UNIVERSITÀ DEGLI STUDI DI MILANO

DOTTORATO DI RICERCA IN SCIENZE DELLA TERRA

Ciclo XXXIII

DIPARTIMENTO DI SCIENZE DELLA TERRA

CONTROLLING FACTORS ON THE DEPOSITIONAL ARCHITECTURE OF CARBONATE SYSTEMS: SEDIMENTOLOGY, FACIES, GEOMETRY, DIAGENESIS AND GEOCHEMISTRY OF EASTERN SARDINIA JURASSIC CARBONATES

GEO/02

PhD Thesis

NEMBRINI MATTIA
ID: R11949

TUTOR

Prof. GIOVANNA DELLA PORTA

Prof. FABRIZIO BERRA

COORDINATORE DEL DOTTORATO

Prof. FERNANDO CAMARA ARTIGAS

Index

Abstract

The evolution through time and space of carbonate platforms and reefs is controlled by the interplay of global (climate, eustasy), regional (tectonic) and local environmental (nutrient levels, light penetration) factors affecting changes in accommodation and in the nature of the carbonate factories. Major tectonic plate reorganizations related to the opening of the Alpine Tethys and climatic fluctuations affected Jurassic carbonate successions, which recorded one of the major peaks in the Phanerozoic for the abundance of coral, sponge and microbialite reefs.

This study focuses on the eastern Sardinia well-exposed Middle-Upper Jurassic carbonate depositional system that evolved in time and space in terms of facies composition and architecture, characters of the carbonate factory and geometry of the depositional profile encompassing four depositional phases. Detailed facies and microfacies analyses, diagenetic and geochemical investigations and new biostratigraphic data and strontium isotope analyses allowed to better constrain the distinctive sedimentological characteristics and age of these depositional phases, building upon the lithostratigraphic framework published in previous studies on eastern Sardinia carbonate succession.

Phase 1 (Callovian-middle Oxfordian) was characterized by the development of a coated-grain dominated carbonate ramp with inner ramp ooidal shoals and peloidal packstone in middle to outer ramp.

Phase 2 (late Oxfordian-late Kimmeridgian) recorded the evolution of a reef-bearing carbonate ramp characterized by three types of build-ups laterally distributed along the depositional profile, reflecting water depth increase and the interplay of water energy and light penetration. Type 1 build-ups (45 m thick, 100 m wide) consisted of coral-stromatoporoid boundstone and coral-stromatoporoid rudstone-grainstone and colonized proximal middle ramp settings. Type 2 build-ups (1-2 m thick, 3-4 m wide) were lens-shaped build-ups made of coral-calcareous sponge-diceratid boundstone, including stromatoporoids and chaetetid sponges associated with bioclastic packstone-grainstone developed in deeper, distal middle ramp settings. Type 3 build-ups (1 m thick and few metres wide) consisted of calcareous and siliceous sponge-coral-microbialite boundstone associated with bioclastic packstone-grainstone colonizing distal middle to outer ramp settings. The evolution from phase 1 to phase 2 was related to the global expansion of coral, stromatoporoid, calcareous and siliceous sponge and microbialite reefs during the middle Oxfordian-late Kimmeridgian due to eustatic sea-level rise and climatic fluctuations.

Phase 3 (late Kimmeridgian) followed a sea-level fall likely driven by regional extensional tectonics recorded by a subaerial exposure surface at the top of phase 2 likely due to fault block uplift. During phase 3 peritidal facies accumulated in the proximal inner platform setting, whereas coated grain dominated facies (ooids and oncoids) were deposited as reworked grains in the more distal middle ramp domains. Differently from previous studies, the age of phase 3 was assigned to late Kimmeridgian according to strontium isotope and biostratigraphic data based on the occurrence of the foraminifer *Alveosepta jaccardi* rather than to the Tithonian. The top of phase 3 is marked by another event of subaerial exposure, also recorded in coeval Tethyan depositional settings as a regional unconformity attributed to extensional tectonics.

The beginning of phase 4 (Tithonian) is characterized by transgressive basinal deposits followed by the recovery of a reefal carbonate factory. Phase 4 recorded a change in depositional geometry from a carbonate ramp to a higher-relief platform with a slope (about 70 m high and 3-15º steep). Basinal deposits consisted of mudstone, wackestone and siltstone and lithoclastic breccia with resedimented clasts from shallower environments through debris-flow mechanisms. Bio-intraclastic grainstone, wackestone with *Clypeina jurassica*, wackestone to floatstone with oncoids and peloidal intraclastic packstone to grainstone were resedimented from inner platform depositional environments. Debris-flow breccias include also lithoclasts of boundstone facies representing Tithonian bioconstructions developed during phase 4, different from the upper Oxfordian-upper Kimmeridgian phase 2 build-up types. Coral-calcareous sponge-microbialite boundstone and *Bacinella* boundstone constituted build-ups in well-illuminated shallow-water settings at the margin of phase 4 platform. Calcareous sponge-*Crescentiella*-coral boundstone and calcareous and siliceous sponge boundstone formed build-ups in the deeper upper slope and were resedimented into the adjacent basinal setting.

The transgression and recovery of the reefal carbonate factory at the beginning of phase 4 were dated to the early Tithonian due to ammonite biostratigraphic data from the basinal deposits. These depositional events were coeval and possibly triggered by tectonic instability during the eustatic sea-level rise that promoted optimal conditions for reef growth during phase 4.

The evolution of eastern Sardinia Callovian-Tithonian carbonate succession was controlled by global changes in the dominant carbonate factory with the onset of reef-building biota (late Oxfordian), regional extensional tectonics affecting the European margin of the Alpine Tethys that controlled relative sea-level changes and accommodation (late Kimmeridgian) and global eustatic rises in sea-level (late Oxfordian and early Tithonian).

Petrographic, cathodoluminescence and carbon and oxygen stable isotope analyses allowed reconstructing the diagenetic evolution of each depositional phase. Phase 1 facies were characterized by replacive burial dolomitization of zoned luminescent dolomite close to the Hercynian basement

and precipitation of blocky calcite cement and microsparite in burial environment and during meteoric telogenesis. Phase 2 facies were characterized by isopachous fibrous cement during early marine diagenesis, burial dolomitization and precipitation of equant blocky calcite and microsparite cement in burial and meteoric telogenetic diagenetic environments. Facies deposited during phase 3 were affected by early marine isopachous fibrous cement (middle ramp facies) or early meteoric vadose cementation by micritic meniscus and pendant cement (inner platform facies). The upper part of phase 3 succession, close to the subaerial exposure surface at the top, is characterized by fabric replacive dolomitization due to evaporitic brines in supratidal settings as inferred from the carbon and oxygen stable isotope signature. Precipitation of equant blocky calcite, fine-grained equant calcite and microsparite took place during burial diagenesis and telogenesis. Phase 4 facies are characterized by early marine (isopachous fibrous cement) and meteoric vadose (micritic meniscus) cementation. Fabric replacive dolomitization took place in the lower part of phase 4 facies close to the subaerial exposure surface due to possibly evaporitic brines. Blocky calcite cement and microsparite precipitated in burial environment and during meteoric telogenesis.

This study, integrating field data, petrographic, biostratigraphic, diagenetic and geochemical stable isotope analyses, highlights how regional tectonics, eustasy and carbonate factory changes affected the evolution of a Jurassic carbonate depositional system and reef growth. These findings have implications for the understanding of the responses of carbonate platforms and reef-building biota to environmental, climate and accommodation changes in the geological record.

Chapter 1

Introduction

1.1 Jurassic carbonate depositional systems and reefs

The Jurassic period was a time characterized by complex geodynamic scenarios and climatic and evolutionary changes in Earth geological history. A major tectonic plate reorganization took place with the gradual break-up of Pangea (Stampfli and Borel, 2002; Golonka, 2004, 2007; Frizon de Lamotte et al., 2015), the opening of the Central Atlantic (Marzoli et al., 2004; Nomade et al., 2007) and the Alpine Tethys (Stampfli and Hochard, 2009; Masini et al., 2013). Climatic fluctuations characterized the whole period (Dera et al., 2011, 2015) and have been subject of scientific debates. Various authors support the hypothesis that the Jurassic was generally a greenhouse period (Hallam, 1985; Sellwood and Valdes, 2008; McKenzie et al., 2016), others suggest that the Late Jurassic was instead an icehouse phase (Frakes et al., 1992; Korte and Hesselbo, 2011; Korte et al., 2015). Various studies disagree about the timing and intensity of such climatic oscillations (Cecca et al., 2005; Martin-Garin et al., 2012, Dera et al., 2011, 2015; Korte et al., 2015).

In this geodynamic and climatic scenario, the Late Jurassic was one of the major peaks in the Phanerozoic for the abundance of coral, stromatoporoid, calcareous and siliceous sponge and microbialite reefs following the Middle Jurassic crises in reef distribution (Leinfelder et al., 2002; Cecca et al., 2005; Kiessling, 2009; Martin-Garin et al., 2012). There is a wealth of studies dealing with possible controlling factors of the Late Jurassic abundance of reef-building organisms pointing out the importance of climatic changes, eustatic sea-level fluctuations, oceanic chemistry and circulation, nutrient regimes and substrate configuration (Leinfelder et al., 2002; Kiessling, 2002, 2009).

The interplay of tectonic activity, climatic and sea-level fluctuations and the contemporaneous diffusion of reef-building biota must have affected the geometry and facies characters of Upper Jurassic carbonate platforms. For instance, the Kimmeridgian evolution of carbonate ramps in the Iberian rift system (Spain) and in western France was influenced by extensional tectonics (Carcel et al., 2010, Aurell et al., 2019a, b). Coral-stromatoporoid reefs formed in tectonically controlled intra-Tethys isolated carbonate platforms (Schlagintweit and Gawlick, 2008; Rusciadelli et al., 2011; Kiani Harchegani and Morsilli, 2019) and Atlantic carbonate platforms and ramps (Leinfelder, 1992; Nose and Leinfelder, 1997). Furthermore, Upper Jurassic carbonate platforms and ramps show differences

in terms of geometry and facies compositon related to their latitudinal distribution and palaeogeographic realm (e.g., northern Tethys, intra-Tethys, southern Tethys and Atlantic Ocean). Notwithstanding, the responses of carbonate depositional systems to global (geodynamic, climate, eustasy, evolutionary trends) and regional (tectonics, oceanography, environmental) controlling factors are still an open question and require further investigations on well-exposed outcrops. This study aims to contribute to the current knowledge on Upper Jurassic reefs, platform facies architectures and the influence of regional tectonics, climatic and sea-level fluctuations on the evolution of carbonate depositional systems.

1.2 Aims of this research

The present PhD thesis focuses on the facies analysis and stratigraphical architecture reconstruction of the Middle-Upper Jurassic carbonate succession of eastern Sardinia (Italy, Fig. 1.1). Facies distribution and depositional geometry of carbonate platforms are governed by the interplay of global, regional and local factors such as the nature of carbonate factories, climate, eustatic sea level changes and regional tectonic. The investigated case study provides a well-exposed example of a carbonate platform evolving through time in terms of facies composition, architecture and depositional geometry.

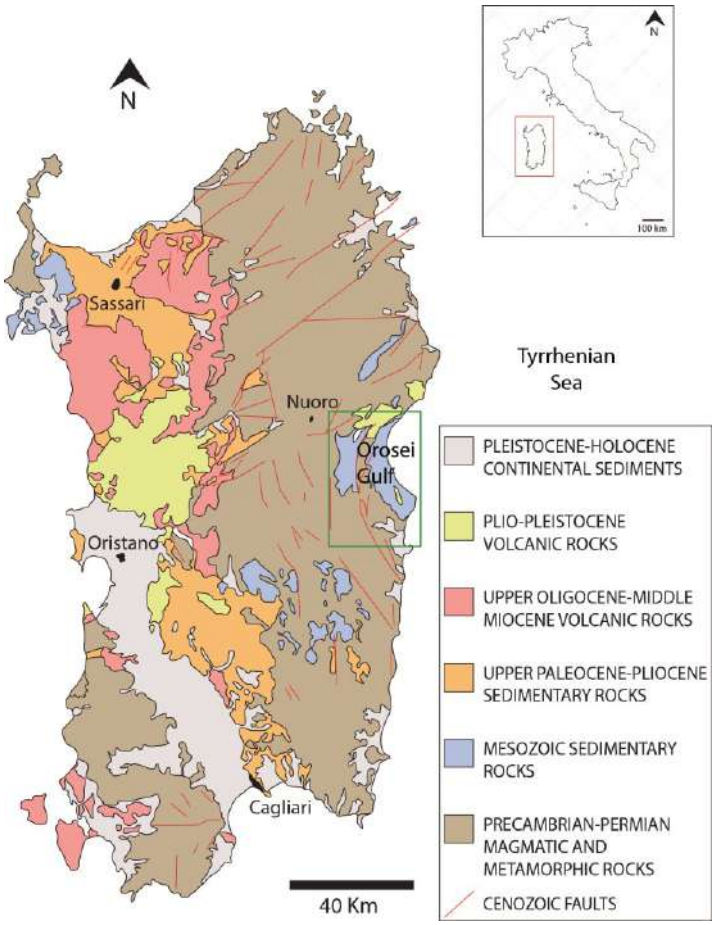

Figure 1.1 Geological map of Sardinia, with the distribution of the Middle Jurassic to Berriasian carbonate succession in eastern Sardinia. The study area is indicated by a green box (modified after Carmignani et al., 2008).

The first aim of this study is to investigate the reef carbonate factory during late Oxfordian-late Kimmeridgian time, dominated by scleractinian corals, stromatoporoids, calcareous and siliceous sponges and microbialites, in order to reconstruct the facies characters and depositional environments of different build-ups along the depositional profile. This study aims to contribute to the knowledge about Upper Jurassic reefs and to provide new insights on scarcely known reefs. Thanks to Sardinia Jurassic palaeogeographic position, between the widely studied northern Tethys (Spain, France, Swiss Jura) and intra-Tethys reefs (Adriatic platform, Apulian platform, Latium-Abruzzi platform), the study of eastern Sardinia reefs contributes to the understanting of the controlling factors on the distribution of reefs during the Late Jurassic.

The second aim of this PhD thesis is to evaluate the effects of global and regional controlling factors on the evolution of the eastern Sardinia depositional system, through a sedimentological and stratigraphical study of the Callovian-Tithonian portion of the succession. The aim is to understand how variations of major reef builders, climate changes, eustatic fluctuations and local tectonic activity influenced facies variability and depositional architecture of the eastern Sardinia carbonate platform

through time and space. This study aims to contribute to the understanding of the responses of carbonate platforms to global and local changes.

To achieve these aims the eastern Sardinia carbonate system was investigated in terms of facies character and architecture through outcrop and petrographic analyses, geochemical and diagenetic investigations.

1.3 Outline of the thesis

This PhD thesis consists of ten chapters. The Introduction (Chapter 1) sets the key open questions concerning Jurassic carbonate systems and reefs and the aims of this PhD research project.

Chapter 2 is a detailed literature review based on published information about the Jurassic period climatic and geodynamic conditions and reef types and carbonate systems, with particular focus on the Late Jurassic. The first part of Chapter 2 presents an overview on Jurassic Tethys geodynamic setting and on global Jurassic climate, eustatic sea-level fluctuations and trends in dominant mineralogies of marine carbonates. The second part of Chapter 2 includes a detailed review of the available information on Jurassic reefs and carbonate platforms presented with respect to their palaeogeographic distribution (northern Tethys, intra-Tethys, southern Tethys, Central Atlantic). This literature review serves to set the background knowledge for the development of Jurassic carbonate systems in Sardinia and demonstrates that Jurassic climate, tectonics, seawater chemistry and eustasy were linked to reef development and that the Middle to Late Jurassic was an important time of global changes reflected in the carbonate rock record.

Chapter 3 focuses on the geological background information about eastern Sardinia Middle Jurassic-Lower Cretaceous carbonate succession summarising published previous studies on the lithostratigraphy, biostratigraphy and magnetostratigraphy of this sedimentary succession.

Chapter 4 reports the approaches and methodologies used in this study: from fieldwork, petrographic analyses to geochemical analyses.

The original contributions of this PhD Tethys are provided in Chapters from 5 to 10.

Chapter 5 deals with the sedimentological study of the Callovian-upper Kimmeridgian portion of the eastern Sardinia carbonate succession in the southern part of the Orosei Gulf and focuses on the characterization of the upper Oxfordian-upper Kimmeridgian reefs comparing them with time-equivalent reefs in the Tethys domains. Chapter 5 reports the results presented in a peer-reviewed scientific paper (Nembrini et al., 2021) and highlights the distinctive features of eastern Sardinia reefs

located in an intermediate palaeogeographic position between the south-eastern intra-Tethys reefs and the north-western European passive margin reefs.

Chapter 6 investigates the role of global sea-level, regional tectonic, environmental and plate motion controls on the Callovian-Tithonian portion of the eastern Sardinia carbonate succession pinpointing the evolution of the carbonate system through four evolutionary phases characterized by specific facies character, architecture and carbonate system geometry. Chapter 6 provides novel age constrain data allowing to revise the stratigraphic framework of eastern Sardinia carbonate succession with respect to previous published studies. Chapter 6 aims at evaluating the role played by regional tectonics vs. eustatic sea-level fluctuations in affecting the development of erosional unconformities and evolutionary phases of the carbonate depositional system. The results presented in this chapter constitute a scientific publication on an international journal in preparation.

Chapter 7 presents the results of facies analysis of Tithonian breccia deposits resedimented from the platform top into the adjacent basinal environment in order to better understand facies composition of the Tithonian carbonate platform. Chapter 7 results help establishing the similarities and differences between upper Oxfordian-upper Kimmeridgian and Tithonian reefs.

Chapter 8 investigates the diagenetic features of the carbonate facies and the stable carbon and oxygen isotope signature of the carbonate succession to complement facies characterization, improve the understanding of the processes of dolomitization and discriminate between possible diagenetic vs. marine, climatic or palaeoceanographic signals recorded in the Upper Jurassic succession.

Chapter 9 is a synthesis of the key findings achieved with this research discussing future perspectives and further investigations.

Final concluding remarks are provided in Chapter 10, synthetizing the main results of this research.

The detailed stratigraphic logs measured on the outcrops within this investigation and the sample list are provided in the Appendix at the end of the thesis.

Chapter 2

Upper Jurassic carbonate systems and reefs: a literature review

2.1 Jurassic time

2.1.1 Geodynamic setting

The Jurassic period was a time of intense continental reshaping driven by the break-up of Pangea (Stampfli and Borel, 2002; Golonka, 2004, 2007; Beutel et al., 2005; Masini et al., 2013; Frizon de Lamotte et al., 2015; Müller et al., 2016), resulting in the formation of numerous rift basins, new oceans and associated passive margins. The most significant tectonic events that resulted in the break-up of Pangea were the rifting and the drifting phases related to the opening of the Central Atlantic Ocean and the opening of the Alpine Tethys (Stampfli and Borel, 2002).

The rifting of the Central Atlantic (Fig. 2.1A) was a long-lasting rifting episode initiated during the Early Triassic that continued and intensified at the beginning of the Norian (Golonka, 2007; Frizon de Lamotte et al., 2015). The rift system developed over a pre-existing weak zone: the Variscan Belt (Frizon de Lamotte et al., 2015). An important magmatic event, known as the Central Atlantic Magmatic Province (CAMP) postdated the rifting onset, sealed the rift system and preceded the drifting in the northern Central Atlantic segment (Marzoli et al., 2004; Frizon de Lamotte et al., 2015; Leleu et al., 2016). Nomade et al. (2007) refined the geochronology of the CAMP magmatism suggesting that it initiated around 201-202 Ma (Rhaetian-Hettangian) with the emplacement of large sills and continued for about 10 Myrs. Sea-floor spreading was probably diachronous along the Central Atlantic rift (Leleu et al., 2016), began during earliest Jurassic in the southern Central Atlantic (Labails et al., 2010) and propagated northeastward toward the Tethys realm (Frizon de Lamotte et al., 2015).

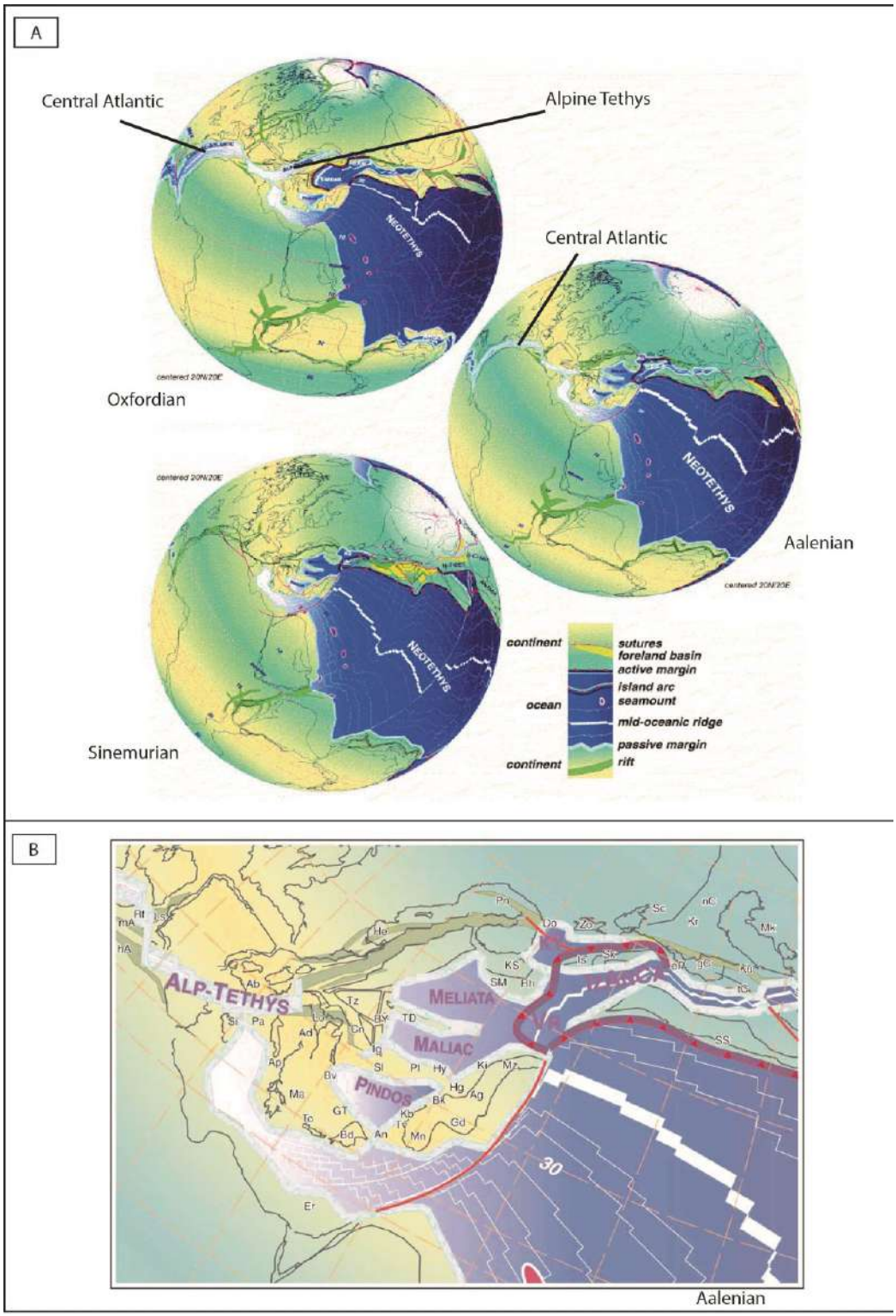

Figure 2.1 A) Ortographic projection of Jurassic earth with Europe fixed in its present-day position, modified after Stampfli and Borel (2002). B) Reconstruction of the western Tethys realm during Aalenian, after Stampfli et al. (2002). Ab - Alboran; Ad - Adria; Ag - Aladag; An - Antalya; Ap - Apulia; Bd - Beydaghlari; Bk - Bolkardag; Bv - Budva; BY - Beyshehir; Cn - Carnic-Julian; Do - Dobrogea; eP - east Pontides; Er - Eratosthen; gC - great Caucasus; Gd - Geydag; GT - Gavrovo-Tripolitza; hA - High-Atlas; He - Helvetic rim basin; Hg - Huglu; Hy - Hydra; Ig - Igal trough; Is - Istanbul; Kb - Karaburun; Ki - Kirshehir; KS - Kotel-Stranja rift; Ku - Kura; Lo - Lombardian; Ls - Lusitanian; mA - Middle Atlas; Ma - Mani; Mk - Mangyshlak rift; Mn - Menderes; Mz - Munzur dag; nC - north Caspian; Pa - Panormides; Pl - Pelagonian; Pn - Pienniny rift; Rf - Rif, external; Rh - Rhodope; Sc - Scythian platform; Si - Sincanian; Sl - Slavonian; Sk – SM - Serbo-Macedonian; SS - Sanandaj-Sirjan; tC - Transcaucasus; TD - Trans-Danubian; To - Talea Ori; Tv - Tavas + Tavas seamount; Tz - Tizia.

The Alpine Tethys opened in Middle Jurassic time, consequence of the break-up of Adria from the Eurasian plate (Fig. 2.1B), following the opening of the Central Atlantic Ocean (Stampfli et al., 2002; Stampfli and Hochard, 2009) and should be regarded as an extension of the Central Atlantic Ocean in the Neo-Tethys realm (Stampfli, 2000). The rifting responsible for the break-up was complex and passed through different stages (Berra et al., 2009; Santantonio and Carminati, 2011; Masini et al., 2013). The extension of the Eurasian lithosphere started in the Late Triassic (Masini et al., 2013) with a period of relative tectonic quiescence (Late Norian-Rhaetian-Hettangian) that allows separating the Norian extensional event from the early Jurassic extensional event (Berra et al., 2009). From the Hettangian time onwards, half-graben basins formed across proximal margins (proximal with respect to the continent) associated with listric faults (Masini et al., 2013). An example of proximal margin is the Lombardy Basin, where the maximum tectonic activity occurred during the Sinemurian (Fantoni and Scotti, 2003) with the deposition of the Moltrasio Limestone (upper Hettangian-Sinemurian), which reaches a present-day thickness of more than 3000 m in western Lombardy (Generoso Basin; Bernoulli, 1964). Another rifting phase was marked by the progressive cessation of rift activity in the proximal margin, together with the migration and localization into the future distal margin from the Late Sinemurian (Masini et al., 2013). In the Western Southern Alps, the major episode of subsidence occurred close to the Pliensbachian-Toarcian boundary and postdated the Jurassic extensional event recorded in the Lombardy Basin (Berra et al., 2009). The second rifting phase terminated with the continental break-up and emplacement of Mid Ocean Ridge Basalt (MORB) in the Bajocian time, at about 165 Ma, also corresponding to the age of the first sedimentary deposits overlying oceanic crust (Baumgartner, 1987; Bill et al., 2001).

The final scattering of Pangea began in the Late Jurassic and climaxed during the Early Cretaceous (Stampfli and Borel, 2002). This rifting episode led to the opening of the South Atlantic Ocean (Jackson et al., 2000; Franke et al., 2007; Moulin et al., 2010; Heine et al., 2013), Indian Ocean (Gaina et al., 2007) and the Bay of Biscay, together with the southern part of the North Atlantic located between the Iberia-Newfoundland conjugate margins (Montadert et al., 1974; Péron-Pinvidic et al., 2007; Tucholke et al., 2007; Tugend et al., 2014).

2.1.2 Jurassic monster plate shift

Recent studies pointed out a global apparent polar wander path showing the existence of a major plate shift during the Late Jurassic based on a compilation of inclination flattering-free palaeomagnetic poles from North America (Kent and Irving, 2010), Italy (Adria, Muttoni et al., 2013; Muttoni and Kent, 2019), Saudi Arabia (Muttoni and Kent, 2016), Argentina (Muttoni and Kent, 2016) and Iran

(Mattei et al., 2014). The shift can be described geometrically as a 30° rotation of the continents about a Euler pole centred on the Equator in the Bight of Benin, off western Africa (Fig. 2.2; Kent et al., 2015; Muttoni and Kent, 2019).

From 160 Ma to 148 Ma (Oxfordian to Tithonian) North America shifted from about 40°N to 70°N (Kent and Irving, 2010), Adria moved from 35°N to 20 N° (Muttoni et al., 2013; Muttoni and Kent, 2019), Saudi Arabia moved from 5°N to 20°S (Muttoni and Kent, 2016), the Neuquén Basin in Argentina shifted from 40°S to 25°S (Muttoni and Kent, 2016) and central Iran shifted from 40°N to 10°N (Mattei et al., 2014).

This motion directly influenced the evolution of sedimentary basins and climate-dependent sedimentary facies modifying the position of the continents through different latitudinal climatic belts. For instance, the Late Jurassic plate shift is considered to be the main controlling factor on the deposition of pelagic deposits on Adria, where radiolarian oozes replaced carbonate oozes as Adria migrated to tropical (or sub-equatorial) palaeolatitudes (Muttoni et al., 2005). The same plate-tectonic stratigraphic approach has been used by Mattei et al. (2014) to interpret the Late Jurassic depositional history of central Iran, where carbonate platform and evaporitic sedimentation took place replacing coal-bearing sedimentation as Iran drifted from the humid temperate belt to arid tropical latitudes. According to Muttoni and Kent (2016), the monster shift influenced also the deposition of the main source rocks of Jurassic petroleum in the Persian Gulf. The Callovian-Oxfordian Tuwaiq Mountain and Hanifa formations were deposited when eastern Saudi Arabia was in the intertropical convergence zone, near to the Equator, whereas the main seal cap rocks, the evaporitic anhydrites of the Tithonian Hith Fm., were deposited as Saudi Arabia rapidly drifted to the arid southern tropics.

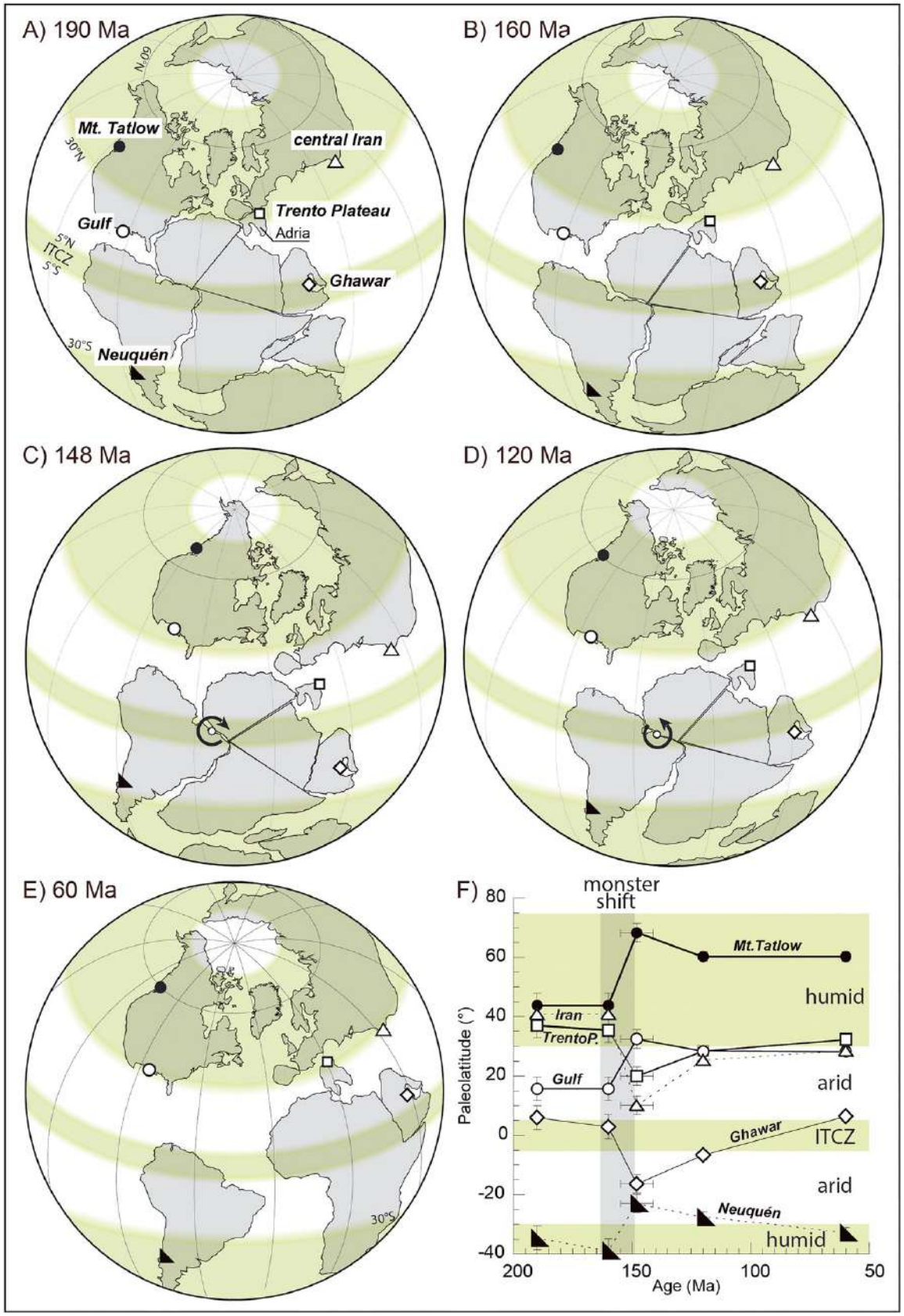

Figure 2.2 Palaeocontinental reconstruction from 190 to 60 Ma (A to E) highlighting the Late Jurassic monster polar shift. The variations of palaeolatitude of some selected sites across the Jurassic monster shift are indicated in F. The green belts in all diagrams represent zonal climate belts where precipitation exceeds evaporation (mid latitude and equatorial humid belts) as opposed to areas with excess evaporation and/or little precipitation (tropical and polar arid belts). From Muttoni and Kent (2019).

2.1.3 Jurassic climate

The worldwide available studies dealing with the sedimentary record of Jurassic climate are difficult to compare because they commonly cover only short stratigraphic intervals or were investigated through different approaches providing diverse results and interpretations. Generally, it is difficult to evaluate whether the proposed climatic reconstructions reflect global or only regional trends.

The Jurassic and Cretaceous palaeoclimate was long considered to be a typical 'greenhouse climate', hot and uniform (Hallam, 1985; Sellwood and Valdes, 2008; McKenzie et al., 2016). There are numerous published studies suggesting a Jurassic global average temperature significaly warmer than today and a more uniform climate in terms of both temperature and atmospheric precipitation, with no ice caps (Hallam, 1985; Sellwood and Valdes, 2008; McKenzie et al., 2016; Vickers et al., 2019; Vickers et al., 2020). For instance, the distribution of temperature-controlled organisms (coral reefs) and tropical carbonate belts extended at least 10° of latitude poleward their present-day distribution, with widespread bauxites and paleosols, evaporites and desert deposits (Sellwood and Valdes, 2008). Oceanic temperatures could have been much warmer than today, not only at the surface but also at great depth, reducing storage capacity both for CO_2 and methane hydrates (Padden et al., 2001). Estimated CO_2 levels are suggested to have been higher than today during the Jurassic (Berner, 1991), causing a pronounced greenhouse effect (Weissert and Mohr, 1996). However, Frakes et al. (1992) pointed out that the hypothesis of the Jurassic and Cretaceous periods as generally warm times is an over-semplification (Fig. 2.3). The idea of a hot and uniform climate during the Jurassic was questioned and, for the majority of the authors, definitively abandoned (Frakes et al., 1992; Dromart et al., 2003; Suan et al., 2010; Dera et al., 2011; Jenkyns et al., 2011; Korte and Hesselbo, 2011; Korte et al., 2015; Ruebsam et al., 2020; Vickers et al., 2020). At first, the finding of ice-drafted deposits at high latitude regions in the Late Jurassic and Early Cretaceous (Bajocian to Albian), suggested that freezing conditions occurred near the poles and that glaciers possibly existed (Frakes and Francis, 1988). According to Frakes et al. (1992) the Late Permian to Middle Jurassic was a warm greenhouse period, whereas the Middle Jurassic to Early Cretaceous was a cool icehouse period. According to Veizer et al. (2000) the whole Jurassic was mostly an icehouse period and the role of pCO_2 as the main driving force of the past global (long-term) climate change is questionable. Instead, according to a wealth of more recent studies between Pliensbachian and Toarcian there was the transition from an icehouse into a greenhouse climate mode (Suan et al., 2010; Korte and Hesselbo, 2011; Krenker et al., 2019; Ruesbam et al., 2019; 2020).

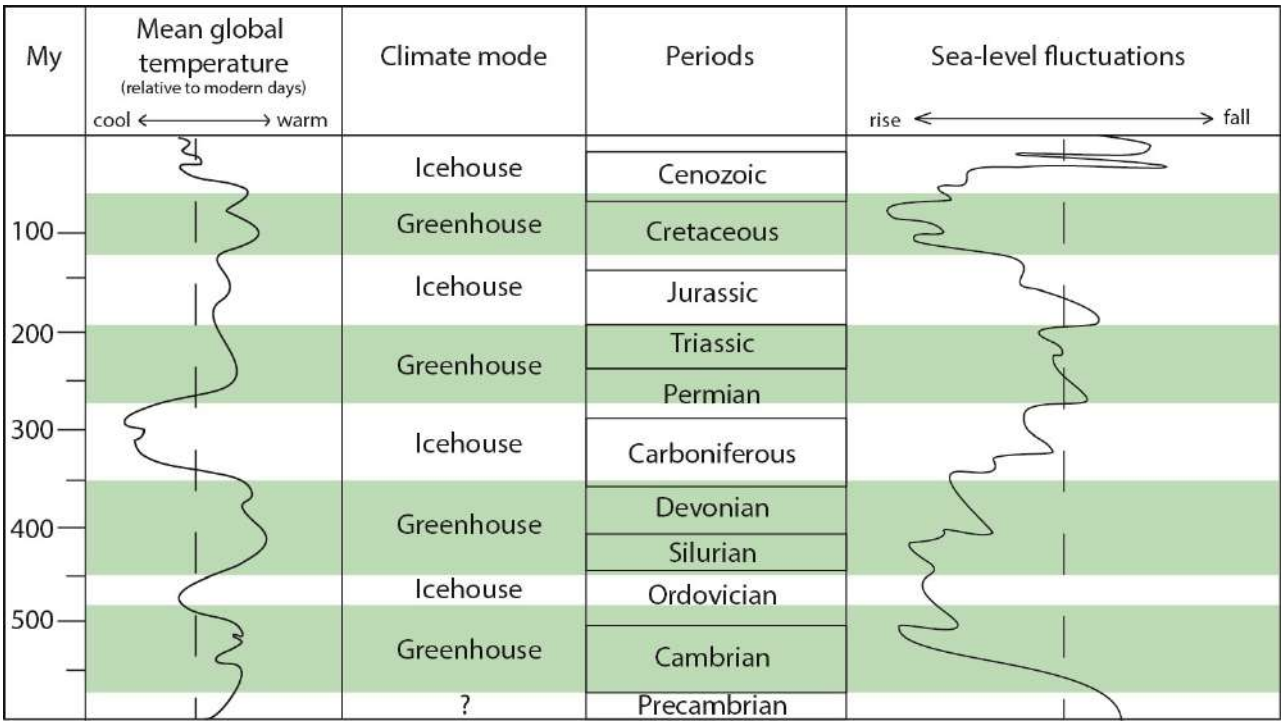

Figure 2.3 Climate mode for the Phanerozoic compared with the mean global temperatures (relative to present-days temperature) and eustatic changes of sea level. Redrafted after Frakes et al. (1992).

Jurassic climatic fluctuations were associated with important global changes. Dera et al. (2011) suggested that there were climate disturbances during the Jurassic that are recorded by major and multiscale $\delta^{18}O$ changes based on data from belemnite and bivalve shells from the European realm. Decrease in the $\delta^{18}O$ during Early Jurassic (Toarcian) and Late Jurassic (Late Oxfordian-Kimmeridgian) were interpreted as consequence of warmer periods preceded and followed by cooler ones. The warm periods correspond to protracted and intensive magmatism in the Karoo-Ferrar and Asian Igneous provinces (Dera et al., 2011).

The time interval between Callovian and Oxfordian was an important turning point in the Jurassic climate. Dromart et al. (2003) suggested a global severe cooling at the Middle-Late Jurassic transition with continental ice formation for about 2.6 My. A short-term cooling followed by a significant increase in temperature of sea-bottom water was also demonstrated in the Central European Basin using palaeotemperature proxies with $\delta^{18}O$ isotopic values from belemnites and brachiopods (Wierzbowski, 2015). This cooling event corresponded to the late Callovian-Oxfordian crisis in carbonate production, the absence of lower Oxfordian reefal formations (Cecca et al., 2005; Martin-Garin et al., 2010, 2012) and global scale sea-level fall that reached the minimum in the latest Callovian (Hallam, 2001; Miller et al., 2005; Haq, 2018). From middle Oxfordian onward, a warming trend, leading to greenhouse type conditions, is suggested on the basis of biogeographical and geochemical data (Cecca et al., 2005). Brigaud et al. (2008) reconstructed the sea-surface temperatures during Oxfordian and Kimmeridgian measuring $\delta^{18}O$ values from oyster shells and

pointed out a warming trend from early to middle Oxfordian, a cooling trend between middle and late Oxfordian and another warming trend in the early Kimmeridgian contrasting with Cecca et al. (2005) suggestion of warming from Middle Jurassic. The $\delta^{18}O$ values provided from belemnites (Russia and New Zeland) by Gröcke et al. (2003) indicate a warming through the Oxfordian-Kimmeridgian, cooler palaeotemperatures within the Early Tithonian and a gradual rise to warmer palaeotemperatures across the Jurassic-Cretaceous boundary.

Also the published $\delta^{13}C$ organic and inorganic trends suggest perturbations of the global carbon cycle possibly related to important climate changes during the Jurassic period. Padden et al. (2001) identified a negative isotopic excursion in both inorganic and organic carbon record from middle Oxfordian deposits attributed to gas hydrate release (Fig. 2.4). Methane hydrate destabilization may have been caused by oceanographic circulation changes following the first significant Tethys-Atlantic connection with the Pacific Ocean. The release in the atmosphere of gas hydrates enhanced the greenhouse effect and led to the warming phase (Padden et al., 2001).

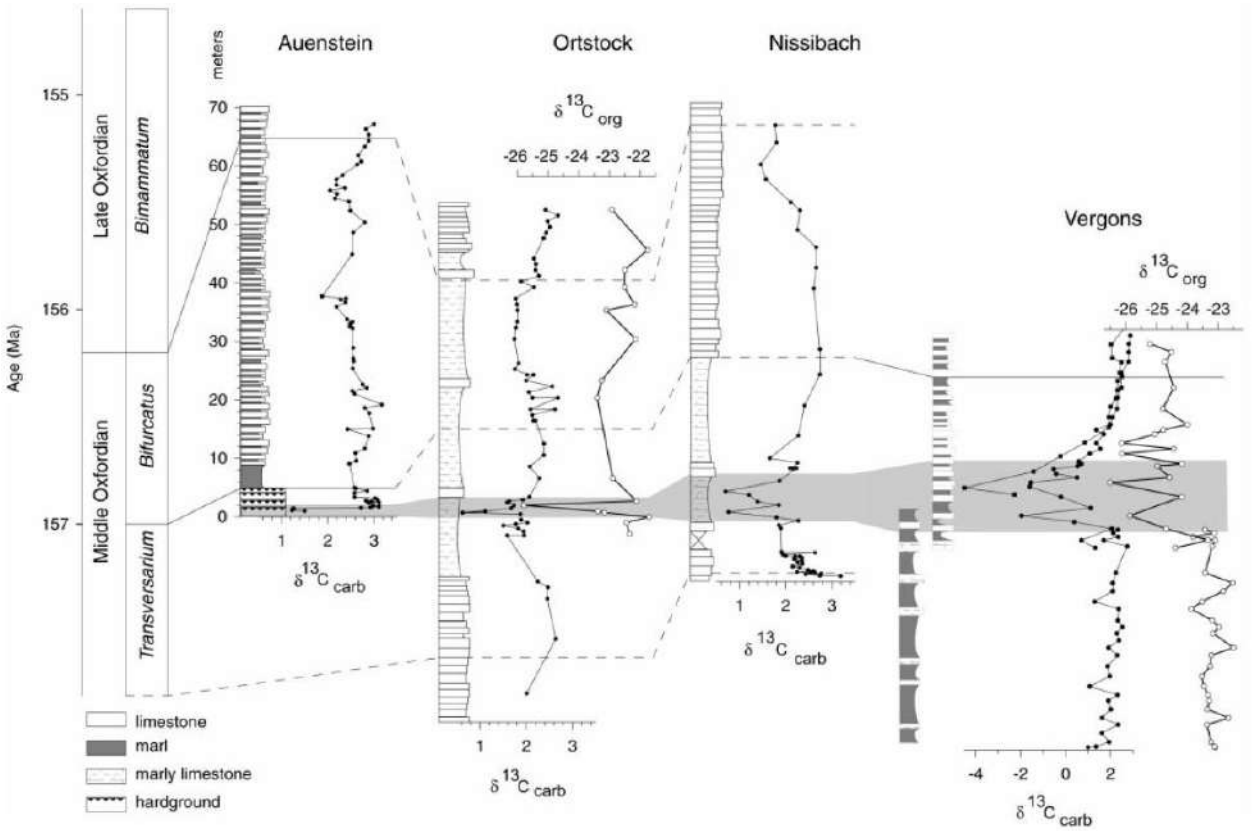

Figure 2.4 Carbon organic and inorganic isotope data from Oxfordian succession of Switzerland and southeastern France studied by Padden et al. (2001).

According to Weissert and Mohr (1996), a large positive $\delta^{13}C$ inorganic and organic excursion in the late Oxfordian may carry a signature of increased organic carbon burial and diminished regional

growth potential of the carbonate platforms (Fig. 2.5). In addition, two positive shifts in the organic carbon isotope record during the Kimmeridgian and Tithonian reflect episodes of globally increased organic carbon burial.

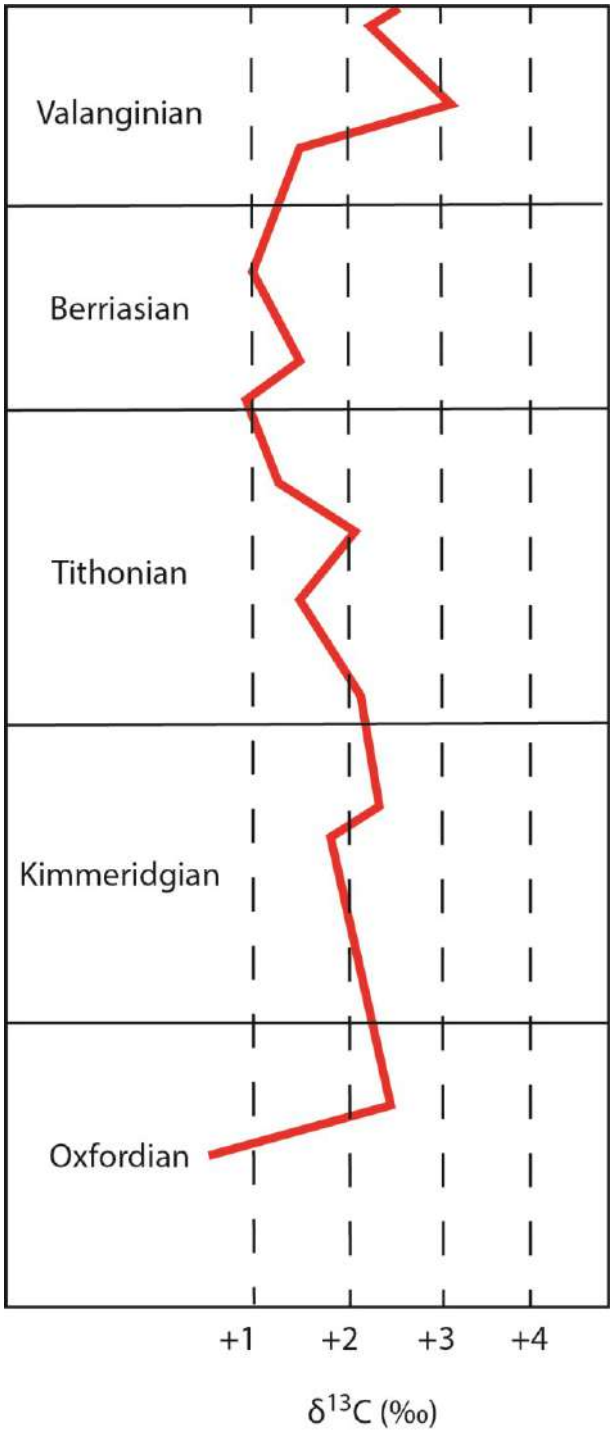

Figure 2.5 Composite carbon organic isotope curve for the Late Jurassic-Early Cretaceous time interval with data from the Southern Alps and northern Swiss Alps, redrafted after Weissert and Mohr (1996).

The latitudinal climate belts were not uniform, especially in the middle Oxfordian, relatively arid conditions between 25°-35° N resulted in low run-off and depleted nutrient supply, whereas humid conditions led to increased run-off and high nutrient flux in the Alpine Tethys (Cecca et al., 2005).
The general rainfall patterns are considered to have been different from today. Plant diversity, evaporite/coal occurrence and dinosaur distribution suggest low-latitude arid climate and high-latitude humid climate during the Late Jurassic (Rees et al., 2004). The lower latitudes were affected by a monsoon-type climate, characterized by very dry conditions in the continental interiors, with hot summers and strong seasonal contrast and precipitations confined to the Tethyan realm (Hallam, 1993; Weissert and Mohr, 1996).

2.1.4 Trends in carbonate mineralogy

It is well established that seawater chemistry has not been stable during all Earth history. There are evidences of oscillating global trends, on a 100-200 My time scale, in the mineralogy of marine carbonate cements, late stage-salts in marine evaporites and calcifying organisms that are interpreted to record change in seawater chemistry (Fig. 2.6; Sandberg, 1983; Stanley and Hardie, 1998, 1999; Montañez, 2002). Sandberg (1983) divided the Phanerozoic Eon into intervals based on the primary mineralogy of ooids and early marine cement whether it was either aragonite and high-Mg calciteor low-Mg calcite (aragonite seas and calcite seas). Stanley and Hardie (1998, 1999) evidenced that the primary mineralogy of important reef-building and carbonate sediment-producing organisms correlated with these Phanerozoic oscillations for non-skeletal carbonates. According to Sandberg (1983), these secular shifts are influenced by the atmospheric CO_2 concentrations, whereas according to Stanley and Hardie (1998), the Mg/Ca ratio of seawaterplays a fundamental role controlling the mineralogy of marine carbonates. A high Mg/Ca ratio (>2) favoured the precipitation of high-Mg calcite and aragonite, whereas Mg/Ca ratio < 2 favoured the precipitation of low-Mg calcite (Stanley and Hardie, 1998, 1999). The Mg/Ca ratio of seawater could be inversely correlated to the Sr/Ca ratio and thus related to oceanic crust alteration, seafloor spreading and carbonate precipitation (Stanley and Hardie 1999; Montañez, 2002; Steuber and Veizer, 2002).
During the Jurassic there was the transition from an aragonite sea to a calcite sea (Stanley and Hardie, 1999). The exact timing of the switch in seawater chemistry is still a matter of debat and was placed at the Triassic/Jurassic boundary by Sandberg (1983) and in between the Early and Middle Jurassic by Stanley and Hardie (1998, 1999) coupled with an abrupt decrease in the Mg/Ca ratio of seawater (Fig 2.6).

Although the Late Jurassic was characterized by a calcite sea, the scleractinian aragonitic coral reefs were widespread in shallow-water bioconstructions until Cretaceous time, when they were replaced by rudists (Stanley and Hardie, 1999). According to Stanley and Hardie (1999) the predominance of aragonitic corals in the Late Jurassic calcite sea resulted from three circumstances. 1) During this time interval the Mg/Ca ratio remained near the calcite-aragonite boundary. 2) The high absolute concentration of Ca^{2+} during this time may have promoted non-equilibrium precipitation of all forms of calcium carbonate. 3) There were no calcitic reef builders that could clearly outcompete corals even though there were calcitic stromatoporoids. Until the Cretaceous time when rudists thrived in shallow-water environments and were the dominant reef-builders, the Mg/Ca ratio remained near the minimum level for aragonite seas (Stanley and Hardie, 1998).

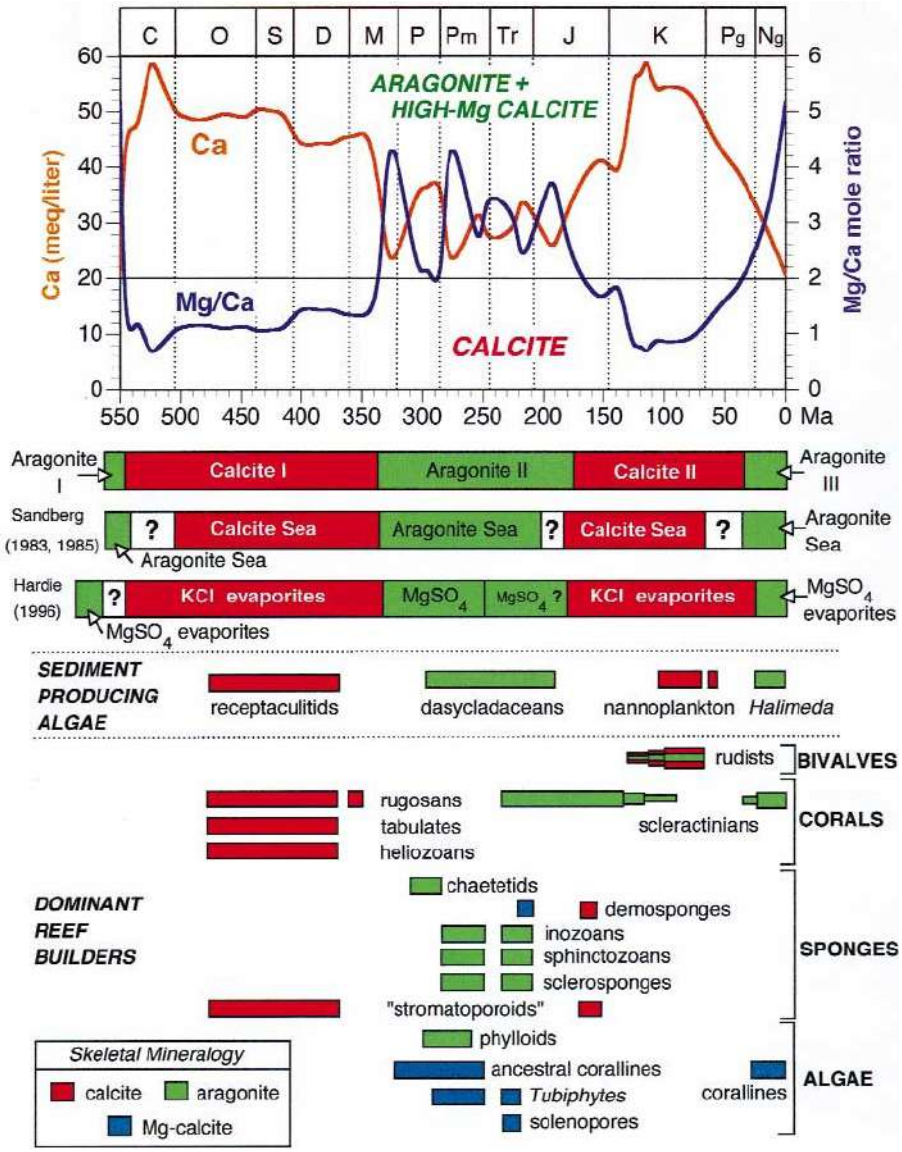

Figure 2.6 Temporal relationship between secular fluctuations in non-skeletal carbonate (aragonite and calcite seas), climate cycles, late-stage marine potash evaporites, skeletal mineralogy of major sediment producers and reef builders and secular variation of Mg/Ca molar ratios throughout the Phanerozoic (after Sandberg, 1983; Stanley and Hardie, 1998).

2.1.5 Eustatic sea-level changes

Eustatic fluctuations are the result of the interplay between global tectonics and climate changes (Miller et al., 2005). Several authors pointed out a general pattern of global sea-level rise, with oscillations (Fig. 2.7), throughout most of the Jurassic until the Kimmeridgian (Hallam, 1981; Haq et al., 1987; Sahagian et al., 1996; Hallam, 2001; Miller et al., 2005; Haq, 2018). Major episodes of eustatic sea-level rise took place in early Hettangian, early Sinemurian, early Pliensbachian, early Toarcian, early and late Bajocian, middle Callovian and late Oxfordian (Hallam, 2001; Haq, 2018).
According to Hallam (2001) there was a strong tectono-eustatic control of Jurassic global sea-level fluctuations, related to the opening of the Central Atlantic and the Indian Ocean. The regression at the Triassic-Jurassic boundary is related to the rifting of the initial break-up of Pangea (Hallam, 2001), whereas the early Toarcian sea-level rise is related to the beginning of the Central Atlantic seafloor spreading (Steiner et al., 1998). The Aalenian regression is a regional event for north-western Europe possibly related to thermal doming in the North Sea with basaltic volcanic activity (Hesselbo and Jenkyns, 1998). The middle Callovian transgression could be related to a pulse of increased oceanic spreading when some plate reorganization took place (Hallam, 2001). The latest pulse of sea-level rise in the late Jurassic was probably driven by the interplay between climate changes and global tectonics. Starting from the middle Oxfordian there was a eustatic sea-level rise, possibly driven by a global warming and ice pole melting (Dromart et al., 2003) and by the initial break-up of Gondwana leading the formation of Indian Ocean (Hallam, 2001). Weissert and Mohr (1996) and Miller et al. (2005) suggested a sea-level maximum in late Oxfordian and early Kimmeridgian, followed by a lowstand in late Kimmeridgian. On the northern Tethys shelf, this is well reflected by the increase of reef sites during middle Oxfordian-early Kimmeridgian times (Fig. 2.8). The Jurassic peak of reef distribution partially mirrors the trend of the eustatic sea-level curve, demonstrating that reef growth had an increase during the transgressive episode of the Oxfordian-Kimmeridgian (Leinfelder et al., 2002).
From this overview it emerges that the Jurassic climate, tectonic, seawater chemistry, atmosphere composition and eustasy are correlated and important changes occurred during different Jurassic ages.

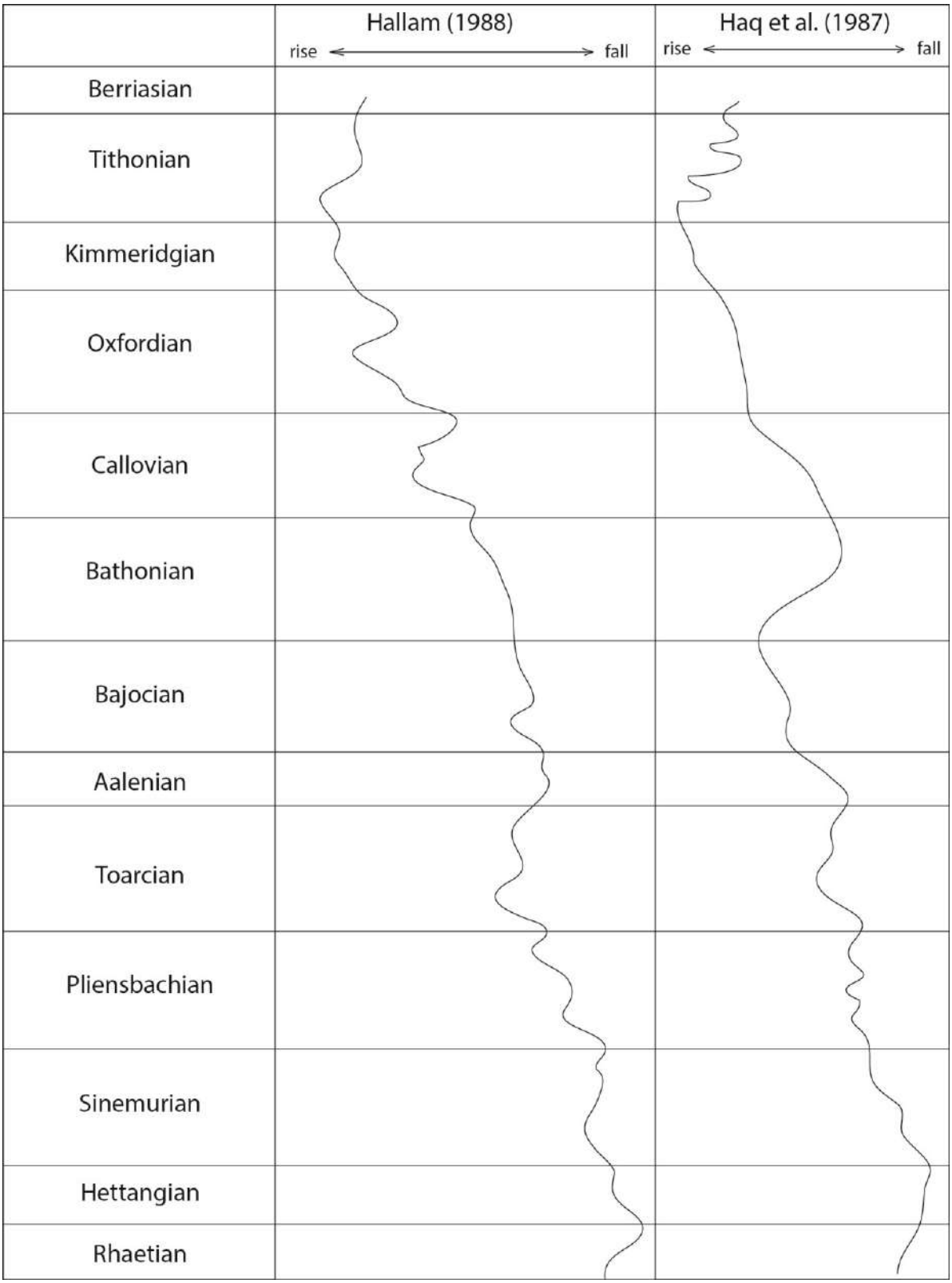

Figure 2.7 Comparison beteween published eustatic sea-level curves for the Jurassic by Hallam (1988) and Haq et al. (1987).

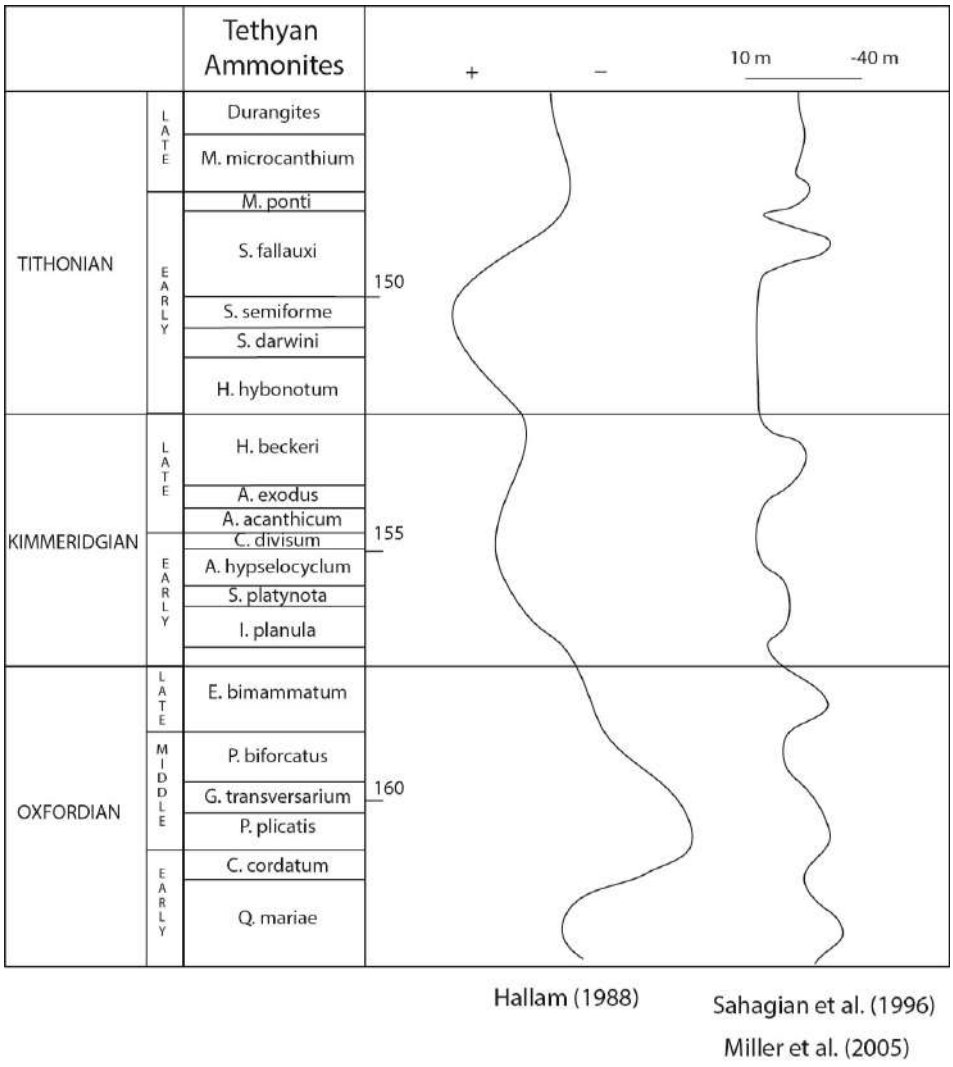

Figure 2.8 Comparison between the published eustatic sea-level curves for the Late Jurassic: a) Hallam (1988); b) Sahagian et al. (1996) and Miller et al. (2005).

2.2 Jurassic reef components

2.2.1 Major biotic changes

The Jurassic was a time of important biotic changes, especially in marine environment, strongly influenced by mass extinction events. Reef organism distribution and proliferation was influenced by these long-term biotic changes. The end Triassic mass extinction is one of the five largest extinctions in Earth history. It was probably the result of the interplay between the onset of the Central Atlantic Magmatic Province (Schaltegger et al., 2008; Schoene et al., 2010) and concomitant drop and rise in sea-level related to global cooling and glaciation (Schoene et al., 2010) that caused the loss of marine shelf habitats during the severe regression (Hallam and Wignall, 1999). There was a dramatic disappearance of numerous groups, particularly of marine organisms, such as corals, demosponges,

brachiopods and ammonoids (Hallam, 2002). The general scarcity of Early Jurassic coral reefs was caused mainly by evolutionary restrictions as well as by the lack of available habitats. Scleractinian corals almost became extinct and Early Jurassic reefs were dominated by survivors of the Triassic faunas (Stanley, 2006). Coral, sponge and microbial reefs were rare in the Hettangian and not recorded in Sinemurian platforms (Fig. 2.9A; Leinfelder et al., 2002), apart from isolated Moroccan domain (Della Porta et al., 2013, 2015). The Pliensbachian represents the climax of reef development in the Early Jurassic for the number of reefs, but they were concentrated in a relatively small area (Western Tethys), between 24°N to 32 N° and 4° W to 19° E (Leinfelder et al., 2002). The Toarcian reef record was affected by strong decline in reef development at the end of the Pliensbachian. Indeed, a second order mass extinction during the Early Toarcian has been reported in the published literature (Hallam, 1996; Gómez et al., 2008; Gómez and Goy, 2011). Many authors suggest that the Toarcian extinction is related to a period of oceanic anoxia (Pálfy and Smith, 2000; Wignall et al., 2005). The Toarcian Oceanic Anoxic Event (T-OAE) corresponds to an important perturbation of the carbon cycle (Mattioli et al., 2009) and the extinction interval coincided with a Tethyan biocalcification crisis in surface waters (Wignall et al., 2005). An increase of pCO_2 in the atmosphere during Early Toarcian either directly affected the biocalcification of nannoplankton or induced climate change that negatively affected nannoplankton biocalcification (Mattioli et al., 2009). This increase in pCO_2 has been related to degassing of CO_2 during the formations of volcanic traps (Wignall et al., 2005) or to a release of methane clathrates from continental margins and their subsequent oxidation in CO_2 (Hesselbo et al., 2000). Consequently, there was a decrease in the abundance of nannoplankton (Mattioli and Pittet, 2002; Mattioli et al., 2009). An important crisis affected also foraminifers at the Pliensbachian and Toarcian boundary (Ruban and Tyszka, 2005). Indeed, in the Toarcian there was the first occurrence of planktonic or quasi-planktonic foraminifers that evolved from benthic taxa (Hart et al., 2003). The environmental perturbations caused by the sea-level rise and associated T-OAE were potential triggers for the change in lifestyle of foraminifera (Hart et al., 2002, 2003). Other studies link the mass extinction with a global climate change that led to a rapid warming (Gómez et al., 2008; Gómez and Goy, 2011).

Despite the availability of shallow-water environments and extensive shelves in the subtropical and tropical belts, Middle Jurassic reefs had a scattered distribution. Aalenian reefs were very rare as a consequence of the Toarcian biotic crisis, whereas Bajocian-Bathonian-Callovian reefs showed a much wider distribution (Leinfelder et al., 2002). However, most reefs exhibited low to moderate diversities, typical of stressed environments. Scleractinian corals rapidly extended mainly on the Northern Tethyan shelf without conquering the high latitude zones (Leinfelder et al., 2002).

During the Oxfordian and Kimmeridgian times, new groups of corals evolved (up to 130 genera) giving birth to highly diversified coral reefs. Encrusting organisms diversified during the Late Jurassic, such as *Crescentiella morronensis, Koskinobulina socialis*, or the newly formed association *Lithocodium-Bacinella* (Dupraz and Strasser, 1999; Schlaginweit and Gawlick, 2010). Several reef-building organisms such as stromatoporoids, chaetetid and calcareous sponges diversified in the Late Jurassic (Wood, 1987; Leinfelder et al., 2005).

The end of the Triassic and the Jurassic were also important turning point for the evolution of scleractinian corals and their adaptation to different environments (Fig. 2.9A; Stanley, 2006). Modern scleractinian corals thrive in nutrient poor settings owing to the development of photosymbiontic relationship with the dynoflagellate algae zooxanthellae (Stanley, 2006). Zooxanthellae live in the endodermal tissues of the corals as symbionts and are thought responsible for enhancing coral rapid calcification and higher metabolic and growth rates (Stanley, 2003, 2006). Several works pointed out that probably many Late Triassic scleractinian corals were zooxhantellate reef builders (Stanley and Swart, 1995; Stanley, 2003, 2006). This observation is based on indirect palaeoecologic evidences of light adaptation such as colony size and shapes, corallite size and skeletal characteristics (Stanley, 2006). In the latest Triassic time, corals seem to have increased both their range of habitats and diversity (Stanley and Swart, 1995). The coevolution of corals and zooxhantellae was considered an important prerequisite for the appereance of constructional framework and reef building (Stanley and Swart, 1995). The hypothesis that the coevolution of coral-zooxanthellae symbiosis occurred at this time is supported by skeletal stable isotopes (Stanley and Swart, 1995) and organic matrix analyses (Muscatine et al., 2005). After the end-Triassic extinction, the earliest Jurassic corals were probably predominantly non-zooxanthellate (Stanley and Swart, 1995). Indeed, throughout the Phanerozoic geological record, reef collapse and recoveries were postulated to correlate with symbiont loss and symbiosis renewal, respectively (Stanley and Swart, 1995; Stanley, 2006). However, symbiosis in Triassic and Jurassic corals may not have been as efficient as in present-day counterparts (Leinfelder et al., 2002; Stanley, 2006). As a consequence, Late Jurassic coral reefs developed also in settings influenced by terrigenous influx or in inferred upwelling zones (Leinfelder et al., 2002). According to Leinfelder et al. (2005) stromatoporoids might have been much more adapted to oligotrophic settings than corals.

From the middle Tithonian onwards, falling global sea level dramatically accelerated withdrawal of reefs in most areas (Leinfelder et al., 2002). Reduction of reefal settings in the late Tithonian and Berriasian coincided with shallowing and subaerial exposure owing to a general sea-level fall (Leinfelder et al., 2002).

2.2.2 Microbialites

Besides corals and calcareous sponges, microbialites are of paramount importance in reef building during the Jurassic time. Microbialites are "organosedimentary deposits that have accreted as a result of a benthic microbial community trapping and binding detrital sediment and/or forming the locus of mineral precipitation" (Burne and Moore, 1987). Microbes are extensively involved in production, accumulation and diagenesis of sediment (Burne and Moore, 1987; Riding, 2000, 2011) and include all the microscopic prokaryotic organisms, such as archaea and bacteria, unicellular eukaryotic algae and protozoans and fungi. Prokaryotic microbes are the key organisms in the formation of microbial carbonates and exhibit immense diversity. Two distinct groups belong to the prokaryotic organisms, termed Archaea and Bacteria (Brock et al., 1994). Cyanobacteria, previously termed in some works as blue-green algae (Stanier, 1977; Carr and Whitton, 1982), blue-green bacteria or cyanophytes, are eubacteria, aerobic phototrophs, using sunlight as energy (Riding, 2000). In shallow-water oxygenated environments cyanobacteria can thrive in the water column and at the sediment-water interface. Many other bacteria are anaerobic heterotrophs and can occupy dark anaerobic conditions such as sediment pore surface (Riding, 2000). Small algae, including brown, green and red filamentous forms, are usually associated with microbial mats in modern microbial carbonates, where they trap and stabilize sediment (Riding, 2000). Microbes occupy a very broad range of environments, including waters of widely differing chemistry and composition. Most microbialites are carbonate in composition, but siliceous, phosphatic, iron, manganese and sulphate examples also occur (Riding, 2011). Moreover, microbes can create intertwined syntrophic communities in which the main individual components require stability, protection, energy and nutrients.

In the formation of microbial carbonates an important contribution is provided by the extracellular polymeric substances (EPS) widely produced by microbes (Decho, 1990). EPS accumulate outside cells to form a protective and adhesive matrix that attaches microbes to substrates, providing physical and chemical protection. A copious amount of EPS can be secreted by heterotrophic bacteria, cyanobacteria and diatoms in order to obtain stability and facilitate metabolic interaction in microbial biofilms that are submillimetre-thick veneers of bacterial population and communities. Instead, microbial mats are complex structures that form the accreting surface of larger scale benthic microbial carbonates such as stromatolites (Riding, 2000). Mats are typically stratified with aerobic phototrophs near the surface, anoxygenic phototrophs below, followed by chemo-organotrophs that require neither light nor oxygen (Riding, 2000).

2.2.2.1 Microbial processes

Microbes are responsible for two main processes that that lead to the deposition of microbial carbonates: grain trapping and mineral precipitation (Burne and Moore, 1987; Riding, 2000, 2011). Both processes are facilitated where microbial mats have irregular surface topography. The process of trapping can involve simple physical blockage (baffling) of grain in movement and also adhesion on, and in, EPS. In contrasts, smooth mats or films with little surface topography trap only very few grains or none at all (Riding, 2000). Trapping can involve fine to coarse sediment, siliciclastic as well as carbonate grains (Riding, 2000). This process is associated with binding processes that correspond to the organic overgrowth of trapped grains by cells, filaments and biofilms, which incorporate them into the mat (Burne and Moore, 1987).

In addition, precipitation is important for the cementation of trapped materials. The conservation of accreted trapped sediment requires early lithification to strengthen the deposit to keep-up with the surrounding sediment accumulation (Riding, 2000). Early lithification is essential for accretion and preservation of benthic microbial carbonates and is both biologically mediated and environmentally dependent (Riding, 2011). Cyanobacteria calcification appears to result from creation of alkalinity gradients in mucilaginous sheaths, associated with photosynthetic uptake of CO_2 and/or HCO_3^-. According to Riding (2000), cyanobacterial calcification appears to be a freshwater phenomenon and scarcely known in modern subtidal environment. Another important feature in microbial calcification is the EPS calcification. Microbially produced EPS can mediate $CaCO_3$ precipitation by providing sites that create alkalinity gradient in response to metabolic processes and by attracting and binding calcium ions to negatively charged sites (Pentecost, 1985). Furthermore, there are a wide range of bacterial processes, in addition to photosynthesis in cyanobacteria, that can lead to HCO_3^- concentration and raised alkalinity favoring $CaCO_3$ such as ammonification, denitrification, sulphate reduction and anaerobic sulphide oxidation (Krumbein, 1979; Visscher et al., 1992; Castanier et al., 2000). These processes are localized where heterotrophic bacteria degrade organic matter, including cyanobacteria microbial mats (Bartley, 1996) and siliceous sponge bodies (Reitner, 1993; Della Porta et al., 2003, 2004, 2013), leading fine grained precipitation, resulting in the creation of a micrite matrix and micrite clots and peloids around the calcified sheath material (Riding, 2000).

2.2.2.2 Microbialite macro and microfabric

Macrofabric, usually readily distinguished in the field, are used to define the main categories of microbial carbonates: stromatolite, thrombolite, dendrolite and leiolite (Fig. 2.9B). All these terms are both structural and genetic terms, because they are defined as microbial (Riding, 2000).

Stromatolites have a macroscopically laminated fabric. The term thrombolite refers to macroscopically clotted fabrics (not to be confused with the clotted peloidal micrite microfabric). Thrombolite clots are discrete rounded to irregular patches that differ in colour and/or texture from intervening areas that create a blotchy, generally unlayered, mesoscale fabric. Dendrolite corresponds to macroscopic centimetre-size bush-like dentritic fabric. Instead, leiolite has a relatively structureless, aphanitic macrofabric, lacking clear lamination, clots or dentritic fabrics (Riding, 2000). Many microbial carbonates are dominated by micritic fabrics whose apparent uniformity masks a range of possible origins. Dense micrite could have microbial origin such as calcified dead bacteria giving rise to discrete rounded bodies, whitings or calcified biofilms. Moreover, micrite could show the typical clotted peloidal fabric formed by an irregular sponge-like network of micrite (Riding, 2000), probably representing EPS calcification. Sometimes calcification of microbial external polysaccharide protective sheaths produces calcified fossils that are readily recognizable such as *Cayeuxia*, *Girvanella* and *Ortonella*. Peloids, silt-size spherules of Mg-calcite micrite, have been regarded as cement fabrics (Macintyre, 1984, 1985) but also as calcified bacterial aggregates rimmed by euhedral calcite crystals (Chafetz, 1986). Microbial precipitated peloids are widespread and often very common in ancient reefs (Flügel and Steiger, 1981; Sun and Wright, 1989). Also microsparite and sparite frequently occur in microbial carbonates. Fibrous, equant and dendritic sparites are common as external crusts on organic tissue and grain and mineral surfaces (Riding, 2000).

2.2.2.3 Geological record of microbial carbonates

Stromatolites are reported from the Late Archean (Hofmann, 2000). The period between 2800 Ma and the end of the Mesoproterozoic (1000 Ma) was the golden age of stromatolites (Riding, 2000). There are evidences of Proterozoic stromatolite decline from 1000 Ma, which coincided with metazoan evolutionary diversification (Awramik, 1971). Thrombolites appeared near the base of the Cambrian, reflecting the development of abundant calcified microbes. During the Cambrian and Early Ordovician, thrombolites and dendrolites participated extensively in reef formation, either in association with metazoans, such as archaeocyaths or alone (Copper, 1974). The Early Paleozoic marked both a recovery for microbial carbonates and changes in their characteristic features (Riding, 2000). The mid-Ordovician appearance of bryozoans, tabulate corals, stromatoporoids and other skeletal metazoans was a major change for reef building (Riding, 2000, 2011). However, stromatolites remained both important and conspicuous in reefs. Both reefal microbial carbonates (Kiessling, 2002) and calcified cyanobacteria (Arp et al., 2001) declined in abundance during the Phanerozoic, but this trend shows marked fluctuations (Riding, 2011). According to Riding (2000), supersaturation of

water with respect to carbonate minerals directly affects microbial carbonate sedimentation rates. Consequently, microbialite history reflects not only microbial mat evolution, but also long-term changes in seawater and atmospheric chemistry that have influenced microbial metabolism and seawater carbonate saturation state (Riding, 1991a, 1993, 2011). The calcification events represent periods of elevated carbonate saturation corresponding to high global temperature, low sea level, and low skeletal abundance. They are common in the Late Cambrian-Early Ordovician and Late Devonian-Late Carboniferous to Permian and scarce during the Cenozoic (Riding, 2011). Comparison with seawater saturation state for $CaCO_3$ minerals calculated from modelled seawater and CO_2 values shows positive correspondence with peaks of microbial/cyanobacterial carbonate abundance during much of the Paleozoic and the Mesozoic. The only lack of correspondence in Cretaceous (between 120 and 80 Ma ago) could reflect removal of carbonate deposition by pelagic calcareous plankton that significantly reduced actual saturation state (Riding, 2011).

2.2.2.4 Jurassic microbialites

The importance of benthic microbial communities in reef development has increased in the course of the Jurassic (Leinfelder et al., 2002). Upper Jurassic reefs contain variable amounts of microbial carbonate crusts, such as in Portugal (Leinfelder, 1993a), Spain (Aurell et al., 2010, 2011; San Miguel et al., 2013, 2017), Germany (Helm and Schülke, 2006) and Jura Mountains (Dupraz and Strasser, 1999, 2002; Samankassou et al., 2003; Colombié and Strasser, 2005; Olivier et al., 2011). Microbial mats, which calcified as microbial crusts, were important stabilizers in Upper Jurassic reefs and were of paramount importance for early cementation and establishment and development of positive build-ups (Leinfelder, 1993a; Leinfelder et al., 2002). In Upper Jurassic reefs, microbialites tended to grow together with metazoan reefs, first accompanying coral growth and then filling the remaining porosity inside the reef, below the living surface (Dupraz and Strasser, 1999). Phototrophic cyanobacteria probably participated in the formation of the first encrustation zone, whereas heterotrophic bacteria in biofilms are thought to have contributed to the microbialites inside the reef body in low-light and low-oxygen conditions (Dupraz and Strasser, 2002). When coral growth could not take place with microbialite development, the microbial front reached the surface and finally covered the reef. The resulting thick interval of microbialite could be interpreted as being related to an ecological crisis in coral-reef evolution (Dupraz and Strasser, 1999). For instance, in the Kimmeridgian Iberian carbonate ramps diverse types of microbial bioconstructions (coral-microbial and microbial-dominated bioconstructions) occurred in different environmental conditions. The microbial-dominated ramps are related to initial platform flooding predating the recovery of benthic carbonate producers and to

local terrigenous/freshwater input involving physico-chemical changes in seawater composition (San Miguel et al., 2017).

2.2.3 Microencrusters

Another important group of organisms, with a fundamental role in Jurassic microbial-cemented reef formation and stabilization, are the so-called microencrusters or *microproblematica*. Microencrusters organisms are microfossils, often of *incertae sedis*, that usually encrust metazoan surface and were object of numerous studies regarding their taxonomy and biostratigraphy (Dupraz and Strasser, 1999; Schlagintweit and Gawlick, 2008; Schlagintweit et al., 2010). Among these fossils, the most studied are *Bacinella irregularis* (Radoičić, 1959; Schlagintweit et al., 2010), *Lithocodium aggregatum* (Elliot, 1956; Schlagintweit et al., 2010), *Crescentiella morronensis* (Crescenti, 1969; Senowbari-Daryan et al., 2008) and *Thaumatoporella parvovesiculifera.*

A wealth of encrusting microorganisms lived on the surface of Jurassic microbialite crusts, such as *Lithocodium aggregatum, Bacinella irregularis* and *Crescentiella morronensis. Lithocodium aggregatum* was interpreted as a codiacean green alga (Elliot, 1956), a lituolid foraminifer (Schmid and Leinfelder, 1995, 1996), calcimicrobial colonies (Cherchi and Schroeder, 2010), ulotrichalean green alga (Schlagintweit et al., 2010), chambers of boring sponges (Cherchi and Schroeder, 2010) or a calcimicrobial crust infested by boring sponges belonging to the ichnogenus *Entobia* (Cherchi and Schroeder, 2013). *Bacinella irregularis* was originally described as an *incertae sedis* alga (Radoičić, 1959); later many authors have suggested cyanobacterial/microbial origin for this *microproblematicum* (Schmid and Leinfelder, 1996). Alternatively, Schlagintweit et al. (2010) and Schlagintweit and Bover-Arnal (2013) interpreted *Bacinella irregularis* as a euendolithic chlorophycean alga. These and other encrusters are often valuable indicators of environmental factors. For instance, according to Dupraz and Strasser, (1999), the *Bacinella-Lithocodium* association indicates oligotrophic, clear, oxygenated and normal-marine waters. However, Schlagintweit et al. (2010) suggested that *Lithocodium aggregatum* could occur in shallow-marine settings together with dasyclad algae, but also in deeper area (slope, outer shelf). Moreover, also increased nutrient concentrations could stimulate blooms of *Lithocodium aggregatum* and *Bacinella irregularis*, such as in the Aptian carbonate succession of Oman (Immenhauser et al., 2005; Rameil et al., 2010). The thickness of the test of *Crescentiella morronensis* (or *Tubiphytes morronensis*) decreases with water depth or increased water turbidity (Dupraz and Strasser, 1999).

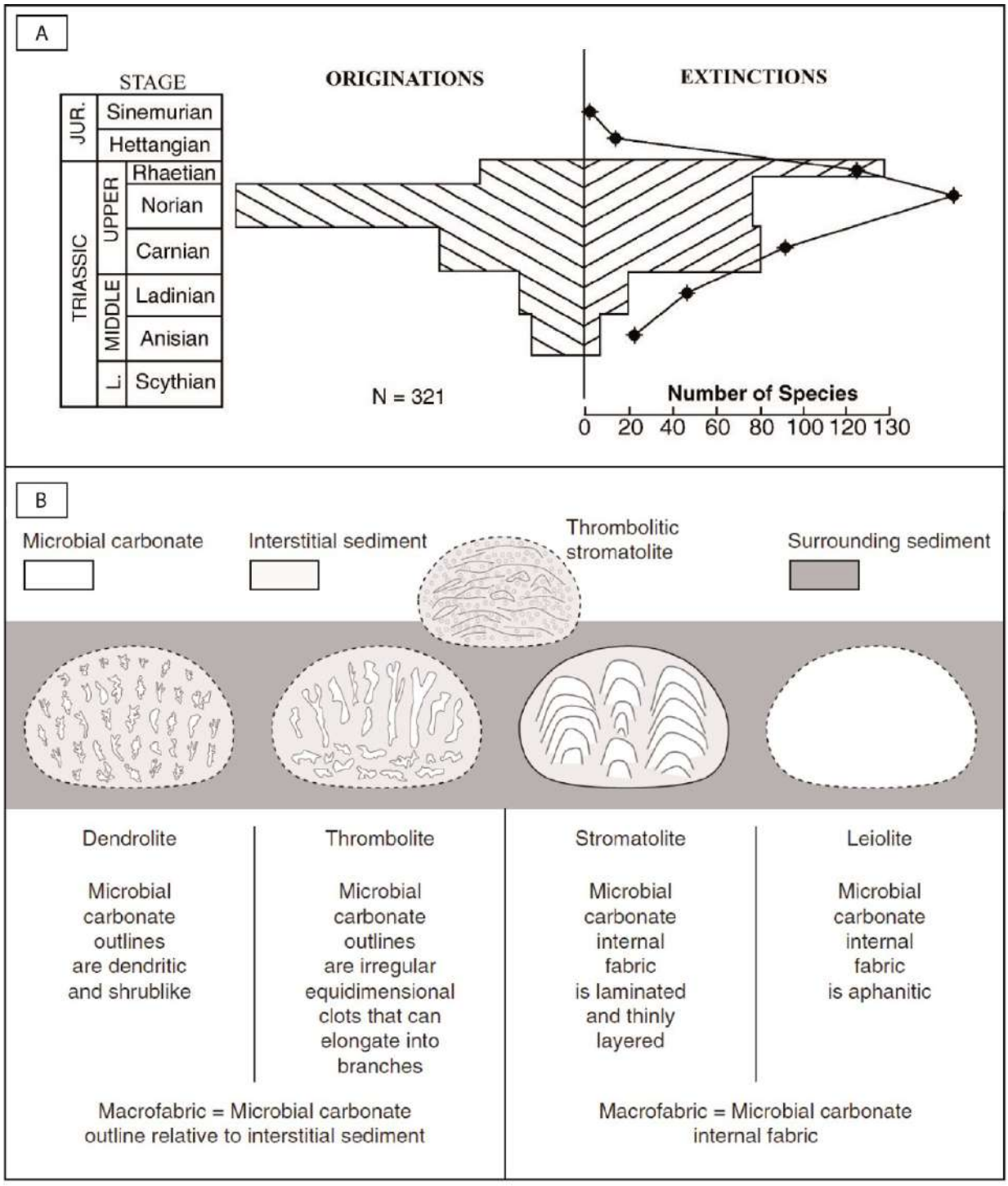

Figure 2.9 A) Abundance of scleractinian coral species from the Middle Triassic to Early Jurassic, after Stanley (2003). B) Macrofabric for microbial carbonates: leiolite (aphanitic), stromatolite (laminated), thrombolite (clotted) dendrolite (dendritic), after Riding (2011).

2.3 Jurassic reef types and carbonate systems

2.3.1 Controlling factors on Jurassic reefs

The Jurassic represents a time of exceptional worldwide abundance of reef proliferation in the Phanerozoic (Leinfelder et al., 2002; Kiessling, 2002, 2009; Cecca et al., 2005; Martin-Garin et al., 2012). In a period characterized by global geodynamic events, such as the break-up and dispersal of Pangea (Stampfli and Borel, 2002; Golonka, 2004, 2007; Frizon de Lamotte et al., 2015) and eustatic sea-level fluctuations (Dromart et al., 2003; Jenkyns et al., 2011; Haq, 2018), reef-building organisms diversified and gave rise to a great variety of reef settings and related reef types (Leinfelder et al., 2002; Kiessling, 2002). The evolution of reef patterns during the Jurassic reflects the modulation and positive feedback of various controlling mechanisms such as: evolution and radiations of scleractinian corals and other reef-building organisms (stromatoporoids, siliceous and calcareous sponges) and microbialites, new adaptational strategies of corals, continental plates reorganization, sea-level rise and climate change (Leinfelder et al., 2002; Kiessling, 2009).

The configuration and the steepness of the carbonate shelves are of paramount importance in determining the appearance and composition of Jurassic reefs. Jurassic reef growth occurred on very stable ramp, passive continental margins and adjacent epicontinental seas, at steepened and tectonically fractured passive margins, within reef basins and at active plate margins (Leinfelder et al., 2002). There was a pronounced structural reorganization during the Jurassic, rifting led to subsequent drowning of shallow-water settings in southwestern Tethys (Leinfelder et al., 2002). A structural revolution was the crustal segmentation and deep connection of Tethys-Atlantic seaway at the transition from Middle to Late Jurassic, resulting in the creation of many new reef environments by transpressional movements (Southern Tethys). Crustal segmentation was followed by increased seafloor spreading, raising sea level further, thus creating new sites for reef development, particularly on the northern Tethys shelves. In the Late Jurassic, a circum-equatorial seaway with a global east-west current facilitated larval distribution, reorganized upwelling zones and equalized the climate, which allowed coral-stromatoporoid reefs to expand into high paleolatitudes (Leinfelder et al., 2002).

Sea level is another important control on the evolution of Jurassic reefs. First order sea-level rises set the conditions for reef development, by enlarging available shelf areas and restricting terrigenous influx to coastal areas. Second to third order sea-level fluctuations provided windows for reef growth, whereas fourth order sea-level changes switched reef growth on and off. Global sea level rose, with oscillations, throughout most of the Jurassic, until the end of Kimmeridgian, well reflected by the

increase of reef sites towards the Late Jurassic on the northern Tethys shelf (Leinfelder et al., 2002; Kiessling, 2002, 2009).

2.3.2 Early Jurassic

The Early Jurassic as a whole was a period not very favourable for reef development (Leinfelder et al., 2002). The Early Jurassic reef biota were dominated by bivalves (lithiotids) and corals (Leinfelder et al., 2002), with some exceptions (cf. Della Porta et al., 2013).

The first lithiotid reef occurred in the Sinemurian, but the climax period was the Pliensbachian, with a continuous distribution belt in warm, low-latitude areas (Leinfelder et al., 2002). Well-preserved examples of lithioid reefs are in the Pliensbachian of Morocco (Fraser et al., 2004; Della Porta et al., 2013; Sadki and Sha, 2018), Trento Platform in Southern Alps (Posenato and Masetti, 2012; Franceschi et al., 2014), Adriatic Platform in Slovenia (Dozet, 2009; Gale, 2015) and Western North America (Fraser et al., 2004). Lithiotid bivalves have been addressed as Early Jurassic recovery taxa within the coral reef niche in a time of low diversity of corals, high atmospheric CO_2 and probable nutrient fluxes onto carbonate shelves (Fraser et al., 2004). Pliensbachian lithiotids are claimed to have partially outcompeted corals in building reefs by occupying the photosymbiontic niche and high-energy platform margin environments as a result of the Early Jurassic coral reef gap (Leinfelder et al., 2002; Wilmsen and Neuweiler, 2008). In the high Altas of Morocco a shoal-rimmed Pliensbachian platform dominated by lithiotid bivalves, for which the lagoonal carbonate factory was the main producer developed (Wilmsen and Neuweiler, 2008). Nevertheless, further studies (Merino Tomé et al., 2012; Della Porta et al., 2013) demonstrated that also in the Lower Jurassic carbonate platforms of the High Atlas, lithiotid reefs occupied the outer platform to lagoonal areas whereas platform margins and uppermost slopes were dominated by coral-stromatoporoid and microbialite reefs similar to the Upper Jurassic reefs.

The oldest known Jurassic coral reef is exposed in the Ardèche region of southern France (Kiessling et al., 2009; Gretz et al., 2015). This reef site, of early Hettangian age, immediately postdates the end-Triassic mass extinction and consists of at least three reefal bodies (Kiessling et al., 2009). This reef is dominated by phaceloid corals with a considerable contribution of microbialites and settled in an epicontinental shelf setting (Kiessling et al., 2009). Hettangian coral reefs are reported also from Scotland (Gretz et al., 2013).

In the Moroccan Central High Atlas, sponge-algal build-ups developed in open marine conditions toward the Lower-Upper Sinermurian boundary (Chafiki et al., 2004). These build-ups closely linked

to tectonic processes, growing on extensional syn-sedimentary faults (Chafiki et al., 2004). The siliceous sponge microbial mounds seem to be limited to the High Atlas marine rift in Morocco during the Early Jurassic time, while similar build-ups are common feature Upper Jurassic ramps (Della Porta et al., 2013).

In the Sinemurian of Southeast France coral-microbial patch reefs are reported as developed in a shallow mixed siliciclastic-carbonate inner ramp setting (Boivin et al., 2018).

In the Central High Atlas of Morocco, Pliensbachian and Toarcian lithiotid and mixed lithiotid-coral reefal deposits occur within carbonate and mixed carbonate-siliciclastic neritic depositional settings. These reefs occur in sheltered, near-shore lagoons along tropical carbonate ramps and platforms (Brame et al., 2019). Lithiotids were frequently associated with phaceloid and solitary corals (Brame et al., 2019).

A well-studied example among Lower Jurassic reefs is the Djebel Bou Dahar carbonate platform in the Moroccan High Atlas (Della Porta et al., 2013). It was a high-relief, flat-topped carbonate platform in which different carbonate factories contributed on its growth and architectural evolution. Here, skeletal and microbial carbonate factories already had the main components that characterized the Upper Jurassic reef (Della Porta et al., 2013). The coral-microbial-debris reefs correspond to high-energy shallow water settings of the Upper Jurassic Tethyan carbonate platforms, but they developed on a platform margin (Della Porta et al., 2013). In terms of geometry, the Djebel Bou Dahar platform is more affine to the Kimmeridgian-Tithonian steepened platform margins, in the subsurface of Nova Scotia, where boundstone lithofacies include microbialites, corals, chaetetids, calcareous and siliceous sponges, *Crescentiella* and stromatolite along the slope (Della Porta et al., 2013). This case study demonstrated that the platform margin of the Pliensbachian platforms was not exclusively dominated by lithioid bivalves and that microbialites were also common in Lower Jurassic reefs associated with corals, stromatoporoids, microencrusters and siliceous sponges (Della Porta et al., 2013). Moreover, it demonstrated that microbialites were not exclusively related to deep, nutrient-rich and oxygen depleted environments because they occur from the slope to intertidal setting and with biotic indicators of oligotrophic conditions such as stromatoporoids (Della Porta et al., 2013, 2015). Della Porta et al. (2013) demonstrated that in the Pliensbachian Djebel Bou Dahar high-relief platform lithioid accumulations represented a minor contribution to the carbonate platform growth and they were not responsible for building the carbonate platform margins, which were instead dominated by coral calcareous sponge microbial boundstone facies.

In the upper Pliensbachian of northern Calabria (Southern Italy) coral-microbial reefs developed on the flanks of uplifted basement highs within the rifted European continental margin of the Western Tethys (Santantonio et al., 2016).

2.3.3 Middle Jurassic

The evolution of the Middle Jurassic carbonate platforms was influenced by carbonate production crisis during Aalenian to early Bajocian and from middle Callovian to early Oxfordian (Andrieu et al., 2016; Bodin et al., 2017). This biotic crisis corresponds to $\delta^{13}C$ positive excursion related to strong seawater eutrophication (Morettini et al., 2002; Hesselbo et al., 2003; Bodin et al., 2017). According to Andrieu et al. (2016), wet climate, during low-eccentricity intervals led to high nutrient inputs. Such eutrophication of seawaters could have damaged the photozoan carbonate producers and dimished the growth potential of carbonate platforms (Bartolini et al., 1996; Andrieu et al., 2016). For instance, during the Middle Jurassic, the Latium-Abruzzi Platform experienced a dramatic decrease in productivity and sedimentation rate (Morettini et al., 2002).

Despite the availability of shallow seas and extensive shelves in the subtropical and tropical belts, Middle Jurassic reefs have a scattered distribution (Leinfelder et al., 2002). Aalenian reef sites are reported only from the southern Tethys shelf (Morocco), Thailand and the western Alps. Bajocian and Bathonian reefs reveal a much wider distribution and have been described from the northern Tethys shelf (Spain, Aurell and Bádenas, 2015; Tomás et al., 2019; England, Hallam, 1975; France, Brigaud et al., 2009; Andrieu et al., 2016; southwestern Germany, Wetzel et al., 2013), southern Tethys margin (Morocco, Tomás et al., 2013), Oman (Watts and Blome, 1990), U.S.A. West (Stanley and Beauvais, 1990) and East coasts (Ryan and Miller, 1981) and Chile (Prinz, 1991). Callovian reefs have been reported from the northern Tethys shelf (France, Brigaud et al., 2009; Poland, Zatoń et al., 2011), Egypt (Farag, 1959), Iran (Schairer et al., 2000) and the southern hemisphere (Saudi Arabia, Youssef and El-Sorogy, 2015; El-Sorogy et al., 2016; Hewaidy et al., 2017; India, Pandey and Fürsich, 1993).

Middle Jurassic reefs, dominated by scleractinian corals, usually developed in shallow platform settings within open shelf environments, such as Madagascar and Morocco along the platform margin. Reefs dominated by siliceous sponges normally grew in deeper platform position, below storm wave base (Leinfelder et al., 2002).

The size of Middle Jurassic reefs varies from small and thin reef structures (10 m thick, lateral extent less than 100 m), to huge build-ups (thickness more than 100 m, lateral extents 500 m).

Primary or secondary reef builders in the Middle Jurassic were scleractinian corals, siliceous sponges, stromatoporoids and chaetetids, red algae, microbes, bivalves, serpulids, encrusting foraminifera (Leinfelder et al., 2002).

From Aalenian to Oxfordian times, western France was positioned at subtropical latitudes (20-30 °N) and was covered by a shallow epicontinental sea. Shallow marine carbonates deposited over a vast

platform open to the Atlantic, Tethys and Arctic oceans (Andrieu et al., 2016). In the Paris Basin an intracratonic carbonate environments with coral reefs and crinoid-rich facies developed in the Early Bajocian (Brigaud et al., 2009). The high carbonate production due to coral-reef development was suggested to be associated to a climate warming (Brigaud et al., 2009). At the transition between Early and Late Bajocian there was a facies change with a clay-rich and ooid-rich carbonate ramp (Brigaud et al., 2009, 2010). The progradation of the ooidal shoals favoured the formation of an inner ramp protected environment with lagoonal, intertidal and supratidal facies in the Bathonian. Exposure episodes during the Bathonian period were coeval with the minimum sea-surface temperature in western Tethyan domain (Brigaud et al., 2009). At the Bathonian/Callovian boundary the lagoonal facies were replaced by an ooid-bioclastic ramp associated with a decrease in carbonate productivity (Brigaud et al., 2009). Siliceous sponge mud mounds are reported from the Bajocian of Southern-Provence Basin (Léonide et al., 2007).

During the Middle Jurassic, Central Europe was occupied by an epeiric sea (Wetzel et al., 2013). In Bajocian-Bathonian times a seaway developed around the London Brabant Massif and carbonate platforms, such as the Burgundy platform were attached to it (Wetzel et al., 2013). The margin of this carbonate platform (Northern Switzerland and south-western Germany) was characterized by the accumulation of ooidal calcarenites (Wetzel et al., 2013).

Microbial mound formed in the normal marine, shallow neritic setting of an inner ramp system from the High Atlas of Morocco. The microbial mounds are embedded in cross-bedded oolitic facies (Tomás et al., 2013). In the central High Atlas coral patch reefs and pinnacle reefs developed at platform margin during the Bajocian (Ait Addi, 2006).

During the Bajocian, in the Iberian Basin, microbial-siliceous mounds developed on carbonate ramp depositional settings (Aurell and Bádenas, 2015; Tomás et al., 2019). In the carbonate platform of Moscardon (Spain), microbial-siliceous sponge lens-shaped build-ups and mounds developed in outer slope settings, below wave base, at depths of about 30-50 m (Aurell and Bádenas, 2015). In the area of Ricla (Spain), the mound framework consisted of various proportions of microbialites (dense to clotted peloidal micrite fabrics), siliceous sponges (both Hexactinellid and Lithistid) and detrital packstone-wackestone matrix (Tomás et al., 2019). The geometry of microbial-siliceous sponge mounds across the carbonate ramp is interpreted to be heterogeneous (Tomás et al., 2019). In the shallower, more proximal ramp, mounds occurred as isolated, single, tabular structures, whereas in the transition area between the relatively shallow and the deep carbonate ramp domains, they form extensive, lenticular, flat-shaped structures. In the deeper more distal domains of the ramp, isolated domal-shaped mounds with preferential vertical accretion occurred. This hydrodynamic gradient is interpreted to be related to the action of storm-induced waves and currents (Tomás et al., 2019).

In the External Subbetic (Spain) coral biostromes formed among oolitic shoals. These build-ups are dominated by phaceloid forms and characterized by a microencruster assemblage and scarce microbial crusts (Reolid et al., 2009).
In the Arabian Peninsula, during Callovian, a carbonate platform (Tuwaiq Fm.) with stromatoporoid-coral reefs and ooidal shoals separating peritidal and lagoonal facies from middle to outer ramp facies developed (Youssef and El-Sorogy, 2015; El-Sorogy et al., 2016; Hewaidy et al., 2017). In the Callovian of Israel, patch reefs made of microsolenoids and stromatoporoids, formed in very shallow waters very close to the palaeoequator (Wilson et al., 2008, 2010).

2.3.4 Evolution of Upper Jurassic carbonate platforms

During the Late Jurassic time, the Tethys Ocean separated Europe and Asia to the north from Africa, Arabia and India to the south (Fig. 2.10). Areas north of the Tethys formed part of the Eurasian continent (Cecca et al., 2005), whereas those to the south were parts of a Western continent (Africa and Arabia). The Late Jurassic Tethys Ocean could be divided in three areas different in terms of emerged land setting and shallow water carbonate distribution and characteristics: northern Tethys, intra-Tethys and southern Tethys (Kiani Harchegani and Morsilli, 2019).
In the northern Tethys the Eurasian continent was separated in some emerged land massif with attached carbonate platforms in the areas prone to shallow-water carbonate development (Leinfelder et al., 2002). Most of the northern Tethys coral-microbial reefs developed in middle ramp settings within attached platforms (Leinfelder et al., 2002).
The intra-Tethys carbonate platforms show a completely different pattern in Late Jurassic reef distribution relative to northern Tethys (Leinfelder et al., 2002). This is due to a different structural setting deriving from rifting extensional tectonics within the Triassic carbonate platforms. Moreover, the isolation from the continent of the intra-Tethys platforms led to lower terrigenous input and more oligotrophic conditions (Leinfelder et al., 2002).
The southern Tethys was the site of an extensive epeiric carbonate platform, with intra-shelf basins, developed and constituted one of the most important petroleum systems in the world (Hughes et al., 2008).
The nature and distribution of coral-sponge reefs and microbial carbonates in the Jurassic carbonate platforms and shelves is complex and diversified and it is synthesized in detail in the next paragraphs.

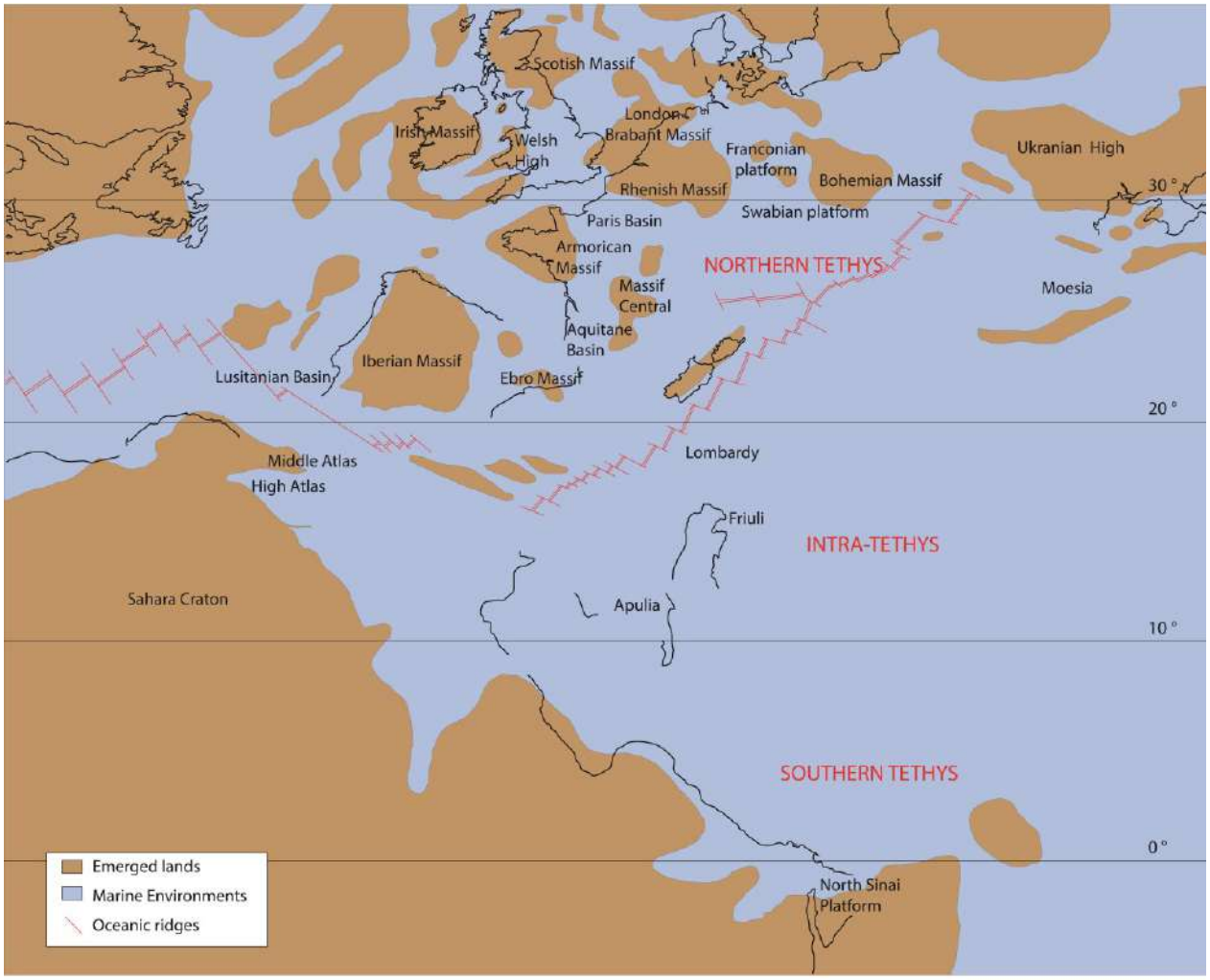

Figure 2.10 Palaeogeographic map showing the distribution of emerged lands and marine environment in the Tethys realm and part of the Atlantic Ocean during the Kimmeridgian. Redrafted after Dercourt et al. (2000).

2.3.4.1 Northern Tethys

In the northern Tethys shelf, there was the development of mainly two types of reefs: coral reefs and siliceous sponge mounds. Almost all of these reefs were partially constructed by microbialites and microencrusters (Leinfelder et al., 2002).

Most of the northern Tethys coral-microbial reefs developed within attached platforms, in environments characterized by high terrestrial run-off, often combined with elevated particulate nutrients (Leinfelder et al., 2002). Coral-microbial northern Tethys reefs generally lacked stromatoporoid and other calcareous sponges with respect to intra-Tethys reefs (Leinfelder et al., 2002; Kiani Harchegani and Morsilli, 2019). The only exceptions were bioherms of chaetetids and *Cladocoropsis mirabilis* in lagoon and back-shoal environments (e.g., Spain, Sequero et al., 2019) and some coral-stromatoporoid-microbial mounds in central Spain (Pomar et al., 2015). This is

considered to be due to the scarce adaptation of stromatoporoids to mesotrophic settings (Leinfelder et al., 2002, 2005).

Siliceous sponges formed mounds in the deeper shelves of the northern Tethys and were mainly Hexactinellid and Lithistid demosponges (Leinfelder, 1993a; Pittet and Mattioli, 2002; Bartolini et al., 2003; Olóriz et al., 2003a, 2006, 2012; Olivier et al., 2004b; Reolid et al., 2005, 2007).

2.3.4.1.1 Oxfordian

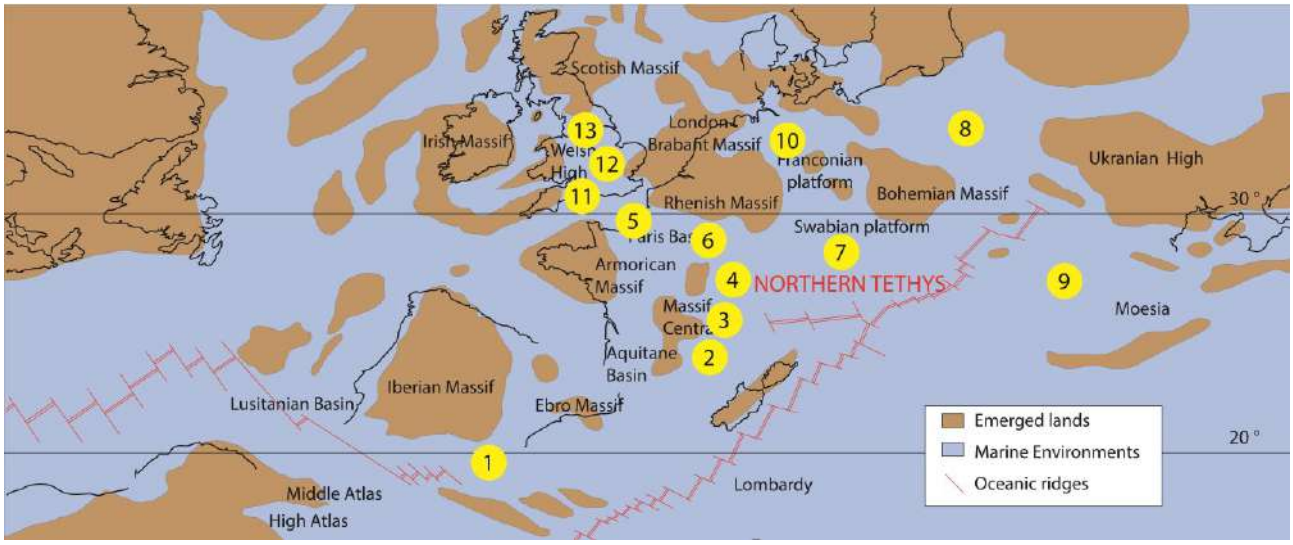

Figure 2.11 Palaeogeographic map of the Northern Tethys realm during Oxfordian with the position of the case studies mentioned in the text: 1 - External Prebetic (Olóriz et al., 2003a; b); 2 - French Jura (Molinges, Olivier et al., 2011); 3 - French Jura (Ornans, Lathuilière et al., 2005); 4 - Swiss Jura (Samankassou et al., 2003; Védrine et al., 2007; Strasser and Védrine, 2009); 5 - Northern Paris Basin (Bertling and Insalaco, 1998); 6 - Eastern Paris Basin (Brigaud et al., 2014); 7 - Southern Germany (Bartolini et al., 2003; Olivier et al., 2004b); 8 - Southern Poland (Matyszkiewicz, 1993; Matyszkiewicz et al., 2012); 9 - Romania (Franţescu, 2011); 10 - Northern Germany (Helm and Schülke, 2006); 11 - England (Wiltshire; Insalaco, 1999); 12 - England (Cambridgeshire; Insalaco, 1999); England (Yorkshire; Insalaco, 1999). Redrafted after Dercourt et al. (2000).

During the early Oxfordian carbonate shallow environments were rare in the northern Tethys and the deposits were characterized by several hiatuses or siliciclastic dominance (Cecca et al., 2005). Instead, carbonate ramps and shelves were widespread in the middle-late Oxfordian, between exposed lands (Fig. 2.11).

In southern Spain, within the external Prebetic, there were carbonate ramps with siliceous sponge-microbial bioherms (Hexactinellid) that occurred in middle-ramp settings (Olóriz et al., 2003a; b, 2008, 2012; Reolid et al., 2005; Reolid and Gaillard, 2007). The development of these bioherms took place in low-energy conditions, nutrient-rich and well-oxygenated waters. The Iberian Basin was connected with the Basque-Cantabrian Basin to the north by the Soria Seaway, a shallow carbonate platform with mixed carbonate-siliciclastic deposition (Pittet and Strasser, 1998).

Deposits similar to those of the Iberian Basin could be found in southern Germany (Pittet and Mattioli, 2002; Bartolini et al., 2003; Olivier et al., 2004b), southern Poland (Trammer, 1989; Matyszkiewicz

and Felisiak, 1992; Matyszkiewicz, 1993; Matyszkiewicz and Krajewski, 1996; Matyszkiewicz et al., 2012) and Romania (Franţescu, 2011). However, the Polish and German sponge bioherms formed below the storm wave base in deep shelf or outer ramp settings.

Between the Bohemian and the Central Massifs, the French Jura was structured as a low-angle, distally steepened ramp with siliceous sponge bioherms located in the outer ramp and/or slope position environments, a well-developed coral fauna in the middle-ramp and ooidal shoals in the inner ramp (Lathuilière et al., 2005; Olivier et al., 2011). The area of Molinges (2 in Figure 2.10) was located at the margin of the platform at the transition between platform interior and the basinal environment. Coral-microbial bioconstructions developed in mid-ramp settings (20-30 m of water depth; Fig. 2.12A). The coral fauna was dominated by dendroid and thamnasterioid forms, in particular *Dimorpharaea, Comoseris, Microsolena, Enalhelia, Montlivatia, Epistreptophyllum* and *Thamnasteria* (Olivier et al., 2011). Instead in the area of Ornans, Lathuilière et al. (2005) recognized a reef tract coral zonation within the ramp, from the more distal zone to the proximal one. The lagoon was dominated by *Stylina* and *Comoseris*, the proximal ramp by *Dendraraea,* the intermediate ramp by *Microsolena* and the most distal part by *Dimorpharaea*. In the highest energy zone, there were ooidal shoals. The development of a reef in this area had a key role in generating a rimmed platform starting from a ramp (Lathuilière et al., 2005).

In the Swiss Jura, carbonate platforms accumulated on an irregular sea-bottom morphology, with topographic highs and lows created by differential subsidence (Samankassou et al., 2003; Védrine et al., 2007; Strasser and Védrine, 2009). Ooidal shoals and coral reefs developed at the top of the elevated areas (Fig. 2.12B). The coral bioconstructions included ramose (*Thamnasteria*), phaceloid (*Calamophylliopsis*), flat (*Actinarae*) and globular (*Stylina*) forms.

North of the Central Massif, in the Paris Basin, there was an epicontinental sea connetting scattered emerged lands, which was open to the Atlantic, Tethys and Arctic oceans (Brigaud et al., 2014). Here carbonate ramps developed with ooidal shoals in the inner ramp and coral-microbial reefs in the middle ramp, especially in late Oxfordian (Bertling and Insalaco, 1998; Brigaud et al., 2014). In the northern part, coral-microbial reefs were built by branching (*Thamnasteria, Dendroelia, Allocoenia, Dendrarea*), phaceloid (*Calamophylliopsis, Cladophyllia, Thecosmilia, Goniocora, Stylosmilia*) and massive (*Diplocoenia, Fungiastraea, Stylina, Latomeandra, Thamnasteria, Mircophyllia*) forms (Bertling and Insalaco, 1998). In the eastern part (Lorraine and Burgundy), there was a transition from a ramp profile to a rimmed platform profile with a microbial and photozoan assemblage due to climatic oscillations from cool to warm conditions (Olivier et al., 2004a; Carpentier et al., 2006, 2007; Brigaud et al., 2014). The coral association included phaceloid (*Aplosmilia, Stylosmilia*) and massive (*Stylina, Isastrea, Microsolena, Thamnasteria*) corals.

In the Hannover Basin, North of the Rhenish Massif (northern Germany), shallow-water microbial-coral patch reefs showed high diversity with *Stylosmilia, Goniocora, Stylina, Actinastrea, Isastrea, microsolenoids, Microphyllia, Helicoenia* and *Dendrohelia* (Helm and Schülke, 2006).

The highest latitude (between 30 and 35 °N) occurrence of coral reefs during the Oxfordian time was in England (Insalaco, 1999). They grew in the shallow sea between the Anglo-Brabant landmass, the Scottish Massif, the Welsh Massif and the Cornubian Massif. Depending on the environmental conditions, diverse types of coral reefs developed in this area. In very shallow waters, with episodic strong siliciclastic input, reefs made of *Thamnasteria, Thecosmilia* and *Isastrea* occurred (Insalaco, 1999). In shallow waters with high-energy conditions a pioneer coral assemblage developed made of *Thamnasteria, Thecosmilia* and *Rhabdophyllia*. Furthermore, there were also monospecific coral bioconstructions made only of *Thamnasteria concinna* (Insalaco, 1999). Instead, in deeper settings, in low energy and low light conditions, in the marginal region of the reef, a distinctive coral association developed, constituted by *Microsolena* and *Dimorpharaea* (Insalaco, 1999).

Romanian coral reefs are other examples of bioconstructions in the Oxfordian northern Tethys. Carbonate ramps occurred with coral reefs in the proximal areas and sponge-microbial bioherms in the deeper parts (Fig. 2.12C; Franţescu, 2011).

All the case studies from the northern Tethys realm reveal that the water trophic level during the Oxfordian was likely particularly high, in many places from mesotrophic to eutrophic conditions. High nutrient level occurred together with a high siliciclastic input in most of the marine environments of the European plate, due to high weathering, especially in humid periods (Dupraz and Strasser, 1999, 2002). Probably these conditions of enhanced nutrient availability could have favoured microbial growth (Dupraz and Strasser, 1999, 2002), which in some places consistuted large volumes of the bioconstructions, encrusting both corals and sponges (Dupraz and Strasser, 1999). The only Oxfordian shallow-water carbonate record without important contribution of microbial growth is in northern England, where probably there where different environmental conditions (Insalaco, 1999). Microencrusters were diffused in almost all the northern Tethys bioconstructions, associated with microbialites. They probably grew in different microenvironments depending on light and water oxygenation. The association *Lithocodium aggregatum-Bacinella irregularis* encrusted corals and other reef builders probably in well-illuminated and oxygenated waters (Dupraz and Strasser, 1999; 2002; Schlagintweit et al., 2010). They were common in the coral reefs of the Swiss Jura, Lorraine and Burgundy (France) and Northern Germany. The association of microencrusters *Crescentiella* and *Terebrella* colonized the less illuminated and less oxygenated waters (Dupraz and Strasser, 1999). These conditions could have favoured the deeper siliceous sponge bioherms of the external Prebetic in Spain (Olóriz et al., 2003a, 2006, 2012; Reolid et al., 2005), southern Germany

(Bartolini et al., 2003; Olivier et al., 2004b) and southern Poland (Matyszkiewicz, 1993; Matyszkiewicz et al., 2012), or could have occurred in the internal pores of the shallow coral bioconstructions, such as in the French Jura (Olivier et al., 2004a, 2011; Olivier, 2019), Swiss Jura (Dupraz and Strasser, 2002; Samankassou et al., 2003; Strasser et al., 2012) and northern Germany (Helm and Schülke, 2006). Other important reef constituents during the Oxfordian were nubeculariid foraminifers, serpulids, bivalves, oysters, calcareous sponges, echinoderms, gastropods, brachiopods, foraminifers and bryozoans. Sometimes the red alga (or chaetetid sponge according to Riding, 2004), *Solenopora* was an important reef component, such as in the reefs of Yorkshire, northern Germany, Swiss Jura, Lorraine and Burgundy (Olivier et al., 2004a; Brigaud et al., 2014). Instead, stromatoporoids were rare in Oxfordian carbonate ramps and shelves of the northern Tethys and are reported only from the Wiltshire reef (Insalaco, 1999). Ooidal shoals were common, especially in inner ramp settings. Some examples are in the ramps of the French Jura (Olivier et al., 2011). In other settings there were isolated ooidal shoals and isolated patch reefs, such as in the Swiss Jura (Samankassou et al., 2003).

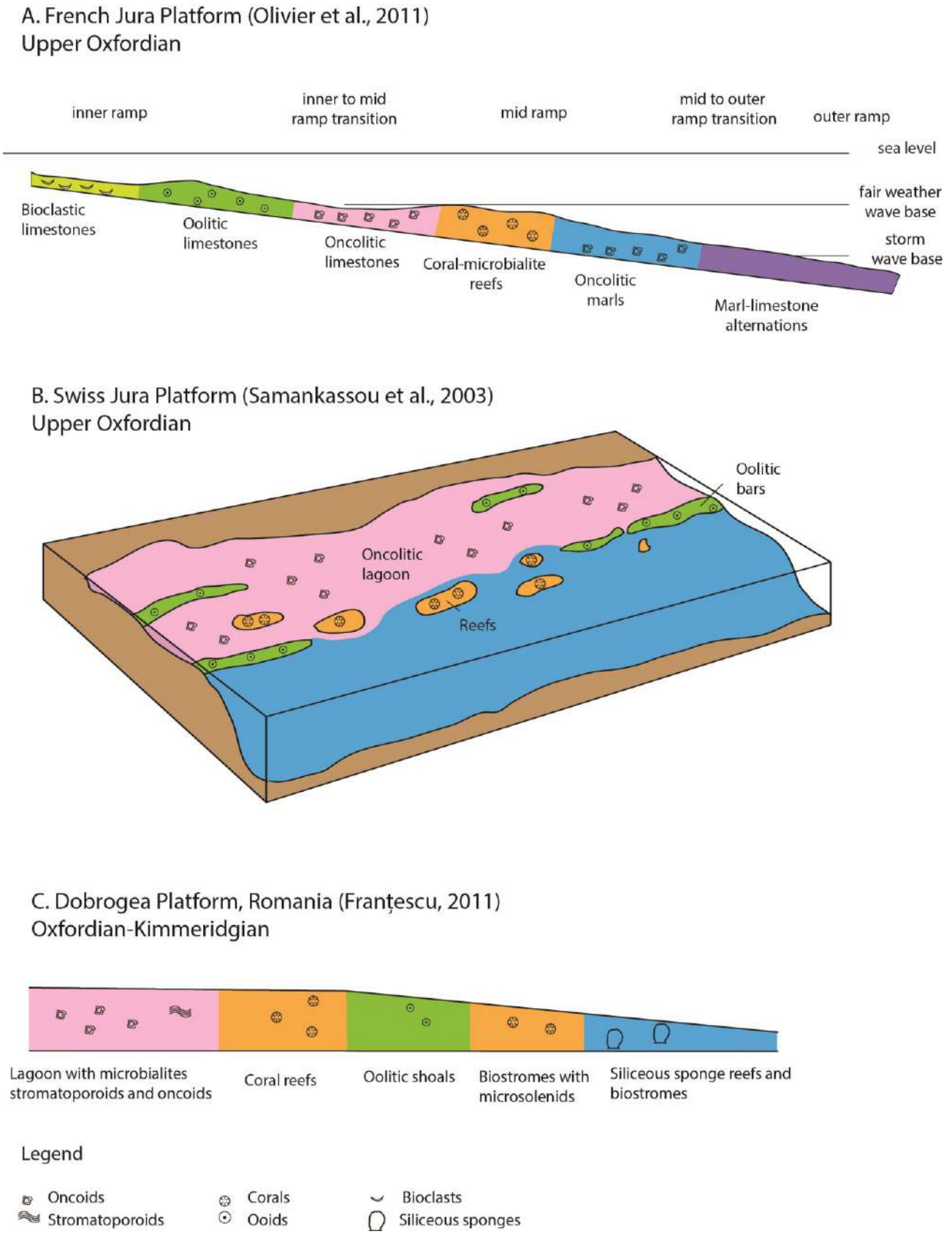

Figure 2.12 A) Depositional profile proposed for the Oxfordian Molinges section (French Jura) redrafted after Olivier et al. (2011). B) Depositional 3D sketch redrafted after Samankassou et al. (2003) for the Oxfordian Swiss Jura Platform. C) Depositional profile proposed for the Oxfordian-Kimmeridgian Dobrogea Platform redrafted after Franţescu (2011).

2.3.4.1.2 Kimmeridgian

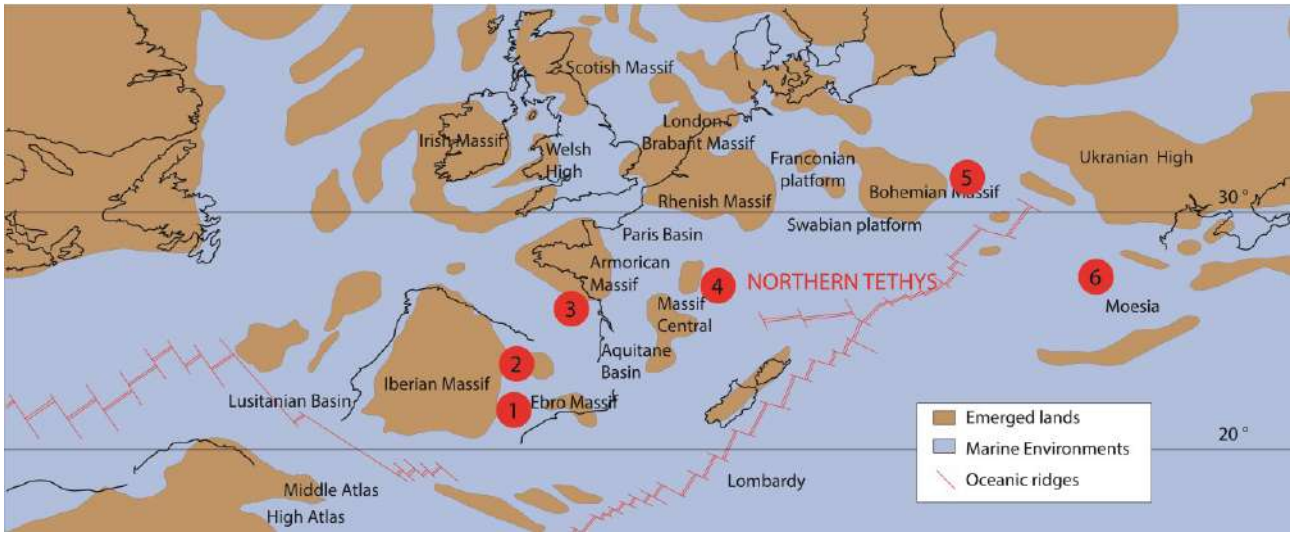

Figure 2.13 Palaeogeographic map of the Northern Tethys realm in Kimmeridgian time, with the position of the case studies mentioned in text: 1 - Iberian Basin (Aurell et al., 2003; San Miguel et al., 2017); 2 - NE Spain (Benito et al., 2005); 3 - La Rochelle (Olivier et al., 2003, 2008); 4 - Swiss Jura (Colombié and Strasser, 2005; Jank et al., 2006); 5 - Poland and Ukraine (Gutowski et al., 2005); 6 - Moesian platform (Ivanova et al., 2008). Redrafted after Dercourt et al. (2000).

The Kimmeridgian was a period of reduced carbonate system development with respect to the Oxfordian time in the Northern Tethys (Fig. 2.13). In particular, coral reefs were less abundant than in the Oxfordian (Cecca et al., 2005). The maximum latitude occurrence of carbonate production shifted toward lower latitudes (Cecca et al., 2005). For instance, coral reefs in UK were drowned and a deep-water environment established (Martin-Garin et al., 2010; 2012). In the Paris Basin, both in the northern and eastern part, there was the complete carbonate platform demise due to intense subsidence (Brigaud et al., 2014). In the Swabian and Franconian platforms (Germany) the depositional conditions of the Oxfordian persisted in the Kimmeridgian with siliceous-sponges patch reefs that developed in outer ramp settings (Bartolini et al., 2003; Olivier et al., 2004b).

During the Kimmeridgian, the Iberian Basin was occupied by an east facing epeiric carbonate ramps with low-angle slopes separating the shallow and deep-water areas (Aurell et al., 2003). In the Early Kimmeridgian a particular carbonate system developed west of Teruel (Pozuel Fm.). It consisted of a carbonate shelf with oolitic sigmoids formed below the wave base due to avalanches generated by storm wave and longshore currents (Pomar et al., 2015). Ooids were formed in the shoreface and transported toward deeper settings. Laterally, coral-stromatoporoid and microbial mounds formed in lower-energy landward settings (Pomar et al., 2015). The main coral genera components were *Stylina, Comoseris, Heliocoenia* and *Microphyllia.* During the Late Kimmeridgian, in the shallow portion of the epeiric ramp, skeletal and ooidal shoals of inner ramp settings separated a lagoon from the open sea. Coral-microbial bioherms and biostromes developed in mid-ramp settings (Alnazghah et al.,

2013; San Miguel et al., 2013, 2017). These coral-microbial reefs formed isolated build-ups (Fig. 2.14A), amalgamated or pinnacle-shaped, up to 20 m high and 40 m wide (San Miguel et al., 2013, 2017). The coral association consisted of dominant *Thamnasteria, Comoseris* and *Microsolena*, associated with *Calamophylliopsis, Stylina, Ovalastrea, Milleporidium, Axosmilia* (San Miguel et al., 2013, 2017). Northward, in NE Spain, there was a shallow platform with coral-microbial fringing reefs and steep margins that evolved into a shallow ramp with lagoonal facies protected by sand shoals (Benito et al., 2005; Benito and Mas, 2006). Corals were mainly platy, branching, massive and solitary forms and the association consisted of microsolenoids, *Clausastraea, Pseudocoenia, Isastraea, Fungiastraea, Calamophylliopsis, Aplosmilia, Stylosmilia, Montlivaltia* (Benito and Mas, 2006). During the latest Kimmeridgian the carbonate system in the Iberian Basin evolved from a ramp with bioconstruction to a ramp with sand shoals, protected back-shoal environments, intertidal environments and restricted lagoons (Alnazghah et al., 2013; Sequero et al., 2018, 2019). In the area of Mezalocha (Higueruelas Fm.) back-shoals and lagoons were rich in peloids and oncoids, whereas stromatoporoids (*Cladocoropsis*), corals and chaetetids colonized sheltered lagoons (Sequero et al., 2018).

South of the Armorican Massif (La Rochelle, Western France) a ramp in relatively low-energy, wave dominated settings developed during the Kimmeridgian (Olivier et al., 2003, 2008). This ramp evolved from a carbonate dominated environment to a mixed carbonate-siliciclastic environment. Coral-microbial patch reefs developed in relatively deep settings, in the upper offshore zone (Olivier et al., 2003, 2008). The coral association was constituted by phaceloid, massive and ramose colonies of the genera *Calamophylliopsis, Microsolena, Thamnasteria, Stylina, Pseudocoenia, Stylosmilia*, and *Isastrea* (Olivier et al., 2008).

In the Swiss Jura a carbonate platform with sufficient carbonate production to keep-up with a sea-level rise, developed (Colombié and Strasser, 2005; Jank et al., 2006). This platform was divided by Colombié and Strasser (2005) in internal and external platform facies belts (Fig. 2.14B) The internal platform was characterized by tidal flats, channels, ponds, beach and a lagoon, divided from the open sea by sand shoals. In the lagoon there were internal shoals and coral patch reefs, dominated by microsolenoids (Colombié and Strasser, 2005).

In Poland (Holy Cross Mt.) and Ukraine a progradational carbonate ramp system developed during the Kimmeridgian. The system was characterized by supra- and intertidal facies with tepees and fenestrae in protected lagoons, oolitic and skeletal shoals and coral-microbial patch reefs and biostromes in the outer ramp (Gutowski et al., 2005). The coral association was dominated by *Isastrea, Fungiastrea, Microsolena, Thamnasteria, Actinaraea, Comoseris, Pseudocoenia, Calamophylliopsis, Meandrophyllia* (Roniewicz and Roniewicz, 1971).

In the Moesian platform (Bulgaria) a rimmed platform with a lagoon, bioclastic shoals and coral-microbial bioherms and biostromes developed. Reef developed in outer platform settings, separated from the inner platform by bioclastic shoals (Ivanova et al., 2008). The corals were mainly solitary, phaceloid, ramose, lamellar and massive and dominated by the genera *Rhipidogyra, Montlivaltia, Calamophylliopsis, Cladophyllia, Latomeandra, Thecosmilia, Microphyllia, Solenocoenia, Thamnarea, Dimorphastrea, Microsolena, Synastrea, Ogilvinella, Placogyra, Cyathophora, Pseudocoenia* (Ivanova et al., 2008; Roniewicz, 2008).

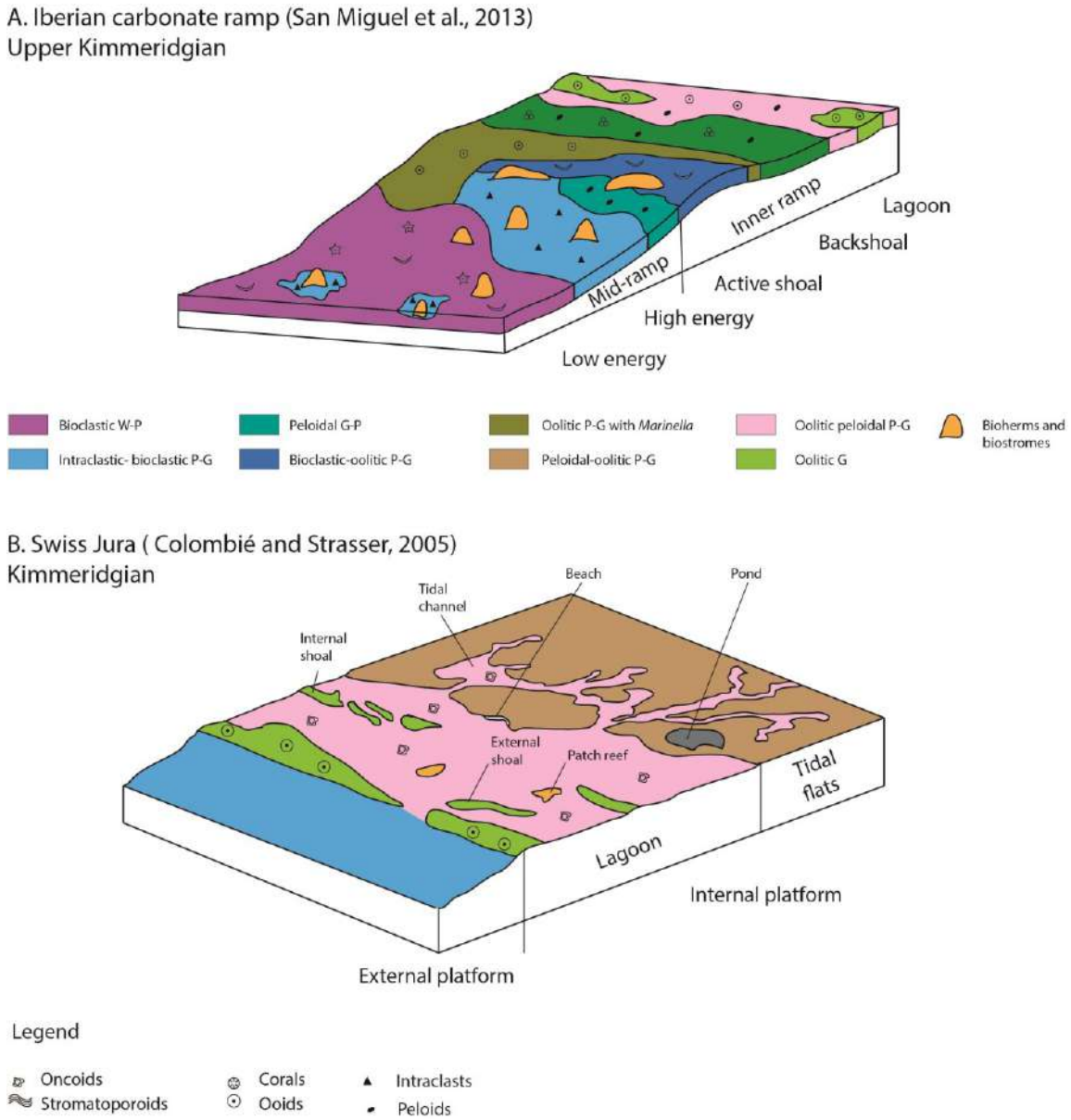

Figure 2.14 A) Facies model proposed for the Kimmeridgian Jabaloyas carbonate ramp; redrafted after San Miguel et al. (2013). B) Depositional model proposed for the Kimmeridgian Swiss Jura Platform; redrafted after Colombié and Strasser (2005).

2.3.4.1.3 Tithonian

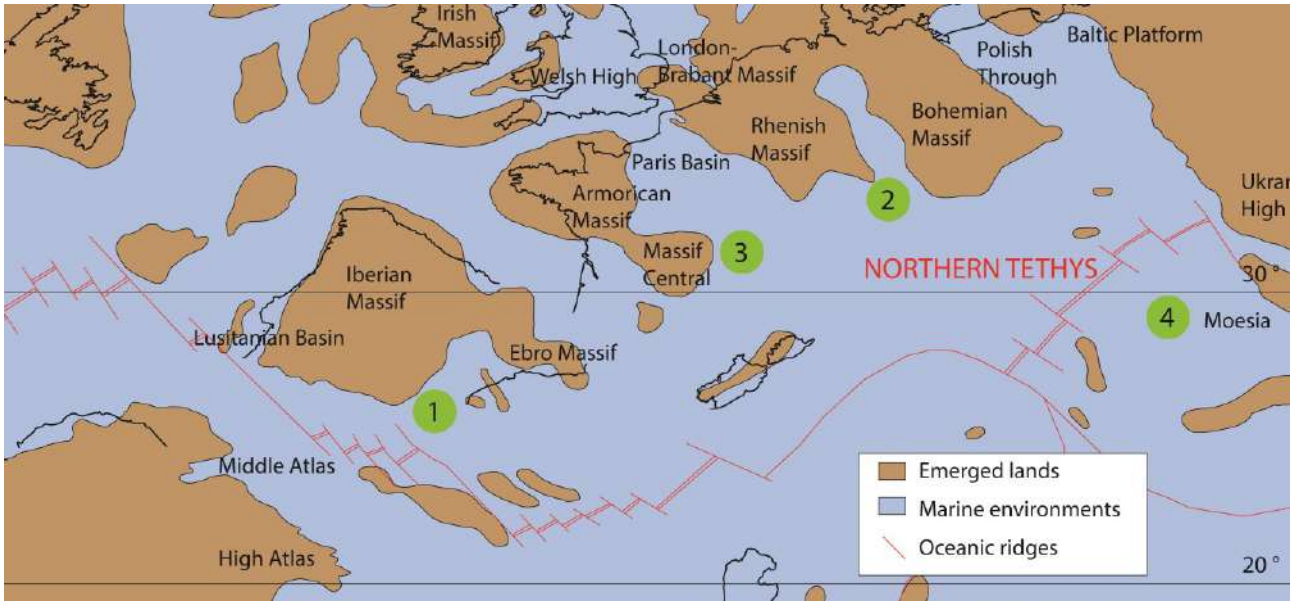

Figure 2.15 Palaeogeographic map of the Northern Tethys realm in Tithonian, with the position of the case studies mentioned in text: 1 - Maestrat Basin, Spain (Bádenas et al., 2004); 2 - NW Germany (Arp et al., 2008; Dragastan and Richter, 2011); 3 - Romania (Pleş et al., 2013, 2019); 4 - Jura platform (Rameil, 2005). Redrafted after Dercourt et al. (2000).

Tithonian bioconstructions in Northern Tethys (Fig. 2.15) were more scattered and less developed compared to the Oxfordian and Kimmeridgian times (Leinfelder et al., 2002). During this period, platforms were commonly rimmed by shoals made of non-skeletal grains or bioclasts and lagoonal facies, rich of peloids and oncoids were widespread.

The Tithonian regression led to shallow carbonate deposition in the Maestrat Basin (Bádenas et al., 2004). In this area a shallow platform, with shoals and coral-rich skeletal banks that isolated a restricted lagoon, developed (Bádenas et al., 2004). In restricted lagoons the deposition was dominated by packstone-wackestone rich in oncoids and peloids, whilst the shoals were mainly ooidal and bioclastic (Bádenas et al., 2004).

In the upper Tithonian of NW Germany, particular bioconstructions were formed under specific environmental conditions. In the area of Thüste, serpulid-stromatolite bioherms developed in shallow-marine carbonate environments (Arp et al., 2008; Dragastan and Richter, 2011). During the late Tithonian, in this area an ooidal shoal separated a schizoaline lagoon from a marine brackish environment. In the lagoon, biocontructions of stromatolites and serpulids accumulated. Landward there was a sabkha environment, testifying arid or semi-arid conditions. The development of this environment was favoured by the alternation of hydrologically closed and open conditions with the influx of brackish waters (Arp et al., 2008). The lagoon was supersaturated with respect to calcium and sulphate minerals and gypsum precipitated within microbial mats (Arp et al., 2008).

In the French and Swiss Jura, the shallow carbonate sedimentation continued from the Kimmeridgian. In particular, platforms were rimmed by sand barriers (Rameil, 2005). Platform interior consisted of tidal flats, ponds and sabkhas, facing a restricted lagoon. Oncoids and peloids were common in these lagoonal settings, whereas ooids and bioclasts accumulated in sand barriers (Rameil, 2005).
Farther East, in Romania, a rimmed platform with coral-microbial bioconstructions developed in settings with low sedimentation rate (Pleş and Schlagintweit, 2013; Pleş et al., 2013, 2019). Reefs consisted of boundstone with corals, stromatolites, thrombolites and microencrusters. The large amount of reef breccia (rudstone with intraclasts) was related to the platform progradation. According to Pleş et al. (2013) this platform is much more similar to the shallow-water carbonates of the southern Tethys than to the ones of the northern Tethys area. Instead, in the Moesian platform shallow carbonate deposition continued during the Tithonian similar to Kimmeridgian times (Ivanova et al., 2008).

2.3.4.2 Intra-Tethys

The intra-Tethys carbonate platforms displayed a different pattern of Late Jurassic reef distribution relative to northern Tethys (Leinfelder et al., 2002). In the intra-Tethys realm, large emerged lands were lacking and the shallow-water carbonates were deposited in isolated platforms. These isolated platforms were characterized by wide reef areas with highly diverse biotic communities dominated by stromatoporoids and corals (Leinfelder et al., 2002, 2005; Kiani Harchegani and Morsilli, 2019). The common characteristics of the intra-Tethys reefs were the widespread presence or dominance of stromatoporoids and the absence of microbialites in the bioconstructions and the zoned character of the reefs (Kiani Harchegani and Morsilli, 2019). A different structural setting derives from rift tectonics within the Triassic carbonate platforms. Moreover, the isolation from the continent of the intra-Tethys platforms led to lower terrigenous input and more oligotrophic conditions (Leinfelder et al., 2002; Kiani Harchegani and Morsilli, 2019) with respect to the northern Tethys shelves.

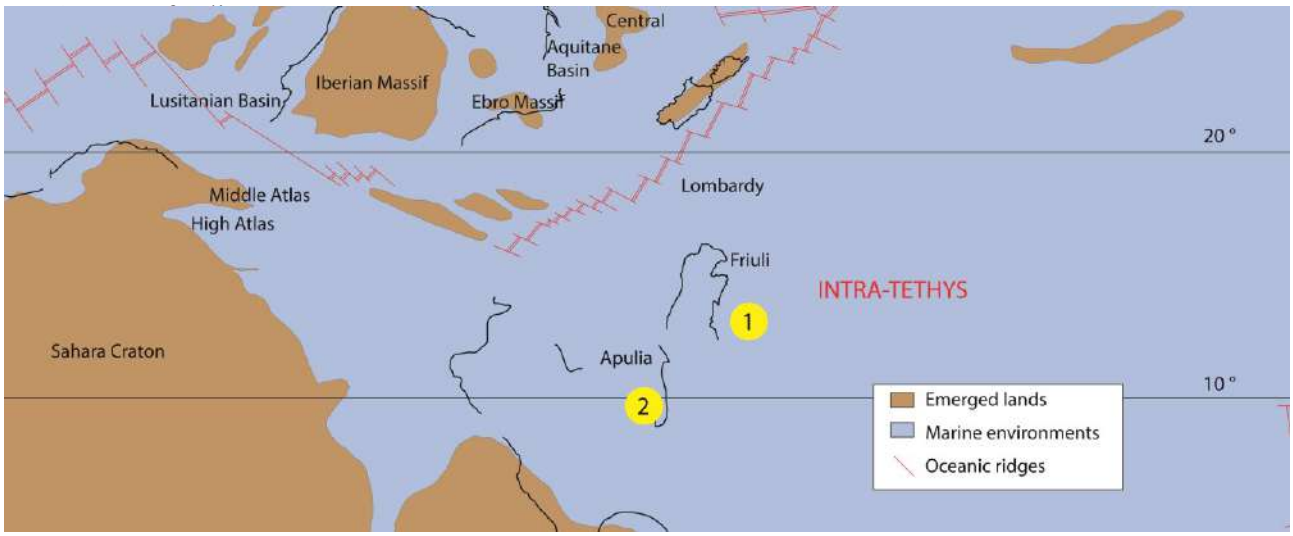

Figure 2.16 Palaeogeographic map (redrafted after Dercourt et al., 2000) of the intra-Tethys realm during Oxfordian, with the position of the case study mentioned in the text: 1- Adriatic Platform (Vlahović et al., 2005); 2- Apulian Platform (Morsilli and Bosellini, 1997).

The structural setting of the Adriatic Platform was caused by Toarcian extensional tectonics (Fig. 2.16) that resulted in the formation of the Adriatic Basin (Vlahović et al., 2005). It was a large platform (more than 700 km long) with relics cropping out in Slovenia, Croatia, Bosnia Herzegovina, Montenegro and Albania (Vlahović et al., 2005).

Oxfordian deposits are almost uniform and mostly of lagoonal origin, except for marginal parts where high-energy grainstone prevailed (Vlahović et al., 2005). Bedded micritic cherty limestone with abundant sponge spicules occurs. This facies indicates deteriorated conditions for carbonate production probably due to more eutrophic seawater (Turnšek et al., 1981; Turnšek, 1997).

The Apulian Platform was a wide carbonate platform that during the Late Jurassic faced the Adriatic and the Ionian pelagic basins (Morsilli and Bosellini, 1997; Bosellini et al., 1999; Santantonio et al., 2013). The Upper Jurassic-Lower Cretaceous succession (Monte Sacro sequence, Gargano Promontory, Southern Italy), ranging from Oxfordian to Valanginian, was deposited within an unrimmed, distally-steepened ramp with a gentle profile (Fig. 2.18A; Morsilli and Bosellini, 1997). A peritidal inner platform environment faced an internal margin with ooidal and skeletal shoals (Morsilli and Bosellini, 1997). Seaward a reef flat with small coral patch reefs and a bioconstructed reef front separated the ooidal shoals from the deeper external margin formed by stromatoporoid-sponge (*Ellipsactinia, Sphaeractinia*) rich deposits (Morsilli and Bosellini, 1997; Russo and Morsilli, 2007).

2.3.4.2.2 Kimmeridgian

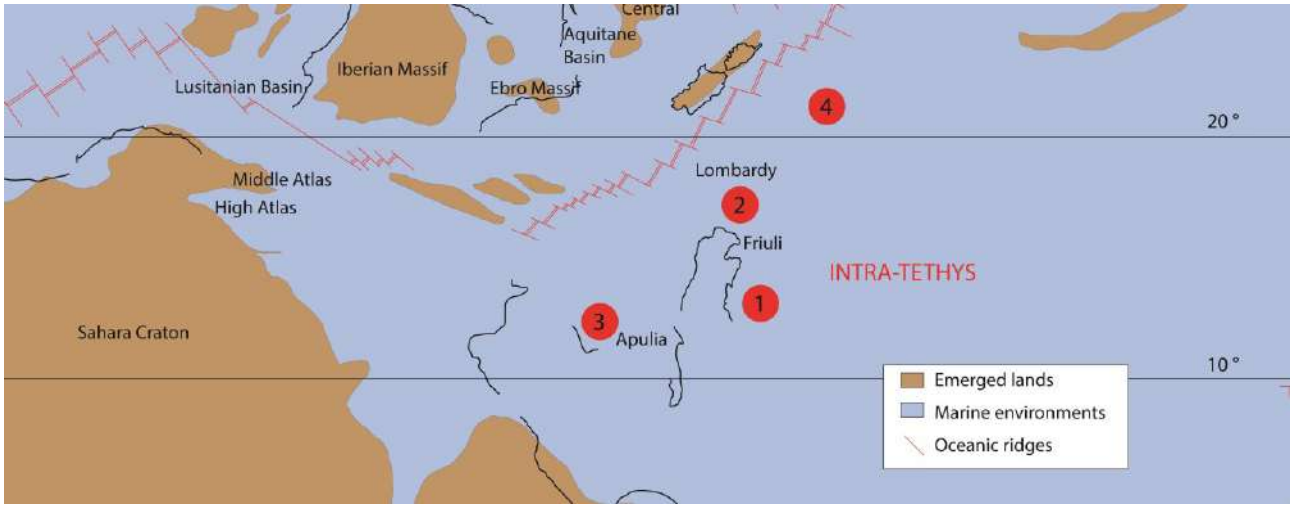

Figure 2.17 Paleogeographic map of the intra-Tethys realm during Kimmeridgian, with the position of the case study mentioned in the text:1 - Adriatic Platform (Tišljar et al., 2002; Vlahović et al., 2005); 2 - Friuli Platform (Picotti and Cobianchi, 2017); 3 - Latium- Abruzzi Platform (Rusciadelli et al., 2011); 4 - Plassen carbonate platform, Austria (Schlagintweit and Gawlick, 2008). Redrafted after Dercourt et al. (2000).

During Kimmeridgian (Fig. 2.17) in the Adriatic Platform syn-sedimentary tectonics led to complex palaeogeographical and depositional facies relationships (Tišljar et al., 2002; Vlahović et al., 2005). A major part of the platform remained within restricted lagoonal settings, whereas some areas where uplifted and karstified (Turnšek, 1997; Vlahović et al., 2005). In the central part of the platform deeper depositional areas where formed as relatively shallow intraplatform troughs (Velić et al., 2002; Vlahović et al., 2005; Bucković, 2008). The margin of the troughs were ideal places for the development of coral-hydrozoan reefs, as far as the NE margin of the platform characterized by hydrozoan-coral-stromatoporoid barrier reefs and bioclastic-ooidal shoals (Turnšek, 1997; Dragičević and Velić, 2002; Vlahović et al., 2005). In the interior part of the platform, patch reefs developed (Turnšek, 1997). Along the SW edge, carbonate sand bars were the most important features (Vlahović et al., 2005). The coral association included massive *Amphiastraea, Comoseris, Clausastraea, Complexastraea, Fungiastraea, Microphyllia, Microsolena, Myriophyllia, Pseudocoenia, Solenocoenia, Actinaraea, Heliocoenia, Meandrophyllia, Stylina, Thamnasteria, Isastraea, branching Calamophylliopsis, Donacosmilia, Apocladophyllia, Dermosmilia, Placophyllia, Stylosmilia, Allocoenia, Diplaraea, Goniocora, Thecosmilia* and solitary coral genera *Epistreptophyllum, Axosmilia, Montlivaltia* (Turnšek, 1997). Stromatoporoids were important and environmentally well differentiated (outer, inner and back reef zone) (Turnšek et al., 1981; Turnšek, 1997).

Upper Jurassic reefs represented by *Ellipsactinia* limestones have also been reported from the Friuli Platform, Southern Alps (Italy) by Picotti and Cobianchi (2017).

In the Central Apennine area during the Late Jurassic isolated platforms were rimmed by wide reef areas with highly diverse biotic communities dominated by corals and stromatoporoids (Colacicchi and Praturlon, 1965; Rusciadelli et al., 2011). In particular, the Latium-Abruzzi platform was well developed during the Kimmeridgian and Tithonian times (Chiocchini et al., 2008). In this area, distally steepened ramps with a gentle profile and clear reef zonation at the margin developed. Stromatoporoids colonized the high-energy reef crests, whereas corals and chaetetids colonized the deeper protected back-reef environments (Fig. 2.18B; Rusciadelli et al., 2011).

At the beginning of the Jurassic the Austroalpine shelf drowned completely and basinal conditions prevailed until the early Cretaceous, with the only exception being the Plassen carbonate platform (Mandl, 1999). Shallow-water carbonate deposition in this area lasted from Kimmeridgian to Berriasian (Gawlick and Schlagintweit, 2006). The reconstruction from the works by Gawlick and Schlagintweit (2006) and Schlagintweit and Gawlick (2008) pointed out the presence of a gently dipping margin with different bioconstructions in different positions (Fig. 2.18C). *Ellipsactina* and microsolenoid corals formed biostromes in the upper slope, whereas stromatoporoid bioconstructions occurred in back-reef environments (Schlagintweit and Gawlick, 2008). A particular type of bioconstruction occurred in this setting: cement-microencruster boundstone, formed by several microencrusters and a high percentage of syn-sedimentary cementation (Schlagintweit and Gawlick, 2008). These bioconstructions occupied an upper fore-reef slope, just seaward of coral-stromatoporoid patch reefs and bindstone with *Bacinella* (Schlagintweit and Gawlick, 2008).

A. Apulian Platform (Morsilli and Bosellini, 1997)
Oxfordian- Lower Cretaceous

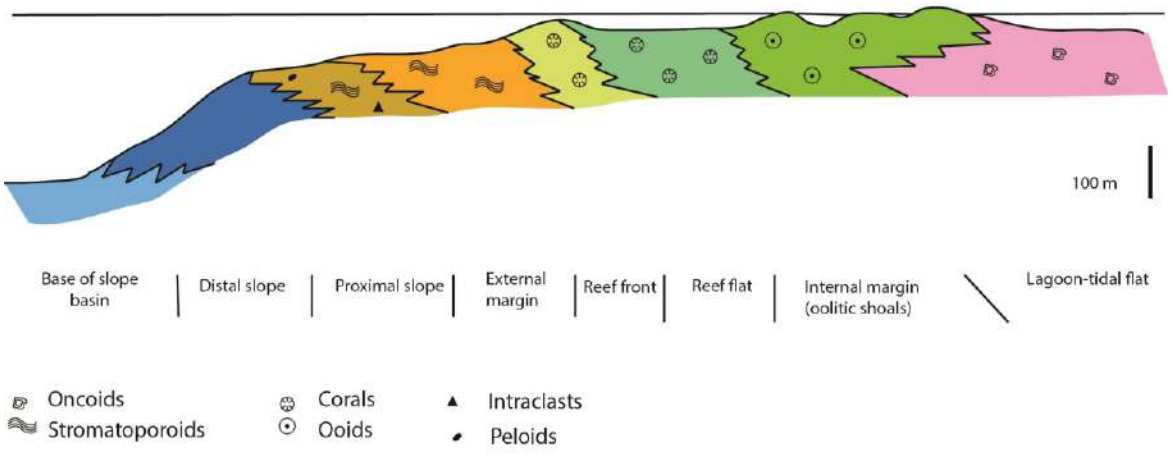

B. Latium-Abruzzi Platform (Rusciadelli et al., 2011)
Kimmeridgian-Tithonian

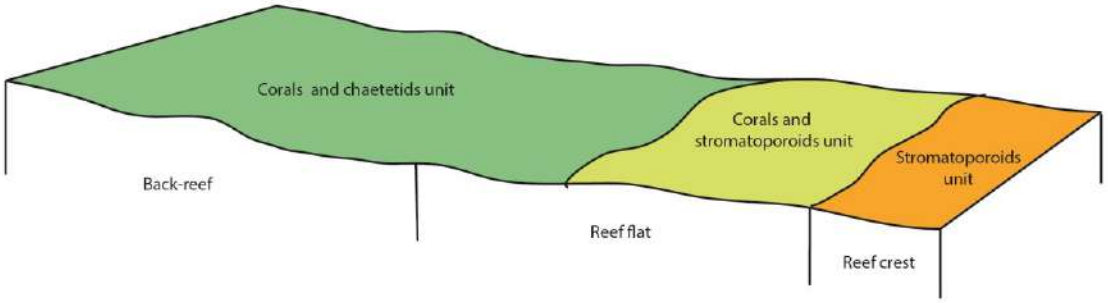

C. Plassen carbonate Platform (Schlagintweit and Gawlick, 2008)
Kimmeridgian- Berriasian

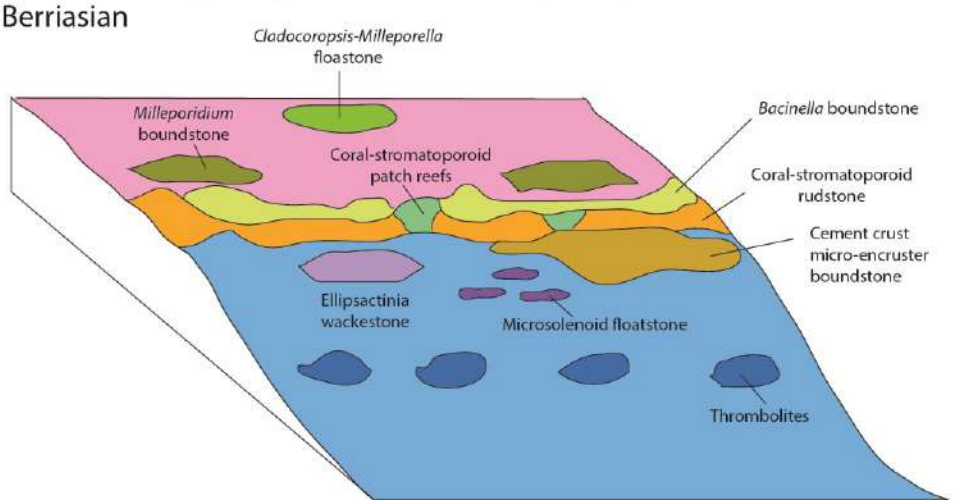

Figure 2.18 Depositional profile of the Upper Jurassic-Lower Cretaceous Apulian carbonate platform redrafted after Morsilli and Bosellini (1997). B) Depositional model proposed for the Kimmeridgian-Tithonian Latium-Abruzzi carbonate platform redrafted after Rusciadelli et al. (2011). C) 3D facies model of the Plassen carbonate Platform redrafted after Schlagintweit and Gawlick (2008).

2.3.4.2.3 Tithonian

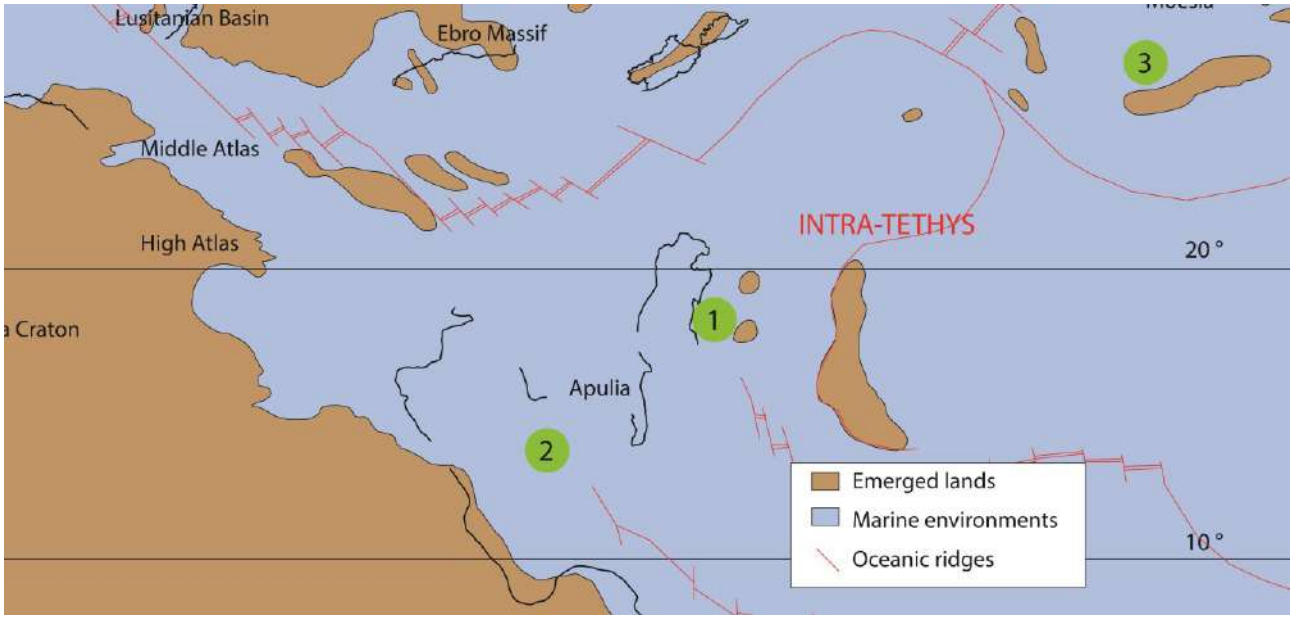

Figure 2.19 Palaeogeographic map of the intra-Tethys realm during Tithonian time, showing the position of the case studies mentioned in the text: 1 - Adriatic carbonate platform (Vlahović et al., 2005); 2 - North Western Sicily (Basilone and Sulli, 2016); 3 - Štramberk reef complex (Hoffmann et al., 2017). Redrafted after Dercourt et al. (2000).

During Tithonian (Fig. 2.19) in the Adriatic Platform the Kimmeridgian intraplatform basins were completely filled by progradation from the surrounding reefs and shallow-water depositional environments re-established over almost the entire platform. Thus, there was a regionally important deposition of peritidal-lagoonal algal wackestone, dominated by dasycladalean algae, labelled as *Clypeina-Campbelliella* limestones (Vlahović et al., 2005).

A Tithonian-Valaginian succession of shallow-water carbonates crops out in North Western Sicily in the Palermo Mountains (Basilone, 2009; Basilone and Sulli, 2016). The shallow rimmed shelf consisted of a wide protected lagoon with coral patch reefs, bordered landward by a tidal flat and seaward by a barrier reef (Fig. 2.20; Basilone and Sulli, 2016). In the tidal flat, large stromatolite microbial mats developed and cyclically were subjected to subaerial exposure. Local interior sand bars-barrier island permitted the development of restricted bays. The reef complex consisted of a reef flat dominated by corals and an outer reef wall dominated by stromatoporoids, in particular *Ellipsactinia* (Basilone and Sulli, 2016). Syn-sedimentary tectonic is well-documented and high subsidence rates created accommodation spaces during a sea-level fall. The resulting irregular sea-bottom enhanced carbonate facies variability (Basilone and Sulli, 2016).

An exception among the intra-Tethys trend is the Tithonian-Berriasian Štramberk reef complex in Czech Republic in which corals outcompeted stromatoporoids as the main reef builders (Hoffmann et al., 2017). Coral assemblages, strongly dominated by phaceloid possibly non-photosymbiontic corals, imply an increased nutrient level (Kolodziej et al., 2012). In the Štramberk Limestone

calcareous sponges contributed to the boundstone framework mostly as a millimetre to centimetre sized crust (Hoffmann et al., 2017).

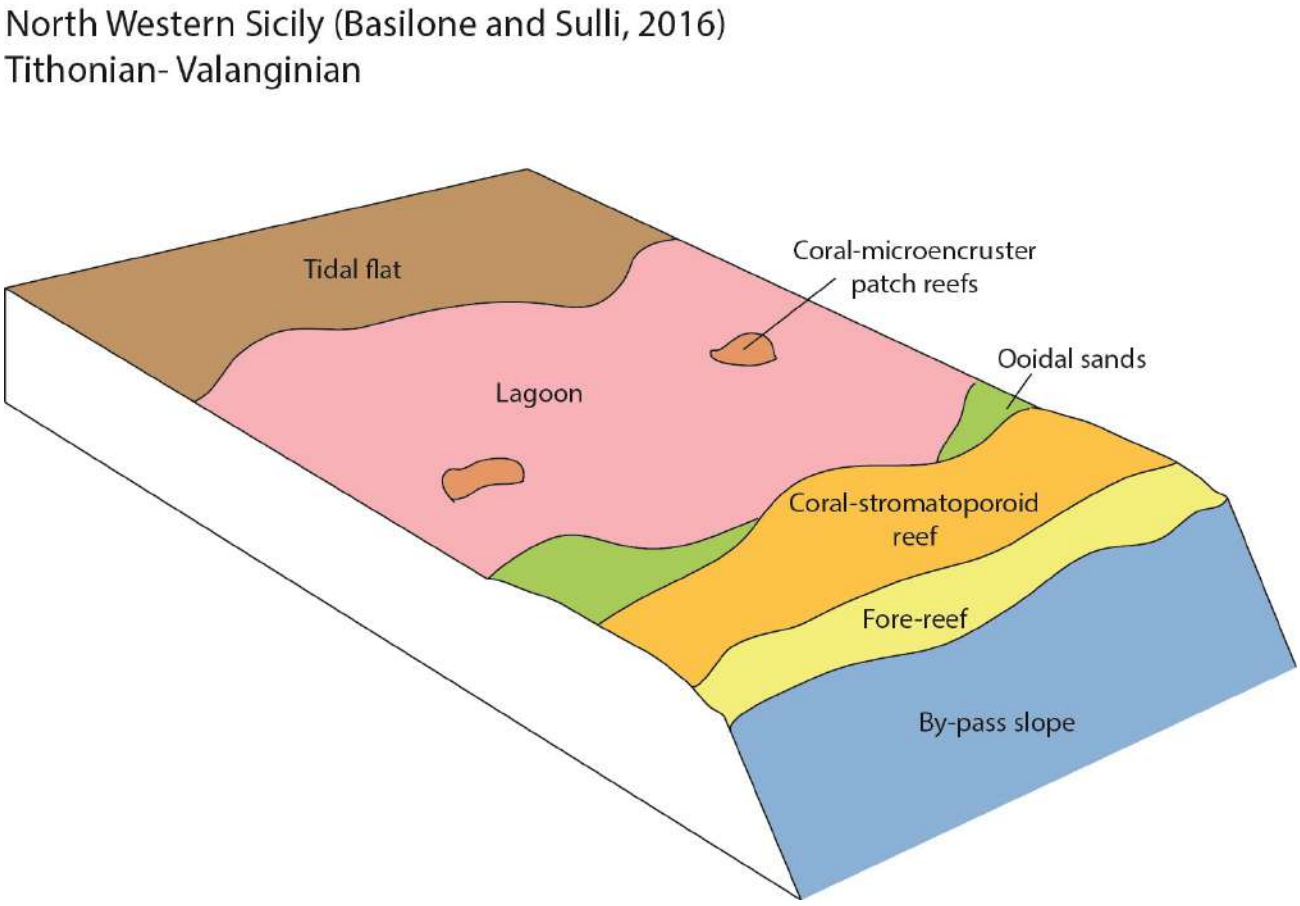

Figure 2.20 Redrafted facies model proposed by Basilone and Sulli (2016) for the Tithonian-Valanginian carbonate platfom in North Western Sicily.

2.3.4.3 Southern Tethys

In the southern Tethys realm, the most extensive Jurassic carbonate deposits are located in the Arabian Peninsula. The Middle and Upper Jurassic carbonates of Saudi Arabia were deposited on a very extensive submarine epeiric platform (Fig. 2.21), in shallow-water environments with adjacent deeper intra-shelf basins (Al-Husseini, 1997; Hughes, 2004; Hughes et al., 2008).

2.3.4.3.1 Oxfordian

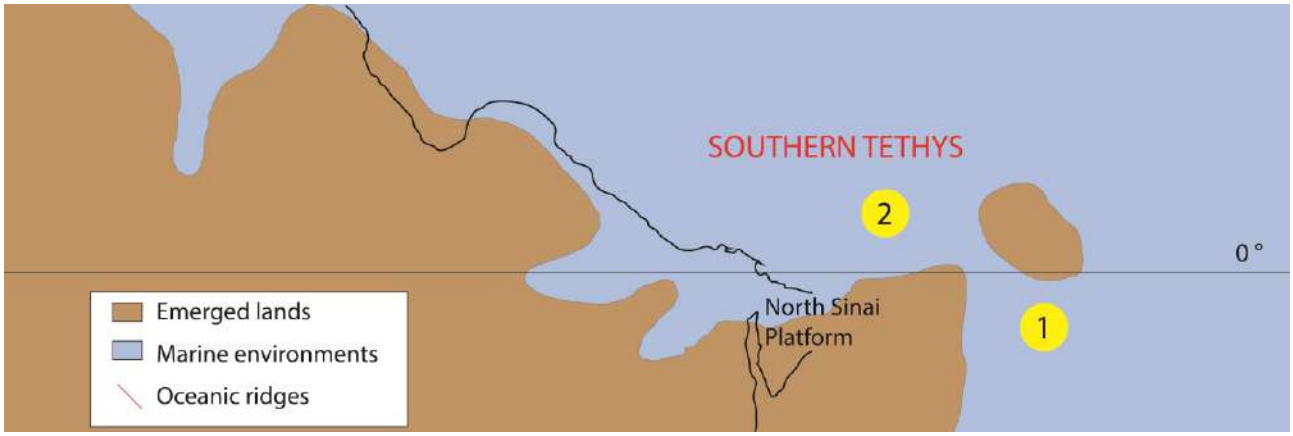

Figure 2.21 Palaeogeographic map of the Southern Tethys realm during Oxfordian time showing the location of the case studies mentioned in the text: 1 - Saudi Arabia (El-Sorogy et al., 2018); 2 - Lebanon (Nader and Swennen, 2004). Redrafted after Dercourt et al. (2000).

During the Oxfordian time (Hanifa Fm.), the intraplatform basins were flanked by stromatoporoid banks and ooidal shoals (Hughes et al., 2008; El-Sorogy et al., 2018) that created sheltered lagoon environments faced by tidal flat influenced by fair-weather wave base (El-Sorogy et al., 2018). Corals were poorly represented compared to stromatoporoids (Hughes et al., 2008) but they sometimes formed build-ups (El-Sorogy et al., 2018). This was probably due to the high water temperatures and restriction of the Arabian Platform during Oxfordian that negatively affected coral growth. Although several studies pointed out that corals were not important builders in the Arabian platform, Fallatah and Kerans (2018) proposed for the Oxfordian Hanifa Fm. a carbonate ramp depositional model with coral-stromatoporoid bioconstructions (bioherms and biostromes) in middle ramp environment (Fig. 2.23A).

In the Lebanon domain, near the palaeoequator (Fig. 2.21), an epicontinental carbonate platform developed during Bathonian, Callovian and Oxfordian with coral reefs. This platform was subaerially exposed in the Kimmeridgian due to extensional tectonic related to a rifting phase (Nader and Swennen, 2004; Collin et al., 2010).

In NE Iran during Oxfordian there was the development of a rimmed carbonate platform with microbial dominated reefs and patch reefs at the platform margin with a nearby deep-marine basin (Kavoosi et al., 2009). During the late Kimmeridgian, an ooidal dominated ramp developed in the Kopet Dagh Basin. The transition from a rimmed shelf to a carbonate ramp was accompanied by climate changing from arid in the early Kimmeridgian to temperate during late Kimmeridgian.

2.3.4.3.2 Kimmeridgian

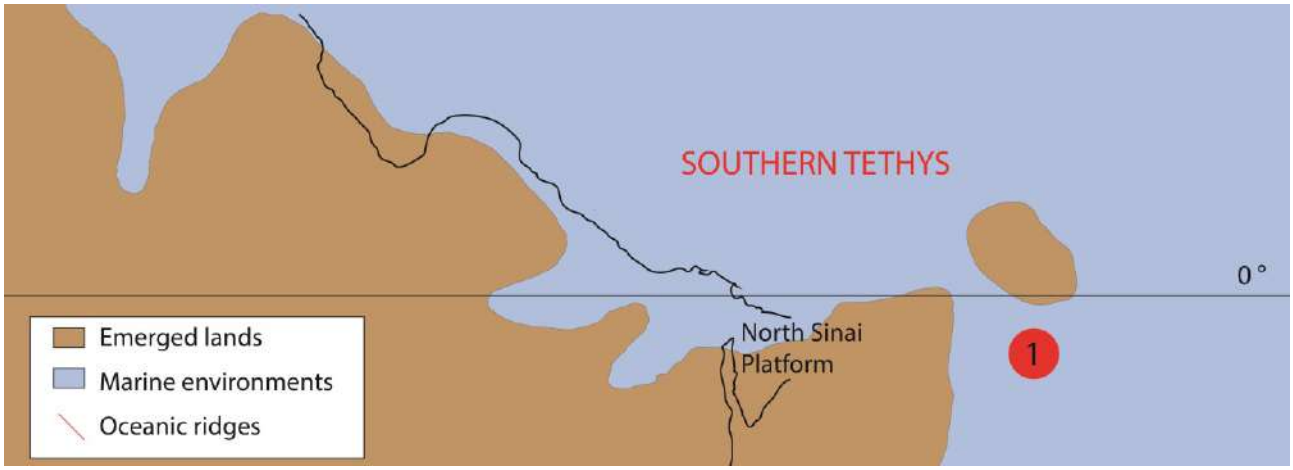

Figure 2.22 Palaeogeographic map of the Southern Tethys realm during Kimmeridgian time, showing the position of the case studies mentioned in the text: 1- Saudi Arabia (El-Asmar et al., 2015). Redrafted after Dercourt et al. (2000).

During the Kimmeridgian (Fig. 2.22), in the Arabian epeiric platform intrashelf basins and carbonate ramp systems are reported (Roberston Handford, 2002). During a sea-level fall (2nd order sequence) that started in the Oxfordian the Arab Fm. and the Arab D reservoir were deposited in a low relief carbonate ramp with ooidal grainstone belts and coral-stromatoporoid biostromes and bioherms (Roberston Handford, 2002). According to Al-Awwad and Collins (2013) it was a prograding, gently sloping, arid, shallow rimmed carbonate shelf with stromatoporoids wave resistant reefs that sheltered a lagoon with dasyclad algae and *Cladocoropsis* meadows. The climate was particularly arid and led to the formation of sabkhas, large anhydrite deposits and hypersaline peritidal facies (Roberston Handford, 2002; Al-Awwad and Collins, 2013). The epeiric seawater was probably overheated and the nutrient supply decreased landward (Al-awwad and Collins, 2013). A depositional model for the Kimmeridgian Jubaila Fm. was provided by El-Asmar et al. (2015) that consists of a carbonate ramp with peloidal-bioclastic facies in the inner ramp and *Cladocoropsis* packstone-grainstone in the proximal portion of the middle ramp (Fig. 2.23B; El-Asmar et al., 2015).

Microbial-coral-stromatoporoid reefs are reported from the Kimmeridgian of central Oman, deposited on a platform margin influenced by extensive tectonic (Pratt and Smewing, 1990).

In NE Iran, during late Kimmeridgian there was the transition from a microbially-dominated rimmed shelf to an ooid-rich carbonate ramp (Kavoosi et al., 2009). This transition was associated with a climate change from arid to temperate conditions (Kavoosi et al., 2009).

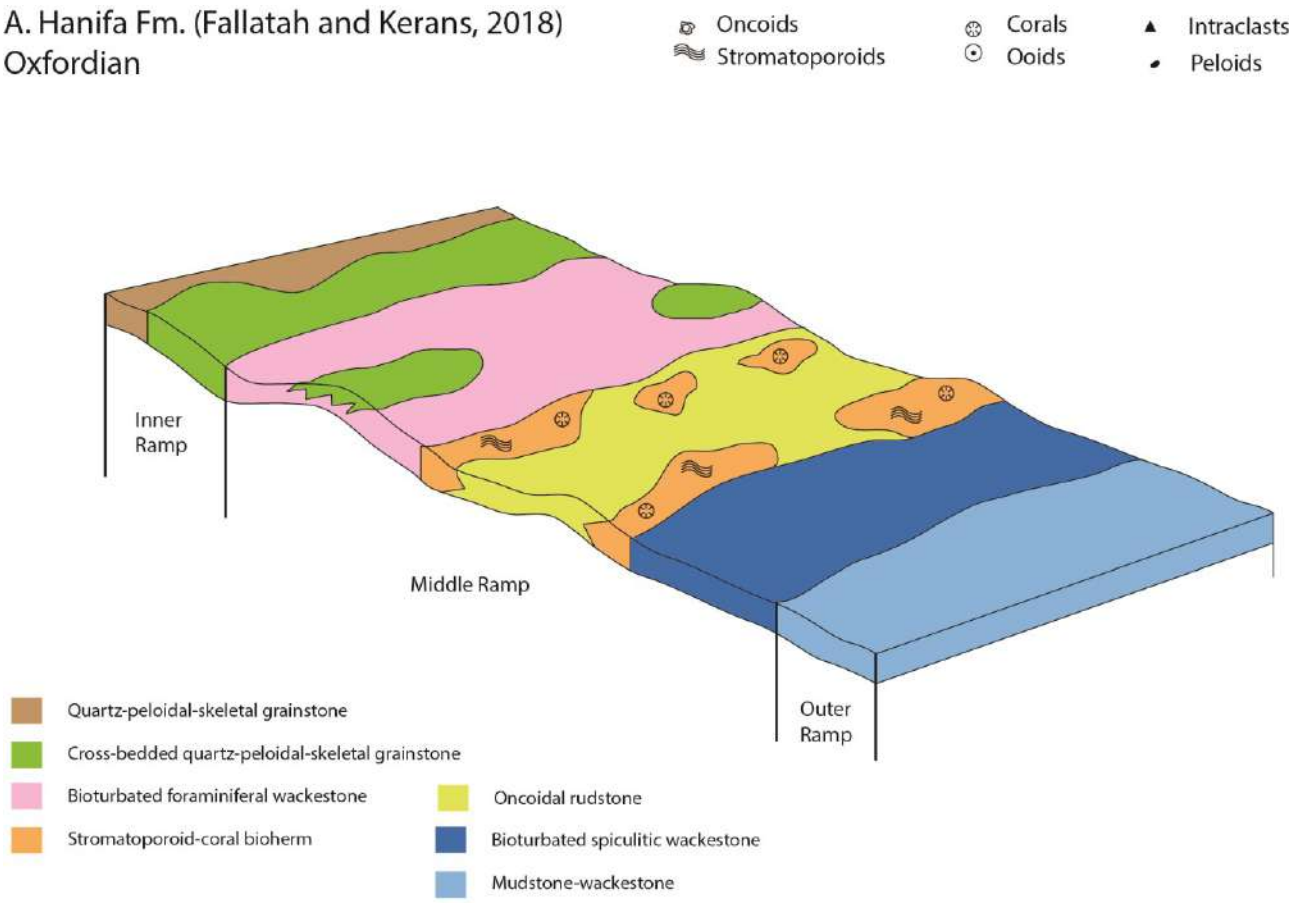

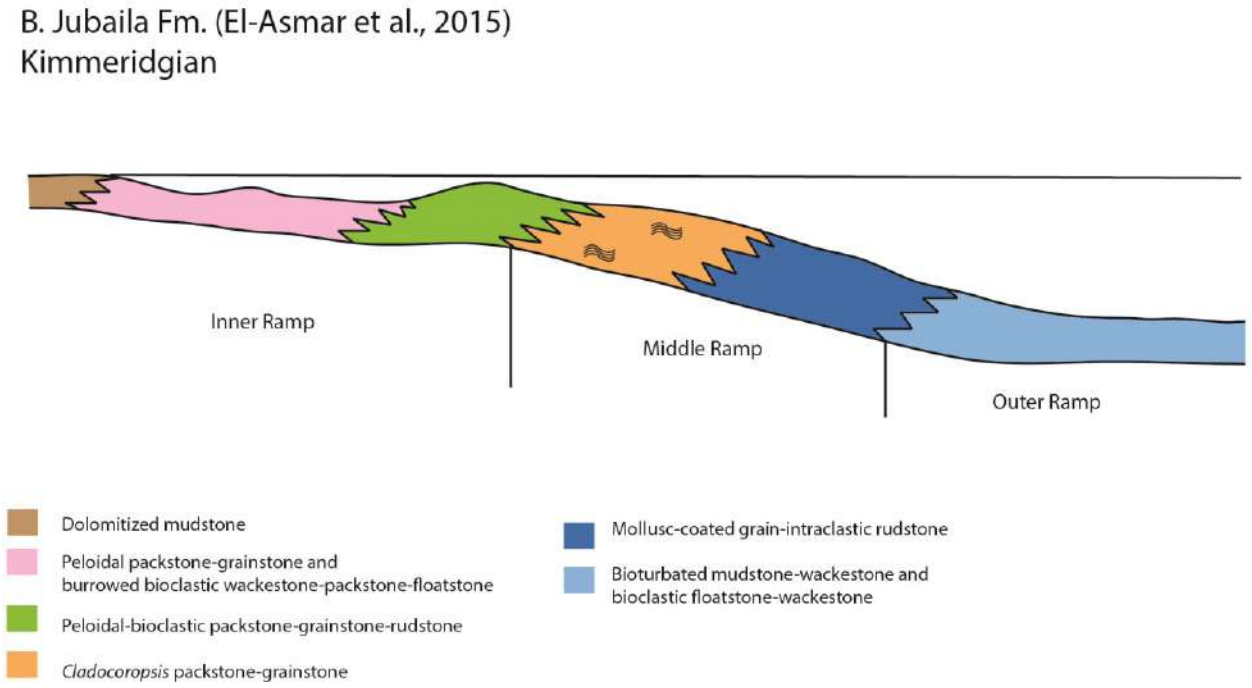

Figure 2.23 A- Depositional model for the Hanifa Fm. (Oxfordian of Saudi Arabia), proposed by Fallatah and Kerans (2018). B- Depositional profile of the Jubaila Fm. (Kimmeridgian of Saudi Arabia) suggested by El-Asmar et al. (2015).

2.3.4.4 Atlantic Province

During the Late Jurassic, the North Atlantic was still a narrow proto-ocean (Fig. 2.24) with a connection to the Tethys Ocean (Leinfelder et al., 2002). In this realm, coral-microbial-sponge reefs developed in different structural settings such as homoclinal ramp, distally-steepened ramp and high-relief platforms (Leinfelder, 1993a).

2.3.4.4.1 Oxfordian-Kimmeridgian

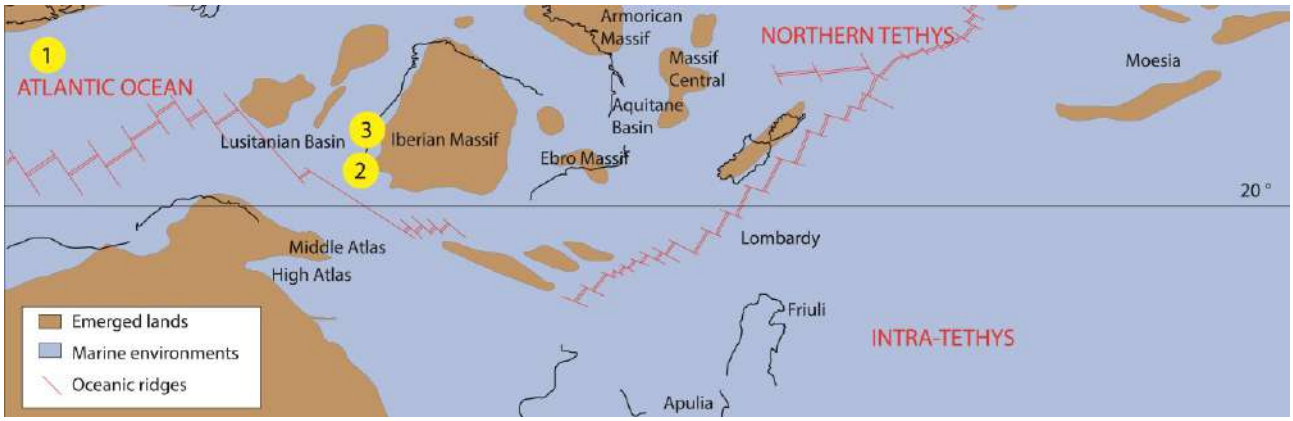

Figure 2.24 Palaeogeographic map of the Atlantic province during Oxfordian-Kimmeridgian, showing the position of the case studies mentioned in the text: 1 - Abenaki Platform, Nova Scotia, Canada (Jansa et al., 1988); 2 - Algarve Basin, Portugal (Leinfelder, 1993a); 3 - Ota Reef, Portugal (Leinfelder, 1992). Redrafted after Dercourt et al. (2000).

In the Western part of the North Atlantic realm Upper Jurassic carbonate platforms were investigated in the subsurface. Along the Gulf Coast, within the Oxfordian Smackover Fm. there are different types of build-ups with considerable variation along the depositional profile (Crevello and Harris, 1984). On carbonate ramps microbial mounds and sponge-coral-microbial build-ups with siliceous and calcified sponges, corals and associated bioclastic debris developed (Baria et al., 1982; Crevello and Harris, 1984). The sponge-coral-microbial build-ups grew in moderately wave agitated environment and show variability in composition related to bathymetry, with the increase in siliceous sponge content in deeper setting and increase in coral content in shallower environments (Crevello and Harris, 1984). Depositional models proposed for the Smackover Fm. show ooidal shoals in the inner ramp, inward with respect to sponge-coral-microbial reefs (Fig. 2.25A; Crevello and Harris, 1984).

A similar situation prevailed along the shelf of eastern Canada (Nova Scotia, Abenaki Fm.) during the Oxfordian and Kimmeridgian, but in a different structural setting. At the margin of a high-relief carbonate platform coral-chaetetid microbial reefs developed facing a steep slope with microbial mounds (Jansa et al., 1988; Pratt and Jansa, 1988).

The eastern part of the North Atlantic province (Portugal) is represented by a wide variety of reefs developed in a diverse spectrum of structural settings. In carbonate ramps, coral reefs with debris piles developed in the distal part of the inner ramp, mixed coral-siliceous sponge reefs were formed in the middle ramp and microbial mounds or siliceous sponge facies occurring mostly as meadows occupied the outer ramp (Leinfelder, 1993a; Leinfelder et al., 1993). In the Algarve Basin during Oxfordian and Kimmeridgian times (Fig. 2.25B), highly diverse coral-stromatoporoid reefs thrived in the shallow inner ramp, whereas below fair-weather wave base lithistid biostromes and microsolenoid boundstone accumulated. Microbial mounds with abundant *Crescentiella* and serpulids colonized the deeper outer ramp settings (Leinfelder, 1993a). In Portugal reefs occurred also on coastal siliciclastic shelves. The proximal part of these shelves could contain coral meadows and patch reefs (Leinfelder, 1993b). In Ota (Portugal) during the Kimmeridgian a coral-microbial reef characterized by large quantity of debris being bounded by microbial crusts and *Crescentiella*, developed on shallow platform margin (Fig. 2.25C). Mixed coral-siliceous sponge reefs grew in deeper settings (Leinfelder, 1992). The outer slope is represented by microbial-coral-siliceous sponge biostromes with crinoids (Leinfelder, 1992; Nose, 1995). In most cases, by-pass margins and escarpments were caused by syn-sedimentary tectonics. Isolated coral build-ups situated on local structural highs, commonly within siliciclastic settings occur in the tectonically active Atlantic type margin basins such as the Lusitanian Basin of west-central Portugal (Leinfelder, 1993b).

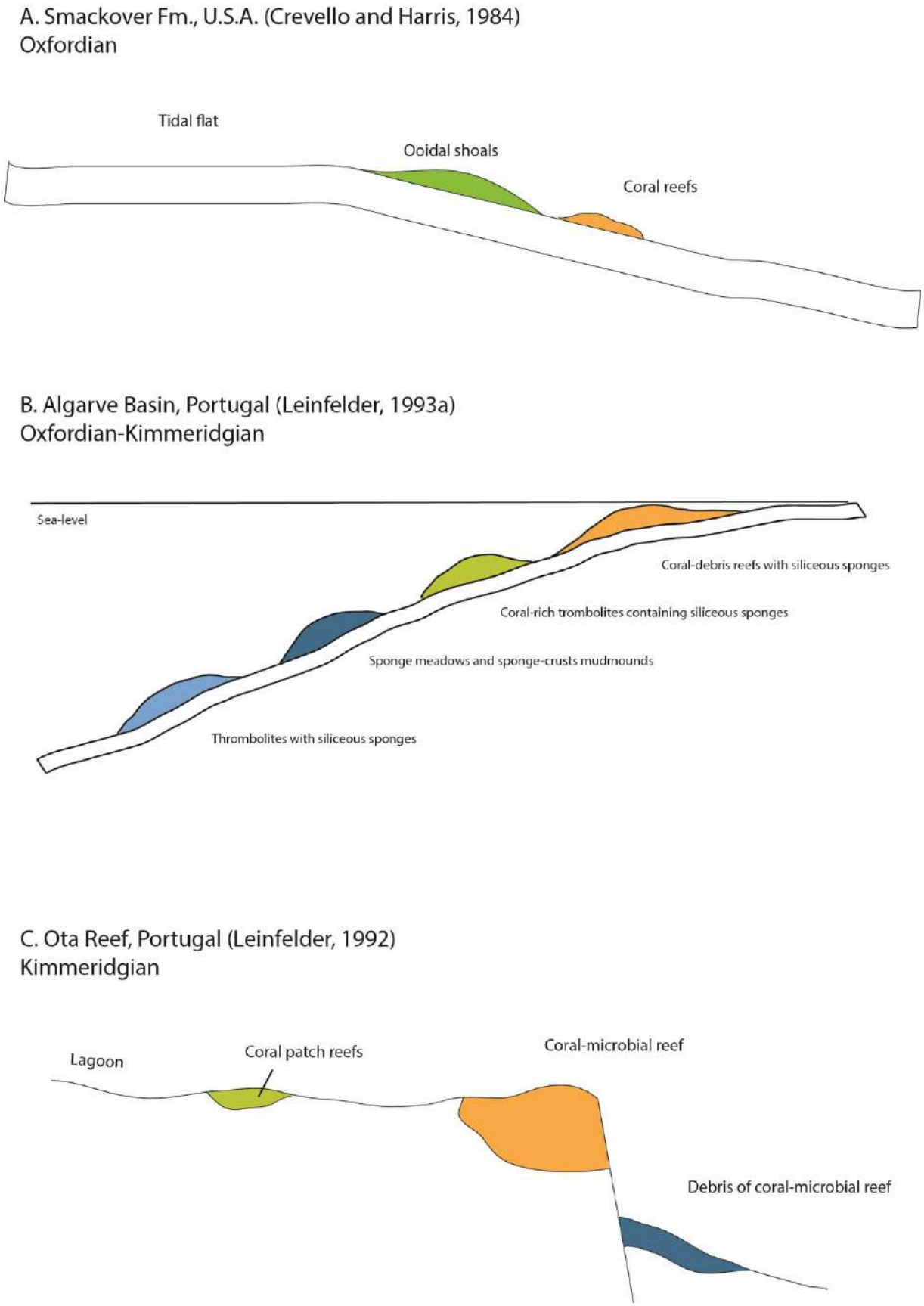

Figure 2.25 A) Depositional sketch of the Oxfordian Smackover Fm. in the subsurface of U.S. Gulf Coast (redrafted after Crevello and Harris, 1984). B) Depositional profile of the Ota Reef (Portugal) showing the location of different reef types (redrafted after Leinfelder, 1992). C) Depositional sketch showing the position of different reef types in the Oxfordian-Kimmeridgian of the Algarve Basin (Portugal, redrafted after Leinfelder, 1993a).

Chapter 3

Geological setting

3.1 Tectonic and palaeogeography

The 650 m thick Middle Jurassic to Lower Cretaceous carbonate succession cropping out in eastern Sardinia (Orosei Gulf, Fig. 3.1) accumulated on the northern passive margin of the Alpine Tethys (Dercourt et al., 2000; Costamagna, 2016ab) at tropical latitude (Fig. 3.2), from 20° to 30° N (Fourcade et al., 1993; Dercourt et al., 2000; Muttoni et al., 2018). The interplay between the geodynamic evolution of the northern passive margin of the Alpine Tethys, regional tectonics and eustatic sea-level fluctuations strongly influenced the sedimentary evolution of the eastern Sardinia carbonate succession (Jadoul et al., 2010; Jadoul, 2018).

In the Middle Jurassic, there was the exhumation of the Hercynian crystalline basement due to extensional tectonics along the European passive margin (Zattin et al., 2008). A link between the opening of the Alpine Tethys and the beginning of sedimentation in eastern Sardinia was proposed by Dieni and Massari (1985). It is suggested that the Alpine Tethys opening led to an extensional tectonic phase in the Early-Middle Jurassic recorded with the deposition of the siliciclastic continental to marine transgressive deposits above the Hercynian basement (Genna Selole Fm., Costamagna et al., 2007; Costamagna, 2016b). The extensional tectonic phase linked with the rifting and opening of the Alpine Tethys was also recorded in other Lower Jurassic successions from the European margin, such as in the Peloritani Mountains (Sicily) and the northern Calabria (Santantonio and Carminati, 2011; Santantonio et al., 2016; Santantonio and Fabbi, 2020). Vardabasso (1959) suggested that in Sardinia, from the Triassic time, there was a N-S oriented (with respect to present-day coordinates) continental structural high separating two different palaeogeographic domains, eastern and western Sardinia (Fig. 3.2). More recently, Costamagna and Barca (2004) and Costamagna (2016b) proposed that this separation was effective only in the Middle Jurassic, whereas Berra et al. (2019) demonstrated that it was effective during all the Mesozoic.

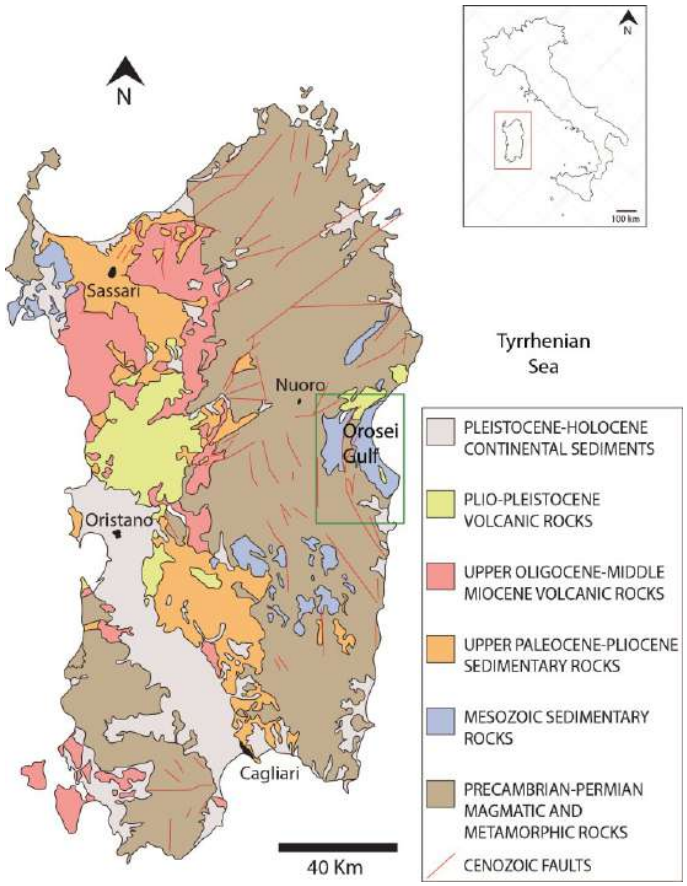

Figure 3.1 Simplified geological map of Sardinia, with the distribution of the Middle Jurassic to Berriasian carbonate succession in eastern Sardinia. The study area is marked by a green box (modified after Carmignani et al., 2008).

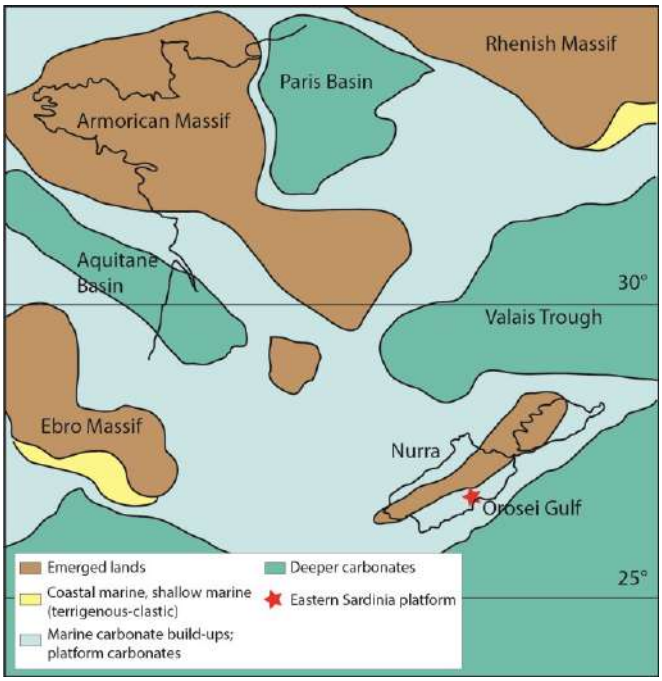

Figure 3.2 Palaeogeographic map showing the position of the eastern Sardinia carbonate platform during the Late Jurassic. Redrafted after Dercourt et al. (2000).

3.2 Lithostratigraphy

The stratigraphy of the Middle Jurassic-Berriasian carbonate succession of the Orosei Gulf (Fig. 3.1) was widely studied by several authors. Amadesi et al. (1961) proposed the first lithostratigraphic framework, refined by Massari (1968) and Dieni and Massari (1985). Costamagna et al. (2007) and Costamagna (2016a) proposed alternative lithostratigraphic subdivision and stratigraphic interpretation of the eastern Sardinia carbonate succession. An updated lithostratigraphic framework was provided by Jadoul et al. (2009, 2010), Casellato et al. (2012) and Jadoul (2018) with the introduction of new lithostratigraphic units and redefinition of previously identified formations (Fig. 3.3).

3.2.1 Genna Selole Fm.

The Genna Selole Fm. was described for the first time by Dieni et al. (1983). It consists of three lithofacies described by Costamagna (2016a): a) the Laconi-Gadoni lithofacies corresponds to massive to poorly stratified quartzose conglomerate and subordinated sandstone lenses interpreted as distal alluvial fan/braided river deposits; b) the Nurri-Escalapiano lithofacies consists of well-stratified alternations of fine sandstone, clayey siltstone and siltstone, linked to alluvial, palustrine and upper delta plains; c) the Ussai-Perdasdefogu lithofacies consists of well-stratified alternations of sandstone, marlstone, marly limestone and limestone with wood coal horizons, interpreted as deposits of littoral to deltaic, partially carbonate environments. The Genna Seloloe Fm. was deposited under an active extensional tectonic regime in a warm-humid climate, which promoted the development of lateritic paleosoils (Costamagna, 2016a). The Genna Selole Fm. represents thin discontinuous siliciclastic strata at the top of the Paleozoic Hercynian basement (Fig. 3.3), with a maximum thickness of about 50 m (Costamagna et al., 2007). It passes gradually upward to the Dorgali Fm. (Costamagna et al., 2007). The presence of plants and sporomorphs in dark clays suggested a Bajocian-Bathonian age (Amadesi et al., 1961; Del Rio, 1976, 1984; Dieni et al., 1983). Dieni et al. (2013) interpreted the upper lithofacies (Ussai-Perdasdefogu) of the Genna Selole Fm. as a lower member of the overlying Dorgali Fm. (Perda Liana Mb.), suggesting an already well-established marine environment. Costamagna (2016a) considered the Ussai-Perdasdefogu lithofacies as part of the Genna Selole Fm., suggesting the persistence of ephemeral palustrine environments. Jadoul et al. (2010) proposed a separation of the entire Genna Selole Fm. from the Dorgali Fm.

depositional cycle due to diffuse indicators of subaerial exposure in the upper lithofacies that led to significant stratigraphic gaps during Callovian times.

3.2.2 Dorgali Fm.

The Dorgali Fm. was introduced by Amadesi et al. (1961) and revised by Jadoul et al. (2009, 2010) who gave to this unit a new lithostratigraphic meaning (Jadoul et al., 2010). The Dorgali Fm. *sensu* Amadesi et al. (1961) is the basal unit of the Eastern Sardinia carbonate succession and consists of brownish dolostone of Bathonian-Oxfordian age. Instead, according to Dieni and Massari (1985) and Costamagna et al. (2007) it represents all the inner platform deposits of Bathonian-Kimmeridgian age and for Dieni and Massari (1985) is partially coeval to the Mt. Tului and S'Adde Limestone.

The Dorgali Fm. (*sensu* Jadoul et al., 2009, 2019) consists of cross-laminated dolostone and conglomerate with quartz grains and laminated massive ooidal dolomitic limestone, associated with planar-laminated oo-crinoidal dolomitic limestone (Jadoul et al., 2010). These facies are interpreted as deposited in high-energy shoals, enclosing mud-dominated lagoonal facies (Jadoul et al., 2010).

The thickness of these deposits is highly variable, from more than 150 m to 10-40 m in the Baunei Supramonte (Jadoul, 2018) to completely absent (Jadoul et al., 2010). The Dorgali Fm. overlies with an unconformity the Hercynian basement (Jadoul et al., 2010) and locally with a gradual transition lenses of the Genna Selole Fm. (Fig. 3.3; Costamagna et al., 2007; Costamagna, 2016a). The upper boundary corresponds to a sharp lithological change, locally characterized by few Fe-hardground surfaces (Jadoul et al., 2010; Casellato et al., 2012). The finding of ammonites and gastropods allow placing the transition from siliciclastic-marine sedimentation to carbonate marine sedimentation, thus the base of the Dorgali Fm., to the Bathonian (Amadesi et al., 1961). Casellato et al. (2012) suggested that the transition to the overlying Mt. Tului Fm. and outer ramp carbonates is upper Bathonian-lower Callovian in the northern portion of the Orosei Gulf, whilst it is upper Callovian-lower Oxfordian in the southern part of the Orosei Gulf.

Jadoul (2018) recognized two different units within the Dorgali Fm. (Upper and Lower Dorgali Fm.), separated by a depositional hiatus marked by regional Fe-rich hardgrounds (upper Bathonian), associated with siliciclastic input. The Upper Dorgali Fm. is thinner and only locally dolomitized with few regional hardgrounds and firmgrounds (middle-upper Callovian hiatus).

3.2.3 Baunei Fm.

The Baunei Fm. was described for the first time by Jadoul et al. (2009) as consisting of thin-bedded (10 cm thick), calcilutites with chert nodules and intercalations of marly limestone, locally dolomitized and bioturbated (Jadoul et al., 2009, 2010). These lithofacies were interpreted as deposited in a basinal area (Jadoul et al., 2009, 2010) or middle-outer ramp setting (Casellato et al., 2012). The total thickness of the Baunei Fm. varies from 30 to 100 m (Fig. 3.3; Jadoul et al., 2010). The lower boundary with the Dorgali Fm. is sharp and marked by a Fe-Hardground surface, as well as the upper boundary with the Mt. Tului Fm., marked by the occurrence of resedimented calcarenites with ooids and crinoids (Jadoul et al., 2010). The base of this unit was dated to the Oxfordian according to the dynoflagellate association found in marly beds (Jadoul et al., 2009). The top of the Baunei Fm. is not younger than early Tithonian, according to its stratigraphic position and the biostratigraphic data from the Pedra Longa Fm. (Jadoul et al., 2009).

3.2.4 Mt. Tului Fm.

The Mt. Tului Fm. was one of the units initially described by Amadesi et al. (1961) and revised by Jadoul et al. (2009, 2010). The first definition of the Mt. Tului Fm. comprised massive ooidal calcarenites and bedded calcilutites of Callovian-Kimmeridgian age (Amadesi et al., 1961). Dieni and Massari (1985) considered this unit in the same way but separated the fine-grained bedded carbonates in a new formation (S'Adde Limestone). Costamagna et al. (2007) considered the Mt. Tului Fm. as a lithofacies of the Genna Silana Fm. and interpreted it as a platform margin facies.

The Mt. Tului Fm. (*sensu* Jadoul et al., 2009, 2010) consists of ooidal and oo-crinoidal grainstone passing vertically to massive boundstone with corals and stromatoporoids, ooidal-bioclastic grainstone and floatstone, coral-stromatoporoid rudstone and floatstone with ooidal matrix and ooidal grainstone with coated grains, lumps, oncoids, benthic foraminifers and bioclasts (Jadoul et al., 2009). These facies are interpreted as representative of ooidal-coated grain shoals vertically passing to coral-stromatoporoid reefs interrupted by tidal channels/inlets and ooidal shoals in the leeward side of the platform (Jadoul et al., 2009). The maximum thickness of the unit is 230 m. The base of Mt. Tului Fm. is often dolomitized, consequently the boundary is difficult to identify (Jadoul et al., 2010). In the northern portion of the Orosei Gulf (Mt. Tuttavista, Dorgali; Fig. 3.4), the Mt. Tului Fm. directly overlies the Dorgali Fm. with a boundary marked by bedded 5-7 m thick dolomicrites (Jadoul et al., 2010). In the southern portion of the Orosei Gulf (Baunei Supramonte) the Mt. Tului Fm. overlies the Baunei Fm. with a sharp boundary characterized by the appearance of resedimented calcarenites with

ooids and crinoids (Jadoul et al., 2010). In the southernmost area of the Orosei Gulf, the base of the Mt. Tului Fm. is represented by an intercalation (7-15 m thick) of resedimented oo-bioclastic calcarenites within the Baunei Fm. (Jadoul et al., 2010). The top of the Mt. Tului Fm. is marked in the Urzulei Supramonte area by an erosional surface overlain by the Urzulei Fm. (Jadoul et al., 2009, 2010). In the southernmost area (Baunei, Pedra Longa) the top of the Mt. Tului Fm. is marked by a sharp hardground surface between the Mt. Tului Fm. and the overlying Pedra Longa Fm. (Jadoul et al., 2010). The stratigraphic position, coeval with the Baunei Fm., suggests an Oxfordian age for the base of this unit, whereas biostragraphic data from the Pedra Longa Fm. placed its top in the lower Tithonian (Jadoul et al., 2009).

3.2.5 S'Adde Limestone

The S'Adde Limestone was defined by Dieni and Massari (1985) including part of the previously defined Mt. Tului Fm. (Amadesi et al., 1961). It consists of thin-bedded (15-40 cm thick), fine calcarenites and calcilutites with crinoids and peloids bounded by hardground surfaces (Jadoul et al., 2010; Casellato et al., 2012). These deposits were interpreted as middle-outer ramp facies (Jadoul et al., 2010; Casellato et al., 2012) and are about 100 to 140 m thick (Casellato et al., 2012). The lower boundary with the Mt. Tului Fm. is transitional, represented by a progressive fining- and thinning-upward trend. Also the lower boundary with the Dorgali Fm. is transitional with a fining-upward trend and dolomitic fine-grained packstone and grainstone with ooids peloids and crinoids followed by peloidal dolomitic calcareous lithofacies characterized by marl-silt intercalations and Fe-rich crusts (Casellato et al., 2012). Locally, the top of the S'Adde Limestone is represented by a chert horizon that marks the sharp boundary with the overlying Mt. Bardia Fm. (Casellato et al., 2012). The boundary with the Mt. Bardia Fm. could also be transitional with a coarsening and thickening upward trend (Jadoul et al., 2010). The base of the S'Adde Limestone was dated to the late Bathonian, whereas the top to the early Tithonian, according to nannoplankton biostratigraphic analyses provided by Casellato et al. (2012). However, more recent studies integrating magnetostratigraphy and biostratigraphy dated the S'Adde Limestone from the Bathonian to late Kimmeridgian (Muttoni et al., 2018)

3.2.6 Urzulei Fm.

The Urzulei Fm. was instituted by Jadoul et al. (2009) and crops out exclusively in the Urzulei Supramonte (Fig. 3.4). It consists of conglomerates with dm-size clasts of intraformational carbonates and black pebbles, cyclically interbedded with fine-grained peloidal carbonates with fenestrae, tepees, mud-cracks, stromatolites, *Charophytes,* gastropods and ostracods passing vertically to bedded massive wackestone, oo-bioclastic packstone-grainstone, oncoid rudstone-floatstone, mud-pebble rudstone and dolostone (Jadoul et al., 2009). These facies are interpreted as related to multiple subaerial exposure, protected lagoon and fresh water/pond environments (Jadoul et al., 2009, 2010). The maximum thickness is around 45 m (Fig 3.3). The lower boundary of the Urzulei Fm. with the Mt. Tului Fm. is characterized by an erosional surface with conglomerates at the top, recording the subaerial exposure of the top of the Mt. Tului Fm. (Jadoul et al., 2009). The top of the Urzulei Fm. is represented by a sharp boundary with the overlying Mt. Bardia Fm., marked by nodular marly-limestone (Codula di Luna) or by a dolostone-cap (Urzulei Supramonte). The Tithonian age of this unit was suggested indirectly on the basis of the stratigraphic position according to Jadoul et al. (2010).

3.2.7 Pedra Longa Fm.

The Pedra Longa Fm. was introduced by Jadoul et al. (2009) and crops out only in the southern area of the Orosei Gulf, from Baunei Supramonte to Pedra Longa (Fig. 3.4). It consists of thin-bedded marly-calcilutites with interbedded lenticular calcirudites with mud-chip and bioclasts of crinoids and corals and chaotic breccia with cobbles and boulders of carbonate rocks (Jadoul et al., 2010). These facies were deposited in basinal environment, with a water depth of at least 100 m, as suggested by the presence of nannoliths and nannoconids (Jadoul et al., 2010). This unit often forms lenticular bodies and is highly variable in thickness, ranging from 0 to 25 m (Jadoul et al., 2009). According to Jadoul et al. (2009), the lower boundary of the Pedra Longa Fm. with the underlying Mt. Tului Fm. is characterized by a Fe-hardground surface. Instead, the top of the Pedra Longa Fm. is characterized by an erosional surface followed by chaotic polygenic carbonate breccia of the Lower Mt. Bardia Formation (Jadoul, 2018). Jadoul et al. (2009, 2010) and Lanfranchi et al. (2011) suggested partial interfingering between the Pedra Longa Fm. and the lower part of the Mt. Bardia Fm. (toe-of-slope of prograding clinoforms; cf., Lanfranchi et al., 2011), whereas according to Casellato et al. (2012) and Jadoul (2018) these units are not coeval, but the Mt. Bardia Fm. is entirely younger than the Pedra

Longa Fm. This unit was dated to the early-late Tithonian on the basis of calcareous nannoplankton biostratigraphy (Jadoul et al., 2010).

3.2.8 Mt. Bardia Fm.

The Mt. Bardia Fm. was described for the first time by Amadesi et al. (1961) and crops out along all the Orosei Gulf area. According to Amadesi et al. (1961), the Mt. Bardia Fm. consists of biohermal and bioclastic limestones with corals, algae, brachiopods and foraminifers of Tithonian age. Massari (1968) provided the first paleoenvironmental interpretation for this lithostratigraphic unit, identifying two members accumulated in different depositional settings. The lower member (lower-middle Tithonian), mostly consisting of bioclastic limestone, was deposited in shallow subtidal settings with patch reefs forming discontinuous barriers. The upper member (upper Tithonian-Berriasian) was deposited in a large platform interior protected by carbonate shoals with cyclic superposition of subtidal or intertidal to supratidal facies.

According to Jadoul et al. (2009, 2010), this lithostratigraphic unit is highly differentiated along the outcropping area in terms of depositional facies and geometries. In the southern part of the Orosei Gulf (Supramonte Baunei) there are sigmoidal clinoforms (inclined from 5° to 15°) mainly composed of bioclastic calcarenites and calcirudites with corals, stromatoporoids and microencrusters (Lower Mt. Bardia Fm., Jadoul et al., 2010; Lanfranchi et al., 2011). These clinostratified bioclastic facies are interpreted as deposited in a slope environment, subdivided in upper, middle and lower slope (Lanfranchi et al., 2011). In the northern part of the study area, the clinostratified bodies consists of calcarenites and calcilutites with ooids, bioclasts, oncoids and foraminifers (Jadoul et al., 2010). Reefal limestone dominated by a very differentiated association of corals, microbialites, stromatoporoids, chaetetids and microframework occur at the platform edge (Ricci et al., 2018), consisting of high-energy reefal facies adjacent to a lower-energy back-reef area (Lower Mt. Bardia Fm., Ricci et al., 2018). On the westernmost part of the Jurassic outcrop area (Supramonte Urzulei), the Lower Mt. Bardia Fm. is represented by restricted inner platform mudstone to packstone with common dasyclad algae, diceratid-nerineid floatstone to rudstone and subtidal skeletal packstone-grainstone (Jadoul, 2018). The Lower Mt. Bardia Fm. evolves vertically (Upper Mt. Bardia Fm.) to shallow-water subtidal skeletal-oncoidal grainstone and packstone and thin intertidal cycles of stromatolitic boundstone and fenestral-ooidal intraclastic-pisoidal packstone-grainstone with tepees in the whole outcropping area (Jadoul, 2018).

The Mt. Bardia Fm. reaches a thickness of about 500 m (Fig 3.3). The base of the unit is characterized in the Baunei Supramonte area by up to 10 m of chaotic, polygenic carbonate breccia overlying a

sharp erosional boundary with the Pedra Longa Fm. (Jadoul, 2018). The clasts of this breccia are made of inner-ramp/lagoonal oo-bioclastic grainstone/packstone, calci-mudstone and poorly lithified calci-mudstone that frequently represent also the breccia matrix (Jadoul, 2018). In the westernmost Jurassic outcrop area (Urzulei Supramonte), the Mt. Bardia Fm. sharply covers the dolostone cap of the Urzulei Fm. The top of the unit is rarely exposed and consists of peritidal carbonates with stromatolites and fenestral fabric and intra-formational breccia with black pebbles (Massari, 1968). According to biostratigraphic data and physical correlations, the base of the unit is diachronous, from the late Tithonian to early Berriasian (Jadoul et al., 2009, 2010).

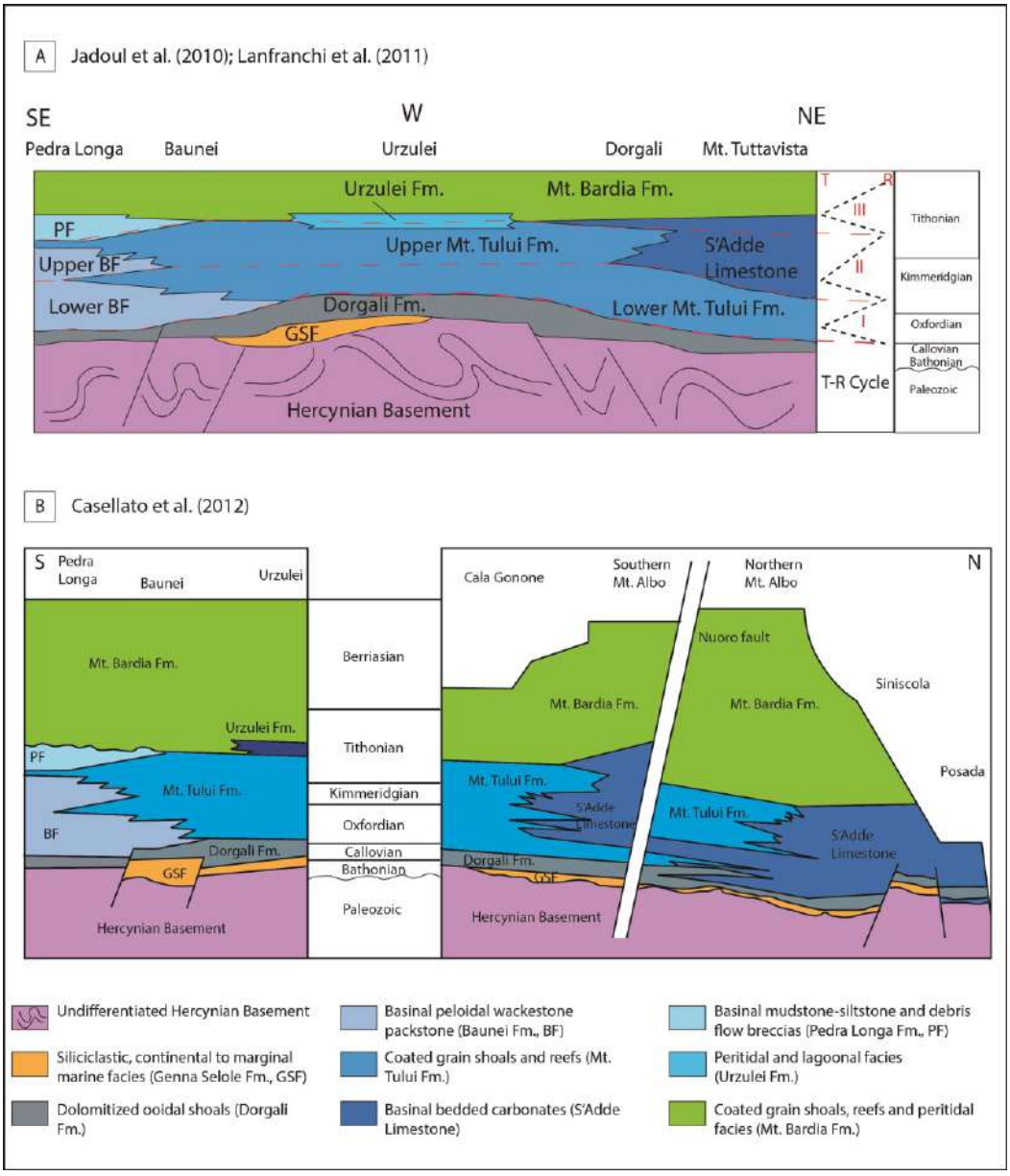

Figure 3.3 A) Stratigraphic scheme of the Middle Jurassic to Berriasian carbonate succession in eastern Sardinia redrafted after Jadoul et al. (2010) and Lanfranchi et al. (2011). B) Stratigraphic scheme of the Middle Jurassic to Berriasian eastern Sardinia carbonate succession redrafted after Casellato et al. (2012).

3.3 Sedimentary evolution of the Jurassic succession in eastern Sardinia

Jadoul et al. (2009, 2010) and Jadoul (2018) reconstructed the stratigraphic evolution of the Middle Jurassic-Lower Cretaceous Orosei Gulf carbonate succession, influenced by regional and local tectonics and eustatic sea level.

The first Middle Jurassic siliclastic unit (Genna Selole Fm.) deposited above the Hercynian basement in a possible active tectonic setting under warm-humid climatic conditions (Costamagna and Barca, 2004; Costamagna, 2016a). The first marine sedimentary cycle, following the Bathonian marine transgression (Amadesi et al., 1961), documents a coastal palaeogeography with open bays generally characterized by low accommodation (Dieni et al., 2013; Jadoul, 2018). From the Bathonian to the early Oxfordian, the palaeogeography of eastern Sardinia was characterized by a shallow marine carbonate environment with prevalent ooidal sedimentation (Dorgali Fm.; Jadoul et al., 2010). The Dorgali Fm. is characterized by the presence of several local and regional hardgrounds, suggesting long periods of non-deposition. These hardground surfaces were interpreted to result from a global decrease in carbonate production (Jadoul, 2018), possibly associated with a climatic cooling event (Louis-Schmid et al., 2007; Rais et al., 2007) or due to regional tectonic activity (late Bathonian-early Oxfordian, Casellato et al., 2012).

The Oxfordian-Tithonian portion of the succession (Mt. Tului, Baunei, S'Adde Limestone, Urzulei and Pedra Longa formations) is characterized by shallow-water carbonates transitional eastward, northward and southward to deeper basinal areas (Fig. 3.4; Jadoul et al., 2009; Casellato et al., 2012). Starting from the Oxfordian, the sedimentation was strongly influenced by relative sea-level fluctuations recorded in three transgressive-regressive (T-R; Fig. 3.3) cycles recognized in the carbonate succession of eastern Sardinia (Jadoul et al., 2009). The basal transgression of the first T-R cycle (T-R I; early Oxfordian), according to biostratigraphic data from a dynoflagellate association (Jadoul et al., 2009), is marked by the deposition of the Baunei Fm. in the southern basin (Fig. 3.3). This cycle is characterized by a prevalent ooidal carbonate production (Mt. Tului Fm.), particularly expressed on the westernmost outcrop area (Urzulei Supramonte; Jadoul et al., 2009).

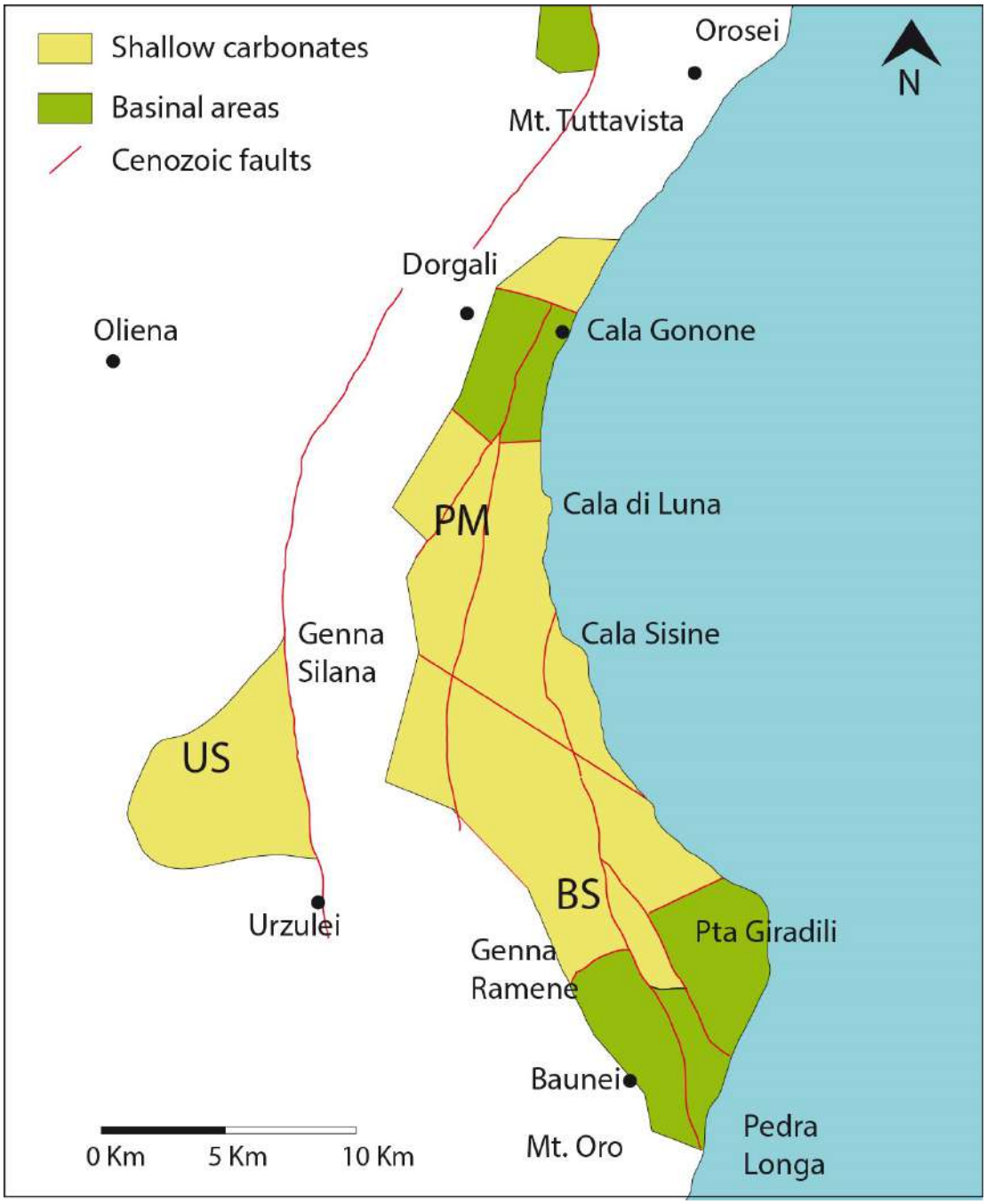

Figure 3.4 Distribution of the outcrops of Jurassic shallow water and basinal carbonates in the Orosei Gulf. US-Urzulei Supramonte, PM-Punta Mureddu, BS-Baunei Supramonte. Modified after Jadoul (2018).

In the southern basin, the regression at the top of the T-R I cycle is marked by the progradation of ooidal and oo-crinoidal grainstone and packstone of the Mt. Tului Fm. above the Baunei Fm. (Jadoul et al., 2009). The transgression was dated indirectly as late Oxfordian by Jadoul et al. (2009), according to similar sedimentation changes in pelagic successions of the Northern Tethys (Jadoul et al., 2009 and references therein).

The beginning of the second T-R cycle (T-R II; Fig. 3.3A) is marked by a transgression that restored distal basinal conditions in the southern basin with the deposition of the Baunei Fm. and in the northern basin with the deposition of the S'Adde Limestone (Fig. 3.3; Jadoul et al., 2009). The second cycle is characterized by the development of coral-stromatoporoid reefs and bioclastic sediment composition (Mt. Tului Fm.). Ooidal shoals persisted in the northern and eastern side of the shallower areas (Fig. 3.4; Jadoul et al., 2009). The basal transgression of this cycle was dated indirectly to the late Kimmeridgian by Jadoul et al. (2009), because a similar switch from an ooidal to a coral-stromatoporoid carbonate factory was dated to the Kimmeridgian along the margins of the Adriatic platform (Tišljar and Velić, 1993). According to Jadoul et al. (2009), this transgression can be probably related to a Kimmeridgian maximum eustatic sea-level rise, documented in Greenland, Gulf of Mexico, Iberian basin and Tethyan realm. Instead, Jadoul (2018) suggested that the basal transgression of this cycle is early Kimmeridgian in age and may be a consequence of early Kimmeridgian tectono-sedimentary and oceanographic events. According to Jadoul et al. (2009, 2010) the regression at the top of the second T-R II cycle is represented in the shallower areas (Urzulei Supramonte) by a subaerial exposure surface followed by the deposition of conglomerate beds with black pebbles and mudstone/wackestone with ostracods, gastropods and *Charophytes* (Urzulei Fm.). Instead, in the northern and southern basins it is recorded by the progradation of the platform with resedimented oo-crinoidal calcarenites and oo-bioclastic packstone of the Mt. Tului Fm. (Jadoul et al., 2009). The end of the second T-R II cycle was dated to the early Tithonian according to biostratigraphic data (Jadoul et al., 2009).

The beginning of the third T-R cycle (T-R III; Fig. 3.3A) is characterized by the recovery of carbonate sedimentation after the subaerial exposure with the deposition of shallow subtidal massive wackestone, oo-bioclastic packstone-grainstone and oncoidal rudstone-floatstone (Urzulei Fm.) on the Urzulei Supramonte area (Jadoul et al., 2009). The basal transgression led to the deposition of the Pedra Longa Fm. on the top of the Mt. Tului Fm. (Baunei Supramonte) and the S'Adde Limestone in the northern basin (Fig. 3.4; Jadoul et al., 2009). The early Tithonian age of the transgression was determined on the basis of nannoplankton biostratigraphic analysis performed by Jadoul et al. (2009) in the Pedra Longa Fm. The top of the third T-R cycle records a late Tithonian regression, which was characterized by the progradational succession of clinostratified sigmoidal bioclastic deposits of the Mt. Bardia Fm. both in the northern and southern basins (Lanfranchi et al., 2011). The base of the Mt. Bardia prograding slope deposits in the southern basin is characterized by an erosional boundary overlain by thick, chaotic, polygenic carbonate breccia. Jadoul (2018) interpreted this erosional surface at the base of the progradational Mt. Bardia clinoforms as deep incisions associated to slump scars or erosional canyons filled by debris flow breccia. The possible mechanisms suggested for

breccia emplacement are catastrophic mass transport and debris flows generated by platform margin collapse. According to Jadoul (2018) these mechanisms were controlled by Tithonian syn-sedimentary tectonics related to fault-block tilting in the underlying Hercynian basement. Similarly, the breccia bodies at the top of the Urzulei Fm. are interpreted as collapse breccia associated with the reactivation of listric faults in the Hercynian basement (Jadoul, 2018). Subsidence related to this late Tithonian tectonic activity probably created the accommodation for the deposition of the thick Mt. Bardia Fm. (Jadoul, 2018). According to Jadoul et al. (2010) the Tithonian transgressive and regressive trend (T-R III cycle in Figure 3.3A) was influenced by extensional tectonic events affecting the western part of the European plate, related to the rifting of the Bay of Biscay and the Iberian Basin. During this third cycle (Mt. Bardia Fm.) stromatoporoid-coral reefs at the platform edge separated the wide bioclastic inner platform factory from the slope facies (Jadoul et al., 2009).

3.4 Post-depositional tectonic events

During the Early Cretaceous the central-eastern Sardinia area was a palaeomargin characterized by outer-shelf to pelagic facies (Zattin et al., 2008). Between Early and Late Cretaceous there is evidence of uplift of the sedimentary succession and Hercynian basement, although not well constrained chronologically. This is confirmed by the common presence of an unconformity in all the Mediterranean area between Albian and Cenomanian (France, Combes 1990; Adriatic platform, Husinec and Jelaska, 2006; Southern Italy, Mindszenty et al., 1995) also widespread in Sardinia (Mameli et al., 2007; Dieni et al., 2008). This tectonic event could be interpreted within the frame of important geodynamic changes in the European margin, including the onset of oceanic subduction under Corsica (Dieni et al., 2008).

The Corsica-Sardinia block was part of the European-Iberian continental margin during the Eocene (Fourcade et al., 1993; Dercourt et al., 2000; Speranza et al., 2002). An Eocene tectonic phase caused the exhumation of crustal blocks, strongly controlled by faults and locally caused the complete erosion of the Mesozoic sedimentary cover (Zattin et al., 2008). The same faults were reactivated during the Oligocene-early Miocene extensional and strike-slip tectonics and control the present outcrops of the Mesozoic succession (Pasci, 1997; Cherchi et al., 2008; Zattin et al., 2008). The extensional tectonic activity started close to the Eocene/Oligocene boundary and preceded calc-alkaline volcanic activity related to the structural extension associated with the Apenninic subduction (Cherchi et al., 2008). The end of the rifting activity is middle Burdigalian (middle Miocene) in age (Cherchi et al., 2008), but extension continued until late Burdigalian-Langhian in the Algero-

Provencal Basin with oceanic accretion and the rotation of the Corsica-Sardina block (Speranza et al., 2002).

The Cenozoic tectonic activity led to the formation of transpressive structures in eastern Sardinia that involved the Hercynian basement and the Mesozoic sedimentary cover (Pasci, 1997). The movements of these faults show an E-W extensional direction as a result of an average N-S shortening (Pasci, 1997). The main structural features of the Orosei Gulf sector related to the Cenozoic tectonic history are represented by different types of faults and several fold systems (Pasci, 1997). One of the most important fault systems is represented by arcuate NE-SW/N-S trending faults (Fig. 3.5; Sovana fault). Toward the northern side of the area, they converge to E-W oriented transpressive faults, producing the strongest deformation of the sector (Pasci, 1997). Another important feature are E-W trending fault systems (Fig. 3.5; Cedrino, S. Giovanni faults). The kinematic indicators show right-reverse transcurrent motions (Pasci, 1997). The third important faults system is represented by arcuate faults (Fig. 3.5; faults of Urzulei and Codula Sisine), whose direction changes from N-S (in the north) to NW-SE (in the south). These faults occur only in the southern part of the area and the kinematic indicators show right transcurrent movements with subordinate normal components (Pasci, 1997). A folding system is associated with the fault systems showing a large scatter of orientations (Pasci, 1997). Fold axis are often sub-horizontal (mainly 10°-20° NE dipping), even if sometimes inclinations up to 45° can be observed. One of the most important folding structures of the whole area is the syncline that characterizes the northern side of the western Supramonte (Pasci, 1997).

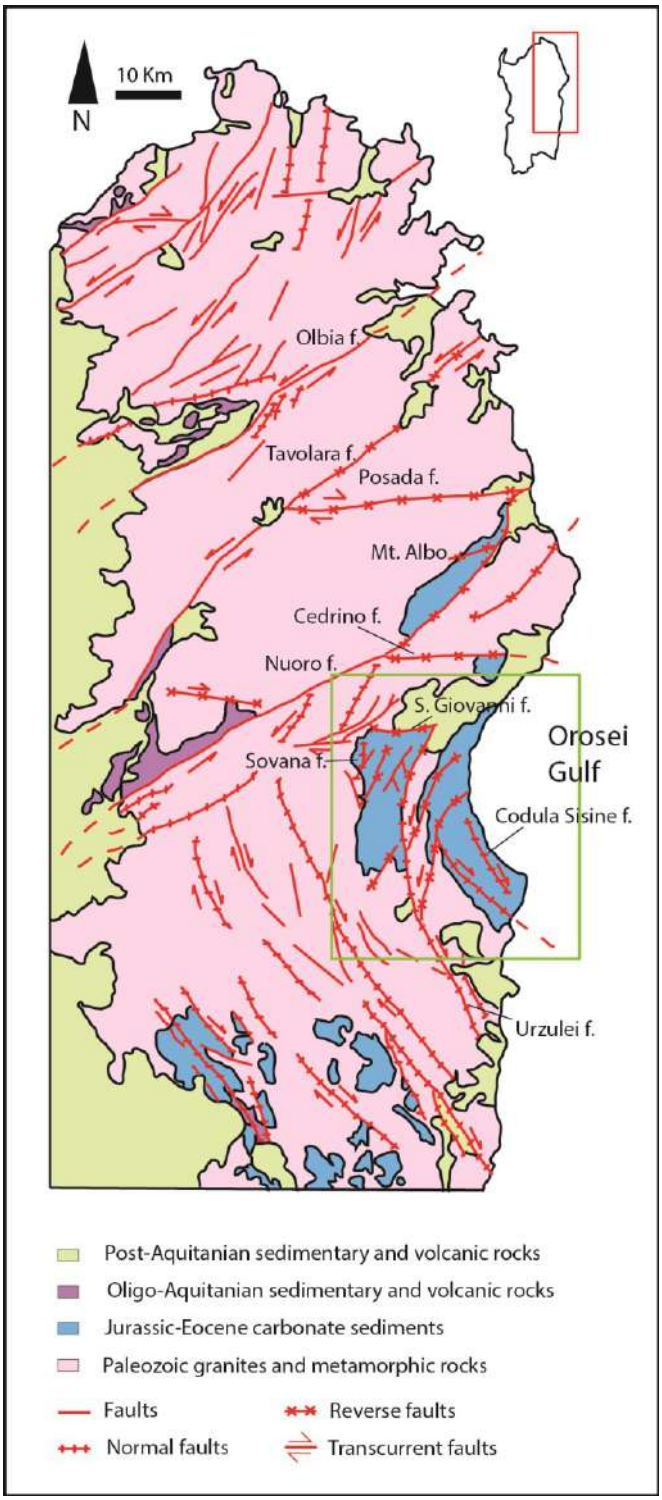

Figure 3.5 Geological-structural map of the north-central Sardinia with the study area in the green square. Modified after Pasci et al. (1997).

3.5 Evolution of western Sardinia

The western Sardinia domain (Nurra) was separated from the eastern Sardinia domain (Orosei Gulf) in Triassic and Jurassic times by an emerged structural high (Vardabasso, 1959) and its evolution was connected to the Iberian-Provençal margin evolution (Cherchi et al., 2010; Simone et al., 2012). In the Nurra area (NW Sardinia), a complete Mesozoic succession was deposited, controlled by extensional tectonics and sea-level fluctuations (Cherchi et al., 2010). The palaeogeographic domain was characterized by epicontinental seas affected by phases of subaerial exposure. From the Bathonian, a marine transgression promoted the deposition of micritic limestone and marls with bioclasts and peloids until the Callovian. A thick dolomitic succession represents the Oxfordian-Kimmeridgian interval, whereas during the late Tithonian there was the deposition of inner platform facies with dasyclad algae. Cherchi et al. (2010) proposed that probably, during the Callovian-Oxfordian time interval, the eastern and western Sardinia basins were connected and the palaeohigh was submerged, but this is still not clearly demonstrated. Indeed, Berra et al. (2019) suggested that the Hercynian basement high persisted through all the Mesozoic. A major latest Jurassic-early Cretaceous regressive event led to lagoonal-lacustrine conditions during the Berriasian. The following transgression led to the deposition of shallow-water limestone during most of the Early Cretaceous, until the early Aptian (Cherchi and Schroeder, 1985; Cherchi et al., 2010) followed by a major regional subaerial exposure at the Aptian-Cenomanian.

Chapter 4

Materials and methods

4.1 Facies analysis

The Callovian-Tithonian portion of eastern Sardinia carbonate succession was investigated in terms of facies character and distribution through 21 stratigraphic logs located in three areas: the SE area (Baunei Supramonte), central NW area (Urzulei Supramonte) and the central northern area (Punta Mureddu). The log list with thickness and latitude and longitude coordinates is reported in Table 4.1; log locations are reported in Figure 4.1.

Log number	***Name***	***Location***	***Thickness***	***Coordinates***
1	Iscra	Urzulei Supramonte	105 m	40°06′17.43″N 9°27′27.01″E
2	Codula Orbisi	Urzulei Supramonte	50 m	40°07′51.63″N 9°29′33.53″E
3	Genna Silana	Urzulei Supramonte	456 m	40°09′30.26″N 9°30′24.08″E
4	Ghispali	Urzulei Supramonte	46 m	40°06′45.77″N 9°30′24.19″E
5	Cave	Urzulei Supramonte	27 m	40°06′11.43″N 9°30′34.79″E
6	Punta Mureddu	Punta Mureddu	25 m	40°09′54.66″N 9°34′49.46″E
7	Genna Scalas	Baunei Supramonte	82 m	40°05′11.10″N 9°36′25.10″E
8	Genna Ramene	Baunei Supramonte	77 m	40°03′39.27″N 9°38′05.28″E
9	Baunei Supramonte	Baunei Supramonte	86 m	40°01′34.93″N 9°40′20.31″E
10	Franciscu 1	Baunei Supramonte	13 m	40°01′32.61″N 9°40′35.15″E

Log number	***Name***	***Location***	***Thickness***	***Coordinates***
10	Franciscu 2	Baunei Supramonte	18 m	40°01′31.79″N 9°40′35.53″E
10	Franciscu 3	Baunei Supramonte	10 m	40°01′26.98″N 9°40′39.37″E
11	Punnaci 1	Baunei Supramonte	16 m	40°01′25.29″N 9°40′41.32″E
11	Punnaci 2	Baunei Supramonte	27 m	40°01′25.02″N 9°40′42.68″E
11	Punnaci 3	Baunei Supramonte	30 m	40°01′24.57″N 9°40′43.88″E
12	Mt. Oro	Baunei Supramonte	108 m	40°01′01.78″N 9°41′00.16″E
13	Cava Litografica	Baunei Supramonte	37 m	40°01′38.19″N 9°41′48.73″E
14	Pedra Longa	Baunei Supramonte	36 m	40°01′44.74″N 9°42′04.13″E
15	Rio Olcoe	Baunei Supramonte	33 m	40°01′53.93″N 9°41′32.17″E
16	Selvaggio Blu	Baunei Supramonte	31 m	40°02′51.06″N 9°41′39.98″E
17	Punta Giradili	Baunei Supramonte	10 m	40°02′28.00″N 9°42′17.16″E

Table 4.1 Stratigraphic log location, thickness and latitude-longitude coordinates.

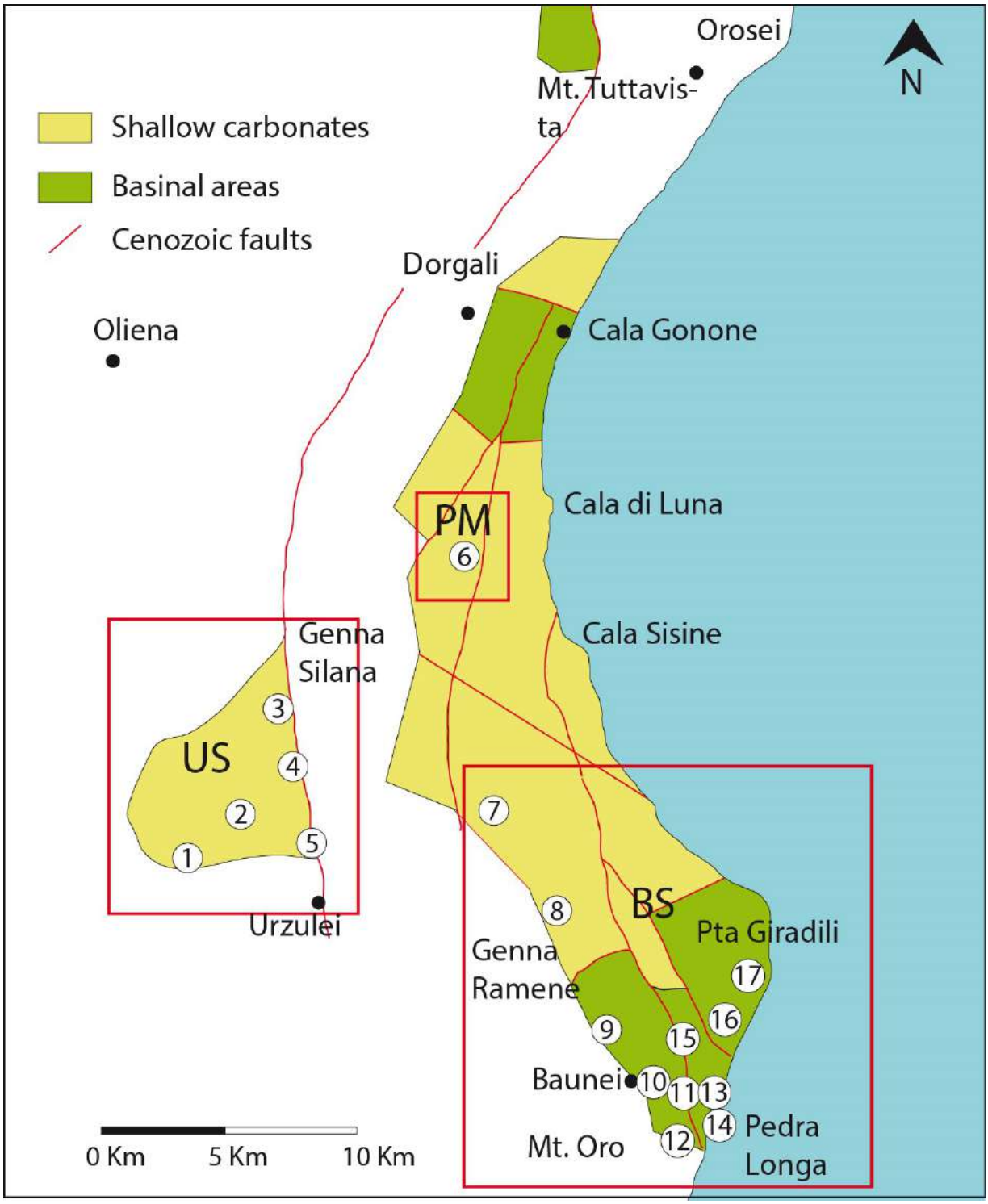

Figure 4.1 Distribution of the outcrops of the studied Jurassic shallow water and basinal carbonates in the Orosei Gulf. The investigated areas are marked by red squares: US-Urzulei Supramonte; PM-Punta Mureddu; BS-Baunei Supramonte. Log location: 1-Iscra; 2-Codula Orbisi; 3-Genna Silana; 4-Ghispali; 5-Cave; 6-Punta Mureddu; 7-Genna Scalas; 8-Genna Ramene; 9-Baunei Supramonte; 10-Fransiscu 1, 2 and 3; 11-Punnaci 1, 2 and 3; 12-Mt. Oro; 13-Cava Litografica; 14-Pedra Longa; 15-Rio Olcoe; 16-Selvaggio Blu; 17-Punta Giradili.

Facies analysis was based on outcrop and sample observation and petrographic analysis of about 700 polished slabs and 365 thin sections. Petrogtraphic analysis was performed with a Zeiss polarized light microscope equipped with a digital camera.

The semi-quantitative analysis of skeletal and non-skeletal grains in thin sections was performed by visual estimates using the comparison charts of percentage of constituents developed for limestones by Baccelle and Bosellini (1965).

For the description of ooids, the nomenclature of Strasser (1986) was adopted. Strasser (1986) defined 6 ooid types (Fig. 4.2): 1) type 1 ooids are well rounded and display fine micritic concentric laminae and possible sparite replacement; 2) type 2 ooids are irregularly shaped with fine micritic laminae (often evolving into oncoids); 3) type 3 ooids display cortices composed of several fine laminae forming a radial structure; they can appear patchily micritized and evolve into irregularly shaped coated grains; 4) type 4 ooids have 1 to 4 laminae and display fine radial structure; 5) type 5 ooids have one lamina with a coarse radial structure; and 6) type 6 ooids display mixed cortices.

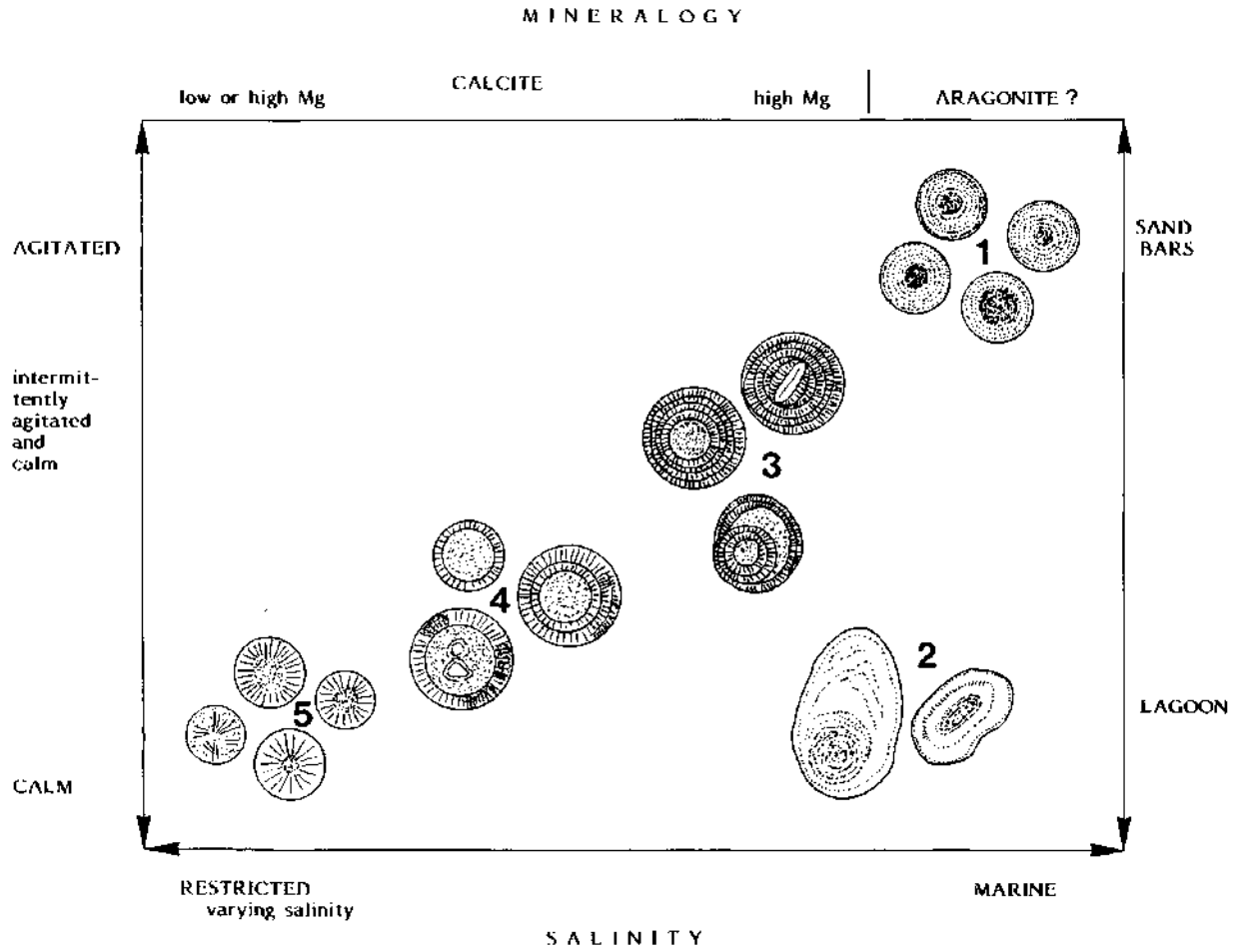

Figure 4.2 Classification of ooids after Strasser et al. (1986) with nomenclature and palaeoenvironmental interpretation.

For the description of oncoids the nomenclature of Dahanayake (1977) was adopted. Dahanayake et al. (1977) defined 4 oncoid types based on their size, shape and internal structure (Fig. 4.3): 1) type I are few millimetres, spherical to elliptical oncoids with concentric and continuous micritic laminae; 2) type II are few millimetres to 1 cm elliptical to sub-spherical oncoids with micritic laminae and organism-bearing encrustations; 3) type III are few centimetres (up to 2 cm) spherical to irregular with wavy contours oncoids with alternating micritic and organism-bearing laminae; 4) type IV are few millimetres to 7 cm, very irregular oncoids with a microbial meshwork without lamination.

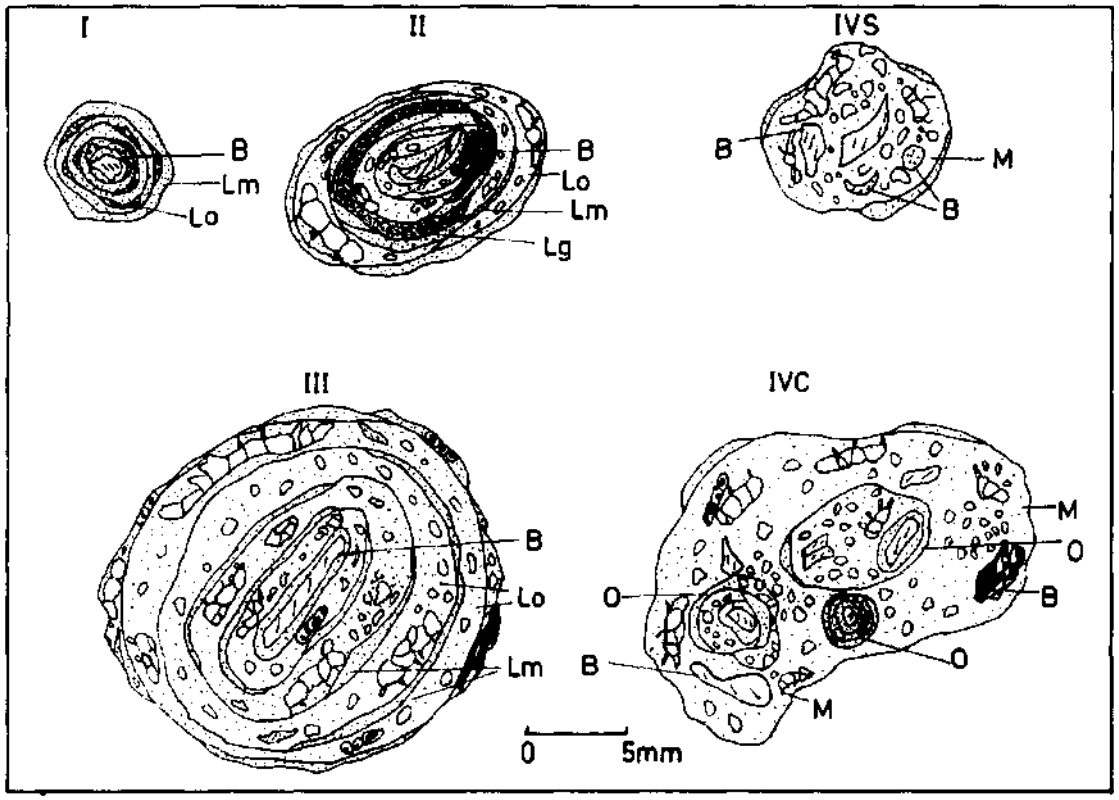

Figure 4.3 Classification of marine oncoid types from Dahanayake (1977) differentiated according to their shape, size and internal structure of the cortex. Lm-micritic laminations; Lg-grumose laminations; Lo-organism-bearing laminations; B-bioclast; M-microbial meshwork; O-oncoid.

Microfacies analysis and nomenclature of sponges is based on Flügel (2004) that defined: a) calcareous sponges as a non-systematic term for calcisponges exhibiting calcite spicules or a calcareous skeleton; b) chaetetids as fossils composed of densely packed, thin calcareous tubes with horizontal partitions; c) stromatoporoids as fossil sponges (regarded as being related to Demosponges or as a separate class of sponges) represented by calcified skeletons of domical to columnar forms, with internal structures parallel and perpendicular to the surface and distinct canal systems (astrorhizae) at the surface; d) siliceous sponges as an informal term for sponges with a skeleton composed of siliceous spicules, including both Demosponges and Hexactinellids.

4.2 Staining techniques and cathodoluminescence microscopy

To identify the presence of dolomite and ferroan calcite cement, some of the thin sections were stained with alizarin red and potassium ferricyanide (cf. Dickson, 1966). Thin sections were examined under cathodoluminescence microscopy with a luminoscope Cambridge Image Technology Limited (CITL), Cambridge, UK (model MK 5-2 operating system at 10-16 kV with a beam current between 200-400 μA, and vacuum gauge 50-70 millitor). Cathodoluminescence microscopy consists of light emission that results when samples are exposed to an electron beam from a cathode ray tube. The electron beam reaches the sample in a vacuum chamber and commonly is about 10-25 kV. The colour and the intensity of the visible light emitted by the sample is useful to find the luminescence activator. Activators are elements that promote active luminescence, the intensity of which decreases above a certain activator concentration. Sensitizers absorb some of the excitation energy and transmit part or all of it to the activators. Quenchers suppress activator and sensitizer luminescence, leading to a lower intensity of luminescence and finally to the extinction of it (Machel, 1985). Important activators are Mn^{2+}, Pb^{2+}, several REEs, Cu^{2+}, Zn^{2-}, Ag, Bi (Machel, 1985; Hiatt and Pufahl, 2014). Important sensitizers are Pb^{2+}, Ce^{2-} and several REEs, whereas Fe^{2+}, Ni^{2+}, Co^{2+} are quenchers (Machel, 1985; Budd et al., 2000). In carbonate rocks, cathodoluminescence is useful for understanding fundamental diagenetic relationships between grains, matrix, cement, porosity evolution, replacement reactions and relative pore water chemistry (Hiatt and Pufahl, 2014).

Mn^{2+} and Fe^{2+} fit into the crystal structure of trigonal carbonates and substitute Ca in calcite and Ca and Mg in dolomite (Hiatt and Pufahl, 2014). Mn and Fe concentrations are useful for determining redox conditions under which the mineral precipitated because they have different redox potential. As oxygen level drops from near atmospheric levels, Mn is reduced and readily incorporated in the diagenetic cements. As oxygen level drops further, Fe is reduced and both elements precipitated in the diagenetic phase (Hiatt and Pufahl, 2014). Different types of luminescence for carbonate cements can indicate that their precipitation could take place in different diagenetic environments. Luminescent cements can indicate the presence of Mn^{2+} in the calcite crystalline structure, typical of reducing conditions. Also Fe^{2+} in calcite crystals is typical of reducing environments and can act as a quencher. Mn^{2+} with no or little Fe^{2+} in the calcite crystal provides to the cement a bright orange luminescence. When the concentration of Fe^{2+} increases and the crystals contain both cations, the cement becomes first dull luminescent and then non-luminescent.

4.3 Strontium isotopes analysis

To constrain the age of the carbonate succession, analyses of strontium isotopes were performed at the CAI Geochronology and Isotope Geochemistry Laboratory at the Geological Science Faculty, Universidad Complutense de Madrid (Spain). Twelve powdered calcite samples, deriving from bulk rocks, brachiopod shells and belemnite rostra from three stratigraphic logs (Genna Silana, Franciscu, Mt. Oro) were extracted with a microdrill. Well-preserved brachiopod shells and belemnite rostra were selected for the analysis, to avoid diagenetic bias. After dissolution in a 5 ml of ultra-pure acetic acid (Merck-Suprapur®), samples were placed in an ultrasound bath for 15 minutes and then centrifuged over 10 minutes at 4000 RPM. Clean vials with the supernatant were evaporated to the dryness over a heat plate at 120 °C. Once samples were completely dried, 1 ml of ultrapure HNO_3 14 M (Merck-Suprapur®) was added and samples were set back on the heat plate (120 °C) to evaporate and 3 ml of HNO_3 were added to the sample for the chromatographic separation. This was performed using an extraction resin Sr-Resin^{TM}. The fractions of Sr were recovered using HNO_3 0.05M as eluent, which were completely dried. Sr samples were recovered in 1 µl of 1 M phosphoric acid and loaded, together with 2 µl of Ta_2O_5, onto a degassed single filament of Re. Sr analyses were performed on an IsotopXPhoenix (TIMS) following a dynamic multi-collection method for 160 cycles, with a stable ion intensity of 3V in the mass ^{88}Sr. Possible ^{87}Rb interferences were corrected in the Sr analysis and the $^{87}Sr/^{86}Sr$ ratio was normalized in order to correct for mass fractionation, taking into account a reference value of $^{86}Sr/^{88}Sr = 0.1194$. NBS 987 Sr isotopic standard ($^{87}Sr/^{86}Sr = 0.710248 \pm 0.000003$. NBS 1982. National Bureau of Standards Certificate of Analysis. Standard Reference Material 987) was checked along with the samples. NBS 987 data were used to correct the samples ratios, attending to the standard drift and taking into account the standard certified value. Analytical error (2STD) achieved during the procedure yields $^{87}Sr/^{86}Sr$ 0.01%. Procedural blanks were always below 0.5 ng. The measured $^{87}Sr/^{86}Sr$ values were analysed against the global marine $^{87}Sr/^{86}Sr$ curve defined for the Late Jurassic by McArthur et al. (2012) and Wierzbowski et al. (2017).

4.4 Oxygen and Carbon stable isotope analyses

Stable oxygen and carbon isotope analyses of 262 samples were performed using an automated carbonate preparation device (Gasbench II) and a Thermo Fisher Scientific Delta V Advantage continuous flow mass spectrometer at the Department of Earth Sciences, University of Milan. Carbonate powder samples, extracted with a microdrill, were reacted with > 99% orthophosphoric acid at 70°C. The carbon and oxygen isotope compositions are expressed in the conventional delta

notation calibrated to the Vienna Pee-Dee Belemnite (V-PDB) scale by the international standards IAEA 603 and NBS-18. Analytical reproducibility for these analyses was better than ± 0.1‰ for both $\delta^{18}O$ and $\delta^{13}C$ values.

4.5 X-ray powder diffraction (XRD)

The mineralogy of 5 powder samples was investigated with X-ray powder diffraction (XRD) analytical technique, by means of an X-RAY Powder Diffractometer Philips X'Pert MPD with high temperature chamber at the laboratory of the University of Milan. For all samples, qualitative analyses were made with Panalytical X'Pert HighScore software to identify the crystalline phases.

4.6 Scanning electron microscope (SEM)

Scanning Electron Microscope (SEM) analyses were performed on 4 polished slabs, thin sections and freshly broken surfaces, gold or carbon coated, with a field emission scanning electron microscope JSM – IT 500 (JEOL, 2019) at the Earth Sciences Department, University of Milan. Major element analyses were made with EDS on carbon coated thin sections.

Chapter 5

Development of coral-sponge-microbialite reefs in a coated grain dominated carbonate ramp

This chapter is extracted from the publication: Nembrini M., Della Porta G., Berra, F. (2021) Development of coral-sponge-microbialite reefs in a coated grain-dominated carbonate ramp (Upper Jurassic, eastern Sardinia, Italy), Facies, 67, 6. DOI: 10.1007/s10347-020-00616-7.

5.1 Abstract

The Late Jurassic is a peak time of diversification of reefs with corals, stromatoporoids, calcareous and siliceous sponges and microbialites during the Phanerozoic. This study focuses on the Callovian-Kimmeridgian carbonate succession of eastern Sardinia, deposited at tropical latitudes on the European passive margin that recorded from the late Oxfordian the evolution from a coated grain-dominated to a reef-bearing carbonate ramp.

The coated grain-dominated carbonate ramp (phase 1; Callovian-middle Oxfordian) includes inner ramp ooidal shoals and peloidal packstone in the middle to outer ramp. The overlying reef-bearing ramp (phase 2; late Oxfordian-late Kimmeridgian) is characterized by three types (1-3) of bioconstructions. The distribution of these build-ups along the middle to outer ramp depositional profile reflects bathymetric parameters, related to the interplay of water energy and light penetration. Type 1 build-ups developed in the proximal middle ramp and consist of 45 m thick, 100 m wide, coral-stromatoporoid boundstone associated with coral-stromatoporoid rudstone-grainstone. Type 2 build-ups, colonizing deeper environments in the middle ramp, are lens-shaped coral-calcareous sponge-diceratid boundstone including stromatoporoids and chaetetid sponges, 1-2 m thick and 3-4 m wide, associated with bioclastic packstone-grainstone. Type 3 lens-shaped calcareous and siliceous sponge-coral-microbialite boundstone build-ups (1 m thick and a few metres wide) formed in lower energy, distal middle to outer ramp settings.

The evolution of the eastern Sardinian carbonate ramp reflects the Oxfordian-Kimmeridgian spread of the coral-sponge-microbialite reefs along the Tethyan European passive margin.

5.2 Introduction

The Late Jurassic represents a time of exceptional abundance of coral, stromatoporoid, calcareous and siliceous sponge and microbialite reefs in the Phanerozoic (Leinfelder et al., 2002; Cecca et al., 2005; Kiessling, 2009; Martin-Garin et al., 2012). This significant phase of reef development is coeval with major tectonic plate reorganizations, marked by the break-up of Pangea, which started in the Late Triassic and led to the opening of the Central Atlantic and Alpine Tethys, followed by the North and South Atlantic, Indian Ocean and the Bay of Biscay (Stampfli and Borel, 2002; Golonka, 2004, 2007; Beutel et al., 2005; Masini et al., 2013; Frizon de Lamotte et al., 2015; Leleu et al., 2016; Müller et al., 2016). In this period of global tectonic reorganization, major climatic changes and sea-level fluctuations (Dromart et al., 2003; Jenkyns et al., 2011; Haq, 2018), reef-building biota diversified and gave rise to a great variety of reef types, dominated by corals, stromatoporoids, various calcareous and siliceous sponges, bivalves and microbialites or a mixture of them (Leinfelder et al., 2002). Starting from the middle Oxfordian, when a eustatic sea-level rise (Cecca et al., 2005), likely driven by climate warming (Dromart et al., 2003; Dera et al., 2011), is documented, reefs consisted of metazoan (mostly corals and stromatoporoids) and microbialites. The record of the global distribution of Upper Jurassic reefs with corals, calcareous and siliceous sponges and microbialites is well-documented in attached platforms of the northern margin of the Alpine Tethys (Spain, Olóriz et al., 2003a; Reolid et al., 2005; Bádenas and Aurell, 2010; San Miguel et al., 2017; Swiss Jura, Dupraz and Strasser, 2002; Samankassou et al., 2003; Strasser and Védrine, 2009; French Jura, Lathuilière et al., 2005; Olivier et al., 2011; Northwestern France, Olivier et al., 2003, 2008; Carcel et al., 2010; Germany, Olivier et al., 2004b), in the intra-Tethys isolated platforms (Plassen, Northern Calcareous Alps, Schlagintweit and Gawlick, 2007, 2008; Adriatic platform, Turnšek et al., 1981; Tišljar and Velić, 1991; Dragičević and Velić, 2002; Velić et al., 2002; Vlahović et al., 2002; Apennine platform, Rusciadelli et al., 2011; Apulian platform, Russo and Morsilli, 2007; Santantonio et al., 2013), in the southern Tethys epeiric platform of Saudi Arabia (Al-Husseini, 1997; Hughes, 2004; El-Sorogy et al., 2018) and in the Atlantic platforms (Portugal, Leinfelder, 1993a; Nose and Leinfelder, 1997; Nova Scotia, Jansa et al., 1988; Pratt and Jansa, 1988).

Laterally extensive well-exposed outcrops of carbonate depositional systems with a wide variety of facies and Oxfordian-Kimmeridgian and Tithonian coral-stromatoporoid-sponge-microbialite reefs are present in the Middle Jurassic to Berriasian (Lower Cretaceous) stratigraphic succession of eastern

Sardinia. Previous studies focused on the stratigraphic reconstruction of the sedimentary succession (Jadoul et al., 2009, 2010; Lanfranchi et al., 2011; Casellato et al., 2012; Jadoul, 2018; Muttoni et al., 2018) and on the characterization of Tithonian reefs (Ricci et al., 2018). This study focuses on the Callovian-Kimmeridgian southern portion of the carbonate ramp system (Dorgali, Mt. Tului and Baunei formations, *sensu* Jadoul et al., 2009, 2010) that recorded a transition from a carbonate succession characterized by coated grains, echinoderms and peloids to a carbonate factory dominated by reefs with variable proportions of corals, stromatoporoids, calcareous and siliceous sponges and microbialites. Thanks to the intermediate palaeogeographic position between the northern Tethys and the intra-Tethys platforms in the south-western portion of the northern margin of the Alpine Tethys (Fig. 5.1; Dercourt et al., 2000) and affinities with both provinces, the study of eastern Sardinia carbonate system provides insights on the factors influencing carbonate lithofacies character, reef composition and architecture during the Late Jurassic.

5.3 Geological setting

The up to 650 m thick Middle Jurassic-Lower Cretaceous carbonate succession of eastern Sardinia (Orosei Gulf; Figure 3.3 in Chapter 3) accumulated on the southern European passive margin of the Alpine Tethys (Fourcade et al., 1993; Costamagna and Barca, 2004; Costamagna, 2016). During the Late Jurassic, Sardinia was located at tropical palaeolatitude (Fig. 5.1) along the northern coast of the Alpine Tethys (Dercourt et al., 2000; Muttoni et al., 2018). The carbonate succession of eastern Sardinia accumulated above a Hercynian basement peneplain, with shallow-water carbonates transitional eastward, northward and southward to deeper basinal areas (Jadoul et al., 2009; Casellato et al., 2012). The carbonate succession started with marine transgressive carbonates covering the Palaeozoic Hercynian basement, Permian volcanic rocks or Bajocian-lower Bathonian discontinuous lenses (up to 50 m thick) of siliciclastic deposits (Genna Selole Fm., Dieni and Massari, 1985; Costamagna et al., 2007; Costamagna, 2016). The first marine carbonate deposits are referred to as Dorgali Fm. (*sensu* Jadoul et al., 2009, 2010), which consists of dolomitized cross-laminated ooidal grainstone to packstone with detrital quartz associated with oo-crinoidal grainstone to packstone of Bathonian-Callovian age (Figure 3.3 in Chapter 3). The overlying Mt. Tului Fm., Baunei Fm. and S'Adde Limestone (Figure 3.3 in Chapter 3) record the evolution through time from a carbonate ramp dominated by coated grains to a reef-bearing carbonate ramp (Jadoul et al., 2009, 2010).

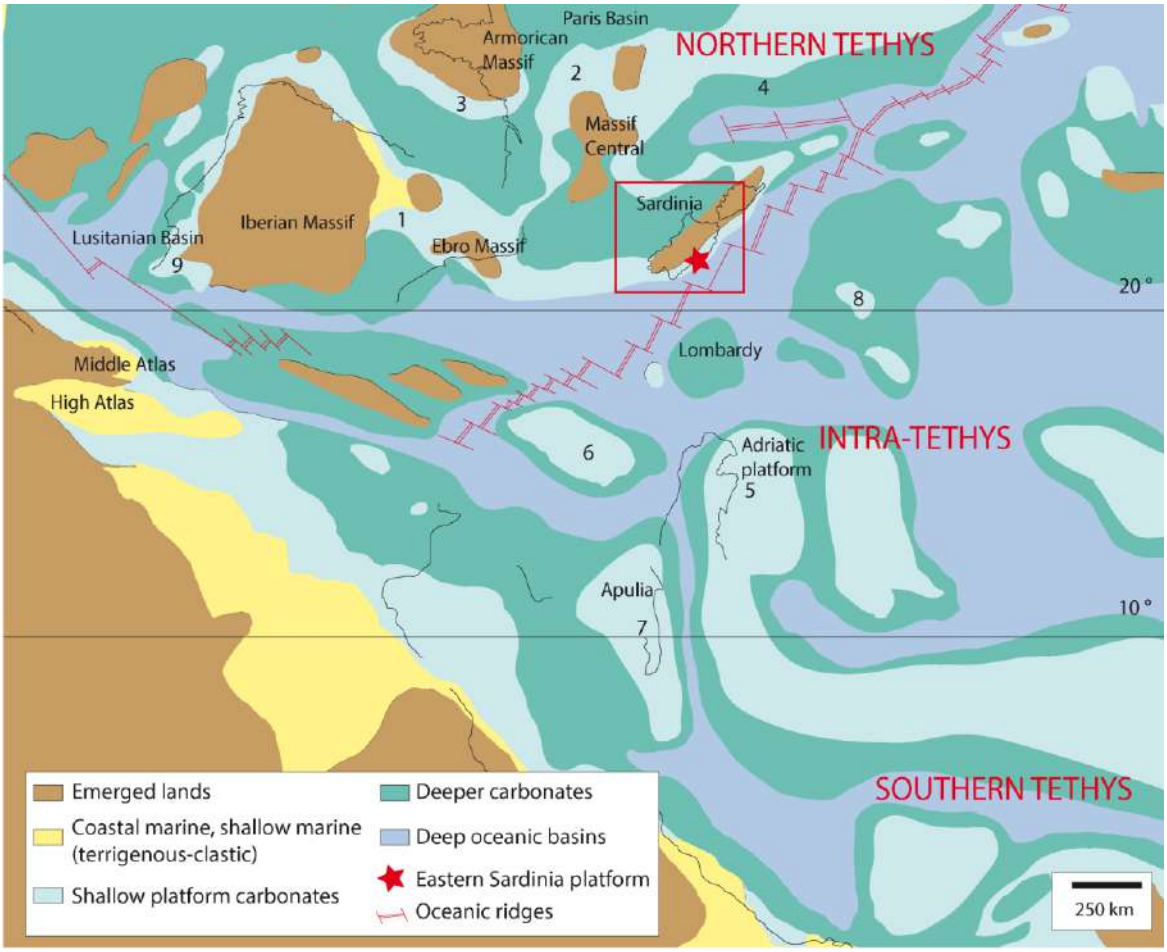

Figure 5.1 Palaeogeographic map of Tethys realm during the Kimmeridgian, with the position of Sardinia (red square); modified after Dercourt et al. (2000). The distribution of coeval reefal carbonate systems is marked as: 1 Iberian Basin coral-microbial build-ups and stromatoporoid carpets (Bádenas and Aurell, 2010); 2 France Lorraine and Jura carbonate platforms with coral-microbialite reefs (Dupraz and Strasser, 2002; Lathuilière et al., 2005; Olivier et al., 2008, 2011); 3 La Rochelle coral-microbialite reefs (Taylor and Palmer, 1994; Olivier et al., 2003, 2008); 4 Germany siliceous sponge mounds (Swabian and Franconian Alb; Olivier et al., 2004b); 5 Adriatic platform stromatoporoid, coral, chaetetid reefs (Vlahović et al., 2002); 6 Apennines carbonate platform with coral stromatoporoid reefs (Rusciadelli et al., 2011); 7 Apulian carbonate platform stromatoporoid-coral reef (Santantonio et al., 2013); 8 Northern Calcareous Alps coral-stromatoporoid reefs (Plassen carbonate platform; Schlagintweit and Gawlick, 2007, 2008); 9 Portugal carbonate platforms in Atlantic realm with reefs with corals, stromatoporoids, siliceous sponges and microbialites (Nose and Leinfelder, 1997).

5.4 Results

5.4.1 Facies types

Outcrop-based facies investigation and petrographic analysis allowed distinguishing 13 carbonate facies, labelled from F1 to F13 (Table 5.1), differently distributed within the Callovian to upper Kimmeridgian succession of the Dorgali, Mt. Tului and Baunei formations (*sensu* Jadoul et al., 2009, 2010). For methods refer to Chapert 4, section 4.1.

Facies	*Texture*	*Grain size and sorting*	*Non-skeletal grains*	*Skeletal grains*	*Bedding and sedimentary structures*	*Diagenetic features*	*Depositional environment*
F1-Cross-bedded ooidal-coated grain grainstone to packstone	G/P, rare W	Well-sorted, mainly 0.3-1 mm, locally up to 2 mm	Radial, sometimes partially micritized ooids (type 3) 0-70%; micritic ooids (type 1) 0-70%; aggregate grains (bound ooids, lumps) <20%; coated grains with micrite envelopes <20%; intraclasts (mudstone and ooidal grainstone) <20%; quartz grains <10%	Crinoids <20%; corals <10%; undetermined calcareous sponges <10%; bivalves <10%; brachiopods <10%; foraminifers (1, 2) <10%; siliceous sponge spicules <10%	Crossed or planar beds 0.5-1 m thick, planar and herringbone cross-lamination, normal grading, fining upward. Locally irregular siliceous sponge spicule wackestone lenses (1-15 mm).	Compaction: concavo-convex grain contacts. Ooids partially dissolved and replaced by equant calcite, except the micritic rim. Interparticle blocky calcite cement (50 µm). Voids filled by scalenohedral calcite cement followed by ferroan blocky calcite (300-600 µm) and rarely replaced by euhedral dolomite. Sparse dolomite euhedral crystals and post-compaction planar-e mosaic of dolomite (50-200 µm) with post-dolomitization blocky calcite cement.	High-energy, inner ramp
F2-Cross-laminated echinoderm packstone to grainstone-rudstone	P-G-R	Well-sorted, 0.5-5 mm	Recrystallized coated grains <20%	Crinoids 40-70%; echinoid spines 20-40%	Planar beds 1 m thick, cross-lamination, fining upward.	Partially dolomitized with: 1) matrix of fine-grained (20-50 µm) planar-s dolomite mosaic, 2) echinoderms recrystallized with a mosaic of coarse grained (50-150 µm) planar-e/-s limpid dolomite crystals; 3) mosaic of planar-e dolomite (100-200 µm) with Fe-oxides between crystals. Blocky equant calcite cement post dolomitization.	High-energy, middle ramp
F3-Peloidal packstone with ooids and echinoderms	P	Moderately-sorted, 50-500 µm	Peloids 50-70%; micritized radial ooids (type 3) <20%; micrite intraclasts <20%	Crinoids <20%; echinoid spines <10%; foraminifers (3) <10%; bivalves <10%	Planar or irregular beds 20 cm-1 m thick.	Compaction with concavo-convex grain contacts and syntaxial cement around echinoderms precipitated before compaction. Microsparite between grains (10-20 µm).	Middle ramp
F4-Peloidal packstone with chert nodules and thin-shelled bivalves	P	Well-sorted, 50-250 µm	Peloids and fine grained (100-200 µm) coated grains with micrite envelopes 50-90%; detrital quartz <10%; micritic ooids (type 1) <10%; micritic intraclasts <10%	Thin-shelled bivalves 10-40%; foraminifers (2, 3) <10%; siliceous sponge spicules <10%; crinoids <10%; echinoid spines <10%	Nodular beds 5-10 cm thick, chert nodules, bioturbation.	Compaction with sutured and concavo-convex grain contacts, syntaxial cement around echinoderms pre-compaction. Locally dolomitized with fine euhedral or subhedral crystals (30-200 µm), with turbid nuclei and limpid outer rim.	Outer ramp
F5- Ooidal grainstone to packstone with intraclasts and bioclasts	G-P, sparse R	Moderately to well-sorted, 0.25-3 mm	Micritized radial ooids (type 3) 40-70%; micritic ooids (type 1) 10-40%; aggregate grains (bound ooids, sometimes by clotted peloidal micrite) <20%; rounded intraclasts (ooidal G-P and clotted peloidal micrite) <20%	Coral fragments (encrusted by clotted peloidal micrite or dense micritic crusts) <20%; crinoids<20%; gastropods <10%	Planar or irregular beds 0.5-1 m thick.	Variable texture: A) Grainstone, not showing compaction evidences, cemented by equant blocky calcite cement (50-70 µm) or microsparite (10-20 µm). Dissolution with mouldic porosity (oo- and bio-mouldic); corals and gastropods replaced by equant blocky calcite mosaic (150-400 µm) locally with drusy fabric. B) Packstone well-compacted with concavo-convex grain contacts; isopachous cement rim (10-15 µm) precipitated before compaction. Some bioclasts dissolved and replaced by fine-grained equant calcite (40-60 µm), followed by blocky calcite (500 µm).	Inner ramp

F6- Peloidal packstone with reworked intraclasts, bioclasts and coated grains	P, sparse R-G	Moderately to poorly sorted, 100 µm-2 mm, up to 6 mm	Peloids 40-70%; intraclasts (dense micrite and clotted peloidal micrite fragments) 10-30%; ooids (type 1) 0-30%; oncoids <10%; coated grains with micrite envelopes <10%	Crinoids 10-30%; coral fragments 0-30%; undetermined calcareous sponges 0-20%, *Neuropora lusitanica* <10%; chaetetids <10%, solenoporaceans <20%; bivalves <10%; foraminifers (1, 2, 3, 5, 6, 7, 8) <10%; siliceous sponge spicules <10%; brachiopods <10%; *Thaumatoporella* <10%; dasyclad algae (very rare)	Planar or irregular beds 20 cm-1 m thick, locally gradation, fining upward	Compaction with concavo-convex grain contacts; syntaxial cement around crinoids pre-compaction. Between grains micrite and microsparite (10-20 µm) or equant blocky calcite cement (80-700 µm).	Middle ramp alternating with build-up type 2 (F8, F11) and 3 (F8, F12)
F7- Peloidal packstone with Lenticulina	P, sparse W	Well-sorted, 30-250 µm, rare 1 mm	Peloids 70-90%; coated grains with micrite envelopes <20%	Crinoids <10%; echinoid spines <10%; foraminifers (3, 4, 5) <10%; bivalves <10%; siliceous sponge spicules <10%	Nodular beds, 5-30 cm thick, bioturbation, burrowing.	Compaction with concavo-convex grain contacts, between grains micrite or rarely microsparite (10 µm).	Distal middle to outer ramp
F8- Bioclastic packstone to grainstone-rudstone with clotted peloidal micrite fragments	P-G-R	Moderately to poorly sorted, 0.25-2 mm, rare up to 1.5 cm	Intraclasts (fragments of clotted peloidal and dense micrite) 30-50%; coated grains with micrite envelopes <20%	Crinoids 10-30%; solenoporaceans 0-30%; corals 0-30%; undetermined calcareous sponges 0-30%; stromatoporoids 0-20%; echinoid spines <10%; *Bacinella irregularis* <10%; foraminifers (1, 2, 3, 5, 6, 9); bivalves <10%; *Lithocodium aggregatum* <10%; siliceous sponges <10%; serpulids <10%; brachiopods <10%; gastropods <10%; *Thaumatoporella parvovesiculifera* <10%	Irregular bedding 0.5-1 m thick, planar and cross-lamination.	Compaction, concavo-convex grain contacts and syntaxial cement around echinoderms pre-compaction. Microsparite cement rim around grains (10-20 µm) followed by a mosaic of equant blocky calcite cement (30-500 µm).	Reworked debris around or within build-ups type 1 (F10), 2 (F11) to 3 (F12) in middle ramp
F9- Coral-stromatoporoid rudstone-grainstone	R-G	Poorly sorted, from 0.1 mm to 20 cm	Intraclasts (clotted peloidal and dense micrite fragments) 10-30%; peloids <10%	Colonial (thamnasterioid, phaceloid) and solitary corals 20-70%; stromatoporoids 0-70%; chaetetids 0-30%; undetermined calcareous sponges 0-30%; solenoporaceans 0-20%; crinoids 10-20%; foraminifers (1, 6, 10) <20%*; Bacinella irregularis*; serpulids <10%; *Lithocodium aggregatum* <10%; *Thaumatoporella parvovesiculifera* <10%; siliceous sponges (forming oncoids) <10%; diceratid bivalves <10%; other bivalves <10%; rare dasyclad algae (*Salpingoporella*); gastropods	Massive; 15 m thick.	Compacted, concavo-convex grain contacts; pre-compaction syntaxial cement on crinoids. Mosaic of equant blocky calcite cement (50-500 µm) in inter- and intraparticle porosity. Geopetal infill in corals, dissolved and replaced by blocky equant calcite (50-200 µm)	Around or within build-ups type 1 (F10) in middle ramp
F10- Coral-stromatoporoid boundstone	B, sediment within build-ups P		Angular and sub-angular intraclasts of clotted peloidal micrite and dense micrite <10%	Coral colonies (5 cm-2 m, phaceloid, cerioid and thamnasterioid) 60-80%; stromatoporoids <20%; undetermined calcareous sponges <10%, *Bacinella irregularis* <10%; *Lithocodium aggregatum* <10%; serpulids <10%; foraminifers (11) <10%; *Thaumatoporella parvovesiculifera* <10%	Thickness 14-45 m of massive B overlying and alternating with F9 beds. Framework of colonial corals in life position, encrusted by clotted peloidal micrite (10-35%) and microencrusters.	Corals dissolved and replaced by equant blocky calcite. Interparticle porosity filled by microsparite or fine-grained equant calcite cement, intraparticle porosity filled by equant blocky, scalenohedral or drusy calcite cement. Primary cavities filled by P with peloids, intraclasts of clotted peloidal and dense micrite and bioclasts.	Build-ups (type 1) in middle ramp

F11- Coral-calcareous sponge-diceratid boundstone	B, sediment between build-ups G-P		Intraclasts made of clotted peloidal micrite fragments and dense micrite fragments 10-20%; peloids <10%	Coral colonies 20-90% (5-50 cm, phaceloid and cerioid); solenoporaceans 10-20%; undetermined calcareous sponges 0-40%; stromatoporoids 0-20%, diceratids <10%; *Bacinella irregularis* <10%; *Lithocodium aggregatum* <10%; *Crescentiella morronensis* <10%; bivalves <10%; crustaceans <10%; crinoids <10%; foraminifers (nubeculars) <10%; serpulids <10%, siliceous sponge spicules <10%	Lens-shaped build-ups, 1-2 m thick and 3-4 m wide constituted by F11 and surrounded by F8. Framework of coral colonies in life-position encrusted by *Solenopora* and *Bacinella irregularis* and clotted peloidal micrite (5-40%).	Compaction, concavo-convex and sutured grain contacts. Rims of microsparite around some grains, followed by blocky calcite cement (500 µm-1 mm) or granular equant calcite (100-200 µm). Geopetal infill in corals, filled by clotted peloidal micrite or intraclastic-peloidal P-G. Corals replaced by blocky calcite (20-70 µm).	Build-ups (type 2) in middle ramp
F12- Sponge-coral-microbialite boundstone	B, sediment within build-ups P		Peloids 10-20%; intraclasts made of angular dense micrite and clotted peloidal micrite fragments <20%; ooids <10% (type 3)	Undetermined calcareous sponges 0-30% (up to 10 mm); chaetetids <20%; solenoporaceans 0-10%; solitary corals 0-30% (3-6 mm); siliceous sponges <20%; *Crescentiella morronensis* <10%	Lens-shaped build-ups, up to 1 m thick and 1 m wide, surrounded by F8. Framework of clotted peloidal micrite (30-40%) with sparse corals and undetermined calcareous sponges encrusted by siliceous sponges and microencrusters. Borings and cavities filled by sediment.	Corals dissolved and replaced by equant blocky calcite (50-200 µm) and geopetal infills. Interparticle space filled by fine-grained equant cement. Dissolution vugs filled by fine-grained (10-30 µm) sediment.	Build-ups (type 3) in distal middle to outer ramp
F13- Stromatoporoid rudstone to packstone with coated grains	R/P rare G	Poorly sorted, 0.2-2 mm with stromatoporoids up to 10 cm	Peloids 10-30%; aggregate grains (bound by *Bacinella irregularis*) <20%; ooids (type 1) <20%; intraclasts (peloidal P) <10%; oncoids <10%	Stromatoporoids 30-40%; crinoids <10%; echinoid spines <10%; brachiopods <10%; chaetetids <10%; undetermined calcareous sponges <10%, *Neuropora lusitanica* <10%	Planar or irregular beds, 50 cm-1 m thick	Geopetal infills, syntaxial cement around echinoderms, compaction, concavo-convex grain contacts, microsparite or fine-grained blocky calcite cement in interparticle porosity (20-30 µm) or scalenohedral calcite cement (60-80 µm), followed by blocky calcite cement (200-300 µm). Locally fractures filled by silt-sized sediment with sparse carbonate lithoclasts.	Middle ramp

Table 5.1 Description of the depositional facies of the investigated Callovian-upper Kimmeridgian portion of the eastern Sardinia carbonate succession. Foraminifers: 1-*Trocholina*; 2-*Protopeneroplis striata;* 3-Textularids*;* 4-*Lenticulina;* 5-Miliolids*;* 6-*Everticyclammina;* 7-*Labyrinthina mirabilis;* 8-*Nautiloculina oolithica;* 9-*Mohlerina basiliensis;* 10-Nubeculars; 11-*Troglotella incrustans.* Texture: M mudstone; W wackestone; P packstone; G grainstone; R rudstone; F floatstone; B boundstone

Facies F1 is a partially dolomitized cross-bedded ooidal-coated grain grainstone to packstone, with beds 0.5-1 m thick and local herringbone cross-lamination (Fig. 5.2A). It contains partially micritized ooids with radial sparitic laminae (type 3), micritic ooids (type 1), aggregate and coated grains with micrite envelopes (Fig. 5.2B). Discontinuous beds (1-15 mm thick) of siliceous sponge spicule wackestone may alternate within fining-upward grainstone beds with dominant type 1 micritic ooids (Fig. 5.2C). Facies F2 is a cross-laminated echinoderm packstone to grainstone-rudstone (Fig. 5.2D) in planar beds up to 1 m thick, with fining-upward grain-size trends, also partially dolomitized as F1 (Table 1). Facies F3 peloidal packstone is well bedded (0.2-1 m thick) and includes ooids and echinoderms. Facies F4 peloidal packstone with chert nodules and thin-shelled bivalves (Fig. 5.2E) is characterized by bioturbated thin nodular beds (5-10 cm) dominated by peloids and fine-grained coated grains (100-200 μm). Facies F5 is an ooidal grainstone to packstone with intraclasts and bioclasts (beds 0.5-1 m thick), dominated by type 3 partially micritized radial ooids and type 1 micritic tangential ooids (Fig. 5.2F-G). Facies F6 (0.2-1 m thick beds) consists of peloidal packstone with reworked intraclasts (mainly clotted peloidal and dense micrite fragments), skeletal fragments, ooids (type 1), oncoids and coated grains with micrite envelopes. Facies F7 consists of burrowed peloidal packstone to locally wackestone with *Lenticulina* foraminifer (Fig. 5.2H) in thin, nodular beds (5-30 cm thick).

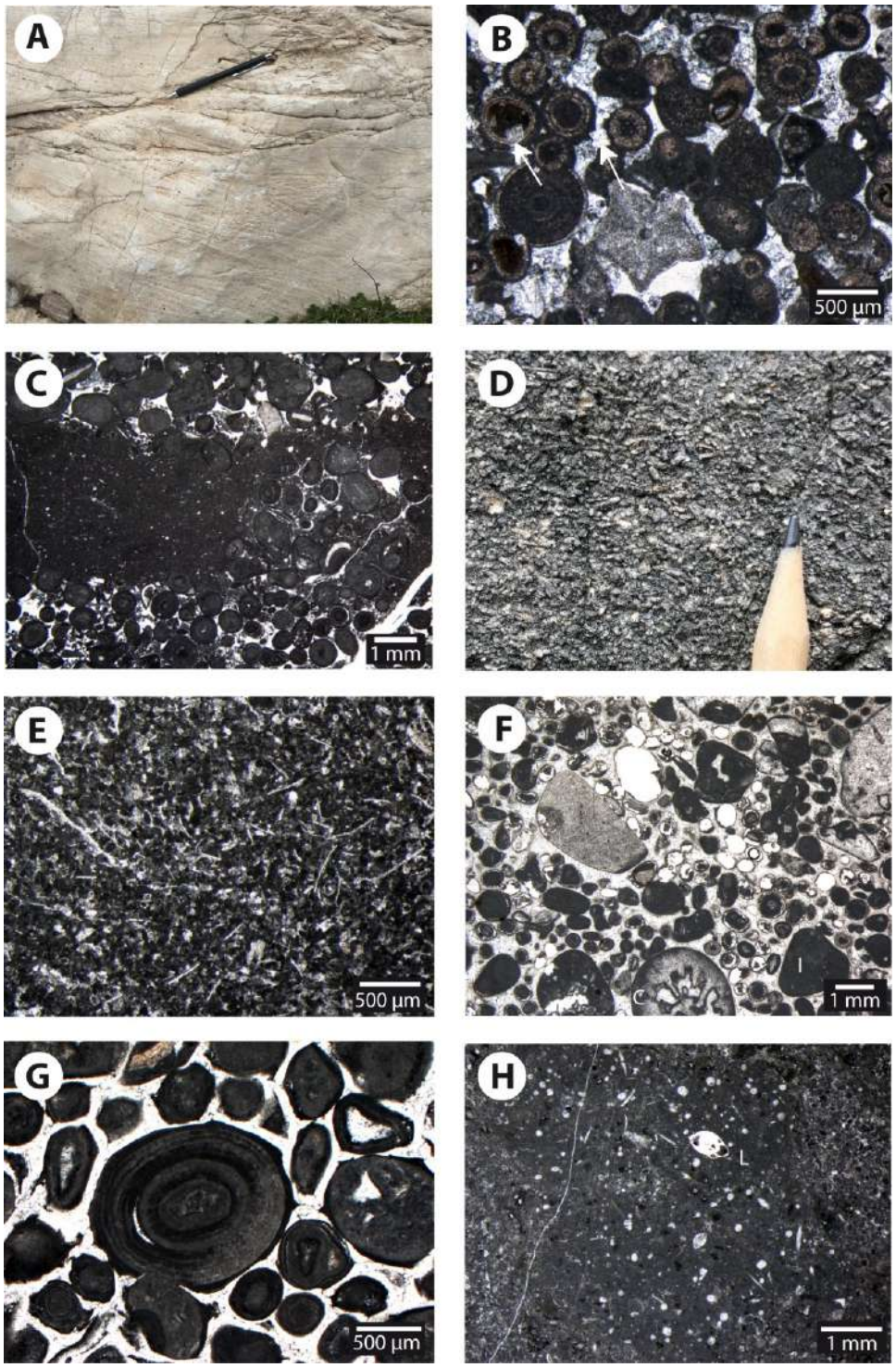

Figure 5.2 A) Outcrop photograph showing herringbone cross-lamination in F1 cross-bedded ooidal-coated grain grainstone to packstone. B) Photomicrograph of F1 cross-bedded ooidal coated grain grainstone showing type 3 ooids and type 1 micritic ooid laminae (which form also aggregate grains) and crinoids, partially dolomitized. Arrows point to euhedral dolomite crystals partially replacing the ooid. C) Photomicrograph of facies F1 showing grainstone with type 1 micritic ooids alternated with irregular wackestone lenses with sponge spicule wackestone. D) Outcrop photograph showing F2 echinoderm packstone to grainstone-rudstone. E) Photomicrograph of F4 peloidal packstone with echinoderms and thin-shelled bivalves. F) Photomicrograph of F5 ooidal grainstone with intraclasts and bioclasts showing type 1 and type 3 ooids, intraclasts (I) and fragments of coral (C) and crinoids, well-cemented by equant blocky calcite cement, with oo-mouldic porosity. G) Ooidal grainstone with intraclasts and bioclasts (F5) showing a compacted fabric with type 1 ooids and intraclasts of clotted peloidal micrite and an isopachous cement rim around grains, precipitated before compaction. H) F7 bioturbated peloidal packstone to wackestone with sponge spicules and *Lenticulina* foraminifers (L).

Facies F8 consists of cross-laminated beds (0.5-1 m thick) of bioclastic packstone to grainstone-rudstone rich in sub-angular to rounded intraclasts of clotted peloidal micrite and dense micrite fragments (Fig. 5.3A-B). Facies F9 is a poorly-sorted, massive, coral-stromatoporoid rudstone-grainstone with common colonial (thamnasterioids) and solitary corals and stromatoporoids (Fig. 5.3C-D), with encrustations by clotted peloidal micrite. Facies F9 contains also sub-angular to rounded intraclasts of clotted peloidal micrite (Fig. 5.3E) and dense micrite and peloids. Facies F10 consists of massive coral-stromatoporoid boundstone (Fig. 5.3F) tens of metres thick (14-45 m) with coral colonies in life position (0.05-2 m, mainly phaceloid, cerioid and thamnasterioid; Fig. 5.3G-H), associated with stromatoporoids, undetermined calcareous sponges and encrusted by clotted peloidal micrite, serpulids and foraminifers (*Troglotella incrustans*, Fig. 5.4A-B). Facies F11 is a coral-calcareous sponge-diceratid boundstone whose framework consists of dominant coral colonies and undetermined calcareous sponges in life position (Fig. 5.4C-E) with sparse stromatoporoids. Coral colonies (mainly phaceloid and cerioid) are often encrusted by solenoporaceans (Fig. 5.4F), *Bacinella irregularis* (Fig. 5.4G), *Lithocodium aggregatum* (Fig. 5.4H) and clotted peloidal micrite associated with diceratid bivalves (Fig. 5.4E). Facies F12 sponge-coral-microbialite boundstone consists of calcareous (Fig. 5.5A) and siliceous sponges (hexactinellid, Fig. 5.5B), chaetetids, solitary and phaceloid corals (Fig. 5.5C) and solenoporaceans showing coatings by micritic clotted peloidal micrite and *Crescentiella morronensis* (Fig. 5.5D). There are boring cavities filled by peloidal packstone (Fig. 5.5E) that also fills some primary growth framework voids. Facies F13 is a planar bedded (50 cm-1 m thick), poorly sorted skeletal rudstone to packstone, rarely grainstone, with coated grains and common stromatoporoids (up to 10 cm in diameter; Fig. 5.5F-H), peloids, aggregate grains (bound by *Bacinella irregularis*) and type 1 ooids.

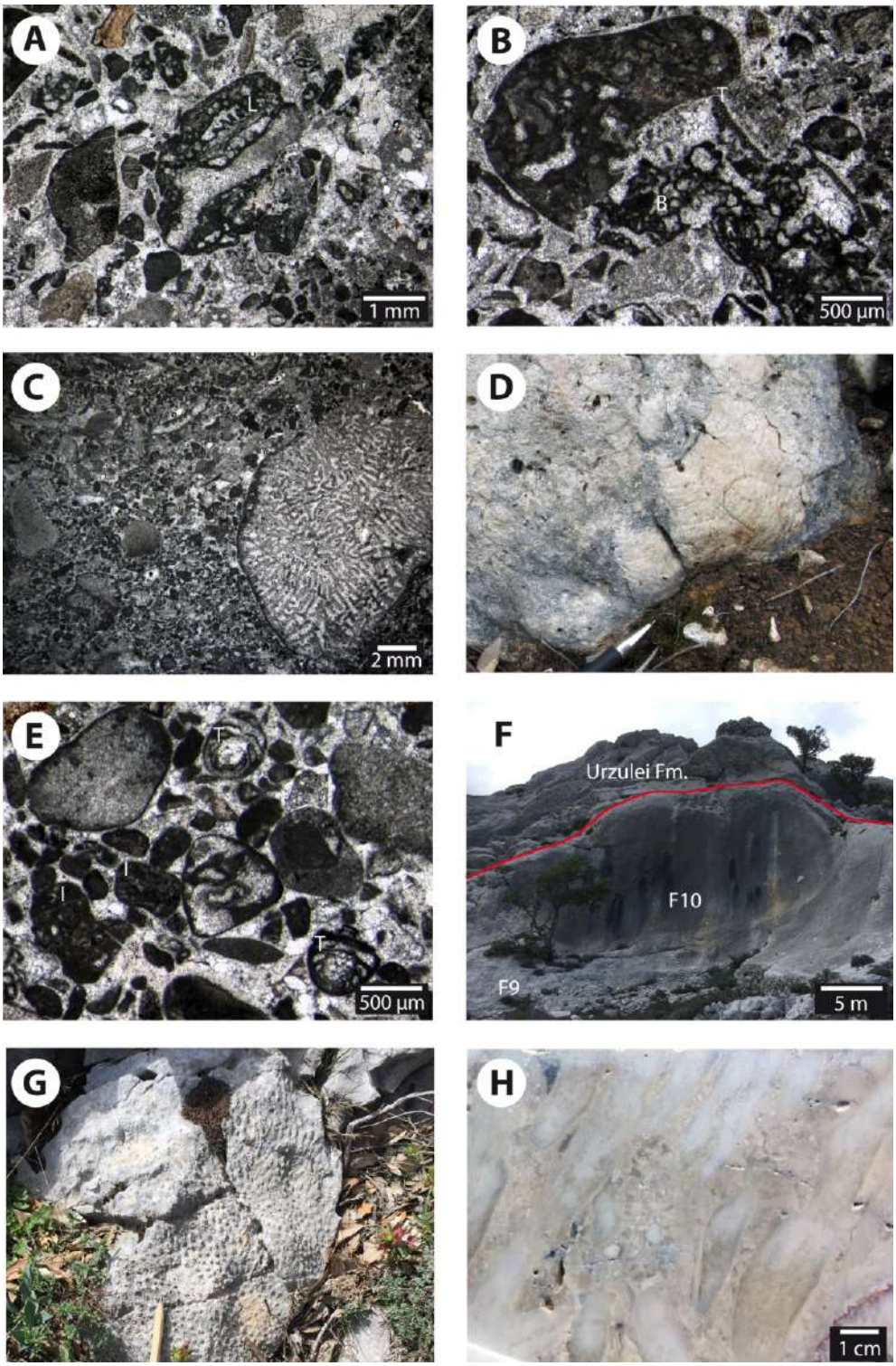

Figure 5.3 A) Photomicrograph of facies F8 bioclastic grainstone to packstone with clotted peloidal micrite and skeletal fragments, locally encrusted by the microencruster *Lithocodium aggregatum* (L). B) F8 bioclastic grainstone to packstone showing an intraclast of clotted peloidal micrite encrusted by *Bacinella irregularis* (B) and *Thaumatoporella parvovesiculifera* (T). C) Photomicrograph of F9 coral-stromatoporoid rudstone-grainstone with bioclasts and intraclasts and a thamnasterioid coral colony. D) Outcrop photograph showing centimetre- to decimetre-size stromatoporoids in facies F9. E) Photomicrograph of F9 grainstone with bioclasts, intraclasts of clotted peloidal micrite (I) and *Trocholina* benthic foraminifer (T). F) Outcrop photograph showing type 1 build-up composed of coral-stromatoporoid boundstone (F10) overlying coral-stromatoporoid rudstone (F9). G) Outcrop photograph of F10 coral-stromatoporoid boundstone showing decimetre-size phaceloid coral colony. H) Polished slab of F10 coral-stromatoporoid boundstone with phaceloid coral colony and intercorallite bioclastic-intraclastic grainstone.

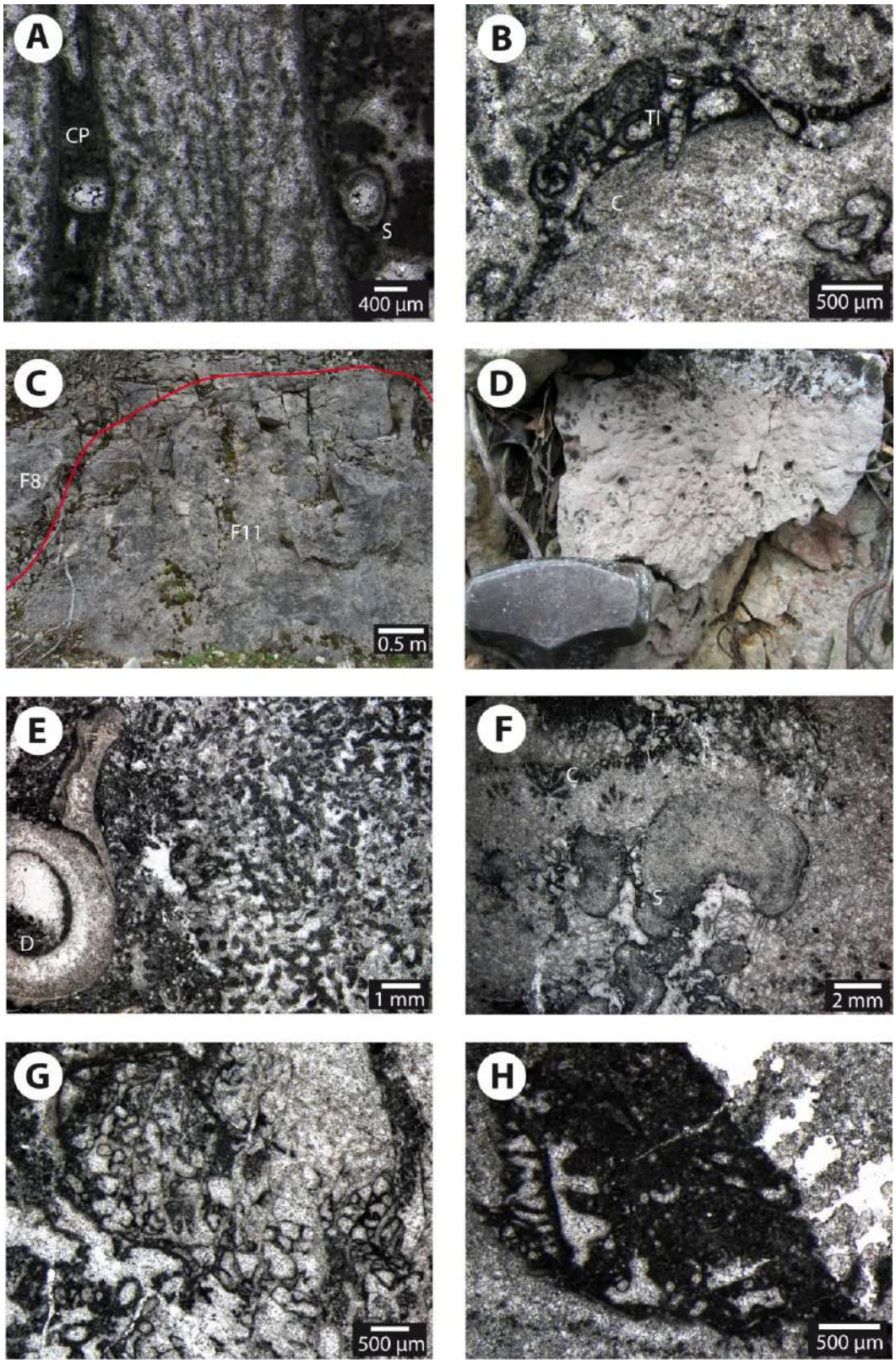

Figure 5.4 Photomicrograph of F10 boundstone with a branching coral colony encrusted by serpulids (S) and clotted peloidal micrite (CP). B) F10 thamnasterioid coral (C) encrusted by *Bacinella irregularis*, clotted peloidal micrite and the foraminifer *Troglotella incrustans* (TI). C) Outcrop photograph showing type 2 build-up composed of facies F8 bioclastic packstone to grainstone-rudstone with clotted peloidal micrite fragments and F11 coral-calcareous sponge-diceratid boundstone. D) Outcrop photograph of F11 phaceloid coral colony. E) Photomicrograph of F11 coral-calcareous sponge-diceratid boundstone with a calcareous sponge and diceratid bivalves (D) with geopetal infill. F) F11 boundstone with cerioid coral colony (C) encrusted by solenoporacean (S) and *Bacinella irregularis*. G) Detail of *Bacinella irregularis* in F11. H) Detail of *Lithocodium aggregatum* in F11.

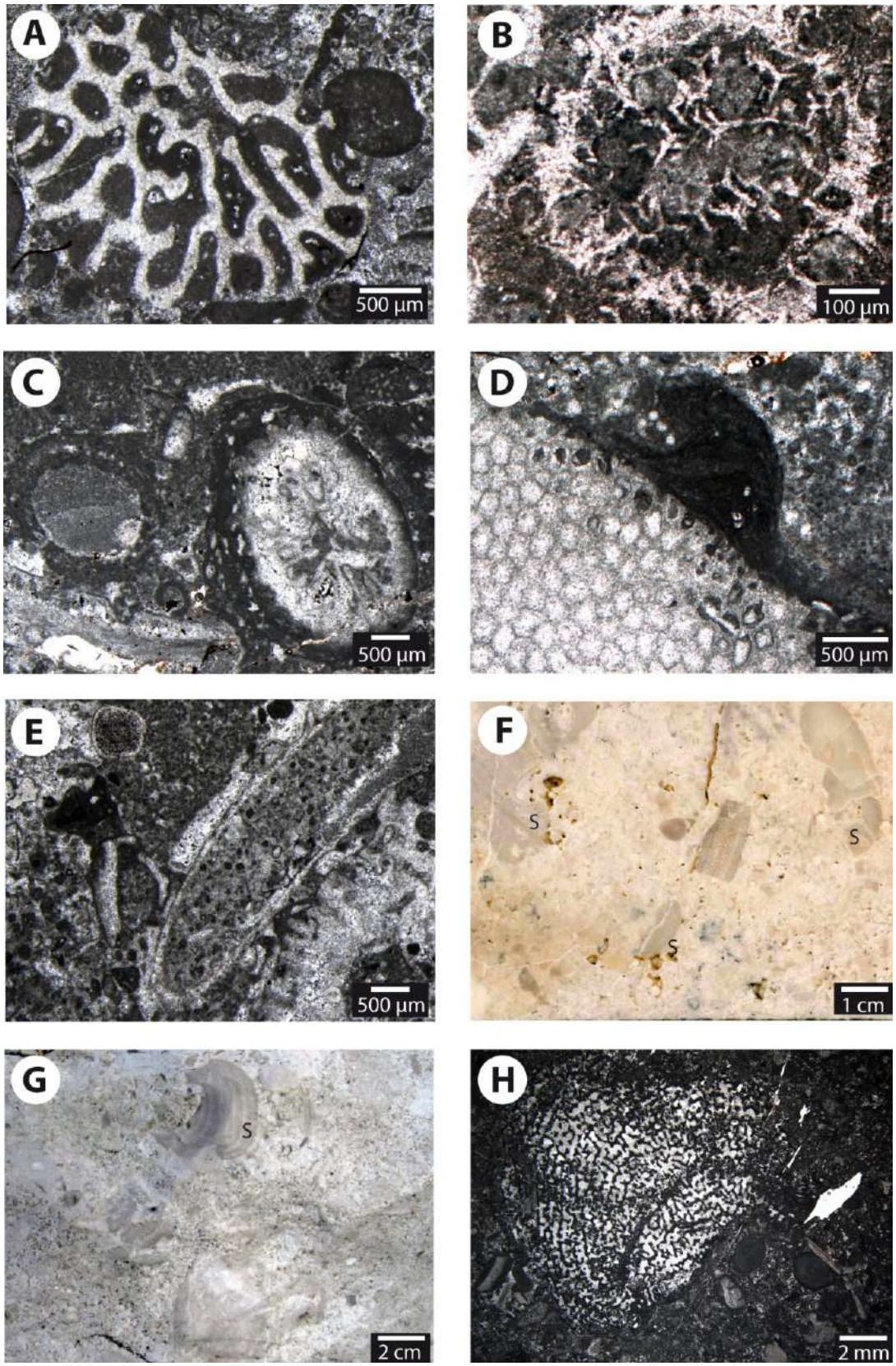

Figure 5.5 A) Photomicrograph of F12 sponge-coral-microbialite boundstone showing a calcareous sponge fragment. B) Facies F12 hexactinellid siliceous sponge. C) F12 boundstone with clotted peloidal micrite embedding corals surrounded by dense micrite and microencrusters. D) Chaetetid sponge encrusted by *Crescentiella morronensis* in F12. E) F12 sponge-coral-microbialite boundstone with millimetre-size boring cavities filled by peloidal sediment. F) Polished slab photograph of F13 stromatoporoid rudstone to packstone with stromatoporoid fragments (S) in a coated grain grainstone to packstone. G) Outcrop photograph of F13 stromatoporoids (S) within coated grain grainstone. H) F13 stromatoporoid within packstone with coated grains and peloids.

5.4.2 Dolomitized facies

As displayed in the stratigraphic logs, facies characterization suffered the widespread presence of replacive dolomitization in the lower part of the succession, close to the Hercynian basement comprising the Dorgali Fm. and lower part of Mt. Tului Fm. (e.g., the basal 20 m at Mt. Oro, 40 m at Genna Scalas, 25 m at Baunei Supramonte to 150 m at Genna Silana). Outcrop exposures show strata-bounding dolomitization or patchily dolomitized volumes (Fig. 5.6A). Some portions of the succession are only partially dolomitized, allowing the recognition of the original facies type (facies F1, F2 and F4). In these facies, dolomitization is characterized by post-compaction planar-e to planar-s mosaics of dolomite (20-200 µm) replacing grains and matrix and sealing grain contacts (Table 5.1). In pervasively dolomitized successions, dolomite consists of: 1) type 1 dolomite of planar-s to planar-e mosaics of dull or bright luminescent subhedral to euhedral crystals with size of 30-120 µm; and 2) type 2 dolomite (Fig. 5.6B) with coarser planar-e mosaic of zoned crystals (200-300 µm) with a turbid non luminescent to dull nucleus and an external limpid bright luminescent rim (Fig. 5.6C-D).

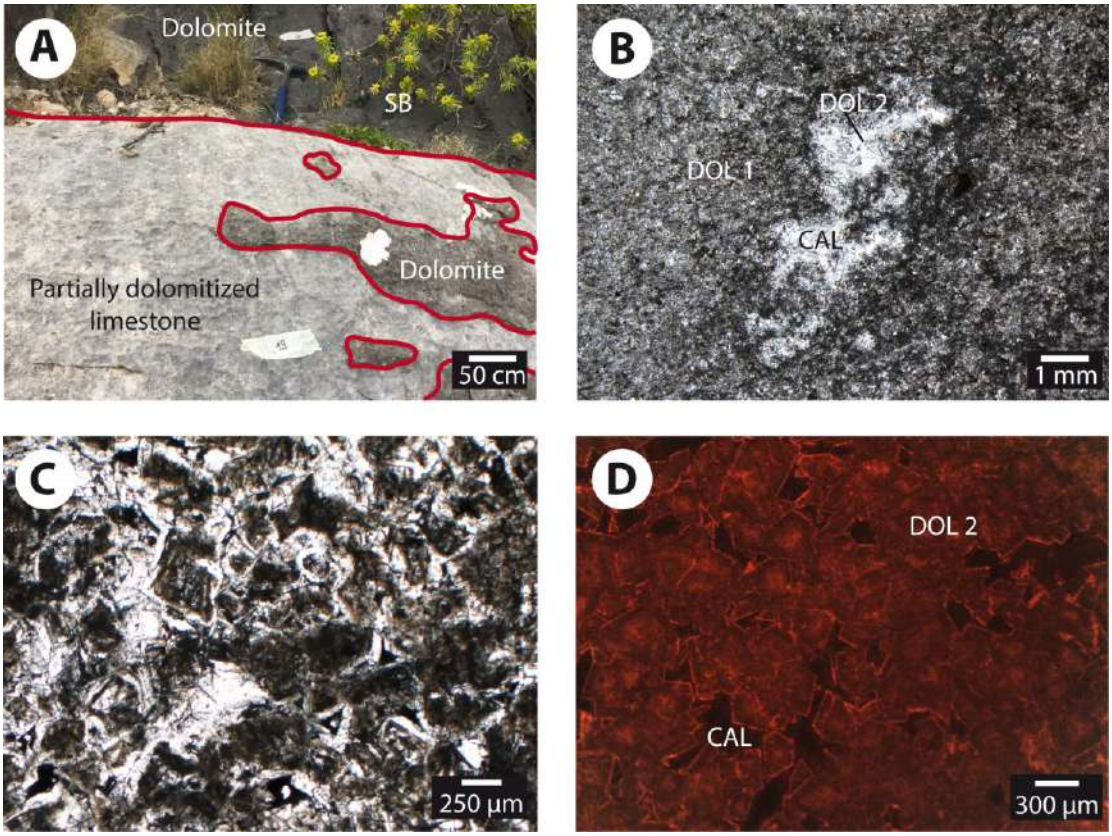

Figure 5.6 A) Outcrop photograph showing irregular dolomitized areas within limestone and strata-bound (SB) dolomitization (Baunei Supramonte). B) Photomicrograph showing a planar-s mosaic of dolomite crystals (DOL-1) and planar-e mosaic of white dolomite crystals in pores (DOL-2) followed by blocky calcite cement (CAL). C) Photomicrograph of DOL-2 showing a planar-e mosaic of dolomite crystals with turbid nucleus and limpid external rim. D) Photomicrograph in cathodoluminescence microscopy showing a luminescent planar-e mosaic of dolomite crystals (DOL-2), zoned, with a more luminescent external rim and non-luminescent blocky calcite cement in pores (CAL).

5.4.3 Facies spatial distribution and build-up types

Vertical and lateral facies distribution and physical correlation among the stratigraphic logs (Fig. 5.7) allowed distinguishing a lower and an upper part of the succession, characterized by different facies composition (Fig. 5.8).

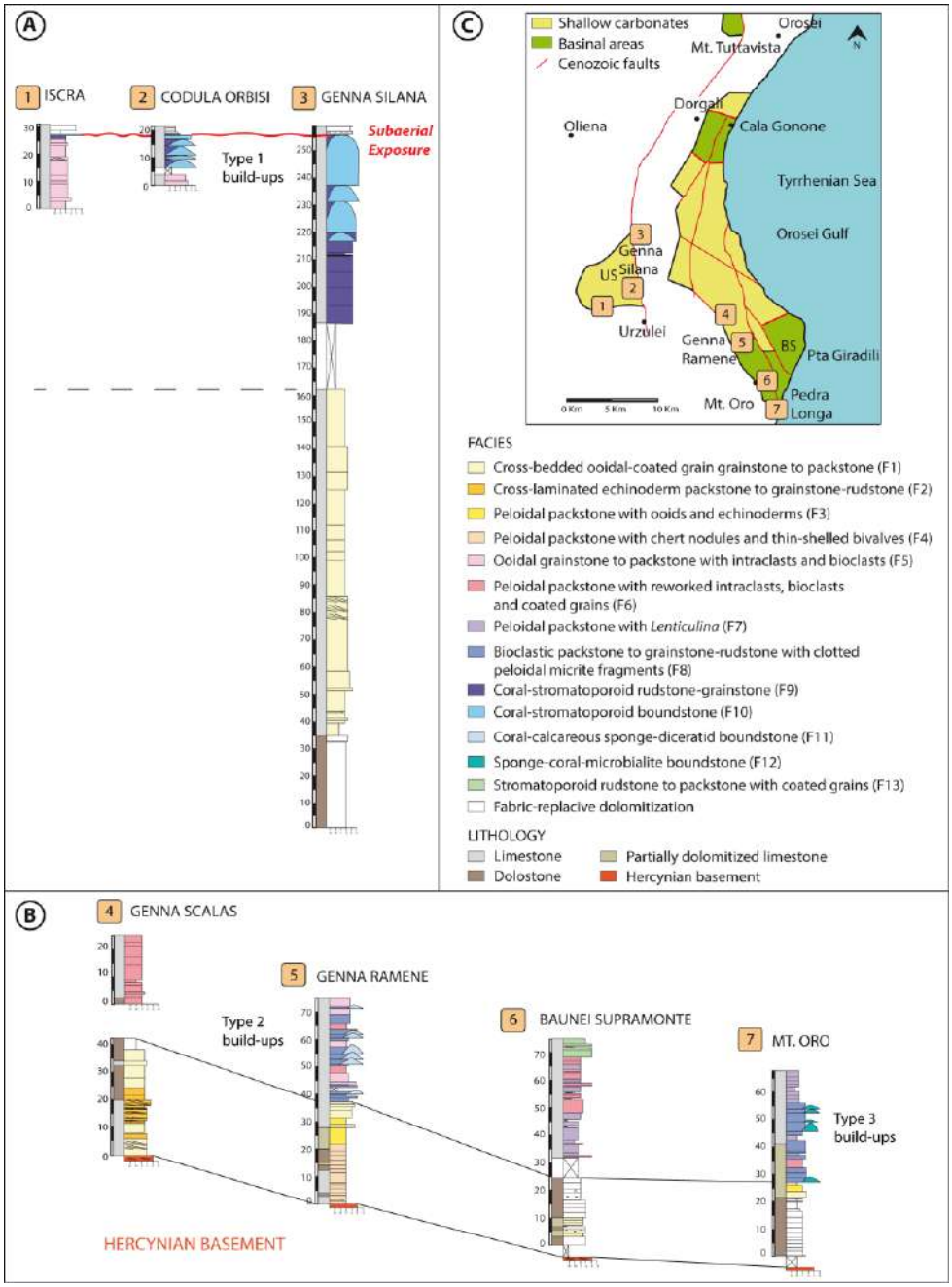

Figure 5.7 A-B) Correlation of stratigraphic logs in the NW (Urzulei Supramonte) shallower central area (A) and in the deeper Baunei Supramonte area (B) showing the vertical and lateral distribution of the distinguished facies types (F1 to F13) of the studied Callovian-upper Kimmeridgian succession. The lower part of the succession includes facies from F1 to F4 belonging to the Dorgali Fm, lower part of Mt. Tului Fm. and Baunei Fm. The upper part of the succession comprises facies from F5 to F15 belonging to the upper part of Mt. Tului Fm. and Baunei Fm. C) Sketch of the study area showing the location of stratigraphic logs.

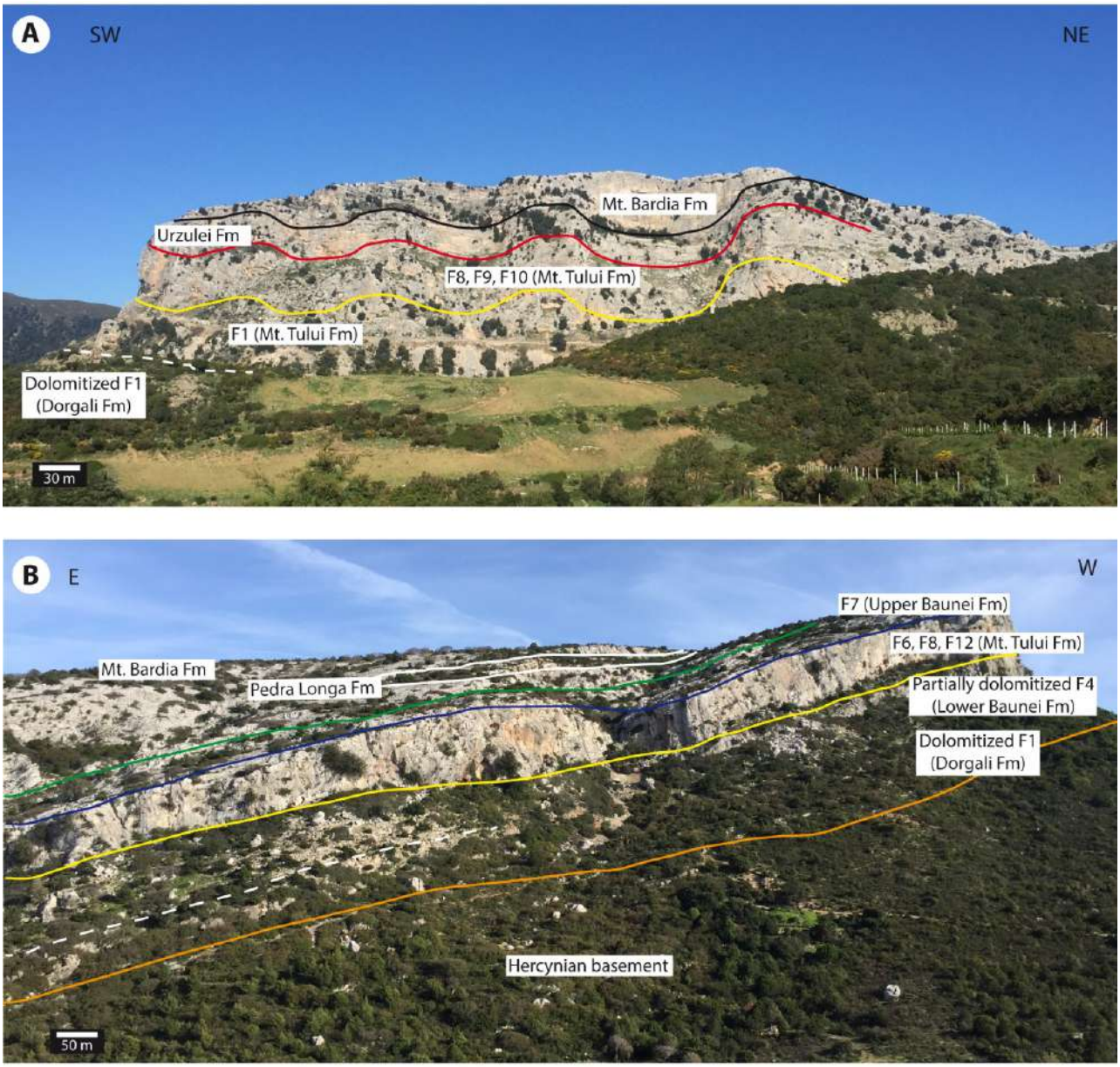

Figure 5.8 A) Panoramic view of the succession in the NW Urzulei Supramonte (Genna Silana stratigraphic log) showing from base to top: 1) the boundary between the dolomitized (Dorgali Fm.) and non-dolomitized (lower Mt. Tului Fm.) F1 (white dashed line); 2) the boundary (yellow line) between F1 (phase 1, Lower Mt. Tului Fm.) and F8, F9 and F10 (phase 2, Upper Mt. Tului Fm.); and 3) the erosional surface due to subaerial exposure at the top of F8, F9 and F10 (red line) overlain by the Mt. Bardia Fm. B) Panoramic view of the succession in the SE Baunei Supramonte (Mt. Oro stratigraphic log) showing from base to top: 1) the top of the Hercynian basement (orange line); 2) the boundary (yellow line) between the lower part of the succession including dolomitized and partially dolomitized F1 and F4 strata (phase 1, Dorgali Fm. and Lower Baunei Fm.) and the upper of the succession made of facies F6, F8 and F12 (phase 2, Mt. Tului Fm.); 3) the boundary (blue line) between F6, F8 and F12 (phase 2; Mt. Tului Fm.) and the overlying facies F7 (phase 2, Upper Baunei Fm.); 4) the top of the studied succession (green line) and the overlying Pedra Longa and Mt. Bardia formations.

The lower part of the studied succession consists of facies from F1 to F4. In the Urzulei Supramonte area (Fig. 5.8A) it is represented by up to 150 m of dolomitized carbonates (Fig. 5.7-5.8), which could not be ascribed to any identified facies due to the replacive dolomitization, capped by 150 m of partially dolomitized facies F1 cross-bedded ooidal-coated grain grainstone to packstone (Fig. 5.7A). Toward the east (Fig. 5.7B-C), F1 beds alternate with cross-laminated echinoderm packstone to grainstone-rudstone (F2, Genna Scalas), whereas towards south-east (Baunei Supramonte; Fig. 5.8B) F1 alternates or overlies facies F3 peloidal packstone with ooids and echinoderms and F4 peloidal packstone with chert nodules and thin-shelled bivalves (Genna Ramene, Mt. Oro; Fig. 5.7B-C). In this south-eastern domain, the succession comprising facies from F1 to F4 (nearly 30-40 m thick; Fig. 5.7B) directly covers the Hercynian basement and at it is overlain by a sharp facies change with the appearance of bioconstructions (F11, F12) and bioclastic grain-supported facies (F6, F8; Fig. 5.8B).
The upper portion of the studied succession is characterized by facies from F5 to F13. The boundstone facies (F10, F11 and F12) and bioclastic facies (F8, F9) are differently associated forming three types of discrete build-ups (labelled as type 1, 2 and 3), which differ for composition, shape, size and spatial distribution, as displayed in the measured stratigraphic logs (Fig. 5.7A-C). The type 1 build-up consists of massive coral-stromatoporoid boundstone (F10), overlying and associated with coral-stromatoporoid rudstone-grainstone (F9) and bioclastic packstone to grainstone-rudstone with clotted peloidal micrite fragments (F8). In the Urzulei Supramonte area (Iscra, Codula Orbisi, Genna Silana logs; Fig. 5.7A-5.8A) type 1 build-up forms the thickest (45 m) and most laterally continuous (few hundred metres) bioconstruction that thins from Genna Silana westward (Codula Orbisi 20 m, Iscra 2 m thick) and overlies in the westernmost part (Codula Orbisi, Iscra) facies F5 ooidal grainstone to packstone with intraclasts and bioclasts. The top of the coral-stromatoporoid boundstone (F10) is marked by an erosional surface caused by a prolonged subaerial exposure (Fig. 5.7A).
South-eastward, in the Baunei Supramonte area (Fig. 5.7B-5.8B), the upper part of the succession (35-40 m thick) includes build-ups type 2 (Genna Ramene) and 3 (Mt. Oro) alternated only with the F6 peloidal packstone with reworked intraclasts, bioclasts and coated grains or with both F6 and F7 peloidal packstone with *Lenticulina*, respectively. Type 2 build-ups are lens-shaped, 1-2 m thick and 3-4 m wide and made of coral-calcareous sponge-diceratid boundstone (F11), including both stromatoporoids and undetermined calcareous sponges, surrounded by bioclastic packstone to grainstone-rudstone with clotted peloidal micrite fragments (F8). Type 3 build-ups are lens-shaped or tabular bioconstructions, about 1 m thick and 1 m wide, made of calcareous and siliceous sponge-coral-microbialite boundstone (F12) surrounded by bioclastic packstone to grainstone-rudstone with clotted peloidal micrite fragments (F8). Bioconstructions were not recognized in Baunei Supramonte and Genna Scalas stratigraphic logs (Fig. 5.7B), where the upper part of the succession is

characterized by common fragments of build-up facies reworked in ooidal grainstone to packstone with intraclasts and bioclasts (F5), peloidal packstone with reworked intraclasts, bioclasts and coated grains (F6) and stromatoporoid rudstone to packstone with coated grains (F13).

5.5 Interpretation

5.5.1 Depositional model

The facies distribution observed in the studied Callovian-upper Kimmeridgian carbonate succession of eastern Sardinia allowed recognizing two superimposed depositional phases (phase 1 and 2) characterized by different carbonate factories and depositional models (Fig. 5.9-5.10). Phase 1 (lower part of the succession, Dorgali Fm., lower part of Baunei and Mt. Tului formations; Callovian-middle Oxfordian) is characterized by a coated-grain dominated carbonate ramp, encompassing facies from F1 to F4, whereas phase 2 (upper part of the succession, upper part of Baunei and Mt. Tului formations; upper Oxfordian-upper Kimmeridgian) represents the development of a carbonate ramp with coral, stromatoporoid, calcareous and siliceous sponge and microbialite build-ups (facies from F5 to F13). The phase 1 carbonate ramp dominated by coated grains was characterized by the gradual lateral facies variability common in a low-angle carbonate system (Fig. 5.8B) with laterally adjacent depositional environments and facies belts (from facies F1 to F4; Fig. 5.9). The detailed reconstruction of facies architecture in the lower part of phase 1 succession (Dorgali Fm.) is frequently prevented by irregularly distributed replacive dolomitization; nevertheless, the local presence of non-dolomitized or partially dolomitized strata confirms facies composition from F1 to F4. The petrographic and cathodoluminescence features of the replacive dolomite mosaics suggest that dolomitization took place during burial diagenesis in contact with fluid rich in Mn^{2+}, in reducing environments (cf. Hiatt and Pufahl, 2014). The irregular distribution of dolomitization, the thickness variability of the dolomitized portions, the irregular shape of the dolomitization front and the evidence of dolomite formation post-dating mechanical compaction, suggest that this burial dolomitization partially overprinted the sedimentary succession in proximity of the contact with the Hercynian basement.

Phase 1 cross-bedded ooidal-coated grain grainstone to packstone (F1) represents ooidal shoals or strand plain in a shallow subtidal environment of the inner ramp, above the effective fair-weather wave base, as demonstrated by the grain-supported texture, well-sorting and sedimentary structures. The presence of herringbone cross-lamination suggests, at least locally, tidal influence on these

deposits. The predominance of high-energy type 3 ooids reflects the continuous agitation of the seafloor. Episodes of low-energy sedimentation are demonstrated by thin irregular wackestone beds, suggesting that coated grain shoals were temporarily abandoned, enabling the deposition of mud in protected areas (cf. Samankassou et al., 2003). The cross-laminated echinoderm packstone to grainstone-rudstone (F2) was deposited in an open-marine, moderate to high-energy environment, probably in a deeper setting with respect to F1, under currents or storms action in a proximal middle ramp environment. This is suggested by the packstone to grainstone texture, good sorting and cross-lamination. The accumulation of crinoid ossicles can form carbonate sand bars in open marine, moderate energy environment on carbonate ramps and at platform margins (cf. Della Porta et al., 2004 and references therein). Facies F3 peloidal packstone with ooids and echinoderms suggests deposition in lower energy environments with respect to F1 and F2. The presence of sparse ooids and echinoderm fragments, frequently broken, suggests that these grains were reworked from adjacent shallower environments. Facies F3 was probably deposited in the middle ramp, not far from ooidal shoals, between fair-weather wave base and storm wave base, where low-energy conditions were occasionally interrupted by storms. Phase 1 more distal deposits consist of peloidal packstone with chert nodules and thin-shelled bivalves (F4). The abundance of micrite matrix and fine grain size that characterize facies F4 suggests deposition in a low-energy environment below the storm wave base. The skeletal biota association suggests open marine conditions, in particular the presence of thin-shelled bivalves (probably *Bositra*-like; Molina et al., 2018). Due to the frequent interfingering with middle ramp facies F3, this environment could be interpreted as an outer ramp setting.

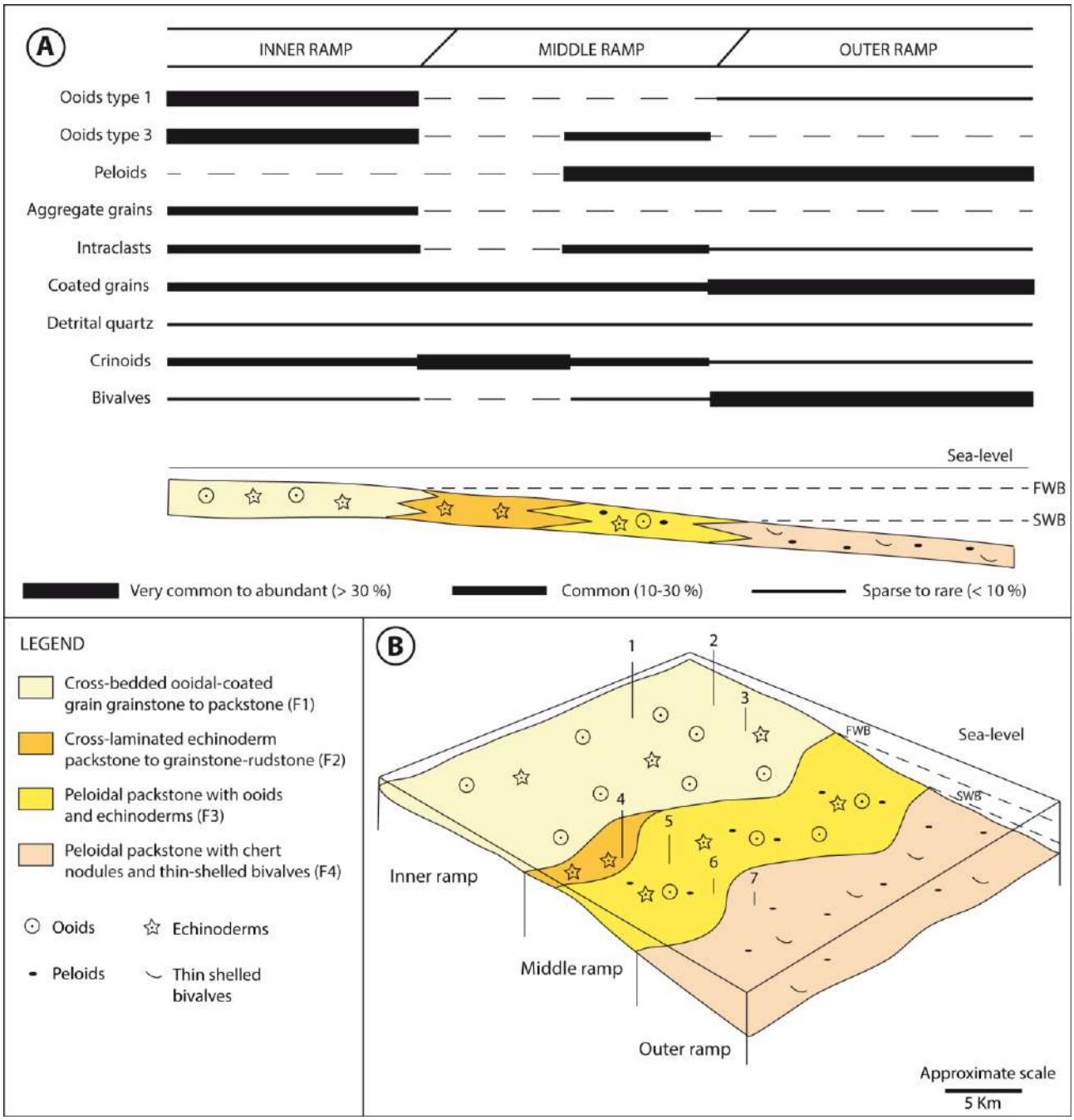

Figure 5.9 A) Semi-quantitative analysis of the carbonate components for different depositional environments and 2D interpretative depositional model of phase 1. B) Schematic sketch showing the spatial distribution of the depositional environments in phase 1 carbonate ramp dominated by ooidal coated grain grainstone facies. Approximate location of stratigraphic logs in Figure 5.7: 1 - Iscra; 2 - Codula Orbisi; 3 - Genna Silana; 4 - Genna Scalas; 5 - Genna Ramene; 6 - Supramonte Baunei; 7 - Mt. Oro.

Phase 2 carbonate ramp is characterized by a change in the carbonate factory (Fig. 5.10) and the onset of build-up growth (type 1 to 3) composed of different proportion of colonial or solitary corals, stromatoporoids, chaetetids, undetermined calcareous sponges, siliceous sponges, solenoporaceans, microencrusters and microbially influenced clotted peloidal and dense micrite precipitates (cf. similar fabrics in Olivier et al., 2003; Della Porta et al., 2013). Microencruster organisms (*Bacinella*

irregularis, Lithocodium aggregatum, Crescentiella morronensis, Thaumatoporella parvovesiculifera) are microfossils, often of *incertae sedis*, which encrust metazoans and were the focus of numerous studies regarding their taxonomy, palaeoecology and biostratigraphy (Elliot, 1956; Radoičić, 1959; Crescenti, 1969; Senowbari-Daryan et al., 2008; Dupraz and Strasser, 1999; Schlagintweit and Gawlick, 2008; Schlagintweit et al., 2010).

During phase 2, the inner ramp was characterized by the deposition of ooidal grainstone to packstone with intraclasts and bioclasts (F5). Phase 2 ooidal grainstone (F5) differs from phase 1 ooidal-coated grain grainstone (F1) for the abundance of bioclasts and intraclasts of clotted peloidal micrite. Facies F5 was deposited in a shallow subtidal high-energy environment, likely above the effective fair-weather wave base in the inner ramp. The common occurrence of micritic (type 1) and micritized radial ooids (type 3), formed in the high-energy environment under the continuous agitation of the sea floor suggests it represents an ooidal shoal. The presence of fragments of corals and clotted peloidal micrite suggests erosion and reworking of nearby coral-stromatoporoid reefs.

The middle ramp was characterized by the deposition of peloidal packstone with reworked bioclasts and coated grains (F6), the stromatoporoid rudstone to packstone with coated grains (F13) and by the development of the coral, stromatoporoid, calcareous and siliceous sponge build-ups (from F8 to F12). F6 peloidal packstone with reworked bioclasts and coated grains indicates deposition in a subtidal open marine environment below the fair-weather wave base in the middle ramp. The occurrence of fragmented skeletal and non-skeletal grains indicates reworking of inner ramp sediment and deposition above the storm wave base in a middle ramp environment. According to Flügel (2004) the benthic foraminifer *Trocholina*, common in facies F6, is typical of high-energy environments.

In type 1 build-ups (F8, F9 and F10), facies F8 bioclastic packstone to grainstone-rudstone with clotted peloidal micrite fragments suggests sedimentation in a relative high-energy environment where most of the grains derive from F10 coral-stromatoporoid boundstone, producing skeletal fragment of reef builders and intraclasts of clotted peloidal and dense micrite. In a similar way, the coral-stromatoporoid rudstone-grainstone (F9) is interpreted as the result of deposition of reefal debris in the higher energy area deriving from the erosion of the build-ups. Indeed, the composition of F9 is similar to F8, with some differences in the size of corals, stromatoporoids and other calcareous sponges. In the coral-stromatoporoid boundstone (F10) the dimension of coral colonies (reaching 2 m in width) and the common presence of stromatoporoids suggest a high-energy depositional environment. According to Leinfelder et al. (2005) stromatoporoids were well-adapted to live in high-energy abrasive environments. Type 1 build-ups formed in the proximal middle-ramp environment seaward with respect to the F5 ooidal shoals of the inner ramp (Fig. 5.10). The widespread presence of debris deriving from the bioconstructions in facies F8 and F9 testifies that

they were periodically exposed to storms and currents. San Miguel et al. (2013) interpreted deposits similar to F8 in the Kimmeridgian of the Iberian Basin as derived from storm-induced flows probably below the fair-weather wave base. Debris sheets rich in reefal material were frequently deposited following storm erosion and disintegration of the reefs (Bertling and Insalaco, 1998).

Type 2 build-ups (F8 and F11) are similar in composition to type 1 build-ups but are thinner and with reduced lateral continuity. The bioclastic packstone to grainstone-rudstone with clotted peloidal micrite fragments (F8) represents the debris deriving from the erosion of F11. In the coral-calcareous sponge-diceratid boundstone (F11) microbialites might have coexisted with the coral growth encrusting inter-corallite space and cryptic cavities, as suggested also by Olivier et al. (2003) for Kimmeridgian coral-microbial reefs in the Aquitanian Basin (France) and by Della Porta et al. (2013) for Lower Jurassic coral-calcareous sponge-microbial reefs in the High Atlas (Morocco). The association *Lithocodium aggregatum-Bacinella irregularis* suggests deposition in the photic zone (Dupraz and Strasser, 1999). The presence of stromatoporoids associated with other calcareous sponges and the dominance of phaceloid coral colonies suggest moderate-energy environments. Build-ups type 2 are interpreted as deposited in middle ramp settings under the action of storm waves associated with peloidal packstone with reworked bioclasts and coated grains (F6; Fig. 5.10).

In type 3 build-ups (F8 and F12) the presence of siliceous sponges suggests relatively deep environments, because typically during the Jurassic siliceous sponge mounds developed in deep shelves, middle to outer ramps or deep slopes, below storm wave-base (cf. Pittet and Mattioli, 2002; Bartolini et al., 2003; Olivier et al., 2004b; Della Porta et al., 2013). This is confirmed by the presence of the microencruster *Crescentiella morronensis* and relatively lack of the light-dependent association *Bacinella-Lithocodium* (cf. Dupraz and Strasser, 1999) with respect to type 1 and 2 build-ups. Type 3 build-ups lack high-energy stromatoporoids and accumulated in association with peloidal packstone with reworked bioclasts and coated grains (F6) and peloidal packstone with *Lenticulina* (F7) in distal middle ramp to outer ramp settings. The abundance of the microbially-mediated clotted peloidal micrite precipitates in the studied build-ups increases from type 1 to 3, i.e., towards more distal domains (Mt. Oro). This trend could be observed in other similar depositional systems, such as in the Kimmeridgian carbonate ramps of Spain, where the relative abundance of microbial crusts increases towards deeper settings (San Miguel et al., 2017). The stromatoporoid rudstone to packstone with coated grains (F13) was probably deposited in the middle ramp during storm events. Stromatoporoids and ooids were reworked respectively from build-ups type 1 and type 2 and shoals in higher energy environments.

The F7 peloidal packstone with *Lenticulina* accumulated in a low-energy distal middle to outer ramp environment based on the common occurrence of these foraminifers in open marine distal settings (cf. Hughes, 2004).

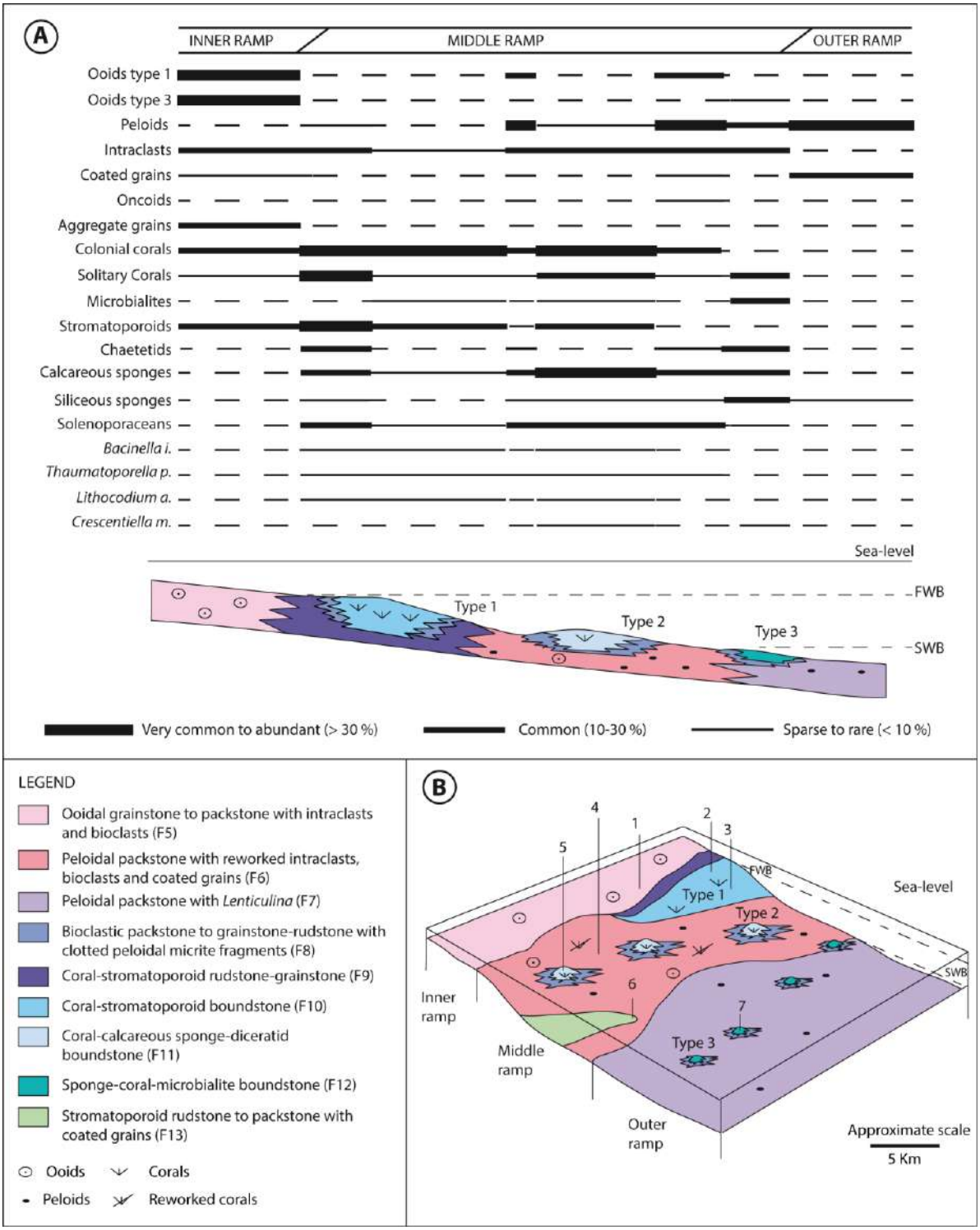

Figure 5.10 A) Semi-quantitative analysis of the carbonate components for different depositional environments and 2D interpretative depositional model of phase 2. B) Schematic sketch showing the spatial distribution of the depositional environments in phase 2 carbonate ramp with build-ups type 1 to 3. Approximate location of stratigraphic logs in Figure 5.7: 1 - Iscra; 2 - Codula Orbisi; 3 - Genna Silana; 4 - Genna Scalas; 5 - Genna Ramene; 6 - Supramonte Baunei; 7 - Mt. Oro.

5.6 Discussion

5.6.1 Global controls on Jurassic reefs

The evolution of Jurassic carbonate platforms was influenced by climatic and oceanographic changes, eustacy as well as syn-sedimentary tectonics (cf. Merino-Tomé et al., 2012; Brigaud et al., 2014). The extension of Upper Jurassic coral reefs at palaeolatitudes higher than 30 N and S suggests that global climate and seawater temperature were generally warm, at least in marine and coastal areas (Hallam, 1985; Leinfelder et al., 2002; Sellwood and Valdes, 2008). The uniformity of climatic conditions during the whole Jurassic is debated and recently questioned (Dromart et al., 2003; Dera et al., 2011; Jenkyns et al., 2011). The early Oxfordian is considered a relatively cool period characterized by a worldwide crisis of coral reef distribution (Martin-Garin et al., 2012), whereas a climate warming is suggested in the middle Oxfordian on the basis of biogeographical and geochemical data (Cecca et al., 2005; Dera et al., 2011), leading to ice pole melting and eustatic sea-level rise (Dromart et al., 2003). During the warm middle Oxfordian time (Cecca et al., 2005), coral reefs expanded towards the northernmost latitudes in the Jurassic (20-35° N) and were absent at low latitudes close to the Equator (Martin-Garin et al., 2012). The late Oxfordian is considered to be cooler with increased precipitation along the northern Tethys margin, lack of coral reefs at the higher latitudes occupied in the middle Oxfordian and their shift towards the equatorial belt (Martin-Garin et al., 2012). Nevertheless, according to Dera et al. (2011, 2015), the Late Oxfordian to Early Tithonian was a global warming event with acceleration of the hydrological cycle and shifts of the humid belts and locally cooler seawater temperatures might have been related to changes in ocean circulation driven by higher sea-level (Dera et al., 2015). Hence, the global peak of reef distribution and their diversity during middle Oxfordian to Kimmeridgian was probably related to optimal environmental conditions favoured by climatic oscillations (Cecca et al., 2005; Martin-Garin et al., 2010; Colombié et al., 2018) and/or by other parameters related to global sea-level and ocean circulation (Kiessling, 2009; Dera et al., 2015).

Eustatic sea-level fluctuations likely affected the accommodation for build-up growth: several studies pointed out a general global sea-level rise, with oscillations, throughout most of the Jurassic until the Kimmeridgian (Haq et al., 1987; Hardenbol et al., 1998; Hallam, 2001; Miller et al., 2005; Haq, 2018). Weissert and Mohr (1996) and Miller et al. (2005) identified a sea-level maximum in the late Oxfordian and early Kimmeridgian time, followed by a lowstand in the late Kimmeridgian. On the northern Tethys shelf, the sea-level rise is well reflected by the increase of reef sites during late Oxfordian and early Kimmeridgian (Leinfelder et al., 2002). The evolution of eastern Sardinia

carbonate system from a coated-grain dominated carbonate ramp (phase 1) to a reef-bearing ramp (phase 2) is likely related to the global spread of reefs with corals, stromatoporoids, calcareous and siliceous sponges and microbialites driven by the middle Oxfordian-Kimmeridgian climatic fluctuations and sea-level rise.

5.6.2 Comparison of eastern Sardinia build-ups with coeval reefs

The distribution of phase 2 build-up types with corals, diverse sponges, microencrusters and microbialites in the eastern Sardinia ramp fits well with the model proposed for the Late Jurassic "reef window" by Leinfelder et al. (2002). According to Leinfelder et al. (2002), three basic intergrading reef types existed throughout the Jurassic: siliceous sponge reefs, microbialite reefs and scleractinian coral and stromatoporoid reefs. The first two types developed in distal middle to outer ramp settings, whereas the scleractinian coral reefs developed at shelf margins or in shallow middle ramp environments (Crevello and Harris, 1984; Leinfelder, 1993b; Leinfelder et al., 2002). Coral-stromatoporoid-microbialite reefs and coral-debris reefs developed around or above storm wave base, whereas siliceous sponge mounds and microbialite reefs occurred in deeper, below storm wave base, settings (Leinfelder et al., 2002).

The Upper Jurassic coral-stromatoporoid, siliceous sponge and microbialite reefs distribution was governed by mechanisms different from present-day reefs. The reef window in the Late Jurassic was relatively wide (Leinfelder et al., 2002): corals thrived both in mesotrophic and oligotrophic settings because the photosymbiontic relationship with zooxanthellae was probably far from being perfect in the Jurassic (Nose and Leinfelder, 1997; Leinfelder et al., 2002). Many coral taxa likely required a higher amount of particulate nutrients and reef settings were influenced by fine siliciclastic input that may have reflected the importance of heterotrophic nutrition for corals (Nose and Leinfelder, 1997). Stromatoporoids could be associated with or result dominant in coral reefs in high-energy oligotrophic settings (Leinfelder et al., 2005).

Build-ups of eastern Sardinia represent a mixture between these end-member reef types and their distribution along the carbonate ramp reflects the modelled global distribution of coral-stromatoporoid, calcareous and siliceous sponge and microbialite reefs. Type 1 (F8, F9 and F10) and 2 (F8 and F11) reefs represent coral reefs with stromatoporoids, chaetetids, various calcareous sponges, diceratid bivalves and microbialite contribution, whereas type 3 build-ups (F8 and F12) are a mixture between siliceous sponges and coral-microbialite reefs, lacking stromatoporoids.

During the Late Jurassic, reefs with corals, stromatoporoids, calcareous or siliceous sponge and microbialites developed in the Alpine Tethys (Fig. 5.1) and in the Central Atlantic. Reefs from these palaeogeographic settings show differences in terms of composition, geometries and distribution along the depositional profile. The build-up types of eastern Sardinia display similarities and differences with coeval reefs from all these palaeogeographic settings.

As for the eastern Sardinia reefs, the northern Tethys reefs mainly developed on carbonate ramps in middle ramp settings exposed to the effect of storm waves, seaward of ooidal shoals representing the inner ramp facies belt. On the western margin of the Iberian Basin during the Kimmeridgian (Aurell et al., 2003; Alnazghah et al., 2013), pinnacle reefs are reported in the middle ramp (San Miguel et al., 2017), with similar composition but different geometry with respect to the type 2 lens-shaped build-ups of eastern Sardinia. Carbonate ramps with ooidal shoals in the inner ramp and coral-microbial reefs in middle-ramp environment are reported from the Oxfordian of the French Jura and Paris Basin (Burgundy, Armorican and Lorraine platforms), where an epicontinental sea flooded the area among scattered emerged lands (Bertling and Insalaco, 1998; Lathuilière et al., 2005; Olivier et al., 2011; Brigaud et al., 2014, Olivier, 2019).

Carbonate-producing biota associations are different in the northern Tethys coral-microbialite reefs that generally lack stromatoporoids (Leinfelder et al., 2002; Kiani Harchegani and Morsilli, 2019) with respect to eastern Sardinia reefs. This is considered to be due to lower water temperatures and scarce adaptation of stromatoporoids to mesotrophic conditions driven by high terrestrial run-off (Leinfelder et al., 2002, 2005). Exceptions are bioherms of chaetetids and *Cladocoropsis mirabilis* in lagoon and back-shoal environments (e.g., Spain, Sequero et al., 2019) and some coral-stromatoporoid-microbialite mounds in the Kimmeridgian of central Spain (Pomar et al., 2015). The microbial contribution to reef growth appears to be higher during the Oxfordian-Kimmeridgian in French (Olivier et al., 2003) and Spanish (San Miguel et al., 2017) reefs than in the eastern Sardinia build-up types.

Type 3 build-ups lack stromatoporoids and contain calcareous and siliceous sponges; the latter typically formed mounds in the northern Tethys in middle to outer ramp settings (Leinfelder, 1993b; Leinfelder et al., 2002). Among the most important occurrences of Upper Jurassic siliceous sponge build-ups, there were the Swabian and Franconian Alb (Oxfordian-Kimmeridgian) of southern Germany (Pittet and Mattioli, 2002; Bartolini et al., 2003; Olivier et al., 2004b), where siliceous sponge reefs formed isolated mounds on a homoclinal ramp. In the Oxfordian of Southern Spain, siliceous sponge-microbial bioconstructions developed in low-energy, nutrient-rich conditions (Olóriz et al., 2003a, b, 2006, 2012; Reolid et al., 2005, 2007). Other coeval examples in similar depositional conditions were described in Poland (Trammer, 1989; Matyszkiewicz et al., 2012) and

Romania (Franţescu, 2011). In eastern Sardinia, type 3 build-ups were probably formed in an ecological window overlapping between coral-stromatoporoid and siliceous sponge and microbialite environmental demands.

The Oxfordian-Kimmeridgian intra-Tethys reefs present similarities with eastern Sardinia reefs type 1 and 2 and show a different distribution pattern with respect to northern Tethys (Leinfelder et al., 2002). The characteristics of the intra-Tethys reefs are related to a structural setting deriving from extensional tectonics and lack of terrigenous input reaching the isolated platforms, favouring oligotrophic conditions (Leinfelder et al., 2002). The Upper Jurassic intra-Tethys reefs are characterized by abundant stromatoporoids and various calcareous sponges and reef zonation (Kiani Harchegani and Morsilli, 2019). For instance, in the Oxfordian-Kimmeridgian of Croatia (Turnšek et al., 1981), the reef complex consists of a back-reef lagoon with *Cladocoropsis* patch reefs, a high-energy zone dominated by stromatoporoids and a lower-energy one dominated by coral-chaetetid facies. Other examples of zoned reefs dominated by stromatoporoids are reported in the central Apennine (Kimmeridgian-Tithonian, *Ellipsactinia* Limestone; Rusciadelli et al., 2011), Apulian carbonate platform (Kiani Harchegani and Morsilli, 2019), Sicily (Tithonian-Valanginian, Basilone and Sulli, 2016), Friuli Platform in northern Italy (Upper Jurassic; Picotti and Cobianchi, 2017) and Northern Calcareous Alps (Austria, Kimmeridgian-Berriasian; Schlagintweit and Gawlick, 2008). The contribution of stromatoporoids, chaetetids and undetermined calcareous sponges in the eastern Sardinia type 1 and type 2 build-ups is important even though corals dominate. Nevertheless, the geometry of isolated platforms of the Alpine Tethys differs from eastern Sardinia carbonate ramp because of the different structural setting. The intra-Tethys platforms are characterized by tectonically controlled high-relief steep margins, with stromatoporoid-rich reefs developing at high-energy platform margin and coral-stromatoporoid patch reefs and microencruster-cement crust boundstone characterizing the fore-reef slope (Schlagintweit and Gawlick, 2008).

Differently from eastern Sardinia and other settings, in the southern Tethys extensive epeiric platform of the Arabian Peninsula, the bioconstructions were dominated by stromatoporoids and corals were not important reef builders (Hughes et al., 2008). This was likely controlled by high water temperature and oligotrophy in arid climate. Among stromatoporoids the most widespread was *Cladocoropsis mirabilis* in shallow protected lagoons (Hughes et al., 2008). The Oxfordian reefs of the Hanifa Fm. represent an exception, because mixed coral-stromatoporoid bioconstructions similar in composition to the eastern Sardinia type 1 and type 2 reefs, developed as well in middle ramp environment (Fallatah and Kerans, 2018).

The eastern Sardinia build-up types 1 to 3 with corals, stromatoporoids, calcareous and siliceous sponges and microbialites show some similar characters with reefs developed on carbonate systems in the Atlantic province in the Gulf Coast and Portugal.

Subsurface data from the Oxfordian Smackover Fm. (U.S. Gulf Coast) show ooidal shoals in the inner ramp facing siliceous and calcareous sponge, coral, microbialite reefs in the middle ramp (Crevello and Harris, 1984) and coral-stromatoporoid reefs in higher energy settings. The depositional model suggested for the Smackover Fm. resembles that proposed for phase 2 of eastern Sardinia. The siliceous and calcareous sponge, coral, microbialite build-ups formed in moderately agitated environment and show variability in composition related to bathymetry, with increasing abundance of siliceous sponges with depth and increase in coral content in shallower environments (Baria et al., 1982; Crevello and Harris, 1984). Transitional reefs (coral-siliceous sponge reefs) formed at intermediate depths between the pure siliceous sponge mounds and the coral-microbial reef environments, as observed in type 3 reefs of eastern Sardinia. Coral-stromatoporoid reefs in high-energy settings are similar in composition to type 1 build-ups. The eastern part of the North Atlantic province (Portugal) is represented by a wide variety of reefs developed in diverse structural settings. The most similar to the eastern Sardinia reefs developed in carbonate ramps (e.g., Algarve Basin, Oxfordian-Kimmeridgian; Leinfelder, 1993a) where coral reefs with debris deposits developed in the distal part of the inner ramp, mixed coral-siliceous sponge reefs accumulated in the middle ramp and microbial or siliceous sponge mounds occurred mostly in the outer ramp (Leinfelder, 1993a). In the Atlantic province, there are also reefs developed in structural settings different from eastern Sardinia showing less similarities with eastern Sardinia type reefs. Examples are the coral-calcareous sponge reefs with stromatoporoids and chaetetids developed at the margin of high-relief platforms in the Oxfordian-Kimmeridgian of the Abenaki Fm. along the shelf of Eastern Canada (Nova Scotia; Jansa et al., 1988; Pratt and Jansa, 1988), in Ota (Portugal, Kimmeridgian; Leinfelder, 1992; Nose, 1995), in the Oxfordian-Kimmeridgian coral-microbialite reefs developed at the margin of a tilted block in the eastern margin of the North Atlantic (Morocco; Ourribane et al., 2000; Olivier et al., 2012) or coral patch reefs occurring on coastal siliciclastic shelves (Portugal; Leinfelder, 1993a).

5.6.3 Controls on eastern Sardinia reef growth

The development of build-ups in the late Oxfordian-late Kimmeridgian (phase 2) carbonate ramp of eastern Sardinia is mostly controlled by light availability and water energy. The distribution of different build-up types reflects the bathymetric position, showing important variations of

composition and geometry related to water depth. The interplay of light penetration and hydrodynamic energy controlled the composition of the build-ups. Type 1 coral-stromatoporoid build-ups developed in the proximal middle ramp, whereas lens-shaped coral-calcareous sponge-diceratid type 2 build-ups, including stromatoporoids, formed in distal middle ramp settings. Type 3 coral-calcareous and siliceous sponge-microbialite build-ups lacking stromatoporoids formed in deeper middle to outer ramp environments, in lower energy and reduced light, where siliceous sponges, indicative of deeper depositional environments (Gaillard, 1983; Crevello and Harris, 1984; Leinfelder, 1993b; Della Porta et al., 2013), were common, associated with microbially-influenced clotted peloidal micritic precipitates. The bathymetric control on the distribution of different reef types reflects the control on the coeval reef distribution within carbonate ramps in northern Tethys and some carbonate platforms in the Atlantic region (Crevello and Harris, 1984; Leinfelder, 1993a; Leinfelder et al., 2002; Della Porta et al., 2013; Kiani Harchegani and Morsilli, 2019).

A secondary control on build-up composition could be nutrient level. The absence of stromatoporoids in coral reefs is considered to be indicative of mesotrophic environments and siliciclastic input in the northern Tethys (Leinfelder et al., 2005). Instead, the contemporaneous occurrence of stromatoporoids and chaetetids is suggested as indicative of oligotrophic settings (Leinfelder et al., 2005). The abundance of stromatoporoids in the intra-Tethys platforms is interpreted as a consequence of the oligotrophic conditions related to scarce siliciclastic input in isolated platforms (Leinfelder et al., 2005).

The composition of the eastern Sardinia upper Oxfordian-upper Kimmeridgian reefs is enriched in stromatoporoids, chaetetids and undetermined calcareous sponges with respect to other northern Tethys coeval reefs. This evidence may suggest for eastern Sardinia reduced nutrient levels and terrestrial run-off with respect to the mesotrophic conditions of the coeval northern Tethys attached carbonate ramps such as those in Spain (Bádenas and Aurell, 2010; San Miguel et al., 2017), France (Lathuiliere et al., 2005; Olivier et al., 2011), Swiss Jura (Dupraz and Strasser, 1999, 2002) and Germany (Olivier et al., 2004b).

5.7 Conclusions

The sedimentological study of the Callovian-upper Kimmeridgian portion of the eastern Sardinia Jurassic-Lower Cretaceous carbonate succession (Dorgali, Mt. Tului and Baunei formations) allowed distinguishing 13 depositional facies belonging to two superimposed carbonate ramp phases. The carbonate system evolved from a coated grain-dominated carbonate ramp (phase 1; Callovian-middle

Oxfordian) to a reef-bearing carbonate ramp (phase 2; upper Oxfordian-upper Kimmeridgian). The evolution of the carbonate ramp reflects the global middle Oxfordian-early Kimmeridgian increase in reef diversity and distribution, driven by sea-level rise and climatic fluctuations. During phase 2, three different build-up types were identified, largely controlled in terms of composition and spatial distribution by bathymetry that influenced light penetration levels and water energy as in coeval northern Tethys and Atlantic carbonate systems. Coral-stromatoporoid and coral-calcareous sponge-diceratid reefs with stromatoporoids (build-up type 1 and 2) developed in middle ramp, intermittent high-energy environments, exposed to the reworking effect of storm currents, whereas calcareous and siliceous sponge-coral-microbialite reefs lacking stromatoporoids (type 3) developed in lower energy environments in the distal middle to outer ramp. The abundance of stromatoporoids, chaetetids and undetermined calcareous sponges in build-up type 1 and 2 differentiate the eastern Sardinia upper Oxfordian-upper Kimmeridgian reefs from the coeval northern Tethys reefs, likely due to reduced nutrient availability and terrestrial run-off in eastern Sardinia with respect to the northern Tethys shelves. Thus, the eastern Sardinia carbonate ramp represents a transitional reef realm bridging the attached northern Tethys platforms and the isolated intra-Tethys platform

Chapter 6

Geometry and carbonate factory changes across a Jurassic carbonate ramp

6.1 Abstract

The development through time of carbonate platforms is affected by the interplay of several factors, among which the most important are the characters of carbonate factories, climate, global sea-level fluctuations and regional tectonics. This study focuses on the Middle-Upper Jurassic eastern Sardinia carbonate succession, a well-exposed carbonate system that recorded four superimposed depositional phases driven by changes in carbonate factories and accommodation. Phase 1 (Callovian-middle Oxfordian) was characterized by a carbonate ramp dominated by coated grains. Phase 2 (late Oxfordian-late Kimmeridgian) recorded the colonization of the carbonate ramp by reefal communities (corals, stromatoporoids, calcareous and siliceous sponges, microbialites). Phase 3 followed a sea-level fall testified by a subaerial exposure surface (late Kimmeridgian) and recorded a change in carbonate production and depositional environments. During phase 3 the depositional system was characterized by peritidal facies in the more proximal areas and coated-grain dominated (ooids and oncoids) middle ramp facies in the more distal areas. The top of phase 3 is marked as well by a subaerial exposure (latest Kimmeridgian), recorded in other depositional settings of the Tethyan realm by an unconformity attributed to extensional tectonics. Phase 4 (Tithonian) is characterized by transgressive basinal deposits followed by the recovery of the reefal carbonate factory and a change in depositional geometry evolving from a carbonate ramp to a higher-relief platform geometry with a slope about 70 m high and 3-15º steep.

The evolution of eastern Sardinia carbonate system was controlled by different factors. Extensional tectonics affecting the European margin of the Alpine Tethys controlled relative sea-level and accommodation changes. Jurassic plate motion modified eastern Sardinia palaeogeographic position leading to the switch of climatic belt from humid to arid conditions directly influencing facies characters. Environmental conditions and the Late Jurassic spread of reefal communities in the Tethys realm promoted the onset of reefal carbonate factories characterized by corals, stromatoporoids, sponges, microbialites and microencrusters during phase 2 and phase 4 as recorded in coeval Tethyan carbonate platforms.

6.2 Introduction

The growth and evolution through time of carbonate platforms in terms of facies characters and architecture is the result of a complex interplay between several variables affecting the nature and rates of carbonate sediment production, redistribution and accumulation and accommodation changes (Pomar, 2001; Schlager, 2003; Pomar and Hallock, 2008; Pomar and Kendall, 2008). These factors are controlled by a variety of parameters, among which the most important are tectonics, eustasy and changes in the carbonate factory.

The Jurassic was a key period for the development of carbonate platforms coeval with major tectonic plate reorganization and climate changes. The gradual break-up of Pangea (Stampfli and Borel, 2002; Golonka, 2004, 2007; Frizon de Lamotte et al., 2015) led to the opening of the Central Atlantic Ocean and the Alpine Tethys (Stampfli and Hochard, 2009; Masini et al., 2013), influencing the sedimentation and the development of carbonate platforms in the Tethys realm. During the Late Jurassic, the European margin of the Alpine Tethys Ocean was affected by extensional tectonics associated with rifting causing variation in subsidence rate and accommodation (Brigaud et al., 2014; Aurell et al., 2019a, b).

Climate during the Jurassic was not uniform with fluctuations associated with important global changes (Dera et al., 2011). The Callovian-Oxfordian time was characterized by a cooling event (Dromart et al., 2003) and a crisis of carbonate production (Cecca et al., 2005; Martin-Garin et al., 2010), followed by a warming trend leading to greenhouse-type conditions (Cecca et al., 2005; Dera et al., 2011). Sea-level fluctuations are the result of the interplay between global tectonics and climate changes (Miller et al., 2005). The eustatic curves proposed by Hallam (1981, 2001), Haq et al. (1987), Miller et al. (2005) and Haq (2018) pointed out sea-level rise episodes in the late Bajocian, middle Callovian, late Oxfordian and early Tithonian. The late Oxfordian rise was probably driven by global warming (Dromart et al., 2003) and the break-up of Gondwana leading to the formation of the Indian Ocean (Hallam, 2001).

In this geodynamic and climatic scenario, a variety of carbonate producing factories, influenced by global and regional changes, characterized the Jurassic carbonate platforms. In particular, the middle Oxfordian-Kimmeridgian spread of reefs built by corals, stromatoporoids, calcareous and siliceous sponges and microbialites affected Jurassic carbonate sedimentation (Leinfelder et al., 2002).

In the Tethys realm, the most studied case studies in which carbonate platform development was controlled by interplay of regional tectonics, eustatic sea-level oscillations and various carbonate producing factories and reef types are in the Central Iberian rift system (Spain, Badenas and Aurell, 2001; Aurell et al., 2003; Aurell et al., 2019a), North Iberian Range (Benito et al., 2001), Swiss Jura

(Jank et al., 2006), La Rochelle Platform (France, Carcel et al., 2010), Provence Platform (France, Jacquin et al., 1998), Mt. Salève Platform (France, Bover-Arnal and Strasser, 2013) and Dinaric Platform (Croatia and Slovenia, Strohmenger et al., 1991).

The well-exposed Bathonian-Berriasian (from Middle Jurassic to Lower Cretaceous) carbonate succession of eastern Sardinia (Orosei Gulf), developed on the European passive margin of the Alpine Tethys (Fig. 6.1), reveals a complex sedimentary evolution affected by the interplay of syn-sedimentary extensional tectonics, eustasy and changes in carbonate factory. Previous studies on the eastern Sardinia Bathonian-Berriasian carbonate succession focused on the stratigraphic reconstruction of the sedimentary succession (Jadoul et al., 2009, 2010; Lanfranchi et al., 2011; Casellato et al., 2012; Jadoul, 2018) and on the characterization of Oxfordian-Kimmeridgian (Chapter 5; Nembrini et al., 2021) and Tithonian reefs (Ricci et al., 2018). This study, on the basis of detailed facies analysis and new biostratigraphic data, proposes a revised interpretation of the Callovian-Tithonian portion of the carbonate system cropping out in the southern part of the Orosei Gulf. The aims of this study are to document in detail the facies characters and changes in facies architectures and platform geometries in time and space and to unravel how intrinsic (type of carbonate factory), regional (tectonics) and global (eustasy) controlling factors affected the evolution of a Middle-Upper Jurassic carbonate platform.

6.3 Geological setting

During the Late Jurassic Sardinia was placed at tropical latitude (Dieni and Massari, 1985; Muttoni et al., 2018) on the northern passive margin of the Alpine Tethys (Fig. 6.1). From the Middle Jurassic to Early Cretaceous a 650 m thick carbonate succession (Fig. 3.3 in Chapter 3) accumulated in eastern Sardinia (Jadoul et al., 2009), recording shallow marine depositional settings in the central area of the Orosei Gulf and deeper basinal ones to North and to the South (Fig. 3.4 in Chapter 3; Jadoul et al., 2009, 2010; Casellato et al., 2012).

The first carbonate deposits consist of dolostone and dolomitized limestone (Bathonian-Callovian, Dorgali Fm., Jadoul et al., 2009) representing a carbonate ramp dominated by ooidal and oo-crinoidal grainstone. In the northern Orosei Gulf, the onset of carbonate sedimentation (Dorgali Fm.) was dated to the late Bathonian based on calcareous nannoplankton biostratigraphy (Casellato et al., 2012). Jadoul et al. (2009) subdivided the stratigraphic succession overlying the Dorgali Fm., ranging from the Oxfordian to the Berriasian, in three transgressive-regressive (T-R) cycles (I-III in Figure 3.3 in Chapter 3). The first T-R cycle (T-R I, Oxfordian-early Kimmeridgian; Jadoul et al., 2009) was characterized by a carbonate ramp dominated by coated grains in the inner and middle ramp (Lower

Mt. Tului Fm.) passing to outer ramp/basinal deposits southward (Lower Baunei Fm.) and northward (S'Adde Limestone; Jadoul et al., 2009, 2010). The occurrence of dynoflagellate associations at the base of the Lower Baunei Fm. constrains the basal transgression of the T-R I cycle to the Oxfordian. The second T-R cycle (T-R II, late Kimmeridgian-early Tithonian; Jadoul et al., 2009) is characterized by coral-stromatoporoid reefs and more bioclastic sediment composition, lithostratigraphically corresponding to the Upper Mt. Tului Fm. (Jadoul et al., 2009; Nembrini et al., 2021; Chapter 5) and outer ramp facies represented by the Upper Baunei Fm. and S'Adde Limestone (Jadoul et al., 2009). The top of the T-R II cycle is marked by a major regressive event that caused the subaerial exposure in the Urzulei Supramonte area (Fig. 3.4 in Chapter 3). The end of this cycle was dated to early Tithonian by Jadoul et al. (2009) in the southern outcropping area, whereas according to Casellato et al. (2012) and Muttoni et al. (2018) the top of S'Adde Limestone in the northern outcropping area is late Kimmeridgian.

The recovery of the carbonate platform corresponds to the beginning of the third T-R cycle (T-R III, early Tithonian-Berriasian; Jadoul et al., 2009) and is characterized by the development of coral-stromatoporoid bioherms with high coral diversity in the northern area (Cala Gonone, Lower Mt. Bardia Fm.; Ricci et al., 2018; Jadoul, 2018). The basal transgression in the southern portion of the Orosei Gulf (Baunei Supramonte) is represented by thin-bedded marly limestone (Pedra Longa Fm.; Jadoul et al., 2009), followed by prograding clinostratified sigmoidal bioclastic deposits (Lower Mt. Bardia Fm., Lanfranchi et al., 2011).

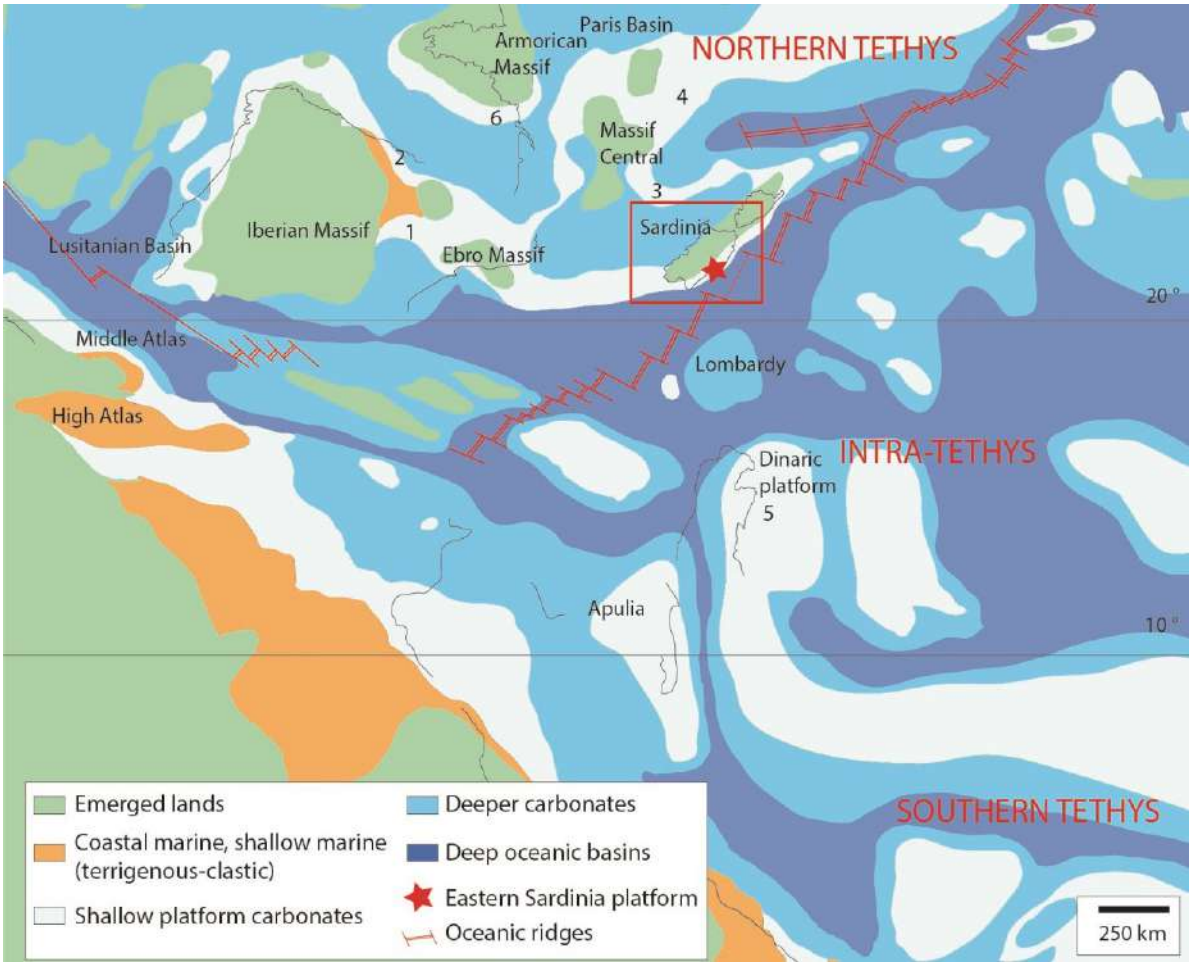

Figure 6.1 Palaeogeographic map of Tethys realm during the Kimmeridgian with the position of Sardinia (red square); modified after Dercourt et al. (2000). The distribution of coeval carbonate platforms controlled by tectonic activity and eustasy is marked as: 1 Central Iberian rift system (Aurell et al., 2019a); 2 North Iberian Range (Benito et al., 2001); 3 Provence Platform (Jacquin et al., 1998); 4 Mt. Salève Platform (Bover-Arnal and Strasser, 2013); 5 Dinaric Platform (Strohmenger et al., 1991); 6 La Rochelle Platform (Carcel et al., 2010).

6.4 Results

6.4.1 Facies characterization

Fieldwork and petrographic analysis (cf. methodology in Chapter 4, 4.1) allowed distinguishing 37 carbonate facies (Table 6.1) differently distributed and vertically stacked in the studied transect from the central NW outcrops of the Urzulei Supramonte to the SE Baunei Supramonte area (Fig. 6.2). Key stratigraphic surfaces allowed correlation among portions of the stratigraphic succession (Fig. 6.2).

	Facies type	*Grain size and sorting*	*Sedimentary features*	*Skeletal grains*	*Non skeletal grains*	*Diagenetic features*	*Spatial distribution*	*Depositional environment*
F1	Cross-bedded ooidal-coated grain grainstone to packstone	Well-sorted, mainly 0.3-1 mm, locally up to 2 mm	Crossed or planar beds 0.5-1 m thick, planar and herringbone cross-lamination, normal grading, fining upward. Locally irregular siliceous sponge spicule wackestone lenses (1-15 mm)	Crinoids; corals; undetermined calcareous sponges; bivalves; brachiopods; foraminifers (1, 2); siliceous sponge spicules	Radial, sometimes partially micritized ooids (type 3); micritic ooids (type 1); aggregate grains (bound ooids, lumps); coated grains with micrite envelopes; intraclasts (mudstone and ooidal grainstone); quartz grains	Compaction: concavo-convex grain contacts. Ooids partially dissolved and replaced by equant calcite, except the micritic rim. Interparticle blocky calcite cement (50 µm). Voids filled by scalenohedral calcite cement followed by ferroan blocky calcite (300-600 µm) and rarely replaced by euhedral dolomite. Sparse dolomite euhedral crystals and post-compaction planar-e mosaic of dolomite (50-200 µm) with post-dolomitization blocky calcite cement.	150 m thick in the Urzulei Supramonte area. In Genna Scalas log F1 alternates with F2 for about 25 m, in Genna Ramene log F1 alternates with F3 for about 15 m. In Baunei Supramonte and Mt. Oro logs partially dolomitized at the base.	Inner ramp
F2	Cross-laminated echinoderm packstone to grainstone-rudstone	Well-sorted, 0.5-5 mm	Planar beds 1 m, cross-lamination, fining upward	Crinoids; echinoid spines	Coated grains with micrite envelopes	Partially dolomitized with: 1) matrix of fine-grained (20-50 µm) planar-s dolomite mosaic, 2) echinoderms recrystallized with a mosaic of coarse grained (50-150 µm) planar-e/-s limpid dolomite crystals; 3) mosaic of planar-e dolomite (100-200 µm) with Fe-oxides between crystals. Blocky equant calcite cement post dolomitization.	Only in Genna Scalas log F2 alternates with F1 for about 25 m.	Proximal middle ramp
F3	Peloidal packstone with ooids and echinoderms	Moderately-sorted, 50-500 µm	Planar or irregular beds 20 cm-1 m	Crinoids; echinoid spines; foraminifers (3); bivalves	Peloids; micritized radial ooids (type 3); micrite intraclasts	Compaction with concavo-convex grain contacts and syntaxial cement around echinoderms precipitated before compaction. Microsparite between grains (10-20 µm).	In the Genna Ramene area F3 alternates with F1 for about 15 m.	Middle ramp
F4	Peloidal packstone with chert nodules and thin-shelled bivalves	Well-sorted, 50-250 µm	Nodular beds 5-10 cm, chert nodules, bioturbation	Thin shelled bivalves; foraminifers (2, 3); siliceous sponge spicules; crinoids; echinoid spines	Peloids and fine grained (100-200 µm) coated grains with micrite envelopes; detrital quartz; ooids (type 1); micritic intraclasts	Compaction with sutured and concavo-convex grain contacts, syntaxial cement around echinoderms pre-compaction. Locally dolomitized with fine euhedral or subhedral crystals (30-200 µm), with turbid nuclei and limpid outer rim.	Only in the Baunei Supramonte area (from Genna Ramene to Mt. Oro logs), 15-25 m thick.	Outer ramp

F5	Ooidal grainstone to packstone with intraclasts and bioclasts	Moderately to well-sorted, 0.25-3 mm	Planar or irregular beds 0.5-1 m	Coral fragments (encrusted by clotted peloidal micrite or dense micritic crusts); Crinoids; gastropods	Micritized radial ooids (type 3); micritic ooids (type 1); aggregate grains (bound ooids, sometimes by clotted peloidal micrite); rounded intraclasts (ooidal G-P and clotted peloidal micrite)	Variable texture: A) Grainstone, not showing mechanical compaction, cemented by equant blocky calcite cement (50-70 µm) or microsparite (10-20 µm). Dissolution with mouldic porosity (oo- and bio-mouldic); corals and gastropods replaced by equant blocky calcite mosaic (150-400 µm) locally with drusy fabric. B) Packstone compacted with concavo-convex grain contacts; isopachous cement rim (10-15 µm) precipitated before compaction. Some bioclasts dissolved and replaced by fine-grained equant calcite (40-60 µm), followed by blocky calcite (500 µm).	In the Urzulei Supramonte area (Iscra, Codula Orbisi) 15-20 m thick. In the Baunei Supramonte area (only Genna Ramene log) F5 alternates with F6, F7, F8 and F11 for an interval of about 30 m.	Inner ramp
F6	Peloidal packstone with reworked intraclasts, bioclasts and coated grains	Moderately to poorly sorted, 100 µm-2 mm, up to 6 mm	Planar or irregular beds 20 cm-1 m, locally gradation, fining upward	Crinoids; coral fragments; undetermined calcareous sponges; *Neuropora lusitanica*; chaetetids; solenoporaceans; bivalves; foraminifers (1, 2, 3, 5, 6, 7, 8); siliceous sponge spicules; brachiopods; *Thaumatoporella*; dasyclad algae (very rare)	Peloids; intraclasts (dense micrite and clotted peloidal micrite fragments); ooids (type1); oncoids (type I and II); coated grains with micrite envelopes	Compaction with concavo-convex grain contacts; syntaxial cement around crinoids pre-compaction. Between grains micrite and microsparite (10-20 µm) or equant blocky calcite cement (80-700 µm).	In the Baunei Supramonte area from Genna Scalas to Mt. Oro logs F6 alternates with F7, F8, F11 and F12 for 35-40 m.	Middle ramp
F7	Peloidal packstone with *Lenticulina*	Well-sorted, 30-250 µm, rare 1 mm	Nodular beds, 5-30 cm bioturbation, burrowing	Crinoids, echinoid spines, foraminifers (3, 4, 5), bivalves, siliceous sponge spicules	Peloids, coated grains with micrite envelopes	Compaction with concavo-convex grain contacts, between grains micrite or rarely microsparite (10 µm).	From Baunei Supramonte to Mt. Oro logs F7 alternates with F6, F8 and F12 for a thickness of about 35-40 m.	Distal middle to outer ramp

F8	Bioclastic packstone to grainstone-rudstone with clotted peloidal micrite fragments	Moderately to poorly sorted, 0.25-2 mm, rare up to 1.5 cm	Irregular bedding 0.5-1 m, planar and cross-lamination	Crinoids; solenoporaceans; corals; undetermined calcareous sponges; stromatoporoids; echinoid spines; *Bacinella irregularis*; foraminifers (1, 2, 3, 5, 6, 9); bivalves; *Lithocodium aggregatum*; siliceous sponges; serpulids; brachiopods; gastropods; *Thaumatoporella parvovesiculifera*	Intraclasts (fragments of clotted peloidal micrite and dense micrite); coated grains with micrite envelopes	Compaction, concavo-convex grain contacts and syntaxial cement around echinoderms pre-compaction. Microsparite cement rim around grains (10-20 μm) followed by a mosaic of equant blocky calcite cement (30-500 μm).	F8 associated with F9 and F10 (build-up type 1) in the Urzulei Supramonte area. F8 associated with F11 (build-up type 2) in Genna Ramene and with F12 (build-up type 3) in the Mt. Oro log.	Reworked debris around bioconstructions in middle ramp
F9	Coral-stromatoporoid rudstone-grainstone	Poorly sorted, from 0.1 mm to 20 cm	Massive, 15 m thick	Colonial (phaceloid, thamnasterioid) and solitary corals; stromatoporoids; chaetetids; undetermined calcareous sponges; solenoporaceans; crinoids; foraminifers (1, 6, 10); *Bacinella irregularis*; serpulids; *Lithocodium aggregatum*; *Thaumatoporella parvovesiculifera*; siliceous sponges (forming oncoids); diceratid bivalves; other bivalves; rare dasyclad algae (*Salpingoporella*); gastropods; brachiopods	Intraclasts (clotted peloidal and dense micrite fragments); peloids	Compacted, concavo-convex grain contacts; pre-compaction syntaxial cement on crinoids. Mosaic of equant blocky calcite cement (50-500 μm) in inter- and intraparticle porosity. Geopetal infill in corals, dissolved and replaced by blocky equant calcite (50-200 μm).	F9 associated with F8 and F10 in the Urzulei Supramonte area (build-up type 1).	Around or within build-ups made of F10 in proximal middle ramp

F10	Coral-stromatoporoid boundstone	Thickness 14-45 m of massive B overlying and alternating with F9 beds. Framework of colonial corals in life position, encrusted by clotted peloidal micrite and microencrusters.	Coral colonies (5 cm-2 m, phaceloid, cerioid and thamnasterioid); stromatoporoids; undetermined calcareous sponges; *Bacinella irregularis*; *Lithocodium aggregatum*; serpulids; foraminifers (11); *Thaumatoporella parvovesiculifera*; brachiopods	Angular and sub-angular intraclasts of clotted peloidal micrite and dense micrite	Corals dissolved and replaced by equant blocky calcite. Interparticle porosity filled by microsparite or fine-grained equant calcite, intraparticle porosity filled by blocky, scalenohedral or drusy cement. Primary cavities filled by P with peloids, intraclasts of clotted peloidal or dense micrite and bioclasts.	F10 associated with F8 and F9 in the Urzulei Supramonte area (build-up type 1).	Build-ups (type 1) in middle ramp
F11	Coral-calcareous sponge-diceratid boundstone	Lens-shaped build-ups, 1-2 m thick and 3-4 m wide made of F11 and surrounded by F8. Framework of coral colonies in life-position encrusted by *Solenopora* and *Bacinella irregularis* and clotted peloidal micrite.	Coral colonies (5-50 cm, phaceloid and cerioid); solenoporaceans; undetermined calcareous sponges; stromatoporoids; diceratids; *Bacinella irregularis; Lithocodium aggregatum; Crescentiella morronensis;* bivalves; crustaceans; crinoids; foraminifers (nubecularids); serpulids; siliceous sponge spicules	Intraclasts of clotted peloidal micrite fragments and dense micrite fragments; peloids	Compaction, concavo-convex and sutured grain contacts. Rims of microsparite around some grains, followed by blocky calcite cement (500 µm-1 mm) or granular equant calcite (100-200 µm). Geopetal infill in corals, filled by clotted peloidal micrite or intraclastic-peloidal P-G. Corals replaced by blocky calcite (20-70 µm).	F11 associated with F8 and F11 in Genna Ramene (build-up type 2), alternating with F5 and F6 for 35 m.	Build-ups (type 2) in middle ramp
F12	Sponge-coral-microbialite boundstone	Lens-shaped build-ups, up to 1 m thick and 1 m wide, surrounded by F8. Framework of clotted peloidal micrite with sparse corals and undetermined calcareous sponges encrusted by siliceous sponges and microencrusters. Borings and cavities filled by sediment.	Undetermined calcareous sponges (up to 10 mm); chaetetids; solenoporaceans; solitary and colonial corals (3-6 mm); siliceous sponges; *Crescentiella morronensis*	Peloids; intraclasts of angular dense micrite and clotted peloidal micrite fragments; ooids (type 3)	Corals dissolved and replaced by equant blocky calcite (50-200 µm) and geopetal infills. Interparticle space filled by fine-grained equant cement. Dissolution vugs filled by fine-grained (10-30 µm) sediment.	F12 associated with F8in the Mt. Oro log (build-up type 3) alternating with F6 and F7 for 40 m.	Build-ups (type 3) in distal middle to outer ramp

F13	Stromatoporoid rudstone to packstone with coated grains	Poorly sorted, 0.2-2 mm with stromatoporoids up to 10 cm	Planar or irregular beds, 50 cm-1m thick	Stromatoporoids; crinoids; echinoid spines; brachiopods; chaetetids; undetermined calcareous sponges; *Neuropora lusitanica*	Peloids; aggregate grains (bound by *Bacinella irregularis*); ooids (type 1); intraclasts (peloidal P); oncoids (type I and II)	Geopetal infills, syntaxial cement around echinoderms, compaction, concavo-convex grain contacts, microsparite or fine-grained blocky calcite cement in interparticle porosity (20-30 µm) or scalenohedral cement (60-80 µm), followed by blocky calcite (200-300 µm). Locally fractures filled by silt-sized sediment with sparse carbonate lithoclasts.	Only in the Baunei Supramonte log, 5 m thick overlying F6.	Middle ramp
F14	Grainstone with ooids, aggregate grains and oncoids	Well-sorted, 0.2-1.5 mm, rare up to 1 cm (belemnites and ammonoids)	Cross-bedding, 40-70 cm thick beds	Belemnites; ammonites; foraminifers (9); crinoids; bivalves; brachiopods; stromatoporoids; gastropods; *Lithocodium aggregatum*	Ooids (type 1 and 3); oncoids (type I-II); aggregate grains (bound ooids); peloids	Compaction, sutured and concavo-convex grain contacts. Locally fibrous cement rim before compaction. Interparticle porosity filled by a fine-grained equant mosaic of blocky calcite. Fractures filled by fine-grained sediment with angular lithoclasts. Around fractures prismatic bladed/scalenohedral calcite cement followed blocky calcite. Red stained stylolites.	Only in the Baunei Supramonte area, 10 m thick overlying F6 and F7.	Middle ramp, open marine environment
F15	Peloidal packstone with oncoids and ooids	Moderately sorted, 0.1-3 mm, rare up to 6 mm	Planar horizontal beds, 30-70 cm thick	*Bacinella irregularis*; foraminifers (7, 9, 3, 6, 2, 1, 5, 8); dasyclad algae (*Salpingoporella annulata*); siliceous sponges; echinoid spines; crinoids; gastropods; bivalves; brachiopods; *Thaumatoporella parvovesiculifera; Lithocodium aggregatum; Cayeuxia;* stromatoporoids; calcareous sponges	Peloids; oncoids (type I-II); ooids (type 1 and type 3); aggregate grains (bound by *Bacinella irregularis,* bound ooids); intraclasts (micritic or clotted peloidal micrite)	Geopetal infillings. Compaction, concavo-convex and sutured grain contacts. Locally fibrous cement before compaction (25-30 µm). Syntaxial cement around echinoderms. Red stained stylolites. Interparticle and intraparticle porosity filled by microsparite, followed by blocky calcite. Irregular fractures filled by micrite and carbonate lithoclasts. Dissolution evidences, such as mouldic porosity filled by blocky cement (10-60 µm). Locally fractures filled by bladed/scalenohedral calcite (50-60 µm).	Only in the Baunei Supramonte area, 20 m thick overlying F14.	Middle ramp
F16	Lithoclastic breccia to conglomerate with black pebbles	Poorly sorted, 0.2 mm-6 cm	Planar horizontal beds (0.3-0.5 m)	Gastropods; foraminifers (3); *Charophytes* gyrogonites; *Thaumatoporella parvovesiculifera*	Lithoclasts and oncoids (type I and II) with clast nuclei (F10, F19, F20, F21); black pebbles; peloids; coated grains with micrite envelopes; pisoids; faecal pellets (*Favreina*)	Reddish matrix, compaction, concavo-convex grain contacts. Grain supported, with micrite matrix, sometimes partially dolomitized with planar-e dolomite crystals, locally with Fe-oxides. Some clasts and clast boundaries dolomitized. Red-stained stylolites.	Only in the Urzulei Supramonte area F16 alternates with F17, F18, F19 and F25 for 2-5 m overlying F10.	Transgressive lag reworking eroded reef, supratidal and pond facies following subaerial exposure at the top of F10

F17	Packstone-grainstone-rudstone with corals, pisoids and black pebbles	Poorly sorted, 0.5-5 mm	Planar horizontal beds (10-30 cm), borings and cavities	Corals (massive plocoid, cerioid colonies); stromatoporoids (*Actinastrea*); other calcareous sponges; *Solenopora;* dasyclad algae; faecal pellets (*Favreina*); foraminifers (10, 11)	Black pebbles; pisoids; peloids; coated grains with micrite envelopes; intraclasts; aggregate grains; clotted peloidal micrite fragments	Irregular cavities (fenestrae) filled by yellow meteoric cement, meniscus cement and thin microsparitic rim (non-isopachous) followed by blocky calcite cement and poikilotopic cement.	Only in the Urzulei Supramonte area F17 alternates with F16 for 2-5 m, overlying F10.	Transgressive lag in supratidal environment
F18	Intraclastic breccia	Poorly sorted, 0.2 mm-10 cm	Irregular chaotic or planar horizontal beds, 30 cm-1 m	*Charophytes* gyrogonites; ostracods; foraminifers (12, 3, 5); calcispheres; brachiopods; dasyclad algae; gastropods; *Thaumatoporella parvovesiculifera*	Intraclasts (facies: wackestone with *Charophytes*, paleosoils, M with gypsum crystal moulds, M with dissolution cavities, peloidal P/G with meniscus cement, gastropod W, M with sponge spicules and gastropods); oncoids with intraclastic nuclei (type II); pisoids; peloids; coated grains with micrite envelopes; faecal pellets	Grain supported, micrite in interparticle porosity. Geopetal infilling in gastropods, compaction, concavo-convex grain contacts. Fractures filled by fine-grained equant calcite cement and fine-grained sediment. Authigenic quartz within matrix. Locally dolomite with planar-s mosaic followed by silicification. Reddish matrix, microsparite and fine-grained equant calcite line pores.	In the Urzulei Supramonte area and in Punta Mureddu log. F18 alternates with F16 and F19 for about 2-5 m and alternates with F19 to F27 for about 45 m. F18 characterizes the upper boundary of the succession of facies from F16 to F27 in the Urzulei Supramonte area.	Breccia related to dissolution and karst
F19	Mudstone-wackestone with desiccation cracks	Rare 0.125-0.1 mm	Planar horizontal beds, 10-15 cm thick. Tubular cavities filled by black sediment (rhizolites)	Ostracods; foraminifers (12, 3); *Charophytes* gyrogonites; calcispheres; faecal pellets	Coated grains with micrite envelopes; pisoids	Dissolution fractures. Laminar or irregular fenestral porosity, desiccation cracks. Cavities and fractures filled by equant blocky calcite cement.	Only in the Urzulei Supramonte area, F19 alternates with F16 and F18 for about 2-5 m and alternates with F18 and from F20 to F27 for about 45 m.	Supratidal environment
F20	Pisoid-intraclastic packstone-rudstone with meniscus cement	Moderately to well-sorted, 0.2-3 mm, rare intraclasts up to 6 mm	Irregular beds 5-20 cm, locally at the bottom sharp erosional surface. Locally cavities filled by dark micrite (rhizolites).	Ostracods; calcispheres; *Charophytes* gyrogonites; foraminifers (3, 5); gastropods; bivalves	Pisoids, intraclasts (micritic clasts with dissolution cavities, M/W with *Charophytes* and ostracods, M); oncoids (type I and II) with intraclastic nuclei (fenestral M); aggregate grains	Micritic meniscus cement between grains. Irregular cavities: with pendant cement, one cavity filled by several crusts of brownish calcite cement (fibrous pendant) and geopetal infills followed by blocky equant calcite cement. Red stained laminar paleosoils.	In the Urzulei Supramonte area F20 alternates with F18, F19 and facies from F21 to F27 for 45 m. In the Punta Mureddu log F20 alternates with F18 and F25.	Supratidal environment

						Fractures filled by micrite followed by calcite cement. Laminar and irregular fenestral porosity and vugs.		
F21	Wackestone-mudstone with ostracods and *Charophytes*	Well-sorted, 0.125-0.1 mm (rare intraclasts up to 1 cm)	Irregular nodular beds (20-30 cm thick). Locally neptunian dikes; laminar and irregular fenestral fabric; desiccation cracks. Locally erosional surface at the bottom.	*Charophytes* gyrogonites and rarely stems; ostracods; calcispheres; gastropods; bivalves	Micrite; peloids, intraclasts; rare black pebbles	Fenestral fabric filled by microsparite or fine-grained equant calcite cement. Geopetal infillings in cavities, gastropods dissolved and replaced by blocky calcite. Intraparticle porosity filled by microsparite or fine-grained equant calcite cement. Locally desiccation cracks and vugs filled by geopetal sediment followed by equant calcite. Fractures filled by equant calcite.	Only in the Urzulei Supramonte area. F21 alternates with F18, F19, F20 and from F22 to F27 for about 45 m.	Pond-lacustrine environment in coastal wetlands with influence of freshwater
F22	Stromatolitic boundstone	Well-sorted, 0.1-1 mm	Well-bedded (20-30 cm thick). Lamination (some laminae made of peloids and coated grains), locally fenestrae and desiccation cracks.	Agglutinated stromatolites	Peloids; coated grains with micrite envelopes	Locally strongly silicified with a mosaic of quartz in cavities. Locally brecciated by subaerial exposure and micrite pendant cement.	Only in the Urzulei Supramonte area F22 alternates with facies from F18 to F21 and from F23 to F27 for 45 m.	Intertidal environment
F23	Microbial boundstone	Moderately sorted, 0.2-3 mm	Massive, locally eroded and brecciated. Irregular texture with clotted peloidal micrite and *Cayeuxia* alternating with dense micrite.	Clotted peloidal micrite; *Cayeuxia*; *Bacinella irregularis; Thaumatoporella parvovesiculifera;* foraminifers (5, 13); ostracods		Vuggy and intraparticle porosity filled by microsparite and equant blocky calcite cement.	Only in the Urzulei Supramonte area F23 alternates with facies from F18 to F22 and from F24 to F27 for 45 m.	Subtidal, open-marine lagoon environment
F24	Wackestone with *Cayeuxia*	Moderately sorted, 0.1-4 mm	Planar, horizontal beds (20-30 cm thick). Irregular and laminar fenestrae.	*Cayeuxia*; foraminifers (3, 5)	Peloids; coated grains with micrite envelopes; intraclasts (mudstone with dissolution cavities)	Fenestrae filled by a first generation of scalenohedral cement or geopetal sediment, locally with peloids, followed by blocky equant calcite. Fractures filled by blocky equant calcite.	Only in the Urzulei Supramonte area F24 alternates with facies from F18 to F23 and from F25 to F27 for 45 m.	Subtidal lagoon environment
F25	Wackestone with ostracods and foraminifers	Well-sorted, 0.1-1.5 mm, rare intraclasts up to 5 mm	Planar horizontal beds, 10-20 cm thick. Bioturbation, locally lamination with more compacted levels with coated grains and less compacted levels with ostracods.	Ostracods; foraminifers (12, 3); calcispheres; brachiopods; bivalves; faecal pellets (*Favreina*)	Coated grains with micrite envelopes; peloids; aggregate grains; intraclasts (fenestral mudstone)	Micrite between grains and fractures filled by fine-grained equant calcite cement.	In the Urzulei Supramonte area, F25 alternates with F16 and F18 for about 2-5 m and alternates with F18 and from F20 to F24 and F26, F27 for about 45 m. In the Punta Mureddu log F25 alternates with F20 and F18 for about 10 m.	Subtidal environment, restricted lagoon

F26	Packstone-wackestone with intraclasts, oncoids and foraminifers	Poorly sorted, 0.1-1 cm	Planar horizontal beds, 10-30 cm thick	Foraminifers (6, 14, 3, 8, 5, 12); brachiopods; corals; crinoids; faecal pellets	Oncoids with bioclastic and intraclastic nuclei with homogeneous micrite coating or organism bearing coating (type I, II and III); intraclasts (mudstone with fenestrae, peloidal packstone with meniscus cement); coated grains with micrite envelopes; peloids; pisoids	Irregular cavities filled by microsparite or blocky equant calcite and fractures filled by fine-grained equant calcite, geopetal infillings in bioclasts, gastropods dissolved and replaced by a mosaic of equant calcite cement.	Only in the Urzulei Supramonte area F26 alternates with facies from F18 to F25 and with F27 for 45 m.	Subtidal lagoon with reworked material
F27	Oncoid floatstone	Poorly sorted, 0.5-4 cm	Planar horizontal beds (10-40 cm)	Foraminifers (13, 12); brachiopods; gastropods; crinoids; ostracods	Oncoids without lamination with *Bacinella irregularis* and sponge spicules (type IV); peloids; coated grains with micrite envelopes; aggregate grains; pisoids	Fractures and vugs filled by equant blocky calcite cement.	Only in the Urzulei Supramonte area F27 alternates with facies from F18 to F26 for 45 m.	Subtidal lagoon
F28	Lithoclastic breccia	Poorly sorted, from 20 µm to 1 m	Irregular and lenticular beds, 30 cm-1.5 m. Locally erosional base.	Crinoids; bivalves; echinoid spines; corals; calcareous sponges (*Neuropora lusitanica, Calcistella jachenhausenensis*); siliceous sponges; serpulids; gastropods; foraminifers (6, 16, 1, 2, 4, 5, 3, 10, 5); *Bacinella irregularis; Lithocodium aggregatum*; *Crescentiella morronensis*; *Cayeuxia; Koskinobulina socialis; Radiomura cautica*; brachiopods; dasyclad algae (*Salpingoporella annulata, Clypeina jurassica*)	Lithoclasts (bioclastic intraclastic grainstone with fibrous cement, calcareous sponge-*Crescentiella*-coral boundstone, coral-calcareous sponge-microbial boundstone, *Bacinella* boundstone, peloidal packstone, peloidal-intraclastic packstone to grainstone, wackestone with dasyclad algae *Clypeina jurassica* and wackestone to floatstone with oncoids); reddish matrix with silt-sized dolomite crystals; clotted peloidal micrite fragments; micritized tangential ooids; aggregate grains	Reddish matrix with Fe-oxides. Geopetal infillings (in corals, gastropods). Syntaxial cement around crinoids. Microsparitic cement rim around some clasts. Coral biomoulds filled by coarse-grained equant calcite cement. Fractures filled by fine-grained blocky calcite cement.	In the Baunei Supramonte area (Franciscu to Pedra Longa logs) F28 alternates at decimetre to metre-scale with F29 for a thickness from 0 to 25 m, overlying F15.	Debris flow deposits with resedimented lithoclasts from reefal and inner platform facies within basin facies (F29)

F29	Mudstone, wackestone, siltstone	Mainly from 10 to 150 µm, rare fragments up to 1.5 mm and very rare up to 6 mm	Nodular beds, 5-15 cm thick. Bioturbation, locally isoriented and broken shells	Bivalves; brachiopods; sponge spicules; echinoid spines; crinoids; calcareous sponges (*Neuropora lusitanica*); ammonites; foraminifers (5, 3)	Peloids; quartz grains; rounded sub-spherical to elongated carbonate lithoclasts (peloidal G/P, M and W with gastropods)		In the Baunei Supramonte area (Franciscu to Pedra Longa logs) F29 alternates at decimetre to metre-scale with F28 for a thickness from 0 to 25 m, overlying F15. In the Punta Mureddu log, 3 m thick, overlying F25.	Basinal deposits with F28 debris flow beds
F30	Compacted peloidal packstone-grainstone with fibrous cement	Well-sorted, 0.1-2 mm	Planar horizontal beds 10-20 cm thick	Foraminifers (3)	Peloids; micritic intraclasts	Microsparitic cement rim around grains (fibrous) precipitated before compaction. Compacted, concavo-convex grain contacts. Fractures filled by microsparite.	A thin bed (10-20 cm thick) in the Urzulei Supramonte area, F30 overlies F18.	Subtidal environment
F31	Laminated dolostone	Crystal size 10-100 µm	Massive to well-bedded (5-10 cm beds), planar lamination			Dolomicrosparite and dolomicrite	Only in the Urzulei Supramonte area, F31 alternates with F32, F33 and F34 for about 10-20 m, overlying F30.	Diagenetic replacive dolomite
F32	Rudstone to packstone with *Clypeina jurassica*	Poorly sorted, 0.1-15 mm	Planar horizontal beds, 30-60 cm thick. Planar lamination	*Clypeina jurassica;* other dasyclad algae; gastropods; foraminifers (5)	Oncoids with intraclastic nuclei (type I and II); intraclasts (fenestral mudstone with ostracods, dolomitized clasts, wackestone with *Clypeina jurassica*); peloids	Compaction, sutured and concavo-convex grain contacts. Fenestral porosity (within intraclasts) filled by scalenohedral cement followed by blocky cement. Geopetal infillings in gastropods with microsparite. Microsparite and fine-grained equant cement in interparticle porosity. Dolomitized matrix with planar-s dolomite crystals with Fe-oxides in porosity.	In the Urzulei Supramonte area F32 alternates with F31, F33 and F34 for about 10-20 m. In the Punta Mureddu log F32 overlies F33 with a thickness of about 10 m.	Subtidal shallow marine inner platform environment
F33	Packstone to rudstone with pisoids, oncoids, foraminifers and meniscus cement	Poorly sorted, 0.2-10 mm	Planar, horizontal beds, 10-50 cm thick. Planar lamination	Foraminifers (1, 15, 3, 5); bivalves; gastropods; dasyclad algae (*Salpingoporella, Clypeina jurassica*); brachiopods	Pisoids; oncoids (type I-II); peloids; coated grains with micrite envelopes; micritic intraclasts; aggregate grains (aggregate pisoids)	Compaction, sutured and concavo-convex grain contacts. Fenestral porosity (within intraclasts) filled by scalenohedral calcite cement followed by blocky calcite. Geopetal infillings in gastropods with microsparite. Microsparite and fine-grained equant cement in interparticle porosity. Dolomitized matrix with a planar-s dolomite mosaic with Fe-oxides in porosity.	In the Urzulei Supramonte area F33 alternates with F31, F32 and F34 for about 10-20 m. In the Punta Mureddu log overlying F29 with a thickness of about 1 m.	Supratidal inner platform environment

F34	Bioturbated wackestone-mudstone with ostracods	0.125-0.1 mm (rare intraclasts up to 0.5 cm)	Planar, horizontal beds 10-20 cm. Bioturbation, planar lamination.	Ostracods; foraminifers (1, 5); dasyclad algae (*Clypeina jurassica, Campbelliella*)	Coated grains with micrite envelopes; intraclasts	Sparse replacive euhedral dolomite crystals.	Only in the Urzulei Supramonte area F34 alternates with F31, F32 and F33 for about 10-20 m.	Subtidal lagoon environment
F35	Breccia with radiaxial fibrous calcite cement	Poorly sorted, 1 mm-10 cm	Massive	*Crescentiella morronensis*; coral fragments; dasyclad algae (*Salpingoporella*); chaetetids; calcareous sponges; serpulids; foraminifers (6, 10, 5, 1); *Lithocodium aggregatum; Bacinella irregularis; Koskinobulina socialis; Thaumatoporella parvovesiculifera*	Carbonate lithoclasts (boundstone, peloidal packstone); micritic intraclasts	Interparticle space filled by radiaxial fibrous calcite cement, followed by equant blocky calcite cement.	Only in the Baunei Supramonte area F35 alternates with F36 and F37 for about 100 m.	Upper to lower slope with marine cement (cf. Lanfranchi et al., 2011)
F36	*Crescentiella* grainstone-packstone	Poorly sorted, mainly from 0.1 to 5 mm, up to 1 cm	10-50 cm thick beds	*Crescentiella morronensis*; *Thaumatoporella parvovesiculifera;* foraminifers (5, 1, 6, 2); crinoids; echinoid spines; chaetetids; siliceous sponges; dasyclad algae (*Clypeina jurassica*); stromatoporoids; bivalves; serpulids; coral fragmentss; *Lithocodium aggregatum; Bacinella irregularis*	Subrounded and subangular micritic lithoclasts; peloids; clotted peloidal micrite lithoclasts; clasts of peloidal packstone-grainstone with *Crescentiella morronensis*	Dissolution and recrystallization, fine grained equant calcite cement (or microsparite) followed by equant blocky calcite cement followed by equant blocky, prismatic calcite cement or radiaxial calcite followed by fine-grained sediment infillings.	Only in the Baunei Supramonte area F36 alternates with F35 and F37 for about 100 m.	Lower slope (cf. Lanfranchi et al., 2011)
F37	Crinoidal peloidal packstone-wackestone	Well-sorted, 0.1-1 mm	5-10 cm thick beds	Crinoids; *Crescentiella morronensis*; bivalves; calcareous sponges; foraminifers (4, 3, 8); *Lithocodium aggregatum*; serpulids	Peloids; micritic lithoclasts	Compaction; concavo-convex grain contacts.	Only in the Baunei Supramonte area F37 alternates with F35 and F36 for about 100 m.	Lower slope (cf. Lanfranchi et al., 2011)

Table 6.1 Description of the depositional facies of the investigated Callovian-Tithonian portion of the eastern Sardinia carbonate succession. Foraminifers: 1-*Trocholina*; 2-*Protopeneroplis striata*; 3-Textularids; 4-L*enticulina*; 5-miliolids; 6-*Everticyclammina*; 7-*Labyrinthina mirabilis*; 8-*Nautiloculina oolithica*; 9-*Mohlerina basiliensis*; 10-Nubeculariids; 11-*Troglotella incrustans;* 12-*Alveosepta jaccardi;* 13-*Redmondoides;* 14-*Parugonia;* 15 -*Kurnubia;* 16-*Pseudocyclammina.*

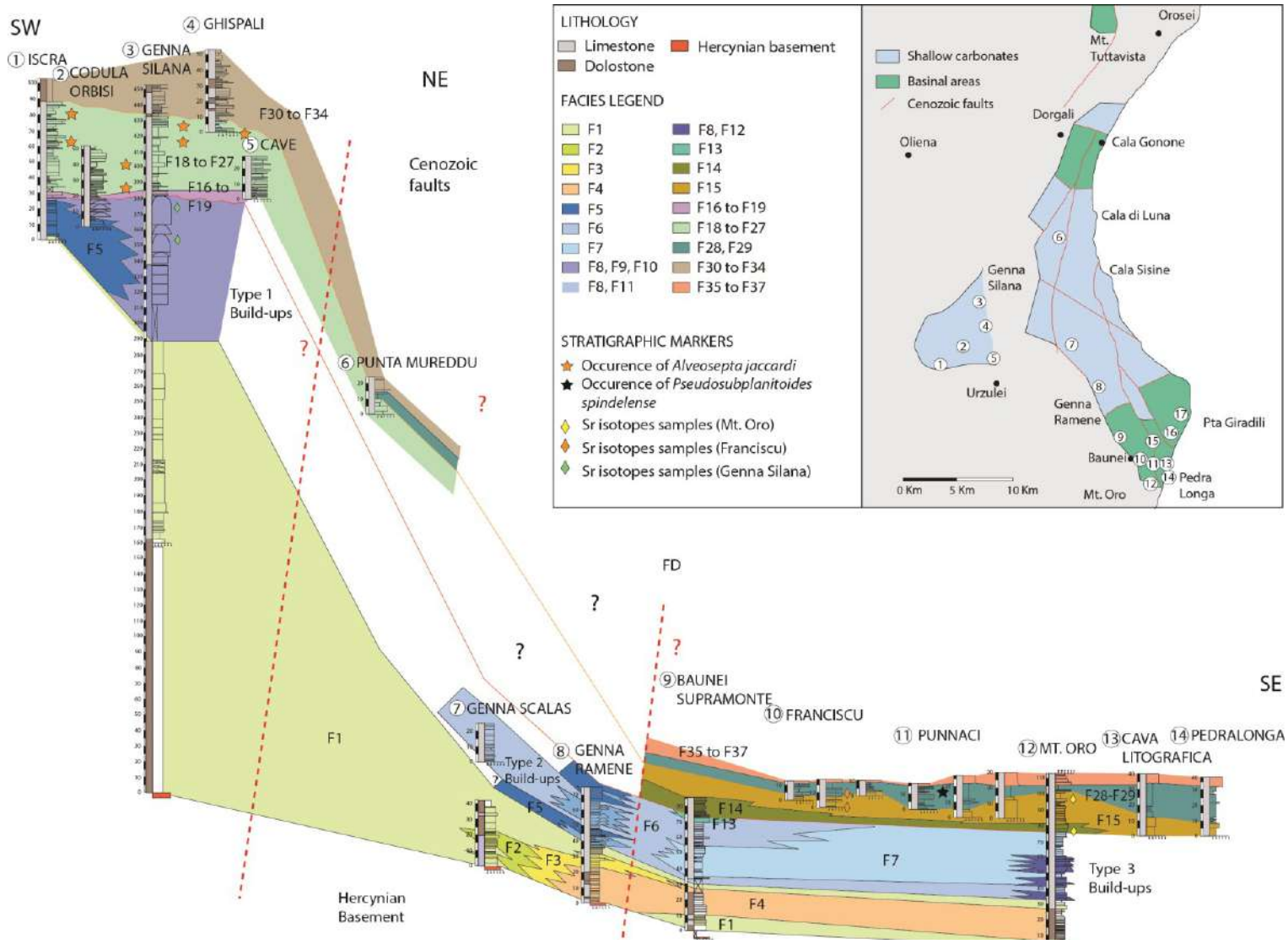

Figure 6.2 Correlation of stratigraphic logs along the study area showing vertical and lateral distribution of facies of the Callovian-Tithonian succession. Log location: 1-Iscra; 2-Codula Orbisi; 3-Genna Silana; 4-Ghispali; 5-Cave; 6-Punta Mureddu; 7-Genna Scalas; 8-Genna Ramene; 9-Baunei Supramonte; 10-Franciscu; 11-Punnaci; 12-Mt. Oro; 13-Cava Litografica; 14-Pedralonga; 15-Rio Olcoe; 16-Selvaggio Blu; 17-Punta Giradili.

Facies F1 is a partially dolomitized cross-bedded ooidal-coated grain grainstone to packstone, with beds 0.5-1 m thick and local herringbone cross-lamination (Fig. 6.3A), dominated by type 1 and 3 ooids (Fig. 6.3B) associated with crinoids, aggregate grains and coated grains with micrite envelopes. F1 crops out widely in the central NW area (Urzulei Supramonte; Fig. 6.2, 6.4A) and in the south-eastern study area (Baunei Supramonte; Fig. 6.2, 6.4B, 6.5). In the central NW area (Urzulei Supramonte; Fig. 6.2), 150 m of F1 ooidal-coated grain grainstone lie above 150 m of dolostone, whose original facies was not possible to characterize due to fabric-destructive replacive dolomitization. Eastward of the Urzulei Supramonte area (Genna Scalas, Baunei Supramonte, Fig. 6.2, 6.5), F1 alternates with facies F2 cross-laminated echinoderm packstone to grainstone-rudstone (Fig. 6.3C) for an interval about 25 m thick above the Hercynian basement (Fig. 6.5). Facies F2 is also partially dolomitized and crops out in planar beds, up to 1 m thick with fining-upward trends.

Facies F3 consists of well-bedded (0.2-1 m thick) peloidal packstone (Fig. 6.3D) with ooids and echinoderms (including abundant crinoids and echinoid spines) associated with foraminifers and bivalves and micritized radial ooids with sparitic laminae (type 3). F3 crops out in the Genna Ramene area alternating with F1 for an interval of about 15 m (Fig. 6.2, 6.5).

Facies F4 peloidal packstone with chert nodules and thin-shelled bivalves (Fig. 6.3E-F) is locally partially dolomitized and is characterized by bioturbated thin nodular beds (5-10 cm), dominated by peloids and fine-grained coated grains with micrite envelopes (100-200 μm in diameter). Facies F4 crops out in the Baunei Supramonte area (from Genna Ramene to Mt. Oro; Fig. 6.2, 6.4B, 6.5), lying above the Hercynian basement and overlain by facies F3 (Genna Ramene; Fig. 6.5), with a thickness of 15-25 m. Facies F5 is an ooidal grainstone to packstone (beds 0.5-1 m thick) with intraclasts and bioclasts (Fig. 6.3G), dominated by partially micritized radial ooids (type 3) and micritic tangential ooids (type 1). F5 crops out in the Urzulei Supramonte area (Iscra, Codula Orbisi, Fig. 6.2, 6.6) where it is about 15-20 m thick and in the Genna Ramene area (Fig. 6.5) where it alternates with F6, F8 and F11 for a thickness of about 30 m.

Facies F6 (0.2-1 m thick beds) is made of peloidal packstone with reworked intraclasts (mainly clotted peloidal and dense micrite fragments), skeletal fragments (crinoids, corals, calcareous sponges, solenoporaceans, bivalves, benthic foraminifers, sponge spicules, brachiopods, microencrusters, *Thaumatoporella parvovesiculifera*), ooids (type 1), oncoids (type I and II) and coated grains with micrite envelopes (Fig. 6.3H). Facies F6 crops out in the Baunei Supramonte area from Genna Scalas stratigraphic log eastward to the Mt. Oro stratigraphic log (Fig. 6.4B, 6.5), alternating with F7, F8, F11 and F12 for a thickness of about 35-40 m.

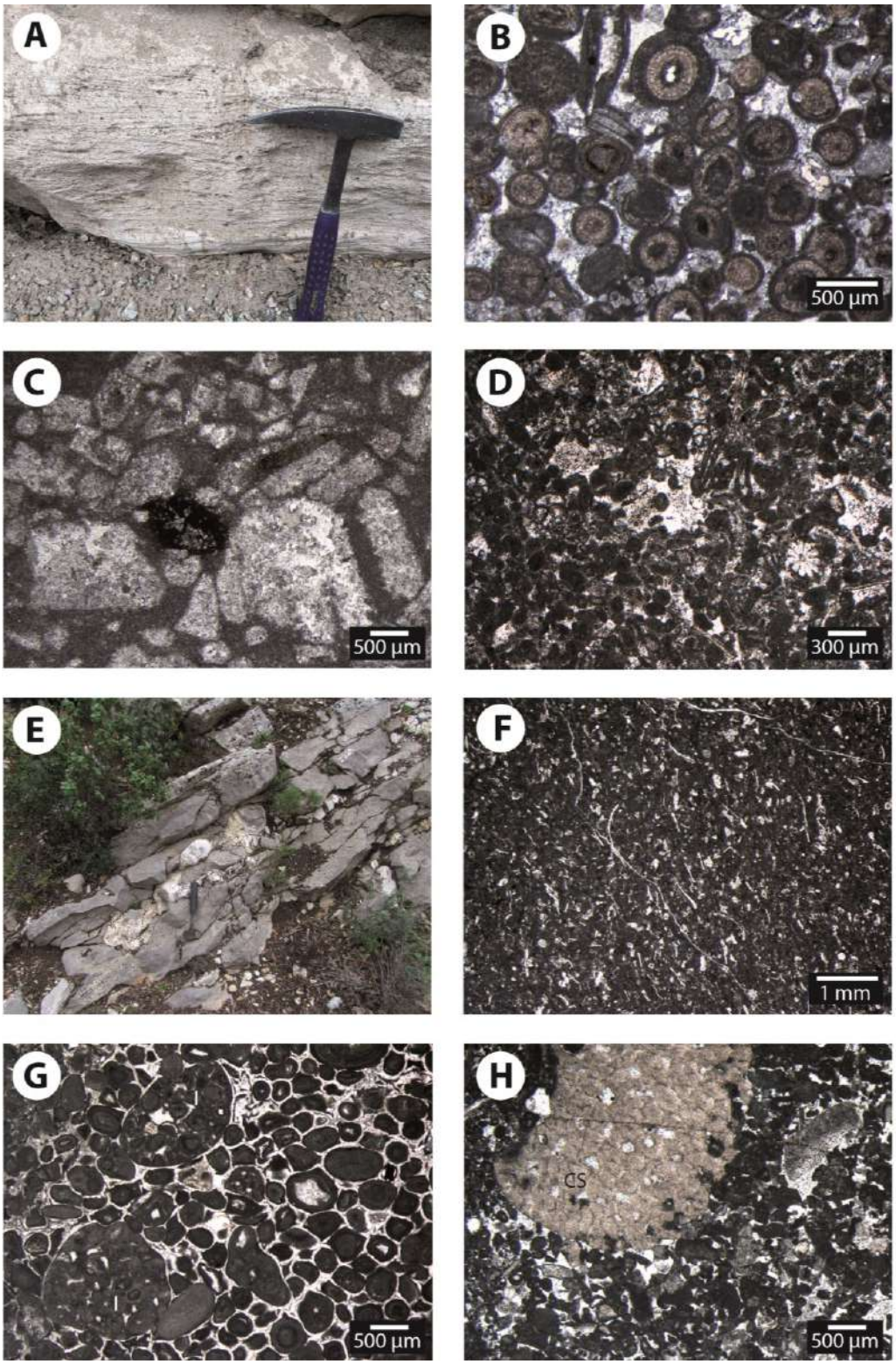

Figure 6.3 A) Outcrop photograph showing herringbone cross-lamination in F1 cross-bedded ooidal-coated grain grainstone to packstone. Hammer for scale. B) Photomicrograph of facies F1 grainstone with type 3 ooids, partially dolomitized. C) Facies F2 packstone with crinoids dissolved and replaced by dolomite, followed by equant blocky calcite. D) Facies F3 peloidal packstone with echinoid spines and benthic foraminifers. E) Outcrop photograph of facies F4 showing a nodular bedded peloidal packstone with chert nodules. Hammer for scale. F) Photomicrograph of facies F4 peloidal packstone with thin-shelled bivalves and crinoid fragments. G) Photomicrograph of facies F5 showing a compacted ooidal grainstone with intraclasts of ooidal grainstone (I) and aggregate grains. H) Facies F6 peloidal packstone with crinoid and a chaetetid fragment (CS).

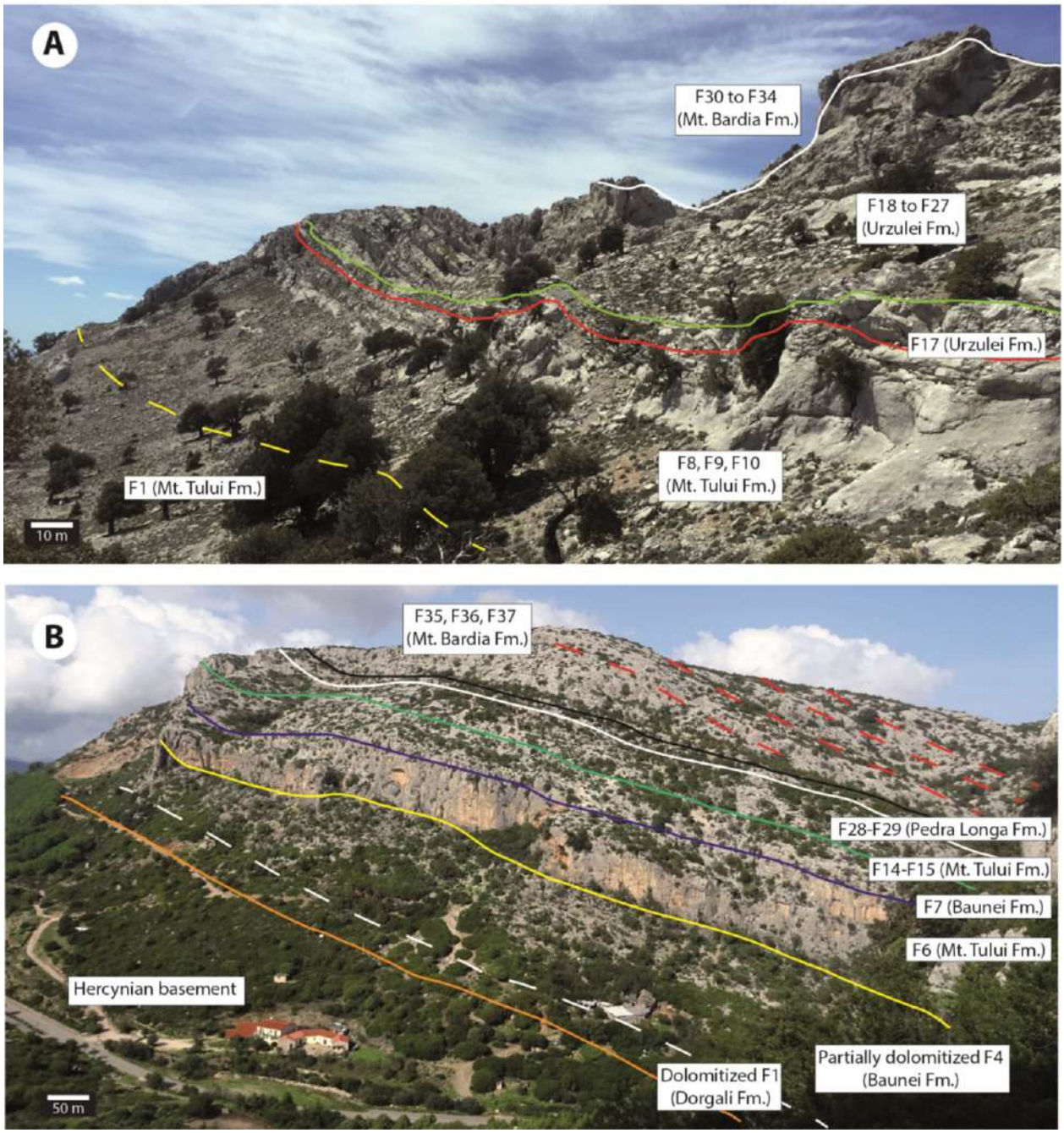

Figure 6.4 A) Panoramic view of the succession showing facies architecture in the Urzulei Supramonte area (Genna Silana log). From the base to the top: 1) Dashed yellow line: boundary between facies F1 and the facies association of F8, F9 and F10 of build-up type 1 (Mt. Tului Fm.); 2) Red line: erosional subaerial exposure surface representing the boundary between the association of facies F8, F9 and F10 (Mt. Tului Fm.) and the overlying F17 (Urzulei Fm.); 3) Green line: boundary between F17 and facies from F18 to F27 (Urzulei Fm.); 4) White line: boundary between facies from F18 to F27 (Urzulei Fm.) and the overlying vertical succession of facies from F30 to F34 (Mt. Bardia Fm.). B) Panoramic view of the succession showing facies architecture in the Baunei Supramonte area (Baunei Supramonte log). From the bottom to the top: 1) Orange line: boundary between the Hercynian basement and the dolomitized facies F1 (Dorgali Fm.); 2) White dashed line: boundary between the dolomitized F1 (Dorgali Fm.) and the partially dolomitized F4 (Lower Baunei Fm.); 3) Yellow line: boundary between partially dolomitized F4 (Lower Baunei Fm.) and F6 (Lower Mt. Tului Fm.); 4) Blue line: boundary between F6 (Lower Mt. Tului Fm.) and F7 (Upper Baunei Fm.); 5) Green line: boundary between F7 (Upper Baunei Fm.) and facies F14 and F15 (Upper Mt. Tului Fm.); 6) White line: boundary between F14 and F15 (Upper Mt. Tului Fm.) and F28-F29 (Pedra Longa Fm.); 7) Black line: boundary between F28-F29 (Pedra Longa Fm.) and facies from F35 to F37 (Mt. Bardia Fm.). 8) Red dashed line: clinoforms redrafted after Lanfranchi et al. (2011).

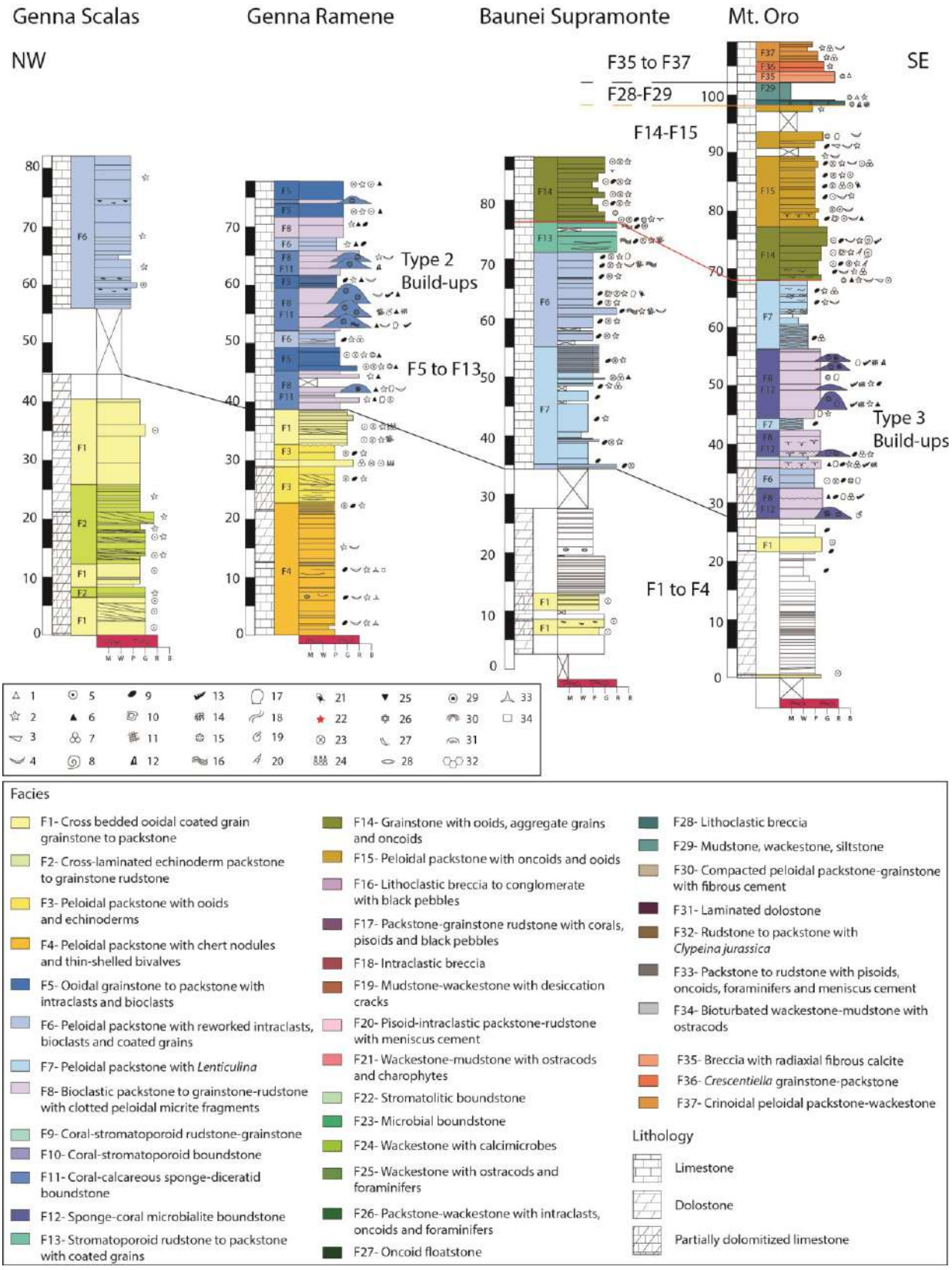

Figure 6.5 Stratigraphic logs showing the lower portion of the succession in the Baunei Supramonte area. Symbol legend: 1-lithoclasts; 2-echinoderms; 3-brachiopods; 4-bivalves; 5-ooids; 6-intraclasts; 7-foraminifers; 8-ammonites; 9-peloids; 10-oncoids; 11-chaetetids; 12-*Crescentiella morronensis*; 13-*Lithocodium aggregatum*; 14-*Bacinella irregularis*; 15-corals; 16-stromatoporoids; 17-siliceous sponges; 18-bioturbation; 19-gastropods; 20-belemnites; 21-dasyclad algae; 22-evidence of subaerial exposure; 23-coated grains; 24-normal gradation; 25-black pebbles; 26-*Charophytes*; 27-ostracods; 28-fenestrae; 29-pisoids; 30-stromatolites; 31-*Cayeuxia*; 32-bryozoans; 33-sponge spicules; 34-detrital quartz. For log location see Figure 6.2.

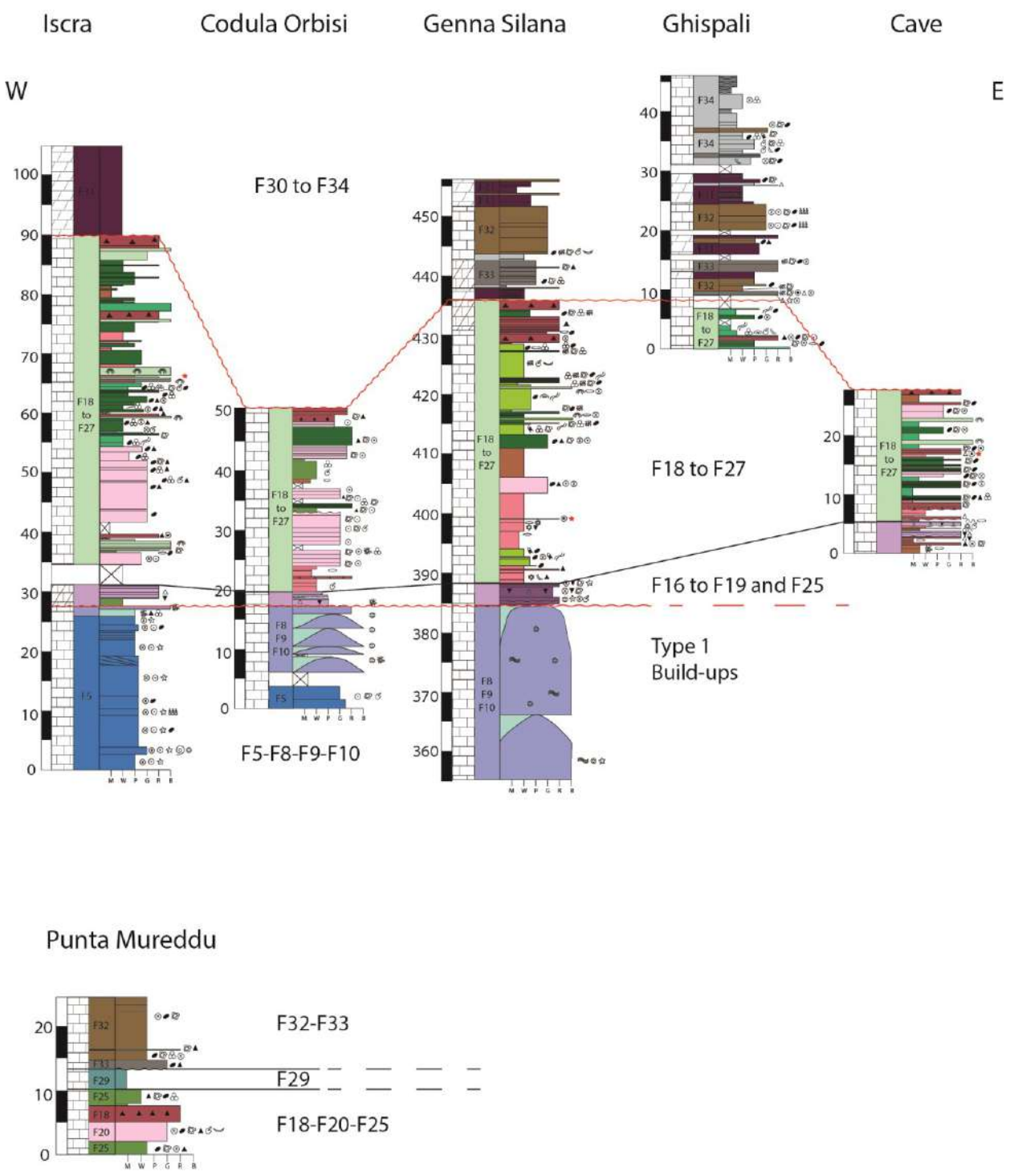

Figure 6.6 Stratigraphic logs showing facies architecture in the Urzulei Supramonte area. For log location see Figure 6.2; for facies and symbol legend refer to Figure 6.5.

Facies F7 consists of burrowed peloidal packstone to locally wackestone with *Lenticulina* foraminifers (Fig. 6.7A) in thin, nodular beds (5-30 cm thick). It crops out in the easternmost part of the Baunei Supramonte area, from the Baunei Supramonte to the Mt. Oro stratigraphic logs (Fig. 6.2, 6.4B, 6.5), alternating with F6, F8 and F12 for a thickness of about 35-40 m.

Facies types F8, F9 and F10 occur alternating and intermixed in the easternmost Urzulei Supramonte area (Genna Silana; Fig. 6.2, 6.4A, 6.6). Facies F8 consists of cross-laminated beds (0.5-1 m thick) of skeletal packstone to grainstone-rudstone rich in sub-angular intraclasts of clotted peloidal micrite and dense micrite fragments (Fig. 6.7B). Facies F9 is a poorly-sorted, massive coral-stromatoporoid rudstone-grainstone with common colonial (phaceloid, thamnasterioids) with microborings and coatings by clotted peloidal micrite crusts (Fig. 6.7C). Facies F9 grainstone-rudstone also contains angular and sub-angular intraclasts of clotted peloidal micrite and dense micrite, peloids and crinoids, undetermined calcareous sponges, benthic foraminifers, rare dasyclad algae, bivalves and gastropods. Facies F10 represents massive coral-stromatoporoid boundstone (Fig. 6.7D), tens of metres thick (14-45 m), with coral colonies in life position (0.5-2 m in size, mainly phaceloid, cerioid and thamnasterioid), associated with stromatoporoids and undetermined calcareous sponges and encrusted by clotted peloidal micrite, *Bacinella irregularis*, *Lithocodium aggregatum* and serpulids. In Genna Silana log (Fig. 6.2, 6.6), there is the thickest (45 m) and most laterally continuous coral-stromatoporoid boundstone (F10), associated with coral-stromatoporoid rudstone-grainstone (F9) and bioclastic packstone to grainstone-rudstone with clotted peloidal micrite fragments (F8). F10 boundstone thins westward (Codula Orbisi 20 m, Iscra 2 m thick), where it overlies F5 ooidal grainstone to packstone (Fig. 6.6). The top of facies F10 massive boundstone is marked by an erosional surface (Fig. 6.2, 6.4B, 6.6, 6.7E) in the Urzulei Supramonte area.

Facies F11 is a coral-calcareous sponge-diceratid boundstone whose framework consists of coral colonies, undetermined calcareous sponges and stromatoporoids in life position (Fig. 6.7F). F11 is associated with bioclastic packstone to grainstone-rudstone with clotted peloidal micrite fragments (F8) in the Genna Ramene log (Fig. 6.2, 6.5), where F11 forms massive lenses, 1-2 m thick and 3-4 m wide. F11 and F8 together alternate with facies F5 and F6 for a thickness of about 35 m, overlying F1 grainstone (Fig. 6.5).

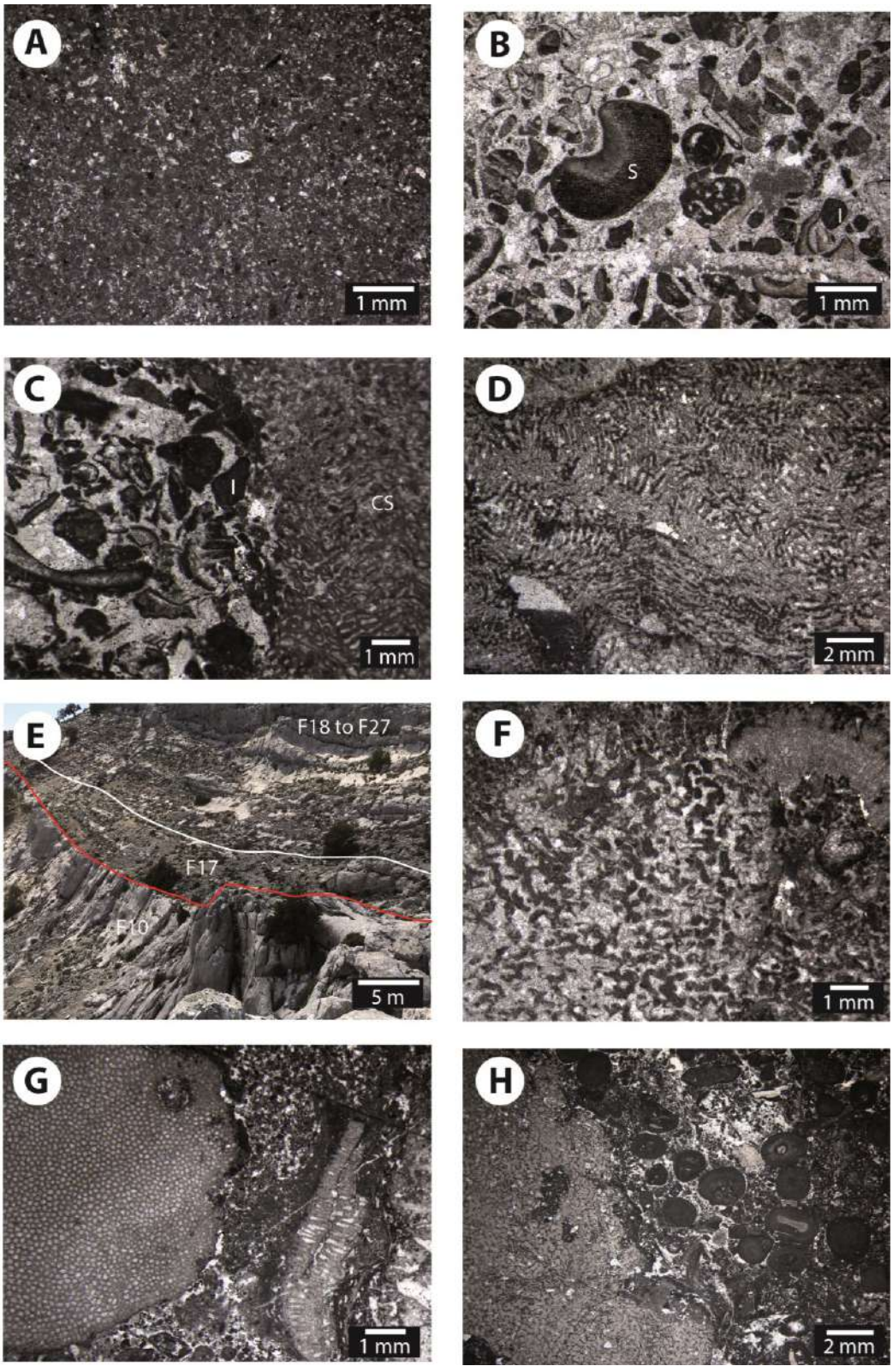

Figure 6.7 A) Photomicrograph of facies F7 peloidal packstone with *Lenticulina* foraminifers. B) Facies F8 bioclastic grainstone with skeletal fragments of solenoporaceans (S) and intraclasts made of clotted peloidal micrite fragments (I) cemented by equant blocky calcite cement. C) Photomicrograph of facies F9 showing a rudstone with an undetermined calcareous sponge (CS), skeletal fragments and intraclasts made of clotted peloidal micrite (I), cemented by blocky calcite cement. D) Facies F10 boundstone with a thamnasterioid coral colony. E) Outcrop photograph showing the erosional surface between the top of facies F10 and F17 (red line). F) Photomicrograph of facies F11 boundstone with an undetermined calcareous sponge and solenoporaceans. G) Facies F12 boundstone with chaetetids. G) Photomicrograph of facies F13 rudstone-packstone with a stromatoporoid and coated grains.

Facies F12 is a sponge-coral-microbialite boundstone with undetermined calcareous sponges, chaetetids (Fig. 6.7G), solenoporaceans, corals and siliceous sponges (Hexactinellid) coated by micritic clotted peloidal micrite and encrusted by *Crescentiella morronensis*. F12 boundstone alternates with bioclastic packstone to grainstone-rudstone with clotted peloidal micrite fragments (F8) in the easternmost part of the Baunei Supramonte area (Mt. Oro log; Fig. 6.2, 6.5), where it forms massive lenses, about 1 m thick and 1 m wide. The association F12 and F8 alternates with F6 and F7 peloidal packstone at the top of partially dolomitized F1 cross-bedded ooidal-coated grain grainstone for a thickness of about 40 m (Mt. Oro log; Fig. 6.5).

Facies F13 is a poorly sorted skeletal rudstone to packstone, rarely grainstone (50 cm-1 m thick beds), with common stromatoporoids (up to 10 cm in diameter; Fig. 6.7H), peloids, aggregate grains (bound by *Bacinella irregularis*), type 1 ooids and associated intraclasts of peloidal packstone, oncoids (type I and II), crinoids, echinoid spines, brachiopods, chaetetids and undetermined calcareous sponges. F13 is about 5 m thick and crops out in the Baunei Supramonte stratigraphic log overlying facies F6 (Fig. 6.5).

Facies F14 is a cross-bedded (40-70 cm thick) grainstone with ooids, aggregate grains and oncoids (Fig. 6.8A) including type 1 and type 3 ooids (Fig. 6.8B), type I and II oncoids, aggregate grains (bound ooids), ammonites (Fig. 6.8C), belemnites and peloids. F14 occurs in the SE area of Baunei Supramonte for a thickness of about 10 m overlying F13 stromatoporoid packstone to rudstone (Baunei Supramonte log) and F7 (Mt. Oro log, Fig. 6.4B, 6.5).

Facies F15 consists of planar beds (30-70 cm thick) of peloidal packstone with oncoids (type I and II) and ooids. The diverse skeletal fragments include echinoderms, molluscs, microencrusters, dasyclad algae (Fig. 6.8D) and benthic foraminifers (*Labyrinthina mirabilis*). F15 crops out in the Baunei Supramonte area, from the Franciscu to the Pedra Longa stratigraphic logs, with a thickness of about 20 m at the top of F14 (Fig. 6.2, 6.5).

Facies from F16 to F27 constitute a vertical succession deposited only in the central NW area (Urzulei Supramonte, Fig. 6.2, 6.4A, 6.6) and in the central northern area (Punta Mureddu, Fig. 6.2, 6.6). The vertical superimposition of facies from F16 to F27 forms a unit nearly 50 m thick, bounded at the base by an erosional surface at the top of F10 (Fig. 6.4A, 6.7E). Facies F16 is a lithoclastic breccia to conglomerate, locally rudstone to packstone, with black pebbles, forming beds 30 to 50 cm thick (Fig. 6.8E). The major components are angular and sub-rounded black pebbles, clasts from coral-stromatoporoid boundstone (F10), mudstone-wackestone with desiccation cracks (F19), pisoid-intraclastic packstone-rudstone with meniscus cement (F20) and wackestone-mudstone with ostracods and *Charophytes* algae (F21) and oncoids with lithoclasts at nuclei.

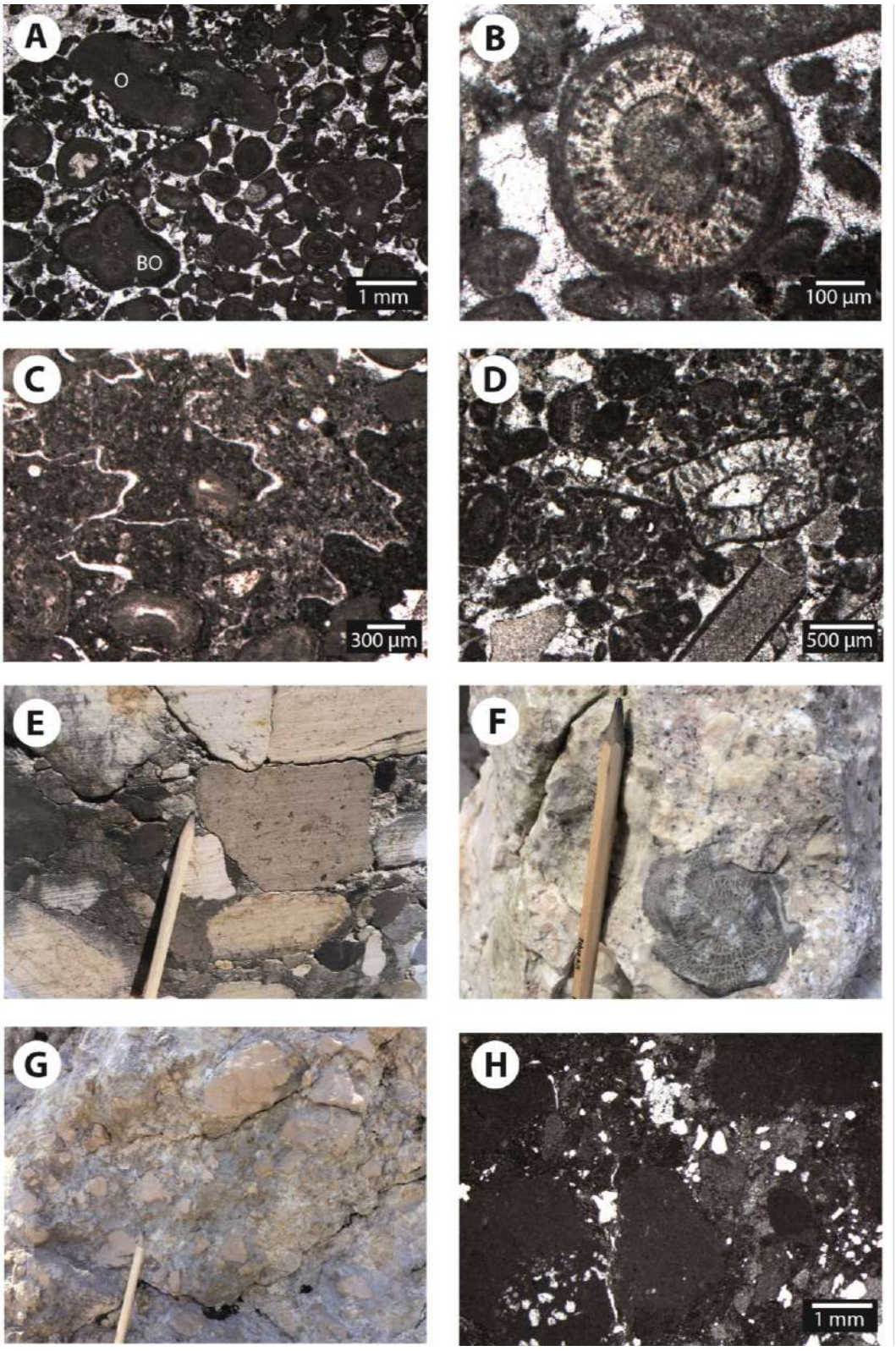

Figure 6.8 A) Facies F14 photomicrograph showing a grainstone with partially micritized radial type 3 ooids, aggregate grains of bound ooids (BO) and type II oncoids with encrustations made by *Lithocodium aggregatum* (O). B) Photomicrograph of type 3 radial ooid in facies F14. C) Ammonite filled by peloidal packstone within the F14 packstone with coated grains with micrite envelopes. D) Facies F15 peloidal packstone with peloids, crinoids and a fragment of a dasyclad alga (*Salpingoporella*). E) Outcrop photograph of facies F16 showing a breccia with black pebbles and lithoclasts made of fenestral mudstone and wackestone with *Charophytes* and gastropods. Pencil for scale. F) Outcrop photograph of facies F17 rudstone with a blackened coral and black pebbles. Pencil for scale. G) Outcrop photograph of facies F18 showing a breccia with mudstone intraclasts. H) Photomicrograph showing F18 partially silicified breccia with mudstone intraclasts.

Facies F17 is a packstone-grainstone to rudstone with corals, pisoids and black pebbles (Fig. 6.8F) with beds 10-30 cm thick. Facies F18 consists of an irregular chaotic (0.3-1 m thick beds) micritic intraclastic breccia (Fig. 6.8G-H). Facies F19 is a mudstone-wackestone with desiccation cracks (10-15 cm thick beds) embedding coated grains with micrite envelopes, pisoids, ostracods, benthic foraminifers (among which *Alveosepta jaccardi*) and *Charophytes* gyrogonites (Fig. 6.9A). Facies F20 is a pisoid-intraclastic packstone-rudstone with meniscus cement forming irregular beds, from 5 to 20 cm in thickness (Fig. 6.9B). Micritic meniscus cement binds the grains, whereas irregular vugs show fibrous pendant cement lining the cavity roof. Facies F20 is characterized by the presence of calcified root mats (rhizolites, Fig. 6.9C) and red stained paleosoils (Fig. 6.9D). Facies F21 is a wackestone-mudstone with ostracods and *Charophytes* stems and gyrogonites forming irregular nodular beds, 20-30 cm thick, with laminar and irregular fenestral fabric and desiccation cracks (Fig. 6.9E). Facies F22 represents a well-bedded (20-30 cm thick beds) stromatolitic boundstone locally with fenestrae and desiccation cracks (Fig. 6.9F-G). Facies F23 consists of massive microbial boundstone, locally brecciated, made of an irregular texture with clotted peloidal micrite and *Cayeuxia*, *Bacinella irregularis* and *Thaumatoporella parvovesiculifera*, alternating with areas filled by dense micrite (Fig. 6.9H). Facies F24 is a wackestone with *Cayeuxia* (20-30 cm thick beds) and irregular and laminar fenestrae (Fig. 6.10A). Facies F25 consists of a bioturbated wackestone (10-20 cm thick beds) with ostracods and foraminifers (*Alveosepta jaccardi;* Fig. 6.10B) and coated grains with micrite envelopes. Facies F26 is a packstone-wackestone with intraclasts, oncoids and foraminifers. Facies F27 consists of an oncoid floatstone (10-40 cm thick beds) with type IV oncoids without lamination (Fig. 6.10C) with *Bacinella irregularis* and coatings including siliceous sponge spicules.

The lower part (2-5 m) of the vertical succession consisting of facies from F16 to F27 (Fig. 6.4a, 6.6) is characterized by the alternation of lithoclastic breccia to conglomerate with black pebbles (F16), packstone-grainstone-rudstone with corals, pisoids and black pebbles (F17), intraclastic breccia (F18), mudstone-wackestone with desiccation cracks (F19) and few beds of wackestone with ostracods and foraminifers (F25). The upper part (Fig. 6.4A, 6.6) is constituted by the alternation of facies from F18 to F27 for about 45 m. The top of the succession from facies F16 to F27 in the Urzulei Supramonte area is characterized by an intraclastic breccia bed (F18), often silicified and with rare quartz grains (Fig. 6.8H, 6.10D), at the boundary with the overlying facies F30 peloidal packstone-grainstone or F31 laminated dolostone (Fig. 6.6). Instead, in the Punta Mureddu area (Fig. 6.6), the top of facies from F18 to F27 is characterized by 2 m of wackestone with ostracods and foraminifers (F25) overlain by mudstone, wackestone and siltstone (F29).

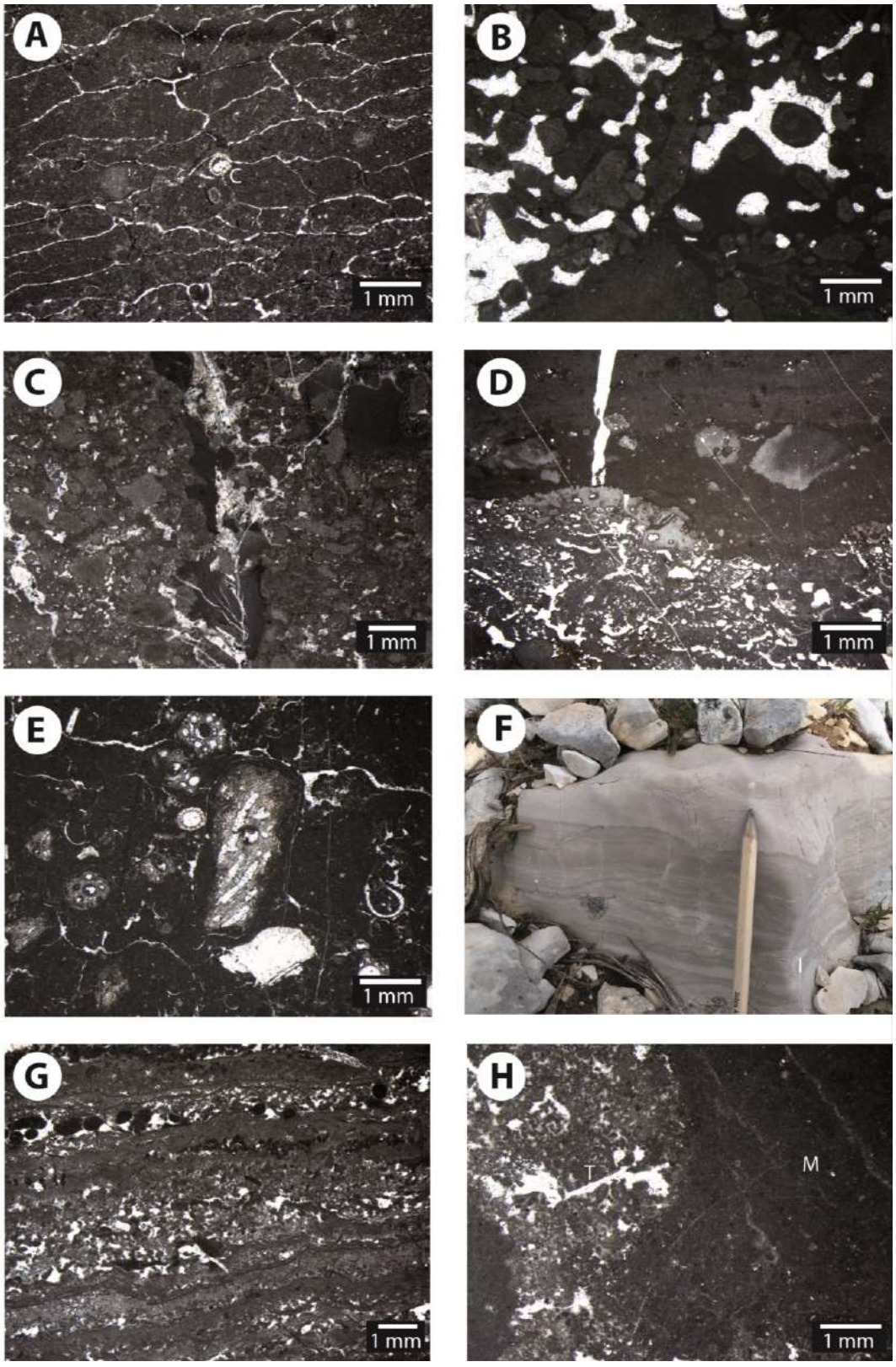

Figure 6.9 A) Photomicrograph of facies F19 mudstone with desiccation cracks and *Charophytes* gyrogonites (C). B) Facies F20 packstone with micritic intraclasts cemented by micritic meniscus cement and porosity filled by blocky calcite cement. C) F20 vertical tubular cavities filled by dark micrite (possible rhizolites). D) Facies F20 photomicrograph showing an oxidised paleosoil. E) Photomicrograph of facies F21 wackestone with *Charophytes* gyrogonites and stems, ostracods and desiccation cracks. F) Outcrop photograph of facies F22 showing stromatolitic boundstone. Pencil for scale. G) Photomicrograph of facies F22 stromatolitic boundstone peloidal agglutinated texture. H) Facies F23 microbial boundstone with clotted peloidal micrite and *Thaumatoporella parvovesiculifera* (T), alternating with areas filled by dense micrite (M).

Facies F28 is a poorly sorted, matrix-supported lithoclastic breccia with irregular and lenticular beds with erosional base, from 0.3 to 1.5 m thick, alternating with F29 mudstone, wackestone and siltstone. F28 includes a wide variety for composition and grain size of lithoclasts and of silt, sand and cobble sized coated grains and bioclasts floating in a micrite matrix (Fig. 6.10E-G). F28 lithoclasts do not resemble any of the identified facies in the succession and include bioclastic intraclastic grainstone with fibrous cement, calcareous sponge-*Crescentiella*-coral boundstone with *Calcistella jachenhausenensis* (Fig. 6.10E-F), coral-calcareous sponge-microbial boundstone, *Bacinella* boundstone, peloidal packstone, peloidal-intraclastic packstone to grainstone, wackestone with dasyclad algae *Clypeina jurassica* (Fig. 6.10G) and wackestone to floatstone with oncoids. Facies F29, embedding the F28 beds, represents 5 to 15 cm thick nodular beds of mudstone, wackestone, siltstone with sparse peloids and quartz grains (Fig. 6.10H). Facies F28 and F29 alternate at the decimetre to metre-scale in the SE Baunei Supramonte area (Fig. 6.4B, 6.11) and Punta Mureddu log (Fig. 6.6) overlying facies F15 and F25 with a sharp boundary. In the SE Baunei Supramonte area (Fig. 6.2), facies F28 and F29 pinch out toward North and West. The total thickness of the vertical succession of F28 breccia beds and F29 mudstone ranges from 0 to 25 m (Fig. 6.6, 6.11). The lower boundary is often characterized by an erosional surface overlain by the lithoclastic breccia (F28), whereas in the easternmost areas (Cava Litografica, Pedra Longa logs, Fig.6.11) it is characterized by a sharp surface overlain by F29 mudstone. The top of facies F29 intervals is overlain by the breccia with radiaxial fibrous calcite (F35; Fig. 6.11, 12A), except in the Punta Mureddu log (Fig. 6.6) where the F29 mudstone is in contact with the overlying rudstone to packstone with *Clypeina jurassica* (F32).

Facies from F30 to F34 alternate at the centimetre to decimetre scale forming a 50 m thick succession in the Urzulei Supramonte (Fig. 6.2, 6.4A, 6.6) and central northern areas (Punta Mureddu, Fig. 6.6). Facies F30 consists of a compacted peloidal packstone-grainstone with fibrous cement around grains, in beds from 10 to 20 cm thick (Fig. 6.12B). Facies F31 is a laminated dolostone with 5-10 cm thick beds (Fig. 6.12C). Facies F32 consists of a partially dolomitized rudstone to packstone (30-60 cm thick beds) with *Clypeina jurassica* (Fig. 6.12D-E). Facies F33 (10-50 cm thick beds) is a packstone to rudstone with pisoids, oncoids, foraminifers and meniscus cement (Fig. 6.12F). Facies F34 is characterized by bioturbated wackestone-mudstone (10-20 cm thick beds) with ostracods and dasyclad algae (*Campbelliella*; Fig. 6.12G). The lower boundary of the succession with alternating facies from F30 to F34 in the central NW area (Urzulei Supramonte, Fig. 6.6) is characterized by a sharp erosional contact between the intraclastic breccia (F18) overlain by a thin bed (10-20 cm thick) of compacted peloidal packstone-grainstone with fibrous cement (F30). The base is characterized by about 3 m of laminated dolostone (F31) at the top of F30, followed by the alternation of F31 with

rudstone to packstone with *Clypeina jurassica* (F32), packstone to rudstone with pisoids, oncoids, foraminifers and meniscus cement (F33) and bioturbated wackestone-mudstone with ostracods. In the central northern area (Punta Mureddu) there is a sharp lower boundary with the mudstone, wackestone and siltstone (F29) (Fig. 6.6).

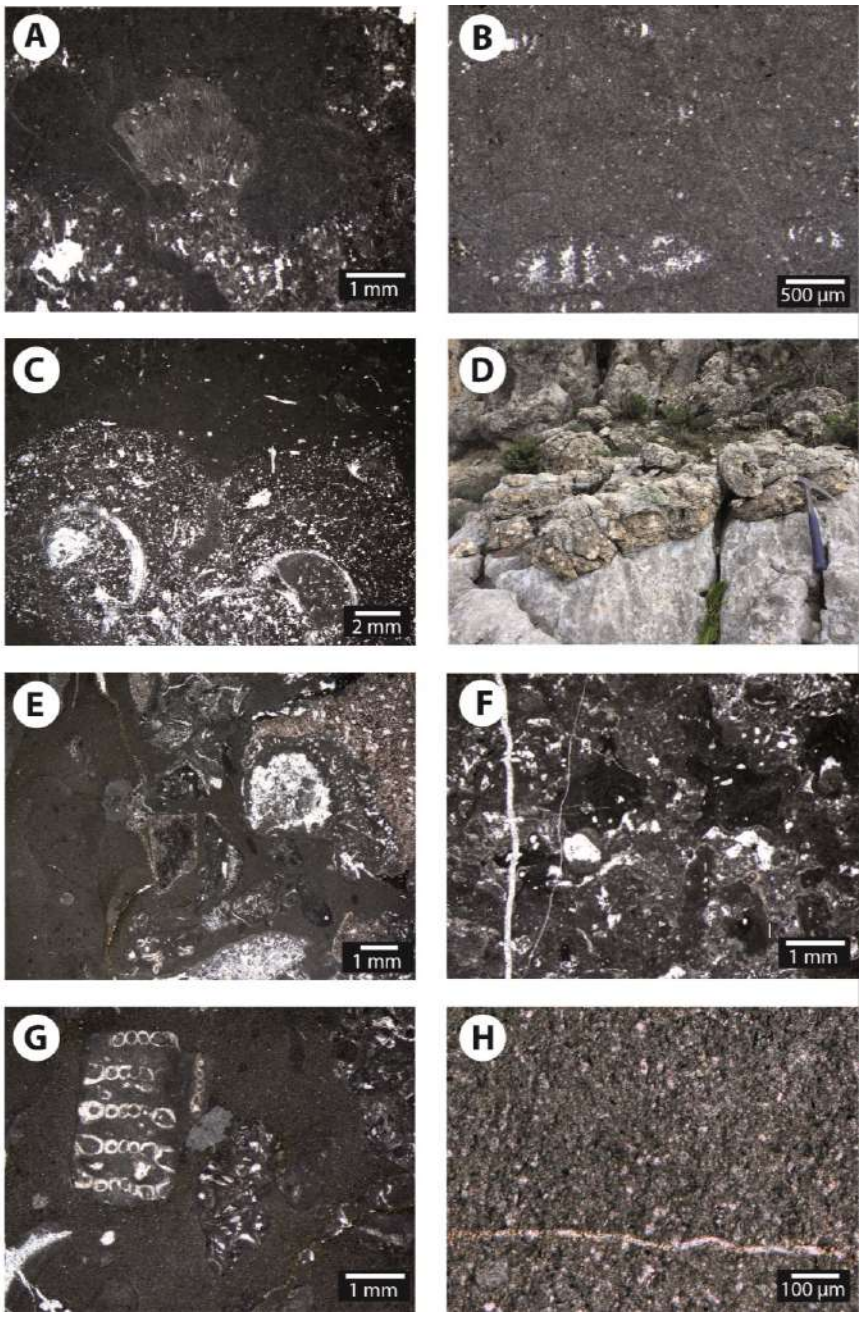

Figure 6.10 A) Facies F24 wackestone with *Cayeuxia*. B) Photomicrograph of facies F25 showing a wackestone with the benthic foraminifer *Alveosepta jaccardi*. C) Photomicrograph of facies F27 floatstone with type IV oncoids. D) Outcrop photograph showing the top of the portion of the succession characterized by facies from F18 to F27 with a silicified horizon of F18 intraclastic breccia. Hammer for scale. E) Facies F28 breccia with lithoclasts made of boundstone with *Calcistella jachenhausenensis*, *Bacinella irregularis* and *Lithocodium aggregatum* and fragments of crinoids and *Crescentiella morronensis*. F) Photomicrograph of facies F28 lithoclast made of boundstone with *Crescentiella morronensis*. G) Photomicrograph of facies F28 breccia with lithoclasts of wackestone with *Clypeina jurassica*. H) Photomicrograph of facies F29 mudstone siltstone.

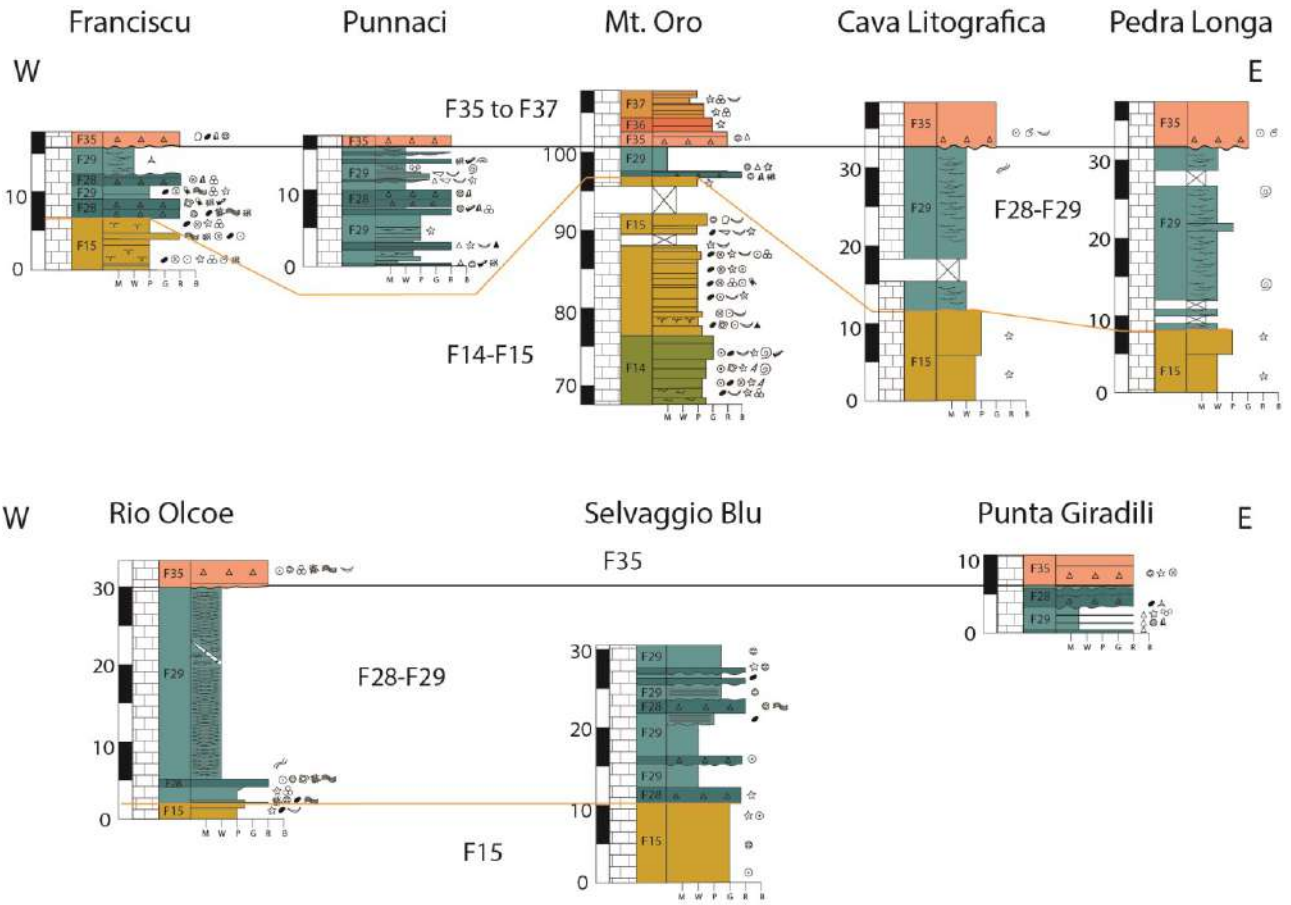

Figure 6.11 Stratigraphic logs showing facies architecture of the upper part of the succession in the Baunei Supramonte area. For log location see Figure 6.2; for facies legend refer to Figure 6.5.

Facies from F35 to F37 form a succession about 100 m thick alternating at the decimetre to metre scale and crop out only in the south-eastern area of the Baunei Supramonte (Fig. 6.2, 6.4B, 6.11). Facies F35 is a massive lithoclastic breccia with clasts bound by radiaxial fibrous calcite cement (Fig. 6.12H, 6.13A). Carbonate lithoclasts are boundstone and peloidal packstone, whereas skeletal fragments are mainly *Crescentiella morronensis*, corals, calcareous sponges and chaetetids. Facies F36 is a grainstone-packstone dominated by *Crescentiella morronensis* (Fig. 6.13B), associated with *Thaumatoporella parvovesiculifera* fragments (Fig. 6.13C) and micritic clasts, with 10-50 cm thick beds. Facies F37 is a crinoidal peloidal packstone-wackestone (Fig. 6.13D). Facies F35 to F37 form gently inclined clinoforms, dipping 3° to 15° with respect to underlying mudstone, wackestone and siltstone (F29) and F28 and F15 beds (Fig. 6.11).

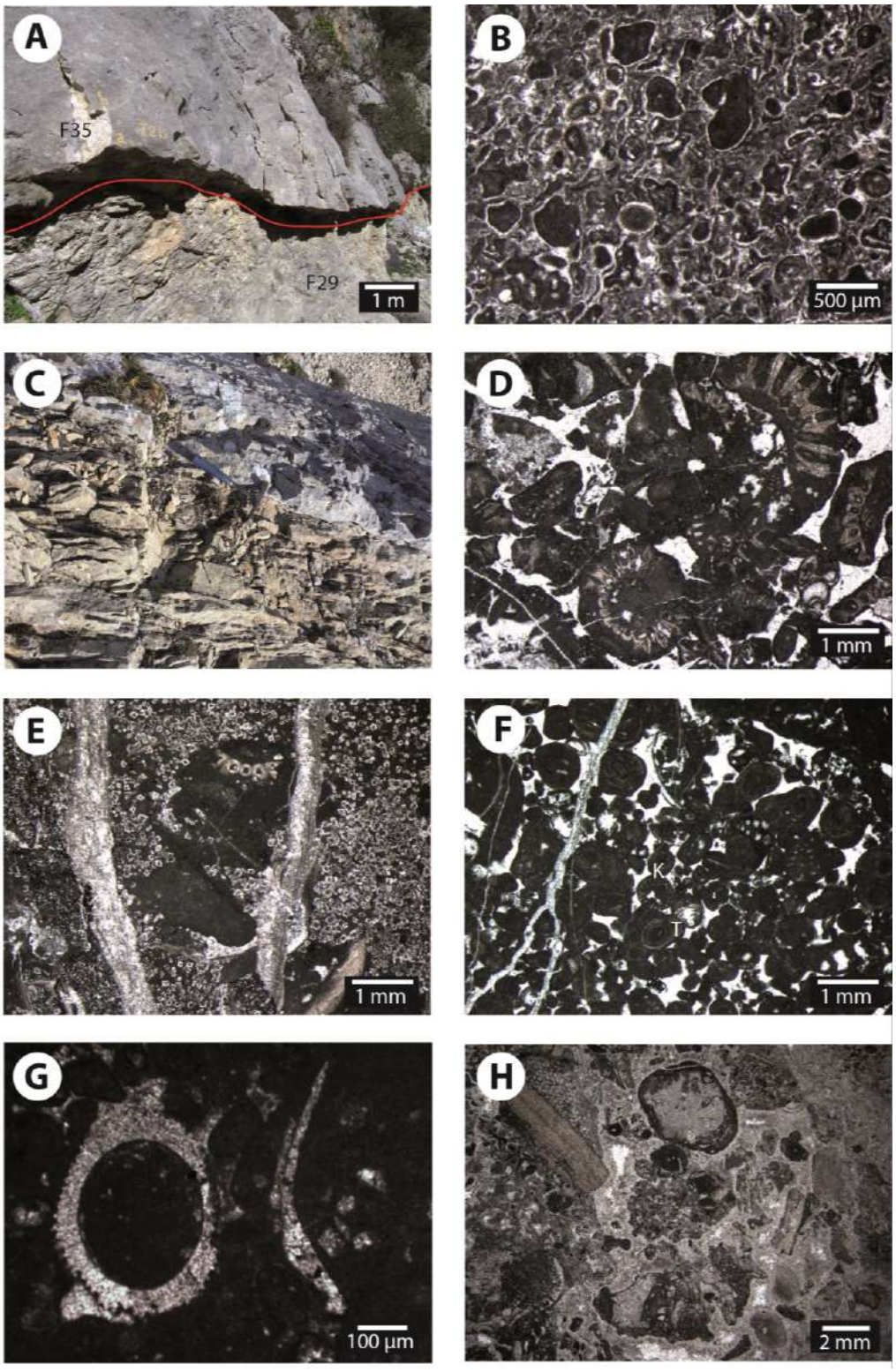

Figure 6.12 A) Outcrop photograph showing the boundary (red line) between F29 (mudstone, wackestone, siltstone) and the overlying F35 breccia with radiaxial fibrous calcite and erosional base. B) Facies F30 compacted packstone with peloids and intraclasts surrounded by a rim of calcite fibrous cement. C) Outcrop photograph showing facies F31 laminated dolostone. D) Photomicrograph of facies F32 rudstone with intraclasts made of wackestone with *Clypeina jurassica* cemented by equant blocky calcite cement. E) Facies F32 rudstone with intraclasts made of wackestone with *Clypeina jurassica*, partially dolomitized by euhedral dolomite crystals. F) Facies F33 grainstone with pisoids and the benthic foraminifers *Kurnubia* (K) and *Trocholina* (T). G) Photomicrograph of facies F34 mudstone with the dasyclad alga *Campbelliella*. H) Facies F35 breccia with lithoclasts made of boundstone with calcareous sponges, corals, clotted peloidal micrite and *Bacinella irregularis* cemented by radiaxial fibrous calcite, followed by equant blocky calcite cement.

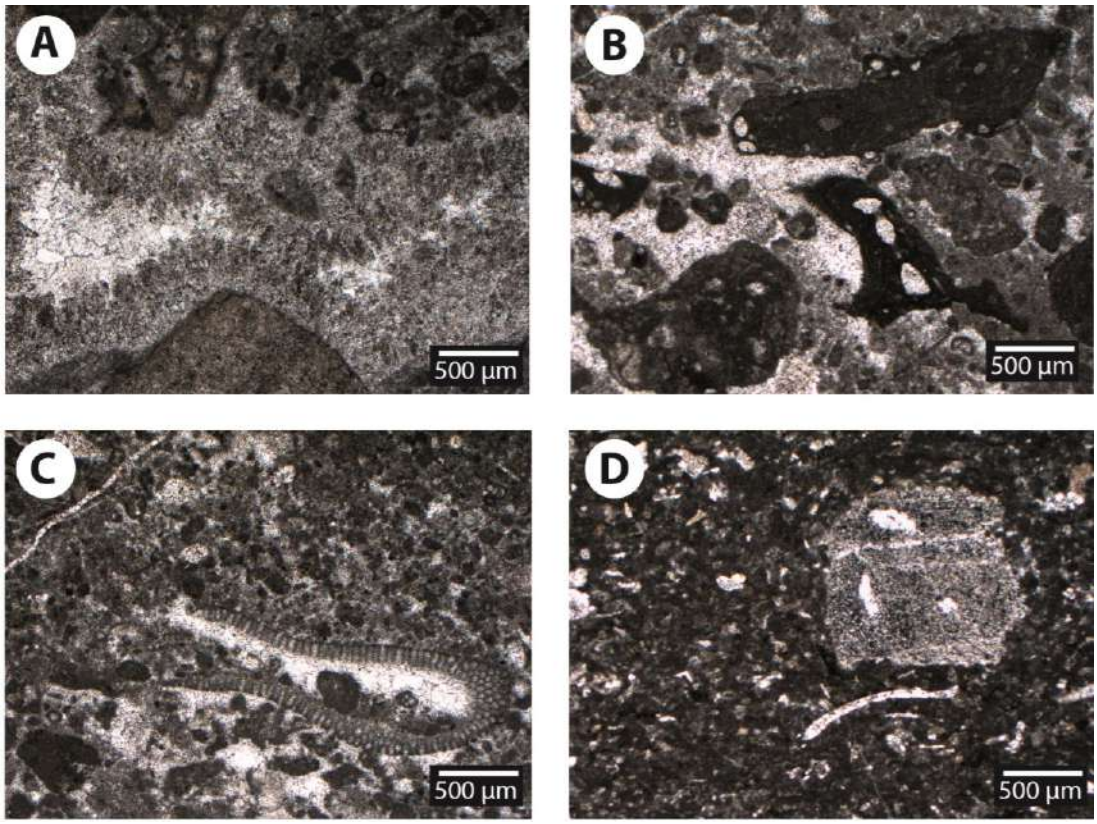

Figure 6.13 A) Photomicrograph of facies F35 showing radiaxial fibrous calcite cement lining pores, followed by equant blocky calcite cement. B) Facies F36 grainstone-packstone with *Crescentiella morronensis* fragments. C) Facies F36 grainstone-packstone with *Thaumatoporella parvovesiculifera* fragments. D) Photomicrograph of facies F37 showing a peloidal packstone with crinoids and bivalves.

6.4.2 Biostratigraphic data

The identification of microfossils and macrofossils assemblages in some of the facies provided constraints on the age of the succession (Fig. 6.14, 6.15). In facies F14 and F15 the benthic foraminifer association includes *Labyrinthina mirabilis* (Fig. 6.14A)*, Mohlerina basiliensis, Everticyclammina, Protopeneroplis striata, Trocholina, Nautiloculina oolithica* associated with the dasyclad alga *Salpingoporella annulata*.

The foraminifer association of facies F18, F19, F23, F25, F26, F27 is characterized by the presence of *Alveosepta jaccardi* (Fig. 6.10B, 6.14B), *Redmondoides, Everticyclammina, Parugonia,* and *Nautiloculina oolithica*.

In facies F29, the ammonite *Pseudosubplanitoides spindelense* (Zeiss, 1968) (Fig. 6.14C) was found in association with the benthic foraminifers *Everticyclammina, Pseudocyclammina, Trocholina, Protopeneroplis striata, Lenticulina*, the calcareous sponges *Neuropora lusitanica, Calcistella jachenhausenensis* and the dasyclad algae *Salpingoporella annulata* and *Clypeina jurassica*.

In the vertically superimposed facies from F30 to F34 the skeletal association is characterized by the benthic foraminifers *Trocholina* and *Kurnubia* and by the dasyclad algae *Clypeina jurassica* and by dasyclad algae belonging to the genus *Campbelliella* (Fig. 6.12G).

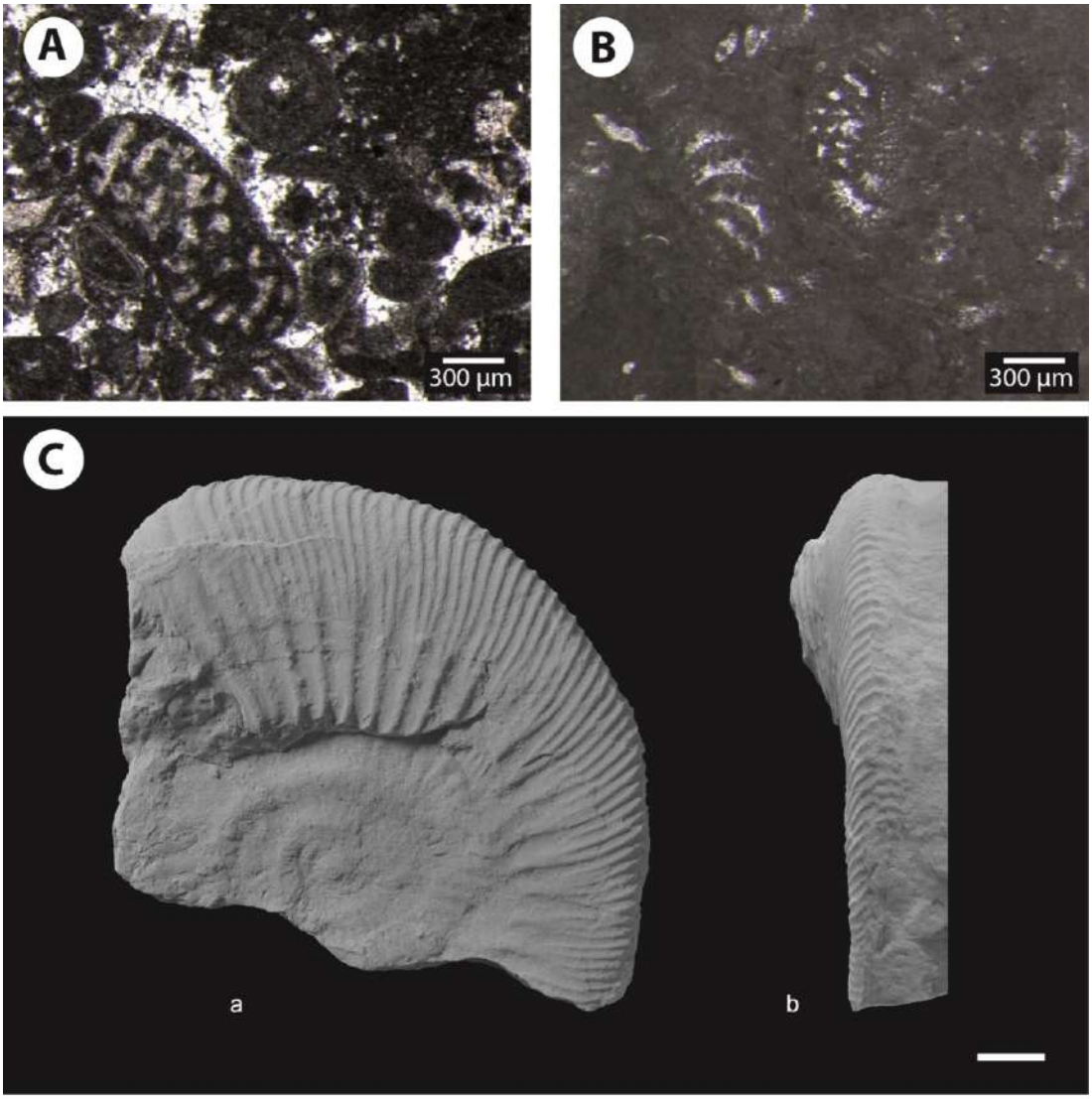

Figure 6.14 A) Photomicrograph of a *Labyrinthina mirabilis* from facies F15. B) Photomicrograph of *Alveosepta jaccardi* from facies F25. C) Ammonite *Pseudosubplanitoides spindelense* (Zeiss, 1968) from Punnaci log (Baunei Supramonte; Fig. 6.2, 6.11), specimen PUN-3. a – lateral view; b – ventral view. Specimen coated with ammonium chloride. Scale bar is 10 mm.

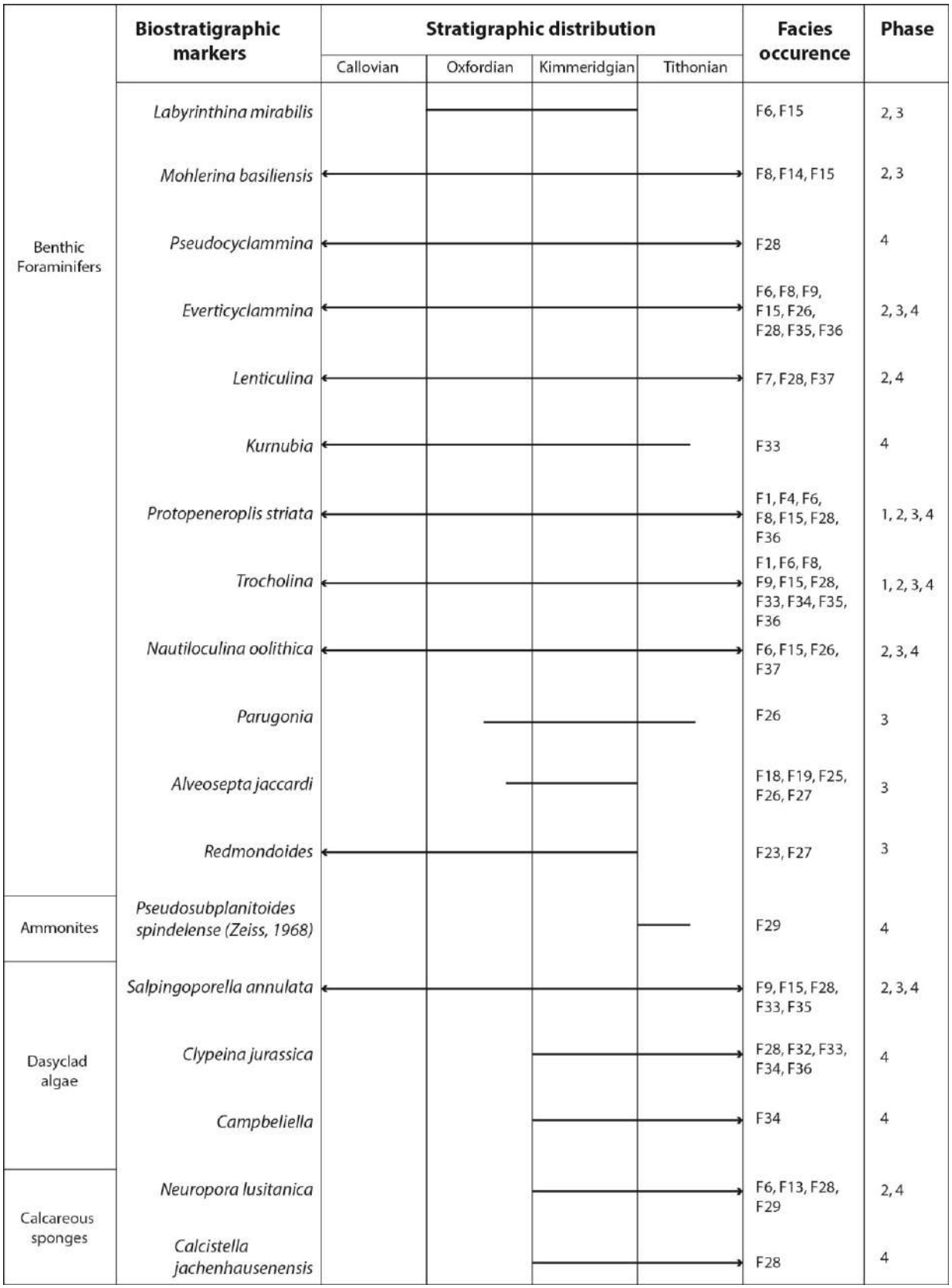

Figure 6.15 Biostratigraphic relevant fossils of eastern Sardinia carbonate succession and their stratigraphic distribution based on Hottinger (1967), Septfontaine (1988), BouDagher-Fadel (2008), Olszewska et al. (2012) and Pleş et al. (2015).

6.4.3 Strontium isotopes

Table 6.2 shows the results of strontium isotopes analyses (for methodology description refer to Chapter 4, 4.3) with $^{87}Sr/^{86}Sr$ ranging from 0.7068 to 0.7072. Due to scarce available suitable sampling material (e.g., brachiopods, belemnites) the results are limited to thin intervals within some stratigraphic logs. In the Baunei Supramonte area, the $^{87}Sr/^{86}Sr$ ratios of facies F15 and F28 samples from the Franciscu stratigraphic section vary between 0.706952 and 0.707207, whereas samples of facies F14, F15 and F35 from the Mt. Oro log range from 0.706860 to 0.707100. The $^{87}Sr/^{86}Sr$ ratios of facies F10 samples from the Urzulei Supramonte area (Genna Silana log; Fig. 6.2, 6.6) vary between 0.706945 and 0.707184.

Stratigraphic log	*Sample*	*Facies*	*$^{87}Sr/^{86}Sr$*	*Sampled component*	*Age according to Wierzbowski et al. (2017)*
Genna Silana	GS2090	F10	0.706968	Brachiopod	**late Kimmeridgian**
Genna Silana	GS2296B	F10	0.706945	Brachiopod	**late Kimmeridgian**
Mt. Oro	O924B	F14	0.706977	Bulk	**late Kimmeridgian**
Mt. Oro	O1133A	F15	0.707017	Brachiopod	**late Kimmeridgian**
Mt. Oro	V9	F36	0.707100	Brachiopod	**early Tithonian**
Franciscu	F77	F15	0.707207	Brachiopod	*late Tithonian-Berriasian*
Franciscu	F98	F15	0.706952	Brachiopod	*late Kimmeridgian*
Franciscu	F125	F29	0.706982	Brachiopod	*late Kimmeridgian*
Genna Silana	GS1800	F10	0.707184	Brachiopod	*early-late Tithonian*
Mt. Oro	O924	F14	0.706860	Belemnite	*Callovian*
Mt. Oro	O1133B	F15	0.706963	Brachiopod	*late Kimmeridgian*

Table 6.2 Results of strontium isotope analyses and possible ages according to Wierzbowski et al. (2017) marine $^{87}Sr/^{86}Sr$ through time.

6.5 Interpretation

6.5.1 Age of the stratigraphic succession

The $^{87}Sr/^{86}Sr$ ratio of selected samples, integrated with biostratigraphic data, provided useful tie-point to constrain the age of the studied succession. The measured values of $^{87}Sr/^{86}Sr$ ratio are compared with the global curve proposed by Wierzbowski et al. (2017), in order to obtain an approximated chronostratigraphic age (Fig. 6.16). Some of the obtained vertical trends fit with the global marine $^{87}Sr/^{86}Sr$ ratio values for the late Kimmeridgian-early Tithonian. Within 11 analysed samples only 5

samples show reliable values fitting with the available biostratigraphic constrains (Fig. 6.15). Thus, the other 6 values were discarded and not considered for the stratigraphic correlation (Table 6.2).

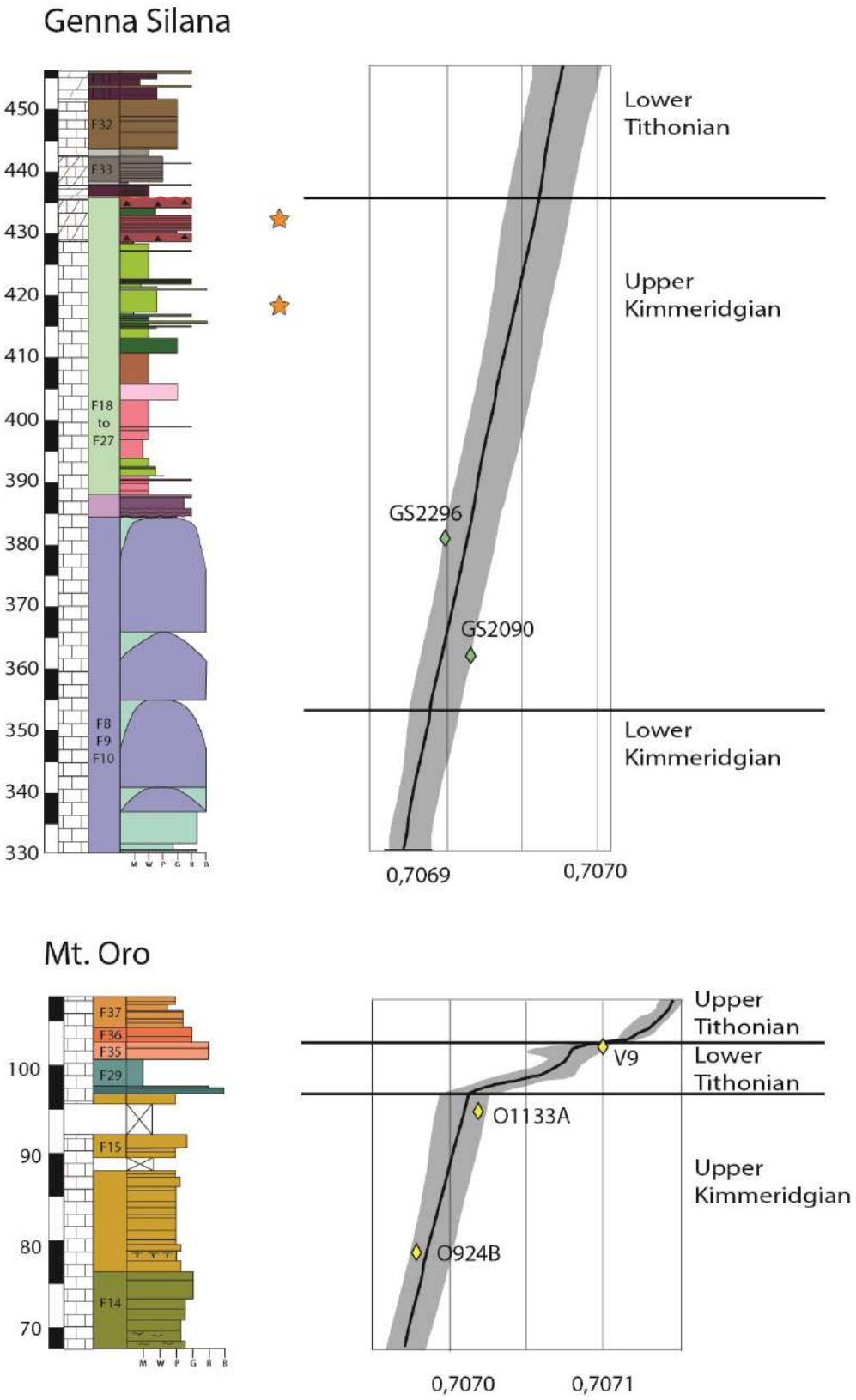

Figure 6.16 Results of the strontium isotope $^{87}Sr/^{86}Sr$ ratio measurements for the Genna Silana and Mt. Oro stratigraphic logs compared with the global curve by Wierzbowski et al. (2017). Occurrence of the benthic foraminifer *Alveosepta*

jaccardi indicative of late Oxfordian-late Kimmeridgian age (Hottinger, 1967) marked by orange stars. For log location refer to Figure 6.2; for facies legend refer to Figure 6.5.

The deposition of facies F8, F9 and F10 in the Genna Silana log results to have ended in the first part of the late Kimmeridgian. This is demonstrated by the $^{87}Sr/^{86}Sr$ ratios of brachiopods from samples GS2090 and GS2296 (0.706968 and 0.706945) indicative of late Kimmeridgian (Wierzbowski et al., 2017) and the occurrence of the benthic foraminifer *Alveosepta jaccardi* in the overlying vertical succession of facies from F16 to F27 (Fig. 6.15, 6.16). The stratigraphic distribution of *Alveosepta jaccardi* is constrained from the late Oxfordian to the late Kimmeridgian (Fig. 6.15; Hottinger, 1967; Septfontaine, 1988; Olszewska et al., 2012; BouDagher-Fadel, 2008; Pleş et al., 2015).

$^{87}Sr/^{86}Sr$ values from bulk matrix and brachiopods of facies F15 and F14 in the Mt. Oro log (O924B: 0.706977 and O1133A: 0.707017) suggest a late Kimmeridgian age (Fig. 6.16). The stratigraphic distribution of the foraminifer *Labyrinthina mirabilis* (Fig. 6.15) identified in facies F14 and F15 in the Baunei Supramonte, Franciscu, Punnaci and Mt. Oro logs (Fig. 6.11) is Oxfordian-Kimmeridgian (BouDagher-Fadel, 2008; Pleş et al., 2015). Instead, the overlying alternating facies F28 and F29 were deposited during the early Tithonian as demonstrated by the occurrence of the ammonite *Pseudosubplanitoides spindelense* (Zeiss, 1968) and the $^{87}Sr/^{86}Sr$ value of a brachiopod sample from the overlying facies F35 (V9: 0.707100) that indicates an approximate early Tithonian age (cf. Wierzbowski et al., 2017). Moreover, the association of benthic foraminifers and dasyclad algae in facies F28 and F29 is indicative of an age not older than early Tithonian (Pleş et al., 2015; Mircescu et al., 2019).

The portion of the succession characterized by facies from F30 to F34 was dated to the early Tithonian based on the paleontological association (*Clypeina jurassica, Campbelliella sp.*) and the stratigraphic position at the top of the upper Kimmeridgian portion of the succession (F16 to F27). The co-occurrence of *Clypeina jurassica* and *Campbelliella* is suggested to be indicative of late Kimmeridgian-Berriasian time interval (Mircescu et al., 2014). *Clypeina jurassica* has a stratigraphic range Kimmeridgian-lower/middle Berriasian (Fig. 6.15) but records an acme in the Kimmeridgian-Tithonian (Mircescu et al., 2019 and references therein).

6.5.2 Stratigraphic evolution

Facies architecture reconstruction and physical correlation among the stratigraphic logs integrated with biostratigraphic and strontium isotopes analysis allowed distinguishing 4 depositional phases for the Callovian-Tithonian eastern Sardinia carbonate succession (Fig. 6.17).

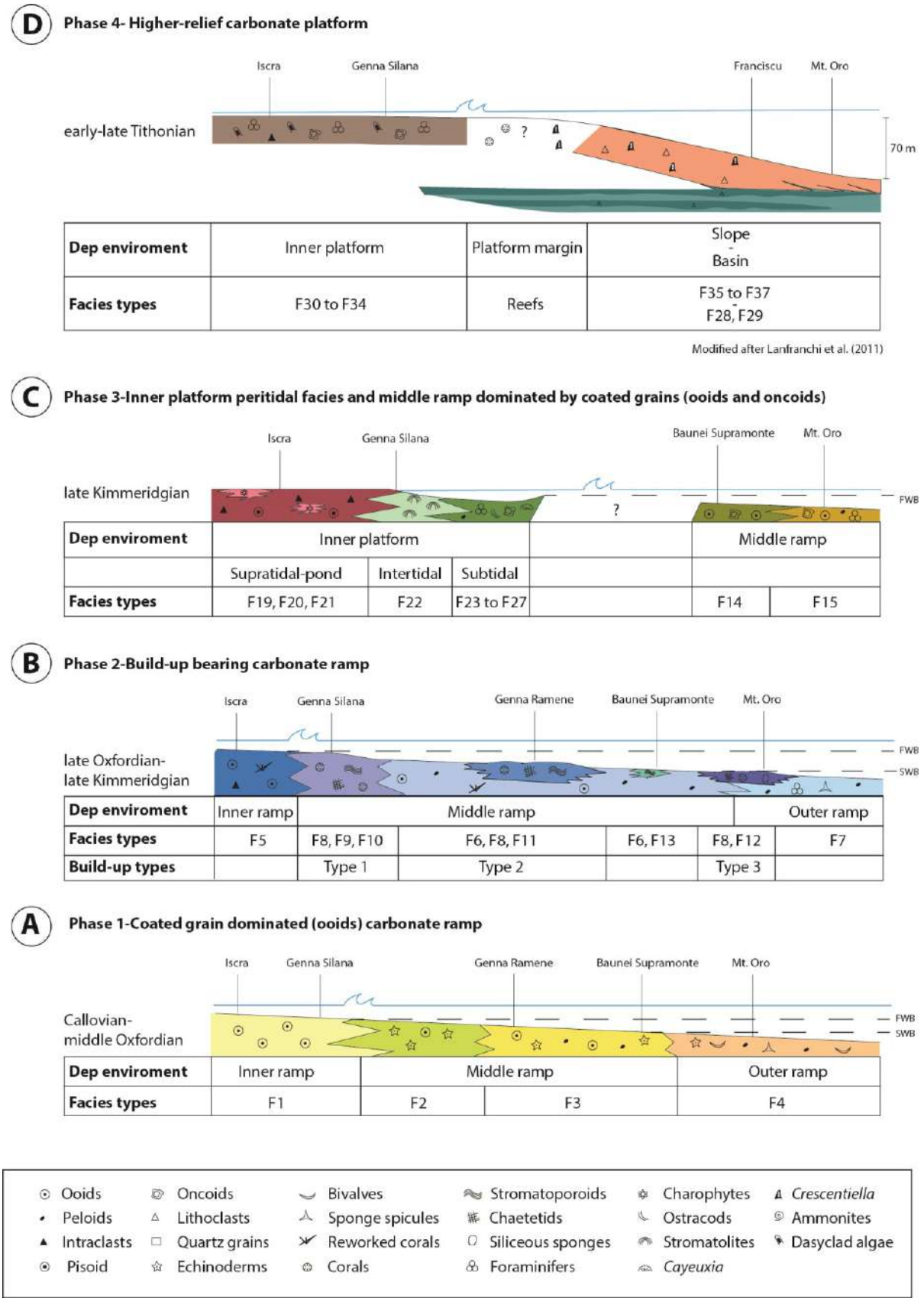

Figure 6.17 Depositional profiles for each depositional phase: A) Phase 1 - Coated grain dominated (ooids) carbonate ramp, Callovian-middle Oxfordian. B) Phase 2 - Build-up bearing carbonate ramp, late Oxfordian-late Kimmeridgian. C) Phase 3 - Inner platform peritidal facies and middle ramp dominated by coated grains (ooids and oncoids), late Kimmeridgian. D) Phase 4 - Higher-relief carbonate platform profile with slope facies, early-late Tithonian (modified after Lanfranchi et al., 2011).

6.5.2.1 Phase 1 (Callovian-middle Oxfordian)

During phase 1, facies F1 to F4 accumulated in a carbonate ramp dominated by coated grains and characterized by gradual facies changes from high-energy shallow water inner ramp to low-energy deeper outer ramp (cf. Chapter 5), with an approximate thickness highly variable from about 300 m in the Urzulei Supramonte to 25-30 m in the Baunei Supramonte (Fig. 6.17A). Facies F1 cross-bedded ooidal coated grain grainstone represents the above fair-weather wave base shoal in the inner ramp setting, whereas the laterally adjacent F2 cross-laminated echinoderm packstone to grainstone-rudstone was deposited at the transition from inner to proximal middle ramp environment, where echinoderm ossicles can form sand bars (cf. Della Porta et al., 2004 and references therein). Facies F3 was deposited in a middle ramp environment, between fair-weather wave base and storm wave base, where low-energy conditions were occasionally interrupted by storms reworking inner-ramp derived ooids and echinoderms. The peloidal packstone with chert nodules and thin-shelled bivalves (F4) accumulated in a low-energy outer ramp, below the fair-weather and storm wave base, as demonstrated by the abundance of micrite matrix, fine grain size and the thin-shelled bivalve association (cf. Hughes, 2004; Molina et al., 2018).

The widespread dolomitization in facies from F1 to F4 prevents to identify biostratigraphic markers for precisely identifying the age for this portion of the succession. However, the onset of carbonate sedimentation in eastern Sardinia was placed in the late Bathonian (Casellato et al., 2012; cf. Chapter 3), whereas the dynoflagellate association identified by Jadoul et al. (2009) in facies F4 in the Baunei Supramonte area indicates an Oxfordian age. Thus, an approximate Callovian-middle Oxfordian age could be suggested for facies from F1 to F4 that are comprised in the Dorgali, Lower Mt. Tului and Lower Baunei formations (cf. Chapter 3 and Chapter 5).

6.5.2.2 Phase 2 (late Oxfordian-late Kimmeridgian)

The laterally adjacent and vertically alternating facies from F5 to F13 represent the carbonate deposition during phase 2, characterized by the development of a ramp dominated by coral, stromatoporoid, calcareous and siliceous sponge, and microbialite bioconstructions (cf. Chapter 5). Phase 2 records a change in the dominant carbonate factory from coated-grain dominated during phase 1 to build-up bearing ramp during phase 2, reaching an approximate thickness from 40 to 60 m (Fig. 6.17B). In facies F5 the common occurrence of micritic (type 1) and micritized radial ooids (type 3) suggests deposition of ooidal shoals in inner-ramp high-energy environments. The middle ramp was characterized by the deposition of peloidal packstone with reworked intraclasts, bioclasts

and coated grains (F6) alternating with three facies associations, representing three different types of build-ups (type 1, 2 and 3), which show high variability in shape, size, composition and distribution as a function of palaeo-water depth (cf. Chapter 5). The occurrence of fragmented skeletal and non-skeletal grains in facies F6 suggests reworking of inner ramp sediment and deposition aáove the storm wave base in the middle ramp environment.

High-energy events in the middle ramp could also be caused by internal waves, which are perturbations propagating along the pycnocline that exert and exerted a fundamental control on carbonate system hydrodynamic regimes at depths, skeletal biota composition, and early marine cementation (Pomar et al., 2012). Their breaking along continental margin and slopes remobilizes sediment. This model has been applied to Jurassic carbonate systems to interpret high-energy deposits in middle ramp environment. In the upper Kimmeridgian carbonate ramp of Ricla (NE Spain) ooidal grainstone within middle ramp deposits were interpreted as reworked by turbulent events related to breaking internal waves because they occur in distal middle ramp, do not show thickening and coarsening upward trends and thin and disappear both up-dip and down-dip (Bádenas et al., 2012). In the upper Kimmeridgian carbonate ramp of Arroyo Cerezo (Iberian Basin, eastern Spain), Alnazghah et al. (2013) suggested that coarse-grained facies of build-up flanks in the middle ramp were the results of turbulence created by propagation of internal waves. Al-Awwad and Pomar (2015) suggested that rudstone-floatstone beds with oncoids and stromatoporoids interbedded with outer ramp peloidal wackestone were deposited due to turbulence related to internal waves in the Kimmeridgian Arab-D subsurface reservoir in the Middle East.

The association of facies F8, F9, F10 represents laterally continuous build-up type 1 formed in the proximal middle ramp environment, seaward with respect to ooidal shoals. In more distal domains of the middle ramp the association of facies F8 and F11 formed lens-shaped build-up type 2.

The association of facies F8 and F12 formed metre-size lens-shaped build-up type 3 in the distal middle ramp and in low-energy outer ramp settings alternated with the peloidal packstone with *Lenticulina* (F7) as suggested by the common occurrence of *Lenticulina* foraminifers in distal settings (cf. Hughes, 2004). Facies F13 was deposited in middle ramp environment during storm events or due to internal wave mechanisms (cf. Pomar et al., 2012; Al-Awwad and Pomar, 2015) that reworked stromatoporoids and other skeletal fragments from the build-up facies associations.

The onset of phase 2 is marked by an abrupt increase in skeletal content in the depositional facies corresponding to a change in the dominant carbonate factory and was dated to the late Oxfordian in analogy with the spread of corals, stromatoporoids and calcareous sponges in the Tethys realm (Leinfelder et al., 2002; Cecca et al., 2005; Martin-Garin et al., 2012; Nembrini et al., 2021). The absence of biostratigraphic indicators in the Oxfordian-early Kimmeridgian portion of the studied

succession prevents to exactly date this facies change. The upper boundary of phase 2 is marked by a subaerial exposure surface at the top of facies F10 in the Urzulei Supramonte area (Fig. 6.2, 6.6). Laterally towards the south-eastern deeper depositional settings in the Baunei Supramonte area (Fig. 6.2, 6.5), the upper boundary of phase 2 is represented by a sharp compositional change in the superimposed facies. The underlying phase 2 outer (F7) to middle (F6, F13) ramp facies F6, F7 and F13 are sharply overlain by grainstone (F14) reworking ooids, aggregate grains and oncoids deriving from the inner ramp. This sharp facies compositional change is interpreted as a shallowing-upward trend laterally equivalent to the subaerial exposure in the north-western shallower setting of the Urzulei Supramonte area (Fig. 6.2). This subaerial exposure event caused the demise of the reefal carbonate factory and marks the end of phase 2. Strontium isotope ratios and biostratigraphic data suggest that phase 2 terminated in the late Kimmeridgian. Phase 2 facies succession from F5 to F13 includes part of the Upper Tului Fm. and the Upper Baunei Fm. by Jadoul et al. (2009, 2010).

6.5.2.3 Phase 3 (late Kimmeridgian)

Phase 3 is characterized by the deposition of facies F14 and F15 in the deeper depositional settings of the south-eastern Baunei Supramonte area (approximate thickness 30 m) and facies from F16 to F27 in the shallower, central north-western Urzulei Supramonte (approximate thickness 50 m) and Punta Mureddu (approximate thickness 20 m) areas (Fig. 6.2).

In the SE Baunei Supramonte area (from Punnaci to Pedra Longa log; Fig. 6.2, 6.11), facies F14 and F15 are interpreted as representing middle ramp environments (Fig. 6.17C). In the grainstone with ooids, aggregate grains and oncoids (F14), these coated grains were reworked, likely during high-energy storm events, from the inner ramp and are associated with ammonites and belemnites suggesting an open marine, deeper environment. The peloidal packstone with oncoids and ooids (F15) was deposited in a low-energy environment in the middle ramp as demonstrated by the abundance of fine-grained peloids. Abundant oncoids (type I-II) and ooids (type 1 and 3) were likely reworked from shallower settings (cf. Sequero et al., 2020). The vertical superposition of facies F14 and F15 on the underlying phase 2 facies F6, F7 and F13 is interpreted as a shallowing-upward trend because of the presence of reworked inner-ramp derived coated grains within facies F14. The upper boundary with the overlying F28 lithoclastic breccia beds within mudstone, wackestone and siltstone (F29) is interpreted as a rapid deepening of the depositional environment into basinal settings. Strontium isotope and biostratigraphic data from the overlying succession (F28, F29) constrain the age of facies F14 and F15 to the late Kimmeridgian. Facies F14 and F15 correspond to the uppermost part of the Upper Mt. Tului Fm. (Jadoul et al., 2009) in the Baunei Supramonte area (from Punnaci to Pedra Longa log; Fig. 6.11).

In the Urzulei Supramonte and Punta Mureddu areas, phase 3 is characterized by deposition of the vertical succession of facies from F16 to F27. The lithoclastic breccia to conglomerate with black pebbles (F16) and the packstone-grainstone-rudstone with corals, pisoids and black pebbles (F17) were deposited during the transgression and reflooding of the platform after the subaerial exposure at the top of phase 2 build-up-bearing carbonate ramp. The abundance of fragments of corals and calcareous sponges suggests erosion and reworking of the subaerially exposed coral-stromatoporoid-sponge microbialite reef accumulated during phase 2 (build-up type 1 F8, F9, F10 in Genna Silana log; Fig. 6.2, 6.6, 6.16). Lithoclasts mainly consist of lacustrine-pond (F21) and supratidal (F19, F20) facies, suggesting subaerial exposure and reworking of terrestrial deposits. The abundance of black pebbles is indicative of reworking during the transgression of subaerially-exposed lithoclasts with the development of calcareous and organic-rich paleosoils. The black pebbles may have derived from erosion and reworking of calcareous paleosoils (Strasser, 1984; Leinfelder, 1987; Platt and Wright, 1992; Sevillano et al., 2019). The blackening is due to impregnation of detrital sediment by organic substances in an anoxic and alkaline environment or microenvironment (Strasser, 1984; Leinfelder, 1987). In some present-day supratidal mangrove zones, the upper few centimetres of sediment are anoxic (Belperio et al., 1988).

The succession of facies from F18 to F27, comprised between the transgressive lag (F16-F17) and facies F30 or F31 at the top of phase 3 (Fig. 6.6, 6.16) represents deposition in a protected low-energy inner platform setting including intertidal, supratidal and subtidal facies and coastal vegetated ponds following events of subaerial exposure (Fig. 6.17C). All the characteristics of the coastal environment suggest deposition in wetlands with vegetated marsh area and facies representative of terrestrial, supratidal and pond environments (Wright and Azerêdo, 2006). The intraclastic breccia (F18) includes a mixture of clasts reworked during high-energy events (such as storm waves) and local autoclastic breccia generated by prolonged and repeated subaerial exposures in the supratidal zone. All the clasts represent supratidal and intertidal facies (F19, F20, F22) and brackish-freshwater deposits (F21 wackestone with *Charophytes)*. The presence of gypsum in some mudstone intraclasts suggests possible periods of arid conditions (Flügel, 2004). Mudstone-wackestone with desiccation cracks (F19) represents low-energy environments in supratidal zones (Tucker and Wright, 1990). The diffuse laminar and irregular fenestral porosity is also indicative of upper intertidal and supratidal areas (Tucker and Wright, 1990). The pisoid-intraclastic packstone-rudstone with meniscus cement (F20) was deposited in supratidal environment. The presence of carbonate meniscus and pendant cement suggests meteoric vadose diagenesis. The paucity of skeletal fragments and low-diversity, limited to *Charophytes* gyrogonites, ostracods and few benthic foraminifers indicates a restricted environment and low-salinity conditions. These deposits were affected by wetting and drying cycles

and by terrestrial vegetation producing calcified root mats (rhizolites). Paleosoil calcretes suggest cyclical periods of subaerial exposure (F20). The wackestone-mudstone with ostracods and *Charophytes* (F21) were deposited in low-energy pond-lacustrine environment, as suggested by the abundance of micrite and the low-diversity fossil assemblage consisting of *Charophytes* gyrogonites and stems, ostracods and few gastropods and bivalves. *Charophytes* and associated ostracods indicate environments influenced by freshwater or brackish water (Shinn et al., 1969; Colombié and Strasser, 2005). Ponds between channel systems could also become brackish during periods of heavy rainfall (Shinn et al., 1969). Indeed, according to Zuo et al. (2019) during the Kimmeridgian, there were fluctuations from humid to arid conditions up to more arid conditions in late Kimmeridgian. The occurrence of fenestrae and desiccation cracks suggests periodical drying cycles in the pond or lacustrine environment.

The intertidal environment was characterized also by the deposition of the stromatolitic boundstone (F22) as demonstrated by the presence of laminated microbialites, such as microbial laminites and fine-grained agglutinated stromatolites (Aitken, 1967). Fenestrae are mainly formed by desiccation and shrinkage or air and gas bubble formation (Shinn, 1968), but they also occur within stromatolites and are formed by the irregular growth processes of the microbial mats (Monty and Hardie, 1976; Playford and Cockbain, 1976; Tucker and Wright, 1990).

The subtidal lagoonal environment was characterized by the deposition of microbialite dominated facies (F23-F24) and mud-supported oncoidal bioclastic facies (F25-F26-F27). Facies F23, with dense micrite and clotted peloidal micrite associated with *Cayeuxia*, *Bacinella irregulari*s and *Thaumatoporella parvovesiculifera*, suggests a microbial origin for this boundstone (Riding, 2000). *Cayeuxia*, abundant in facies F23 and F24, is considered a calcified cyanobacterium (Riding, 1991b). Calcification of cyanobacteria sheaths is attributed to photosynthetic inorganic carbon uptake that increases the pH adjacent to cyanobacterial cells, promoting $CaCO_3$ precipitation (Arp et al., 2001; Riding, 2006; Planavsky et al., 2009; Săsăran et al., 2014). Periods of increased abundance of calcified cyanobacteria are indicative of high supersaturation of seawater (Riding and Liang, 2005; Della Porta et al., 2013). According to Reolid et al. (2007) and Palma et al. (2007) the occurrence of *Cayeuxia*, *Bacinella irregulari*s and *Thaumatoporella parvovesiculifera* is indicative of shallow-water marine lagoon environment. The wackestone with ostracods and foraminifers (F25) is characterized by low biotic diversity and mud-supported texture and is interpreted as deposited in a low-energy shallow subtidal environment, most probably in a restricted lagoon with fluctuations in seawater salinity and temperature, which inhibited the proliferation of normal marine benthic organisms (cf. Sevillano et al., 2019). The packstone-wackestone with intraclasts, oncoids and foraminifers (F26) was deposited in a subtidal environment. Abundance of benthic foraminifers

associated with brachiopods, corals and crinoid fragments indicates normal marine salinity. Abundant micrite and the irregular shapes and nature of oncoid cortices and nuclei suggest a shallow low-energy environment (Flügel, 2004). Type II and type III oncoids are typical of protected environment (Dahanayake, 1978; Sequero et al., 2020), suggesting for F26 a subtidal, relatively open lagoon environment. The oncoid floatstone (F27) was deposited in a low-energy subtidal environment as suggested by the dominance of type IV oncoids (typical of low energy environments) and the abundance of micrite (Dahanayake, 1978; Sequero et al., 2020).

The vertical succession of facies from F18 to F27 in phase 3 suggests a prolonged period of low accommodation with very shallow sedimentation characterized by a peritidal environment affected by high-frequency subaerial exposures and transgressions. The deposition of facies from F16 to F27 was dated to the late Kimmeridgian due to the occurrence of the benthic foraminifer *Alveosepta jaccardi,* whose distribution is late Oxfordian-late Kimmeridgian (Hottinger, 1967) and the stratigraphic position overlying the subaerial exposure at the top of phase 2 dated to the late Kimmeridgian according to strontium isotopes data. The top of phase 3, with facies from F16 to F27, is characterized by the intraclastic breccia (F18), suggesting a second subaerial exposure event. Facies from F16 to F27 characterize the Urzulei Fm. after Jadoul et al. (2009, 2010).

6.5.2.4 Phase 4 (early-late Tithonian)

Phase 4 was characterized by sharp facies and depositional environment changes across the whole studied transect form the deeper south-eastern Baunei Supramonte area (approximate thickness 100 m) to the shallower central north-western Urzulei Supramonte areas (approximate thickness 50 m) with the deposition of facies F28 to F37 (Fig. 6.2).

In the SE Baunei Supramonte, the association of facies F28 and F29 represents deposition in basinal environment (Fig. 6.17D), where the lithoclastic breccia (F28) represents resedimentation of shallow-water carbonate facies through subaqueous mass transport processes (debris flow) and F29 mudstone, wackestone and siltstone the background basinal sedimentation. This is suggested by the chaotic massive character of the lenticular breccia beds, the erosional bases and the size and facies variability of the angular carbonate lithoclasts (up to 1 m in diameter) representing different depositional environments, from inner platform to reefs (Pray et al., 1968; Cook et al., 1972; Crevello and Schlager, 1980). F28 debris-flow deposits are embedded within the F29 mudstone, wackestone and siltstone that constitute also the matrix between lithoclasts. The lithoclasts represent early cemented facies mainly belonging to build-ups formed by corals, calcareous sponges, *Crescentiella morronensis* and *Bacinella irregularis* or derive from reworking of inner platform deposits. F29

facies represents a low-energy basin, as suggested by the grain size, abundance of micrite, widespread bioturbation, thin nodular-bedding and the presence of ammonites and sponge spicules. Some of the beds with isoriented and broken shells of bivalves, brachiopods and other skeletal fragments may represent transportation and deposition by turbidity currents (Cook et al., 1972). The presence of fine-grained quartz grains suggests influence of siliciclastic input. F28 deposits were probably emplaced rapidly relative to the normal rate accumulation of the F29 basinal facies (Cook et al., 1972).

The sharp lower boundary of facies F28 and F29 with the underlying middle ramp F14 grainstone with reworked ooids, aggregate grains and oncoids in the Baunei Supramonte area (from Punnaci to Pedra Longa logs; Fig. 6.11) and with the underlying lagoonal facies F25 wackestone with ostracods and foraminifers in the Punta Mureddu log (Fig. 6.6) is interpreted as a deepening-upward trend leading to basinal conditions. The occurrence of the ammonite *Pseudosubplanitoides spindelense* (Zeiss, 1968), strontium isotope data and the stratigraphic position suggest for the basinal facies association F28 and F29 an early Tithonian age. The age and lithoclast composition reveal the presence of lower Tithonian bioconstructions (Lanfranchi et al., 2011; Ricci et al., 2018; Chapter 7) different from the upper Oxfordian-Kimmeridgian build-up type 1 to 3 (facies from F8 to F12; Chapter 5) reworked through the F28 debris-flow breccia beds. This evidence suggests the recovery of a reefal carbonate factory in the Tithonian phase 4 after the subaerial exposure events and peritidal facies characterizing the late Kimmeridgian phase 3 in the north-western Urzulei Supramonte area. The association of facies F28 and F29 constitutes the Pedra Longa Fm. by Jadoul et al. (2009; 2010).

In the Urzulei Supramonte area, facies from F30 to F34 represent an association indicative of subtidal to supratidal inner platform environment (Fig. 6.17D), overlying the F18 intraclastic breccia attributed to karstic dissolution. This vertical trend suggests a reflooding of the platform top after the subaerial exposure marked by the F18 breccia. The compacted peloidal packstone-grainstone with fibrous cement (F30) was deposited and early cemented in a subtidal marine environment. This is suggested by the widespread fibrous marine calcite cement that lines pores, precipitated before compaction. In the laminated dolostone (F31) the replacive dolomitization prevents identification of the depositional facies. The rudstone to packstone with *Clypeina jurassica* (F32) was deposited in a subtidal shallow-water environment. The abundance of *Clypeina jurassica* associated with other dasyclad algae and molluscs suggests a shallow-marine, illuminated environment with normal-marine salinity (Elliot, 1991; Génot, 1991; Barattolo and Bigozzi, 1996; Sevillano et al., 2019). Dasyclad algae are common in warm waters with 3-5 m of water depth but could extend to 30 m of depth (Wray, 1977). They are typical in low-energy regimes, below wave base or in protected settings typical of lagoons (Wray, 1977). The packstone to rudstone with pisoids, oncoids, foraminifers and meniscus cement (F33) was deposited in supratidal environment. The abundance of pisoids and

micrite meniscus cement between grains suggests periods of subaerial exposure and vadose meteoric diagenesis. The bioturbated wackestone-mudstone with ostracods (F34) with dasyclad algae (*Clypeina jurassica* and *Campbelliella*) was deposited in a low-energy lagoonal environment.

The thin bed (10-20 cm) of facies F30 characterizes the lower boundary of phase 4 strata with facies F18 and marks the beginning of the transgression of phase 4 inner platform facies in the Urzulei Supramonte area. The early Tithonian age is suggested by the stratigraphic position and the skeletal biota association of facies from F32 to F34. The vertical succession of facies from F30 to F34 characterizes the Lower Mt. Bardia Fm. (Jadoul et al., 2009, 2010) in the Urzulei Supramonte area.

Facies from F35 to F37 are interpreted as deposited in a slope depositional environment as previously proposed by Lanfranchi et al. (2011), who described a carbonate slope with sigmoidal clinoforms 3° to 15° steep and nearly 70 m high in the Baunei Supramonte area (Fig. 6.4B, 6.11, 6.17D). The breccia with radiaxial fibrous calcite (F35) represents the accumulation of debris deriving from rock falls and avalanches coeval to boundstone growth cemented during early marine diagenesis (cf. Della Porta et al., 2004), probably an upper slope setting (Fig. 6.17D). Lithoclasts derived from reefs mainly composed by corals, calcareous sponges and *Crescentiella morronensis* (cf. Lanfranchi et al., 2011). The clast-supported and widespread presence of radiaxial fibrous calcite both in lithoclasts and lining pore spaces suggest early marine cementation both in the upper slope/platform margin boundstone and F35 breccias. Syn-depositional marine cement precipitation of radiaxial fibrous calcite occurs typically in the platform margin-upper slope facies (e.g., Russo et al., 2000) but could extend to the lower slope within the pore space of detrital deposits (e.g., Della Porta et al., 2004). In the lower part of the slope, breccias are associated with layers of grainstone and packstone, represented by the *Crescentiella* grainstone-packstone (F36) and the crinoidal peloidal packstone-wackestone (F37). The *Crescentiella* grainstone-packstone contains reef debris such as *Crescentiella morronensis*, chaetetids, corals, calcareous sponges and serpulids and shows marine cementation with prismatic and radiaxial calcite cement. The crinoidal peloidal packstone-wackestone (F37) was deposited in a lower energy environment, probably in the distal part of the lower slope to toe of slope, as demonstrated by the texture and abundance of peloids, bivalves and the benthic foraminifer *Lenticulina.*

The boundary between facies F35 breccias and the association of facies F28 and F29 represents the progradation of the carbonate platform margin/slope in the basin towards the SE.

The characters of facies F35 to F37 and the depositional architecture showing clinoforms (cf. Lanfranchi et al., 2011) demonstrate the development of steeper depositional angles with respect to the phase 1 and 2 from the proximal to the distal slope depositional environments, probably starting from the early Tithonian. The depositional profile evolved from a homoclinal carbonate ramp (phase

1 and 2) to a higher relief carbonate system with clinoforms (Lanfranchi et al., 2011). Facies from F35 to F37 in the Baunei Supramonte area were dated to the Late Tithonian by Lanfranchi et al. (2011) and this age fits well with the stratigraphic position. These facies characterize the Lower Mt. Bardia Fm. by Jadoul et al. (2009) in the Baunei Supramonte area (from Punnaci to Pedra Longa logs; Fig. 6.2, 6.11).

6.6 Discussion

6.6.1 Comparison with previous studies on eastern Sardinia carbonate succession

This study proposes a revision of the evolutionary phases of the eastern Middle-Upper Jurassic Sardinia carbonate system and their ages with respect to Jadoul et al. (2009, 2010). In the south-eastern study area of the Baunei Supramonte, phase 1 (Callovian-middle Oxfordian) comprises the Dorgali Fm. sedimentary cycle and the transgressive-regressive T-R I cycle by Jadoul et al. (2009, 2010). Jadoul et al. (2010) established the Dorgali Fm. as a lithostratigraphic unit consisting of dolomitized ooidal grainstone of Bathonian-Callovian age overlying the Hercynian basement and capped by a Fe-rich hardground surface, preceding the three Upper Jurassic T-R cycles (Fig. 3.3, Chapter 3). Nevertheless, in the studied area of the southern part of the Orosei Gulf, the replacive dolomitization affects portions of different facies belonging to the Dorgali, Mt. Tului and Baunei formations. Dolomitization is pervasive in the lower part of the succession at the contact with the Hercynian basement and its upper limit is an irregular diagenetic boundary affecting different stratigraphic levels (Fig. 6.2; cf. Chapter 5 and Chapter 8). Hence, the Callovian partially dolomitized ooidal grainstone succession was included in phase 1 representing the coated-grain dominated carbonate ramp. The end of phase 1, originally dated as early Kimmeridgian by Jadoul et al. (2009), is proposed to be middle Oxfordian in this study, in analogy with regional coral, stromatoporoid and calcareous and siliceous sponge reef diffusion in the Tethys realm (Cecca et al., 2005; Martin-Garin et al., 2010, 2012) due to the absence of biostratigraphic markers (Nembrini et al., 2021; Chapter 5). This age is confirmed by biostratigraphic nannoplankton and magnetostratigraphic analyses performed by Casellato et al. (2012) and Muttoni et al. (2018) in the northern basinal outcrops on the S'Adde Limestone (Fig. 3.3 and 3.4 in Chapter 3) suggesting low sedimentation rates for Callovian-Oxfordian times and higher sedimentation rates for the Kimmeridgian. This could be explained by the switch in carbonate factory between phase 1 and phase 2 with consequential increase in carbonate production and export into the northern basin.

Phase 2 partially corresponds to the T-R II cycle characterized by the change from an ooidal to a reefal carbonate factory. Indeed, T-R II cycle by Jadoul et al. (2009) comprises also the uppermost part of the Mt. Tului Fm. in the Baunei Supramonte area and the lower part of the Urzulei Fm., placed in phase 3 in this study (Fig. 3.3. in Chapter 3). The T-R II cycle was originally dated by Jadoul et al. (2009) to the late Kimmeridgian-early Tithonian. Biostratigraphic and strontium isotope data from this study indicate that phase 2 ended in the early part of the late Kimmeridgian; hence phase 2 was assigned to the late Oxfordian-late Kimmeridgian. The subaerial exposure at the top of phase 2 must have occurred in the late Kimmeridgian, as demonstrated by the presence of *Alveosepta jaccardi* in the overlying phase 3 peritidal facies and not in the early Tithonian as proposed by Jadoul et al. (2009, 2010; Fig. 3.3. in Chapter 3).

Phase 3 corresponds to the upper part of the T-R II cycle including the peritidal facies forming the Urzulei Fm. and the uppermost Upper Tului Fm. (*sensu* Jadoul et al., 2009). The original early Tithonian age proposed by Jadoul et al. (2009) for the Urzulei Fm. was revised in this study and assigned to the late Kimmeridgian on the basis of biostratigraphic (*Alveosepta jaccardi*) and strontium isotope data. Phase 4 corresponds to the third T-R III cycle by Jadoul et al. (2009), whose early-late Tithonian age is confirmed by the biostratigraphic data from this study.

6.6.2 Controls on the sedimentary evolution and global and regional controls

The sedimentary evolution of the Upper Jurassic carbonate succession of eastern Sardinia records the interplay between the changes in carbonate factory with development of build-ups, linked to local and global environmental and climatic conditions favouring reef biota, and changes in accommodation driven by eustasy and tectonic activity.

Phase 1 (Callovian-middle Oxfordian) was characterized by a non-skeletal coated grain dominated carbonate factory likely linked to the global late Callovian-early Oxfordian crisis in reef distribution and carbonate productivity (Cecca et al., 2005; Martin-Garin et al., 2010, 2012) related to a climate cooling period (Dromart et al., 2003). The development of reefal carbonate factories during phase 2 and phase 4 reflects the onset of optimal environmental conditions and increase in accommodation. As discussed in Chapter 5, reef distribution patterns in the northern Tethys indicate a spreading of reefal carbonate factories towards high latitudes (up to 35 °N) during middle Oxfordian and a subsequent shift towards lower latitudes during late Oxfordian (Cecca et al., 2005; Martin-Garin et al., 2012). This shift might have influenced the eastern Sardinia carbonate ramp located at latitude of about 20-25 °N (Muttoni et al., 2018), which was colonized by corals, stromatoporoids, calcareous

and siliceous sponges associated with microbialites at the beginning of phase 2 (late Oxfordian). The global pattern of reef distribution during middle Oxfordian to Kimmeridgian was probably influenced by climatic oscillations (Cecca et al., 2005; Martin-Garin et al., 2012). Nevertheless, there is no consensus in the published literature about the Late Jurassic climatic regimes. Martin-Garin et al. (2012) suggested a warming trend during the middle Oxfordian followed by a cooling trend from the late Oxfordian onward, whereas Dera et al. (2011, 2015) suggested a general warming trend from the middle Oxfordian through the Kimmeridgian. Therefore, although some studies propose that the distribution of reefal carbonate factories in the Tethys realm during middle Oxfordian-Kimmeridgian time was likely influenced by climate changes (Cecca et al., 2005; Martin-Garin et al., 2012), there might have been the co-occurrence of other driving factors besides climate (Kiessling, 2009; Dera et al., 2015).

Another important controlling factor on the development of build-ups is nutrient availability. Internal waves play an important role in carbonate systems by determining the flux of dissolved nutrients around the pycnocline depth, which is a zone of both high-nutrient concentration and internal-wave propagation (Pomar et al., 2012). Suspension-feeding metazoans (such as for phase 2 build-ups) would have preferentially formed reefs at the depth of pycnocline corresponding to middle to outer ramp settings (cf. Pomar et al., 2012; Alnazghah et al., 2013; Kiani Harchegani and Morsilli, 2019). Probably nutrient levels needed by coral-calcareous sponge-diceratid build-ups (type 2) and sponge-coral-microbialite build-ups (type 3) were provided in relative low-energy environments in the distal middle ramp and outer ramp by internal wave mechanisms.

A regional tectonic control on the evolution of the Middle-Upper Jurassic eastern Sardinia carbonate succession can be suggested due to similarities and differences with coeval carbonate systems that record the influence of syn-rift syn-sedimentary tectonics. In the central Iberian rift system, Aurell et al. (2019a) identified four Kimmeridgian-Tithonian sequences (Ki1, Ki2, Ki3, Ti1) in the carbonate succession. Sequence Ki1 (lower Kimmeridgian) and Ki2 (lower part of upper Kimmeridgian) are coeval to eastern Sardinia phase 2 and are characterized by diffused open marine carbonate facies. The Ki3 sequence (uppermost Kimmeridgian) records a shallowing upward trend with the progradation of shallow-water facies of the Higueruelas Fm. at the top of open marine carbonate facies (Aurell et al., 2019a; Sequero et al., 2019) and may correspond to eastern Sardinia phase 3 following the first subaerial exposure (Fig. 6.18). The subsequent switch-off of the phase 2 reefal carbonate factory in eastern Sardinia marks the transition to a carbonate factory dominated by coated grains, such as ooids and oncoids identified as reworked in deeper areas, and peritidal facies in the shallow areas (phase 3). In the central Iberian rift system, the top of Ki3 is marked by a major unconformity overlain by upper Valanginian-Hauterivian or lower Berriasian continental facies,

whereas only in one subbasin (Galve subbasin) there was the onset of a Tithonian marine sequence (Ti1) marked by a sharp increase in silicilastic input (Aurell et al., 2019a). The unconformity at the top of Ki3 likely corresponds to the second major subaerial exposure at the top of eastern Sardinia phase 3 (latest Kimmeridgian, Fig. 6.18). The general progradation and offlap starting from late Kimmeridgian (Ki2 and Ki3) in the central Iberian rift system have been related to the uplift of the northern and western marginal areas of the carbonate ramps because the Iberian plate was surrounded by divergent boundaries affected by extensional tectonics (Aurell et al., 2019b). Thus, the subaerial exposures at the top of phase 2 and phase 3 in eastern Sardinia, linked to the late Kimmeridgian Ki2 and Ki3 sequences in the central Iberian rift, might be related to the extensional tectonic activity affecting the European margin of the Alpine Tethys. Differently from eastern Sardinia, the Tithonian increase in extensional tectonics in the central Iberian rift system caused the interruption of carbonate sedimentation or the onset of siliciclastic input (Aurell et al., 2019b; Val et al., 2019). Instead, in eastern Sardinia, probably due to its palaeogeographic position nearer to the Alpine Tethys margin or due to tectonically driven increase in accommodation, there were the conditions for the flooding of the previously exposed platform top, the recovery of the reefal carbonate factory and the development of the Tithonian higher-relief carbonate platform (phase 4, Mt. Bardia Fm.). The debris flows associated with the accumulation of the lithoclastic breccia (F28, Pedra Longa Fm.) in the basin (F29) at the beginning of eastern Sardinia phase 4 were probably triggered by tectonic activity as well (Jadoul, 2018).

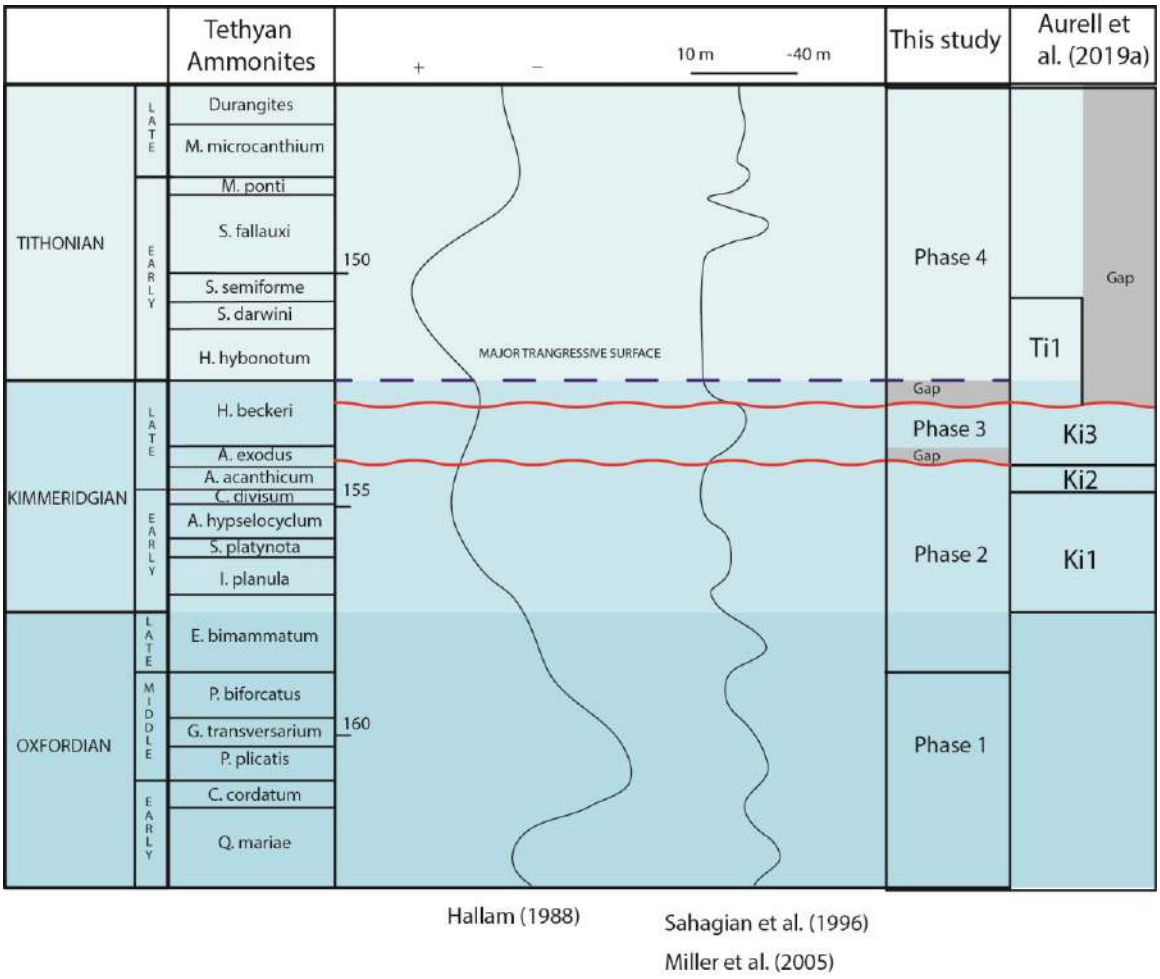

Figure 6.18 Comparison between the published eustatic sea-level curves by Hallam (1988) and Sahagian et al. (1996) and Miller et al. (2005), the depositional sequences proposed by Aurell et al. (2019a) in the Iberian Basin and the depositional phases of this study.

According to Jadoul (2018) there was a collapse of the platform margin controlled by Tithonian syn-sedimentary tectonics with reactivation of growth faults and syn-depositional flexuring. Tithonian carbonate breccias deposited by submarine debris flows mechanisms can be found also in the south-eastern France subalpine basin (northern part of the "Vocotian Through"; Courjault et al., 2011). In this area, debris flows were triggered by tectonic activity related to syn-sedimentary fault movements (Courjault et al., 2011). This tectonic influence fits well with the regional extensional tectonics recorded in coeval carbonate platforms in the central Iberian rift system during the Tithonian (Aurell et al., 2019b). The influence of these extensional movements is confirmed by the evidence of increased accommodation in the Tithonian strata of eastern Sardinia, documented by the up to 550 m thick Mt. Bardia Fm. deposited in 5-6 Myr (Jadoul, 2018). Extensional faulting could have favoured the creation of accommodation and a differential subsidence between the Urzulei Supramonte and Baunei Supramonte areas leading to the creation of a steeper slope (Lanfranchi et al., 2011) and the

consequential change in the depositional geometry from the phase 1 to 3 carbonate ramp into a higher relief platform.

Other Tethyan carbonate platforms recorded similar regional trends. In the northern Iberian range, due to tectonically-induced forced regression, Kimmeridgian reefal carbonates (Torrecilla reef complex) are separated from overlying Tithonian-Berriasian fluvial and lacustrine deposits by an unconformity (matching the subaerial exposure at the top of phase 3 in eastern Sardinia) marked by brecciation and karstification (Benito et al., 2001; Benito and Mas, 2006). In western France, the progradation of La Rochelle carbonate platform during the late Kimmeridgian has been associated with extensional tectonics by Carcel et al. (2010). In the Adriatic platform, some areas were uplifted due to syn-sedimentary tectonics in the late Kimmeridgian (Tišlar et al., 2002; Velić et al., 2002; Vlahović et al., 2005) and were capped by subaerial exposure surfaces with pronounced karstification (matching the subaerial exposure at the top of phase 3 in eastern Sardinia) overlain by Tithonian deposits with the dasyclad alga *Clypeina jurassica* (comparable to eastern Sardinia phase 4 inner platform subtidal facies). In the subsurface Apulia-Adriatic domain, available borehole cores and seismic reflection profiles indicate possible Late Jurassic faulting due to extensional tectonics by the reactivation of pre-existing faults (Santantonio et al., 2013).

However, eustatic sea-level fluctuations interfering with extensional tectonics might have played a role as well in the evolution of eastern Sardinia carbonate succession. The changes in accommodation available for the reef colonization of carbonate systems are connected to global sea-level fluctuations (Leinfelder et al., 2002). According to the published global sea-level curves (Hallam, 1988; Sahagian et al., 1996; Miller et al., 2005; Haq, 2018), a major sea-level rise started from the middle Oxfordian with the maximum transgression in the latest early Kimmeridgian at the boundary between the *A. hypselocyclum* and *C. divisum* ammonite biozones (Fig. 6.18). A sea-level fall characterized the beginning of the late Kimmeridgian starting from the *A. exodus* biozone followed by a sea-level rise at the end of late Kimmeridgian (*H. beckeri* biozone) according to Sahagian et al. (1996) and Miller et al. (2005) or during the early Tithonian according to Hallam (1988).

The eustatic sea-level rise starting from the middle Oxfordian is probably recorded in the eastern Sardinia carbonate succession and was likely responsible of the creation of accommodation for the development of the reefal carbonate factory of phase 2 on the shallow, high-energy coated grain dominated ramp of phase 1. The eustatic sea-level fall in the early late Kimmeridgian could correspond to the subaerial exposure at the top of phase 3 in combination with the extensional tectonics reported in the Iberian rift system. The sea-level rise of latest Kimmeridgian (Sahagian et al., 1996; Miller et al., 2005) or early Tithonian (Hallam, 1988) might correspond to the transgressive trend recorded at the base of phase 4 (early Tithonian) with development of basinal deposition (F28,

F29) and the establishment of renewed optimal environmental conditions for the development of the reefal carbonate factory of phase 4. The accommodation necessary for the development of phase 4 carbonate platform was likely created by the interplay of extensional tectonics at the margin of Alpine Tethys and the flooding driven by the eustatic rise (Fig. 6.18).

Another possible global control on Late Jurassic sedimentary successions that might have affected eastern Sardinia and coeval carbonate depositional system is linked to the Jurassic monster plate shift identified by Kent and Irving (2010). Several studies demonstrated that from the Oxfordian to Tithonian a 30° rotation of the continental plates about a pole centered in western Africa (Kent et al., 2015; Muttoni and Kent, 2019) caused the shift of regions such as Saudi Arabia, Northern Italy (Adria) and Central Iran from arid to humid climate belts or vice versa (Muttoni et al., 2013; Mattei et al., 2014; Muttoni and Kent, 2016; 2019). This latitudinal and climatic belt changes likely influenced carbonate platform sedimentation. Muttoni and Kent (2019) placed the Trento Plateu (NE Italy, Adria) during the Oxfordian in the humid climatic belt at 35°N of palaeolatitude. According to this palaeogeographic reconstruction, the European margin of the Alpine Tethys (Sardinia, France, Iberia) was few degrees north of the Adria plate in the humid climatic belt as well (Muttoni and Kent, 2019). During the Kimmeridgian and Tithonian, the Adria plate shifted southward to 20°N and the European margin of the Alpine Tethys reached the tropical arid climatic belt (Muttoni and Kent, 2019). This event may have been recorded in eastern Sardinia carbonate succession during phase 3 and 4 as suggested by facies characters identified in the Urzulei Supramonte area. The occurrence of wackestone-mudstone with ostracods and *Charophytes* (F21) in the lower part of phase 3 deposits suggests the presence of ponds in coastal wetlands, indicative of humid or at least semi-arid climatic conditions. Instead, the top of phase 3 facies is characterized by the occurrence of supratidal intraclastic breccia (F18) locally with clasts rich of gypsum pseudomorphs. The first deposit of phase 4 consist of laminated dolostone (F31) probably formed in arid evaporitic conditions, suggesting the climate change towards more arid climate at the end of the Kimmeridgian and in the early Tithonian, probably driven by the Late Jurassic plate motion.

The evolution of eastern Sardinia Middle-Upper Jurassic carbonate succession was the result of the interplay of plate motion, regional tectonics, carbonate factory changes related to environmental, climate and eustatic fluctuations. One of the controls was extensional tectonics affecting the European margin of the Alpine Tethys as demonstrated by coeval regional trends in similar carbonate systems, but the effects of colonization by reefal communities due to favourable environmental conditions (Chapter 5), climate changes and eustatic fluctuations are recorded as well in the carbonate succession as in coeval carbonate systems.

6.7 Conclusions

The sedimentological and stratigraphic investigation of the Callovian-Tithonian portion of the eastern Sardinia carbonate succession allowed the identification of 37 carbonate facies differently distributed in the study area and the recognition of 4 different depositional phases. Phase 1 (Callovian-middle Oxfordian) is characterized by a ramp with a carbonate factory dominated by ooids and other coated grains. Phase 2 (late Oxfordian-late Kimmeridgian) is characterized by a change in the dominant carbonate factory with the development of coral, stromatoporoid, calcareous and siliceous sponge and microbialite reefs. Phase 3 (late Kimmeridgian) followed a major subaerial exposure and is characterized by a peritidal succession in the inner platform and middle ramp deposits in the more distal areas with the development of a coated-grain dominated carbonate factory (mainly ooids and oncoids) and is capped by a subaerial exposure. Phase 4 (Tithonian) represents the onset of a different carbonate system in terms of facies and geometry following the early Tithonian transgression after a second major subaerial exposure at the top of phase 3 (latest Kimmeridgian). A higher-relief carbonate platform with tens of metres high slope clinoforms developed characterized by a renewed reefal carbonate factory.

Facies composition and architecture were influenced by the interplay of different factors such as regional tectonics, plate motion, the varying environmental condition favouring the growth of reef biota and changes in carbonate factories, Late Jurassic climate and global sea-level fluctuations. One of the major controls on the evolution of the eastern Sardinia carbonate systems was likely extensional tectonics affecting the European margin of the Alpine Tethys as demonstrated by similar trends in coeval platforms in the central Iberian rift system, in the North Iberian range and western France. However, eastern Sardinia sedimentary evolution was also influenced by the colonization by the reef community during Late Jurassic and global rises in sea-level during middle Oxfordian-early Kimmeridgian and in early Tithonian leading to optimal conditions for reef development (phase 2 and phase 4).

Chapter 7

Facies analysis of resedimented lithoclasts in the basinal Pedra Longa Fm.

7.1 Abstract

The determination of the composition of resedimented deposits in basinal successions is often of paramount importance to reconstruct the sedimentological features of their provenance environment. The clasts of the Tithonian lithoclastic breccia (facies F28) resedimented in basinal environment with mudstone, wackestone and siltstone (F29, Pedra Longa Fm., phase 4) by debris-flow processes were analysed in this study and 8 facies types were identified. Facies, labelled from FA to FD, are: bio-intraclastic grainstone with fibrous cement (FA), wackestone with *Clypeina jurassica* (FB), wackestone to floatstone with oncoids, *Cayeuxia*, foraminifers and dasyclad algae (FC), and peloidal-intraclastic packstone to grainstone (FD). These resedimented facies are indicative to have been originally deposited in an inner platform depositional environment. Facies from FE to FH originally formed different types of build-up in possible platform margin and upper slope settings. Coral-calcareous sponge-microbialite boundstone (FE) and *Bacinella* boundstone (FF) formed build-ups in well-illuminated shallow-water environments, whereas calcareous sponge-*Crescentiella*-coral boundstone and calcareous and siliceous sponge boundstone formed bioconstructions in deeper, possibly upper slope environments. The identified resedimented facies show similarities with the inner platform facies deposited during the Tithonian phase 4 (facies from F30 to F34, Mt. Bardia Fm.) and with Tithonian reef facies described in previous studies in different outcrops of the Mt. Bardia Fm. (Lanfranchi et al., 2011; Ricci et al., 2018). The resedimented clasts of the lithoclastic breccia (F28) record the recovery of the reefal carbonate factory during early Tithonian (phase 4).

7.2 Introduction

Deep-water basins adjacent to carbonate platforms and reefs are frequently filled by fine-grained carbonate mud with variable to absent amount of terrigenous clay. The fall-out basinal sedimentation may be occasionally interrupted by carbonate breccias and conglomerates made of clasts from shallower-water facies (Cook et al., 1972; Tucker and Wright, 1990; Flügel, 2004). These deposits

are relatively rapidly emplaced by debris-flow mechanisms with respect to the low sedimentation rates of the background fall-out deposition (Pray and Cook, 1968; Cook et al., 1972). The recognition and characterization of these resedimented deposits is significant because clast composition may suggest facies characters of adjacent shallow-water platforms, where a detailed statigraphical and sedimentological analysis is prevented due to scarce outcrop control. There are several studies on resedimented carbonate deposits, such as on the Devonian platform margins in Canada (Pray and Cook, 1968; Cook et al., 1972), the Devonian of the Canning Basin (W Australia, George et al., 1995), the Triassic of Yangtze Platform (China, Lehrmann et al., 2020), the Lower Jurassic of northern Calabria (Italy, Innamorati and Santantonio, 2018), the Upper Jurassic of south-eastern France (Courjault et al., 2011), the Lower Cretaceous of the Dinaric Platform (Slovenia, Kukoč et al., 2012), the Upper Cretaceous of the south-central Pyrenees (Spain, Drzewiecki and Simó, 2002), the Upper Cretaceous of the Apulian Platform (Italy and Albania, Santantonio et al., 2013; Hairabian et al., 2015; Morsilli et al., 2017; Le Goff et al., 2019), the Cretaceous of western Sicily (Italy, Randazzo et al., 2020) and Majella platform (Italy, Eberli et al., 2004), and the Eocene of Sinai (Egypt, Corlett et al., 2018).

In the eastern Sardinia Upper Jurassic carbonate succession, the lower Tithonian lithoclastic breccia beds (facies F28, phase 4; cf. Chapter 6) consist of resedimented material transported and deposited by debris-flow mechanisms in basinal environment (facies F29 mudstone, wackestone and siltstone; cf. Chapter 6). Lithoclast facies analysis may contribute to identify the clast provenance. either from coeval different depositional environments of the same carbonate systems (phase 4; cf. Chapter 6) or from facies deposited during previous depositinal phases (phase 2 or 3; cf. Chapter 5 and 6). Considering the limited outcrop control on some portions of the carbonate system, analysis of lithoclastic breccia composition helps revealing the characteristics of the primary depositional environments and may provide insights on the upper Oxfordian-upper Kimmeridgian (phase 2 and 3) or Tithonian (phase 4) facies composition and architecture.

7.3 Results

7.3.1 Clast facies analysis

The lithoclastic breccia (F28), described in Chapter 6 Table 6.1 and in Table 7.1, crops out exclusively in the Baunei Supramonte area (Figure 4.1 in Chapter 4), alternating with facies F29 mudstone, wackestone and siltstone (Fig. 7.1), overlying facies F15 peloidal packstone with oncoids and ooids (Mt. Tului Fm.) for a thickness variable from 0 to 25 m (Chapter 6). Facies F28 consists of a variety

in composition and size of carbonate lithoclasts and a wide range of silt, sand and cobble-sized coated grains and bioclasts floating in a micrite matrix (Fig. 7.2A). The analysis of carbonate lithoclasts allowed recognizing 9 different facies labelled from FA to FH (Table 7.1). For methodology description refer to Chapter 4, section 4.1.

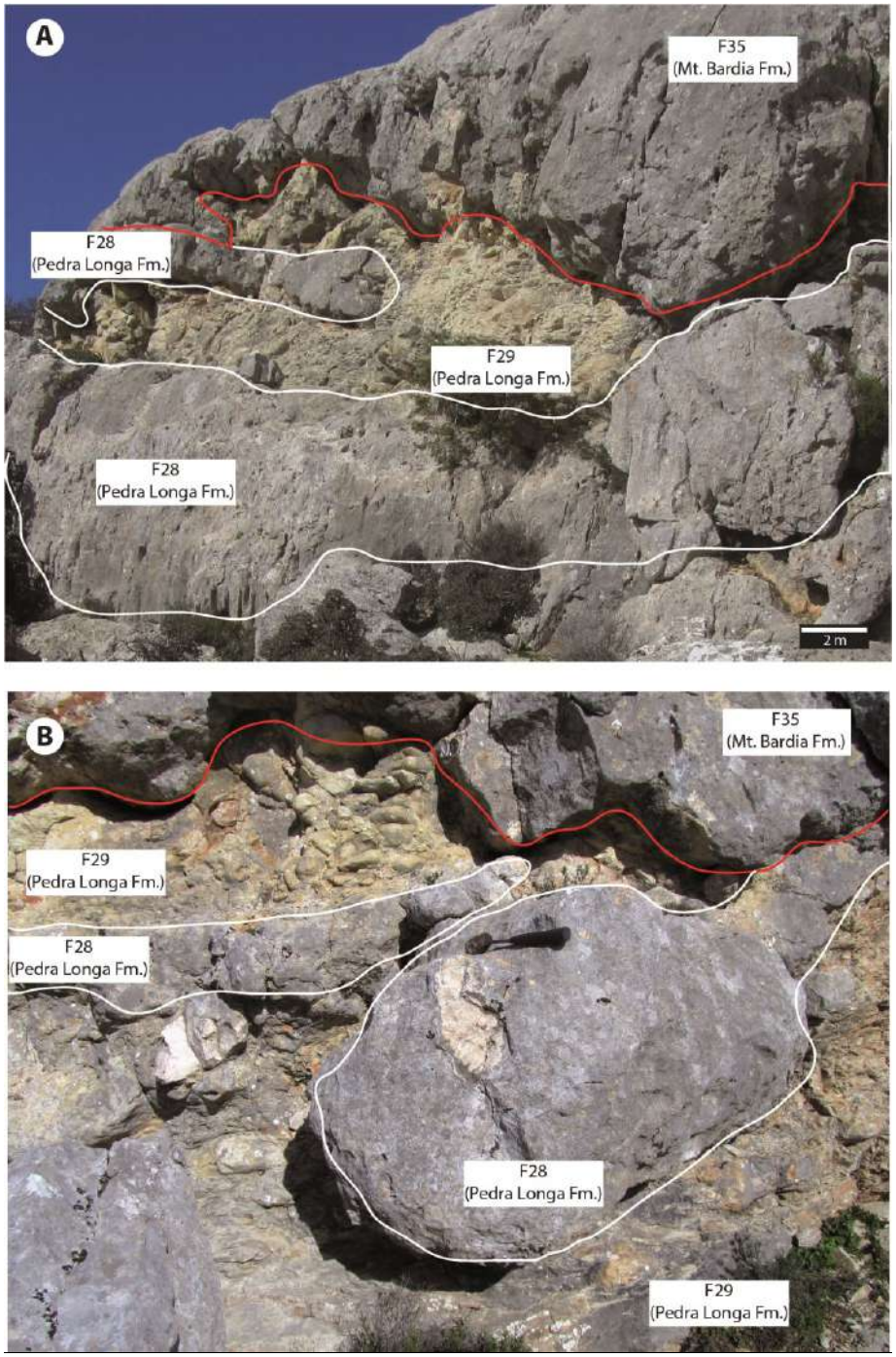

Figure 7.1 A) Outcrop photograph showing the lithoclastic breccia F28 alternating with mudstone, wackestone and siltstone F29 (Pedra Longa Fm.) overlain by the breccia with radiaxial fibrous calcite (F35, Mt. Bardia Fm.) with an erosional boundary (red line). B) Outcrop photograph showing lithoclastic breccia (F28) lenses within mudstone, wackestone and siltstone (F29, Pedra Longa Fm.) overlain by breccia with radiaxial fibrous calcite, (F35, Mt. Bardia Fm.) with an erosional boundary (red line).

Facies FA is a bio-intraclastic grainstone with fibrous cement. The main components are high diversity benthic foraminifers, dasyclad algae (*Salpingoporella annulata*) and intraclasts made of micrite or peloidal packstone (Fig. 7.2B). It is characterized by the abundance of isopachous fibrous cement that forms a rim around grains (40 μm thick), whereas the remaining interparticle porosity is filled by equant blocky calcite cement (Fig. 7.2C).

Facies FB is a wackestone with the dasyclad alga *Clypeina jurassica* (Fig. 7.2D). Facies FC is a wackestone to floatstone with oncoids with bioclastic and intraclastic nuclei (type I and II), *Cayeuxia*, foraminifers, dasyclad algae, *Crescentiella morronensis* fragments and bivalves (Fig. 7.2E).

Facies FD consists of a peloidal-intraclastic packstone to grainstone including, besides peloids, micritic intraclasts and coated grains with micrite envelopes associated with skeletal fragments such as *Crescentiella morronensis,* bivalves, benthic foraminifers, crinoids, brachiopods and dasyclad algae (Fig. 7.2F).

Facies FE consists of a coral-calcareous sponge-microbialite boundstone and is characterized by colonial corals (mainly phaceloid and thamnasterioid, Fig. 7.2G), a framework of clotted peloidal micrite, calcareous sponges (*Calcistella jachenhausenensis*) and stromatoporoids associated with siliceous sponges, solenoporaceans and microencrusters (*Bacinella irregularis, Lithocodium aggregatum, Thaumatoporella parvovesiculifera* and *Koskinobulina socialis*).

Facies FF is a *Bacinella* boundstone made of a framework of *Bacinella irregularis* (Fig. 7.2H). This facies is often characterized by dissolution cavities filled by equant blocky calcite cement.

Facies FG is a calcareous sponge-*Crescentiella*-coral boundstone consisting of calcareous sponges (mainly *Calcistella jachenhausenensis* and *Neuropora lusitanica,* Fig. 7.3A) and locally densely packed *Crescentiella morronensis* and *Terebella lapilloides* (Fig. 7.3B-C), associated with colonial corals (Fig. 7.3D), serpulids and microencrusters (*Koskinobulina socialis*). Microbialites consist of clotted fine peloidal fabrics between the *Crescentiella* colonies. Facies FH is a calcareous-siliceous sponge boundstone (Fig. 7.3E-F).

The carbonate lithoclasts represented by facies from FA to FH are associated with coated grains and bioclasts floating in the micrite matrix. The bioclastic content includes crinoids, bivalves, echinoid spines, corals, calcareous sponges (*Neuropora lusitanica, Calcistella jachenhausenensis*), siliceous sponges, serpulids, various benthic foraminifers, microencrusters (*Bacinella irregularis, Lithocodium aggregatum, Koskinobulina socialis, Radiomura cautica*), brachiopods and dasyclad algae (*Salpingoporella annulata, Clypeina jurassica*). The matrix surrounding the lithoclasts consists of facies F29 mudstone, wackestone and siltstone that reepresents the background basinal sedimentation.

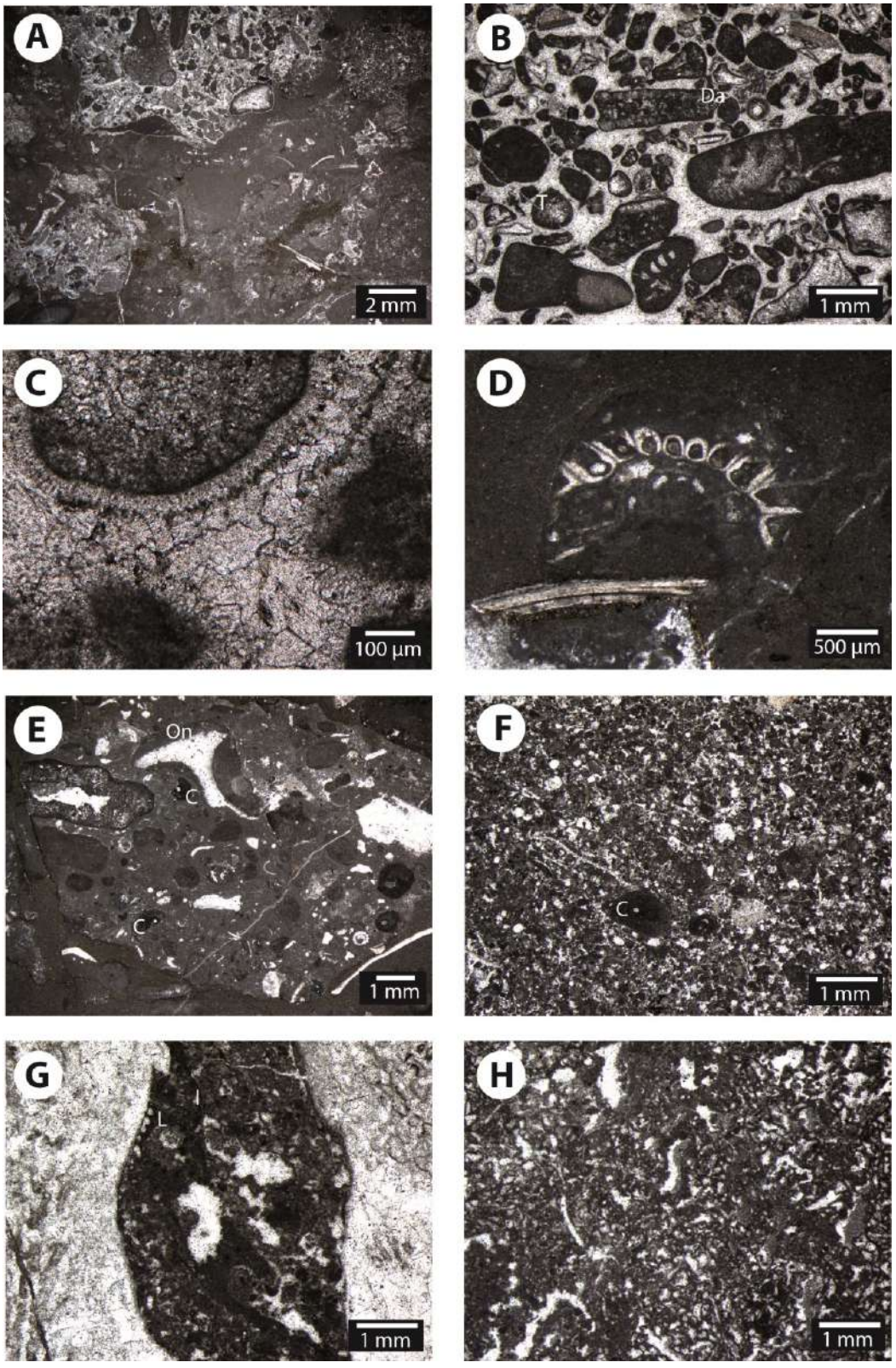

Figure 7.2 A) Photomicrograph of F28 lithoclastic breccia with clasts made of bio-intraclastic grainstone with fibrous cement (FA). B) Lithoclast of facies FA showing a grainstone with dasyclad algae (Da), benthic foraminifers (*Trocholina*; T) and micritic intraclasts. C) Photomicrograph of facies FA lithoclast showing isopachous fibrous calcite cement around grains and equant blocky calcite cement in interparticle porosity. D) Lithoclasts of facies FB showing a wackestone with *Clypeina jurassica.* E) Facies FC lithoclast represented by a wackestone with type II oncoids (On), micritic intraclasts and *Crescentiella morronensis* (C) fragments. F) Photomicrograph of facies FD showing a peloidal packstone with *Crescentiella morronensis* fragments (C). G) Facies FE boundstone with phaceloid coral colonies encrusted by *Lithocodium aggregatum* (L) and clotted peloidal micrite. H) Facies FF boundstone with *Bacinella irregularis*.

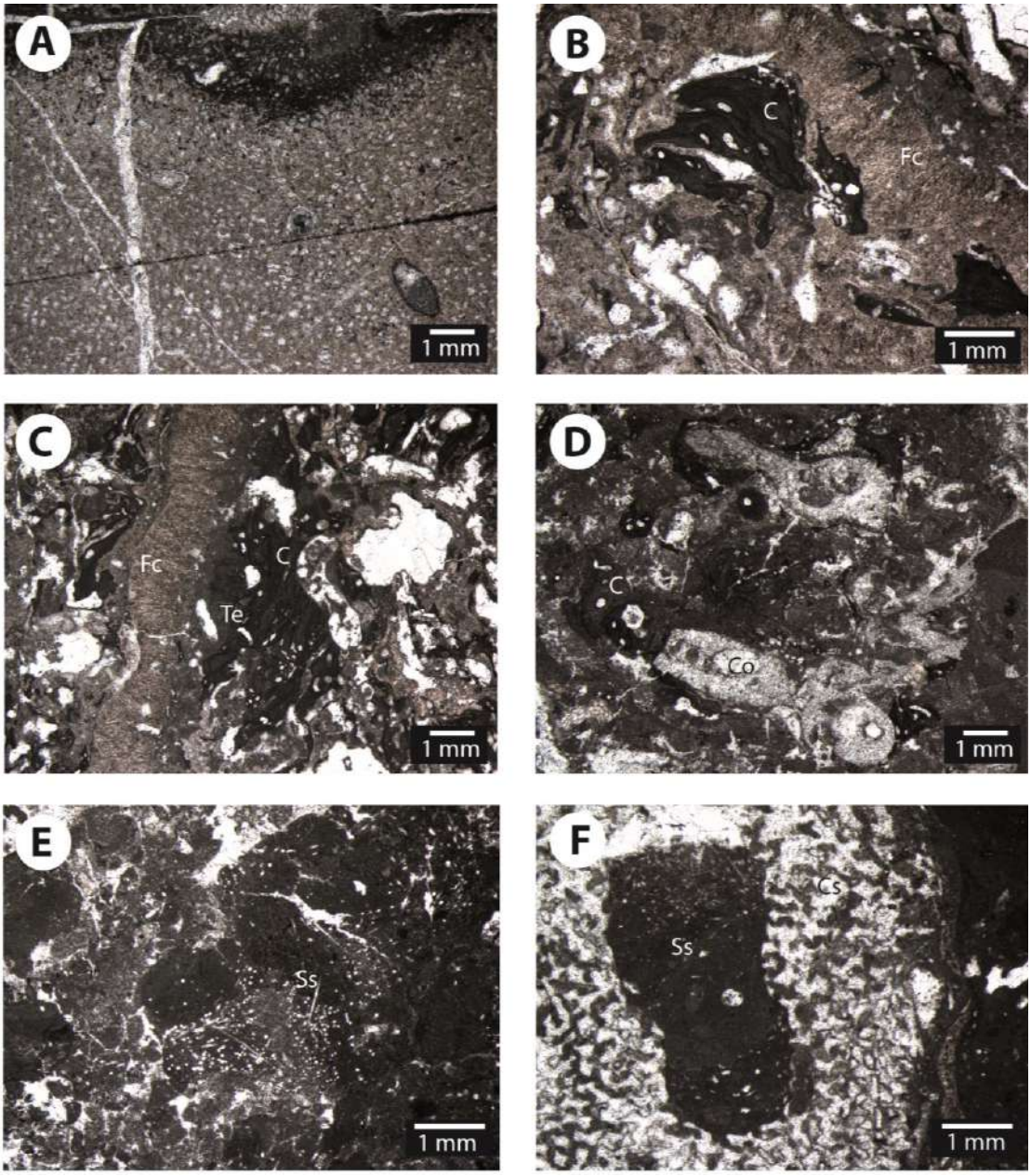

Figure 7.3 A) Photomicrograph of facies FG showing a boundstone with an undetermined calcareous sponge. B) Facies FG boundstone with *Crescentiella morronensis* (C) and fibrous calcite cement (Fc). C) Lithoclast of facies FG showing a boundstone with *Crescentiella morronensis* (C), *Terebella lapilloides* (Te) and fibrous calcite cement (Fc). D) Facies FG boundstone with corals (Co) and *Crescentiella morronensis* (C). E) Facies FH siliceous sponge (Ss) boundstone. F) Facies FH showing a boundstone with an undetermined calcareous sponge (Cs) and a siliceous sponge (Ss).

Facies type	*Grain size and sorting*	*Sedimentary and diagenetic features*	*Skeletal grains*	*Non skeletal grains*	*Depositional environment*
FA-Bio-intraclastic grainstone with fibrous cement	Well-sorted, grain size mainly from 0.1 mm to 0.5 mm (rarely fragments up to 1 cm)	Isopachous fibrous cement (40 µm) precipitated around grains and in intraparticle porosity before compaction. Syntaxial cement around echinoderms, whereas the interparticle and intraparticle porosity is filled by equant blocky calcite cement (300-400 µm) and poikilotopic cement. Evidence of dissolution, mouldic porosity filled by calcite microsparite and equant blocky calcite cement.	Benthic foraminifers (*Everticyclammina, Trocholina, Labyrinthina mirabilis, Nautiloculina oolithica, Mohlerina basiliensis, Pseudocyclammina,* miliolids, textularids), Dasyclad algae (*Salpingoporella annulata*), gastropods, microencruster fragments (*Bacinella irregularis, Crescentiella morronensis)* calcareous sponges, echinoid spines, crinoids and bivalves	Intraclasts (micritic or peloidal packstone), oncoids	High-energy, inner platfrom
FB-Wackestone with Clypeina jurassica	Moderately sorted, grain size from 0.1 to 2 mm	Locally dissolution vugs filled by equant blocky calcite cement.	*Clypeina jurassica*	-	Well-illuminated, low-energy inner platform
FC-Wackestone to floatstone with oncoids, Cayeuxia, foraminifers, and dasyclads	Moderately to poorly sorted, grain size from 0.1 to 4 mm-	Abundant micrite between grains	*Cayeuxia*, benthic foraminifers (*Everticyclammina*), dasyclad algae, *Cresecentiella* fragments, bivalves	Type I and type II oncoids with bioclastic and intraclastic nuclei, micritic intraclasts	Low-energy, inner platform
FD-Peloidal-intraclastic packstone to grainstone	Well-sorted, grain size from 0.01 to 1 mm	Compaction, concavo-convex grain contacts, locally equant blocky calcite cement filling pores, syntaxial cement around echinoderms. Dissolution cavities filled by geopetal micritic sediment followed by equant blocky calcite cement.	*Crescentiella* fragments, bivalves, benthic foraminifers (textularids, miliolids, trocholina, everticyclammina), crinoids, brachiopods, dasyclad algae, calcisphere, sponge spicules, calcareous sponges (*Neuropora lusitanica*)	Peloids, micritic intralcasts, coated grains with micrite envelopes	Inner platform
FE-Coral-calcareous sponge microbialite boundstone	Grain size from 0.1 mm to 2 cm	Borings, dissolution of corals filled by equant blocky calcite cement.	Colonial corals (phaceloid, thamnasterioid), clotted peloidal micrite, calcareous sponges (*Neuropora lusitanica Calcistella jachenhausenensis*), stromatoporoids, solenoporaceans, *Bacinella irregularis*, *Lithocodium aggregatum, Thaumatoporella parvovesiculifera*, *Koskinobulina socialis*, bivalves, *Troglotella incrustans*, echinoid spines, serpulids, dasyclad algae, brachiopods	Peloids, micritic intraclasts	Well-lit, shallow possible platform margin
FF-Bacinella boundstone		Fenestrae filled by geopetal micritic sediment and equant blocky calcite cement.	*Bacinella irregularis*	-	Well-lit shallow possible platform margin
FG-Calcareous sponge-Crescentiella-coral boundstone	Grain size from 0.1 mm to 1.5 cm	Yellowish fibrous cement. Dissolution of corals filled by microsparite followed by a mosaic of equant blocky calcite cement.	Calcareous sponges (*Calcistella jachenhausenensis, Neuropora lusitanica*), *Crescentiella morronensis*, *Terebella lapilloides*, colonial corals, serpulids, *Koskinobulina socialis, Troglotella incrustans*, clotted peloidal micrite	Peloids, micritic intraclasts	High-energy upper slope
FH-Calcareous-siliceous sponge boundstone	Grain size from 0.1 mm to 2 cm	Geopetal infillings, dissolution of corals filled by equant blocky calcite cement	Undetermined calcareous sponges, siliceous sponges, crustaceans, solitary corals, *Koskinobulina socialis*	Peloids, micritic intralcasts	Slope, below storm wave base

Table 7.1 Facies character description of the lower Tithonian breccia lithoclasts (F28)

7.4 Interpretation

7.4.1 Facies character and inferred depositional environments of breccia lithoclasts

The lack of outcrop control prevents a precise reconstruction of facies distribution and depositional geometry of the portions of the carbonate platform characterized by the reworked facies from FA to FH. However, facies characters of the resedimented clasts suggest deposition in an inner platform setting and in a possible platform margin and upper slope environment.

The bio-intraclastic grainstone with fibrous cement (FA) is interpreted as deposited in a high-energy subtidal environment as demonstrated by the widespread isopachous fibrous calcite cement lining pores of early marine diagenesis. The abundance of dasyclad algae (*Salpingoporella annulata*) suggests reworking from a low-energy well-lit protected, shallow-water environment with normal marine saline (Wray, 1977; Barattolo and Bigozzi, 1996). The wackestone with *Clypeina jurassica* (FB) was deposited in a shallow water, low-energy lagoonal environment. The abundance of the dasyclad alga *Clypeina jurassica* suggests a well-lit environment with normal-marine salinity (Barattolo and Bigozzi, 1996; Sevillano et al., 2019). The wackestone to floatstone with oncoids, *Cayeuxia*, foraminifers, and dasyclads (FC) was deposited in a relatively shallow, subtidal environment. The occurrence of *Cayeuxia*, dasyclad algae and type I and II oncoids is indicative of shallow inner platform, open marine environment (Reolid et al., 2007). The peloidal-intraclastic packstone to grainstone (FD) was deposited in a subtidal high-energy environment, as suggested by the texture and the presence of the benthic foraminifer *Trocholina*. The abundance of dasyclad algae suggests reworking from shallower water settings. The presence of crinoids and the diverse benthic foraminifer fauna suggest open-marine conditions. *Crescentiella morronensis* fragments suggest reworking from near bioconstructions, probably made of calcareous sponge-*Crescentiella*-coral boundstone (FG). The coral-calcareous sponge-microbialite boundstone (FE) derived from bioconstructions developed in shallow waters within the photic zone as suggested by the widespread presence of *Bacinella irregularis* and *Lithocodium aggregatum* (Dupraz and Strasser, 1999). The *Bacinella* boundstone (FF) consists of a framework almost totally made of *Bacinella irregularis*. The *Bacinella-Lithocodium* association is interpreted to occur in well-oxygenated, shallow-water environments and normal marine salinity (Dupraz and Strasser, 1999; Pittet et al., 2002). The clasts belonging to this facies could be fragments of the bioconstructions formed by the coral-calcareous sponge-microbialite boundstone (FE) or *Bacinella irregularis* could form bioconstructions itself in shallow-water environments (cf. Pittet et al., 2002; Schlagintweit and Gawlick, 2008). The calcareous

sponge-*Crescentiella*-coral boundstone (FG) probably derived from bioconstructions developed in deeper, possible upper-slope environment. The abundance of *Crescentiella morronensis* and *Terebella lapilloides* and the lack of typical shallow-water *microproblematica* (*Lithocodium-Bacinella-Thaumatoporella*) suggest several metres of water depth (Schlagintweit and Gawlick, 2008; Krajewski and Schlagintweit, 2018). In particular, *Terebella lapilloides* (typically associated with *Crescentiella morronensis*) exhibits a wide spatial distribution on carbonate platforms, spanning from outer platform to slope to middle-outer ramp settings (Della Porta et al., 2013; Kaya and Altiner, 2014 and references therein). The occurrence of fibrous syn-depositional marine cement suggests that these bioconstructions formed in high-energy environments, where pumping of seawater through the sediment was favoured by interconnected vugs (Krajewski and Schlagintweit, 2018). The calcareous sponge *Neuropora lusitanica* preferred cryptic habitats (Fürsich and Werner, 1991; Schlagintweit and Gawlick, 2008; Krajewski and Schlagintweit, 2018) and formed upper-slope bioconstructions in association with *Crescentiella morronensis* and microbialites (cf. Crimea, Krajewski and Schlagintweit, 2018). The calcareous-siliceous sponge boundstone (FH) probably derived from build-ups formed in relatively deep-water environments as demonstrated by the presence of siliceous sponges. During the Jurassic, siliceous sponge mounds developed in deep shelves, middle to outer ramps or deep slopes below the storm wave base (Pittet and Mattioli, 2002; Bartolini et al., 2003; Olivier et al., 2004b; Della Porta et al., 2013).

7.5 Discussion

7.5.1 Comparison of lithoclast facies with Oxfordian-Kimmeridgian (phase 2) and Tithonian (phase 4) facies

In order to reconstruct the origin of the carbonate lithoclasts of the lower Tithonian F28 lithoclastic breccia a comparison between their composition and the composition of phase 2 and phase 4 facies was necessary. In particular, the comparison with the composition of the upper Oxfordian-upper Kimmeridgian (Mt. Tului Fm., Chapter 5) and Tithonian reefs (Mt. Bardia Fm., Lanfranchi et al., 2011; Ricci et al., 2018) provides valuable insights.

The composition of Tithonian reefs (phase 4, Mt. Bardia Fm.) was analysed in the study by Ricci et al. (2018). Two types of microencruster associations were distinguished forming two different microframeworks: 1) poorly diversified association with *Crescentiella morronensis, Labes atramentosa, Terebrella lapilloides* (MFK1); 2) complex multi-layered crusts with *Bacinella*

irregularis, Lithocodium aggregatum, Thaumatoporella parvovesiculifera, Koskinobulina socialis, and *Calcistella jachenhausenensis* (MFK2). The MFK1 was found in association with colonial, solitary corals and calcareous sponges (Ricci et al., 2018) and corresponds to the resedimented facies labelled in this study as calcareous sponge-*Crescentiella*-coral boundstone (FG). Instead, the MFK2 is associated with corals and stromatoporoids (Ricci et al., 2018) and has been observed in the resedimented facies labelled as coral-calcareous sponge-microbialite boundstone (FE) in this study. In the build-up types described in Chapter 5 (phase 2; late Oxfordian-late Kimmeridgian) the microencruster association *Crescentiella morronensis, Labes atramentosa, Terebrella lapilloides* (MFK1) is absent and there is only sparse occurrence of *Crescentiella morronensis* in type 3 build-up (facies F8, F12). Moreover, the microencruster *Koskinobulina socialis* and the calcareous sponge *Calcistella jachenhausenensis,* widespread in the Tithonian reefs (Mt. Bardia Fm., Ricci et al., 2018) and in clasts of the lithoclastic breccia (F28), are absent in the upper Oxfordian-upper Kimmeridgian reefs of phase 2 (F8-F12). Ricci et al. (2018) described boundstone facies with a microframework consisting of abundant *Bacinella irregularis* associated with *Lithocodium aggregatum* such as the resedimented facies labelled here as *Bacinella* boundstone (FF).

The dasyclad alga *Clypeina jurassica* was found only in facies from phase 4 (cf. Chapter 6), such as rudstone to packstone with *Clypeina jurassica* (F32), packstone to rudstone with pisoids, oncoids, foraminifers and meniscus cement (F33) and bioturbated wackestone-mudstone with ostracods (F34) and the wackestone with *Clypeina jurassica* (FB) widespread in F28 (Pedra Longa Fm.) clasts. As a result, the composition of the resedimented carbonate lithoclasts of the F28 lithoclastic breccia and the stratigraphic position suggest their provenience from the Tithonian carbonate platform (phase 4, Mt. Bardia Fm.) during an active extensional tectonic phase (cf. Chapter 6). In contrast, the hypothesis of an origin from the erosion of reefal facies deposited during phase 2 (F8-F12, upper Oxfordian-upper Kimmeridgian, Mt. Tului Fm.) can be excluded.

Facies from FE to FH suggest the recovery of the reefal carbonate factory after the second Kimmeridgian subaerial exposure at the top of phase 3 (cf. Chapter 6) and probably the calcareous sponge-*Crescentiella*-coral boundstone (FG) flourished in the initial stage of platform recovery (cf. Crimea, Krajewski and Schlagintweit, 2018).

7.5.2 Comparison with coeval similar depositional facies

The absence of outcrop control prevents the reconstruction of a precise depositional model for the possible margin/upper slope environment during the Tithonian phase 4. However, in published

literature (cf. Chapter 2 literature review), it is possible to find case studies with similar facies composition in which facies distribution and the depositional architecture of the platform were investigated in preserved outcrops. In the Northern Calcareous Alps (Austria), from late Kimmeridgian to Berriasian the Plassen carbonate platform developed with platform margin occupied by *Bacinella* boundstone and coral-stromatoporoid rudstone and the upper slope characterized by cement crust-microencruster boundstone (Schlagintweit and Gawlick, 2008). The facies characters of the *Bacinella* boundstone and the coral-stromatoporoid rudstone are similar to the *Bacinella* boundstone (FF) and coral-calcareous sponge microbialite boundstone (FE) of the Pedra Longa Fm. breccia lithoclasts. Instead, the cement crust-microencruster boundstone are dominated by syn-depositional marine cement and include the association of *Crescentiella morronensis* and *Terebella lapilloides*, similar to the calcareous sponge-*Crescentiella*-coral boundstone (FG). In the upper Kimmeridgian-Tithonian of the Jalta platform (Crimea) the calcareous sponge *Neuropora lusitanica* and the microencruster *Crescentiella morronensis* in association with syn-depositional cement formed biocostructions, with similar composition to facies FG, in the upper slope environment and constituted a transitional facies zone between typical slope facies and margin facies characterized by high diversity of calcareous sponges, corals and microencrusters (Krajewski and Schlagintweit, 2018). In the Jalta platform, most of the facies rich in *Neuropora lusitanica* and *Crescentiella morronensis* developed in the initial phase of the cycle of restoration and blooming of reefs in late Kimmeridgian-early Tithonian. Similarly, in the eastern Sardinia carbonate system, the calcareous sponge-*Crescentiella*-coral boundstone (FG) could represent the dominant build-up facies during the initial stage of phase 4 corresponding to the recovery of the reefal carbonate factory (early Tithonian) after the subaerial exposure at the top of phase 3 and the initial transgression of phase 4 represented by the basinal facies F28 and F29. This is also demonstrated by the abundance of *Crescentiella morronensis* fragments in the matrix of the lithoclastic breccia (F28). Facies FG could colonize the upper part of the slope as well and form a transitional facies zone between the slope facies (F35 to F37) and the *Bacinella* boundstone (FF) and the coral-calcareous sponge microbialite boundstone (FE) that were deposited in shallower domains of the Tithonian platform (phase 4). In the Štamberk carbonate platform (Czech Republic) two types of boundstone facies developed. The first type is similar to facies FF and FE dominated by the *Bacinella-Lithocodium* association and phaceloid corals and was deposited in well-illuminated low-energy environments of the inner platform (Hoffman et al., 2017). The second type shows a similar composition to facies FG, rich in *Crescentiella morronensis* and marine fibrous cement and was deposited in high-energy upper slope environment (Hoffman et al., 2017).

7.6 Conclusions

Facies analysis of resedimented lithoclasts from breccia beds (F28) within the Pedra Longa Fm., belonging to the Tithonian phase 4, allow the recognition of 8 resedimented facies (FA to FH). FA to FD were deposited in an inner platform subtidal environment, whereas FE to FH formed different types of build-ups in different environmental settings. Coral-calcareous sponge microbialite boundstone (FE) and *Bacinella* boundstone (FF) were deposited in well-illuminated shallow-water environment in a possible platform margin setting. The calcareous sponge-*Crescentiella*-coral boundstone (FG) probably formed build-ups in a high-energy upper slope environment, whereas the calcareous-siliceous sponge boundstone (FH) characterized deeper slope environments. The facies of lithoclasts within the debris-flow breccia beds of the Pedra Longa Fm. show similarities with platform interior facies deposited during the Tithonian phase 4 described in Chapter 6 (F30 to F34) and with Tithonian reef facies described in other outcrop areas (Cala Gonone) by Ricci et al. (2018). Thus, the facies of the lithoclasts of Pedra Longa Fm. were resedimented from inner platform, possible platform margin and slope of the progradational Tithonian carbonate platform (phase 4, Mt. Bardia Fm.) during events of instability probably triggered by tectonic activity (cf. Jadoul, 2018).

Chapter 8

Diagenetic features and stable isotope geochemical signature

8.1 Abstract

Petrographic, cathodoluminescence (CL) and carbon and oxygen stable isotope analyses allowed reconstructing the diagenetic history of eastern Sardinia Callovian-Tithonian carbonate succession and proposing a paragenetic sequence for each depositional phase.

Facies from F1 to F4 (phase 1, Dorgali, Lower Mt. Tului and Lower Bauunei formations) were affected by mechanical compaction, dissolution and fracturing during burial diagenesis. This portion of the succession was affected by replacive burial dolomitization close to the Hercynian basement that totally or partially overprinted facies characters (DOL-1 and DOL-2). Dolomite crystals show a zoned pattern in CL and isotopic signatures with $\delta^{13}C$ between 0.1 ‰ and 3.0 ‰ and $\delta^{18}O$ between -1.0 ‰ and 1.2 ‰. Blocky equant calcite and microsparite cement precipitated in burial environment and partially in telogenetic meteoric environment. Dedolomitization affected locally phase 1 dolomitized facies (Mt. Oro log) modifying the CL response and isotopic signal of dolomite (depleted in both ^{13}C and ^{18}O).

In phase 2 facies (from F5 to F13, Upper Mt. Tului and Baunei formations) isopachous fibrous marine cement precipitated during early marine diagenesis whereas dissolution, mechanical compaction and fracturing took place in burial environment. Blocky equant calcite cement and microsparite precipitated in burial environment and possibly during meteoric telogenesis. Burial dolomitization by DOL-1 and DOL-2 replaced phase 2 facies only locally in the lower part of the succession.

In middle ramp facies F14 and F15 (phase 3, uppermost Mt. Tului Fm.) early marine cementation is represented by isopachous fibrous calcite cement, whereas in the inner platform facies (from F16 to F27) micrite meniscus and pendant cement precipitated during early meteoric diagenesis. The intraclastic breccia (F18) in the upper part of the succession of facies from F16 to F27 (Urzulei Fm.) is affected by early dolomitization possibly due to evaporitic fluids (DOL-3, DOL-4, DOL-5) based on the dolomite isotopic signature with values of $\delta^{13}C$ between 1.9 ‰ and 3.0 ‰ and $\delta^{18}O$ between 0.7 ‰ and 3.6 ‰. Equant blocky calcite, fine-grained equant calcite and microsparite cement precipitated in burial and meteoric environment and during meteoric telogenesis. Isotopic signature

of phase 3 is locally depleted in ^{18}O, especially near the subaerial exposure surfaces enclosing phase 3 facies at the bottom and the top.

Phase 4 inner platform facies (F32 and F33, Mt. Bardia Fm.) were early cemented by isopachous fibrous cement in marine phreatic environment, whereas supratidal facies F33 is characterized by micritic meniscus cement precipitated in meteoric vadose environment. Dolomitization due to evaporitic brines (DOL-3, DOL-4, DOL-5) affected the lower portions of phase 4 succession close to the subaerial exposure boundary such as in the underlying phase 3 facies. Equant blocky calcite cement and microsparite precipitated in burial and meteoric telogenetic environment.

Carbon and oxygen stable isotope values for the analysed samples mostly do not match with the Late Jurassic pristine marine values proposed in published literature, with the exception of few portions of the stratigraphic logs. In particular, the isotopic signature of cemented grain-supported grainstone and boundstone appears to be reset by meteoric and burial diagenesis. Wackestone, mudstone and floatstone textures may more frequently preserve marine original values, whereas the isotopic signatures of only some facies with packstone texture were clearly reset by burial or meteoric diagenesis.

8.2 Introduction

Carbon and oxygen stable isotopes composition of ancient shallow-water marine carbonates are strongly influenced by several factors, related to the chemical composition of shallow seawater (e.g. changes in salinity, evaporation, carbon transfer; Patterson and Walter, 1994; Immenhauser et al., 2003; Zuo et al., 2019), the vital effects of different marine organisms (McConnaughey, 1989; Nelson and Smith, 1996; Swart, 2015) and post-depositional diagenetic processes (Lohmann, 1988; Moore, 1989; Immenhauser et al., 2002; Lavastre et al., 2011; Huck et al., 2017). For these reasons it is challenging to reconstruct the original marine isotopic signature of marine shallow-water carbonates for stratigraphic, palaeoceanographic and palaeoclimatic reconstructions.

The effect of burial or meteoric diagenesis on $\delta^{13}C$ and $\delta^{18}O$ values of marine carbonates has been reported by several authors (Hudson, 1977; Lohmann, 1988; Immenhauser et al., 2002, 2003; Lavastre et al., 2011; Swart, 2015; Bahamonde et al., 2017). Diagenetic alteration generally causes a decrease in $\delta^{18}O$ values due to the interaction with high-temperature burial fluids or ^{18}O-depleted meteoric waters (Hudson, 1977; Allan and Matthews, 1982; Moore, 1989; Lohmann, 1988; Immenhauser et al., 2003; van der Kooij et al., 2009). Furthermore, negative $\delta^{13}C$ values are often the consequence of rock interaction with meteoric water rich in ^{12}C deriving from organic matter from soil alteration (Hudson, 1977; Allan and Matthews, 1982; Lohmann, 1988; Patterson and Walter,

1994; Immenhauser et al., 2003; Lavastre et al., 2011; Swart, 2015; Chesnel et al., 2016; Bahamonde et al., 2017). Facies characters influence the magnitude of diagenetic alteration, particularly texture and grain-size. Coarser sediment and grain-supported textures are characterized by higher degree of primary porosity and permeability facilitating the infiltration of diagenetic fluids (Marshall, 1992; Immenhauser et al., 2002; Vincent et al., 2004).

Dolomite formation is largely a replacive processes that in some cases may overprint facies texture and the original oxygen and carbon isotopic signature of carbonate rocks (Machel and Anderson, 1989; Machel and Burton, 1994; Reinhold, 1998; Warren, 2000). The formation of dolomite is still a controversial subject and numerous dolomitization models have been proposed (e.g., reflux, sabkha, mixing zone, burial, hydrothermal, seawater, microbial; Adams and Rhodes, 1960; Butler, 1969; Mattes and Mountjoy, 1980; Saller, 1984; Simms, 1984; Ward and Halley, 1985; Machel and Burton, 1994; Muchez and Viaene, 1994; Vasconcelos and McKenzie, 1997; Wright, 1997; Machel, 2004). The isotopic composition of dolomite combined with petrography and cathodoluminescence analyses gives insights on the nature of the parent fluid responsible for dolomitization and the diagenetic environment of precipitation (Machel and Burton, 1994; Reinhold, 1998; Warren, 2000).

This study aims at identifying the diagenetic features of Middle-Upper Jurassic eastern Sardinia carbonate succession through petrographic, cathodoluminescence analyses and stable oxygen and carbon isotopes analyses. Furthermore, the study aims to separate facies that could record an original marine Upper Jurassic stable isotopic signature from facies with isotopic signature is reset by burial or meteoric diagenesis.

8.3 Results

8.3.1 Petrographic characters and cathodoluminescence analysis

Limestone and dolostone samples from the Middle-Upper Jurassic carbonate succession of eastern Sardinia include a wide variety of diagenetic petrographic features. This study summarises the common diagenetic features observed in most of the facies and the distinctive features characterizing specific facies and depositional phases (Table 8.1). For detailed methodology description for cathodoluminescence (CL) and carbon and oxygen stable isotope analyses refer to Chapter 4, sections 4.2 and 4.4.

	FACIES TYPE	*DIAGENETIC FEATURES*	*DEPOSITIONAL ENVIRONMENT*
F1	Cross-bedded ooidal-coated grain grainstone to packstone	Compaction: concavo-convex grain contacts. Ooids partially dissolved and replaced by equant calcite, except the micritic rim. Interparticle blocky calcite cement (50 µm). Voids filled by scalenohedral calcite cement followed by ferroan blocky calcite (300-600 µm) and rarely replaced by euhedral dolomite. Sparse dolomite euhedral crystals and post-compaction planar-e mosaic of dolomite (50-200 µm) with post-dolomitization blocky calcite cement.	Inner ramp
F2	Cross-laminated echinoderm packstone to grainstone-rudstone	Partially dolomitized with: 1) matrix of fine-grained (20-50 µm) planar-s dolomite mosaic, 2) echinoderms recrystallized with a mosaic of coarse grained (50-150 µm) planar-e/-s limpid dolomite crystals; 3) mosaic of planar-e dolomite (100-200 µm) with Fe-oxides between crystals. Blocky equant calcite cement post dolomitization.	Proximal middle ramp
F3	Peloidal packstone with ooids and echinoderms	Compaction with concavo-convex grain contacts and syntaxial cement around echinoderms precipitated before compaction. Microsparite between grains (10-20 µm).	Middle ramp
F4	Peloidal packstone with chert nodules and thin-shelled bivalves	Compaction with sutured and concavo-convex grain contacts, syntaxial cement around echinoderms pre-compaction. Locally dolomitized with fine euhedral or subhedral crystals (30-200 µm), with turbid nuclei and limpid outer rim.	Outer ramp
F5	Ooidal grainstone to packstone with intraclasts and bioclasts	Variable texture: A) Grainstone, not showing mechanical compaction, cemented by equant blocky calcite cement (50-70 µm) or microsparite (10-20 µm). Dissolution with mouldic porosity (oo- and bio-mouldic); corals and gastropods replaced by equant blocky calcite mosaic (150-400 µm) locally with drusy fabric. B) Packstone compacted with concavo-convex grain contacts; isopachous cement rim (10-15 µm) precipitated before compaction. Some bioclasts dissolved and replaced by fine-grained equant calcite (40-60 µm), followed by blocky calcite (500 µm).	Inner ramp
F6	Peloidal packstone with reworked intraclasts, bioclasts and coated grains	Compaction with concavo-convex grain contacts; syntaxial cement around crinoids pre-compaction. Between grains micrite and microsparite (10-20 µm) or equant blocky calcite cement (80-700 µm).	Middle ramp
F7	Peloidal packstone with *Lenticulina*	Compaction with concavo-convex grain contacts, between grains micrite or rarely microsparite (10 µm)	Distal middle to outer ramp
F8	Bioclastic packstone to grainstone-rudstone with clotted peloidal micrite fragments	Compaction, concavo-convex grain contacts and syntaxial cement around echinoderms pre-compaction. Microsparite cement rim around grains (10-20 µm) followed by a mosaic of equant blocky calcite cement (30-500 µm).	Reworked debris around bioconstructions in middle ramp
F9	Coral-stromatoporoid rudstone-grainstone	Compacted, concavo-convex grain contacts; pre-compaction syntaxial cement on crinoids. Mosaic of equant blocky calcite cement (50-500 µm) in inter- and intraparticle porosity. Geopetal infill in corals, dissolved and replaced by blocky equant calcite (50-200 µm)	Around or within build-ups made of F10 in proximal middle ramp
F10	Coral-stromatoporoid boundstone	Corals dissolved and replaced by equant blocky calcite. Interparticle porosity filled by microsparite or fine-grained equant calcite, intraparticle porosity filled by blocky, scalenohedral or drusy cement. Primary cavities filled by P with peloids, intraclasts of clotted peloidal or dense micrite and bioclasts.	Build-ups (type 1) in middle ramp
F11	Coral-calcareous sponge-diceratid boundstone	Compaction, concavo-convex and sutured grain contacts. Rims of microsparite around some grains, followed by blocky calcite cement (500 µm-1 mm) or granular equant calcite (100-200 µm). Geopetal infill in corals, filled by clotted peloidal micrite or intraclastic-peloidal P-G. Corals replaced by blocky calcite (20-70 µm).	Build-ups (type 2) in middle ramp

F12	Sponge-coral-microbialite boundstone	Corals dissolved and replaced by equant blocky calcite (50-200 µm) and geopetal infills. Interparticle space filled by fine-grained equant cement. Dissolution vugs filled by fine-grained (10-30 µm) sediment.	Build-ups (type 3) in distal middle to outer ramp
F13	Stromatoporoid rudstone to packstone with coated grains	Geopetal infills, syntaxial cement around echinoderms, compaction, concavo-convex grain contacts, microsparite or fine-grained blocky calcite cement in interparticle porosity (20-30 µm) or scalenohedral cement (60-80 µm), followed by blocky calcite (200-300 µm). Locally fractures filled by silt-sized sediment with sparse carbonate lithoclasts.	Middle ramp
F14	Grainstone with ooids, aggregate grains and oncoids	Compaction, sutured and concavo-convex grain contacts. Locally fibrous cement rim before compaction. Interparticle porosity filled by a fine-grained equant mosaic of blocky calcite. Fractures filled by fine-grained sediment with angular lithoclasts. Around fractures prismatic bladed/scalenohedral calcite cement followed blocky calcite. Red stained stylolites	Middle ramp, open marine environment
F15	Peloidal packstone with oncoids and ooids	Geopetal infillings. Compaction, concavo-convex and sutured grain contacts. Locally fibrous cement before compaction (25-30 µm). Syntaxial cement around echinoderms. Red stained stylolites. Interparticle and intraparticle porosity filled by microsparite, followed by blocky calcite. Irregular fractures filled by micrite and carbonate lithoclasts. Dissolution evidences, such as mouldic porosity filled by blocky cement (10-60 µm). Locally fractures filled by bladed/scalenohedral calcite (50-60 µm)	Middle ramp
F16	Lithoclastic breccia to conglomerate with black pebbles	Reddish matrix, compaction, concavo-convex grain contacts. Grain supported, with micrite matrix, sometimes partially dolomitized with planar-e dolomite crystals, locally with Fe-oxides. Some clasts and clast boundaries dolomitized. Red-stained stylolites	Transgressive lag reworking eroded reef, supratidal and pond facies following subaerial exposure at the top of F10
F17	Packstone-grainstone-rudstone with corals, pisoids and black pebbles	Irregular cavities (fenestrae) filled by yellow meteoric cement, meniscus cement and thin microsparitic rim (non-isopachous) followed by blocky calcite cement and poikilotopic cement.	Transgressive lag in supratidal environment
F18	Intraclastic breccia	Grain supported, micrite in interparticle porosity. Geopetal infilling in gastropods, compaction, concavo-convex grain contacts. Fractures filled by fine-grained equant calcite cement and fine-grained sediment. Authigenic quartz within matrix. Locally dolomite with planar-s mosaic followed by silicification. Reddish matrix, microsparite and fine-grained equant calcite cement line pores	Breccia related to dissolution or karst
F19	Mudstone-wackestone with desiccation cracks	Dissolution fractures. Laminar or irregular fenestral porosity, desiccation cracks. Cavities and fractures filled by equant blocky calcite cement	Supratidal environment
F20	Pisoid-intraclastic packstone-rudstone with meniscus cement	Micritic meniscus cement between grains. Irregular cavities: with pendant cement, one cavity filled by several crusts of brownish calcite cement (fibrous pendant) and geopetal infills followed by blocky equant calcite cement. Red stained laminar paleosoils. Fractures filled by micrite followed by calcite cement. Laminar and irregular fenestral porosity and vugs.	Supratidal environment
F21	Wackestone-mudstone with ostracods and *Charophytes*	Fenestral fabric filled by microsparite or fine-grained equant calcite cement. Geopetal infillings in cavities, gastropods dissolved and replaced by blocky calcite. Intraparticle porosity filled by microsparite or fine-grained equant calcite cement. Locally desiccation cracks and vugs filled by geopetal sediment followed by equant calcite. Fractures filled by equant calcite.	Pond-lacustrine environment in coastal wetlands with influence of fresh water
F22	Stromatolitic boundstone	Locally strongly silicified with a mosaic of quartz in cavities. Locally brecciated by subaerial exposure and micrite pendant cement.	Intertidal environment
F23	Microbial boundstone	Vuggy and intraparticle porosity filled by microsparite and equant blocky calcite cement	Subtidal, open-marine lagoon environment
F24	Wackestone with *Cayeuxia*	Fenestrae filled by a first generation of scalenohedral cement or geopetal sediment, locally with peloids, followed by blocky equant calcite. Fractures filled by blocky equant calcite.	Subtidal lagoon environment
F25	Wackestone with ostracods and foraminifers	Micrite between grains and fractures filled by fine-grained equant calcite cement.	Subtidal environment, restricted lagoon

F26	Packstone-wackestone with intraclasts, oncoids and foraminifers	Irregular cavities filled by microsparite or blocky equant calcite and fractures filled by fine-grained equant calcite, geopetal infillings in bioclasts, gastropods dissolved and replaced by a mosaic of equant calcite cement.	Subtidal lagoon with reworked material
F27	Oncoid floatstone	Fractures and vugs filled by equant blocky calcite cement.	Subtidal lagoon
F28	Lithoclastic breccia	Reddish matrix with Fe-oxides. Geopetal infillings (in corals, gastropods). Syntaxial cement around crinoids. Microsparitic cement rim around some clasts. Coral biomoulds filled by coarse-grained equant calcite cement. Fractures filled by fine-grained blocky calcite cement	Debris flow deposits with resedimented lithoclasts from reefal and inner platform facies within basin facies (F29)
F29	Mudstone, wackestone, siltstone		Basinal deposits with F28 debris flow beds
F30	Compacted peloidal packstone-grainstone with fibrous cement	Microsparitic cement rim around grains (fibrous) precipitated before compaction. Compacted, concavo-convex grain contacts. Fractures filled by microsparite	Subtidal environment
F31	Laminated dolostone	Dolomicrosparite and dolomicrite	Diagenetic overprint.
F32	Rudstone to packstone with *Clypeina jurassica*	Compaction, sutured and concavo-convex grain contacts. Fenestral porosity (within intraclasts) filled by scalenohedral calcite cement followed by equant blocky cement. Geopetal infillings in gastropods followed by microsparite. Microsparite and fine-grained equant calcite cement in interparticle porosity. Dolomitized matrix with a mosaic of planar-s dolomite crystals with Fe-oxides in porosity.	Subtidal shallow marine inner platform environment
F33	Packstone to rudstone with pisoids, oncoids, foraminifers and meniscus cement	Compaction, sutured and concavo-convex grain contacts. Fenestral porosity (within intraclasts) filled by scalenohedral calcite cement followed by equant blocky calcite cement. Geopetal infillings in gastropods followed by microsparite. Microsparite and fine-grained equant calcite cement in interparticle porosity. Dolomitized matrix with a mosaic of planar-s dolomite crystals with Fe-oxides in porosity.	Supratidal inner platform environment
F34	Bioturbated wackestone-mudstone with ostracods	Sparse replacive euedral dolomite crystals	Subtidal lagoon environment
F35	Breccia with radiaxial fibrous calcite cement	Interparticle space filled by radiaxial fibrous calcite cement, followed by equant blocky calcite cement	Upper to lower slope with marine cement (cf. Lanfranchi et al. 2011)
F36	*Crescentiella* grainstone-packstone	Dissolution and recrystallization, fine grained equant calcite cement (or microsparite) followed by equant blocky calcite cement followed by equant blocky, prismatic calcite cement or radiaxial calcite followed by fine-grained sediment infillings	Lower slope (cf. Lanfranchi et al. 2011)
F37	Crinoidal peloidal packstone-wackestone	Compaction, concavo-convex grain contacts	Lower slope (cf. Lanfranchi et al. 2011)

Table 8.1 Diagenetic features of the distinguished facies types (cf Chapter 6) and interpreted depositional environment of the eastern Sardinia Callovian-Tithonian portion of the succession.

8.3.1.1 Phase 1

The majority of the facies deposited during phase 1 (F1, F3, F4) shows evidences of mechanical compaction with concavo-convex and locally sutured grain contacts.

In the inner ramp facies F1 cross-bedded ooidal-coated grain grainstone to packstone, ooids are partially dissolved leaving only a micrite envelope filled by non-luminescent equant blocky calcite

cement, whereas voids are filled by scalenohedral calcite followed by non-luminescent equant blocky calcite cement. Locally (lower part of Baunei Supramonte stratigraphic log; Fig. 6.2, 6.5 in Chapter 6), ooids in facies F1 are dull luminescent and equant blocky calcite between grains is zoned with non-luminescent, dull and bright luminescent rims (Fig. 8.1A). In the middle ramp peloidal packstone with ooids and echinoderms (F3) and outer ramp peloidal packstone with chert nodules and thin-shelled bivalves (F4), non-luminescent syntaxial (50 to 600 μm in size) cement precipitated before compaction surrounding echinoderms (Fig. 8.1B). Locally in facies F3 non-luminescent microsparite (crystal size 10-20 μm) surrounds pores.

Phase 1 facies (Dorgali, Lower Mt. Tului and Lower Baunei formations) are characterized by widespread dolomitization close to the Hercynian basement with a variable thickness (e.g., the basal 20 m at Mt. Oro, 40 m at Genna Scalas, 25 m at Baunei Supramonte to 150 m at Genna Silana; Figure 6.2 in Chapter 6). The outcrops are characterized by strata-bounding dolomitization, patchy dolomitized volumes or partially dolomitized portions in which it is possible to recognize the original facies. In completely dolomitized facies, dolomite consists of: 1) planar-s to planar-e mosaics of subhedral to euhedral crystals with size of 30-120 μm (DOL-1; Fig. 8.1C); 2) planar-e mosaics of zoned crystals (200-300 μm) with a turbid nucleus and an external limpid rim (DOL-2; Fig. 8.1D). In partially dolomitized facies F1, it is possible to observe post mechanical compaction planar-e to planar-s mosaics of dolomite (20-200 μm) replacing grains and matrix and sealing grain contacts. In the middle ramp cross-laminated echinoderm packstone to grainstone-rudstone (F2), there are fine-grained planar-s dolomite crystals (20-50 μm) and echinoderms are recrystallized by a mosaic of coarser (50-150 μm) planar-e/planar-s limpid dolomite crystals and planar-e dolomite (100-200 μm) with Fe-oxides between crystals. Facies F3 and F4 are locally dolomitized by fine planar-e or planar-s dolomite (30-200 μm in size) with a turbid nucleus and limpid outer rim (DOL-2). Dolomite is generally luminescent in CL with a variable zoned pattern and is generally followed by non-luminescent equant blocky calcite cement in interparticle porosity.

In the lower part of the Genna Silana log (Fig. 8.2), in facies F1 planar-e dolomite (DOL-2) is usually zoned with a dull-luminescent nucleus and alternating non-luminescent, dull-luminescent and bright luminescent rims (Fig. 8.1E). In the Genna Scalas log, planar-e dolomite crystals (DOL-2) are characterized by a dull-luminescent nucleus, followed, from the nucleus toward the outer rim, by a bright luminescent rim, a non-luminescent or dull-luminescent rim and an external bright luminescent rim (Fig. 8.1F) or only a dull-luminescent nucleus followed by a bright luminescent rim. In the same samples, planar-s dolomite (DOL-1) crystals are generally dull-luminescent, whereas the finer dolomite crystals are usually non-luminescent.

In the Genna Ramene log (Fig. 8.3), for a thickness of about 30 m in facies F4 and F3 the planar-e and planar-s zoned dolomite (DOL-2) shows a dull-luminescent nucleus, followed by alternating dull- and bright luminescent rims or a non-luminescent nucleus with bright luminescent rims (Fig. 8.1G). In the Mt. Oro stratigraphic log (Fig. 8.4), for a thickness of about 25 m, in facies F1 (or undetermined facies due to dolomitization) the first metres of dolostone are characterized by dull-luminescent planar-e crystals (DOL-2) with a bright luminescent rim (Fig. 8.1H, 8.5A). In the overlying 20 m (Fig. 8.4) a dedolomitization process affected DOL-1 and DOL-2 with the presence of calcite within the remaining dolomite rhombic crystals as identified by alizarin red staining (Fig. 8.5B). The planar-e dolomite (DOL-2) is characterized by a non-luminescent dedolomitized calcite nucleus with a bright luminescent rim (Fig. 8.5B-C) and dull to bright luminescent dolomite crystals (DOL-1; Fig. 8.5D) for about 8 m (from m 2 to m 10 in log in Figure 8.4). For about 1 m, the dolomite is generally non-luminescent and dull-luminescent with a bright luminescent rim line pores, whereas for the overlying 7 m (from m 11 to m 18) dolomite crystals are completely non-luminescent. In the Baunei Supramonte stratigraphic log in facies F1 (or undetermined facies due to dolomitization) DOL-1 is bright to dull luminescent for a thickness of about 30 m.

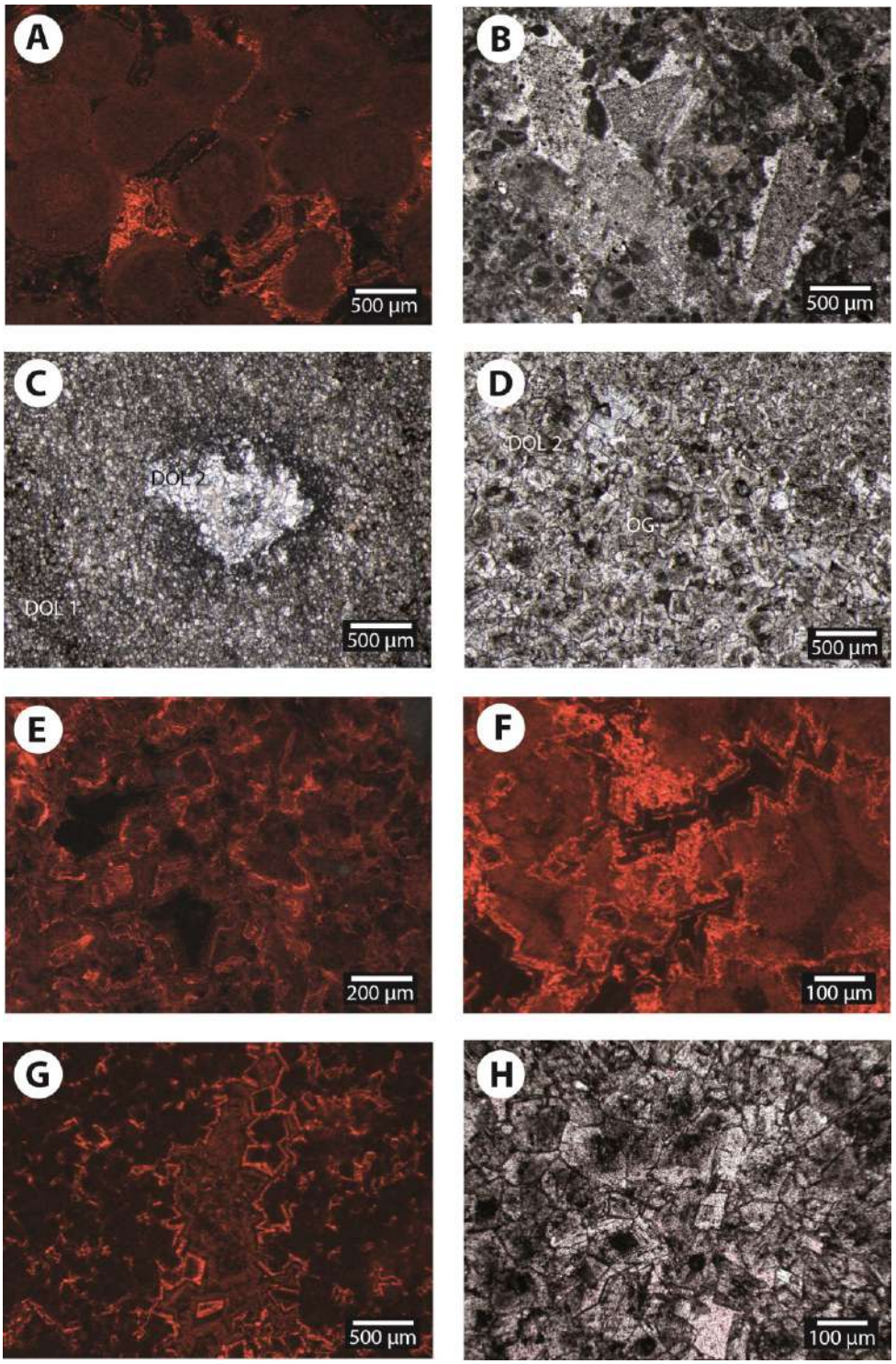

Figure 8.1 A) CL image of F1 showing dull-luminescent ooids and zoned blocky equant calcite cement lining pores. B) Photomicrograph of facies F3 showing syntaxial calcite cement surrounding crinoid fragments. C) Photomicrograph of dolostone showing a mosaic of planar-s turbid dolomite crystals (DOL-1) and coarser planar-e dolomite crystals (DOL-2) in porosity followed by equant blocky calcite cement (CAL). D) Photomicrograph of dolostone showing a planar-e mosaic of dolomite crystals with a turbid nucleus and a limpid external rim (DOL-2) and an ooid ghost (OG). E) CL image showing a mosaic of zoned planar-e dolomite crystals with a dull-luminescent nucleus followed by a bright luminescent rim and a dull-luminescent rim and non-luminescent equant blocky calcite in pores. F) CL image of a mosaic of planar-e dolomite a dull-luminescent nucleus, followed by a bright luminescent rim, a non-luminescent rim and an external bright luminescent rim. G) CL image of a mosaic of planar-e dolomite crystals showing a non-luminescent nucleus and alternated bright luminescent, non-luminescent and dull-luminescent external rims. H) Photomicrograph showing DOL-2 dolomite with a turbid nucleus and limpid external rim and equant blocky calcite in pores stained with alizarin red.

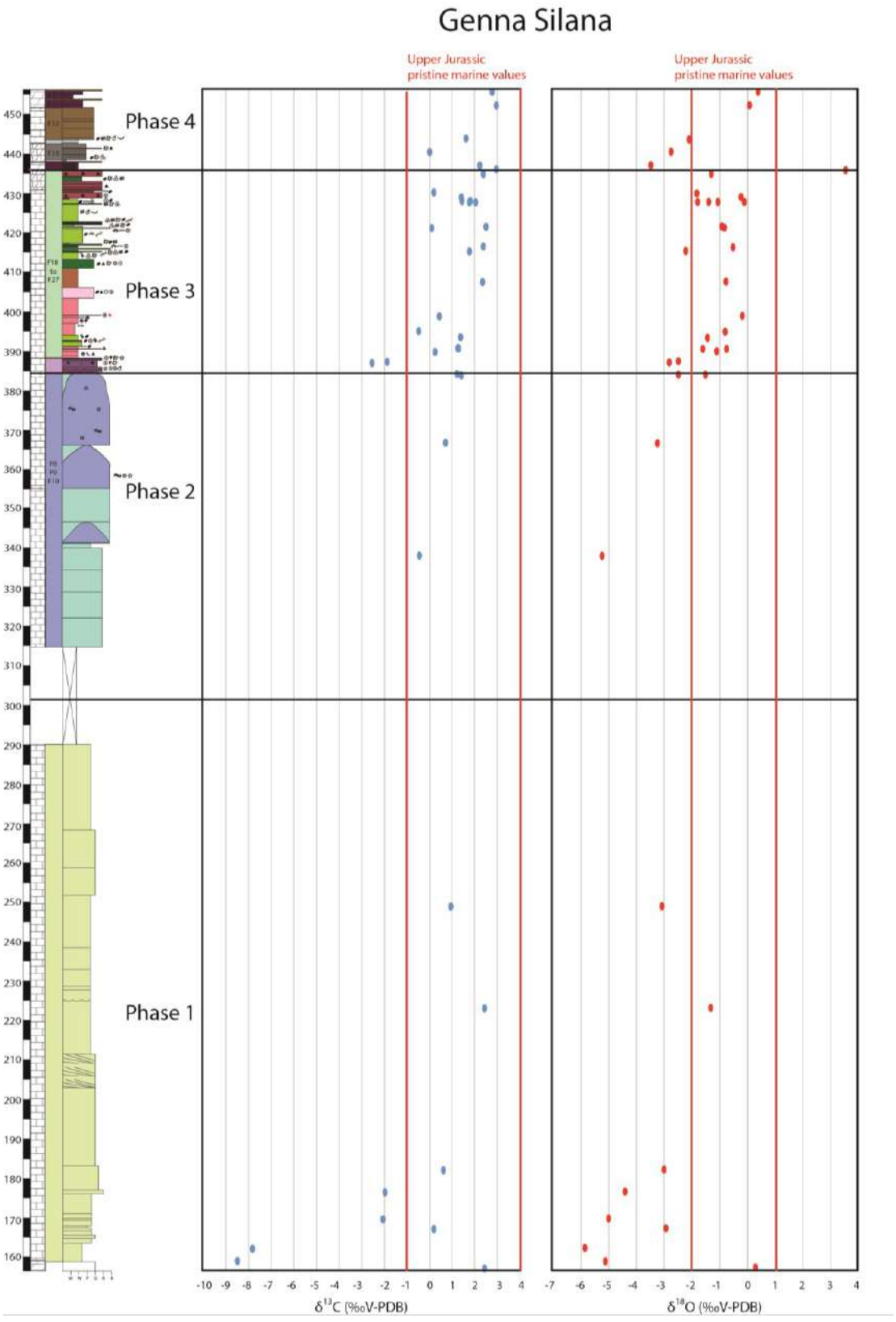

Figure 8.2 Genna Silana stratigraphic log with $\delta^{13}C$ and $\delta^{18}O$ plotted values. Red lines represent the field of Upper Jurassic pristine marine values based on published stable-isotope compositions obtained from well-preserved fossils (particularly belemnites) in Jenkyns et al. (2002), Weissert and Erba (2004), Wierzbowski et al. (2004), Brigaud et al. (2008), Nunn et al. (2009), Price and Rogov (2009), Nunn and Price (2010).

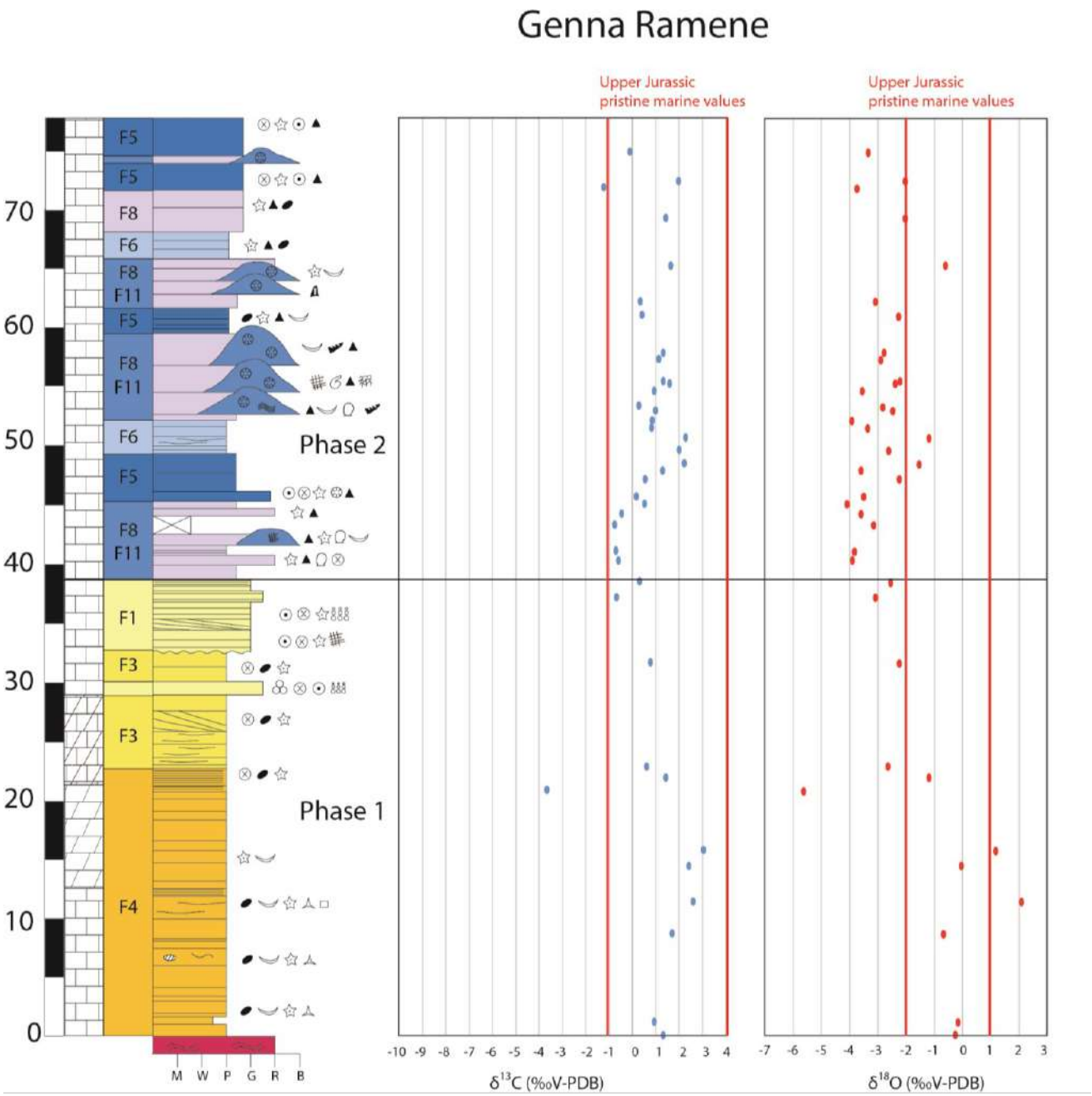

Figure 8.3 Genna Ramene stratigraphic log with $\delta^{13}C$ and $\delta^{18}O$ plotted values. Red lines represent the field of Upper Jurassic pristine marine values based on published stable-isotope compositions obtained from well-preserved fossils (particularly belemnites) in Jenkyns et al. (2002), Weissert and Erba (2004), Wierzbowski et al. (2004), Brigaud et al. (2008), Nunn et al. (2009), Price and Rogov (2009), Nunn and Price (2010).

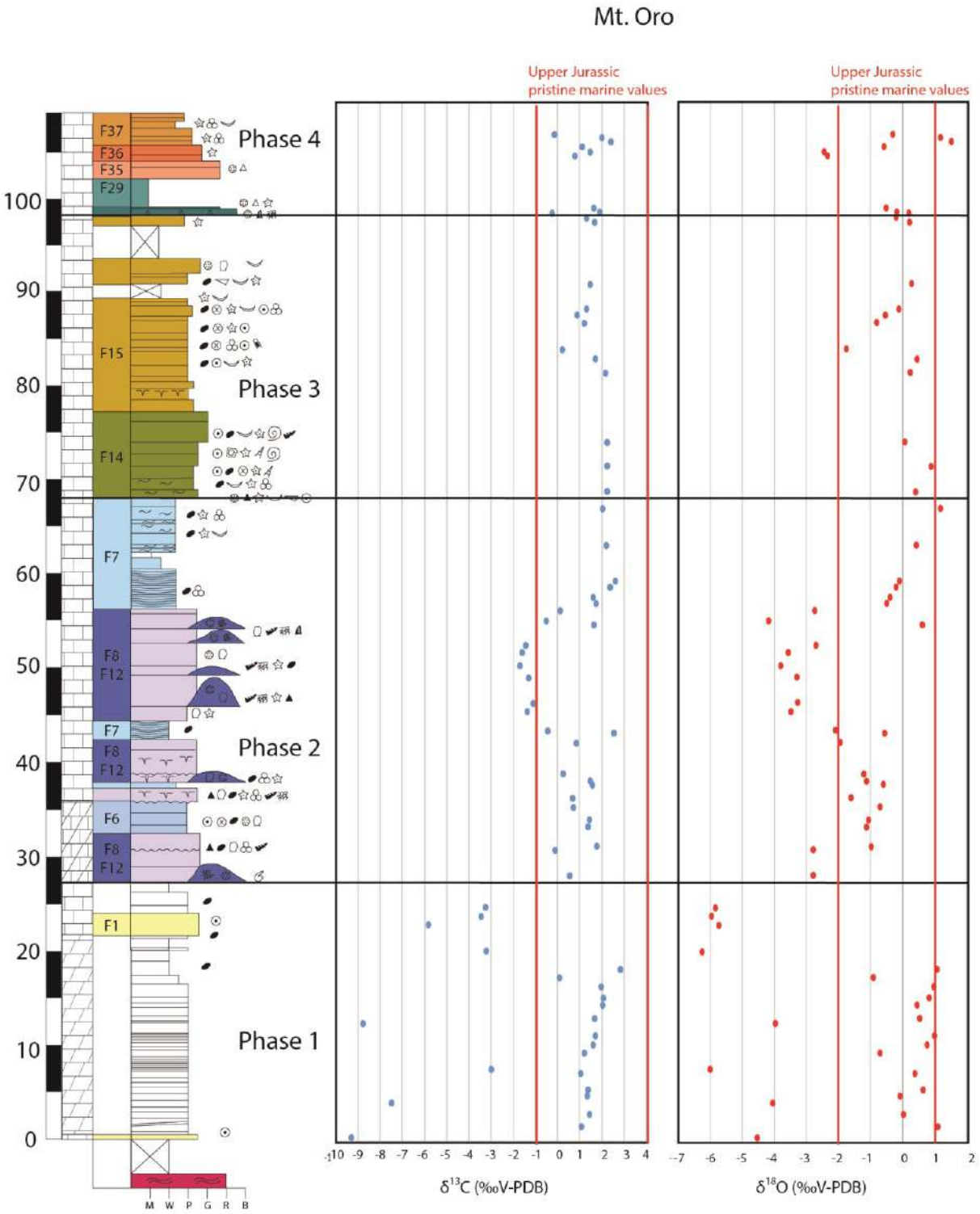

Figure 8.4 Mt. Oro stratigraphic log with $\delta^{13}C$ and $\delta^{18}O$ plotted values. Red lines represent the field of Upper Jurassic pristine marine values based on published stable-isotope compositions obtained from well-preserved fossils (particularly belemnites) in Jenkyns et al. (2002), Weissert and Erba (2004), Wierzbowski et al. (2004), Brigaud et al. (2008), Nunn et al. (2009), Price and Rogov (2009), Nunn and Price (2010).

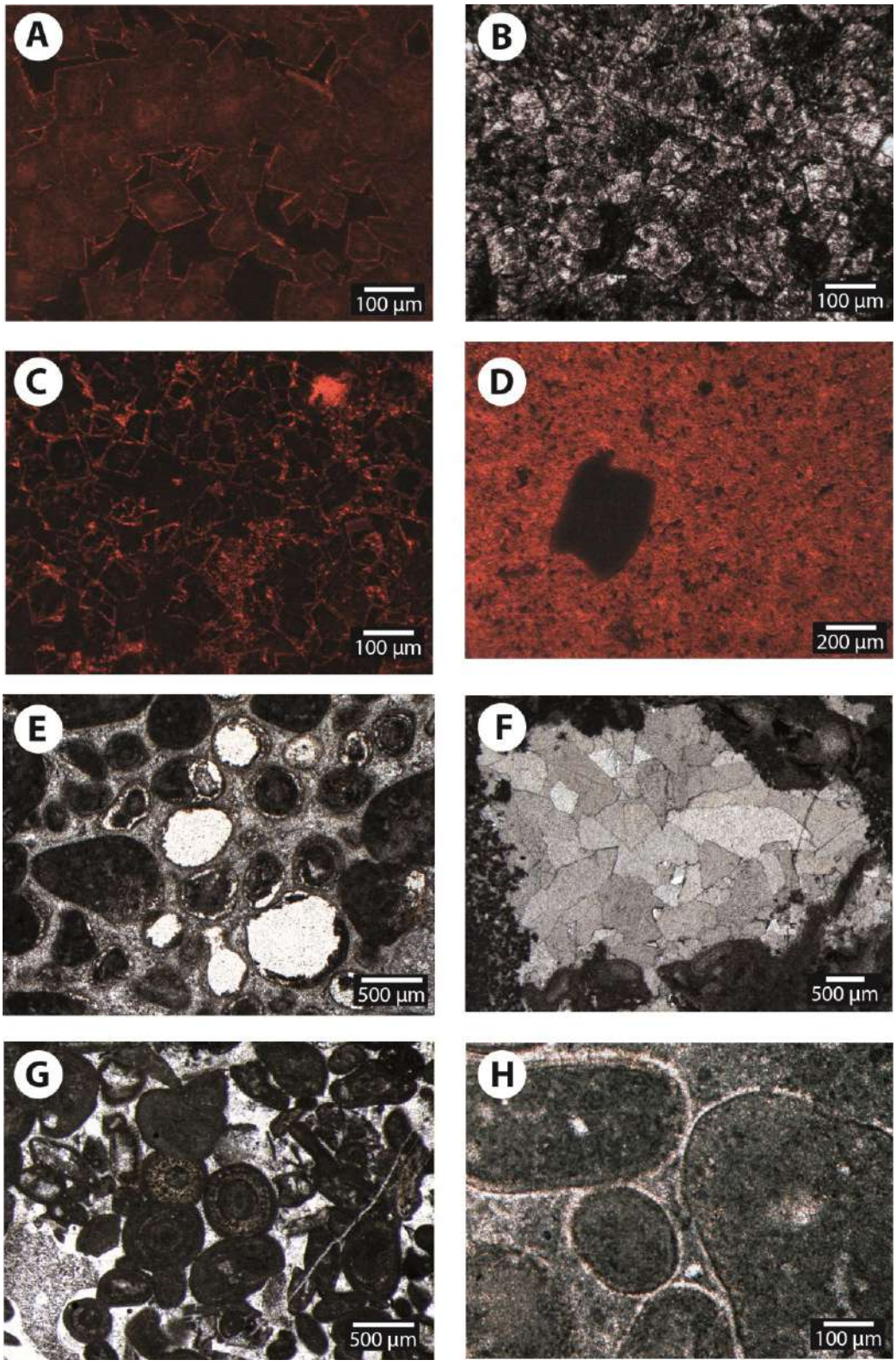

Figure 8.5 A) CL image of a planar-e mosaic of dolomite with dull-luminescent nucleus and a bright luminescent external rim and non-luminescent equant blocky calcite in pores. B) Photomicrograph showing a planar-e mosaic of DOL-2 with dedolomitized calcite nucleus stained with alizarin red and a limpid external rim. C) CL image of a planar-e mosaic of dolomite with dedolomitized calcite non-luminescent nucleus and an external bright luminescent rim. D) CL image showing a bright-luminescent planar-s mosaic of DOL-1 and a non-luminescent quartz fragment. E) Facies F1 showing oo-mouldic porosity. F) Facies F10 photomicrograph showing a mosaic of equant blocky calcite cement. G) Facies F14 showing concavo-convex grain contacts between ooids. H) Photomicrograph of facies F15 showing intraclasts with a thin isopachous fibrous cement rim.

8.3.1.2 Phase 2

Facies deposited during phase 2 (from F5 to F13) are generally well compacted with concavo-convex grain contacts, with the exception of facies F5. The ooidal grainstone to packstone with intraclasts and bioclasts (F5) show a variable texture passing from a grainstone without compaction evidences to a compacted packstone with concavo-convex grain contacts. F5 grainstone shows oo- and bio-mouldic porosity (Fig. 8.5E) and is cemented by non-luminescent equant blocky calcite cement (50-70 μm in size) or microsparite (10-20 μm) filling the interparticle and mouldic porosity. F5 packstone shows an isopachous fibrous cement rim (10-15 μm), some bioclasts are dissolved and replaced by non-luminescent fine-grained equant calcite (40-60 μm) and equant non-luminescent blocky calcite cement fills interparticle porosity (500 μm).

In the peloidal packstone with reworked intraclasts, bioclasts and coated grains (F6) non-luminescent syntaxial cement precipitated around grains before compaction and non-luminescent microsparite (10-20 μm) or equant blocky calcite (80-700 μm) cements line pores. The peloidal packstone with *Lenticulina* (F7) is poorly cemented and shows only rare non-luminescent microsparite (10 μm). In the bioclastic packstone to grainstone-rudstone with clotted peloidal micrite fragments (F8) non-luminescent syntaxial cement surrounds echinoderms, non-luminescent microsparite lines pores and non-luminescent equant blocky calcite cement fills the interparticle and intraparticle porosity.

The coral-stromatoporoid rudstone-grainstone (F9), coral-stromatoporoid boundstone (F10), coral-calcareous sponge-diceratid boundstone (F11) and sponge-coral-microbialite boundstone (F12) are characterized by geopetal infill (clotted peloidal micrite and intraclastic peloidal packstone-grainstone) and dissolution of corals replaced by non-luminescent equant blocky calcite cement (50-200 μm). In facies from F9 to F12 non-luminescent microsparite lines pores (10-20 μm) and a mosaic of non-luminescent equant blocky calcite cement (50 μm-1 mm) fills interparticle porosity (Fig. 8.5F). In the stromatoporoid rudstone to packstone with coated grains (F13) non-luminescent syntaxial cement surrounds echinoderms, whereas the interparticle porosity is filled by non-luminescent fine-grained equant calcite cement (20-30 μm), scalenohedral cement (60-80 μm) or equant blocky calcite cement (200-300 μm). Locally in F13 there are fractures filled by silt-size sediment with sparse carbonate lithoclasts.

Facies deposited during phase 2 are affected by dolomitization only in the Mt. Oro stratigraphic log (F6, F8, F12, Fig. 8.4) for about 7 m at the top of facies F1 (phase 1). Dolomitization is characterized by sparse planar-e dolomite crystals (DOL 1 and DOL 2), often dedolomitized as demonstrated by staining with alizarine red.

8.3.1.3 Phase 3

The middle ramp grainstone with ooids, aggregate grains and oncoids (F14) and peloidal packstone with oncoids and ooids (F15) show evidences of mechanical compaction with concavo-convex and sutured grain contacts (Fig. 8.5G). In these facies (F14-F15), a non-luminescent fibrous cement rim (25-30 μm, Fig. 8.5H) and syntaxial cement precipitated around grains before compaction. Interparticle and intraparticle porosity are filled by non-luminescent microsparite (10-20 μm, Fig. 8.6A), fine-grained equant calcite (30-40 μm, Fig. 8.6B) and blocky equant calcite cement (50-60 μm). Locally there are fractures filled by silt-size sediment (Fig. 8.6C) with angular lithoclasts and scalenohedral calcite cement (50-60 μm) followed by equant calcite cement (50-200 μm).

Within the facies deposited during the transgressive lag in supratidal environment, the lithoclastic breccia to conglomerate with black pebbles (F16) and the packstone-grainstone-rudstone with corals, pisoids and black pebbles (F17), there are irregular cavities (fenestrae) filled by yellowish pendant cement (Fig. 8.6D), and micrite meniscus cement between grains (Fig. 8.6E). In facies F17 a microsparitic rim surrounds the grains.

The intraclastic breccia (F18) indicative of exposure and karstic dissolution (cf. Chapter 6) is characterized by fractures filled by non-luminescent equant blocky calcite cement (50-500 μm) and silicification with authigenic quartz within matrix. In supratidal (F19, F20) and pond (F21) facies laminar or irregular fenestral porosity is filled by non-luminescent equant blocky calcite, fine-grained equant or fibrous pendant cement. Fine-grained equant cement filling intraparticle porosity in F21 (*Charophytes*) is locally dull-luminescent. Dessication cracks are diffused in F19 mudstone-wackestone and in F21 wackestone-mudstone with *Charophytes* and ostracods. The pisoid-intraclastic packstone rudstone (F20) shows widespread cementation by micritic meniscus cement and red-stained laminar paleosoils. The intertidal stromatolitic boundstone (F22) is characterized by micritic pendant cement and is often silicified with quartz mosaic filling cavities. The subtidal lagoon facies (F23 to F27) are poorly cemented and are characterized by vuggy and rare fenestral porosity and fractures filled by non-luminescent microsparite (10-20 μm), scalenohedral (60-80 μm), fine grained equant (30-40 μm) or equant blocky calcite cement (50-400 μm).

Facies F18 is partially dolomitized with planar-s crystals in the Genna Silana log (Fig. 8.2) for about 4 m below the subaerial exposure boundary overlain by F30 (phase 4).

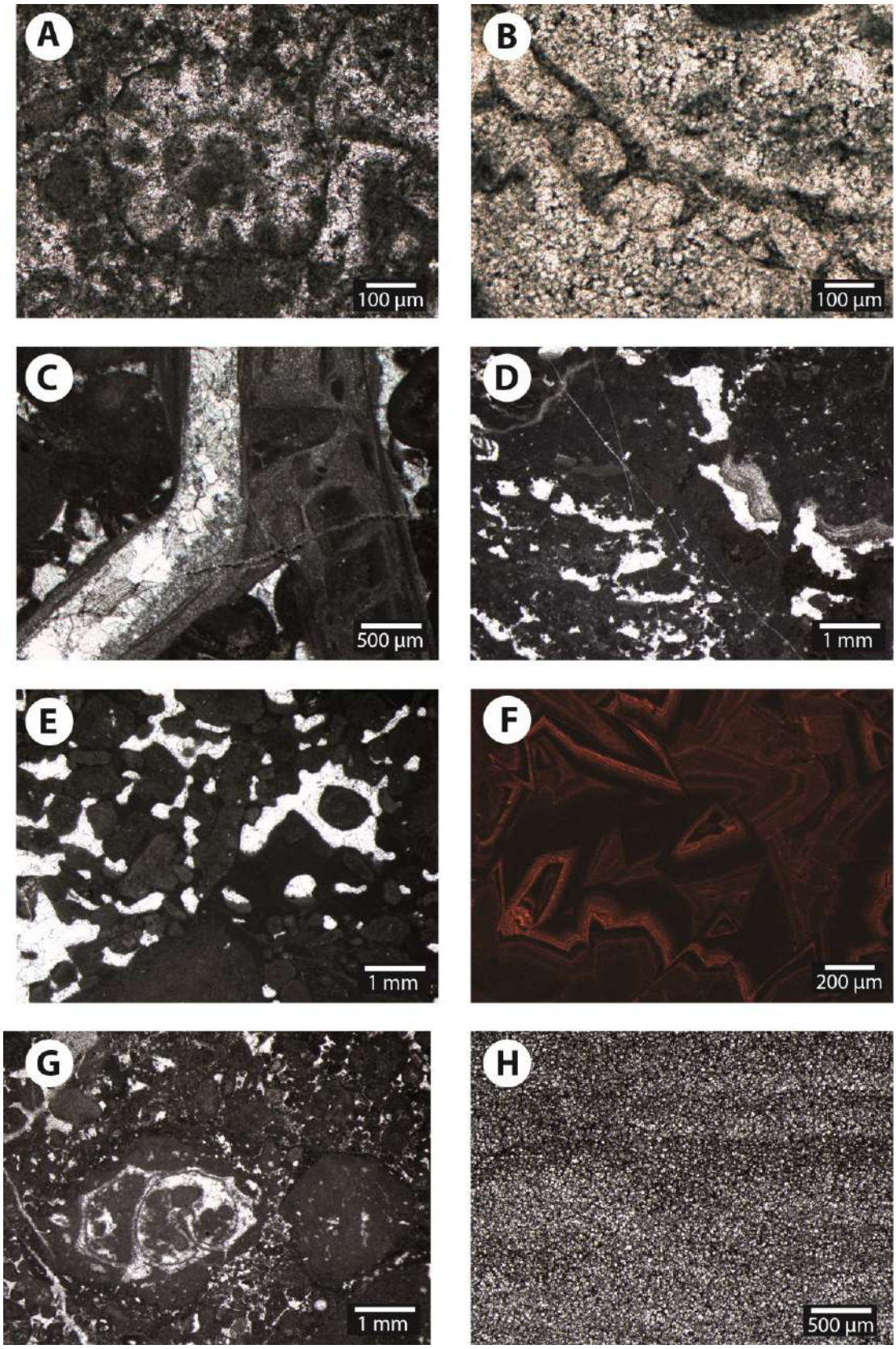

Figure 8.6 A) Photomicrograph of facies F15 showing a dasyclad alga partially dissolved and replaced by microsparite. B) Facies F14 photomicrograph showing a mosaic of fine-grained equant calcite cement. C) Facies F14 showing a fracture filled by sediment with carbonate lithoclasts and equant blocky calcite cement. D) Photomicrograph of facies F20 showing pendant calcite cement in vugs. E) Facies F20 showing micrite meniscus cement between grains. F) CL image of a mosaic of zoned blocky equant calcite cement. G) Photomicrograph of F26 showing a gastropod with geopetal infillings H) Photomicrograph of a planar-s mosaic of dolomite crystals (DOL-3).

8.3.1.4 Phase 4

The basinal facies deposited during phase 4 (F28, F29) in the south-eastern Baunei Supramonte area (cf. Chapter 6 and Chapter 7) are poorly cemented and are characterized by a reddish matrix with Fe-oxides. In the lithoclastic breccia (F28) there is locally a non-luminescent microsparite cement rim (10-20 μm) surrounding clasts. Within lithoclasts, there are corals dissolved and replaced by equant blocky calcite cement generally non-luminescent and rarely showing a zoned pattern with non-luminescent zones alternating with dull- and bright-luminescent zones (Fig. 8.6F) or dull-luminescent zones alternating to bright-luminescent zones especially in fractures.

The inner platform facies (F30 to F34) deposited during phase 4 in the central north-western Urzulei Supramonte area (cf. Chapter 6) are generally well-compacted with concavo-convex grain contacts. In the compacted F30 peloidal packstone-grainstone a fibrous cement rim (10-30 μm) precipitated before compaction around grains; fractures are filled by non-luminescent microsparite.

In the rudstone to packstone with *Clypeina jurassica* (F32) and in the packstone to rudstone with pisoids, oncoids and foraminifers (F33), gastropods are rich in geopetal infillings (Fig. 8.6G) and there is non-luminescent microsparite (10-20 μm) and fine-grained equant calcite cement (30-50 μm) in interparticle porosity. Fenestral porosity within intraclasts is filled by scalenohedral calcite cement followed by non-luminescent equant blocky calcite cement. In F33 micrite meniscus cement precipitated between grains.

The inner platform facies (F31 to F34) are dolomitized or partially dolomitized for a stratigraphic interval of about 20 m exclusively in the Urzulei Supramonte area (Iscra, Codula Orbisi, Genna Silana and Ghispali stratigraphic logs, Figure 6.6 in Chapter 6). Dolomite consists of pervasively dolomitized intervals, forming planar horizontal beds (5-10 cm thick) of laminated dolostone (F31) and of partially dolomitized facies affecting the rudstone to packstone with *Clypeina jurassica* (F32), the packstone to rudstone with pisoids, oncoids, foraminifers and meniscus cement (F33) and the bioturbated wackestone-mudstone with ostracods (F34). In the pervasively dolomitized succession (F31, Genna Silana and Iscra logs, Fig. 8.2, 8.7) dolomite forms a fine grained planar-s mosaic of turbid crystals (10-100 μm, DOL-3; Fig. 8.6H). Instead, in the partially dolomitized facies (F32, F33, F34) dolomite consists of planar-e mosaic of euhedral zoned dolomite crystals (100-300 μm) with a turbid nucleus and external limpid rim (DOL-4; Fig. 8.8A-B) and a planar-s or planar-e mosaic of limpid dolomite crystals (60-250 μm, DOL-5; Fig. 8.8C). Dolomitization in facies from F31 to F34 is generally non-luminescent or slightly dull-luminescent.

Within the slope facies (F35 to F37; cf. Chapter 6), in F35 lithoclastic breccia and F36 *Crescentiella* grainstone-packstone non-luminescent radiaxial fibrous calcite cement (100-400 μm) lines pores

(Fig. 8.8D) and non-luminescent equant blocky calcite cement (100-500 μm) or silt-size sediment fills interparticle porosity. The crinoidal peloidal packstone-wackestone (F37) shows evidences of mechanical compaction such as concavo-convex grain contacts and are poorly cemented.

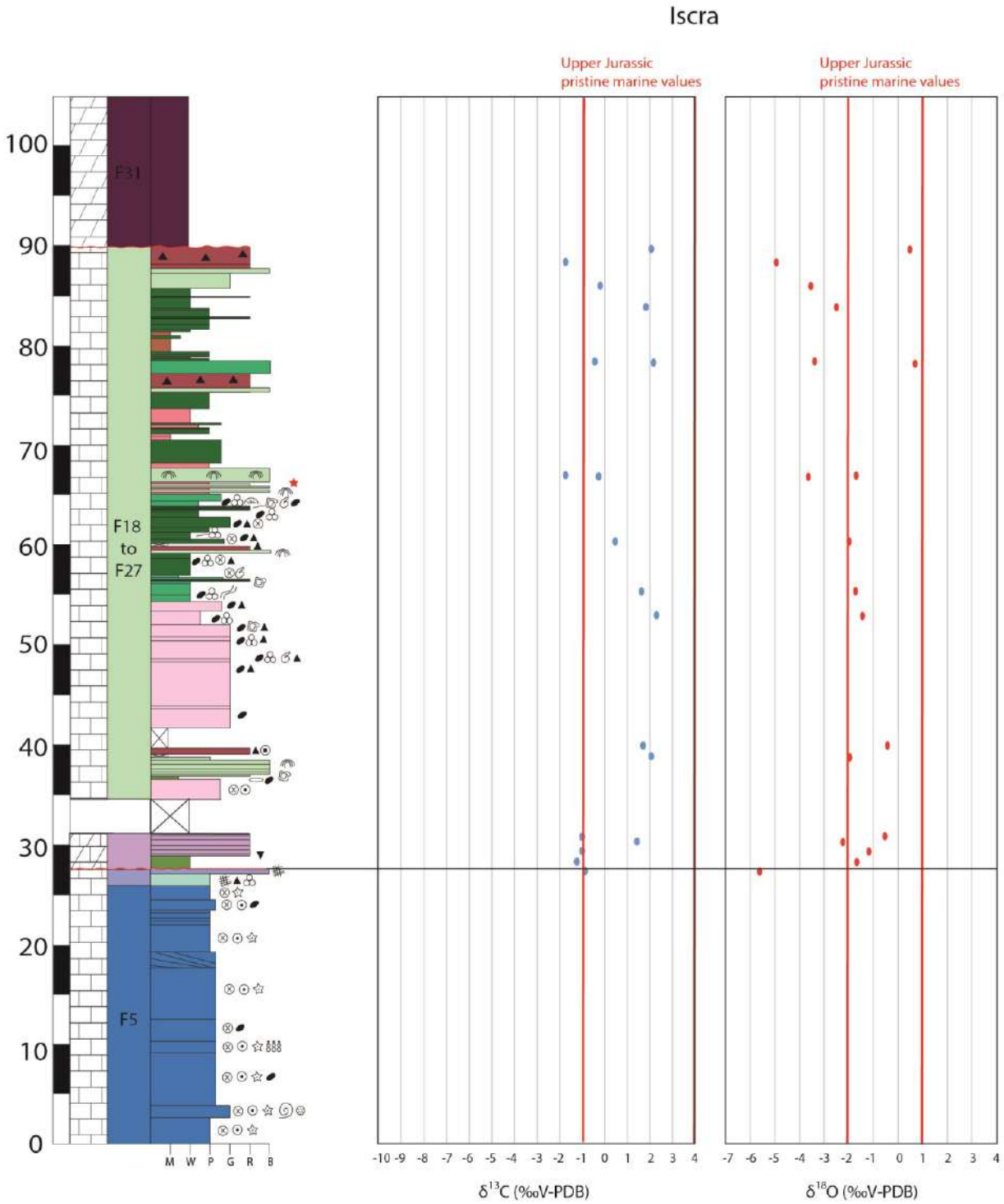

Figure 8.7 Iscra stratigraphic log with $\delta^{13}C$ and $\delta^{18}O$ plotted values. Red lines represent the field of Upper Jurassic pristine marine values based on published stable-isotope compositions obtained from well-preserved fossils (particularly belemnites) in Jenkyns et al. (2002), Weissert and Erba (2004), Wierzbowski et al. (2004), Brigaud et al. (2008), Nunn et al. (2009), Price and Rogov (2009), Nunn and Price (2010).

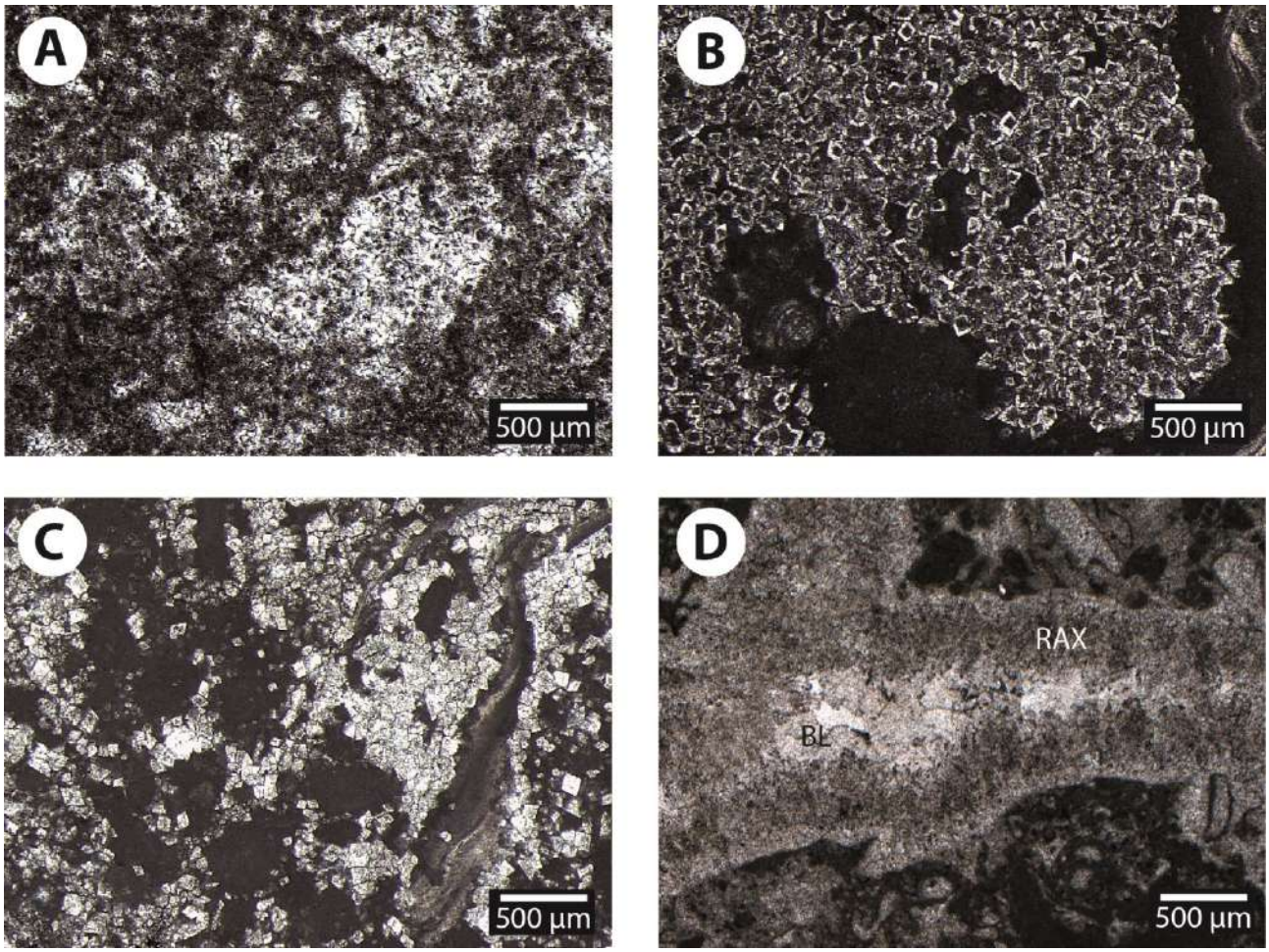

Figure 8.8 A) Photomicrograph of a dolostone showing a planar-s mosaic of dolomite crystals (DOL-3) and a planar-e mosaic of dolomite crystals with a turbid nucleus and an external limpid rim (DOL-4) 4B) Photomicrograph of partially dolomitized facies F32 showing a planar-e mosaic of dolomite crystals with a turbid nucleus and a limpid external rim (DOL-4). C) Photomicrograph of partially dolomitized facies F32 showing a planar-e mosaic of limpid dolomite crystals (DOL-5). D) Photomicrograph of facies F35 showing radiaxial fibrous calcite (RAX) cement followed by equant blocky calcite cement (BL).

8.3.2 Calcite carbon and oxygen stable isotope analyses

Carbon and oxygen stable isotope analyses performed on limestone and partially dolomitized limestone bulk and skeletal grain samples (corals and calcareous sponges dissolved and replaced by equant blocky calcite cement) are summarized in Tables from 8.2 to 8.10. For detailed methodology description refer to Chapter 4, section 4.4.

In the Mt. Oro stratigraphic log (Fig. 8.4), the $\delta^{13}C$ values range between -9.3 ‰ and 2.6 ‰, whereas $\delta^{18}O$ values are between -6.0 ‰ and 1.5 ‰ (Table 8.2). The cross-plot of the $\delta^{13}C$ and $\delta^{18}O$ values per facies types indicates differentiated isotopic composition patterns (Fig. 8.9).

SAMPLE	*SAMPLED COMPONENT*	*FACIES*	*PHASE*	*$\Delta^{13}C$ (‰ V-PDB)*	*ST. DEV $\Delta^{13}C$*	*$\Delta^{18}O$ (‰ V-PDB)*	*ST. DEV $\Delta^{18}O$*
O04	Bulk	F1	1	-9.29	0.04	-4.53	0.02
O16	Bulk	DOL	1	1.08	0.05	1.11	0.04
O29	Bulk	DOL	1	1.44	0.04	0.02	0.04
O41A	Bulk	DOL	1	-7.47	0.05	-4.05	0.06
O41B	Bulk	DOL	1	-4.13	0.04	-2.81	0.05
O48	Bulk	DOL	1	1.34	0.03	-0.09	0.09
O55A	Bulk	DOL	1	1.37	0.03	0.64	0.03
O55B	Bulk	DOL	1	2.73	0.06	1.18	0.06
O55B	Bulk	DOL	1	2.70	0.03	0.62	0.03
O72A	Bulk	DOL	1	1.05	0.02	0.38	0.04
O77	Bulk	DOL	1	-2.96	0.05	-6.02	0.05
O94	Bulk	DOL	1	1.22	0.03	-0.70	0.05
O102	Bulk	DOL	1	1.62	0.04	0.76	0.06
O112	Bulk	DOL	1	1.70	0.09	0.99	0.12
O125	Bulk	DOL	1	-8.75	0.02	-3.97	0.06
O130	Bulk	DOL	1	1.68	0.04	0.52	0.04
O144	Bulk	DOL	1	2.06	0.06	0.45	0.07
O152A	Bulk	DOL	1	2.08	0.02	0.83	0.05
O152B	Bulk	DOL	1	1.31	0.03	0.23	0.03
O164	Bulk	DOL	1	1.97	0.04	0.96	0.05
O173	Bulk	DOL	1	0.09	0.03	-0.92	0.05
O182	Bulk	DOL	1	2.84	0.04	1.08	0.03
O182	Bulk	DOL	1	1.25	0.02	0.05	0.03
O201	Bulk	DOL	1	-3.21	0.02	-6.27	0.02
O229	Bulk	F8	2	-5.80	0.03	-5.73	0.06
O238	Bulk	F8	2	-3.44	0.01	-5.96	0.05
O247	Bulk	F8	2	-3.25	0.03	-5.83	0.04
O281	Bulk	F12	2	0.54	0.02	-2.80	0.06
O308	Bulk	F8	2	0.23	0.07	-2.62	0.05
O308	Bulk	F8	2	-0.12	0.04	-2.79	0.05
O312	Bulk	F8	2	1.76	0.03	-0.99	0.04
O332	Bulk	F8	2	1.37	0.05	-1.13	0.07
O340	Bulk	F8	2	1.43	0.03	-1.08	0.04
O340	Fracture	F8	2	-3.42	0.10	-5.03	0.10
O353	Bulk	F8	2	0.72	0.07	-0.71	0.07
O363	Bulk	F8	2	0.68	0.03	-1.62	0.03
O377	Bulk	F7	2	1.58	0.02	-0.60	0.04
O381	Bulk	F8	2	1.52	0.02	-0.98	0.04
O381	Bulk	F8	2	1.48	0.04	-1.14	0.04
O381	Fracture	F8	2	-7.94	0.07	-4.26	0.06
O388	Bulk	F8	2	0.27	0.04	-1.22	0.04
O388	Bulk	F8	2	0.28	0.05	-1.12	0.06
O421	Bulk	F8	2	0.84	0.03	-1.95	0.02
O431	Bulk	F8	2	2.54	0.03	-0.56	0.07
O434	Bulk	F8	2	-0.43	0.04	-2.09	0.07
O454	Bulk	F8	2	-1.37	0.03	-3.49	0.07
O463	Bulk	F8	2	-1.08	0.02	-3.29	0.04
O490	Bulk	F12	2	-1.30	0.04	-3.31	0.04
O502	Bulk	F12	2	-1.70	0.04	-3.80	0.03
O516	Bulk	F12	2	-1.58	0.06	-3.58	0.12
O524	Bulk	F12	2	-1.43	0.03	-2.72	0.05
O545	Bulk	F8	2	1.64	0.02	0.61	0.04
O550	Bulk	F12	2	-0.50	0.05	-4.19	0.06
O550	Fracture	F12	2	-3.24	0.03	-3.42	0.05
O560	Bulk	F8	2	0.12	0.03	-2.75	0.04
O568	Bulk	F7	2	1.76	0.02	-0.49	0.06
O568	Bulk	F7	2	1.76	0.03	-0.71	0.04
O575	Bulk	F7	2	1.63	0.04	-0.40	0.06
O585	Bulk	F7	2	2.38	0.08	-0.20	0.12

SAMPLE	*SAMPLED COMPONENT*	*FACIES*	*PHASE*	*$\Delta^{13}C$ (‰ V-PDB)*	*ST. DEV $\Delta^{13}C$*	*$\Delta^{18}O$ (‰ V-PDB)*	*ST. DEV $\Delta^{18}O$*
O592	Bulk	F7	2	2.59	0.02	-0.10	0.03
O849	Bulk	F7	2	2.22	0.03	0.43	0.03
O888	Bulk	F7	2	2.05	0.04	1.19	0.06
O906	Bulk	F14	3	2.24	0.01	0.41	0.04
O906	Bulk	F14	3	2.26	0.05	0.40	0.06
O933	Bulk	F14	3	2.23	0.02	0.88	0.04
O933	Fracture	F14	3	1.51	0.03	0.38	0.02
O958	Bulk	F14	3	2.23	0.03	0.07	0.05
O958	Bulk	F14	3	2.27	0.05	0.47	0.06
O1013	Bulk	F15	3	2.18	0.03	0.24	0.02
O1046	Bulk	F15	3	1.71	0.06	0.44	0.07
O1056	Bulk	F15	3	0.22	0.03	-1.76	0.04
O1084	Bulk	F15	3	1.23	0.03	-0.82	0.06
O1092	Bulk	F15	3	0.88	0.02	-0.55	0.04
O1109	Bulk	F15	3	1.31	0.04	-0.13	0.06
O1125	Bulk	F15	3	1.50	0.05	0.29	0.02
O1125	Bulk	F15	3	1.56	0.05	0.50	0.10
V11	Bulk	F15	3	1.52	0.04	-0.19	0.05
V11	Bulk	F15	3	1.67	0.10	0.22	0.05
V10	Bulk	F15	3	1.32	0.03	-0.20	0.07
MO A	Bulk	F28	4	-0.25	0.03	0.20	0.05
MO A	Bulk	F28	4	-0.19	0.04	0.11	0.04
V9	Bulk	F28	4	1.90	0.04	-0.19	0.06
V8	Bulk	F29	4	1.65	0.03	-0.52	0.05
V6	Bulk	F36	4	0.80	0.06	-2.35	0.08
V6	Bulk	F36	4	0.84	0.04	-2.19	0.04
V5	Bulk	F36	4	1.49	0.03	-2.45	0.05
V4	Bulk	F37	4	1.11	0.01	-0.59	0.03
V3	Bulk	F37	4	2.40	0.02	1.52	0.04
V2	Bulk	F37	4	2.00	0.03	1.18	0.06
V1	Bulk	F37	4	-0.13	0.07	-0.32	0.06

Table 8.2 $\delta^{13}C$ and $\delta^{18}O$ values with standard deviations for measured samples from Mt. Oro log.

The majority of the facies from phase 1 in the Mt. Oro log are dolomitized, the one sample from facies F1 1 m above the Hercynian basement shows the lowest $\delta^{13}C$ value -9.3 ‰ and a $\delta^{18}O$ value of -4.5 ‰. The isotopic values for the peloidal packstone with *Lenticulina* (F7, phase 2) are comprised between 1.6 ‰ and 2.1 ‰ for $\delta^{13}C$ and between -0.7 ‰ and 1.2 ‰ for $\delta^{18}O$. Samples from bioclastic packstone to grainstone-rudstone with clotted peloidal micrite fragments (F8, phase 2) show a wide range of values, between -5.8 ‰ and 2.5 ‰ for $\delta^{13}C$ and between -6.0 ‰ and 0.6 ‰ for $\delta^{18}O$. The sponge-coral-microbialite boundstone (F12, phase 2) shows an isotopic composition pattern, with $\delta^{13}C$ values between -3.2 ‰ and 0.5 ‰ and $\delta^{18}O$ values between -4.2 ‰ and -2.8 ‰. The isotopic values for the grainstone with ooids, aggregate grains and oncoids (F14, phase 3) and peloidal packstone with oncoids and ooids (F15, phase 3) range from 0.2 ‰ to 2.3 ‰ $\delta^{13}C$ and from -1.8 ‰ to 0.9 ‰ $\delta^{18}O$.

The basinal lithoclastic breccia (F28, phase 4) and the mudstone, wackestone and siltstone (F29, phase 4) are characterized by $\delta^{13}C$ values between -0.2 ‰ and 1.6 ‰ and $\delta^{18}O$ values between -0.5

‰ and 0.1 ‰. The *Crescentiella* grainstone-packstone (F36, phase 4) shows $\delta^{13}C$ values ranging between 0.8 ‰ and 1.5 ‰ and $\delta^{18}O$ values between -2.5 ‰ and -2.2 ‰, whereas the crinoidal peloidal packstone-wackestone (F37, phase 4) shows a range of values between -0.1 ‰ and 2.4 ‰ for the $\delta^{13}C$ and from -0.6 ‰ to 1.5 ‰ $\delta^{18}O$. Sampled sparite from fractures shows values between -7.9 and -1.0 for $\delta^{13}C$ and between -5.0 ‰ and -3.4 ‰ for $\delta^{18}O$, with the exception of one value showing 1.5 ‰ $\delta^{13}C$ and 0.4 ‰ $\delta^{18}O$.

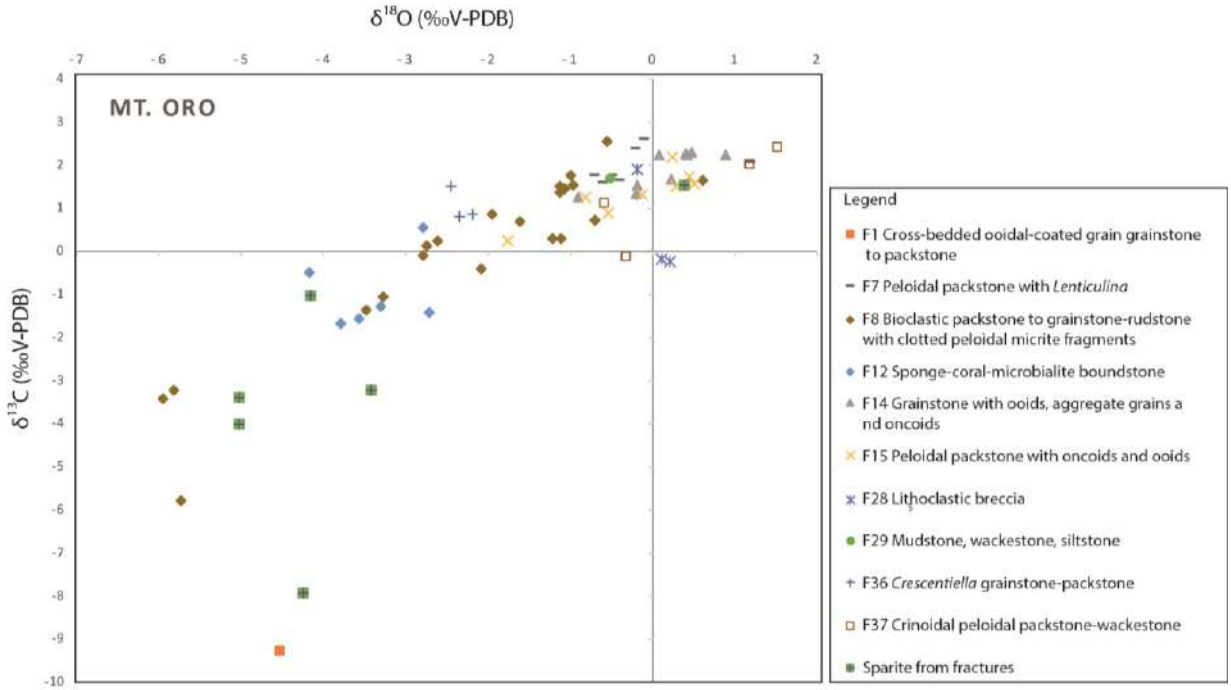

Figure 8.9 Cross-plots of $\delta^{13}C$ and $\delta^{18}O$ of the analysed bulk and skeletal grains from limestones and partially dolomitized limestones in Mt. Oro stratigraphic section according to facies types.

Sample	*Sampled Component*	*Facies*	*Phase*	*$\delta^{13}C$ (‰ V-PDB)*	*St. dev $\delta^{13}C$*	*$\delta^{18}O$ (‰ V-PDB)*	*St. dev $\delta^{18}O$*
F05	Bulk	F15	3	-0.68	0.06	-3.75	0.06
F08	Bulk	F15	3	-0.58	0.02	-2.82	0.04
F15	Bulk	F15	3	-0.53	0.10	-3.37	0.08
F30	Bulk	F15	3	-0.78	0.03	-3.25	0.04
F38	Bulk	F15	3	-1.49	0.05	-4.02	0.09
F43	Bulk	F15	3	-0.89	0.03	-3.64	0.13
F50	Bulk	F15	3	0.74	0.04	-2.02	0.04
F62	Bulk	F15	3	1.23	0.08	-1.09	0.03
F77	Bulk	F15	3	0.60	0.03	-1.90	0.03
F91	Bulk	F15	3	0.67	0.02	-2.41	0.04
F98	Bulk	F15	3	-0.40	0.01	-3.55	0.05
F111	Bulk	F15	3	-0.66	0.05	-2.81	0.06
F120	Bulk	F28	4	-0.93	0.03	-2.00	0.06
F125	Bulk	F28	4	2.06	0.05	-0.24	0.10
F126	Bulk	F29	4	1.99	0.06	0.03	0.07
F131	Bulk	F29	4	2.10	0.02	0.03	0.04
F140	Bulk	F29	4	2.17	0.04	-0.57	0.07

Sample	*Sampled Component*	*Facies*	*Phase*	*$\delta^{13}C$ (‰ V-PDB)*	*St. dev $\delta^{13}C$*	*$\delta^{18}O$ (‰ V-PDB)*	*St. dev $\delta^{18}O$*
F147	Bulk	F29	4	2.38	0.04	0.43	0.06
F147	Bulk	F29	4	2.33	0.05	0.20	0.04
F160	Bulk	F29	4	0.92	0.04	-1.36	0.07
F163	Bulk	F29	4	0.98	0.05	-0.34	0.06
F165A	Bulk	F35	4	1.27	0.07	-1.96	0.11
F165B	Bulk	F35	4	1.00	0.12	-1.68	0.14
F172	Bulk	F35	4	0.25	0.05	-3.20	0.05

Table 8.3 $\delta^{13}C$ and $\delta^{18}O$ values with standard deviations for measured samples from Franciscu log.

In the Franciscu stratigraphic log (Fig. 8.10 and Table 8.3), the $\delta^{13}C$ values range from -1.5 ‰ to 2.4 ‰, whereas $\delta^{18}O$ values between -4.0 ‰ and 0.4 ‰ (Fig. 8.11). The depositional facies from this log show specific isotopic patterns. In the peloidal packstone with oncoids and ooids (F15, phase 3), $\delta^{13}C$ values range between -1.5 ‰ and 1.2 ‰, whereas $\delta^{18}O$ values are between -4.0 ‰ and -1.1 ‰. Two samples of facies lithoclastic breccia (F28, phase 4) shows $\delta^{13}C$ values between -1.0 ‰ and 2.0 ‰, and $\delta^{18}O$ values between -2.0 ‰ and -0.2 ‰. The mudstone, wackestone and siltstone (F29, phase 4) shows $\delta^{13}C$ values varying between 1.0 ‰ and 2.4 ‰, whereas $\delta^{18}O$ values varies between -1.4 ‰ and 0.4 ‰. The breccia with radiaxial fibrous calcite cement (F35, phase 4) shows $\delta^{13}C$ values ranging between 0.3 ‰ and 1.3 ‰ and $\delta^{18}O$ values between -3.2 ‰ and -1.7 ‰.

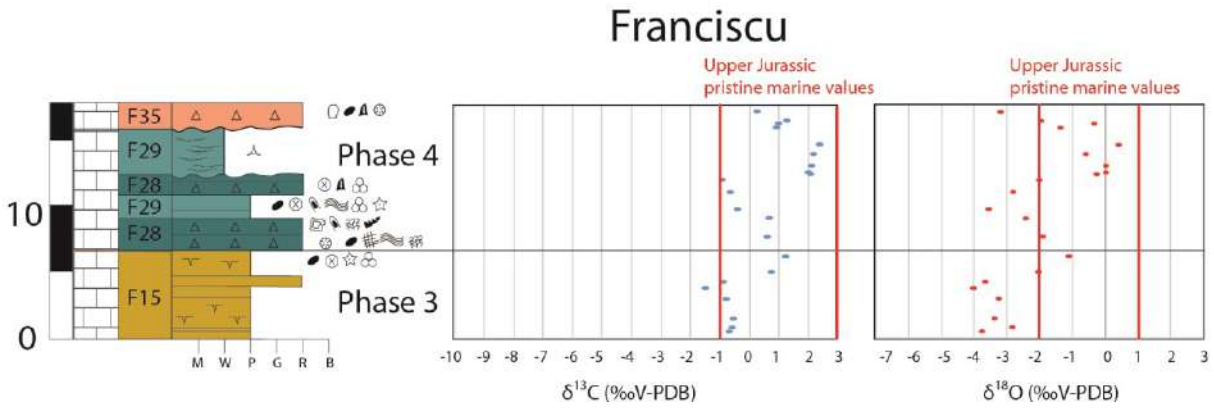

Figure 8.10 Franciscu stratigraphic log with $\delta^{13}C$ and $\delta^{18}O$ plotted values. Red lines represent the field of Upper Jurassic pristine marine values based on published stable-isotope compositions obtained from well-preserved fossils (particularly belemnites) in Jenkyns et al. (2002), Weissert and Erba (2004), Wierzbowski et al. (2004), Brigaud et al. (2008), Nunn et al. (2009), Price and Rogov (2009), Nunn and Price (2010).

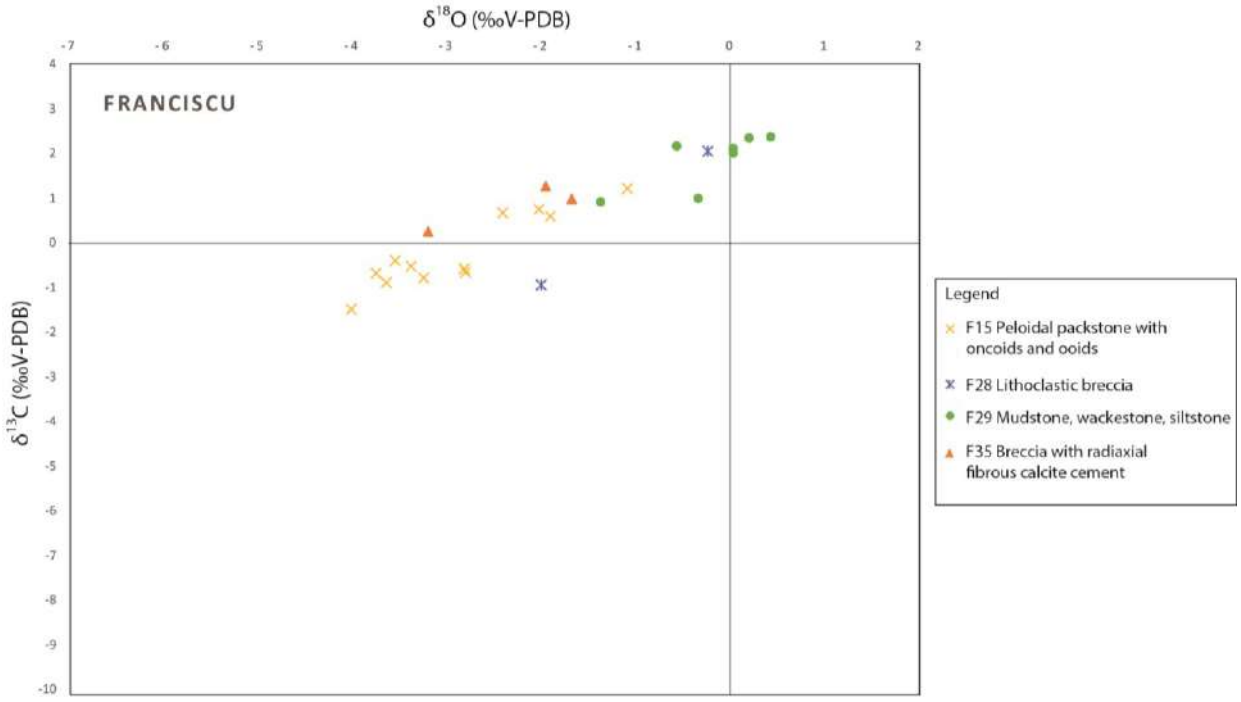

Figure 8.11 Cross-plots of $\delta^{13}C$ and $\delta^{18}O$ of the analysed bulk and skeletal grains from limestones and partially dolomitized limestones in Franciscu stratigraphic section according to facies types.

Sample	*Sampled Component*	*Facies*	*Phase*	*$\delta^{13}C$ (‰ V-PDB)*	*St. dev $\delta^{13}C$*	*$\delta^{18}O$ (‰ V-PDB)*	*St. dev $\delta^{18}O$*
R00	Bulk	F4	1	1.31	0.07	-0.26	0.07
R11	Bulk	F4	1	0.91	0.03	-0.16	0.05
R11	Bulk	F4	1	0.94	0.03	-0.02	0.07
R85	Bulk	F4	1	1.69	0.05	-0.68	0.06
R112A	Bulk	F4	1	2.58	0.02	2.07	0.05
R112B	Fracture	F4	1	-0.29	0.04	-1.49	0.04
R142	Bulk	F4	1	2.40	0.03	-0.06	0.05
R155	Bulk	DOL	1	3.03	0.04	1.16	0.05
R205	Bulk	F4	1	-3.69	0.05	-5.65	0.04
R216	Bulk	F4	1	1.40	0.03	-1.21	0.04
R225	Bulk	F3	1	0.60	0.03	-2.64	0.04
R312A	Bulk	F1	1	0.77	0.05	-2.25	0.04
R312B	Bulk	F1	1	0.64	0.06	-2.29	0.10
R312C	Bulk	F1	1	0.88	0.03	-0.77	0.04
R367	Bulk	F1	1	-0.70	0.04	-3.10	0.07
R380	Bulk	F8	2	0.30	0.02	-2.56	0.08
R398	Bulk	F8	2	-0.62	0.03	-3.90	0.03
R406A	Bulk	F8	2	-0.71	0.03	-3.85	0.03
R406B	Fracture	F8	2	0.10	0.03	-3.22	0.06
R428	Bulk	F8	2	-0.78	0.03	-3.16	0.04
R437	Bulk	F8	2	-0.47	0.03	-3.62	0.03
R445	Bulk	F5	2	0.52	0.02	-4.10	0.05
R451	Bulk	F5	2	0.16	0.02	-3.51	0.03
R466	Bulk	F5	2	0.53	0.03	-2.25	0.07
R473	Bulk	F5	2	1.29	0.02	-3.61	0.05
R479	Bulk	F6	2	2.21	0.02	-1.55	0.06
R490	Bulk	F6	2	1.98	0.04	-2.62	0.05

Sample	*Sampled Component*	*Facies*	*Phase*	*$\delta^{13}C$ (‰ V-PDB)*	*St. dev $\delta^{13}C$*	*$\delta^{18}O$ (‰ V-PDB)*	*St. dev $\delta^{18}O$*
R501	Bulk	F6	2	2.25	0.02	-1.20	0.03
R509	Bulk	F11	2	0.82	0.05	-3.37	0.05
R515A	Bulk	F11	2	0.85	0.02	-3.94	0.04
R515B	Bulk	F11	2	-0.04	0.03	-4.46	0.08
R523	Bulk	F11	2	0.97	0.04	-2.48	0.05
R527	Bulk	F11	2	0.26	0.03	-2.84	0.03
R540	Bulk	F8	2	0.91	0.04	-3.55	0.05
R546	Bulk	F8	2	1.58	0.03	-2.38	0.04
R548A	Bulk	F11	2	1.31	0.02	-2.23	0.02
R548B	Coral	F11	2	0.69	0.04	-3.02	0.07
R566	Bulk	F8	2	1.12	0.04	-2.90	0.09
R566	Bulk	F8	2	1.20	0.04	-3.17	0.06
R572	Bulk	F8	2	1.29	0.03	-2.80	0.04
R603	Bulk	F5	2	0.41	0.03	-2.28	0.04
R615A	Bulk	F11	2	0.31	0.05	-3.09	0.07
R615B	Calc sponge	F11	2	0.45	0.06	-3.64	0.04
R645	Bulk	F8	2	1.63	0.05	-0.62	0.07
R645A	Bulk	F8	2	0.41	0.03	-3.08	0.04
R645A	Bulk	F8	2	0.45	0.03	-2.57	0.07
R685	Bulk	F6	2	1.41	0.03	-2.03	0.03
R710	Bulk	F8	2	-1.25	0.03	-3.75	0.06
R716	Bulk	F11	2	1.97	0.04	-2.04	0.04
R740	Bulk	F5	2	-0.11	0.02	-3.36	0.06

Table 8.4 $\delta^{13}C$ and $\delta^{18}O$ values with standard deviations for measured samples from Genna Ramene log.

In the Genna Ramene stratigraphic log (Fig. 8.3 and Table 8.4), the $\delta^{13}C$ values varies from -3.7 ‰ to 2.6 ‰, whereas $\delta^{18}O$ values between -5.7 ‰ and 2.1 ‰ (Fig. 8.12). The cross-plot of the $\delta^{13}C$ and $\delta^{18}O$ values per facies types indicates differentiated isotopic signatures. The isotopic values for cross-bedded ooidal-coated grain grainstone to packstone (F1, phase 1) and peloidal packstone with ooids and echinoderms (F3) range between -0.7 ‰ and 0.8 ‰ for $\delta^{13}C$ and between -3.1‰ and -0.8 ‰ for $\delta^{18}O$. The peloidal packstone with *Lenticulina* (F4) shows a different isotopic signature with the majority of values varying between 0.6 ‰ and 2.4 ‰ for $\delta^{13}C$ and between -2.6 ‰ and -0.0 ‰ for $\delta^{18}O$ with the exception of two samples showing low, negative (-3.7; -5.7) or high, positive (2.6; 2.1) values.

The ooidal grainstone to packstone with intraclasts and bioclasts (F5, phase 2), peloidal packstone with reworked intraclasts, bioclasts and coated grains (F6, phase 2) and bioclastic packstone to grainstone-rudstone with clotted peloidal micrite fragments (F8, phase 2) are comprised between -1.3 ‰ and 2.3 ‰ for $\delta^{13}C$ and between -4.5 ‰ and -0.6 ‰ for $\delta^{18}O$. Within this trend, two defined isotopic patterns can be identified for facies F5 and F6. Samples from facies F5 show $\delta^{13}C$ values between -0.1 ‰ and 1.3 ‰ and $\delta^{18}O$ values between -4.1 ‰ and -2.3 ‰. Instead, facies F6 shows $\delta^{13}C$ values from 1.4 ‰ to 2.3 ‰ and $\delta^{18}O$ values from -2.6 ‰ and -1.2 ‰. Samples from bulk and coral and calcareous sponge fragments from the coral-calcareous sponge-diceratid boundstone (F11) show isotopic signature between -0.0 ‰ and 2.0 ‰ for $\delta^{13}C$ and -4.5 ‰ and -2.0 ‰ for $\delta^{18}O$.

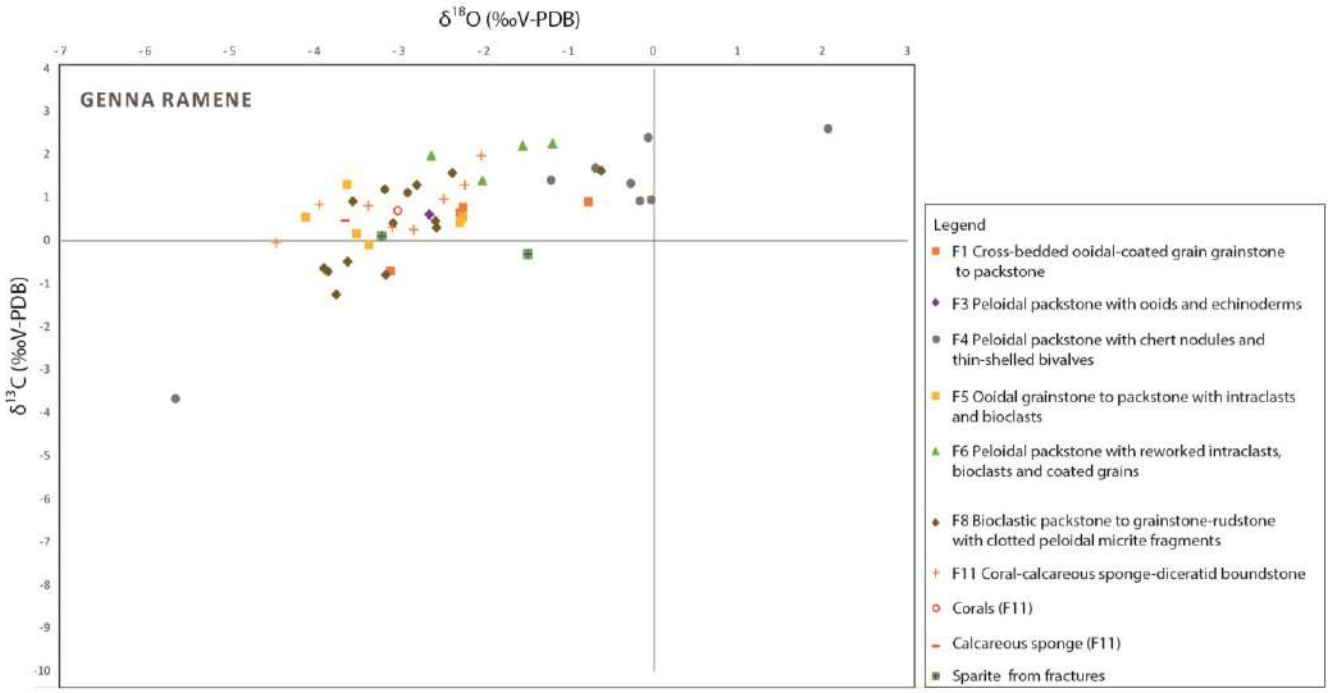

Figure 8.12 Cross-plots of $\delta^{13}C$ and $\delta^{18}O$ of the analysed bulk and skeletal grains from limestones and partially dolomitized limestones in Genna Ramene stratigraphic section according to facies types.

In the Genna scalas log (Table 8.5) three partially dolomitized samples of cross-bedded ooidal-coated grain grainstone to packstone (F1, phase 1) and cross-laminated echinoderm packstone to grainstone (F2, phase 1) were analysed. The isotopic values are comprised between 0.4 ‰ and 2.5 ‰ for $\delta^{13}C$ and between -0.2 ‰ and 0.5 ‰ for $\delta^{18}O$.

Sample	*Sampled Component*	*Facies*	*Phase*	*$\delta^{13}C$ (‰ V-PDB)*	*St. dev $\delta^{13}C$*	***$\Delta^{18}O$ (‰ V-PDB)***	***ST. DEV $\Delta^{18}O$***
SK03	Bulk	F1	1	0.40	0.03	-0.17	0.05
SK76	Bulk	F2	1	1.43	0.03	0.02	0.05
SK200	Bulk	F1	1	2.54	0.05	0.53	0.04
SK390	Bulk	DOL	1	-2.01	0.05	-5.17	0.04

Table 8.5 $\delta^{13}C$ and $\delta^{18}O$ values with standard deviations for measured samples from Genna Scalas log

In the Ghispali stratigraphic log (Table 8.6) three limestone samples of rudstone to packstone with *Clypeina jurassica* (F32, phase 4) were analysed and shows $\delta^{13}C$ values from 2.0 ‰ to 2.9 ‰ and $\delta^{18}O$ values between -1.7 ‰ and 1.8 ‰.

SAMPLE	*SAMPLED COMPONENT*	*FACIES*	*PHASE*	*$\Delta^{13}C$ (‰ V-PDB)*	*ST. DEV $\Delta^{13}C$*	*$\Delta^{18}O$ (‰ V-PDB)*	*ST. DEV $\Delta^{18}O$*
G161	Bulk	F31	4	2.59	0.06	3.07	0.08
G170	Bulk	F32	4	2.87	0.07	1.78	0.06
G186A	Bulk	F32	4	2.03	0.05	-1.74	0.07
G186B	Bulk	F32	4	2.87	0.04	1.56	0.04
G255	Bulk	F31	4	2.92	0.03	1.19	0.04
G255	Bulk	F31	4	2.92	0.04	1.09	0.05
G297A	Bulk	F31	4	1.87	0.03	-3.44	0.06
G297B	Bulk	F31	4	2.74	0.01	0.65	0.06

Table 8.6 $\delta^{13}C$ and $\delta^{18}O$ values with standard deviations for measured samples from Ghispali log.

SAMPLE	*SAMPLED COMPONENT*	*FACIES*	*PHASE*	*$\Delta^{13}C$ (‰ V-PDB)*	*ST. DEV $\Delta^{13}C$*	*$\Delta^{18}O$ (‰ V-PDB)*	*ST. DEV $\Delta^{18}O$*
GS06	Bulk	DOL	1	2.45	0.03	0.28	0.03
GS23A	Bulk	F1	1	-8.51	0.03	-5.11	0.03
GS23B	Bulk	F1	1	-9.09	0.03	-4.69	0.03
GS55	Bulk	F1	1	-7.81	0.03	-5.86	0.03
GS107C	Bulk	F1	1	0.18	0.08	-2.93	0.10
GS130	Bulk	F1	1	-2.06	0.03	-4.99	0.03
GS257	Bulk	F1	1	0.63	0.04	-3.00	0.01
GS257	Bulk	F1	1	0.61	0.03	-2.92	0.02
GS670BA	Bulk	F1	1	2.45	0.03	-1.32	0.05
GS670BB	Bulk	F1	1	0.77	0.01	-2.81	0.05
GS931	Bulk	F1	1	0.95	0.04	-3.07	0.04
GS1830	Bulk	F1	1	-0.44	0.02	-5.23	0.04
GS201BA	Bulk	F1	1	-1.97	0.04	-4.40	0.04
GS201BB	Bulk	F9	2	-2.22	0.05	-4.68	0.05
GS2120A	Coral	F10	2	1.51	0.03	-2.10	0.02
GS2120B	Bulk	F10	2	0.72	0.03	-3.25	0.04
GS2294	Bulk	F10	2	1.41	0.05	-1.51	0.06
GS2296A	Bulk	F17	3	1.24	0.06	-2.49	0.05
GS2296B	Bulk	F17	3	1.45	0.04	-1.80	0.04
GS2325	Bulk	F17	3	-2.54	0.07	-2.82	0.09
GS2328	Bulk	F17	3	-1.87	0.03	-2.48	0.03
GS2354	Bulk	F19	3	0.27	0.04	-1.11	0.04
GS2361	Bulk	F19	3	1.25	0.02	-0.76	0.05
GS2362	Bulk	F19	3	1.30	0.06	-1.60	0.06
GS2390	Bulk	F19	3	1.38	0.05	-1.43	0.03
GS2405	Bulk	F19	3	-0.48	0.02	-0.80	0.04
GS2444A	Bulk	F20	3	0.44	0.03	-0.18	0.03
GS2444B	Bulk	F20	3	0.02	0.06	-0.86	0.05
GS2533	Bulk	F21	3	2.35	0.08	-0.78	0.07
GS2612	Bulk	F22	3	1.77	0.07	-2.22	0.05
GS2622	Bulk	F26	3	2.39	0.02	-0.51	0.05
GS2670	Bulk	F27	3	0.10	0.05	-0.83	0.04
GS2674	Bulk	F27	3	2.49	0.04	-0.93	0.09
GS2736	Bulk	F24	3	1.76	0.03	-1.80	0.04
GS2737	Bulk	F20	3	2.04	0.05	-1.05	0.04
GS2738B	Bulk	F20	3	1.45	0.02	-1.40	0.03
GS2739A	Bulk	F18	3	1.80	0.08	-0.10	0.05
GS2739B	Bulk	F18	3	1.71	0.03	0.09	0.03
GS2750	Bulk	F18	3	1.42	0.04	-0.23	0.05
GS2760	Bulk	F18	3	0.21	0.03	-1.83	0.05
GS2810	Bulk	F30	4	2.38	0.05	-1.30	0.07
GS2820	Bulk	F31	4	2.97	0.04	3.55	0.04

SAMPLE	*SAMPLED COMPONENT*	*FACIES*	*PHASE*	*$\Delta^{13}C$ (‰ V-PDB)*	*ST. DEV $\Delta^{13}C$*	*$\Delta^{18}O$ (‰ V-PDB)*	*ST. DEV $\Delta^{18}O$*
GS2831	Bulk	F34	4	2.22	0.06	-3.48	0.06
GS2866	Bulk	F32	4	0.02	0.02	-2.74	0.05
GS2899	Bulk	F33	4	1.61	0.04	-2.10	0.03
GS2986	Bulk	F33	4	2.96	0.10	0.07	0.03
GS3020	Bulk	F33	4	2.78	0.04	0.39	0.06

Table 8.7 $\delta^{13}C$ and $\delta^{18}O$ values with standard deviations for measured samples from Genna Silana log.

In samples from Genna Silana stratigraphic log (Fig. 8.2 and Table 8.7) $\delta^{13}C$ values range from -9.1 ‰ to 3.0 ‰ and $\delta^{18}O$ varies between -5.9 ‰ and 0.4 ‰ (Fig. 8.13). Cross-bedded ooidal-coated grain grainstone to packstone (F1, phase 1) samples show a wide pattern, with $\delta^{13}C$ values from -9.1 ‰ to 2.5 ‰ and $\delta^{18}O$ values between -5.9 ‰ and -1.3 ‰. The sample analysed from coral-stromatoporoid rudstone-grainstone (F9, phase 2) shows $\delta^{13}C$ of -0.4 ‰ and $\delta^{18}O$ of -5.2 ‰. Coral-stromatoporoid boundstone (F10, phase 2) bulk samples a few metres below the subaerial exposure surface (top of phase 2) show isotopic signature between 0.7 ‰ and 1.4 ‰ for $\delta^{13}C$ and -3.3 ‰ and -1.5 ‰ for $\delta^{18}O$, whereas a coral fragment from facies F10 shows 1.5 ‰ for $\delta^{13}C$ and -2.1 ‰ for $\delta^{18}O$. The majority of values from the peritidal and inner platform phase 3 and phase 4 facies (F17, F18, F19, F20, F21, F22, F24, F26, F27, F30, F32, F33 and F34) show $\delta^{13}C$ between -0.5 ‰ and 3.0 ‰ and $\delta^{18}O$ between -3.5 ‰ and 0.4 ‰. The exception are two samples from packstone-grainstone-rudstone with corals, pisoids and black pebbles (F17, phase 3) that show different $\delta^{13}C$ values ranging from -2.5 ‰ to -1.9 ‰ at the top of the subaerial exposure surface (boundary between phase 3 and phase 4).

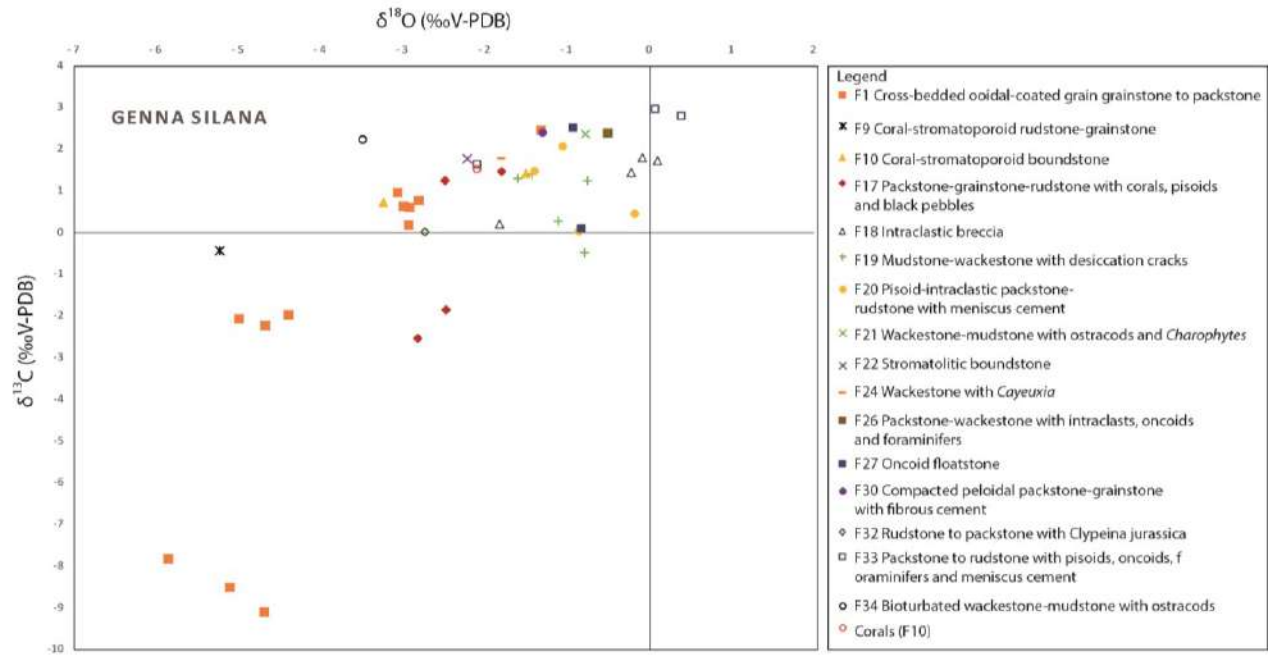

Figure 8.13 Cross-plots of $\delta^{13}C$ and $\delta^{18}O$ of the analysed bulk and skeletal grains from limestones and partially dolomitized limestones in Genna Silana stratigraphic section according to facies types.

Sample	*Sampled Component*	*Facies*	*Phase*	*$\delta^{13}C$ (‰ V-PDB)*	*St. dev $\delta^{13}C$*	*$\delta^{18}O$ (‰ V-PDB)*	*St. dev $\delta^{18}O$*
CO29BULK	Bulk	F5	2	-0.98	0.06	-2.93	0.10
CO29FRACT	Fracture	F5	2	-0.09	0.06	-5.73	0.03
CO83BULK	Bulk	F10	2	-0.97	0.05	-3.99	0.06
CO83FRACT	Fracture	F10	2	-1.16	0.01	-6.20	0.05
CO110	Bulk	F10	2	-1.19	0.06	-3.93	0.08
CO150	Bulk	F10	2	-0.93	0.06	-3.12	0.06
CO174	Bulk	F17	3	-1.36	0.03	-3.87	0.05
CO174	Bulk	F17	3	-1.37	0.05	-3.95	0.05
CO185	Bulk	F25	3	0.01	0.04	-2.11	0.10
CO218	Bulk	F19	3	-1.41	0.03	0.11	0.03
CO476	Bulk	F26	3	1.58	0.06	-1.07	0.09
CO495	Bulk	F18	3	1.62	0.05	-1.46	0.14

Table 8.8 $\delta^{13}C$ and $\delta^{18}O$ values with standard deviations for measured samples from Codula Orbisi log.

Samples from the Codula Orbisi log (Fig. 8.14, Table 8.8) are characterized by different isotopic signatures depending on the depositional facies. The stable C and O isotope values vary between -1.4 ‰ and 1.6 ‰ for $\delta^{13}C$ and between -6.2 ‰ and 0.1 ‰ for $\delta^{18}O$ (Fig. 8.15).

For the ooidal grainstone to packstone with intraclasts and bioclasts (F5, phase 2) and coral-stromatoporoid boundstone (F10, phase 2) the values range between -1.2 ‰ and -0.9 ‰ for $\delta^{13}C$ and -4.0 ‰ and -2.9 ‰ for $\delta^{18}O$. The packstone-grainstone-rudstone with corals, pisoids and black

pebbles (F17, phase 3) above the subaerial exposure surface (end of phase 2) shows an isotopic signature with $\delta^{13}C$ of -1.3 ‰ and $\delta^{18}O$ of -3.9 ‰. The isotopic values for peritidal facies deposited during phase 3 (F18, F19, F25, F26) are comprised between -1.4 ‰ and 1.6 ‰ for $\delta^{13}C$ and between -2.1 ‰ and 0.1 ‰ for $\delta^{18}O$. Sparite sampled from fractures shows a distinctive isotopic signature with $\delta^{13}C$ from -1.2 ‰ and -0.1 ‰ and $\delta^{18}O$ from -6.2 ‰ and -5.7 ‰.

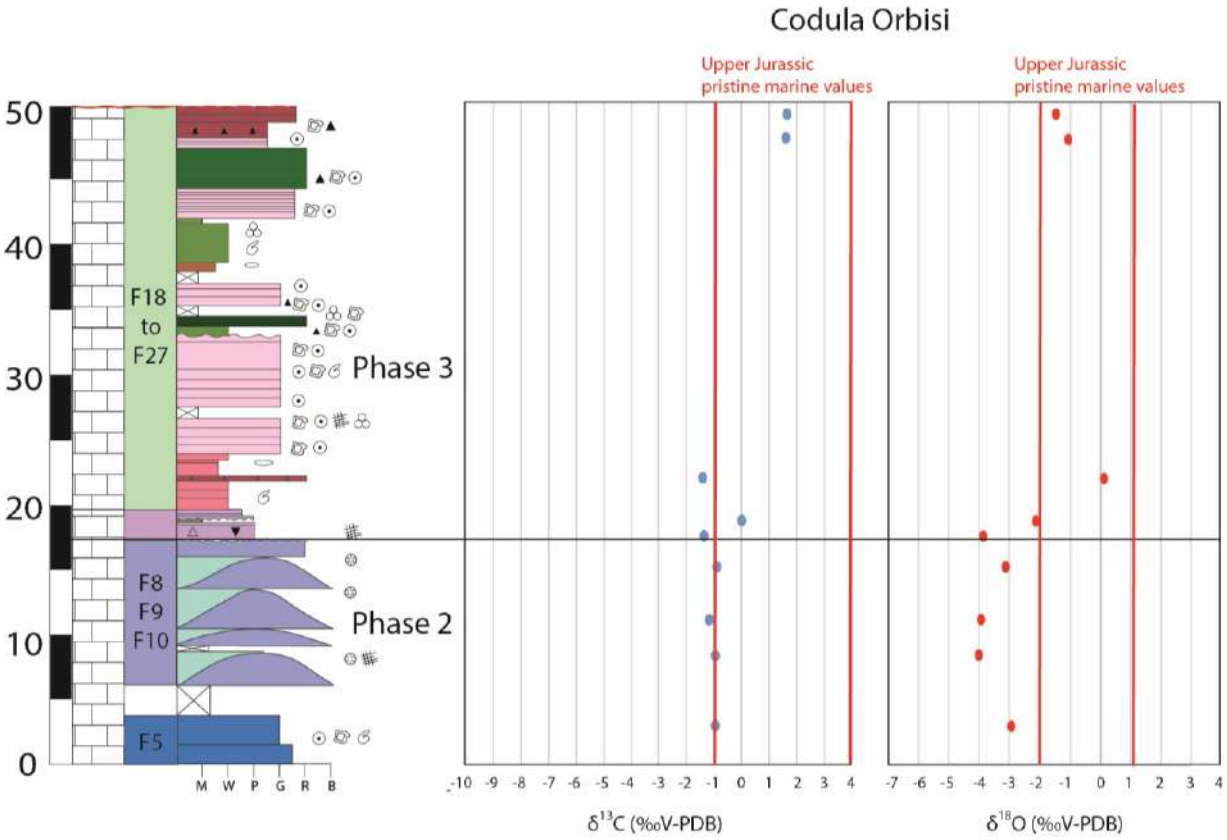

Figure 8.14 Codula Orbisi stratigraphic log with $\delta^{13}C$ and $\delta^{18}O$ plotted values. Red lines represent the field of Upper Jurassic pristine marine values based on published stable-isotope compositions obtained from well-preserved fossils (particularly belemnites) in Jenkyns et al. (2002), Weissert and Erba (2004), Wierzbowski et al. (2004), Brigaud et al. (2008), Nunn et al. (2009), Price and Rogov (2009), Nunn and Price (2010).

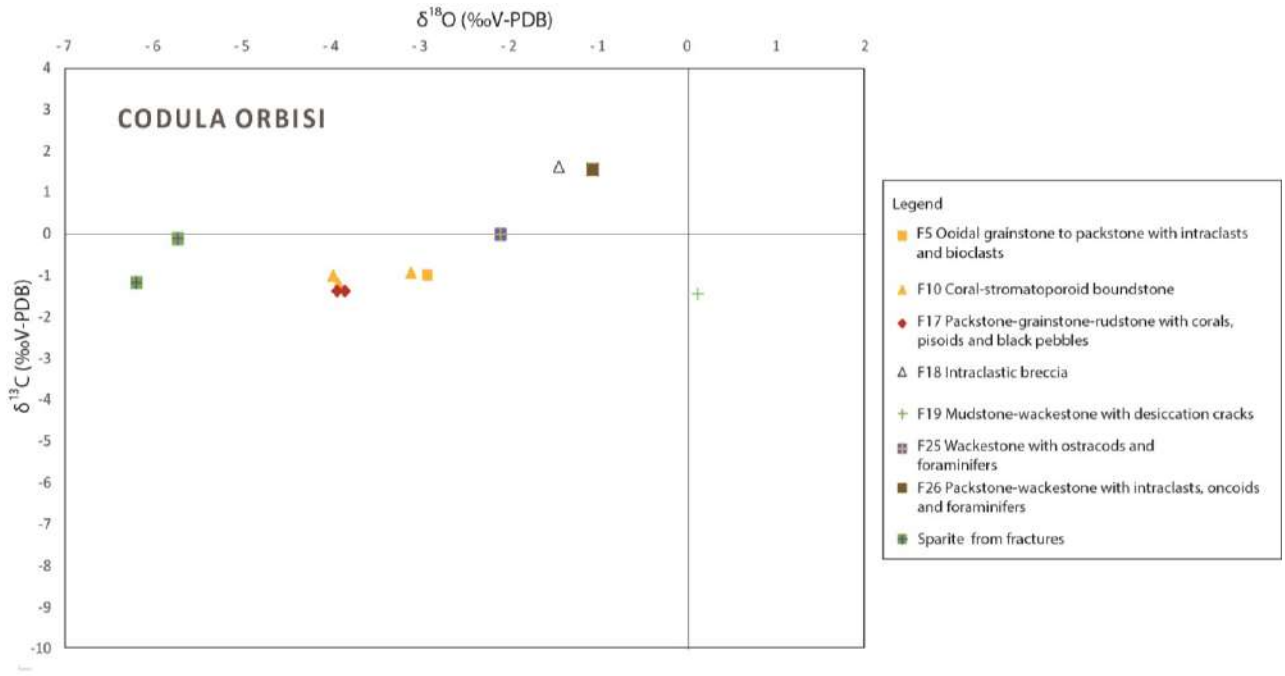

Figure 8.15 Cross-plots of $\delta^{13}C$ and $\delta^{18}O$ of the analysed bulk and skeletal grains from limestones and partially dolomitized limestones in Codula Orbisi stratigraphic section according to facies types.

Sample	*Sampled Component*	*Facies*	*Phase*	*$\delta^{13}C$ (‰ V-PDB)*	*St. dev $\delta^{13}C$*	*$\delta^{18}O$ (‰ V-PDB)*	*St. dev $\delta^{18}O$*
I34	Bulk	F23	3	2.06	0.08	-1.96	0.03
I45	Bulk	F16	3	1.70	0.02	-0.44	0.03
I174	Bulk	F20	3	2.30	0.02	-1.45	0.02
I198	Bulk	F23	3	1.64	0.06	-1.75	0.07
I247	Bulk	F22	3	0.47	0.06	-2.00	0.08
I312	Bulk	F22	3	-0.26	0.08	-3.65	0.08
I313	Bulk	F19	3	-1.72	0.04	-1.70	0.07
I424	Bulk	F18	3	2.16	0.04	0.69	0.06
I426	Bulk	F23	3	-0.42	0.03	-3.39	0.04
I480	Bulk	F27	3	1.83	0.02	-2.51	0.03
I501	Bulk	F23	3	-0.19	0.03	-3.55	0.04
I524A	Bulk	F22	3	1.49	0.03	-1.62	0.06
I524B	Bulk	F22	3	-1.73	0.01	-4.95	0.04
I537	Bulk	F18	3	2.06	0.04	0.47	0.04
IS273	Bulk	F10	2	-0.87	0.09	-5.62	0.09
IS276	Bulk	F25	3	-1.22	0.04	-1.68	0.05
IS287	Bulk	F16	3	-0.99	0.04	-1.19	0.05
IS291	Bulk	F16	3	1.45	0.03	-2.25	0.03
IS309A	Bulk	F16	3	-0.99	0.02	-0.54	0.04

Table 8.9 $\delta^{13}C$ and $\delta^{18}O$ values with standard deviations for measured samples from Iscra log.

In samples from the Iscra stratigraphic log (Fig. 8.7 and Table 8.9) $\delta^{13}C$ values are between -1.7 ‰ and 2.3 ‰ and $\delta^{18}O$ values between -5.6 ‰ and 0.7 ‰.

The one sample from coral-stromatoporoid boundstone (F10, phase 2) show $\delta^{13}C$ of -0.9 ‰ and $\delta^{18}O$ of -5.6 ‰ (Fig. 8.16). Some samples from the lithoclastic breccia to conglomerate with black pebbles (F16, phase 3), the mudstone-wackestone with desiccation cracks (F19) and wackestone with ostracods and foraminifers (F25) show a particular isotopic signature with $\delta^{13}C$ between -1.7 ‰ and -1.0 ‰ and $\delta^{18}O$ between-1.7 ‰ and -0.5 ‰. Some samples from the stromatolitic boundstone (F22, phase 3) and the microbial boundstone (F23, phase 3) show $\delta^{13}C$ between -1.7 ‰ and -0.2 ‰ and $\delta^{18}O$ from -4.9 ‰ to -3.4 ‰. Samples from the intraclastic breccia (F18, phase 3) show $\delta^{13}C$ values between 2.0 ‰ and 2.2 ‰ and $\delta^{18}O$ from 0.5 ‰ to 0.7 ‰.

The other samples from phase 3 facies (F16, F20, F22, F23 and F27) show isotopic values from 0.5 ‰ to 2.3 ‰ for $\delta^{13}C$ between and from -2.5 ‰ to -0.5 ‰ for $\delta^{18}O$.

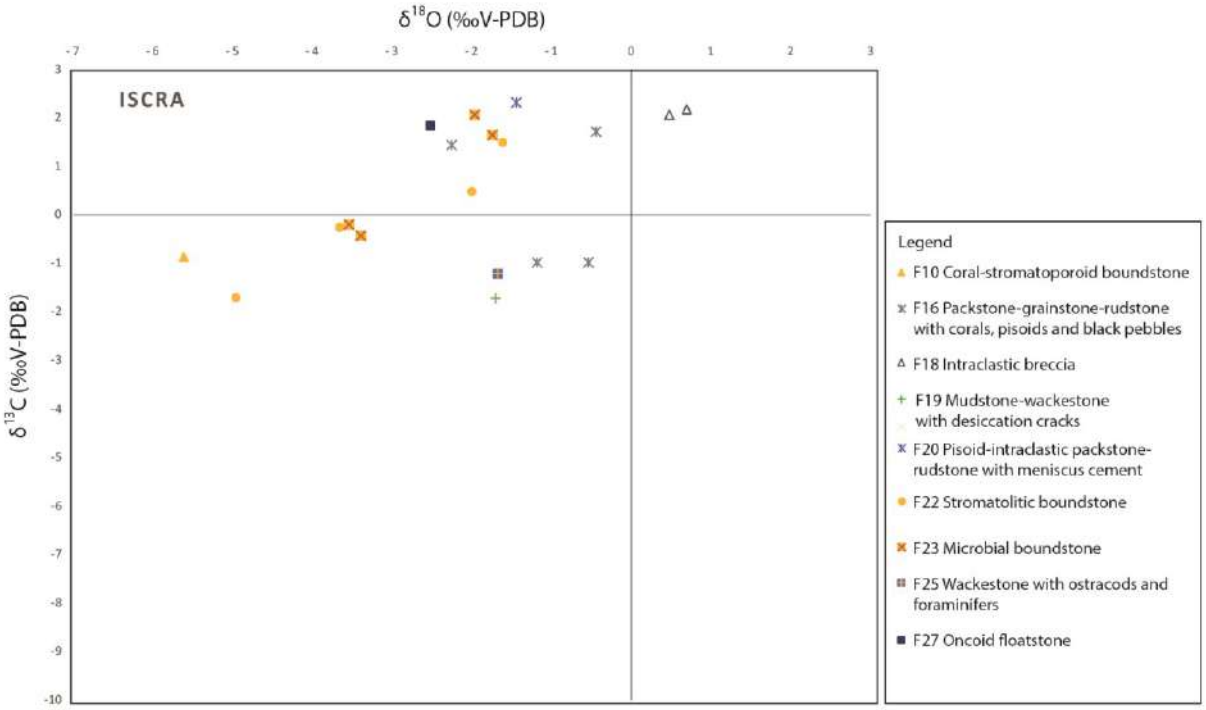

Figure 8.16 Cross-plots of $\delta^{13}C$ and $\delta^{18}O$ of the analysed bulk and skeletal grains from limestones and partially dolomitized limestones in Iscra stratigraphic section according to facies types.

In the Punta Mureddu stratigraphic log (Fig. 8.17, Table 8.10) all samples from intraclastic breccia (F18, phase 3), wackestone with ostracods and foraminifers (F25, phase 4) and rudstone to packstone with *Clypeina jurassica* (F32, phase 4) show $\delta^{13}C$ between 1.4 ‰ and 2.4 ‰ and $\delta^{18}O$ from -1.4 ‰ to 0.2 ‰ (Fig. 8.10).

Sample	*Sampled Component*	*Facies*	***PHASE***	***Δ^{13}C (‰ V-PDB)***	***ST. DEV Δ^{13}C***	***Δ^{18}O (‰ V-PDB)***	***ST. DEV Δ^{18}O***
BA1A	Bulk	F25	3	1.45	0.05	0.17	0.06
BA1B	Intraclast	F25	3	1.37	0.07	-0.71	0.07
BA2	Bulk	F32	4	2.39	0.04	-0.69	0.03
BA9	Bulk	F18	3	1.75	0.04	0.06	0.10
BA11	Bulk	F25	3	2.31	0.06	-1.35	0.05

Table 8.10 $\delta^{13}C$ and $\delta^{18}O$ values with standard deviations for measured samples from Punta Mureddu log.

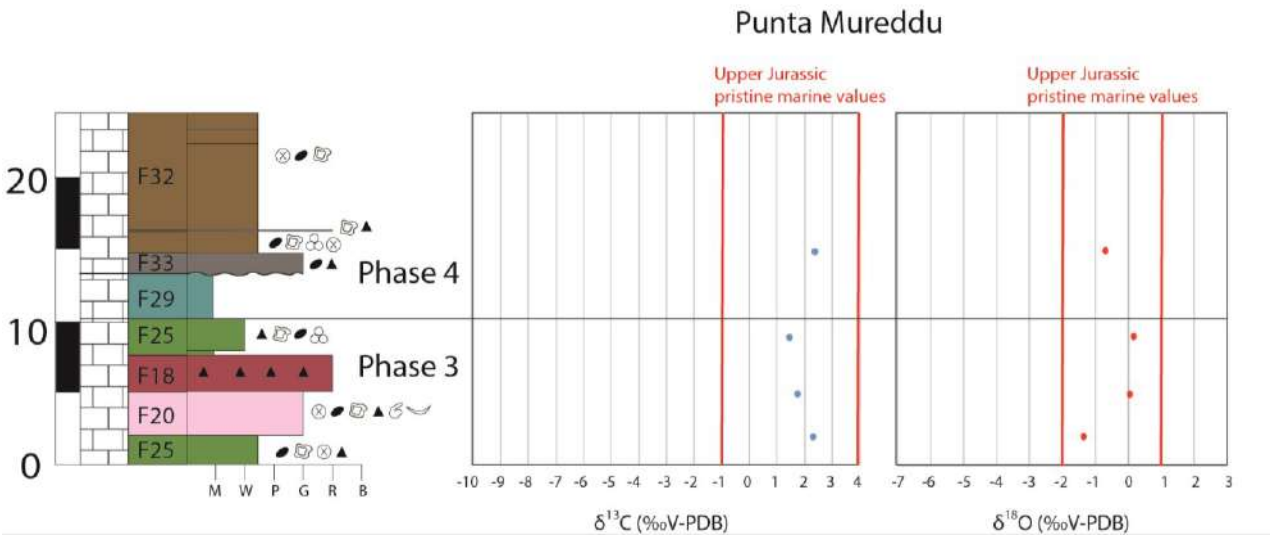

Figure 8.17 Punta Mureddu stratigraphic log with $\delta^{13}C$ and $\delta^{18}O$ plotted values. Red lines represent the field of Upper Jurassic pristine marine values based on published stable-isotope compositions obtained from well-preserved fossils (particularly belemnites) in Jenkyns et al. (2002), Weissert and Erba (2004), Wierzbowski et al. (2004), Brigaud et al. (2008), Nunn et al. (2009), Price and Rogov (2009), Nunn and Price (2010).

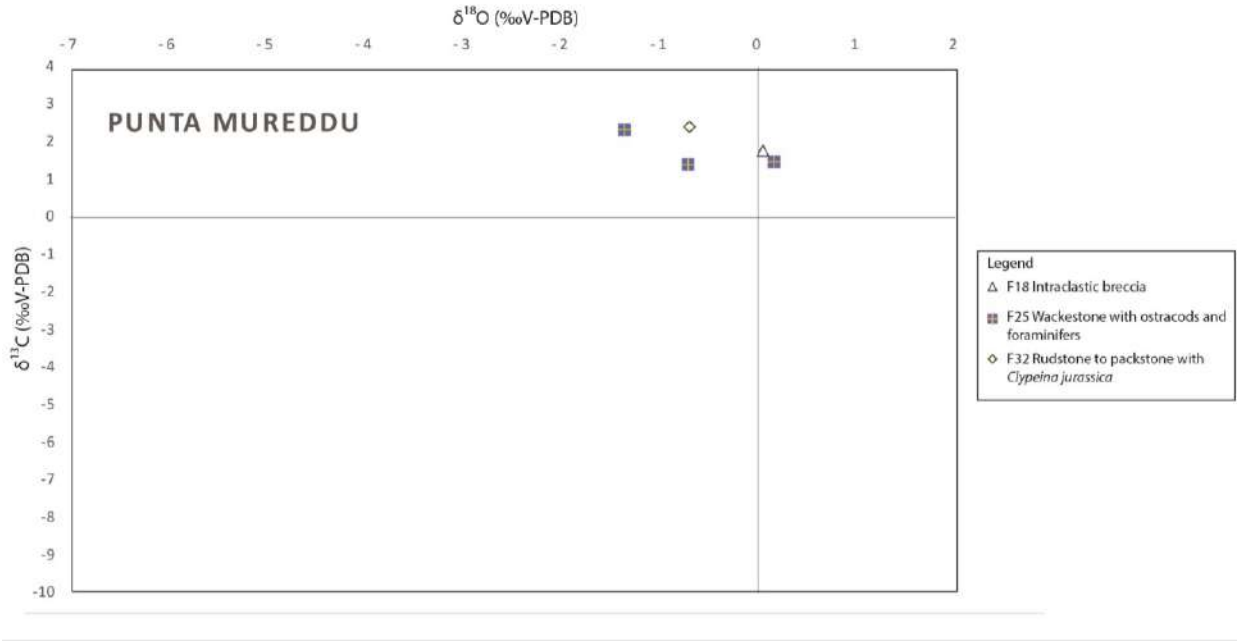

Figure 8.18 Cross-plots of $\delta^{13}C$ and $\delta^{18}O$ of the analysed bulk and skeletal grains from limestones and partially dolomitized limestones in Codula Orbisi stratigraphic section according to facies types.

8.3.3 Dolomite stable carbon and oxygen analyses

Carbon and oxygen stable isotope analyses performed on bulk dolostone samples are reported in Table 8.11 and plotted in Figure 8.19.

Sample	*Sampled Component*	*Dol Type*	*Phase*	*$\delta^{13}C$ (‰ V-PDB)*	*St. dev $\delta^{13}C$*	*$\delta^{18}O$ (‰ V-PDB)*	*St. dev $\delta^{18}O$*
GS06	Bulk	DOL-1, DOL2	1	2.45	0.03	0.28	0.03
GS2820	Bulk	DOL-3, DOL-4, DOL-5	4	2.97	0.04	3.55	0.04
G161	Bulk	DOL-3, DOL-4, DOL-5	4	2.59	0.06	3.07	0.08
G170	Bulk	DOL-3, DOL-4, DOL-5	4	2.87	0.07	1.78	0.06
G186A	Bulk	DOL-3, DOL-4, DOL-5	4	2.03	0.05	-1.74	0.07
G186B	Bulk	DOL-3, DOL-4, DOL-5	4	2.87	0.04	1.56	0.04
G255	Bulk	DOL-3, DOL-4, DOL-5	4	2.92	0.03	1.19	0.04
G255	Bulk	DOL-3, DOL-4, DOL-5	4	2.92	0.04	1.09	0.05
G297A	Bulk	DOL-3, DOL-4, DOL-5	4	1.87	0.03	-3.44	0.06
G297B	Bulk	DOL-3, DOL-4, DOL-5	4	2.74	0.01	0.65	0.06
O29	Bulk	DOL-1, DOL-2	1	1.44	0.04	0.02	0.04
O41A	Bulk	DOL-1, DOL-2	1	-7.47	0.05	-4.05	0.06
O41B	Bulk	DOL-1, DOL-2	1	-4.13	0.04	-2.81	0.05
O55A	Bulk	DOL-1, DOL-2	1	1.37	0.03	0.64	0.03
O55B	Bulk	DOL-1, DOL-2	1	2.73	0.06	1.18	0.06
O55B	Bulk	DOL-1, DOL-2	1	2.70	0.03	0.62	0.03
O72A	Bulk	DOL-1, DOL-2	1	1.05	0.02	0.38	0.04
O77	Bulk	DOL-1, DOL-2	1	-2.96	0.05	-6.02	0.05
O94	Bulk	DOL-1, DOL-2	1	1.22	0.03	-0.70	0.05
O102	Bulk	DOL-1, DOL-2	1	1.62	0.04	0.76	0.06
O112	Bulk	DOL-1, DOL-2	1	1.70	0.09	0.99	0.12

Sample	*Sampled Component*	*Dol Type*	*Phase*	*$\delta^{13}C$ (‰ V-PDB)*	*St. dev $\delta^{13}C$*	*$\delta^{18}O$ (‰ V-PDB)*	*St. dev $\delta^{18}O$*
O125	Bulk	DOL-1, DOL-2	1	-8.75	0.02	-3.97	0.06
O144	Bulk	DOL-1, DOL-2	1	2.06	0.06	0.45	0.07
O152A	Bulk	DOL-1, DOL-2	1	2.08	0.02	0.83	0.05
O152B	Bulk	DOL-1, DOL-2	1	1.31	0.03	0.23	0.03
O164	Bulk	DOL-1, DOL-2	1	1.97	0.04	0.96	0.05
R155	Bulk	DOL-1, DOL-2	1	3.03	0.04	1.16	0.05
SK390	Bulk	DOL-1, DOL-2	1	-2.01	0.05	-5.17	0.04

Table 8.11 Table 8.10 $\delta^{13}C$ and $\delta^{18}O$ values with standard deviations for measured dolostone samples.

Samples from DOL-1 and DOL-2 from completely dolomitized facies close to Hercynian basement show $\delta^{13}C$ from -8.8 ‰ to 3.0 ‰ and $\delta^{18}O$ between -6.3 ‰ and 1.2 ‰. The isotopic signature for DOL-1 and DOL-2 can be divided in two groups with different isotopic values. The first group concerns completely dolomitized phase 1 samples from Genna Silana, Genna Ramene and Mt. Oro logs (from m 1 to m 4 and from m 12 to m 20) and is characterized by $\delta^{13}C$ between 0.1 ‰ and 3.0 ‰ and $\delta^{18}O$ between -1.0 ‰ and 1.2 ‰. This first group includes both non-luminescent and luminescent samples. The second group includes samples from phase 1 completely dolomitized facies in the Mt. Oro log from m 5 to m 12 that show $\delta^{13}C$ values ranging from -8.8 ‰ and -2.0 ‰ and $\delta^{18}O$ between -6.3 ‰ and -2.8 ‰. This second group of dolomite samples consists almost totally of non-luminescent dolostone samples. DOL-3, DOL-4 and DOL-5 identified in the F31 laminated dolostone samples (phase 4), in the Genna Silana and Ghispali stratigraphic logs above the subaerial exposure surface separating phase 3 from phase 4, show positive $\delta^{13}C$ between 1.9 ‰ and 3.0 ‰ and positive $\delta^{18}O$ generally from 0.7 ‰ to 3.6 ‰, with the exception of one sample characterized by a $\delta^{18}O$ value of -3.4 ‰ associated with $\delta^{13}C$ of 1.9 ‰ occurring in the Ghispali log.

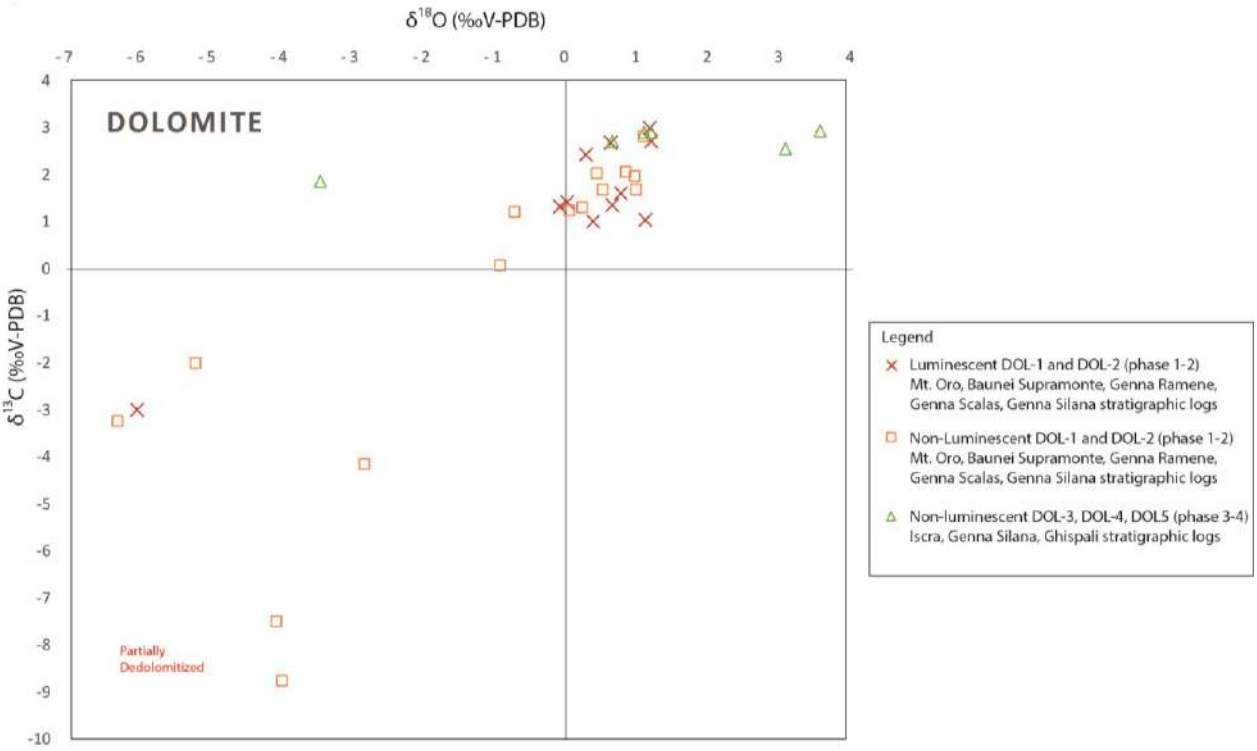

Figure 8.19 Cross-plots of $\delta^{13}C$ and $\delta^{18}O$ of the analysed bulk dolostone samples according to dolomitization type.

8.4 Interpretation and Discussion

8.4.1 Diagenetic alteration of limestone carbon and oxygen isotope values

In shallow-water carbonate systems the original $\delta^{13}C$ and $\delta^{18}O$ values reflecting the isotopic composition of precipitating water, DIC (Dissolved Inorganic Carbon), vital effects for skeletal carbonates and environmental factors (e.g., temperature, pH, climate, palaeoceanography and carbon cycle perturbation) are usually modified by diagenetic effects (c.f. Immenhauser et al., 2003; Badenas et al., 2005; Ahm et al., 2018; Higgins et al., 2018 and references therein). In order to assess this diagenetic effect, carbon and oxygen stable isotope data from this study were compared with values reported in literature for Upper Jurassic pristine marine carbonates provided from basinal succession: approximately -1 ‰ to 4 ‰ for $\delta^{13}C$ and -2 ‰ to 1 ‰ for $\delta^{18}O$ with differences between Oxfordian, Kimmeridgian and Tithonian (e.g., Veizer et al., 1999; Jenkyns et al., 2002; Weissert and Erba, 2004; Wierzbowski et al., 2004; Brigaud et al., 2008; Nunn et al., 2009; Price and Rogov, 2009; Nunn and Price, 2010). A general decrease characterizes $\delta^{13}C$ from early Oxfordian (3 ‰) to Tithonian (-1 ‰). Oxfordian $\delta^{13}C$ values range between 1 ‰ and 3 ‰, Kimmeridgian values are around 1 ‰, whereas Tithonian values range between -1 ‰ and -1 ‰ (Nunn and Price, 2010). Instead, $\delta^{18}O$ values decrease

from Oxfordian (between 0 ‰ and -1 ‰) to Kimmeridgian (between -0.5 ‰ and -2 ‰) and increase during Tithonian from -1 ‰ to 0 ‰ (Nunn and Price, 2010).

In the Mt. Oro stratigraphic log (Fig. 8.4), the one sample from facies F1 (phase 1) 1 m above the Hercynian basement records an isotopic signature depleted both in ^{13}C and ^{18}O (Fig. 8.20). This significant depletion is interpreted as consequence of the interaction with circulating ^{18}O-depleted meteoric waters with high concentrations in ^{12}C deriving from soil weathering during meteoric diagenesis (e.g., Hudson, 1977; Allan and Matthews, 1982; Lohmann, 1988; Patterson and Walter, 1994; Immenhauser et al., 2003; Lavastre et al., 2011; Swart, 2015; Chesnel et al., 2016; Bahamonde et al., 2017).

Assuming the published pristine marine stable O and C values valid for the eastern Sardinia marine environments, in the Mt. Oro stratigraphic log facies F8 and F12 appears depleted in ^{18}O (Fig. 8.20) likely due to the interaction with higher temperature burial fluids or ^{18}O depleted meteoric waters (Hudson, 1977; Allan and Matthews, 1982; Moore, 1989; Lohmann, 1998; Immenhauser et al., 2003; van der Kooij et al., 2009). The other facies accumulated during phase 2 and phase 3 and 4 could record the original marine isotopic signatures. Sparite sampled from fractures is depleted both in ^{18}O and ^{13}C and probably records the interaction with burial and meteoric telogenetic fluids (Fig. 8.20).

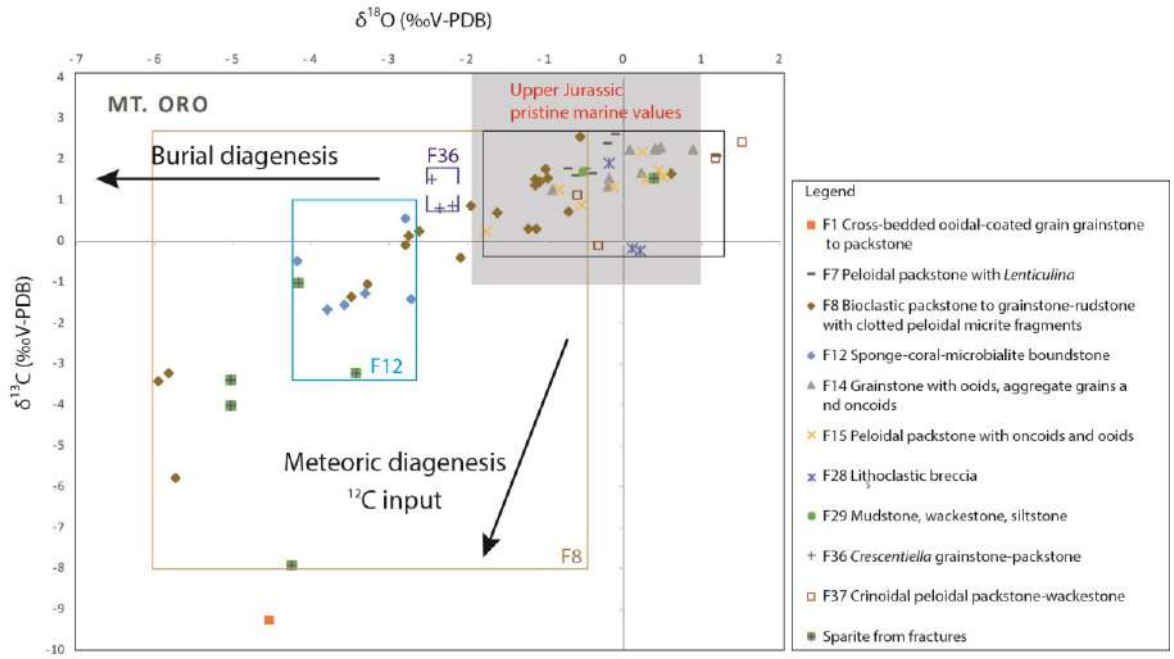

Figure 8.20 Cross-plot of $\delta^{13}C$ and $\delta^{18}O$ of the analysed bulk and skeletal fragments of limestones and partially dolomitized limestones in Mt. Oro stratigraphic section according to facies types with evidenced the major isotopic signature trends. The grey square represents the field of Upper Jurassic pristine marine values based on published stable-isotope compositions obtained from well-preserved fossils (particularly belemnites) in Jenkyns et al. (2002), Weissert and Erba (2004), Wierzbowski et al. (2004), Brigaud et al. (2008), Nunn et al. (2009), Price and Rogov (2009), Nunn and Price (2010).

In the Franciscu stratigraphic log (Fig. 8.10) some values from phase 3 facies (F15) are depleted in ^{18}O and were diagenetically altered, likely in contact with burial fluids (Fig. 8.10, 8.21). Phase 4 facies F28 and F29 probably record the original isotopic marine signal, whereas some samples from F35 were altered by burial diagenetic fluids.

In the Genna Ramene log (Fig. 8.3) phase 1 facies (F1, F3, F4) likely preserve the original marine values except for a few samples or dolomitized facies. Phase 2 facies F5, F8 and F11 record an isotopic signature depleted in ^{18}O and were altered by burial diagenetic fluids (Fig. 8.3, 8.22). Instead, facies F6 (phase 2) probably records an original marine isotopic signature (Fig. 8.22).

In the Genna Silana log (Fig. 8.2) the isotopic signal of facies F1(phase 1) is depleted in both ^{13}C and ^{18}O in the first 5 m above the boundary with completely dolomitized facies overlying the Hercynian basement (Fig. 8.2). It suggests diagenetic alteration in contact with burial and meteoric fluids. For the following 15 m, F1 samples are depleted in ^{18}O and were likely altered by burial fluids (Fig. 8.2). Phase 2 facies F9 and F10 (from 0 to 45 m below the subaerial exposure separating phase 2 and phase 3; Fig. 8.2) are depleted in ^{18}O with respect to mean Upper Jurassic pristine marine values suggesting influence by high-temperature diagenetic fluids (Fig. 8.23). Two samples of facies F17 (phase 3 above the subaerial exposure surface; Fig. 8.2) were altered during diagenesis likely in contact with burial fluids. Instead, the isotopic composition of the majority of the phase 3 facies F18, F19, F20, F21, F22, F24, F26 and F27, could possibly record an original marine signal (Fig. 8.23). However, the lower $\delta^{13}C$ and $\delta^{18}O$ values for phase 3 facies were measured in samples collected a few metres above the subaerial exposure surface between phase 2 and phase 3. Upward, C and O isotopic values slightly increase and newly decrease near the second subaerial exposure surface between phase 3 and phase 4. This small local positive shift of $\delta^{13}C$ and $\delta^{18}O$ seems to be related to sea-level fluctuations and different degrees of early meteoric diagenesis near the subaerial exposure surfaces rather than possible global palaeoceanographic trends (cf., Immenhauser et al., 2003).

Phase 4 facies F30, F32 and F33 might record the original marine signal (Fig. 8.23), except just above the subaerial exposure dividing phase 3 and phase 4 where a sample from facies F34 is depleted in ^{18}O suggesting diagenesis in contact with high-temperature burial fluids (Fig. 8.2).

In the Codula Orbisi stratigraphic log (Fig. 8.14) the isotopic composition of facies F5 and F10 (phase 2) below the subaerial exposure surface is clearly reset showing ^{18}O depleted values (Fig. 8.24). Also the isotopic signature of F17 (phase 3) just above the subaerial exposure surface is ^{18}O depleted (Fig. 8.14) suggesting influence from high-temperature burial fluids. Fractures show the lower $\delta^{18}O$ values and record percolation of high-temperature fluids in burial environment. Instead, phase 3 F18, F25 and F26 could have preserved the original marine isotopic signal (Fig. 8.24).

In the Iscra stratigraphic log (Fig. 8.7), the unique F10 boundstone (phase 2) sample below the subaerial exposure surface is depleted in ^{18}O suggesting that it was likely modified in burial environment. Some phase 3 supratidal facies (F16, F19 and F20) show values slightly depleted in ^{13}C probably modified by meteoric waters. In particular, the lowest value of $\delta^{13}C$ in the lower part of phase 3 succession corresponds to the first 4 m above the subaerial exposure surface, suggesting the influence of ^{12}C rich meteoric fluids (cf., Immenhauser et al., 2003). The other phase 3 facies could record an original marine signal, with exception of some samples from F22 and F23 that are depleted in ^{18}O due to burial diagenesis (Fig. 8.25), especially just below (up to 10 m) the subaerial exposure surface at the top of phase 3 (Fig. 8.7). The intraclastic breccia samples (F18, phase 3) are slightly enriched in ^{18}O, probably due to the effect of partial dolomitization.

In the Punta Mureddu log (Fig. 8.17) facies F18, F25 (phase 3) and F32 (phase 4) likely preserve the original isotopic marine composition (Fig. 8.26).

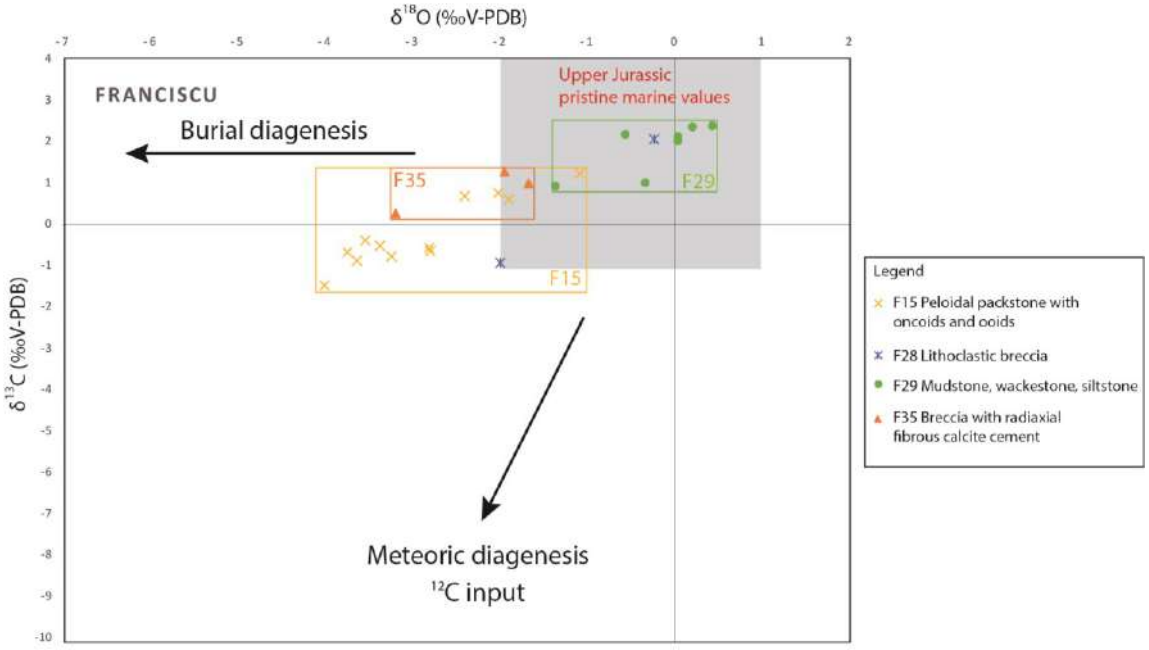

Figure 8.21 Cross-plot of $\delta^{13}C$ and $\delta^{18}O$ of the analysed bulk and skeletal fragments of limestones and partially dolomitized limestones in Franciscu stratigraphic section according to facies types with evidenced the major isotopic signature trends. The grey square represents the field of Upper Jurassic pristine marine values based on published stable-isotope compositions obtained from well-preserved fossils (particularly belemnites) in Jenkyns et al. (2002), Weissert and Erba (2004), Wierzbowski et al. (2004), Brigaud et al. (2008), Nunn et al. (2009), Price and Rogov (2009), Nunn and Price (2010).

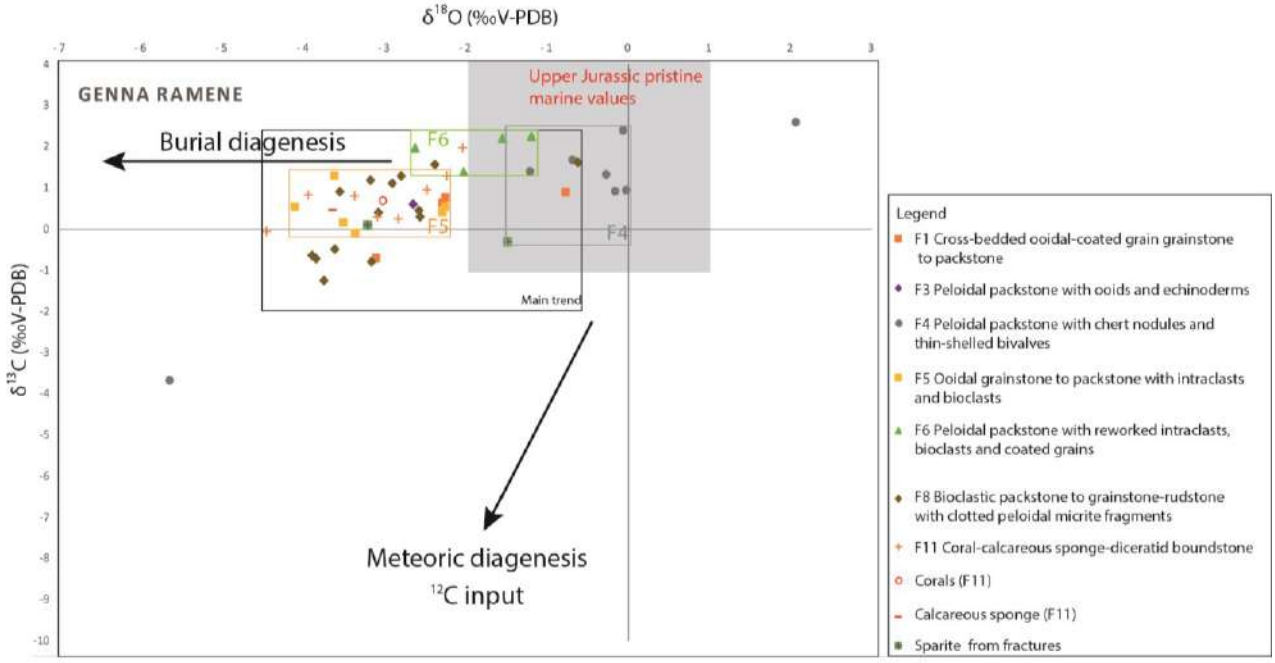

Figure 8.22 Cross-plot of $\delta^{13}C$ and $\delta^{18}O$ of the analysed bulk and skeletal fragments of limestone and partially dolomitized limestones in Genna Ramene stratigraphic section according to facies types with evidenced the major isotopic signature trends. The grey square represents the field of Upper Jurassic pristine marine values based on published stable-isotope compositions obtained from well-preserved fossils (particularly belemnites) in Jenkyns et al. (2002), Weissert and Erba (2004), Wierzbowski et al. (2004), Brigaud et al. (2008), Nunn et al. (2009), Price and Rogov (2009), Nunn and Price (2010).

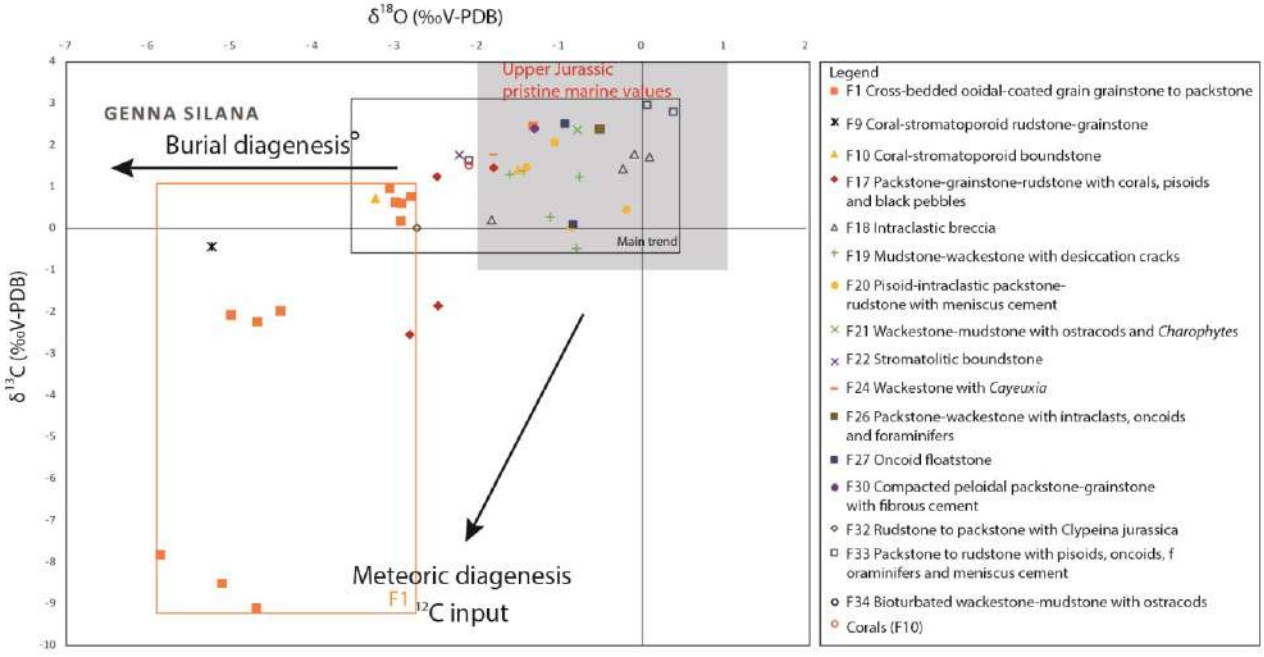

Figure 8.23 Cross-plot of $\delta^{13}C$ and $\delta^{18}O$ of the analysed bulk and skeletal fragments of limestones and partially dolomitized limestones in Genna Silana stratigraphic section according to facies types with evidenced the major isotopic signature trends. The grey square represents the field of Upper Jurassic pristine marine values based on published stable-isotope compositions obtained from well-preserved fossils (particularly belemnites) in Jenkyns et al. (2002), Weissert and Erba (2004), Wierzbowski et al. (2004), Brigaud et al. (2008), Nunn et al. (2009), Price and Rogov (2009), Nunn and Price (2010).

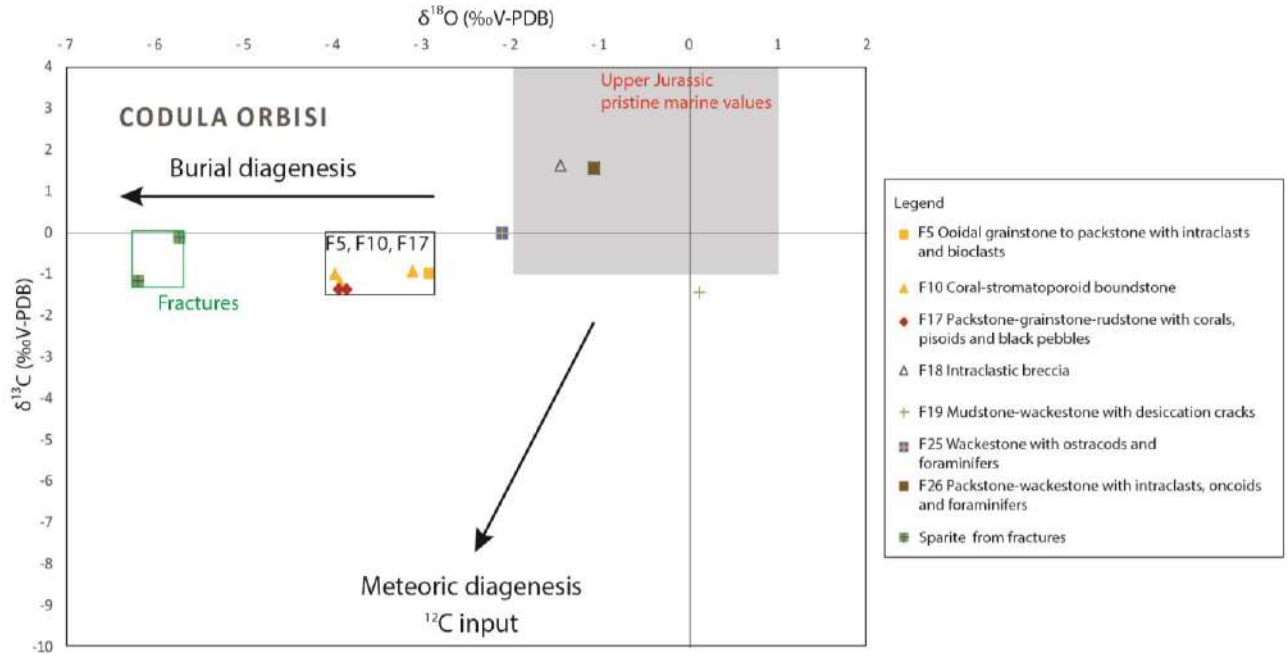

Figure 8.24 Cross-plot of $\delta^{13}C$ and $\delta^{18}O$ of the analysed bulk and skeletal fragments in limestones and partially dolomitized limestones in Codula Orbisi stratigraphic section according to facies types with evidenced the major isotopic signature trends. The grey square represents the field of Upper Jurassic pristine marine values based on published stable-isotope compositions obtained from well-preserved fossils (particularly belemnites) in Jenkyns et al. (2002), Weissert and Erba (2004), Wierzbowski et al. (2004), Brigaud et al. (2008), Nunn et al. (2009), Price and Rogov (2009), Nunn and Price (2010).

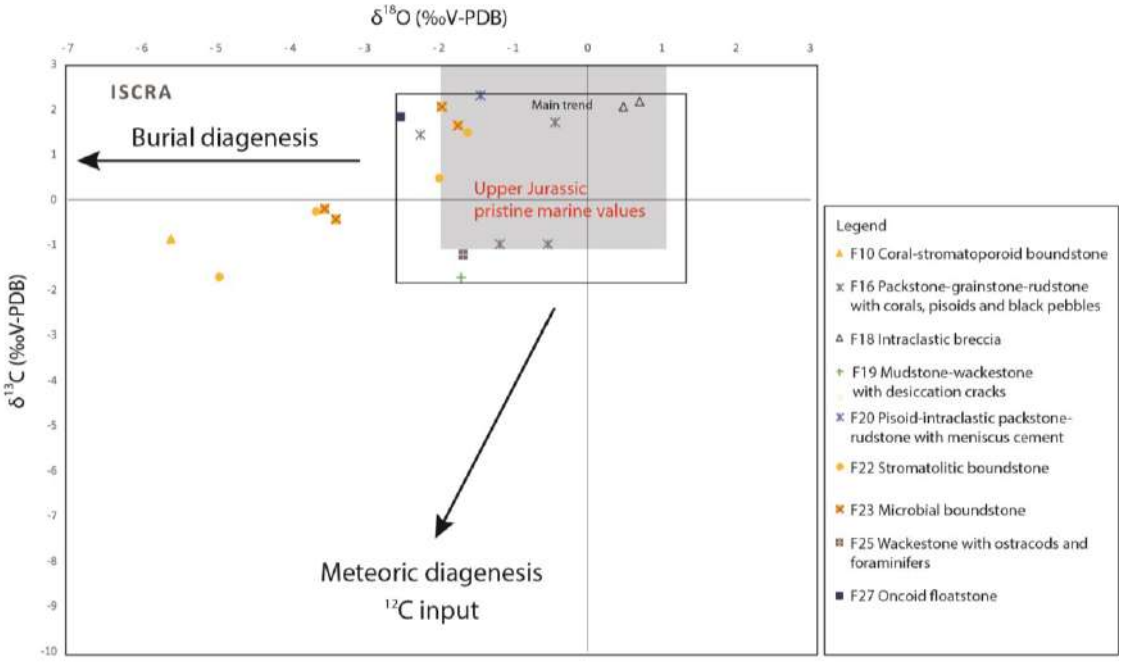

Figure 8.25 Cross-plot of $\delta^{13}C$ and $\delta^{18}O$ of the analysed bulk and skeletal fragments in limestones and partially dolomitized limestones in Iscra stratigraphic section according to facies types with evidenced the major isotopic signature trends. The grey square represents the field of Upper Jurassic pristine marine values based on published stable-isotope compositions obtained from well-preserved fossils (particularly belemnites) in Jenkyns et al. (2002), Weissert and Erba (2004), Wierzbowski et al. (2004), Brigaud et al. (2008), Nunn et al. (2009), Price and Rogov (2009), Nunn and Price (2010).

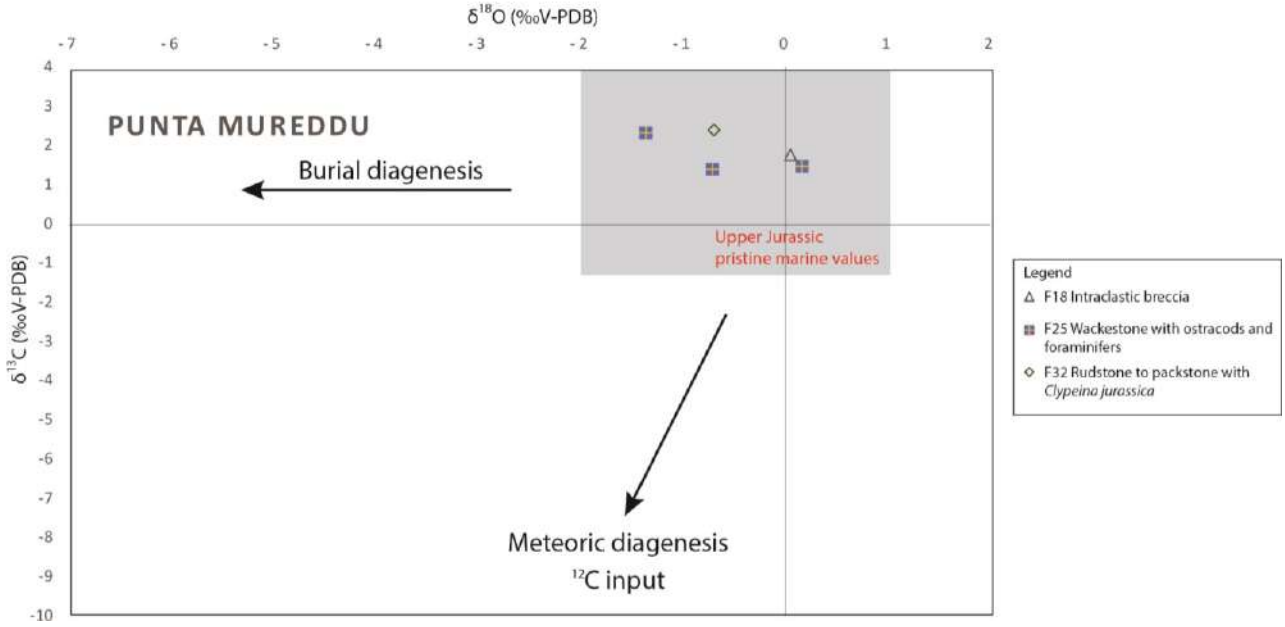

Figure 8.26 Cross-plot of $\delta^{13}C$ and $\delta^{18}O$ of the analysed bulk and skeletal fragments of limestones and partially dolomitized limestones in Punta Mureddu stratigraphic section according to facies types. The grey square represents the field of Upper Jurassic pristine marine values based on published stable-isotope compositions obtained from well-preserved fossils (particularly belemnites) in Jenkyns et al. (2002), Weissert and Erba (2004), Wierzbowski et al. (2004), Brigaud et al. (2008), Nunn et al. (2009), Price and Rogov (2009), Nunn and Price (2010).

8.4.2 Dolomite stable carbon and oxygen isotopic signature

The stable carbon and oxygen isotopic signatures of the dolostone samples provide insights on the origin of the replacive dolomite and dolomitization process.

In the Mt. Oro stratigraphic log (DOL-1, DOL-2, phase 1 close to the Hercynian basement; Fig. 8.4, 8.27) the isotopic signature of dolomite can be divided in two groups. The first group ($\delta^{13}C$ between 0.1 ‰ and 3.0 ‰ and $\delta^{18}O$ between -1.0 ‰ and 1.2 ‰) records the same isotopic signature of DOL-1 and DOL-2 in Genna Ramene (Fig. 8.3), Genna Scalas and the lower part of the Genna Silana log (phase 1; Fig. 8.2).

Burial dolomite precipitated at temperature higher than 60°C usually shows negative oxygen isotope signature (Warren, 2000). Thus, a precipitation at temperatures lower than 60°C could be suggested for this group of dolomite (from DOL-1, DOL-2) that generally shows a positive oxygen isotope signature (e.g., Reinhold, 1998; Hou et al., 2016; Berra et al., 2020). However, luminescence in dolomite crystals suggests precipitation in reducing environments characterized by conditions with relatively high concentrations of manganese (Mn^{2+}, activator of bright luminescence) and relatively low concentrations of iron (Fe^{2+}, quencher). These conditions are common in reducing environments typical of burial diagenesis (Hiatt and Pufahl, 2014). The CL zoning likely reflects fluctuations in the

manganese and iron proportions in the parent fluid during DOL-1 and DOL-2 dolomite precipitation, probably related to variations in redox conditions (Gaswirth et al., 2007; Choquette and Hiatt, 2008). Thus, DOL-1 and DOL-2 precipitated in burial environment and the isotopic signal was modified by fluids enriched in ^{18}O or the positive oxygen isotopic signature reveals relative low temperatures of precipitation (Kyser et al., 2002; Choquette and Hiatt, 2008). Dolomitization by DOL-1 and DOL-2 was the result of probably high-saline burial fluids circulating at the boundary between the impermeable Hercynian basement and the highly permeable ooidal grainstone of facies F1, echinoderm packstone to grainstone-rudstone (F2) and less permeable peloidal packstone with ooids and echinoderms (F3) and peloidal packstone with chert nodules and thin shelled bivalves (F4, phase 1). The source of Mg was likely the Hercynian basement constituted by metamorphic and magmatic rocks.

The second group of DOL-1 and DOL-2 in the Mt. Oro stratigraphic log (Fig. 8.4, Fig. 8.27) records lower isotopic values for both $\delta^{13}C$ and $\delta^{18}O$. The petrographic characters of samples stained with alizarin red and the non-luminescence response to CL suggest that this portion of the succession was affected by dedolomitization processes. Dedolomitization affected only DOL-1 and DOL-2 dolomite and took place in contact with meteoric waters during telogenesis (e.g., Arenas et al., 1999; Kyser et al., 2002; Nader et al., 2007; Makhloufi and Samankassou, 2019). Thus, the isotopic signature of these dolomite samples was modified by ^{12}C and ^{16}O enriched meteoric waters.

The isotopic signatures of DOL-3, DOL-4 and DOL-5 in Genna Silana (Fig. 8.2) and Ghispali log (phase 4) show high positive $\delta^{13}C$ (1.9 ‰ to 3.0 ‰) and $\delta^{18}O$ (0.7 ‰ to 3.6 ‰) values (Fig. 8.27). The isotopic signature enriched in ^{18}O suggests dolomite origin from evaporative fluids (Warren, 2000). The non-luminescent response to CL confirms this hypothesis of early formation of dolomite in oxygenated environment. The exception of one sample characterized by a $\delta^{18}O$ value of -3.4 ‰ associated with $\delta^{13}C$ of 1.9 ‰ (Fig. 8.27) in Ghispali log suggests isotopic signature modification by high-temperature burial fluids.

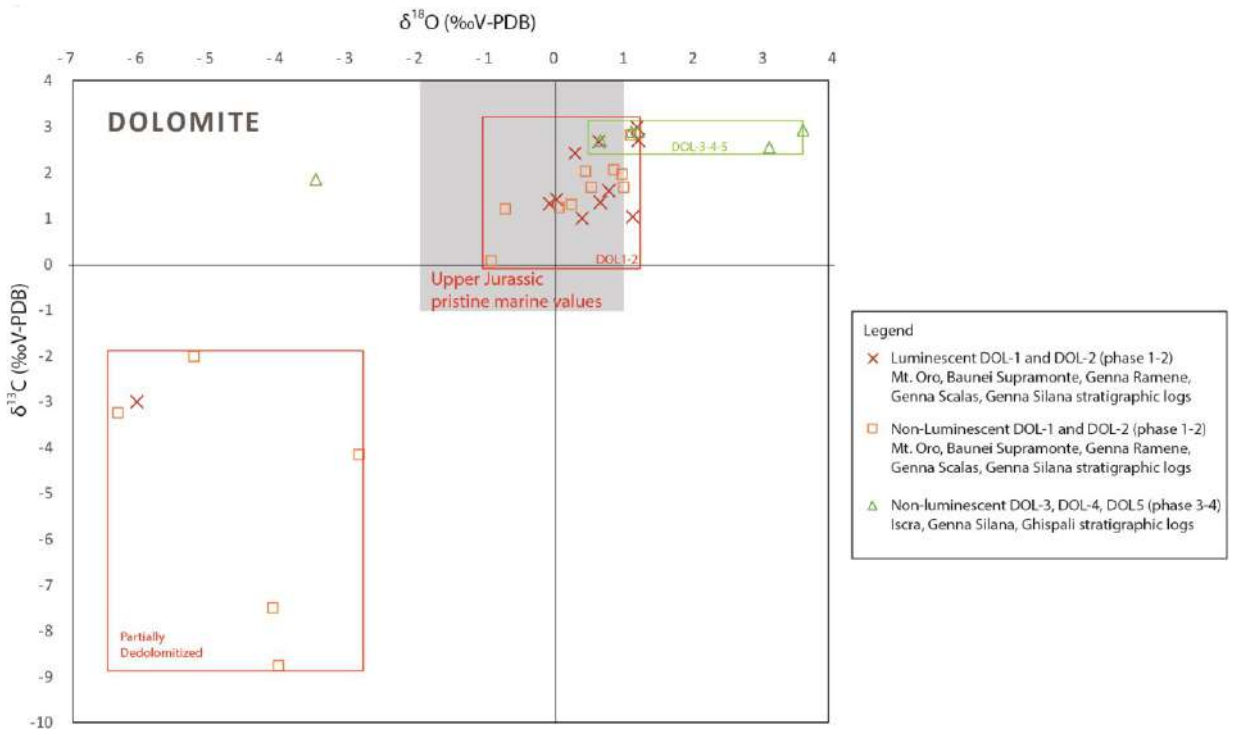

Figure 8.27 Cross-plot of $\delta^{13}C$ and $\delta^{18}O$ of the analysed bulk of dolostone samples according to dolomitization type with evidenced the major isotopic signature trends. The grey square represents the field of Upper Jurassic pristine marine values based on published stable-isotope compositions obtained from well-preserved fossils (particularly belemnites) in Jenkyns et al. (2002), Weissert and Erba (2004), Wierzbowski et al. (2004), Brigaud et al. (2008), Nunn et al. (2009), Price and Rogov (2009), Nunn and Price (2010).

8.4.3 Diagenetic features interpretation and paragenetic sequences

The petrographic analyses of diagenetic features combined with cathodoluminescence and stable isotope analyses allowed to tentatively reconstruct the paragenetic sequences of the diagenetic features vs. time for the depositional phases of the eastern Sardinia carbonate succession (Fig. 8.28 and 8.29).

Early marine cementation is absent in facies deposited during phase 1 (Fig. 8.28A); syntaxial calcite cement precipitated around crinoids in burial environment predating mechanical compaction. Dissolution with oo- and bio-mouldic porosity and fracturing occurred in burial environment. Dolomitization by DOL-1 and DOL-2 in phase 1 facies took place possibly in burial environment as demonstrated by the zoned luminescence pattern (e.g., Kyser et al., 2002; Choquette and Hiatt, 2008). Zattin et al. (2008) provided thermochronological evidences with apatite fission-track analysis that eastern Sardinia experienced a rapid burial from the late Jurassic until Barremian-Aptian with the Hercynian basement reaching temperature of about 80°C. Considering a normal geothermal gradient

of about 30°C km^{-1}, Zattin et al. (2008) calculated a burial thickness of about 2000 m. The erosion of a sedimentary cover of unknown thickness, today not preserved, has been suggested by Dieni et al. (2012) due to an Eocene major erosional event associated with transpressional tectonics. This is demonstrated by the clast lithologies contained in the Eocene Cucurru ‘e Flores Conglomerate spanning from the Hercynian basement to Ypresian limestones (Dieni et al., 2012). Burial dolomitization occurs at temperatures exceeding 60-70°C (Warren, 2000; Machel, 2004). As a result, assuming the first carbonate strata above the Hercynian basement replaced by DOL-1 and DOL-2 (Dorgali Fm.) reaching that temperatures, the interpretation of the burial origin of dolomite is well-supported. Furthermore, the apatite fission-track analysis by Zattin et al. (2008) suggests the uplift of the Hercynian basement and of the sedimentary cover between 120 and 95 Ma. This finding constrains the time occurrence of dolomitization by DOL-1 and DOL-2 between the end of Late Jurassic and Early Cretaceous. The rare luminescent zoned equant blocky calcite cement probably precipitated in burial environment under fluctuating redox conditions (Choquette and Hiatt, 2008; Hiatt and Pufahl, 2014). The non-luminescent equant blocky calcite cement and microsparite fill a wide variety of pores, postdate dolomitization and partially precipitate or were probably altered during telogenesis by meteoric fluids. This is demonstrated by the non-luminescent response to cathodoluminescence suggesting precipitation or modification in oxidised conditions (Hiatt and Pufahl, 2014) and is confirmed by the isotopic signature with low oxygen and carbon isotope values for the bulk of facies F1 (Mt. Oro and Genna Silana logs close to dolomitized facies) characterized by a great amount of equant blocky calcite cement. Dedolomitization occurred locally (Mt. Oro log) during telogenesis and interactions with meteoric fluids.

In facies deposited during phase 2 (Fig. 8.28B) isopachous fibrous marine cement precipitated during early marine diagenesis in facies F5, whereas syntaxial cement precipitated around echinoderms in the initial stage of burial diagenesis predating mechanical compaction and fracturing. Dissolution created mouldic porosity in burial environment and DOL-1 and DOL-2 precipitated in the lower part of phase 2 in Mt. Oro log. Equant blocky calcite cement and microsparite formed in burial environment as demonstrated by the isotopic signature in Mt. Oro (F8, F12), Genna Ramene (F5, F8, F11), Genna Silana (F8, F9, F10) and Codula Orbisi (F8, F9, F10) stratigraphic logs showing values depleted in ^{18}O. The-non luminescent response to CL probably is due to interaction with meteoric fluids during telogenesis.

In phase 3 facies (Fig. 8.29A) different types of calcite cement precipitated during early diagenesis in marine phreatic or meteoric vadose environments according to the cement habit (isopachous vs. pendant and meniscus) and non-luminescent response in CL. Isopachous fibrous cement precipitated around grains in high-energy marine conditions in facies F14 and F15 (cf. Chapter 6). Micritic

meniscus and pendant cement precipitated in supratidal and intertidal environment in vadose meteoric conditions (cf. Chapter 6). Dissolution took place both in early meteoric environment with dissolution cavities and vuggy porosity and in burial environment. Mechanical compaction and fracturing occurred in burial environment in middle ramp facies F14 and F15.

Dolomitization by DOL-3, DOL-4 and DOL-5 in facies F18 below the subaerial exposure surface occurred during early diagenesis due to evaporitic brines. This is suggested by the fine-grained texture of dolomite crystals, the presence of gypsum pseudomorph and the widespread silicification (Chapter 6) at the top of F18 (cf., Flügel, 2004) and the geochemistry of dolomite reflecting those of the evaporitic fluids with high positive $\delta^{18}O$ (Warren, 2000; Machel, 2004). The intensity of dolomitization decreases downward (phase 3 facies) and upward (phase 4 facies) of the horizon represented by the subaerial exposure surface between phase 3 and phase 4 facies. Dolomites may form from evaporated seawater either due to reflux brines or because of evaporation within supratidal facies during early diagenesis in sabkha settings (Machel, 2004). The reflux model was originally proposed by Adams and Rhodes (1960) and suggests that dolomitizing evaporated seawater, both hypersaline and mesohaline (cf. Melim and Scholle, 2002), flows downward and seaward through sediments. Considering phase 4 laminated dolostone (F31) beds deposited in supratidal environment (Chapter 6), hypersaline (or at least mesohaline) fluids could have flown downward through permeable facies causing the replacive dolomitization by DOL-3, DOL-4 and DOL-5. Instead, sabkha dolomites are syn-depositional, thin (<1-2m thick) stratiform, micritic and confined to restricted to marine supratidal facies (Warren, 2000). Seawater has normal slightly elevated salinity but becomes significantly evaporated beyond gypsum saturation within the supratidal flats, through which it refluxes due to its increased density with capillary mechanism (Machel, 2004). Dolomite in sabkhas is a pore precipitate or replaces aragonite mud less than a metre beneath the surface (Warren, 2000). Recently, a role of microbial mats in dolomite precipitation has been pointed out by several studies (Brauchli et al., 2016; Al Disi et al., 2017; Riechelmann et al., 2020). Only DOL-3 in the laminated dolostone (F31) could represent syn-depositional dolomite precipitation in sabkha environment due to the thickness of F31 beds (1-2 m), the positive $\delta^{18}O$ values, the fine-grained petrography and the alternation with supratidal and subtidal facies (F32, F33, F34). However, the reflux model is preferred because it better explains the precipitation of DOL-3, DOL-4 and DOL-5 dolomite types and their spatial distribution within the succession. Equant blocky calcite, microsparite and fine-grained equant cement precipitated during burial diagenesis and were altered during telogenesis.

In phase 4 facies (Fig. 8.29B) early diagenetic calcite cement precipitated in marine phreatic and meteoric vadose environment. Radiaxial fibrous cement precipitated in marine phreatic environment in high-energy slope settings (F35, F36: Chapter 6, cf. Della Porta et al., 2004). In inner platform

facies isopachous fibrous cement formed around grains in F30, whereas micritic meniscus cement formed in supratidal facies (F33) in meteoric vadose environment. Dissolution took place in supratidal early diagenetic environment and in burial environment. Dolomitization (DOL-3, DOL-4, DOL-5) occurred during early diagenesis due to evaporitic brines either related to reflux mechanisms or due to evaporation in supratidal settings as in the sabkha model for early dolomitization (cf. Flügel, 2004 and references therein).

Mechanical compaction affected inner platform facies (F32 and F33) during burial diagenesis, whereas equant blocky calcite and microsparite precipitated during burial diagenesis and were altered during telogenesis by meteoric fluids.

A) Phase 1

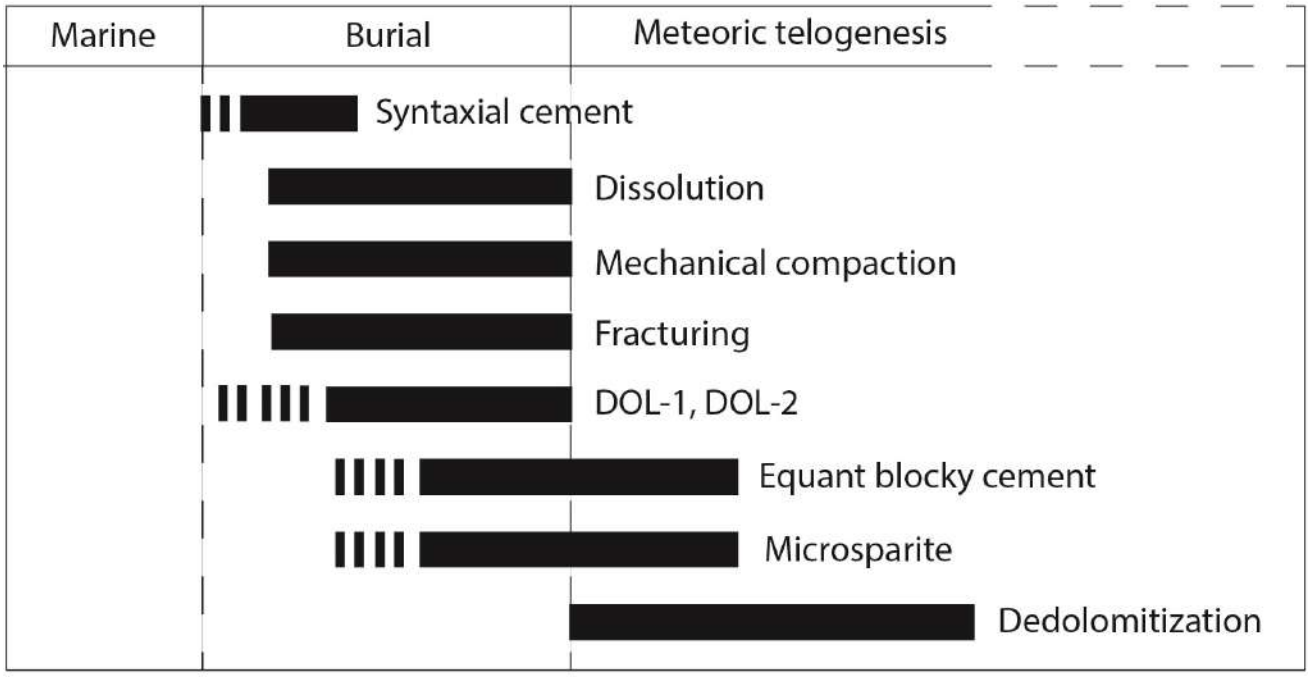

B) Phase 2

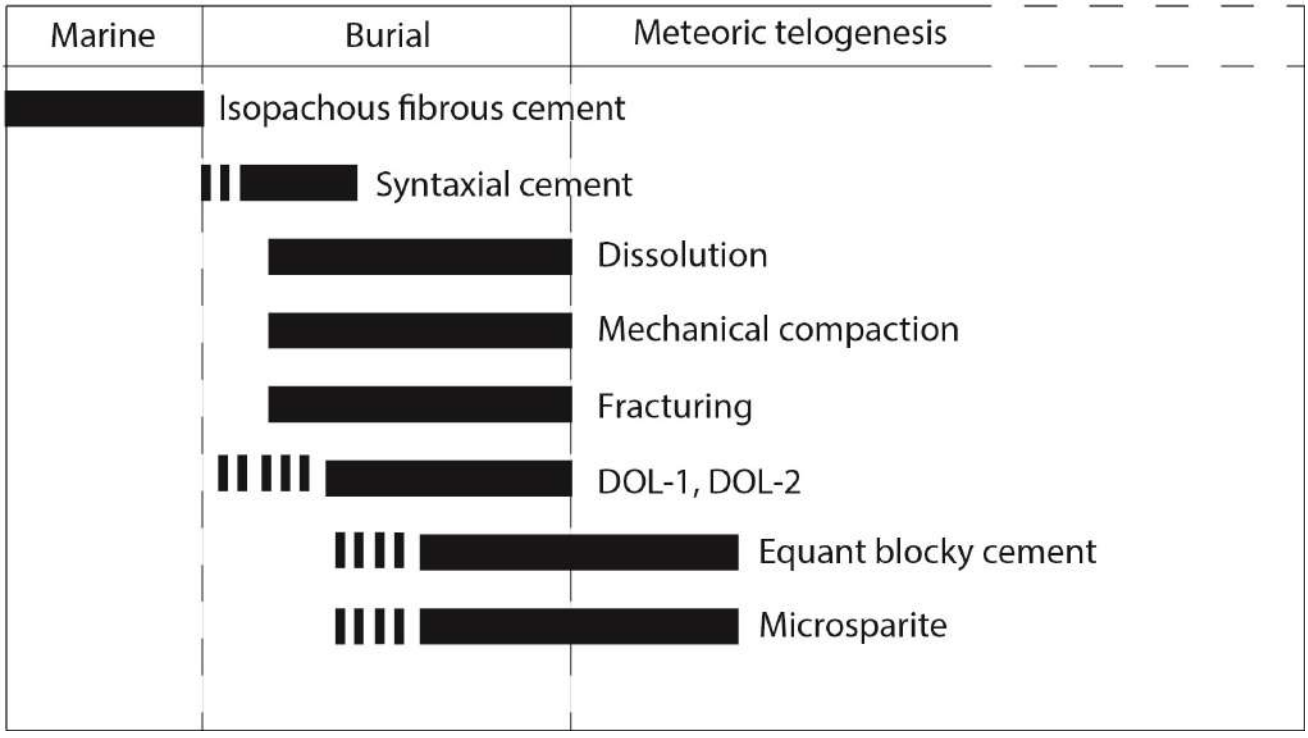

Figure 8.28 Paragenetic sequences for phase 1 (A) and phase 2 (B) facies.

A) Phase 3

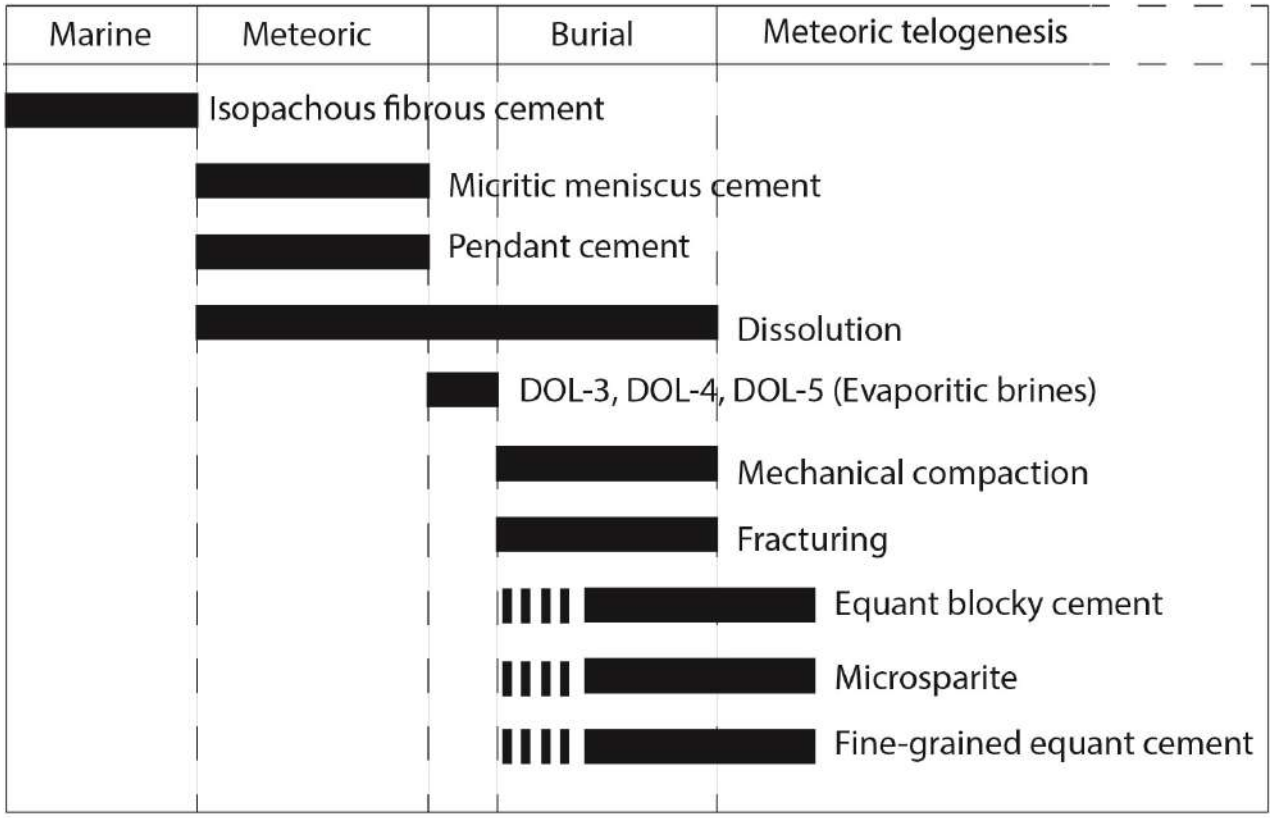

B) Phase 4

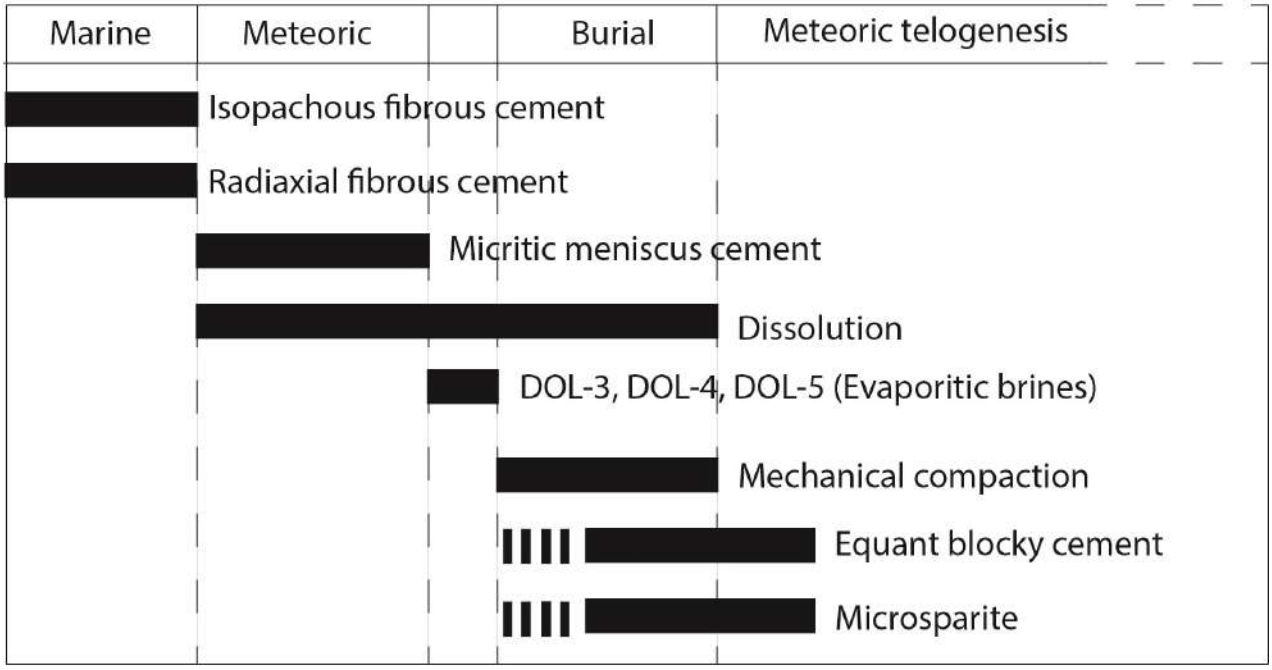

Figure 8.29 Paragenetic sequences for phase 3 (A) and phase 4 (B) facies.

8.4.4 Facies dependent diagenetic alteration

Results of carbon and oxygen stable isotopes on the eastern Sardinia carbonate succession reveal that isotopic signature resetting by diagenetic fluids is strongly affected by facies texture. Grain-supported textures are considered to be more favourable for fluid circulation and could record a more pronounced modification of carbon and oxygen signatures (e.g., Marshall, 1992; Immenhauser et al., 2002; Vincent et al., 2004). Samples from eastern Sardinia grainstone, rudstone and boundstone facies were reset and their isotopic signature is generally depleted in both ^{13}C and ^{18}O with respect to mean Upper Jurassic marine values (Fig. 8.30). The depletion in ^{18}O record a burial diagenetic signal.

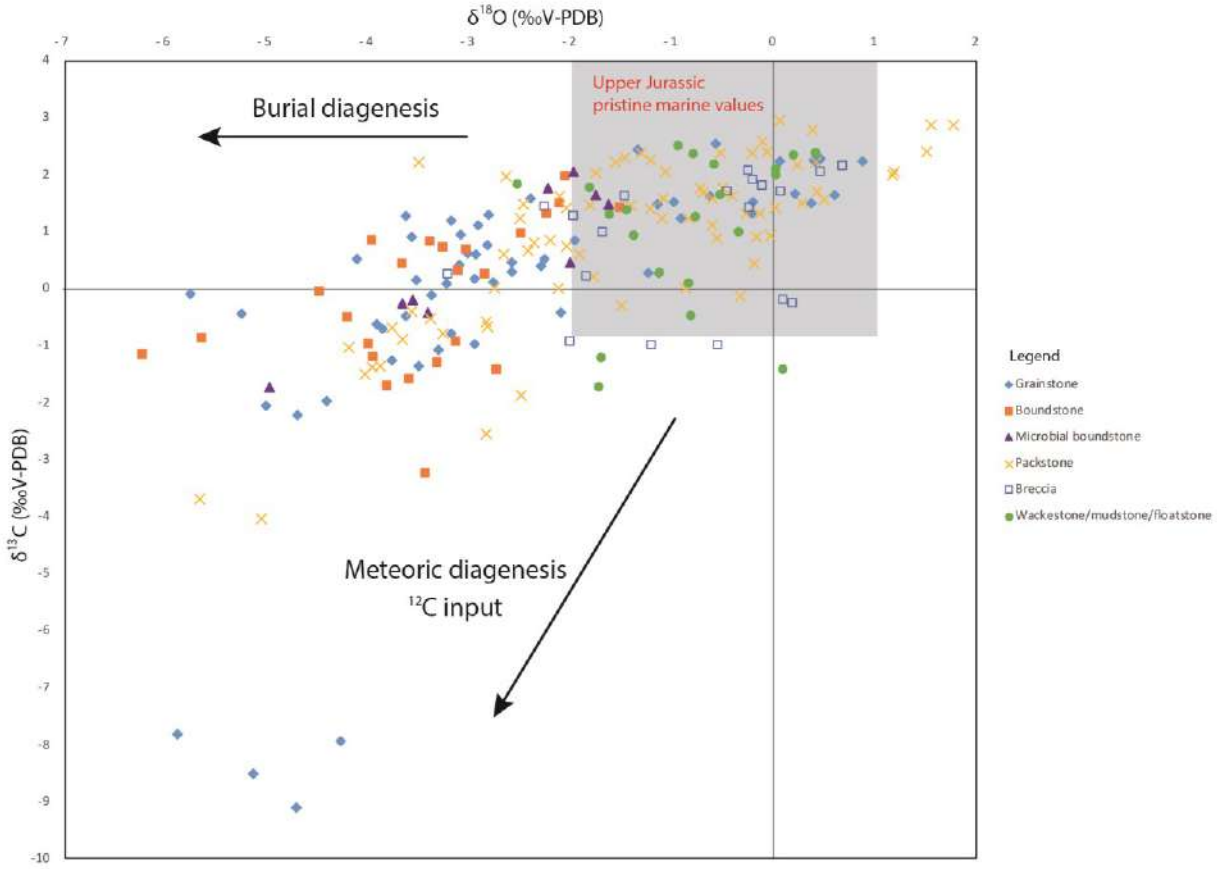

Figure 8.30 Cross-plot of $\delta^{13}C$ and $\delta^{18}O$ of all the analysed bulk and skeletal fragments of limestones and partially dolomitized limestones according to facies texture. The grey square represents the field of Upper Jurassic pristine marine values based on published stable-isotope compositions obtained from well-preserved fossils (particularly belemnites) in Jenkyns et al. (2002), Weissert and Erba (2004), Wierzbowski et al. (2004), Brigaud et al. (2008), Nunn et al. (2009), Price and Rogov (2009), Nunn and Price (2010). Arrows point to isotopic signature fields from burial and meteoric diagenesis (after Lavastre et al., 2011).

Instead, the isotopic signatures of wackestone, mudstone, floatstone and breccia facies appear to be less influenced by diagenetic evolution and apparently records the original marine values. The breccia bulk isotopic trends were probably influenced by the fine-grained micrite matrix of facies F18 and F28. The most isotopically altered breccia samples are from facies F35 that is cemented by radiaxial fibrous calcite. The samples with packstone textures are characterized by the more scattered $\delta^{13}C$ and $\delta^{18}O$ values, suggesting that some samples were reset by meteoric diagenesis (values depleted in both ^{13}C and ^{18}O) whereas other samples possibly reflect the original marine signatures. A more detailed analysis allows to point out which packstone facies were altered by diagenetic fluids (Fig. 8.31). One sample from F4 shows very low $\delta^{13}C$ and $\delta^{18}O$ values and was probably reset by diagenetic fluids, but the other sample from the same facies probably records original marine values. Some samples from F15 were altered. The deposition of F17 followed the subaerial exposure separating depositional phase 3 and phase 4 (cf. Chapter 6), thus this facies was probably in contact with meteoric fluids enriched in ^{12}C during deposition. The isotopic signature of some samples of facies F32 was probably influenced by DOL-4 and DOL-5 partial dolomitization and shows more positive oxygen values with respect to Upper Jurassic marine values. One sample from F33 and three samples from F37 were altered by diagenetic fluids. Among the packstone facies types, the original marine isotopic signature was possibly recorded only by F2, F3, F4 (except one sample), F6, F7, F20, F26, F30, F32 and F36. As a result, all the facies that possibly retain the original marine values are F2, F3, F4 (except one altered sample), F6, F7, F16 matrix, F18 matrix, F19, F20, F21, F24, F25, F26, F27, F28 matrix, F29, F30, F33 (except one altered sample) and F36. However, the sedimentological analysis of F16, F18, F19, F20 and F21 (cf. Chapter 6) suggests a supratidal and pond-lacustrine depositional environment for these facies and a fresh-water influence in their isotopic signature cannot be excluded. The realization of a possible curve showing the isotopic signature of marine trend for the Upper Jurassic of eastern Sardinia must take into account only analyses from facies F2, F3, F4, F6, F7, F24, F25, F26, F27, F28 matrix, F29, F30, F33 (except one sample) and F36.

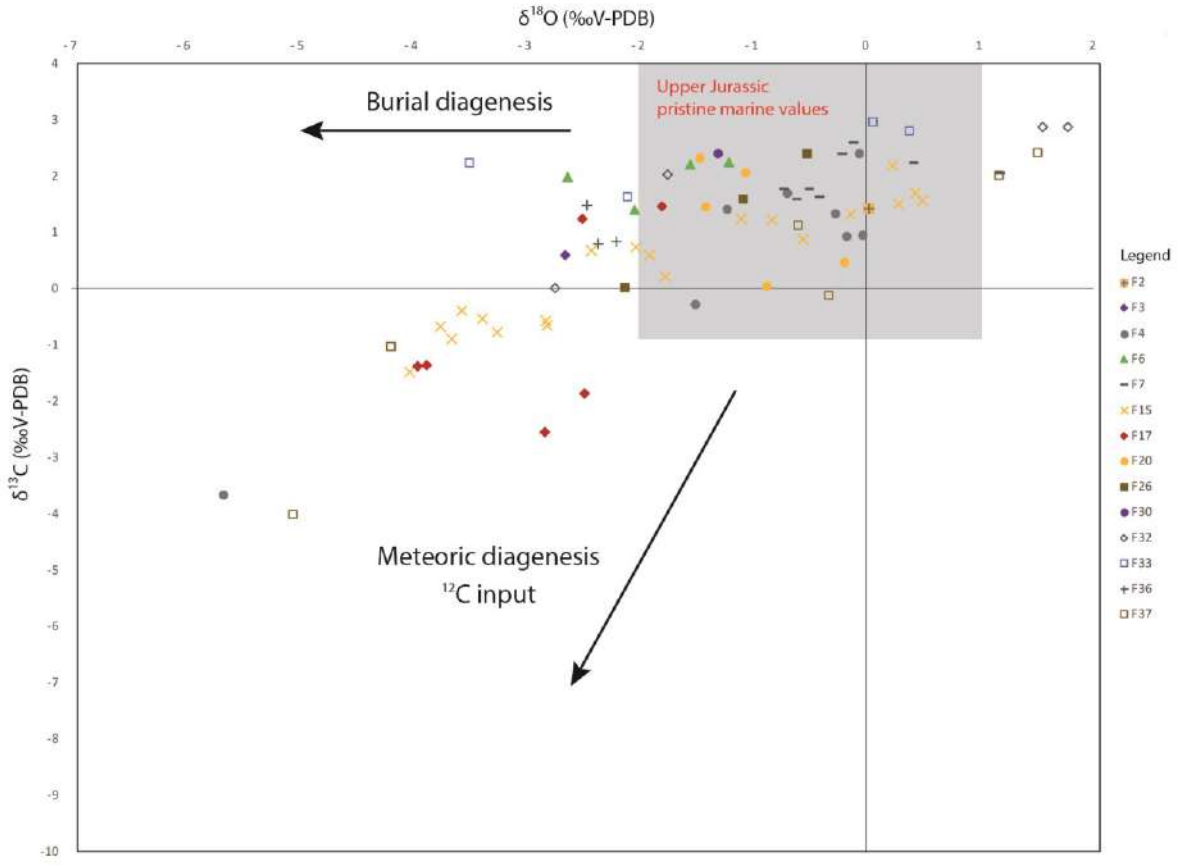

Figure 8.31 Cross-plot of $\delta^{13}C$ and $\delta^{18}O$ of the analysed bulk and skeletal fragments of packstone according to facies types. The grey square represents the field of Upper Jurassic pristine marine values based on published stable-isotope compositions obtained from well-preserved fossils (particularly belemnites) in Jenkyns et al. (2002), Weissert and Erba (2004), Wierzbowski et al. (2004), Brigaud et al. (2008), Nunn et al. (2009), Price and Rogov (2009), Nunn and Price (2010). Arrows point to isotopic signature fields from burial and meteoric diagenesis (after Lavastre et al., 2011).

8.4.5 Comparison with published Upper Jurassic stable C and O isotope curves

The published $\delta^{18}O$ and $\delta^{13}C$ values exhibit possible trends in marine isotopic signature variation during the Late Jurassic.

Curves proposed in basinal succession by Price and Rogov (2009) based on belemnites from the Russian platform and by Nunn and Price (2010), based on belemnites from Scotland (Fig. 8.32), show a general $\delta^{13}C$ decrease from early Oxfordian (3 ‰) to late Tithonian (-1 ‰). The $\delta^{13}C$ proposed by Dera et al. (2011) based on belemnite samples show a positive peak of $\delta^{13}C$ (about 2.5 ‰) in early Oxfordian, a decrease in $\delta^{13}C$ in middle Oxfordian to 0.5 ‰ and another positive peak in late Oxfordian (about 2 ‰). Instead, $\delta^{13}C$ curves of inorganic carbon proposed by Jenkyns (1996) and Weissert and Mohr (1996) for the Tethyan realm show a general decrease from about 2.5 ‰ in middle Oxfordian to 1.5 ‰ in early Tithonian (Fig. 8.32).

The $\delta^{18}O$ curves proposed by Price and Rogov (2009), Nunn and Price (2010) and Dera et al. (2011), based on belemnite samples, show a decrease of $\delta^{18}O$ values during Oxfordian from about 0 ‰ to -1 ‰. The curve proposed by Price and Rogov and Nunn and Price (2010) suggests a decrease in $\delta^{18}O$ also during Kimmeridgian until late Kimmeridgian (-2 ‰) and a decrease in $\delta^{18}O$ from latest Kimmeridgian to Tithonian up to 0 ‰ (Fig. 8.32). Dera et al. (2011) proposed an increase throughout Kimmeridgian to 0 ‰. and another decrease during Early Tithonian to -1.5 ‰.

The $\delta^{13}C$ and $\delta^{18}O$ values measured for eastern Sardinia carbonate succession in this study do not match with the curves proposed in literature (Fig. 8.32). Plotted $\delta^{13}C$ and $\delta^{18}O$ values appear to be more scattered and the isotopic signature of a large number of samples appears to be reset by burial or meteoric diagenesis. There are exceptions regarding $\delta^{13}C$ values for portions of the succession, probably less modified by diagenesis. In the Mt. Oro stratigraphic log (Fig. 8.4) from nearly the top of phase 2 facies (about 55 m, upper Kimmeridgian) to the top of phase 3 facies (about 100 m, upper Kimmeridgian) there is a general decrease in $\delta^{13}C$ with some exceptions with values ranging from 2 ‰ to 1.5 ‰ as in the curves proposed by Jenkyns (1996) and Weissert and Mohr (1996) for the Tethyan realm. In the Genna Ramene log (Fig. 8.3), in the lower part of phase 2 facies (from about 47 m to about 55 m, upper Oxfordian-upper Kimmeridgian?) $\delta^{13}C$ values with some exceptions appear to slightly decrease from 2.5 ‰ to 2 ‰ like in the curves proposed by Jenkyns (1996) and Weissert and Mohr (1996).

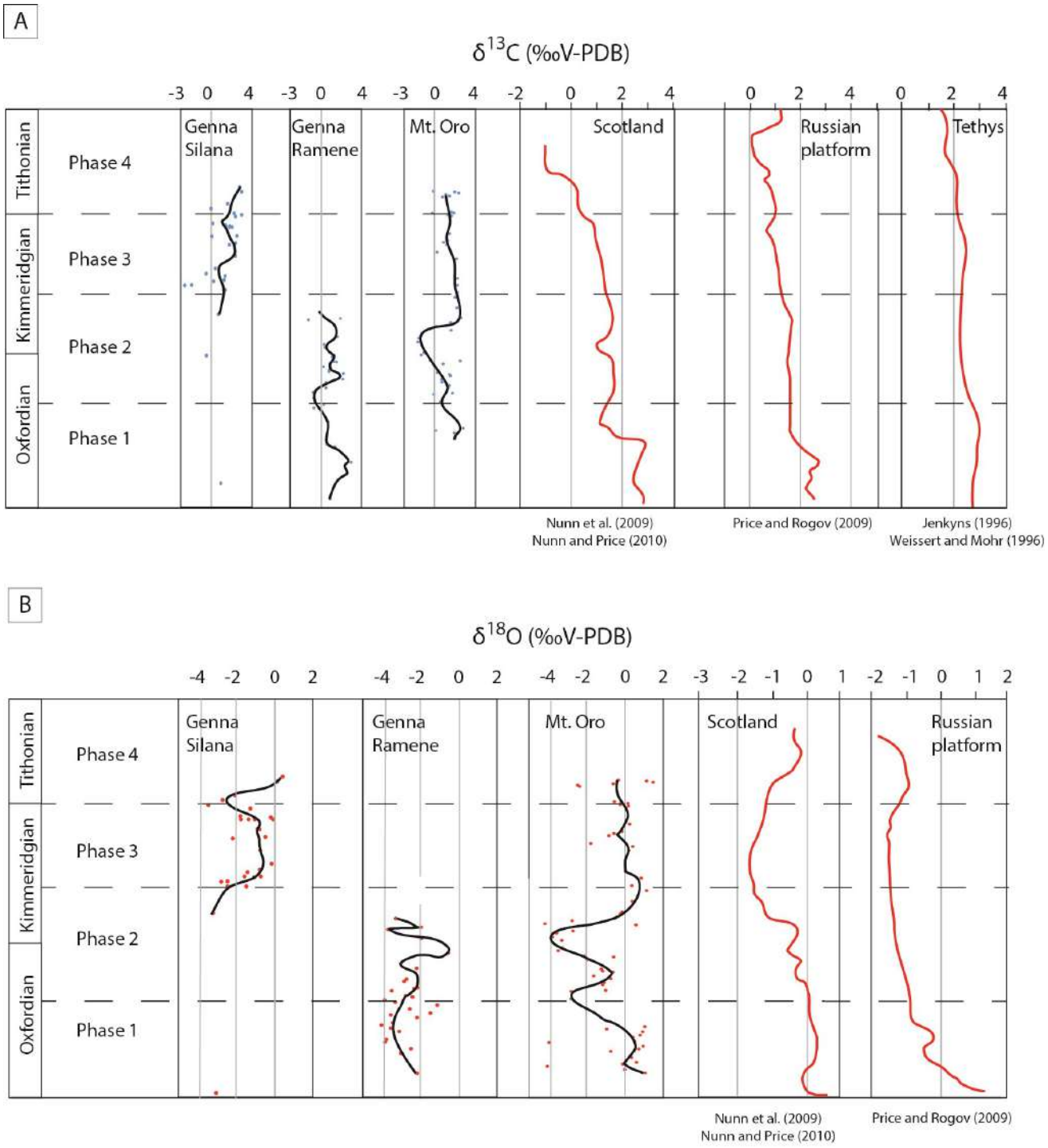

Figure 8.32 A) Comparison between $\delta^{13}C$ curves from this study and composite $\delta^{13}C$ curves of marine pristine carbonates from Scotland (Nunn et al., 2009; Nunn and Price, 2010), Russian Platform (Price and Rogov (2009) and Tethys (Jenkyns, 1996; Weissert and Mohr, 1996); B) Comparison between $\delta^{18}O$ curves from this study and composite $\delta^{18}O$ curves from Scotland (Nunn et al., 2009; Nunn and Price, 2010) and Russian Platform (Price and Rogov (2009).

8.5 Conclusions

The petrographic, cathodoluminescence and stable isotope analyses of the eastern Sardinia Callovian-Tithonian carbonate succession allowed the reconstruction of its diagenetic history.

Phase 1 facies (from F1 to F4) were affected by mechanical compaction, dissolution and fracturing in burial environment. Burial dolomitization characterized this portion of the succession close to the Hercynian basement (DOL-1, DOL-2) with zoned luminescence in CL and isotopic signature with $\delta^{13}C$ between 0.1 ‰ and 3.0 ‰ and $\delta^{18}O$ between -1.0 ‰ and 1.2 ‰. Blocky equant calcite cement and microsparite precipitated in burial environment and partially in meteoric environment during telogenesis. Dedolomitization took place during telogenesis recorded with depletion in both ^{13}C and ^{18}O and non-luminescence response to CL by some dolostone samples (Mt. Oro log). Some samples from F1 were altered by ^{12}C enriched meteoric fluids.

In Phase 2 facies (from F5 to F13) isopachous fibrous marine cement precipitated during early marine diagenesis; dissolution, mechanical compaction and fracturing occurred during burial diagenesis. These facies were dolomitized in burial environment in the lower part of Mt. Oro stratigraphic log (DOL-1 and DOL-2). Blocky equant calcite cement and microsparite precipitated in burial environment and possibly during meteoric telogenesis.

Phase 3 middle ramp facies (F14 and F15) are characterized by early marine cementation by isopachous fibrous calcite cement. Inner platform facies (from F16 to F27) are characterized by early meteoric cementation by micrite meniscus and pendant cement. Dissolution occurred in meteoric and possibly burial environment. The upper part of the succession of facies from F16 to F27 was affected by early dolomitization due to evaporitic brines (DOL-3, DOL-4, DOL-5). Equant blocky calcite, fine-grained equant calcite and microsparite cement precipitated in burial and meteoric environment and during meteoric telogenesis. The isotopic signal of phase 3 facies might have preserved the original marine values, but sometimes it appears depleted in ^{18}O, probably due to resetting by high-temperature burial fluids, especially near the subaerial exposure surfaces at the bottom and the top of phase 3.

Phase 4 facies show early marine phreatic cementation in inner platform facies (F32 and F33) with isopachous fibrous cement and in slope facies (F35 and F36) with radiaxial fibrous calcite cement. Micritic meniscus cement precipitated in supratidal facies in early meteoric vadose conditions and dissolution occurred in early meteoric and burial environments. Fabric replacive dolomitization, with an isotopic signal characterized by $\delta^{13}C$ between 1.9 ‰ and 3.0 ‰ and positive $\delta^{18}O$ from 0.7 ‰ to 3.6 ‰, took place near the subaerial exposure boundary with phase 3 in inner platform facies due to

evaporitic brines. Equant blocky calcite cement and microsparite precipitated in burial environment and likely in meteoric environment during telogenesis.

Carbon and oxygen stable isotope analyses allowed recognizing the facies for which the isotopic signature was influenced by meteoric and burial diagenesis (low $\delta^{13}C$ and $\delta^{18}O$ values). Generally, the isotopic signatures of cemented grain-supported grainstone and boundstone facies types were altered by diagenetic fluids, whereas wackestone, mudstone and floatstone records marine original values. Among, packstone facies types, only facies F15, F17, F32, F33 and F37 were reset during diagenesis, whereas facies F2, F3, F4, F6, F7, F20, F26, F30, F32 and F36 could retain the Late Jurassic marine pristine isotopic signature. However, the comparison with published $\delta^{13}C$ and $\delta^{18}O$ curves of pristine marine carbonates revealed that numerous samples appear to be reset by burial or meteoric diagenesis with the exception of scattered portions of the succession.

Chapter 9

Final remarks on controlling factors of Upper Jurassic reef distribution

Upper Jurassic reef distribution and composition are controlled by several factors such as tectonics, eustatic fluctuations, climate oscillations, nutrient levels and oceanographic parameters. The study of eastern Sardinia carbonate succession contributes to the assessment of how each of these factors influences carbonate platform evolution and reef growth.

9.1 Tectonics

In Chapter 6 the role of extensional tectonic activity as an important controlling factor of the evolution of carbonate ramps and platforms and reef growth and demise was pointed out. Tectonics controlled relative sea-level and accommodation changes influencing the development of reefal carbonate factories. For instance, a likely tectonically driven relative sea-fall in the late Kimmeridgian caused the switch off of the reefal carbonate factory at the end of eastern Sardinia phase 2. The effects of extensional tectonics during Kimmeridgian and Tithonian times in the European margin of the Alpine Tethys are reported from the Central Iberian rift system (Aurell et al., 2019ab), North Iberian Range (Benito et al., 2001), western France (Carcel et al., 2010) and Apulian-Adriatic platforms (Santantonio et al., 2013). As in eastern Sardinia, in these settings shallowing and deepening-upward trends and subaerial exposures, and consequently facies character and architecture, are influenced by accommodation changes driven by extensional tectonics.

However, besides the influence on vertical facies evolution, tectonics is a primary control on the geometry of the depositional profile. One of the differences between the northern Tethys and intra-Tethys reefs is the structural setting. The intra-Tethys isolated carbonate platforms are characterized by tectonically controlled high-relief steep margins, whereas northern Tethys reefs developed on low relief carbonate ramps on the northern European passive margin. Indeed, in the northern Tethys and in some Atlantic carbonate ramp systems, reefs developed in middle (coral-stromatoporoid, coral-microbial or coral reefs) to outer ramp (siliceous sponge reefs) environments and their distribution and composition were primarily controlled by bathymetry (cf. Crevello and Harris, 1984; Leinfelder,

1993a; Leinfelder et al., 2002; Della Porta et al., 2013; San Miguel et al., 2017). Eastern Sardinia phase 2 (late Oxfordian-late Kimmeridgian) reefs show a similar distribution on the depositional profile and similar facies to other coeval case studies but with some differences (Chapter 5). Instead, in intra-Tethys isolated carbonate platforms coral-stromatoporoid reefs formed in platform margin to upper-slope environments (cf. Turnšek et al., 1981; Schlagintweit and Gawlick, 2008; Rusciadelli et al., 2011; Kiani Harcegani and Morsilli, 2019). Syn-depositional cement is widespread in this type of reefs due to the high-energy conditions and high porosity in the boundstone facies favouring pumping of seawater and early cementation in marine phreatic environment. Eastern Sardinia phase 4 (Tithonian) reef facies characters analysed in resedimented breccias (F28) resemble much more intra-Tethys reef facies developed at high-relief platform margins and on upper slopes rather than the phase 2 build-ups developed on the upper Oxfordian-upper Kimmeridgian ramp (Chapter 7). Indeed, Eastern Sardinia phase 4 carbonate platform (Tithonian) with inner platform, slope and basin environments show a different higher-relief depositional profile with respect to phase 2 carbonate ramp (late Oxfordian-late Kimmeridgian) due to syn-depositional normal faulting (Jadoul, 2018).

9.2 Eustasy

Besides tectonics, global eustatic sea-level is another important controlling factor on reef evolution. According to Leinfelder et al. (2002), eustatic sea-level rises may favour conditions for reef growth enlarging available shallow-water habitat areas and restricting terrigenous influx and the Late Jurassic peak of reef distribution partially mirror the general outline of the eustatic sea-level curve.
Kiessling (2002, 2009) suggested that large scale eustatic sea-level changes show a significant cross-correlation with preserved reef numbers and volume at million-year time scale. A comparison with the published eustatic curves (Hallam, 1988; Sahagian et al., 1996; Miller et al., 2005; Haq, 2018) confirmed that the two phases of reef growth in eastern Sardinia (phase 2 late Oxfordian-late Kimmeridgian and phase 4 Tithonian) are coeval and possibly triggered by periods of major eustatic sea-level rise (cf. Chapter 6).

9.3 Climate

Eustatic sea-level changes cannot be decoupled from climatic fluctuations because they result from the interplay of global geodynamics and climate. The debate about Jurassic climate and Late Jurassic climatic fluctuations are discussed in Chapter 2, Chapter 5 and Chapter 6. Despite the majority of the

authors in disagreement about Late Jurassic climatic oscillations (Cecca et al., 2005; Dera et al., 2011, 2015; Martin-Garin et al., 2012), there is agreement on a climate warming in the middle Oxfordian, possibly related to ice-pole melting (Dromart et al., 2003). The ice-pole melting led to a global sea-level rise paralleled by climate warming.

According to several studies (Cecca et al., 2005; Martin-Garin et al., 2010, 2012), the Late Jurassic latitudinal occurrence of reef sites is related to climatic fluctuations. During the warmer middle Oxfordian, corals reefs expanded towards higher latitudes (up to 35 °N), whereas in the late Oxfordian, due to cooling climate, reefs shifted toward the Equator (Cecca et al., 2005; Martin-Garin et al., 2012). However, stable isotope analyses (Dera et al., 2011; 2015) suggest that the late Oxfordian to early Tithonian was a global warming trend in contrast with the suggested cooling at the late Oxfordian proposed by Martin-Garin et al. (2012).

For the Late Jurassic, it appears difficult to separate the role of contemporaneous climate warming and global sea-level rise on reef site distribution, because they appear correlated. However, it is suggested that it is misleading to assign the primary control on latitudinal reef distribution only to climate, as proposed by Dera et al. (2011, 2015). Indeed, according to Kiessling (2009), studies linking reef expansion to climate changes (e.g., Cecca et al., 2005) did not explain why other similar changes in global temperature did not lead to similar reef responses. Climate must be one of the driving factors, but together with other parameters related to sea-level rise, oceanic circulation and environmental factors (Kiessling, 2009).

Besides global climatic fluctuations another controlling factor on climate, often underestimated, is plate motion (Kent and Irving, 2010). From the Oxfordian to Tithonian the global monster plate shift caused a 30° rotation of the continental plates about a pole centered in western Africa (Kent et al., 2015; Muttoni and Kent, 2019). It is demonstrated that this plate motion affected carbonate platform sedimentation in Saudi Arabia, Northern Italy (Adria) and Central Iran modyfing the palaeolatitude of these places and consequently their climatic belt (Muttoni et al., 2013; Mattei et al., 2014; Muttoni and Kent, 2016, 2019). As a consequence, global plate motion and the deriving local climate changes are controlling factors on Jurassic carbonate sedimentation and reef growth that cannot be ignored.

9.4 Nutrient supply

Modern scleractinian corals obtain the necessary nutrient supply thanks to the photosymbiontic relationship with the dynoflagellate algae zooxanthellate (Stanley, 2006). For this reason, present-day scleractinian corals typically thrive in oligotrophic setting. However, there are geological evidences that during Jurassic corals thrived both in mesotrophic and oligotrophic settings (Nose and

Leinfelder, 1997) and the symbiontic relationship with zooxanthellae was probably far from being perfect (Nose and Leinfelder, 1997; Leinfelder et al., 2002). Indeed, numerous coral taxa required a higher amount of particulate nutrients and probably heterotrophic nutrition for corals was much more important than in modern settings (Nose and Leinfelder, 1997). Instead, according to Leinfelder et al. (2005) stromatoporoids were more adapted to high-energy oligotrophic settings.

The global distribution of reef-building organisms could reflect nutrient availability in Late Jurassic seawater. In the northern Tethys realm, reefs developed on carbonate ramps attached to continental areas and were influenced by fine siliciclastic input (Leinfelder et al., 2002). Dupraz and Strasser (1999, 2002) described coral-microbialite reefs with microencrusters developed from oligotrophic to mesotrophic conditions depending on the amount of terrigenous input. In the Oxfordian-Kimmeridgian Atlantic region (Portugal) coral patch reefs formed also on coastal siliciclastic shelves (Leinfelder, 1993a).

The absence or lack of stromatoporoids among the reef-building biota in the northern Tethys reefs could be interpreted in trophic terms due to relatively elevated nutrient particulates in seawaters with high terrestrial runoff (Leinfelder et al., 2005). Instead, in the intra-Tethys isolated platforms, stromatoporoids dominated in coral-stromatoporoid reefs in high-energy platform margin environments and are considered indicative of oligotrophic conditions (Leinfelder et al., 2005). However, stromatoporoid build-ups associated with microbialites can be adapted to mesotrophic environment (Kiani Harchegani and Morsilli, 2019). Thus, the interpretation of reef building biota distribution according to nutrient availability and nutrition modes appears to be simplistic and probably different stromatoporoid taxa required different trophic levels (Leinfelder et al., 2005).

9.5 Distribution of microbialites

Despite microbialites were important reef builders during the Late Jurassic period, build-ups in different palaeogeographic realms show a variable content of microbial crusts. Microbialites were abundant in the Atlantic realm (Portugal, Leinfelder, 1993a), in the Kimmeridgian of the Iberian Basin (Aurell et al., 2010, 2011; San Miguel et al., 2013, 2017), northern Germany (Helm and Schülke, 2006) and in carbonate platforms in the Swiss and French Jura Mountains (Dupraz and Strasser, 1999, 2002; Samankassou et al., 2003; Colombié and Strasser, 2005; Olivier et al., 2011). Eastern Sardinia build-ups lack abundant microbial boundstone precipitates, which occur only in the deeper middle to outer ramp sponge-coral-microbialite type 3 build-ups. Similarly, intra-Tethys reefs generally lack abundant microbialite content.

In the Iberian Basin and Jura Mountains excess in nutrient supply related to terrestrial run-off in seawater is interpreted to be unfavourable for coral and stromatoporoid growth and could have facilitated high amount of microbialites development in build-ups (Dupraz and Strasser, 1999, 2002; Olivier et al., 2011; San Miguel et al., 2017). During the Phanerozoic microbialites colonized reefal environments in periods of crises of skeletal reef builders or where environmental conditions prevented coral growth (cf. Della Porta et al., 2003, 2004; Bahamonde et al., 2004; Mata and Bottjer, 2012). The lack of microbial content in eastern Sardinia and intra-Tethys reefs suggests that these environments were favourable for coral and stromatoporoid growth due to their trophic, light penetration and climatic conditions. Instead, in northern Tethys attached platforms, the abundance of microbialites could possibly indicate that environmental conditions were less prone to coral growth, especially during periods of high terrigenous input (Dupraz and Strasser, 1999, 2002; Olivier et al., 2011).

9.6 Open questions and further perspectives

Despite there is a wealth of studies on Upper Jurassic reefs and carbonate platforms, this study on eastern Sardinia contributes to the knowledge on controlling factors on reef and platform evolution. Nevertheless, the full understanding of how carbonate platforms and reefs responded and respond to global and local environmental, climatic and accommodation changes is far from being achieved.

The climatic control on the spreading of reef-building biota during middle Oxfordian-early Kimmeridgian time is still a matter of debate (Cecca et al., 2005; Martin-Garin et al., 2012; Dera et al., 2011). If for Oxfordian-Kimmeridgian times climate warming and coral diffusion appear to be related, other global warming trends in the geological history did not match with coral reefs diffusion (Kiessling, 2009). Instead, the contribution of eustatic sea-level rises in creating available space for reef growth is well-established and appears of paramount importance (Kiessling, 2002, 2009; Leinfelder et al., 2002). This accommodation control is also recorded in the evolution of eastern Sardinia carbonate succession for the onset of the reefal carbonate factories in phase 2 and phase 4.

The role of nutrient availability is also likely very significant in Upper Jurassic reef distribution, but further research is needed to better understand how corals and stromatoporoids were adapted to different trophic conditions. Probably a specific nutrient mode should be suggested for different coral and stromatoporoid taxa.

An evolutionary trend of reef-building biota can be excluded, because Lower Jurassic reefs are characterized by the same reef builders and types of build-ups that characterized Upper Jurassic reefs

(Della Porta et al., 2013). The only difference is the limited corals, stromatoporoids, calcareous and siliceous sponge, microbialite reefs distribution in Early Jurassic with respect to wider Late Jurassic distribution following the extinction event and biotic crises at the Triassic/Jurassic boundary. Certainly, environmental conditions changed during the whole Jurassic, but it is difficult to individuate which are the limiting parameters that prevented reef distribution during Early Jurassic and further investigations are needed.

Regarding the Middle-Upper Jurassic eastern Sardinia carbonate succession future investigations are needed, especially in the northern Orosei Gulf outcropping area. Biostratigraphic and magnetostratigraphic studies are available (Casellato et al., 2012; Muttoni et al., 2018), but there is a lack of extensive age dating of the stratigraphic succession integrated with detailed sedimentological and facies analysis studies. Facies analyses and stratigraphic reconstructions in the northern Orosei Gulf area could allow a comparison with the results of this study, focussing on the southern area, and could lead to the overall comprehension of the whole Middle-Upper Jurassic eastern Sardinia carbonate succession.

In the southern portion of the Orosei Gulf analysed in this study further studies are needed in the portion of the succession between depositional phases 1 and 2. The age of the switch in carbonate factory was assigned indirectly in comparison with coeval similar depositional system. However, more detailed age constrain data area needed to pinpoint the precise evolutionary history of the depositional system.

Chapter 10

Conclusions

The sedimentological and stratigraphic study of the Callovian-Tithonian portion of the eastern Sardinia carbonate succession cropping out in the southern portion of the Orosei Gulf allowed recognizing 37 carbonate facies differently distributed in the study area and the identification of four depositional phases (from phase 1 to phase 4) improving and expanding previous published studies on the lithostratigraphy of the Jurassic succession.

Phase 1 (Callovian-middle Oxfordian) was characterized by a low-angle coated grain dominated carbonate ramp with ooidal shoals and middle ramp peloidal packstone. From phase 1 to phase 2 the depositional system evolved into a reef-bearing carbonate ramp (upper Oxfordian-upper Kimmeridgian) with three types of build-ups controlled in composition and spatial distribution by bathymetry (light penetration, hydrodynamic energy), as in coeval northern Tethys and Atlantic carbonate systems. Coral-stromatoporoid (type 1) and coral-calcareous sponge-diceratid (type 2) reefs developed in middle ramp environment exposed to the effect of storm currents and internal waves, whereas calcareous and siliceous sponge-coral-microbialite reefs lacking stromatoporoids (type 3) formed in lower-energy distal, middle to outer ramp settings. The colonization by reef-building biota of the eastern Sardinia carbonate ramp was related to the global expansion of corals, stromatoporoids, calcareous and siliceous sponges and microbialites caused by the interplay of eustatic sea-level rise and climatic fluctuations. The low-angle carbonate ramp depositional geometry and development of build-ups in middle ramp environment characterized upper Oxfordian-upper Kimmeridgian eastern Sardinia and northern Tethys reefs. However, the abundances of stromatoporoids, chaetetids and undetermined calcareous sponges in build-up type 1 and type 2 differentiate eastern Sardinia reefs from the northern Tethys reefs, possibly due to lower nutrient availability and terrestrial run-off in eastern Sardinia. For this reason, eastern Sardinia carbonate ramp could be considered a transitional domain linking the attached northern Tethys carbonate systems and the isolated intra-Tethys platforms. Strontium isotopes and biostratigraphic analyses allowed placing the top of phase 2 in the late Kimmeridgian.

Phase 3 (late Kimmeridgian) followed a subaerial exposure surface associated with a relative sea-level fall at the top of phase 2, probably driven by regional extensional tectonics in the European margin of the Alpine Tethys. Phase 3 was characterized by peritidal facies in the inner platform setting and coated grain dominated (ooids and oncoids) reworked in middle ramp facies. New

biostratigraphic data showing the presence of *Alveosepta jaccardi* in the phase 3 inner platform facies allowed dating this depositional phase to the late Kimmeridgian. Phase 3 was capped by a second major subaerial exposure surface due to a relative sea-level fall recorded in other Tethyan depositional systems by a regional unconformity attributed to uplift driven by extensional tectonics. Phase 4 (Tithonian) recorded the onset of a different depositional system following the early Tithonian transgression at the onset of phase 4. The early Tithonian age of these transgressive basinal deposits was assigned on the basis of new ammonite biostratigraphic data. A high-relief carbonate platform with a slope up to 70 m high developed in parallel with the recovery of the reefal carbonate factory; the growth of different types of build-ups in phase 4 contributed to the development of a different depositional geometry with respect to upper Oxfordian-upper Kimmeridgian reefs (phase 2). Facies analysis of lithoclasts resedimented by debris flow in basinal environment allowed recognizing 8 facies and reconstructing portions of the Tithonian carbonate platform not cropping out but identified through the resedimented debris into the adjacent basin. Bio-intraclastic grainstone, wackestone with *Clypeina jurassica*, wackestone to floatstone with oncoids and peloidal intraclastic packstone to grainstone deposited in inner platform environment. Coral-calcareous sponge-microbialite boundstone and *Bacinella* boundstone constituted build-ups in well-illuminated shallow water environment, whereas the calcareous sponge-*Crescentiella*-coral boundstone probably formed build-ups in high-energy upper slope settings and the calcareous-siliceous sponge boundstone colonized deeper slope environments.

The onset of the Tithonian phase 4 and the recovery of the reefal carbonate factory were probably controlled by early Tithonian eustatic sea-level rise that restored optimal conditions for reef growth. Jurassic plate motion probably led to the southern shift of eastern Sardinia modifying its latitudinal belt from a humid to an arid climate belt directly influencing facies characters.

Facies composition and architecture of eastern Sardinia carbonate succession were controlled by the interplay of regional tectonics, plate motion, the varying environmental conditions favouring the growth of reef biota and changes in carbonate factories, Late Jurassic climate and eustatic sea-level fluctuations. Kimmeridgian and Tithonian extensional tectonics affecting the European margin of the Alpine Tethys was a major controlling factor as well as eustatic sea-level rises and substrates available for reef development.

Petrographic, cathodoluminescence (CL) and carbon and oxygen isotopes analyses allowed investigating the diagenetic evolution for each depositional phase. Phase 1 facies were affected by burial replacive dolomitization close to the Hercynian basement with isotopic values of $\delta^{13}C$ between 0.1 ‰ and 3.0 ‰ and $\delta^{18}O$ between -1.0 ‰ and 1.2 ‰. Blocky calcite cement and microsparite precipitated in burial environment and during meteoric telogenesis. Dedolomitization took place in

telogenetic meteoric environment and caused depletion in both ^{13}C and ^{18}O and non-luminescence response to CL by some dolostone samples. Phase 2 facies were affected by early marine cementation (isopachous fibrous cement), burial dolomitization and precipitation of equant blocky calcite and microsparite cement in burial and meteoric telogenetic environment.

Phase 3 facies were characterized by isopachous fibrous cement precipitation in marine phreatic environment (middle ramp facies) or micritic meniscus and pendant cement in meteoric vadose environment (inner platform facies). Replacive dolomitization took place at the top of phase 3 facies, close to the subaerial exposure surface due to evaporitic brines as demonstrated by the high $\delta^{13}C$ and $\delta^{18}O$ values. Equant blocky calcite, fine-grained equant calcite and microsparite precipitation took place in burial environment and during telogenesis. Phase 4 facies were affected by early marine phreatic and meteoric vadose cementation as demonstrated by the occurrence of isopachous fibrous cement and micritic meniscus cement, respectively. The lower part of phase 4 facies, close to the subaerial exposure surface, was affected by fabric replacive dolomitization due to evaporitic brines as at the top of phase 3. The isotopic signal of this dolomite is characterized by $\delta^{13}C$ between 1.9 ‰ and 3.0 ‰ and positive $\delta^{18}O$ from 0.7 ‰ to 3.6 ‰. Precipitation of blocky calcite cement and microsparite took place in burial environment and during meteoric telogenesis.

This study contributes to the knowledge on the controlling factors of Upper Jurassic carbonate platform evolution. The development of different carbonate factories and reef growth is influenced by bathymetry, hydrodynamic energy and changes in ecologic and oceanographic parameters, such as nutrient fluxes. The role of the numerous Jurassic climatic fluctuations, including local climate changes related to plate motion, is still unclear, whereas sea-level fluctuations are considered of paramount importance in driving the onset and growth of reef carbonate factories. Furthermore, this study evaluates the importance of regional tectonics in affecting platform evolution growth phases and facies architecture.

Acknowledgements

First of all, I wish to warmly thank my supervisor professor Giovanna Della Porta for scientific, moral and financial support during my master thesis and PhD, particularly for the great deal of patience in correcting my mistakes and inspiring my research day by day. Professor Fabrizio Berra is thanked for the great contribute in this research, especially stimulating discussion and bringing out questions and for his help on the field.

I am grateful to my wife Elisa that accompanies me in life, forgives all my distractions and failings and supported me during all the duration of my PhD. I would like also to thank all my family, in particular my brother and my parents for the continuous support they have given me since I was a child.

Professor Flavio Jadoul is thanked for stimulating my passion for carbonate sedimentology, introducing the study area and stimulating discussion. I would like to thank Alessandro Lanfranchi as well, for guiding me to key outcrops and provide inspiration in the geological interpretation.

Professors Marcos Aurell, Michele Morsilli and Giovanni Muttoni are thanked for the careful and highly detailed reviews that greatly improved this thesis.

I am also grateful to all the PhD students and researchers that share these three years with me at Milan University, in particular Irene Bollati, Ruben Marchesi, Facheng Ye, Gabrielle Bindellini and Alessandro Mancini. I wish to thank all the people I knew during my internship at the University of Zaragoza, particularly professor Beatriz Bádenas, professor Marcos Aurell and Cristina Sequero for introducing me to the Upper Jurassic of the Iberian Basin and providing inspiration on the interpretation of my data. Thanks also to the PhD students that I met during my stay, Alicia, Angel, Blanca and Urbez for the great welcome they gave me.

I am also grateful to Curzio Malinverno for thin section preparation, Elena Ferrari for the analyses with the mass spectrometer, Stefania Crespi for SEM analyses and Monica Dapiaggi for XRD analyses. Ruben Marchesi is thanked for ammonite sample preparation and photography and together with Luis Moliner for help in ammonite determination. José Manuel Fuenlabrada Pérez from the Universidad Complutense Madrid (Spain) is thanked for the Sr analyses. I wish also to thank Ilaria Menga, Lorenzo Cariati and Luigi Vignati for the help on the field and sample preparation for stable isotope analyses.

Finally, I would like to thank all my friends that supported me in difficult moments and share with me the joy for achieving this important goal and all the people that I did not mention in this paragraph but supported me during these years.

References

Adams, J.E. and Rhodes, M.L. (1960). Dolomitization by seepage refluxion. Bulletin of the American Association of Petroleum Geologists, 44 (12), 1912-1920.

Ahm, A.-S.C., Bjerrum, C.J., Blättler, C.L., Swart, P.K. and Higgins, J.A. (2018) Quantifying early marine diagenesis in shallow-water carbonate sediments. Geochimica et Cosmochimica Acta, 236, 140-159.

Ait Addi, A. (2006) The dogger reef horizons of the Moroccan Central High Atlas: New data on their development. J. African Earth Sci., 45, 162–172.

Aitken, J.D. (1967) Classification and environmental significance of cryptalgal limestones and dolomites, with illustrations from the Cambrian and Ordovician of southwestern Alberta. J. Sediment. Petrol., 37, 1163–1178.

Al Disi, Z.A., Jaoua, S., Bontognali, T.R.R., Attia, E.S.M., Al-Kuwari, H.A.A.S. and Zouari, N. (2017) Evidence of a role for aerobic bacteria in high magnesium carbonate formation in the evaporitic environment of Dohat Faishakh sabkha in Qatar. Frontiers of Environmental Science, 5, 1-11.

Al-awwad, S.F. and Collins, L.B. (2013) Carbonate-platform scale correlation of stacked high-frequency sequences in the Arab-D reservoir, Saudi Arabia. Sediment. Geol., 294, 205–218.

Al-awwad, S.F. and Pomar, L. (2015) Origin of the rudstone-floatstone beds in the Upper Jurassic Arab-D reservoir, Khurais Complex, Saudi Arabia. Marine and Petroleum Geology, 67, 743-768.

Al-Husseini, M.I. (1997) Jurassic Sequence Stratigraphy of the Western and Southern Arabian Gulf. GeoArabia, 2, 361–382.

Allan, J.R. and Matthews, R.K. (1982). Isotope signatures associated with early meteoric diagenesis. Sedimentology, 29, 797-817.

Alnazghah, M.H., Bádenas, B., Pomar, L., Aurell, M. and Morsilli, M. (2013) Facies heterogeneity at interwell-scale in a carbonate ramp, Upper Jurassic, NE Spain. Mar. Pet. Geol., 44, 140–163.

Amadesi, E., Cantelli, C., Carloni, G.C. and Rabbi, E. (1961) Ricerche geologiche sui terreni sedimentari del Foglio 208-Dorgali. Giorn di Geol., 28, 59–87.

Andrieu, S., Brigaud, B., Barbarand, J., Lasseur, E. and Saucède, T. (2016) Disentangling the control of tectonics , eustasy , trophic conditions and climate on shallow-marine carbonate production during the Aalenian – Oxfordian interval : From the western France platform to the western Tethyan domain. Sediment. Geol., 345, 54–84.

Arenas, C., Alonso Zarza, A.M. and Pardo, G. (1999) Dedolomitization and other early diagenetic processes in Miocene lacustrine deposits, Ebro Basin (Spain). Sedimentary Geology, 125, 23-45.

Arp, G., Ostertag-Henning, C., Yücekent, S., Reitner, J. and Thiel, V. (2008) Methane-related microbial gypsum calcitization in stromatolites of a marine evaporative setting (Münder Formation, Upper Jurassic, Hils Syncline, north Germany). Sedimentology, 55, 1227–1251.

Arp, G., Reimer, A. and Reitner, J. (2001) Photosynthesis-induced biofilm calcification and calcium concentrations in phanerozoic oceans. Science (80-.)., 292, 1701–1704.

Aurell, M. and Bádenas, B. (2015) Facies architecture of a microbial – siliceous sponge-dominated ´ n carbonate platform: the Bajocian of Moscardo (Middle Jurassic, Spain). In: Microbial Carbonates in Space and Time: Implications for Global Exploration and Production (Ed. D.W.J. Bosence, K.A. Gibbons, D.P. Le Heron, W.A. Morgan, T. Pritchard, and B.A. Vining), Geological Society, Special Publications, 418, London.

Aurell, M., Robles, B., Bádenas, B., Rosales, I., Quesada, S., Meléndez, G. and García-ramos, J.C. (2003) Transgressive – regressive cycles and Jurassic palaeogeography of northeast Iberia. Sediment. Geol., 162, 239–271.

Aurell, M., Bádenas, B., Ipas, J. and Ramajo, J. (2010) Sedimentary evolution of an Upper Jurassic carbonate ramp, Iberian Basin, NE Spain. Geol. Soc. Spec. Publ., 329, 89–111.

Aurell, M., Bádenas, B. and Bernard, C. (2011) The Kimmeridgian-Lower Tithonian Iberian carbonate ramps (Upper Jurassic, NE Spain): architecture, facies distribution and cyclostratigraphy. Post-meeting field trip guidebook, 28th IAS Meeting of Sedimentologists: Sociedad Geologica de España, Geo-Guias, 8, 45-86.

Aurell, M., Bádenas, B., Canudo, J.I., Castanera, D., García-Penas, A., Gasca, J.M., Martín-Closas, C., Moliner, L., Moreno-Azanza, M., Rosales, I., Santas, L., Sequero, C. and Val, J. (2019a) Kimmeridgian–Berriasian stratigraphy and sedimentary evolution of the central Iberian Rift System (NE Spain). Cretaceous Research, 103, 10415 https://doi.org/10.1016/j.cretres.2019.05.011

Aurell, M., Fregenal-Martìnez, M., Bádenas, B. Muñoz-Garcia, M.B., Élez, J., Meléndez, N. and de Santisteban, C. (2019b) Middle Jurassic–Early Cretaceous tectono-sedimentary evolution of the southwestern Iberian Basin (central Spain): Major palaeogeographical changes in the geotectonic framework of the Western Tethys. Earth-Science Reviews, 199, 102983.

Awramik, S.M. (1971) Precambrian columnar stromatolite diversity: reflection of metazoan appearance. Science (80-.)., 174, 825–827.

Baccelle, L. and Bosellini, A. (1965) Diagrammi per la stima visiva della composizione percentuale delle rocce sedimentarie. Ann Uni Ferrara, NS, Sez IX; Sci Geol Paleontol, 1, 59–62.

Bádenas, B., Aurell, M. (2001) Proximal - distal facies relationships and sedimentary processes in a storm dominated carbonate ramp (Kimmeridgian, northwest of the Iberian Ranges, Spain). Sedimentary Geology, 139, 319–340.

Bádenas, B. and Aurell, M. (2010) Facies models of a shallow-water carbonate ramp based on distribution of non-skeletal grains (Kimmeridgian, Spain). Facies 56:89–110.

Bádenas, B., Salas, R. and Aurell, M. (2004) Three orders of regional sea-level changes control facies and stacking patterns of shallow platform carbonates in the Maestrat Basin (Tithonian-Berriasian, NE Spain). Int. J. Earth Sci. (Geol Rundsch), 93, 144–162.

Bádenas, B., Aurell, M. and Gröcke, D.R. (2005) Facies analysis and correlation of high-order sequences in middle–outer ramp successions: variations in exported carbonate on basin-wide $\delta^{13}C_{carb}$ (Kimmeridgian, NE Spain). Sedimentology, 52, 1253-1275.

Bádenas, B., Pomar, L., Aurell, M. and M. Morsilli (2012) A facies model for internalites (internal wave deposits) on a gently sloping carbonate ramp (Upper Jurassic, Ricla, NE Spain). Sedimentary Geology, 271-272, 44-57.

Bahamonde, J.R., Della Porta, G., Merino-Tomé, O. (2017) Lateral variability of shallow-water facies and high-frequency cycles in foreland basin carbonate platforms (Pennsylvanian, NW Spain). Facies 63, 6.

Barattolo, F. and Bigozzi, A. (1996) Dasycladaleans and depositional environments of the Upper Triassic-Liassic carbonate platform of the Gran Sasso (Central Apennines, Italy). Facies, 35, 163–208.

Baria, L.R., Stoudt, D.L., Harris, P.M. and Crevello, P.D. (1982) Upper Jurassic reefs of Smackover Formation, United States Gulf Coast. Am. Assoc. Pet. Geol. Bull., 66, 1449–1482.

Bartley, J.K. (1996) Actualistic taphonomy of cyanobacteria: implications for the Precambrian Fossil Record. Palaios, 11, 571–586.

Bartolini, A., Baumgartner, P.O. and Hunziker, J. (1996) Middle and Late Jurassic carbon stable-isotope stratigraphy and radiolarite sedimentation of the Umbria-Marche Basin (Central Italy). Eclogae Geol. Helv., 89, 811–844.

Bartolini, A., Pittet, B., Mattioli, E. and Hunziker, J.C. (2003) Shallow-platform palaeoenvironmental conditions recorded in deep-shelf sediments: C and O stable isotopes in Upper Jurassic sections of southern Germany (Oxfordian – Kimmeridgian). Sediment. Geol., 160, 107–130.

Basilone, L. (2009) Mesozoic tectono-sedimentary evolution of Rocca Busambra. 115–135.

Basilone, L. and Sulli, A. (2016) A facies distribution model controlled by a tectonically inherited sea bottom topography in the carbonate rimmed shelf of the Upper Tithonian – Valanginian Southern Tethyan continental margin (NW Sicily, Italy). Sediment. Geol., 342, 91–105.

Baumgartner, P.O. (1987) Age and genesis of Tethyan Jurassic Radiolarites. Eclogae Geol Helv, 80, 831–879.

Belperio, A.P., Gostin, V.A., Cann, J.H. and Murray-Wallace, C. V. (1988) Sediment-organism zonation and the evolution of Holocene tidal sequences in Southern Australia. In: Tide-Influenced Sedimentary Environments and Facies (Ed. P.L. de Boer, A. van Gelder, and S.D. Nio), D. Reidel Publishing Company, Dordrecth, 475–497.

Benito, M.I., Lohmann, K.C. and Mas, R. (2001). Discrimination of multiple episodes of meteoric diagenesis in a kimmeridgian reefal complex, north iberian range, Spain. Journal of Sedimentary Research 71, 380–393. https://doi.org/10.1306/2DC4094C-0E47-11F22-8643000102F14865D

Benito, M.I., Lohmann, K.C. and Mas, R. (2005) Late Jurassic paleogeography and paleoclimate in the Northern Iberian Basin of Spain: Constraints from diagenetic records in reefal and continental carbonates. J. Sediment. Res., 75, 82–96.

Benito, M.I. and Mas, R. (2006) Sedimentary evolution of the Torrecilla Reef Complex in response to tectonically forced regression (Early Kimmeridgian, Northern Spain). Sediment. Geol., 183, 31–49.

Berner, R.A. (1991) A model for atmospheric CO_2 over Phanerozoic time. Am. J. Sci., 291, 339–376.

Bernoulli, D. (1964) Zur Geologie des Monte Generoso (Lombardische Alpen). Beitr. Geol. Karte Schweiz, 118, 135.

Berra, F., Galli, T., Reghellin, F., Torricelli, S. and Fantoni, R. (2009) Stratigraphic evolution of theTriassic ^ Jurassic succession in the Western Southern Alps (Italy): the record of the two-stage rifting on the distal passive margin of Adria. Basin Res., 21, 335–353.

Berra, F., Stucchi, E.M. and Moretti, S. (2019). New information from “old” seismic lines: an update geological interpretation from the re-processing of the CROP line M-2A/I (Bonifacio Straits) at shallow depths. Italian Journal of Geosciences, 138, 31-42.

Berra, F., Azmy, K. and Della Porta, G. (2020) Stable-isotope and fluid inclusion constraints on the timing of diagenetic events in the dolomitized Dolomia Principale inner platform (Norian, Southern Alps of Italy). Marine and Petroleum Geology, 121, 104615.

Bertling, M. and Insalaco, E. (1998) Late Jurassic coral/microbial reefs from the northern Paris Basin - facies, palaeoecology and palaeobiogeography. Palaeogeogr. Palaeoclimatol. Palaeoecol., 139, 139–175.

Beutel, E.K., Nomade, S., Fronabarger, A.K. and Renne, P.R. (2005) Pangea’s complex breakup: A new rapidly changing stress field model. Earth Planet. Sci. Lett., 236, 471–485.

Bill, M., O’Dogherty, L., Guex, J., Baumgartner, P.O. and Masson, H. (2001) Radiolarite ages in Alpine-Mediterranean ophiolites: Constraints on the oceanic spreading and the Tethys-Atlantic connection. Bull. Geol. Soc. Am., 113, 129–143.

Bodin, S., Hönig, M.R., Krencker, F.N., Danisch, J. and Kabiri, L. (2017) Neritic carbonate crisis during the Early Bajocian: Divergent responses to a global environmental perturbation. Palaeogeogr. Palaeoclimatol. Palaeoecol., 468, 184–199.

Boivin, S., Gretz, M., Lathuilière, B., Olivier, N., Bartolini, A. and Martini, R. (2018) Coral- and oyster-microbialite patch reefs in the aftermath of the Triassic–Jurassic biotic crisis (Sinemurian, Southeast France). Swiss J. Geosci., 111, 509–520.

Bosellini, A., Morsilli, M. and Neri, C. (1999) Long-term event stratigraphy of the Apulia Platform Margin (Upper Jurassic to Eocene, Gargano, southern Italy). J. Sediment. Res., 69, 1241–1252.

BouDagher-Fadel, M.K. (2008) The Mesozoic Larger Benthic Foraminifera. In: BouDagher-Fadel, M.K. (Ed.), Evolution and Geological Significance of Larger Benthic Foraminifera. Elsevier, Amsterdam, pp. 285–386.

Bover-Arnal, T. and Strasser, A. (2013) Relative sea-level change, climate, and sequence boundaries: insights from the Kimmeridgian to Berriasian platform carbonates of Mount Salève (E France). Int J Earth Sci (Geol Rundsch), 102, 493-515.

Brame, H.M.R., Martindale, R.C., Ettinger, N.P., Debeljak, I., Vasseur, R., Lathuilière, B., Kabiri, L. and Bodin, S. (2019) Stratigraphic distribution and paleoecological significance of Early Jurassic (Pliensbachian-Toarcian) lithiotid-coral reefal deposits from the Central High Atlas of Morocco. Palaeogeogr. Palaeoclimatol. Palaeoecol., 514, 813–837.

Brauchli, M., McKenzie, J.A., Strohmenger, C.J., Sadooni, F., Vasconcelos, C. and Bontognali, T.R.R. (2016) The importance of microbial mats for dolomite formation in the Dohat Faishakh sabkha, Qatar. Carbonates Evaporites, 31, 339-345.

Brigaud, B., Pucéat, E., Pellenard, P., Vincent, B. and Joachimski, M.M. (2008) Climatic fluctuations and seasonality during the Late Jurassic (Oxfordian–Early Kimmeridgian) inferred from $\delta^{18}O$ of Paris Basin oyster shells. Earth and Planetary Science Letters, 273, 58–67

Brigaud, B., Durlet, C., Deconinck, J., Vincent, B., Pucéat, E., Thierry, J. and Trouiller, A. (2009) Facies and climate/environmental changes recorded on a carbonate ramp: A sedimentological and geochemical approach on Middle Jurassic carbonates (Paris Basin, France). Sediment. Geol., 222, 181–206.

Brigaud, B., Vincent, B., Durlet, C., Deconinck, J.-F., Blanc, P. and Trouiller, A. (2010) Acoustic Properties of Ancient Shallow-Marine Carbonates: Effects of Depositional Environments and Diagenetic Processes (Middle Jurassic, Paris Basin, France). J. Sediment. Res., 80, 791–807.

Brigaud, B., Vincent, B., Carpentier, C., Robin, C., Guillocheau, F., Yven, B. and Huret, E. (2014) Growth and demise of the Jurassic carbonate platform in the intracratonic Paris Basin (France): Interplay of climate change, eustasy and tectonics. Mar. Pet. Geol., 53, 3–29.

Brock, T.D., Madigan, M.T., Martinko, J.M. and Parker, J. (1994) Biology of Microorganisms, 7th editio. Prentice Hall, New Jersey.

Bucković, D. (2008) Upper Jurassic Platform succession with characteristics of a deeper water intraplatform trough (Mt. Svilaja, Croatia). Cent. Eur. Geol., 51, 17–34.

Budd, D.A., Hammes, U. and Ward, W.B. (2000) Cathodoluminescence in calcite cements: new insights on Pb and Zn sensitizing, Mn activation, and Fe quenching at low trace-element concentrations. Journal of Sedimentary Research, 70 (1), 217–226.

Burne, R. V. and Moore, L.S. (1987) Microbialites: Organosedimentary Deposits of Benthic Microbial Communities. Palaios, 2, 241.

Butler, G.P. (1969) Modern evaporative deposition and geochemistry of coexisting brines, the sabkha, Trucial Coast, Arabian Gulf. Journal of Sedimentary Petrology, 39, 70-89.

Carcel, D., Colombié, C., Giraud, F. and Courtinat, B. (2010) Tectonic and eustatic control on a mixed siliciclastic-carbonate platform during the Late Oxfordian-Kimmeridgian (La Rochelle platform, western France). Sedimentary Geology, 223, 334-359.

Carmignani, L., Oggiano, G., Funedda, A., Conti, P., Pasci, S. and Barca, S. (2008) Carta Geologica della Sardegna, Scala 1:250.000. Litografia artistica Cartografia, Firenze.

Carpentier, C., Martin-garin, B., Lathuilie, B. and Ferry, S. (2006) Correlation of reefal Oxfordian episodes and climatic implications in the eastern Paris Basin (France). Terra Nov., 18, 191–201.

Carpentier, C., Lathuilière, B., Ferry, S. and Sausse, J. (2007) Sequence stratigraphy and tectonosedimentary history of the Upper Jurassic of the Eastern Paris Basin (Lower and Middle Oxfordian, Northeastern France). Sediment. Geol., 197, 235–266.

Carr, N.G. and Whitton, B.A. (1982) The biology of cyanobacteria, Vol.19. University of California Press.

Casellato, C.E., Jadoul, F. and Lanfranchi, A. (2012) Calcareous nannofossil biostratigraphy of the S'Adde Limestone (Mt. Albo, Orosei Gulf): insights into the Middle-Late Jurassic eastern Sardinia passive margin evolution. Riv. Ital. di Paleontol. e Stratigr., 118, 439–460.

Castanier, S., Le Métayer-Levrel, G. and Perthuisot, J.-P. (2000) Bacterial roles in the precipitation of carbonate minerals. In: Microbial Sediments (Ed. R. Riding and M. Awramik), Springer-Verlag, Berlin, Heidelberg, 32–39.

Cecca, F., Martin Garin, B., Marchand, D., Lathuiliere, B. and Bartolini, A. (2005) Paleoclimatic control of biogeographic and sedimentary events in Tethyan and peri-Tethyan areas during the Oxfordian (Late Jurassic). Palaeogeogr. Palaeoclimatol. Palaeoecol., 222, 10–32.

Chafetz, H.S. (1986) Marine peloids: a product of bacterially induced precipitation of calcite. J. Sediment. Petrol., 56, 812–817.

Chafiki, D., Canérot, J., Souhel, A., Hariri, K. El and Eddine, K.T. (2004) The Sinemurian carbonate mud-mounds from central High Atlas (Morocco): Stratigraphy, geometry, sedimentology and geodynamic patterns. J. African Earth Sci., 39, 337–346.

Cherchi, A. and Schroeder, R. (1985) Mesozoic of northwestern Sardinia. In: Cherchi A (ed) 19th European Micropaleontological Colloquium. Micropaleontological researches in Sardinia. Guidebook, 44–56.

Cherchi, A. and Schroeder, R. (2010) Boring sponges (ichnogenus Entobia) in mesozoic Lithocodium calcimicrobial crusts. Riv. Ital. di Paleontol. e Stratigr., 116, 351–356.

Cherchi, A. and Schroeder, R. (2013) Revision of the holotype of Lithocodium aggregatum Elliott, 1956 (Lower Cretaceous, Iraq): New interpretation as sponge-calcimicrobe consortium. Facies, 59, 49–57.

Cherchi, A., Mancin, N., Montadert, L., Murru, M., Putzu, M.T., Schiavinotto, F. and Verrubbi, V. (2008) The stratigraphic response to the Oligo-Miocene extension in the western

Mediterranean from observations on the Sardinia graben system (Italy). Bull. la Soc. Geol. Fr., 179, 267–287.

Cherchi, A., Simone, L. and Schroeder, R. (2010) I sistemi carbonatici giurassici della Sardegna orientale (Golfo di Orosei) ed eventi deposizionali nel sistema carbonatico giurassico-cretacico della Nurra (Sardegna nord-occidentale). Parte seconda, i sistemi carbonatici giurassico-cretacei della Nurra. Period Semest del Serv Geol d'Italia - ISPRA e della Soc Geol Ital GeolFTrips, 2, 122.

Chesnel, V., Merino-Tomé, O., Fernández, L.P., Villa, E. and Samankassou, E. (2016) Isotopic fingerprints of Milankovitch cycles in Pennsylvanian carbonate platform-top deposits: the Valdorria record, Northern Spain. Terra Nova, 28, 364-373.

Chiocchini, M., Chiocchini, R.A., Didaskalou, P. and Potetti, M. (2008) Microbiostratigrafia del Triassico superiore, Giurassico e Cretacico in facies di piattaforma carbonatica del Lazio centro-meridionale e Abruzzo: revisione finale. Mem. Descr. della Cart. Geol. d'Italia, 84, 5–170.

Choquette, P.W. and Hiatt, E.E. (2008) Shallow-burial dolomite cement: a major component of many ancient sucrosic dolomites. Sedimentology, 55, 423-460.

Colacicchi, R. and Praturlon, A. (1965) Stratigraphical and paleogeographical investigations on the Mesozoic shelf-edge facies in eastern Marsica (Central Apennines, Italy). Geol. Rom., 4, 89–118.

Collin, P.Y., Mancinelli, A., Chiocchini, M., Mroueh, M., Hamdam, W. and Higazi, F. (2010) Middle and Upper Jurassic stratigraphy and sedimentary evolution of Lebanon (Levantine margin): palaeoenvironmental and geodynamic implications. Geol. Soc. London, Spec. Publ., 341, 227–244.

Colombié, C. and Strasser, A. (2005) Facies, cycles, and controls on the evolution of a keep-up carbonate platform (Kimmeridgian, Swiss Jura). Sedimentology, 52, 1207–1227.

Colombié, C., Carcel, D., Lécuyer, C., Ruffel, A. and Schnyder, J. (2018) Temperature and cyclone frequency in Kimmeridgian Greenhouse period (late Jurassic). Global and Planetary Change, 170, 126-145.

Combes, P.J. (1990). Typologie, cadre géodynamique et génèse des bauxites Françaises. Geodin. Acta, 4 (2), 91-109.

Cook, H.E., McDaniel, P.N., Mountjoy, E.W. and Pray, L.C. (1972) Allochthonous Carbonate Debris Flows at Devonian Bank ("Reef") Margins, Alberta, Canada. Bull. Can. Pet. Geol., 20, 439–497.

Copper, P. (1974) Structure and development of Early Paleozoic reefs. In: Second international Coral Reef Symposium, 365–386.

Corlett, H.J., Bastesen, E., Gawthorpe, R.L., Hirani, J., Hodgetts, D., Hollis, C. and Rotevatn, A. (2018) Origin, dimensions, and distribution of remobilized carbonate deposits in a tectonically active zone, Eocene Thebes Formation, Sinai, Egypt. Sediment. Geol., 372, 44–63.

Costamagna, L.G. (2016a) Middle Jurassic continental to marine transition in an extensional tectonics context: the Genna Selole Fm depositional system in the Tacchi area (central Sardinia, Italy). Geol. J., 51, 722–736.

Costamagna, L.G. (2016b) The Middle Jurassic Alpine Tethyan Unconformity and the Eastern Sardinia - Corsica Jurassic High : A sedimentary and regional analysis. J. Iber. Geol., 42, 311–334.

Costamagna, L.G. and Barca, S. (2004) Stratigraphy, facies analysis, paleogeography and regional framework of the Jurassic succession of the "Tacchi" area (Middle-Eastern Sardinia). Boll. della Soc. Geol. Ital., 123, 477–495.

Costamagna, L.G., Barca, S. and Lecca, L. (2007) The Bajocian – Kimmeridgian Jurassic sedimentary cycle of eastern Sardinia: Stratigraphic, depositional and sequence interpretation of the new 'Baunei Group'. C. R. Geosci., 339, 601–612.

Courjault, T., Grosheny, D., Ferry, S. and Sausse, J. (2011) Detailed anatomy of a deep-water carbonate breccia lobe (Upper Jurassic, French subalpine basin). Sedimentary Geology, 238, 156-171.

Crescenti, U. (1969) Biostratigrafia delle facies mesozoiche dell'Appennino centrale. Geol Rom, 8, 15–40.

Crevello, P.D. and Harris, P.M. (1984) Depositional models for Jurassic reefal buildups. Gulf Coast Sect. SEPM Found. third Annu. Res. Conf. Proc., 57–102.

Crevello, P.D. and Schlager, W. (1980) Carbonate debris sheet and turbidites, Exuma Sound, Bahamas. J. Sediment. Petrol., 50, 1121–1148.

Dahanayake, K. (1977) Classification of oncoids from the Upper Jurassic carbonates of the French Jura. Sediment. Geol., 18, 337–353.

Dahanayake, K. (1978) Sequential position and environmental significance of different types of oncoids. Sediment. Geol., 20, 301–316.

Decho, A.W. (1990) Microbial exopolymer secretions in ocean environments: their role(s) in food webs and marine processes. Oceanogr. Mar. Biol. - An Annu. Rev., 28, 73–153.

Del Rio, M. (1976) Analisi palinologica del Giurese della Sardegna centrale. Boll. della Soc. Geol. Ital., 95, 619–631.

Del Rio, M. (1984) Palynology of the Middle Jurassic black organic shale of "Tacco di Laconi", Central Sardinia, Italy. Boll. della Soc. Paleontol. Ital., 23, 325–342.

Della Porta, G., Kenter, J.A:M., Bahamonde, J.R., Immenhauser, A. and Villa, E. (2003) Microbial Boundstone Dominated Carbonate Slope (Upper Carboniferous, N Spain): Microfacies, Lithofacies Distribution and Stratal Geometry. Facies, 49, 175-208.

Della Porta, G., Kenter, J.A.M. and Bahamonde, J.R. (2004) Depositional facies and stratal geometry of an Upper Carboniferous prograding and aggrading high-relief carbonate platform (Cantabrian Mountains, N Spain). Sedimentology, 51, 267–295.

Della Porta, G., Merino-Tomé, O., Kenter, J.A.M. and Verwer, K. (2013) Lower jurassic microbial and skeletal carbonate factories and platform geometry (Djebel Bou Dahar, High Atlas, Morocco). SEPM Spec. Publ., 105, 237–263.

Della Porta, G., Webb, G.E. and McDonald, I. (2015) REE patterns of microbial carbonate and cements from Sinemurian (Lower Jurassic) siliceous sponge mounds (Djebel Bou Dahar, High Atlas, Morocco). Chem. Geol., 400, 65–86.

Dera, G., Brigaud, B., Monna, F., Laffont, R., Pucéat, E., Deconinck J.-F., Pellenard, P., Joachimski, M.M. and Durlet, C. (2011). Climatic ups and downs in a disturbed Jurassic world. Geology, 39, 215-218. https://doi.org/10.1130/G31579.1

Dera, G., Prunier, J., Smith, P.L., Haggart, J.W., Popov, E., Guzhov, A., Rogov, M., Delsate, D., Thies, D., Cuny, G., Pucéat, E., Charbonnier, G. and Bayon, G. (2015) Nd isotope constraints on ocean circulation, paleoclimate, and continental drainage during the Jurassic breakup of Pangea. Gondwana Research, 27, 1599-1615. https://doi.org/10.1016/j.gr.2014.02.006

Dercourt, J., Gaetani, M., Vrielynck, B., Barrier, E., Biju-Duval, B., Brunet, M.F., Cadet, J.P., Crasquin, S. and Sandulescu, M. (2000) Atlas Peri-Tethys, Palaeogeographical Maps. 24 Maps and Explanatory Notes. CCGM/CGMW, Paris, pp 1-269.

Dickson, J.A.D. (1966). Carbonate identification and genesis as revealed by staining. Journal of Sedimentary Research, 36(2), 491-505.

Dieni, I. and Massari, F. (1985) Mesozoic of eastern Sardinia. In: Cherchi A (ed)19th European Micropaleontological Colloquium. Micropaleontological researches in Sardinia. Guidebook, 66–77.

Dieni, I., Fischer, J.C., Massari, F., Salard-Cheboldaeff, M. and Vozenin-Serra, C. (1983) La sucession de Genna Selole (Baunei) dans le cadre de la paléogéographie mésojurassique de la Sardigne orientale.

Dieni, I., Massari, F., Médus, J. (2008) Age, depositional environment and stratigraphic value of the Cuccuru ‘e Flores Conglomerate: insight into the Palaeogene to Early Miocene geodynamic evolution of Sardinia. Bull. Soc. géol. Fr., 179, 51-72.

Dieni, I., Massari, F., Radulovic, V. (2012) Clasts of uppermost Albian (Vraconian) limestone in the Eocene Cuccuru'e Flores Conglomerate of the M. Albo massif (eastern Sardinia). Rivista Italiana di Paleontologia e Stratigrafia, 118(1).

Dieni, I., Massari, F. and Radulović, V. (2013) The Mt Perda Liana section (Middle Jurassic, central-eastern Sardinia): revised stratigraphy and brachiopod faunas. Boll. della Soc. Paleontol. Ital., 52, 123–138.

Dozet, S. (2009) Lower Jurassic carbonate succession between Predole and Mlačevo , Central Slovenia. RMZ–Materials and Geoenvironment, 56, 164–193.

Dragastan, O.V.N. and Richter, D.E.K. (2011) Stromatolites and calcareous algae of Münder Formation (Tithonian-Berriasian) from NW Germany. Acta Palaeontol. Rom., 7, 139–168.

Dragičević, I. and Velić, I. (2002) The Northeastern margin of the Adriatic carbonate platform. Geol. Croat., 55, 185–232.

Dromart, G., Garcia, J.P., Picard, S., Atrops, F., Lécuyer, C. and Sheppard, S.M.F. (2003) Ice age at the Middle-Late Jurassic transition? Earth Planet. Sci. Lett., 213, 205–220.

Drzewiecki, P.A. and Simó, J.A. (2002). Depositional processes, triggering mechanisms and sediment composition of carbonate gravity flow deposits: examples from the Late Cretaceous of the south-central Pyrenees, Spain. Sedimentary Geology, 146, 155-189.

Dupraz, C. and Strasser, A. (1999) Microbialites and micro-encrusters in shallow coral bioherms (Middle to Late Oxfordian, Swiss Jura Mountains). Facies, 101–130.

Dupraz, C. and Strasser, A. (2002) Nutritional Modes in Coral-Microbialite Reefs (Jurassic, Oxfordian, Switzerland): Evolution of Trophic Structure as a Response to Environmental Change. Palaios, 17, 449–471.

Eberli, G.P., Anselmetti, F.S., Betzler, C., Van Konijnenburg, J.-H. and Bernoulli, D. (2004) Carbonate platform to basin transitions on seismic data and in outcrops: Great Bahama Bank and the Maiella Platform Margin, Italy. In: Eberli, G.P., Masaferro, J.L., Sarg, F.R. (eds) Seismic imaging of carbonate reservoirs and systems, AAPG Memoir, 81, pp 207-250.

El-asmar, H.M., Assal, E.M., El-sorogy, A.S. and Youssef, M. (2015) Facies analysis and depositional environments of the Upper Jurassic Jubaila Formation, Central Saudi Arabia. J. African Earth Sci., 110, 34–51.

El-Sorogy, A.S., Almadani, S.A. and Al-Dabbagh, M.E. (2016) Microfacies and diagenesis of the reefal limestone, Callovian Tuwaiq Mountain Limestone Formation, central Saudi Arabia. J. African Earth Sci., 115, 63–70.

El-Sorogy, A., Al-Kahtany, K., Almadani, S. and Tawfik, M. (2018) Depositional architecture and sequence stratigraphy of the Upper Jurassic Hanifa Formation, central Saudi Arabia. J. African Earth Sci., 139, 367–378.

Elliot, G.F. (1956) Further records of fossil calcareous algae from the Middle East. Micropaleontology, 2, 327–334.

Elliot, G.F. (1991) Dasycladalean Algae of the Palaeozoic and Mesozoic. In: Calcareous Algae and Stromatolites (Ed. R. Riding), Springer-Verlag, Berlin, Heidelberg, 125–130.

Fallatah, M.I. and Kerans, C. (2018) Stratigraphic evolution of the Late Jurassic Hanifa Formation along the Tuwaiq Escarpment, Saudi Arabia: Evidence for a carbonate ramp system. Sediment. Geol., 363, 152–180.

Fantoni, R. and Scotti, P. (2003) Thermal record of the Mesozoic rifting in the Southern Alps. Atti Ticinesi Sci. Terra Spec Ser, 9, 83–87.

Farag, I.A.M. (1959) Contribution to the study of the Jurassic formations in the Maghara massif (northern Sinai, Egypt). Egyptian Journal of Geology, 3, 175–199.

Flügel, E. (2004) Microfacies of carbonate rocks – Analysis, interpretation and application. Springer, Berlin.

Flügel, E. and Steiger, T. (1981) An upper Jurassic sponge-algal buildup from the northern Frankenalb, West Germany. In: European Fossil Reef Models (Ed. D.. F. Toomey), SEPM Special Publications, 30, 371–397.

Fourcade, E., Azema, J., Cecca, F., Dercourt, J., Vrielynck, B., Bellio, Y., Sandulescu, M. and Ricou, L.E. (1993) Late Tithonian palaeoenvironments. In: Dercourt, J, Ricou, LM, Vrienlynck, B (eds) Atlas Téthys Palaeoenvironmental Maps, and Explanatory Notes, CGMW, pp 113-134.

Frakes, L.A. and Francis, J.E. (1988) A guide to Phanerozoic cold polar climates from high-latitude ice-rafting in the Cretaceous. Nature, 333, 547-549.

Frakes, L.A., Francis, J.E., Syktus, J.I. (1992) Climate modes of the Phanerozoic: The History of the Earth's Climate over the past 600 Million Years. Cambridge University Press, Cambridge.

Franceschi, M., Dal Corso, J., Posenato, R., Roghi, G., Masetti, D. and Jenkyns, H.C. (2014) Early Pliensbachian (Early Jurassic) C-isotope perturbation and the diffusion of the Lithiotis Fauna: Insights from the western Tethys. Palaeogeogr. Palaeoclimatol. Palaeoecol., 410, 255–263.

Franke, D., Neben, S., Ladage, S., Schreckenberger, B. and Hinz, K. (2007) Margin segmentation and volcano-tectonic architecture along the volcanic margin off Argentina/Uruguay, South Atlantic. Mar. Geol., 244, 46–67.

Franţescu, O.D. (2011) Brachyuran decapods (including five new species and one new genus) from Jurassic (Oxfordian-Kimmeridgian) coral reef limestones from Dobrogea, Romania. N. Jb. Geol. Paläont. Abh., 259, 271–297.

Fraser, N.M., Bottjer, D.J. and Fischer, A.G. (2004) Dissecting "Lithiotis" Bivalves: Implications for the Early Jurassic Reef Eclipse. Palaios, 19, 51–67.

Frizon de Lamotte, D., Fourdan, B., Leleu, S., Leparmentier, F. and de Clarens, P. (2015) Style of rifting and the stages of Pangea breakup. Tectonics, 34, 1009–1029.

Fürsich, F. T., Werner, W. (1991) Palaeoecology of coralline sponge-coral meadows from the upper jurassic of Portugal. Paläontologische Zeitschrift, 65, 35.

Gaillard, C (1983) Les biohermes à spongiaires et leur environment dans l'Oxfordian du Jura meridional. Documents des Laboratoires de Géologie Lyon 90: 515.

Gaina, C., Müller, R.D., Brown, B., Ishihara, T. and Ivanov, S. (2007) Breakup and early seafloor spreading between India and Antarctica. Geophys. J. Int., 170, 151–169.

Gale, L. (2015) Microfacies characteristics of the lower jurassic lithiotid limestone from northern Adriatic Carbonate Platform (central Slovenia). Geologija, 58, 121–138.

Gaswirth, S.B., Budd, D.A. and Lang Farmer, G. (2007) The role and impact of freshwater–seawater mixing zones in the maturation of regional dolomite bodies within the proto Floridan Aquifer, USA. Sedimentology, 54, 1065-1091.

Gawlick, H.J. and Schlagintweit, F. (2006) Berriasian drowning of the Plassen carbonate platform at the type-locality and its bearing on the early Eoalpine orogenic dynamics in the Northern Calcareous Alps (Austria). Int. J. Earth Sci. (Geol Rundsch), 95, 451–462.

Génot, P. (1991) Cenozoic and Recent Dasycladales. In: Calcareous Algae and Stromatolites (Ed. R. Riding), Springer-Verlag, Berlin, Heidelberg, 131–144.

George, A.D., Playford, P.E. and Powell, C.M. (1995) Platform-margin collapse during Famennian reef evolution, Canning Basin, Western Australia. Geology, 23, 691-694.

Golonka, J. (2004) Plate tectonic evolution of the southern margin of Eurasia in the Mesozoic and Cenozoic. Tectonophysics, 381, 235–273.

Golonka, J. (2007) Late Triassic and Early Jurassic palaeogeography of the world. Palaeogeogr. Palaeoclimatol. Palaeoecol., 244, 297–307.

Gómez, J.J. and Goy, A. (2011) Warming-driven mass extinction in the Early Toarcian (Early Jurassic) of northern and central Spain. Correlation with other time-equivalent European sections. Palaeogeogr. Palaeoclimatol. Palaeoecol., 306, 176–195.

Gómez, J.J., Goy, A. and Canales, M.L. (2008) Seawater temperature and carbon isotope variations in belemnites linked to mass extinction during the Toarcian (Early Jurassic) in Central and Northern Spain. Comparison with other European sections. Palaeogeogr. Palaeoclimatol. Palaeoecol., 258, 28–58.

Gretz, M., Lathuilière, B., Martini, R. and Bartolini, A. (2013) The Hettangian corals of the Isle of Skye (Scotland): An opportunity to better understand the palaeoenvironmental conditions during the aftermath of the Triassic-Jurassic boundary crisis. Palaeogeogr. Palaeoclimatol. Palaeoecol., 376, 132–148.

Gretz, M., Lathuilière, B. and Martini, R. (2015) A new coral with simplified morphology from the oldest known Hettangian (Early Jurassic) reef in southern France. Acta Palaeontol. Pol., 60, 277–286.

Gröcke, D.R., Price, D.P., Ruffell, A.H., Mutterlose, J. and Baraboshkin, E. (2003) Palaeogeography, Palaeoclimatology, Palaeoecology, 202, 97-118.

Gutowski, J., Popadyuk, I. V and Olszewska, B. (2005) Late Jurassic-earliest Cretaceous evolution of the epicontinental sedimentary basin of southeastern Poland and Western Ukraine. Geol. Q., 49, 31–44.

Hairabian, A., Borgomano, J., Masse, J.P. and Nardon, S. (2015) 3-D stratigraphic architecture, sedimentary processes and controlling factors of Cretaceous deep-water resedimented carbonates (Gargano Peninsula, SE Italy). Sedimentary Geology, 317, 116-136.

Hallam, A. (1975) Coral patch reefs in the Bajocian (Middle Jurassic) of Lorraine. Geological Magazine, 112, 383-392.

Hallam, A. (1981) A revised sea-level curve for the early Jurassic. J. Geol. Soc. London., 138, 735–743.

Hallam, A. (1985) A review of Mesozoic climates. J. - Geol. Soc. London, 142, 433–445.

Hallam, A. (1988) A re-evaluation of Jurassic eustasy in the light of new data and the revised Exxon curve. In: Wilgus, C.K., Hastings, B.S., Kendall, C.G.S.C., Posamatir, H.W., Ron,

C.A. and van Wagner, J.C. (Eds.), Sea-Level Changes - An Integrated Approach. SEPM Special Publication 42, pp. 261–273.

Hallam, A. (1993) Jurassic climates as inferred from the sedimentary and fossil record. Phil. Trans. R. Soc. London B, 341, 287–296.

Hallam, A. (1996) Recovery of the marine fauna in Europe after the end-Triassic and Early Toarcian mass Extinctions. Geol. Soc. London, Spec. Publ., 102, 231–236.

Hallam, A. (2001) A review of the broad pattern of Jurassic sea-level changes and their possible causes in the light of current knowledge. Palaeogeogr. Palaeoclimatol. Palaeoecol., 167, 23–37.

Hallam, A. (2002) How catastrophic was the end-Triassic mass extinction? Lethaia, 35, 147–157.

Hallam, A. and Wignall, P.B. (1999) Mass extinctions and sea-level changes. Earth Sci. Rev., 48, 217–250.

Haq, B.U. (2018) Jurassic sea-level variations: A reappraisal. GSA Today, 28, 4–10.

Haq, B.U., Hardenbol, J. and Vail, P.R. (1987) Chronology of fluctuating sea levels since the Triassic. Science (80-.)., 235, 1156–1167.

Hardenbol, J., Thierry, J., Farley, M.B., Jacquin, T., De Graciansky, P.-C. and Vail, P.R. (1998) Mesozoic and Cenozoic sequence chronostratigraphic framework of European basins. In: De Graciansky P-C, Hardenbol J, Jacquin T, Vail PR (eds) Mesozoic and Cenozoic Sequence Stratigraphy of European Basins, SEPM Spec Publ, 60, 13.

Hart, M.B., Oxford, M.J. and Hudson, W. (2002) The early evolution and palaeobiogeography of Mesozoic planktonic foraminifera. Geol. Soc. Spec. Publ., 194, 115–125.

Hart, M.B., Hylton, M.D., Oxford, M.J., Price, G.D., Hudson, W. and Smart, C.W. (2003) The search for the origin of the planktic Foraminifera. J. Geol. Soc. London., 160, 341–343.

Heine, C., Zoethout, J. and Müller, R.D. (2013) Kinematics of the South Atlantic rift. Solid Earth, 4, 215–253.

Helm, C. and Schülke, I. (2006) Patch reef development in the florigemma-Bank Member (Oxfordian) from the Deister Mts (NW Germany): a type example for Late Jurassic coral thrombolite thickets. Facies, 52, 441–467.

Hesselbo, S.P. and Jenkyns, H.C. (1998) British Lower Jurassic Sequence Stratigraphy. In: de Graciansky, P.C., Hardenbol, J., Jacquin, T., Vail, P.R. (Eds) SEPM Special Publications 60, 561–581.

Hesselbo, S.P., Gröcke, D.R., Jenkyns, H.C., Bjerrum, C.J., Farrimond, P., Morgans Bell, H.S. and Green, O.R. (2000) Massive dissociation of gas hydrate during a Jurassic oceanic anoxic event. Nature, 406, 392–395.

Hesselbo, S.P., Morgans-Bell, H.S., McElwain, J.C., Rees, P.M.A., Robinson, S.A. and Ross, C.E. (2003) Carbon-cycle perturbation in the Middle Jurassic and accompanying changes in the terrestrial paleoenvironment. J. Geol., 111, 259–276.

Hewaidy, A.G.A., Abd El-Moghny, M.W., Farouk, S. and El Kahtani, K. (2017) Microfacies and depositional environments of Jurassic (Callovian) Tuwaiq Mountain Formation in central Saudi Arabia. Carbonates and Evaporites, 32, 497–512.

Hiatt, E.E. and Pufahl, P.K. (2014) Cathodoluminescence petrography of carbonate rocks: application to understanding diagenesis, reservoir quality, and pore system evolution. Mineral Assoc Canada Short Course, 45, 75–96.

Higgins, J.A., Blättler, C.L., Lundstrom, E.A., Santiago-Ramos, D.P., Akhtar, A.A., Crüger Ahm, A.-S., Bialik, O., Holmden, C., Bradbury, H., Murray, S.T. and Swart, P.K. (2018). Mineralogy, early marine diagenesis, and the chemistry of shallow-water carbonate sediments. Geochimica et Cosmochimica Acta, 220, 512-534.

Hoffmann, M., Kołodziej, B. and Skupien, P. (2017) Microencruster-microbial framework and synsedimentary cements in the Štramberk Limestone (Carpathians, Czech Republic): Insights into reef zonation. 87, 325–347.

Hofmann, H.J. (2000) Archean stromatolites as microbial archives. In: Microbial Sediments (Ed. R. Riding and M. Awramik), Springer-Verlag, Berlin, Heidelberg, 315–327.

Hottinger, L. (1967) Foraminiferes imperforés du Mésozoique marocain, Notes et Mémoires du Service Géologique du Maroc 209. Editions du Service Geologique du Maroc, Rabat, pp. 168.

Hou, Y., Azmy, K., Berra, F., Jadoul, F., Blamey, N.J.F., Gleeson, S.A. and Brand, U. (2016) Origin of the Breno and Esino dolomites in the western Southern Alps (Italy): Implications for a volcanic influence. Marine and Petroleum Geology 69, 38-52.

Huck, S., Wohlwend, S., Coimbra, R., Christ, N. and Weissert, H. (2017) Disentangling shallow-water bulk carbonate carbon isotope archives with evidence for multi-stage diagenesis: An in-depth component-specific petrographic and geochemical study from Oman (mid-Cretaceous). The Depositional record 3, 233-257.

Hudson, J.D. (1977) Stable isotopes and limestone lithification. Journal of the Geological Society, 133 (6), 637-660.

Hughes, G.W. (2004) Middle to Late Jurassic biofacies of Saudi Arabia. Riv. Ital. di Paleontol. e Stratigr., 110, 173–179.

Hughes, G.W., Varol, O. and Al-khalid, M. (2008) Late Oxfordian micropalaeontology, nannopalaeontology and palaeoenvironments of Saudi Arabia. GeoArabia, 13, 15–30.

Husinec, A., Jelaska, V. (2006) Relative sea-level changes recorded on an isolated carbonate platform: Tithonian to Cenomanian succession, Southern Croatia. Journal of Sedimentary Research 76 (10), 1120-1136.

Immenhauser, A., Kenter, J.A.M., Ganssen, G., Bahamonde, J.R., Van Vliet, A., Saher, M.H. (2002) Origin and significance of isotope shifts in pennsylvanian carbonates (Asturias, NW Spain). Journal of Sedimentary Research 72 (1), 82-94.

Immenhauser, A., Della Porta, G., Kenter, J.A.M. and Bahamonde, J. (2003) An alternative model for positive shifts in shallow-marine carbonate $\delta^{13}C$ and $\delta^{18}O$. Sedimentology, 50, 953-959.

Immenhauser, A., Hillgärtner, H. and Van Bentum, E. (2005) Microbial-foraminiferal episodes in the Early Aptian of the southern Tethyan margin: ecological significance and possible relation to oceanic anoxic event 1a. Sedimentology, 52, 77-99.

Innamorati, G. and Santantonio, M. (2018) Evidence for extended Hercynian basement and a preserved Jurassic basin-margin tract in Northern Calabria (Southern Italy): The Longobucco Basin. Sedimentary Geology, 376, 147-163.

Insalaco, E. (1999) Facies and palaeoecology of Upper Jurassic (Middle Oxfordian) Coral Reefs in England. Facies, 40, 81–100.

Ivanova, D., Kołodziej, B., Koleva-Rekalova, E. and Roniewicz, E. (2008) Oxfordian to Valanginian palaeoenvironmental evolution on the western Moesian Carbonate Platform: a case study from SW Bulgaria. Ann. Soc. Geol. Pol., 78, 65–90.

Jackson, M.P.A., Cramez, C. and Fonck, J.M. (2000) Role of subaerial volcanic rocks and mantle plumes in creation of South Atlantic margins: Implications for salt tectonics and source rocks. Mar. Pet. Geol., 17, 477–498.

Jacquin, T. and De Graciansky, P.-C. (1998) Transgressive/regressive (second order) facies cycles: the effects of tectonoeustacy. In: De Graciansky, P.-C., Hardenbol, J., Jacquin, T. and Vail, P.R. (Eds.), Mesozoic and Cenozoic Sequence Stratigraphy of European Basins, SEPM Special Publication 60. pp. 445–466.

Jadoul, F. (2018) Stratigraphic-paleogeographic evolution of Eastern Sardinia Jurassic passive margin carbonates: synthesis and future developments. J. Mediterr. Earth Sci., 10, 147–154.

Jadoul, F., Lanfranchi, A. and Berra, F. (2009) Evolution of late Jurassic to Berriasian carbonate platforms of Eastern Sardinia. 27th IAS Meet. Sedimentol., pre congre, 51–71.

Jadoul, F., Lanfranchi, A., Berra, F., Erba, E., Casellato, C.E., Cherchi, A., Simone, L., Schroeder, R., Carannante, G. and Ibba, A. (2010) I sistemi carbonatici giurassici della Sardegna orientale (Golfo di Orosei) ed eventi deposizionali nel sistema carbonatico giurassico-

cretacico della Nurra (Sardegna nord-occidentale). Period. Semest. del Serv. Geol. d'Italia - ISPRA e della Soc. Geol. Ital. Geol.F.Trips, 2, 122.

Jank, M., Meyer, C.A. and Wetzel, A. (2006) Late Oxfordian to Late Kimmeridgian carbonate deposits of NW Switzerland (Swiss Jura): Stratigraphical and palaeogeographical implications in the transition area between the Paris Basin and the Tethys. 186, 237–263.

Jansa, L.F., Pratt, B.R. and Dromart, G. (1988) Deep water thrombolite mounds from the Upper Jurassic of offshore Nova Scotia. In: Geldsetzer HHJ, James NP, Tebbutt GE (eds) Reefs, Canada and Adjacent Area, Canadian Society of Petroleum Geologists Memoir 13, 725–735.

Jenkyns, H.C., Jones, C.E., Darren, R. Gröcke, D.R., Hesselbo, S.P. and Parkinson, D.N. (2002) Chemostratigraphy of the Jurassic System: applications, limitations and implications for palaeoceanography. Journal of the Geological Society, 159 (4), 351–378.

Jenkyns, H.C., Schouten-Huibers, L., Schouten, S. and Sinninghe Damsté, J.S. (2011) Middle Jurassic-Early Cretaceous high-latitude sea-surface temperatures from the Southern Ocean. Clim. Past Discuss., 7, 1339–1361.

Kavoosi, M.A., Lasemi, Y., Sherkati, S. and Moussavi-Harami, R. (2009) Facies analysis and depositional sequences of the Upper Jurassic Mozduran Formation, a carbonate reservoir in the Kopet Dagh Basin, NE Iran. J. Pet. Geol., 32, 235–259.

Kaya, M.Y. and Altiner, D. (2015) Microencrusters from the Upper Jurassic–Lower Cretaceous Inaltı Formation (Central Pontides, Turkey): remarks on the development of reefal/peri-reefal facies. Facies, 61, 18.

Kent, D.V. and Irving, E. (2010) Influence of inclination error in sedimentary rocks on the Triassic and Jurassic apparent pole wander path for North America and implications for Cordilleran tectonics. Journal of Geophysical Research. 115, B10.

Kent, D.V., Kjarsgaard, B.A., Gee, J.S., Muttoni, G. and Heaman, L.M. (2015) Tracking the Late Jurassic apparent (or true) polar shift in U-Pb-dated kimberlites from cratonic North

America (Superior Province of Canada). Geochemistry, Geophysics, Geosystems, 16, 983–994.

Kiani Harchegani, F. and Morsilli, M. (2019) Internal waves as controlling factor in the development of stromatoporoid-rich facies of the Apulia Platform margin (Upper Jurassic-Lower Cretaceous, Gargano Promontory, Italy). Sediment. Geol., 380, 1–20.

Kiessling, W. (2002) Secular Variations in the Phanerozoic Reef Ecosystem. In: Phanerozoic Reef Patterns (Ed. W. Kiessling, E. Flügel, and J. Golonka), SEPM Special Publications 72, Tulsa, 625–690.

Kiessling, W. (2009) Geologic and biologic controls on the evolution of reefs. Annual Review of Ecology, Evolution and Systematics, 40, 173-192.

Kiessling, W., Roniewicz, E., Villier, L., Leonide, P. and Struck, U. (2009) An early Hettangian coral reef in southern France: Implications for the end-Triassic reef crisis. Palaios, 24, 657–671.

Kolodziej, B., Ivanov, M. and Idakieva, V. (2012) Prolific development of pachythecaliines in late Barremian, Bulgaria: Coral taxonomy and sedimentary environment. Ann. Soc. Geol. Pol., 82, 291–330.

Korte, C. and Hesselbo, S.P. (2011) Shallow marine carbon and oxygen isotope and elemental records indicate icehouse-greenhouse cycles during the Early Jurassic. Paleoceanography, 26(4).

Korte, C., Hesselbo, S.P., Ullmann, C.V., Dietl, G., Ruhl, M., Schweigert, G. and Thibault, N. (2015) Jurassic climate mode governed by ocean gateway. Nature communications, 6(1), 1-7.

Krajewski, M. and Schlagintweit, F. (2018) *Crescentiella*-microbial-cement microframeworks in the Upper Jurassic reefs of the Crimean Peninsula. Facies 64, 21.

Krencker, F.N., Lindström, S., Bodin, S., 2019. A major sea-level drop briefly precedes the Toarcian oceanic anoxic event: implication for Early Jurassic climate and carbon cycle. Scientific Reports 9, 12518.

Krumbein, W.E. (1979) Calcification by bacteria and algae. In: Biogeochemical Cycling of Mineral-Forming Elements (Ed. P.A. Trudinger and D.J. Swaine), Elsevier, Amsterdam, 47–68.

Kukoč, D., Goričan, Š., Košir, A. (2012) Lower Cretaceous carbonate gravity-flow deposits from the Bohinj area (NW Slovenia): evidence of a lost carbonate platform in the Internal Dinarides. Bull. Soc. géol. France, 183, 383-392.

Kyser, T.K., James, N.P. and Bone, Y. (2002) Shallow burial dolomitization and dedolomitization of cenozoic cool-water limestones, Southern Australia: geochemistry and origin. Journal of Sedimentary Research, 72, 146-157.

Labails, C., Olivet, J., Aslanian, D. and Roest, W.R. (2010) An alternative early opening scenario for the Central Atlantic Ocean. Earth Planet. Sci. Lett., 297, 355–368.

Lanfranchi, A., Berra, F. and Jadoul, F. (2011) Compositional changes in sigmoidal carbonate clinoforms (Late Tithonian, eastern Sardinia, Italy): Insights from quantitative microfacies analyses. Sedimentology, 58, 2039–2060.

Lathuilière, B., Bodeur, Y., Enay, R., Hanzo, M., Marchand, D. and Jura, F. (2005) Coral zonation of an Oxfordian reef tract in the northern French Jura. Facies, 50, 545–559.

Lavastre, V., Ader, M., Buschaert, S., Petit, S. and Javoy, M. (2011) Water cir culation control on carbonate- $\delta^{18}O$ records in a low permeability clay formation and surrounding limestones: the Upper Dogger–Oxfordian sequence from the eastern Paris basin, France. Applied Geochemistry, 26 (5), 818-827.

Le Goff, J., Reijmer, J.J.G., Cerepi, A., Loisy, C., Swennen, R., Heba, G., Cavailhes, T. and De Graaf, S. (2019). The dismantling of the Apulian carbonate platform during the late Campanian e early Maastrichtian in Albania. Cretaceous Research, 96, 83-106.

Lehrmann, D.J., Minzoni, M., Enos, P., Kelleher, C., Stepchinski, L., Li, X., Payne, J.L. and Yu, M. (2020) Giant sector-collapse structures (scalloped margins) of the Yangtze Platform and Great Bank of Guizhou, China: Implications for genesis of collapsed carbonate platform margin systems. Sedimentology, 67, 3167-3198.

Leinfelder, R.R. (1987) Formation and significance of black pebbles from the ota limestone (Upper Jurassic, Portugal). Facies, 17, 159–169.

Leinfelder, R.R. (1992) A modern-type Kimmeridgian reef (Ota Limestone, Portugal): Implications for Jurassic reef models. Facies, 26, 11–34.

Leinfelder, R.R. (1993a) Upper Jurassic reef types and controlling factors- a preliminary report. Profil, 5, 119–140.

Leinfelder, R.R. (1993b) A sequence stratigraphic approach to the Upper Jurassic mixed carbonate - siliciclastic succession of the central Lusitanian Basin, Portugal. Profil, 5, 119–140.

Leinfelder, R.R., Krautter, M., Nose, M., Ramalho, M.M. and Werner, W. (1993) Siliceous sponge facies from the Upper Jurassic of Portugal. N. Jb. Geol. Paläont. Abh., 189, 199–254.

Leinfelder, R.R., Schmid, D.U., Nose, M. and Werner, W. (2002) Jurassic Reef Patterns-the Expression of a Changing Globe. In: Kiessling W, Flügel E, Golonka J (eds) Phanerozoic Reef Patterns, SEPM special publication, vol 72, Tulsa, 465–520.

Leinfelder, R.R., Schlagintweit, F., Werner, W., Ebli, O., Nose, M., Schmid, D.U. and Hughes, G.W. (2005) Significance of stromatoporoids in Jurassic reefs and carbonate platforms-concepts and implications. Facies, 51, 287–325.

Leleu, S., Hartley, A.J., Oosterhout, C. Van, Kennan, L., Ruckwied, K. and Gerdes, K. (2016) Structural, stratigraphic and sedimentological characterisation of a wide rift system: The Triassic rift system of the Central Atlantic Domain. Earth Sci. Rev., 158, 89–124.

Léonide, P., Floquet, M. and Villier, L. (2007) Interaction of tectonics, eustasy, climate and carbonate production on the sedimentary evolution of an early/middle Jurassic extensional basin (Southern Provence Sub-basin, SE France). Basin Res., 19, 125–152.

Louis-Schmid, B., Rais, P., Bernasconi, S.M., Pellenard, P., Collin, P.Y. and Weissert, H. (2007) Detailed record of the mid-Oxfordian (Late Jurassic) positive carbon-isotope excursion in two hemipelagic sections (France and Switzerland): A plate tectonic trigger? Palaeogeogr. Palaeoclimatol. Palaeoecol., 248, 459–472.

Lohmann, K.C: (1988) Geochemical patterns of meteoric diagenetic systems and their application to studies of paleokarst. In: James, N.P., Choquette, P.W. (eds.) Paleokarst. Springer-Verlag, Berlin, pp.50-80.

Machel, H.-G. (1985) Cathodoluminescence in calcite and dolomite and its chemical interpretation. Geoscience Canada, 12, 139-147.

Machel, H.G. (2004) Concepts and models of dolomitization: a critical reappraisal. In: Braithwaite, C. J. R., Rizzl, G. and Darke, G. (eds) 2004. The Geometry and Petrogenesis of Dolomite Hydrocarbon Reservoirs. Geological Society, London, Special Publications, 235, 7-63.

Machel, H.G. and Anderson, J.H. (1989) Pervasive subsurface dolomitization of the Nisku Formation in Central Alberta. Journal of Sedimentary Petrology, 59 (6), 891-911.

Machel, H.G. and Burton, E.A. (1994) Golden Grove dolomite, Barbados; origin from modified seawater. Journal of Sedimentary Research, 64, 741-751.

Macintyre, I.G. (1984) Extensive submarine lithification in a cave in the Belize Barrier Reef Platform. J. Sediment. Petrol., 54, 221–235.

Macintyre, I.G. (1985) Submarine cements - the peloidal question. In: Carbonate Cements (Ed. N. Schneidermann and P.M. Harris), SEPM Special Publications, 109–116.

Makhloufi, Y. and Samankassou, E. (2019) Geochemical constrains on dolomitization pathways of the Upper Jurassic carbonate rocks in the Geneva Basin (Switzerland and France). Swiss Journal of Geosciences, 112, 579-596.

Mameli, P., Mongelli, G., Oggiano, G. and Dinelli, E. (2007) Geological, geochemical and mineralogical features of some bauxite deposits from Nurra (Western Sardinia, Italy): insights on conditions of formation and parental affinity. Int. J. Earth Sci., 96, 887-902.

Mandl, G. (1999) The Alpine sector of the Tethys shelf – Examples of Triassic to Jurassic sedimentation and deformation from the Northern Calcareous Alps. Mitt. Österr. Geol. Ges., 92, 61–77.

Marshall, J.D. (1992) Climatic and oceanographic isotopic signals from the carbonate rock record and their preservation. Geological Magazine, 129, 143-160.

Martin-Garin, B., Lathuilière, B., Geister, J. and Ramseyer, K. (2010) Oxygen isotopes and climatic control of Oxfordian coral reefs (Jurassic, Tethys). Palaios, 25, 721-729.

Martin-Garin, B., Lathuilière, B. and Geister, J. (2012) The shifting biogeography of reef corals during the Oxfordian (Late Jurassic). A climatic control? Palaeogeogr. Palaeoclimatol. Palaeoecol., 365–366, 136–153.

Marzoli, A., Bertrand, H., Knight, K.B., Cirilli, S., Buratti, N., Vérati, C., Nomade, S., Renne, P.R., Youbi, N., Martini, R., Allenbach, K., Neuwerth, R., Rapaille, C., Zaninetti, L. and Bellieni, G. (2004). Synchrony of the Central Atlantic magmatic province and the Triassic-Jurassic boundary climatic and biotic crisis. Geology, 32, 973-976.

Masini, E., Manatschal, G. and Geoffroy, M. (2013) The Alpine Tethys rifted margins: Reconciling old and new ideas to understand the stratigraphic architecture of magma-poor rifted margins. Sedimentology, 60, 174–196.

Massari, F. (1968) Aspetti sedimentologici in una serie calcarea Titonico-Berriasiana di bassa profondità nella Sardegna Orientale. Mem. Soc. Geol., 26, 1–56.

Mattei, M., Muttoni, G. and Cifelli, F. (2014) A record of the Jurassic massive plate shift from the Garedu Formation of central Iran. Geology, 42, 555-558.

Mattes, B.W. and Mountjoy, E.W. (1980) Burial dolomitization of the Upper Devonian Miette build-up, Jasper National Park, Alberta. In: Zenger, D.H., Dunham, J.B., Ethington, R.L. (eds.), Concepts and models of Dolomitization. SEPM Special Publication, 28, pp. 259-297.

Mattioli, E. and Pittet, B. (2002) Contribution of calcareous nannoplankton to carbonate deposition: A new approach applied to the Lower Jurassic of Central Italy. Mar. Micropaleontol., 45, 175–190.

Mattioli, E., Pittet, B., Petitpierre, L. and Mailliot, S. (2009) Dramatic decrease of pelagic carbonate production by nannoplankton across the Early Toarcian anoxic event (T-OAE). Glob. Planet. Change, 65, 134–145.

Matyszkiewicz, J. (1993) Genesis of stromatactis in an Upper Jurassic carbonate buildup (Mlynka, Cracow region, Southern Poland): Internal reworking and erosion of organic growth cavities. Facies, 28, 87.

Matyszkiewicz, J. and Felisiak, I. (1992) Microfacies and diagenesis of an Upper Oxfordian carbonate buildup in Mydlniki (Cracow area, Southern Poland). Facies, 27, 179–189.

Matyszkiewicz, J. and Krajewski, M. (1996) Lithology and sedimentation of Upper Jurassic massive limestone near Bolechowice, Kraków-Wieluń Upland, South Poland. Ann. Soc. Geol. Pol., 66, 285–301.

Matyszkiewicz, J., Kochman, A. and Du, A. (2012) Influence of local sedimentary conditions on development of microbialites in the Oxfordian carbonate buildups from the southern part of the Kraków – Częstochowa Upland (South Poland). Sediment. Geol., 264, 109–132.

McArthur, J.M., Howarth, R.J. and Shields, G.A. (2012). Strontium isotope stratigraphy. In: Gradstein, F.M., Ogg, J.G., Schmitz, M., Ogg, G. (eds.), The Geologic Time Scale 2012. Elsevier, Amsterdam, Boston, Heidelberg, London, New York, Oxford, Paris, San Diego, San Francisco, Singapore, Sydney, Tokyo, pp. 127–144.

McConnaughey, T.A. (1989)^{13}C and ^{18}O isotopic disequilibrium in biological carbonates. I. Patterns. Geochimica et Cosmochimica acta, 53, 151-162.

McKenzie, N.R., Horton, B.K., Loomis, S.E., Stockli, D.F., Planavsky, N.J., Lee, C.-T. A (2016) Continental arc volcanism as the principal driver of icehouse-greenhouse variability. Science 352, 444-445.

Melim, L.A. and Scholle, P.A. (2002) Dolomitization of the Capitan Formation forereef facies (Permian, west Texas and New Mexico): seepage reflux revisited. Sedimentology, 49, 1207-1227.

Merino-Tomé, Ó., Della Porta, G., Kenter, J.A.M., Verwer, K., Harris, P.M., Adams, E.W., Playton T. and Corrochano, D. (2012) Sequence development in an isolated carbonate platform (Lower Jurassic, Djebel Bou Dahar, High Atlas, Morocco): Influence of tectonics, eustacy and carbonate production. Sedimentology, 59, 118–155.

Miller, K.G., Kominz, M.A., Browning, J. V., Wright, J.D., Mountain, G.S., Katz, M.E., Sugarman, P.J., Cramer, B.S., Christie-Blick, N. and Pekar, S.F. (2005) The phanerozoic record of global sea-level change. Science (80-.)., 310, 1293–1298.

Mindszenty, A., D'Argenio, B. and Aiello, G. (1995) Lithospheric bulges recorded by regional unconformities. The case of the Mesozoic-Tertiary Apulia. Tectonophysics, 252, 137-161.

Mircescu, C., Bucur, I. and Săsăran, E. (2014) Dasycladalean algae from Upper Jurassic-Lower Cretaceous limestones of Piatra Craiului Massif (South Carpathians, Romania) and their relationship to paleoenvironment. Stud. Univ. Babes-Bolyai, Geol., 59, 5–27.

Mircescu, C.V., Bucur, I.I., Săsăran, E., Pleş, G., Ungureanu, R. and Oprişa, A. (2019) Facies evolution of the Jurassic-Cretaceous transition in the Eastern Getic Carbonate Platform, Romania: Integration of sequence stratigraphy, biostratigraphy and isotope stratigraphy. Cretaceous Research, 99, 71-95.

Molina, J.M., Reolid, M. and Mattioli, E. (2018) Thin-shelled bivalve buildup of the lower Bajocian, South Iberian paleomargin: development of opportunists after oceanic perturbations. Facies 64:1–17.

Montadert, I., Winnock, E., Deltiel, J.R. and Grau, G. (1974) Continental margins of Galicia-Portugal and Bay of Biscay. In: Burk, C.A., Drake, C.L (eds) The Geology of Continental Margins, Springer, Berlin, Heidelberg, 323–342.

Montañez, I.P. (2002) Biological skeletal carbonate records changes in major-ion chemistry of paleo-oceans. Proc. Natl. Acad. Sci. U. S. A., 99, 15852–15854.

Monty, C.L. V. and Hardie, L.A. (1976) The geological significance of the freshwater blue-green algal calcareous marsh. In: Stromatolites (Ed. M.R. Walter), Elsevier, Amsterdam, 447–477.

Moore, C.H. (1989) Carbonate Diagenesis and Porosity. Developments in Sedimentology 46, Amsterdam, Elsevier, pp.337.

Morettini, E., Santantonio, M., Bartolini, A., Cecca, F., Baumgartner, P.O. and Hunziker, J.C. (2002) Carbon isotope stratigraphy and carbonate production during the Early-Middle Jurassic: Examples from the Umbria-Marche-Sabina Apennines (central Italy). Palaeogeogr. Palaeoclimatol. Palaeoecol., 184, 251–273.

Morsilli, M. and Bosellini, A. (1997) Carbonate facies zonation of the Upper Jurassic-Lower Cretaceous Apulia Platform Margin (Gargano Promontory, Southern Italy). Riv. Ital. di Paleontol. e Stratigr., 103, 193–206.

Morsilli, M., Hairabian, A., Borgomano, J., Nardon, S., Adams, E. and Gartner, G.B. (2017) The Apulia Carbonate Platform-Gargano Promontory, Italy (Upper Jurassic–Eocene). AAPG Bulletin 101, 523–531.

Moulin, M., Aslanian, D. and Unternehr, P. (2010) Archimer. Earth-Science Rev., 98, 1–37.

Muchez, P. and Viaene, W. (1994) Dolomitization caused by water circulation near the mixing zone: an example from the Lower Visean of the Campine Basin (northern Belgium). In: H. Purser, M.E. Tucker and D.H. Zenger (eds.) Dolomites–A Volume in Honour of Dolomieu SEPM Spec. Publ. Tulsa, 21, 155–166.

Müller, D.R., Seton, M., Zahirovic, S., Williams, S.E., Matthews, K.J., Wright, N.M., Shephard, G.E., Maloney, K.T., Barnett-moore, N., Hosseinpour, M., Bower, D.J. and Cannon, J. (2016) Ocean Basin Evolution and Global-Scale Plate Reorganization Events Since Pangea Breakup. Annu. Rev. Earth Planet. Sci., 44, 107–38.

Muscatine, L., Goiran, C., Land, L., Jaubert, J., Cuif, J.P. and Allemand, D. (2005) Stable isotopes (δ13C and δ15N) of organic matrix from coral skeleton. Proc. Natl. Acad. Sci. U. S. A., 102, 1525–1530.

Muttoni, G. and Kent, D.V. (2016) A novel plate tectonic scenario for the genesis and sealing of some major Mesozoic oil fields. GSA Today, 26, 4-11.

Muttoni, G. and Kent, D.V. (2019) Jurassic monster polar shift confirmed by sequential paleopoles from Adria, promontory of Africa. Journal of Geophisical Research: Solid Earth, 124, 3288-3306.

Muttoni, G. Erba, E., Kent, D.V. and Bachtadse, V. (2005) Mesozoic Alpine facies deposition as a result of past latitudinal plate motion. Nature, 434, 59-63.

Muttoni, G., Dallanave, E. and Channell, J.E.T. (2013) The drift history of Adria and Africa from 280 Ma to Present, Jurassic true polar wander, and zonal climate control on Tethyan sedimentary facies. Palaeogeogr. Palaeoclimatol. Palaeoecol., 386, 415-435.

Muttoni, G., Visconti, A., Channell, J.E.T., Emanuela, C., Maron, M. and Jadoul, F. (2018) An expanded Tethyan Kimmeridgian magneto-biostratigraphy from the S'Adde section (Sardinia): Implications for the Jurassic timescale. Palaeogeogr. Palaeoclimatol. Palaeoecol., 503, 90–101.

Nader, F.H. and Swennen, R. (2004) Petroleum prospects of Lebanon: some remarks from sedimentological and diagenetic studies of Jurassic carbonates. Mar. Pet. Geol., 21, 427–441.

Nader, F.H., Swennen, R. and Ellam, R.M. (2007) Field geometry, petrography and geochemistry of a dolomitization front (Late Jurassic, central Lebanon). Sedimentology, 54, 1093-1119.

Nelson, C.S. and Smith, A.M. (1996) Stable oxygen and car bon isotope compositional fields for skeletal and diagenetic components in New Zealand Cenozoic nontropical carbonate sediments and limestones: a synthesis and review. New Zealand Journal of Geology and Geophysics, 39, 93-107.

Nembrini, M., Della Porta, G. and Berra, F. (2021) Development of coral–sponge–microbialite reefs in a coated grain-dominated carbonate ramp (Upper Jurassic, eastern Sardinia, Italy). Facies, 67, 6.

Nomade, S., Knight, K.B., Beutel, E., Renne, P.R., Verati, C. and Féraud, G. (2007) Chronology of the Central Atlantic Magmatic Province: Implications for the Central Atlantic rifting processes and the Triassic – Jurassic biotic crisis. 244, 326–344.

Nose, M. (1995) Comparative facies analysis and palaeoecology of coral-bearing shallowing-upwards successions from the Upper Jurassic of Iberia. Profil, 8, 1–237.

Nose, M. and Leinfelder, R.R., (1997) Upper Jurassic coral communities within siliciclastic settings (Lusitanian Basin, Portugal): Implications for symbiotic and nutrient strategies. In: 8th International Coral Reef Symposium, Panamá City, Proceedings. pp 1755–1760.

Nunn, E.V. and Price, G.D. (2010) Late Jurassic (Kimmeridgian–Tithonian) stable isotopes ($\delta^{18}O$, $\delta^{13}C$) and Mg/Ca ratios: New palaeoclimate data from Helmsdale, northeast Scotland. Palaeogeography, Palaeoclimatology, Palaeoecology, 292, 325–335

Nunn, E.V., Price, G.D., Hart, M.B., Page, K.N. and Leng, M.J. (2009) Isotopic signals from Callovian–Kimmeridgian (Middle–Upper Jurassic) belemnites and bulk organic carbon, Staffin Bay, Isle of Skye, Scotland. Journal of the Geological Society, London, 166, 633–641.

Olivier, N. (2019) Distribution of coral-microbialite reefs along the French Jura platform during the Bimammatum Zone (Oxfordian, Late Jurassic). Bulletin of Geosciences, 94(3), 257-277.

Olivier, N., Hantzpergue, P., Gaillard, C., Pittet, B., Leinfelder, R.R., Schmid, D.U. and Werner, W. (2003) Microbialite morphology, structure and growth: A model of the Upper Jurassic reefs of the Chay Peninsula (Western France). Palaeogeogr. Palaeoclimatol. Palaeoecol., 193, 383–404.

Olivier, N., Carpentier, C., Martin-garin, B., Lathuilière, B., Gaillard, C., Ferry, S., Hantzpergue, P. and Geister, J. (2004a) Coral-microbialite reefs in pure carbonate versus mixed carbonate-

siliciclastic depositional environments: the example of the Pagny-sur-Meuse section (Upper Jurassic, northeastern France). Facies, 50, 229–255.

Olivier, N., Pittet, B. and Mattioli, E. (2004b) Palaeoenvironmental control on sponge- microbialite reefs and contemporaneous deep-shelf marl-limestone deposition (Late Oxfordian, southern Germany). Palaeogeogr. Palaeoclimatol. Palaeoecol., 212, 233–263.

Olivier, N., Pittet, B., Werner, W., Hantzpergue, P. and Gaillard, C. (2008) Facies distribution and coral-microbialite reef development on a low-energy carbonate ramp (Chay Peninsula, Kimmeridgian, western France). Sediment. Geol., 205, 14–33.

Olivier, N., Colombié, C., Pittet, B. and Lathuilière, B. (2011) Microbial carbonates and corals on the marginal French Jura platform (Late Oxfordian, Molinges section). Facies, 57, 469–492.

Olóriz, F., Reolid, M. and Rodríguez-Tovar, F.J. (2003a) A Late Jurassic Carbonate Ramp Colonized by Sponges and Benthic Microbial Communities (External Prebetic, Southern Spain). Palaios, 18, 528–545.

Olóriz, F., Reolid, M. and Rodríguez-Tovar, F.J. (2003b) Palaeogeographic and stratigraphic distribution of mid-late Oxfordian foraminiferal assemblages in the Prebetic Zone (Betic Cordillera, Southern Spain). Geobios, 36, 733–747.

Olóriz, F., Reolid, M. and Rodríguez-Tovar, F.J. (2006) Approaching trophic structure in Late Jurassic neritic shelves: A western Tethys example from southern Iberia. Earth-Science Rev., 79, 101–139.

Olóriz, F., Reolid, M. and Rodríguez-Tovar, F.J. (2008) Taphonomy of fossil macro-invertebrate assemblages as a tool for ecostratigraphic interpretation in Upper Jurassic shelf deposits (Prebetic Zone, southern Spain). Apport de la taphonomie des assemblages fossiles à macro-invertébrés à l'interprétation écostratigraphique des dépôts de plate-forme du Jurassique supérieur (zone Prébétique, Sud de l'Espagne). Geobios 41, 31–42.

Olóriz, F., Reolid, M. and Rodríguez-Tovar, F.J. (2012) Palaeogeography and relative sea-level history forcing eco-sedimentary contexts in Late Jurassic epicontinental shelves (Prebetic Zone, Betic Cordillera): An ecostratigraphic approach. Earth Sci. Rev., 111, 154–178.

Olszewska, B., Matyszkiewicz, J., Katarzyna, K. and Krajewski, M. (2012) Correlation of the Upper Jurassic-Cretaceous epicontinental sediments in Southern Poland and Southwestern Ukraine based on thin sections. Biuletyn Państwowego Instytutu Geologicznego, 453, 29-80.

Ourribane, M., Chellai, H. and Zaghib-Turki, D. (2000) Role des microbialites et des micro-encroutants dans la lithification récifale: exemples du Jurassique supérieur de l'Atlas maghrébin (Maroc et Tunisie) C R Acad Sci Paris Sci Planetes, 330: 407-414.

Padden, M., Weissert, H. and De Rafelis, M. (2001) Evidence for Late Jurassic release of methane from gas hydrate. Geology, 29, 223–226.

Pálfy, J. and Smith, P.L. (2000) Synchrony between Early Jurassic extinction, oceanic anoxic event, and the Karoo-Ferrar flood basalt volcanism. Geology, 28, 747–750.

Palma, R.M., López-Gómez, J. and Piethé, R.D. (2007) Oxfordian ramp system (La Manga Formation) in the Bardas Blancas area (Mendoza Province) Neuquén Basin, Argentina: Facies and depositional sequences. Sediment. Geol., 195, 113–134.

Pandey, D.K., and Fürsich, F.T. (1993) Contributions to the Jurassic of Kachchh, western India. I. The coral fauna. Beringeria, 8, 3–69.

Pasci, S. (1997) Tertiary transcurrent tectonics of North-Central Sardinia. Bull. Soc. géol. Fr., 168, 301–312.

Patterson, W.P. and Walter, L.M. (1994) Depletion of 13C in seawater ΣCO2 on modern carbonate platforms. Significance for the carbon isotopic record of carbonates. Geology 22, 885-888.

Pentecost, A. (1985) Association of cyanobacteria with tufa deposits: identity, enumeration and nature of the sheath material revealed by histochemistry. Geomicrobiol. J., 4, 285–298.

Péron-Pinvidic, G., Manatschal, G., Minshull, T.A. and Sawyer, D.S. (2007) Tectonosedimentary evolution of the deep Iberia-Newfoundland margins: Evidence for a complex breakup history. Tectonics, 26, 1–19.

Picotti, V. and Cobianchi, M. (2017) Jurassic stratigraphy of the Belluno Basin and Friuli Platform: a perspective on far-field compression in the Adria passive margin. Swiss J Geosci, 110, 833–850.

Pittet, B. and Mattioli, E. (2002) The carbonate signal and calcareous nannofossil distribution in an Upper Jurassic section (Balingen-Tieringen , Late Oxfordian, southern Germany). Palaeogeogr. Palaeoclimatol. Palaeoecol., 179, 71–96.

Pittet, B. and Strasser, A. (1998) Long-distance correlations by sequence stratigraphy and cyclostratigraphy: Examples and implications (Oxfordian from the Swiss Jura, Spain, and Normandy). Int. J. Earth Sci., 86, 852–874.

Pittet, B., Van Buchem, F.S.P., Hillgartner, H., Razin, P., Grötsch and Droste (2002) Ecological succession, palaeoenvironmental change, and depositional sequences of Barremian–Aptian shallow-water carbonates in northern Oman. Sedimentology, 49, 555-581.

Planavsky, N., Reid, R.P., Lyons, T.W., Myshrall, K.L. and Visscher, P.T. (2009) Formation and diagenesis of modern marine calcified cyanobacteria. Geobiology, 7, 566–576.

Platt, N.H. and Wright, V.P. (1992) Palustrine carbonates and the Florida Everglades: towards an exposure index for the fresh-water environment. J. Sediment. Petrol., 62, 1058–1071.

Playford, P.E. and Cockbain, A.E. (1976) Modern algal stromatolites at Hamelin Pool, a hyper-saline barred basin in Shark Bay, Western Australia. In: Stromatolites (Ed. M.R. Walter), Elsevier, Amsterdam, 389–411.

Pleş, G. and Schlagintweit, F. (2013) New data on Perturbatacrusta leini Schlagintweit & Gawlick, 2011 (Calcareous sponge ?) from the Late Jurassic (Tithonian) of the southern Carpathians, Romania. Acta Palaeontol. Rom., 9, 3–9.

Pleş, G., Mircescu, C. V., Bucur, I.I. and Săsăran, E. (2013) Encrusting micro-organisms and microbial structures in Upper Jurassic limestones from the Southern Carpathians (Romania). Facies, 59, 19–48.

Pleş, G., Bucur, I.I. and Păcurariu, A. (2015) Foraminiferal assemblages and facies associations in the Upper Jurassic carbonates from Ardeu Unit (Metaliferi Mountains, Romania). Acta Palaeontologica Romaniae, 11(2), 43-57.

Pleş, G., Oprişa, A., Bucur, I.I., Săsăran, E., Mircescu, C. V, Oltean, G. and Iacob, R.G. (2019) The central - western Getic Carbonate Platform: Upper Jurassic to Lower Cretaceous biostratigraphy and sedimentary evolution of the Cioclovina – Băniţa sector (Southern Carpathians , Romania). Facies, 65, 1–25.

Pomar, L. (2001) Types of carbonate platforms: a genetic approach. Basin Research 13, 313–334.

Pomar, L. and Hallock, P. (2008) Carbonate factories: A conundrum in sedimentary geology. Earth-Science Reviews 87, 134–169. https://doi.org/10.1016/j.earscirev.2007.12.002

Pomar, L. and Kendall, C.G.S.C. (2008) Architecture of Carbonate Platforms: A Response to Hydrodynamics and Evolving Ecology, Controls on Carbonate Platform and Reef Development. SEPM Special Publication 89, 187-216. https://doi.org/10.2110/pec.08.89.0187

Pomar, L., Morsilli, M., Hallock, P. and Badenas, B. (2012) Internal waves, an under-explored source of turbulence events in the sedimentary record. Earth-Science Reviews, 111, 56-81.

Pomar, L., Aurell, M., Beatriz, B., Morsilli, M. and Al-Awwad, S.F. (2015) Depositional model for a prograding oolitic wedge, Upper Jurassic, Iberian basin. Mar. Pet. Geol., 67, 556–582.

Posenato, R. and Masetti, D. (2012) Environmental control and dynamics of Lower Jurassic bivalve build-ups in the Trento Platform (Southern Alps, Italy). Palaeogeogr. Palaeoclimatol. Palaeoecol., 361–362, 1–13.

Pratt, B.R. and Jansa, L.F. (1988) Upper Jurassic shallow-water reefs of offshore Nova Scotia. In: Geldsetzer HHJ, James NP, Tebbutt GE (eds) Reefs, Canada and Adjacent Area, Canadian Society of Petroleum Geologists Memoir 13, 741–747.

Pratt, B.R. and Smewing, J.D. (1990) Jurassic and Early Cretaceous platform margin configuration and evolution, central Oman Mountains. Geol. Soc. Spec. Publ., 49, 69–88.

Pray, L.C., Cook, H.E., Mountjoy, E.W. and Mcdaniel, P.N. (1968) Allochthonous carbonate debris flow at Devonian Bank ("Reef") Margins, Alberta. Am. Assoc. Pet. Geol. Bull., 52, 545–546.

Price, G.D. and Rogov, M.A. (2009) An isotopic appraisal of the Late Jurassic greenhouse phase in the Russian Platform. Palaeogeography, Palaeoclimatology, Palaeoecology, 273, 41–49

Prinz, P. (1991) Mesozoische Korallen aus Nordchile. Palaeontographica Abt. A, 216, 147–209.

Radoičić, R. (1959) Nekoliko problematicnih mikrofosila iz dinarske krede (some problematic microfossils from the Dinarian Cretaceous). Vesnik, 17, 87–92.

Rais, P., Louis-Schmid, B., Bernasconi, S.M. and Weissert, H. (2007) Palaeoceanographic and palaeoclimatic reorganization around the Middle-Late Jurassic transition. Palaeogeogr. Palaeoclimatol. Palaeoecol., 251, 527–546.

Rameil, N. (2005) Carbonate sedimentology, sequence stratigraphy, and cyclostratigraphy of the Tithonian in the Swiss and French Jura Mountains A high-resolution record of changes in sea level and climate. GeoFocus, 13, 245.

Rameil, N., Immenhauser, A., Warrlich, G., Hillgärtner, H. and Droste, H.J. (2010) Morphological patterns of Aptian *Lithocodium–Bacinella* geobodies: relation to environment and scale. Sedimentology, 57, 883-911.

Randazzo, V., Le Goff, J., Di Stefano, P., Reijmer, J., Todaro, S. and Cacciatore, M.S. (2020) Carbonate slope re-sedimentation in a tectonically-active setting (Western Sicily Cretaceous Escarpment, Italy). Sedimentology, 67, 2360-2391.

Rees, P.M., Noto, C.R., Parrish, J.M. and Parrish, J.T. (2004) Late Jurassic climates, vegetation, and dinosaur distributions. J. Geol., 112, 643–653.

Reinhold, C. (1998) Multiple episodes of dolomitization and dolomite recrystallization during shallow burial in Upper Jurassic shelf carbonates: eastern Swabian Alb, southern Germany. Sedimentary Geology, 121, 71-95.

Reitner J. (1993) Modern cryptic microbialite/metazoan facies from Lizard Island (Great Barrier Reef, Australia) Formation and concepts. Facies, 29, 3-40.

Reolid, M. and Gaillard, C. (2007) Microtaphonomy of bioclasts and paleoecology of microencrusters from Upper Jurassic spongiolithic limestones (External Prebetic, Southern Spain). Facies, 53, 97–112.

Reolid, M., Gaillard, C., Olóriz, F. and Rodríguez-Tovar, F.J. (2005) Microbial encrustations from the Middle Oxfordian-earliest Kimmeridgian lithofacies in the Prebetic Zone (Betic Cordillera, southern Spain): characterization, distribution and controlling factors. Facies, 50, 529–543.

Reolid, M., Gaillard, C. and Lathuilière, B. (2007) Microfacies, microtaphonomic traits and foraminiferal assemblages from Upper Jurassic oolitic-coral limestones: Stratigraphic fluctuations in a shallowing-upward sequence (French Jura, Middle Oxfordian). Facies, 53, 553–574.

Reolid, M., Molina, J.M., Löser, H., Navarro, V. and Ruiz-ortiz, P.A. (2009) Coral biostromes of the Middle Jurassic from the Subbetic (Betic Cordillera, southern Spain): facies, coral taxonomy, taphonomy, and palaeoecology. Facies, 55, 575–593.

Ricci, C., Rusciadelli, G., Della Porta, G., Lanfranchi, A., Jadoul, F. and Lathuilière, B. (2018) Sedimentary evolution of a coral- microbialites- and debris-rich Upper Jurassic reef (upper Tithonian, eastern Sardinia, Italy). Sediment. Geol., 376, 113–135.

Riding, R. (1991a) Classification of Microbial Carbonates. In: Calcareous Algae and Stromatolites (Ed. R. Riding), Springer-Verlag, Berlin, 21–51.

Riding, R. (1991b) Calcified cyanobacteria. In: Calcareous Algae and Stromatolites, Springer, Berlin, Heidelberg, 55–87.

Riding, R. (1993) Phanerozoic patterns of marine CaCO3 precipitation. Naturwissenschaften, 80, 513–516.

Riding, R. (2000) Microbial carbonates: The geological record of calcified bacterial-algal mats and biofilms. Sedimentology, 47, 179–214.

Riding, R. (2004) Solenopora is a chaetetid sponge, not and alga. Paleontology, 47, 117–122.

Riding, R. (2006) Cyanobacterial calcification, carbon dioxide concentrating mechanisms, and Proterozoic-Cambrian changes in atmospheric composition. Geobiology, 4, 299–316.

Riding, R. (2011) Microbialites, stromatolites, and thrombolites. In: Encyclopedia of Geobiology (Ed. J. Reitner and V. Thiel), Encyclopedia of Earth Science Series, Springer, Heidelberg, 635–654.

Riding, R. and Liang, L. (2005) Geobiology of microbial carbonates: Metazoan and seawater saturation state influences on secular trends during the Phanerozoic. Palaeogeogr. Palaeoclimatol. Palaeoecol., 219, 101–115.

Riechelmann, S., Mavromatis; V., Buhl, D., Dietzel, M. and Immenhauser, A. (2020) Controls on formation and alteration of early diagenetic dolomite: A multi-proxy $\delta^{44/40}$Ca, δ^{26}Mg, δ^{18}O and δ^{13}C approach. Geochimica et Cosmochimica Acta, 283, 167-183.

Roberston Handford, C. (2002) Regional Facies Relationships and Sequence Stratigraphy of a Super-Giant Reservoir (Arab-D Member), Saudi Arabia. In: Sequence Stratigraphic Models for Exploration and Production: Evolving Methodology, Emerging Models and Application Histories. 22nd Annual Bob F. Perkins Research Conference. Gulf Coast Section SEPM (GCSSEPM), TX, Houston, 564.

Roniewicz, E. (2008) Kimmeridgian-Valanginian reef corals from the Moesian Platform from Bulgaria. Ann. Soc. Geol. Pol., 78, 91–134.

Roniewicz, E. and Roniewicz, P. (1971) Upper Jurassic coral assemblages of the Central Polish Uplands.

Ruban, D.A. and Tyszka, J. (2005) Diversity dynamics and mass extinctions of the Early-Middle Jurassic foraminifers: A record from the Northwestern Caucasus. Palaeogeogr. Palaeoclimatol. Palaeoecol., 222, 329–343.

Ruebsam, W. Mayer, B. and Schwark, L. (2019) Cryosphere carbon dynamics control early Toarcian global warming and sea level evolution. Glob. Planet. Chang. 172, 440–453.

Ruebsam, W., Reolid, M., Marok, A. and Schwark, L. (2020) Drivers of benthic extinction during the early Toarcian (Early Jurassic) at the northern Gondwana paleomargin: Implications for paleoceanographic conditions. Earth-Sciences Reviews, 203, 103-117.

Rusciadelli, G., Ricci, C. and Lathuilière, B. (2011) The Ellipsactinia Limestones of the Marsica area (Central Apennines): A reference zonation model for Upper Jurassic Intra-Tethys reef complexes. Sediment. Geol., 233, 69–87.

Russo, A. and Morsilli, M. (2007) New insight on architecture and microstructure of *Ellipsactinia* and *Sphaeractinia* (Demosponges) from the Gargano promontory (southern Italy). Geol. Rom., 40, 215–225.

Russo, F., Mastandrea, A., Stefani, M. and Neri, C. (2000) Carbonate facies dominated by syndepositional cements: A key component of middle Triassic platforms. The Marmolada case history (Dolomites, Italy). Facies, 42, 211–226. https://doi.org/10.1007/bf02562573

Ryan, W.B.F. and Miller, E.L. (1981) Evidence of a carbonate platform beneath Georges Bank. Marine Geology, 44, 213–228.

Sadki, D. and Sha, J.G. (2018) Jurassic reef events in the Moroccan Atlas: A review. Palaeoworld, 27, 458–466.

Sahagian, D., Pinous, O., Olferiev, A. and Zakharov, V. (1996) Eustatic curve for the middle jurassic-cretaceous based on Russian platform and Siberian Stratigraphy: Zonal resolution. Am. Assoc. Pet. Geol. Bull., 80, 1433–1458.

Saller, A.H. (1984) Petrologic and geochemical constraints on the origin of subsurface dolomite, Enewatak Atoll: an example of dolomitization by normal sea-water. Geology, 12, 217-220.

Samankassou, E., Strasser, A., Dupraz, C., Samankassou, E., Strasser, A., Gioia, E. Di, Rauber, G. and Dupraz, C. (2003) High-resolution record of lateral facies variations on a shallow carbonate platform (Upper Oxfordian, Swiss Jura Mountains). Eclogae geol Helv, 96, 425–440.

San Miguel, G., Aurell, M., Bádenas, B., Martinez, V., Caline, B., Pabian-Goyheneche, C., Rolando, J.P. and Grasseau, N. (2013) Facies heterogeneity of a Kimmeridgian carbonate ramp (Jabaloyas, eastern Spain): a combined outcrop and 3D geomodelling analysis. J. Iber. Geol., 39, 233–252.

San Miguel, G., Aurell, M. and Bádenas, B. (2017) Occurrence of high-diversity metazoan - to microbial - dominated bioconstructions in a shallow Kimmeridgian carbonate ramp (Jabaloyas, Spain). Facies, 63, 1–21.

Sandberg, P.A. (1983) An oscillating trend in Phanerozoic nonskeletal carbonate mineralogy. Nature, 305, 19–22.

Santantonio, M. and Carminati, E. (2011) Jurassic rifting evolution of the Apennines and Southern Alps (Italy): Parallels and differences. GSA Bulletin, 123, 468-484.

Santantonio, M. and Fabbi, S. (2020) Anatomy and Jurassic evolution of a Hercynian basement high (Caloveto High - Calabria, Southern Italy). Italian Journal of Geosciences, 139, 30-53.

Santantonio, M., Scrocca, D. and Lipparini, L. (2013) The Ombrina-Rospo Plateau (Apulian Platform): Evolution of a Carbonate Platform and its Margins during the Jurassic and Cretaceous. Mar. Pet. Geol., 42, 4–29.

Santantonio, M., Fabbi, S. and Aldega, L. (2016) Mesozoic architecture of a tract of the European–Iberian continental margin: Insights from preserved submarine palaeotopography in the Longobucco Basin (Calabria, Southern Italy). Sedimentary Geology, 331, 94-113.

Săsăran, E., Bucur, I.I., Pleş, G. and Riding, R. (2014) Late Jurassic Epiphyton-like cyanobacteria: Indicators of long-term episodic variation in marine bioinduced microbial calcification? Palaeogeogr. Palaeoclimatol. Palaeoecol., 401, 122–131.

Schairer, G., Seyed-Emami, K., Fürsich, F.T., Senowbari-Daryan, B., Aghanabati, S.A. and Majidifard, M.R. (2000) Stratigraphy, facies analysis and ammonite fauna of the Qal'eh Dokhtar formation (Middle–Upper Jurassic) at the type locality west of Boshrouyeh (east central Iran). Neues Jahrbuch für Geologie und Paläontologie, Abhandlungen, 216, 35–66.

Schaltegger, U., Guex, J., Bartolini, A., Schoene, B. and Ovtcharova, M. (2008) Precise U-Pb age constraints for end-Triassic mass extinction, its correlation to volcanism and Hettangian post-extinction recovery. Earth Planet. Sci. Lett., 267, 266–275.

Schick, H.W. (2004) Bio-and lithostratigraphic study on the lower Kimmeridgian of the Swabian and Franconian Alb (Germany). Rivista Italiana di Paleontologia e Stratigrafia, 110, 279-278.

Schlager, W. (2003) Benthic carbonate factories of the Phanerozoic. International Journal of Earth Sciences, 92, 445–464. https://doi.org/10.1007/s00531-003-0327-x

Schlagintweit, F. and Bover-Arnal, T. (2013) Remarks on Bačinella Radoičić, 1959 (type species B. irregularis) and its representatives. Facies, 59, 59–73.

Schlagintweit, F. and Gawlick, H.J. (2007) Analysis of Late Jurassic to Early Cretaceous algal debris-facies of the Plassen carbonate platform in the Northern Calcareous Alps (Germany, Austria) and in the Kurbnesh area of the Mirdita zone (Albania): a tool to reconstruct tectonics and palaeogeography of eroded platforms. Facies 53:209–227.

Schlagintweit, F. and Gawlick, H.J. (2008) The occurrence and role of microencruster frameworks in Late Jurassic to Early Cretaceous platform margin deposits of the Northern Calcareous Alps (Austria). Facies, 54, 207–231.

Schlagintweit, F. and Bover-Arnal, T. (2013) Remarks on *Bacinella* Radoičic, 1959 (type species B. irregularis) and its representatives. Facies, 59, 59-37.

Schlagintweit, F., Bover-Arnal, T. and Salas, R. (2010) New insights into *Lithocodium aggregatum* Elliott 1956 and *Bacinella irregularis* Radoičić 1959 (Late Jurassic-Lower Cretaceous): Two ulvophycean green algae (?Order Ulotrichales) with a heteromorphic life cycle (epilithic/euendolithic). 509–547 pp.

Schmid, D.U. and Leinfelder, R.R. (1995) Lithocodium aggregatum Elliott n'est pas une algue mais un foraminifère encroûtant, commensalisé par le foraminifère *Troglotella incrustans* Wernli et Fookes. Comptes rendus l'Académie des Sci. Série 2. Sci. la terre des planètes, 320, 531–538.

Schmid, D.U. and Leinfelder, R.R. (1996) The Jurassic Lithocodium aggregatum - Troglotella incrustans foraminiferal consortium. Palaeontology, 39, 21–52.

Schoene, B., Guex, J., Bartolini, A., Schaltegger, U. and Blackburn, T.J. (2010) Correlating the end-Triassic mass extinction and flood basalt volcanism at the 100 ka level. Geology, 38, 387–390.

Sellwood, B.W. and Valdes, P.J. (2008) Jurassic climates. Proc. Geol. Assoc., 119, 5–17.

Senowbari-Daryan, B., Bucur, I.I., Schlagintweit, F., Săsăran, E. and Matyszkiewicz, J. (2008) Crescentiella, a new name for "Tubiphytes" morronensis CRESCENTI, 1969: An enigmatic Jurassic - Cretaceous microfossil. Geol. Croat., 61, 185–214.

Septfontaine, M. (1988) Vers une classification évolutive des Lituolidés (Foraminifères) jurassiques en milieux de plate-forme carbonatée. Revue de Paléobiologie, 2, 229-256.

Sequero, C., Bádenas, B. and Aurell, M. (2018) Facies mosaic in the inner areas of a shallow carbonate ramp (Upper Jurassic, Higueruelas Fm, NE Spain). Facies. doi: 10.1007/s10347-018-0521-8

Sequero, C., Aurell, M. and Bádenas, B. (2019) Sedimentary evolution of a shallow carbonate ramp (Kimmeridgian, NE Spain): Unravelling controlling factors for facies heterogeneities at reservoir scale. Mar. Pet. Geol., 109, 145–174.

Sequero, C., Aurell, M. and Bádenas, B. (2020) Oncoid distribution in the shallow domains of a Kimmeridgian carbonate ramp (Late Jurassic, NE Spain). Sedimentary Geology, 398, 105585.

Sevillano, A., Rosales, I., Bádenas, B., Barnolas, A. and María, J. (2019) Spatial and temporal facies evolution of a Lower Jurassic carbonate platform, NW Tethyan margin (Mallorca, Spain). Facies, 65, 1–34.

Shinn, E.A. (1968) Practical Significance of Birdseye Structures in Carbonate Rocks. J. Sediment. Petrol., 38, 215–223.

Shinn, E.A., Loyd, R.M. and Ginsburg, R.N. (1969) Anatomy of a Modern Carbonate Tidal-flat, Andros Island, Bahamas. J. Sediment. Petrol., 39, 1202–1228.

Simms, M.A., Dolomitization by groundwater-flow systems in carbonate platforms. Trans. Gulf Coast Association Geol. Soc., 34, 411-420.

Simone, L., Carannante, G., Bassi, D. and Cherchi, A. (2012) Rudist-bearing rhodalgal facies in the post-Turonian recovery of peri-Tethyan carbonate systems: a case history from the Nurra region (northwestern Sardinia, Italy). Geodiversitas, 34, 167–187.

Speranza, F., Villa, I.M., Sagnotti, L., Florindo, F., Cosentino, D., Cipollari, P. and Mattei, M. (2002) Age of the Corsica-Sardinia rotation and Liguro-Provençal Basin spreading: New paleomagnetic and Ar/Ar evidence. Tectonophysics, 347, 231–251.

Stampfli, G.M. (2000) Tethyan oceans. Geol. Soc. Spec. Publ., 173, 1–23.

Stampfli, G.M. and Borel, G.D. (2002) A plate tectonic model for the Paleozoic and Mesozoic constrained by dynamic plate boundaries and restored synthetic oceanic isochrons. Earth Planet. Sci. Lett., 196, 17–33.

Stampfli, G.M., Borel, G.D., Marchant, R. and Mosar, J. (2002) Western Alps geological constraints on western Tethyan reconstructions. 77–106.

Stampfli, G.M. and Hochard, C. (2009) Plate tectonics of the Alpine realm. In: Murphy, J. B., Keppie, J. D. & Hynes, A. J. (eds) Ancient Orogens and Modern Analogues. Geological Society, London, Special Publications, 327, 89–111.

Stanier, R.Y. (1977) The position of cyanobacteria in the world of phototrophs. Carlsberg Res. Commun., 42, 77–98.

Stanley, G.D. (2003) The evolution of modern corals and their early history. Earth Sci. Rev., 60, 195–225.

Stanley, G.D. (2006) Photosymbiosis and the evolution of modern coral reefs. Science (80-.)., 312, 857–858.

Stanley G.D. and Beauvais L. (1990) Middle Jurassic corals from the Wallowa Terrane, west-central Idaho. Journal of Paleontology, 64, 352-362.

Stanley, G.D. and Swart, P.K. (1995) Evolution of the coral-zooxanthenllae symbiosis during the Triassic: a geochemical approach. Paleobiology, 21, 179–199.

Stanley, S.M. and Hardie, L.A. (1998) Secular oscillations in the carbonate mineralogy of reef-building and sediment-producing organisms driven by tectonically forced shifts in seawater chemistry. Palaeogeogr. Palaeoclimatol. Palaeoecol., 144, 3–19.

Stanley, S.M. and Hardie, L.A. (1999) Hypercalcification: Paleontology links plate tectonics. GSA Today, 9, 1–7.

Steiner, C., Hobson, A., Favre, P., Stampfli, G.M. and Hernandez, J. (1998) Mesozoic sequence of Fuerteventura (Canary Islands): Witness of early Jurassic sea-floor spreading in the central Atlantic. Bull. Geol. Soc. Am., 110, 1304–1317.

Steuber, T. and Veizer, J. (2002) Phanerozoic record of plate tectonic control of seawater chemistry and carbonate sedimentation. Geology, 30, 1123–1126.

Strasser, A. (1984) Black-pebble occurrence and genesis in Holocene carbonate sediments (Florida Keys, Bahamas and Tunisia). J. Sediment. Petrol., 54, 1097–1109.

Strasser, A. (1986) Ooids in Purbeck limestones (lowermost Cretaceous) of the Swiss and French Jura. Sedimentology 33:711–727

Strasser, A. and Védrine, S. (2009) Controls on facies mosaics of carbonate platforms : a case study from the Oxfordian of the Swiss Jura. Spec. Publ. Int. Assoc. Sedimentol., 41, 199–213.

Strasser, A., Védrine, S. and Stienne, N. (2012) Rate and synchronicity of environmental changes on a shallow carbonate platform (Late Oxfordian, Swiss Jura Mountains). Sedimentology, 59, 185–211.

Strohmenger, C., Deville, Q. and Fookes, E. (1991) Kimmeridgian/Tithonian eustacy and its imprints on carbonate rocks from the Dinaric and the Jura carbonate platforms. Bulletin de la Societé géologique de France, 162, 661–671.

Suan, G. Nikitenko, B.L., Rogov, M.A., Baudin, F., Spangenberg, J.E., Knyazev, V.G., Glinskikh, L.A., Goryacheva, A.A., Adatte, T., Riding, J.B., Föllmi, K.B., Pittet, B., Mattioli, E. and Lécuyer, C. (2011) Polar record of Early Jurassic massive carbon injection. Earth Planet. Sci. Lett. 312, 102–113.

Sun, S.Q. and Wright, V.P. (1989) Peloidal fabrics in Upper Jurassic reefal limestones, Weald Basin, southern England. Sediment. Geol., 65, 165–181.

Swart, P.K. (2015) The geochemistry of carbonate diagenesis: The past, present and future. Sedimentology, 62, 1233-1304.

Taylor, P.D: and Palmer, T.J. (1994) Submarine Caves in a Jurassic Reef (La Rochelle, France). Naturwissenschaften, 81, 357-360.

Tišljar, J. and Velić, I. (1991) Carbonate facies and depositional environments of the Jurassic and Lower Cretaceous of the coastal Dinarides (Croatia). Geološki Vjesn 44:215–234

Tišljar, J. and Velić, I. (1993) Upper Jurassic (Malm) shallow-water carbonates in the Western Gorski Kotar area: facies and depositional environments (Western Croatia). Geologia Croatica, 46, 263-279.

Tišljar, J., Vlahović, I., Velić, I. and Sokač, B. (2002) Carbonate Platform Megafacies of the Jurassic and Cretaceous Deposits of the Karst Dinarides. Geologia Croatica 139–170.

Tomás, S., Homann, M., Mutti, M., Amour, F., Christ, N., Immenhauser, A., Agar, S.M. and Kabiri, L. (2013) Alternation of microbial mounds and ooid shoals (Middle Jurasssic , Morocco): Response to paleoenvironmental changes. Sediment. Geol., 294, 68–82.

Tomás, S., Aurell, M., Bádenas, B., Bjorge, M., Duaso, M. and Mutti, M. (2019) Architecture and paleoenvironment of Mid-Jurassic microbial – siliceous sponge mounds, northeastern Spain. J. Sediment. Res., 89, 110–134.

Trammer, J. (1989) Middle to Upper Oxfordian sponges of the Polish Jura. Acta Geol. Pol., 39, 49–91.

Tucholke, B.E., Sawyer, D.S. and Sibuet, J.C. (2007) Breakup of the Newfoundland-Iberia rift. In: Karner, G.D., Manatschal, G., Pinheiro, L.M. (eds) Imaging, Mapping and Modelling Continental Lithosphere Extension and Breakup. Geological Society, London, Special Publication, 282, 9–46.

Tucker, M.E. and Wright, V.P. (1990) Carbonate sedimentology. Blackwells Scientific.

Tugend, J., Manatschal, G., Kusznir, N.J., Masini, E., Mohn, G. and Thinon, I. (2014) Formation and deformation of hyperextended rift systems: Insights from rift domain mapping in the Bay of Biscay-Pyrenees. Tectonics, 33, 1239–1276.

Turnšek, D. (1997) Mesozoic corals of Slovenia. ZRC SAZU, Ljubljana, 513 pp.

Turnšek, D., Buser, S. and Ogorolec, B. (1981) An Upper Jurassic reef complex from Slovenia, Yugoslavia. In: Tomey D.F. (ed) European Fossils Reefs Models, SEPM Special Publication 30, 361–369.

Val, J., Aurell, M., Bádenas, B., Castanera, D. and Subías, S. (2019) Cyclic carbonate–siliciclastic sedimentation in a shallow marine to coastal environment (latest Kimmeridgian–early Tithonian, Galve sub-basin, Spain). Journal of Iberian Geology 45, 195–222. https://doi.org/10.1007/s41513-018-00098-1

van der Kooij, B., Immenhauser, A., Csoma, A., Bahamonde, J. and Steuber, T. (2009). Spatial geochemistry of a Carboniferous platform-margin-to-basin transect: balancing environmental and diagenetic factors. Sedimentary Geology, 219, 136-150.

Vardabasso, S. (1959) Il Mesozoico epicontinentale della Sardegna. Rend Sc Fis Mat Nat, 27, 178–184.

Vasconcelos, C. and McKenzie J.A. (1997). Microbial mediation of modern dolomite precipitation and diagenesis under anoxic conditions (Lagoa Vermelha, Rio De Janeiro, Brazil). Journal of Sedimentary Research, 67, 378-391.

Védrine, S., Strasser, A. and Hug, W. (2007) Oncoid growth and distribution controlled by sea-level X uctuations and climate (Late Oxfordian , Swiss Jura Mountains). 535–552.

Veizer, J., Godderis, Y. and François, L.M. (2000) Evidence for decoupling of atmospheric CO 2 and global climate during the Phanerozoic eon. Nature, 408, 698–701.

Velić, I., Tišljar, J., Vlahović, I., Velić, J., Koch, G. and Matičec, D. (2002) Palaeogeographic Variability and Depositional Environments of the Upper Jurassic Carbonate Rocks of Velika Kapela Mt. (Gorski Kotar Area, Adriatic Carbonate Platform, Croatia). Geol. Croat., 55, 121–138.

Vickers, M.L., Bajnai, B., Price, G.D., Linckens, J. and Fiebig, J. (2019) Southern high latitude warmth during Jurassic-Cretaceous: new evidence from clumped isotope thermometry. Geology, 47 (8), 724-728.

Vickers, M.L., Fernandez, A., Hesselbo, S.P., Price, G.D., Bernasconi, S.M., Lode, S., Ullmann, C.V., Thibault, N., Hougaard, I.B. and Korte, C. (2020) Unravelling Middle to Late Jurassic palaeoceanographic and palaeoclimatic signals in the Hebrides Basin using belemnite clumped isotope thermometry. Earth and Planetary Science Letters, 546, 116401.

Vincent, B., Emmanuel, L., Loreau, J.P. (2004) Significance of the isotopic signal ($\delta^{18}O$, $\delta^{13}C$) of neritic carbonates: diagenetic component and original component (Upper Jurassic of the East of the Paris Basin, France). Comptes Rendus Geoscience, 336 (1), 29-39.

Visscher, P.T., Prins, R.A. and van Gemerden, H. (1992) Rates of sulfate reduction and thiosulfate consumption in a marine microbial mat. FEMS Microbiol. Lett., 86, 283–294.

Vlahović, I., Tišljar, J., Velić, I., Matičec, D. (2002) The Karst Dinarides are Composed of Relics of a Single Mesozoic Platform: Facts and Consequences. Geol Croat 55:171–184

Vlahović, I., Tišljar, J., Velić, I. and Matičec, D. (2005) Evolution of the Adriatic Carbonate Platform: Palaeogeography, main events and depositional dynamics. Palaeogeogr. Palaeoclimatol. Palaeoecol., 220, 333–360.

Ward, W.C. and Halley, R.B. (1985) Dolomitization in a mixing zone of near-seawater composition, Late Pleistocene, northeastern Yucutan Peninsula. Journal of Sedimentary Petrology, 55, 407-420.

Warren, J. (2000). Dolomite: occurrence, evolution and economically important associations. Earth-Science Reviews 52, 1-81.

Watts, K.F. and Blome, C.D. (1990) Evolution of the Arabian carbonate platform margin slope and its response to orogenic closing of a Cretaceous ocean basin, Oman. In: Tucker, M.E., Wilson, J.L., Crevello, P.D., Sarg, J.F., and Read, J.F. (eds) Carbonate Platforms: Facies, Sequences and Evolution: International Association of Sedimentologists, Special Publication 9, 291–323.

Weissert, H. and Mohr, H. (1996) Late Jurassic climate and its impact on carbon cycling. Palaeogeogr. Palaeoclimatol. Palaeoecol., 122, 27–43.

Wetzel, A., Weissert, H., Schaub, M. and Voegelin, A.R. (2013) Sea-water circulation on an oolite-dominated carbonate system in an epeiric sea (Middle Jurassic, Switzerland). Sedimentology, 60, 19–35.

Wierzbowski, H. (2015) Seawater temperatures and carbon isotope variations in central European basins at the Middle-Late Jurassic transition (Late Callovian-Early Kimmeridgian). Palaeogeogr. Palaeoclimatol. Palaeoecol., 440, 506–523.

Wierzbowski, H., Anczkiewicz, R., Pawlak, J., Rogov, M.A. and Kuznetsov, A.B. (2017) Revised Middle–Upper Jurassic strontium isotope stratigraphy. Chemical Geology, 466, 239–255. https://doi.org/10.1016/j.chemgeo.2017.06.015

Wignall, P.B., Newton, R.J. and Little, C.T.S. (2005) The timing of paleoenvironmental change and cause-and-effect relationships during the early Jurassic mass extinction in Europe. Am. J. Sci., 305, 1014–1032.

Wilmsen, M. and Neuweiler, F. (2008) Biosedimentology of the Early Jurassic post-extinction carbonate depositional system, central High Atlas rift basin, Morocco. Sedimentology, 55, 773–807.

Wilson, M.A., Feldman, H.R., Bowen, J.C. and Avni, Y. (2008) A new equatorial, very shallow marine sclerozoan fauna from the Middle Jurassic (late Callovian) of southern Israel. Palaeogeogr. Palaeoclimatol. Palaeoecol., 263, 24–29.

Wilson, M.A., Feldman, H.R. and Krivicich, E.B. (2010) Bioerosion in an equatorial Middle Jurassic coral-sponge reef community (Callovian, Matmor Formation, southern Israel). Palaeogeogr. Palaeoclimatol. Palaeoecol., 289, 93–101.

Wood, R. A. (1987) The biology and taxonomy of Mesozoic stromatoporoids. PhD thesis

Wray, J.L. (1977) Calcareous algae. Elsevier, Amsterdam, 185 pp.

Wright, D.T. (1997) An organogenic origin for widespread dolomite in the Cambrian Eilean Dubh Formation, north-western Scotland. Journal of Sedimentary Research, 67, 54-65.

Wright, V.P. and Azerêdo, A.C. (2006) How relevant is the role of macrophytic vegetation in controlling peritidal carbonate facies ?: Clues from the Upper Jurassic of Portugal. 186, 147–156.

Youssef, M. and El-Sorogy, A.S. (2015) Paleoecology of benthic foraminifera in coral reefs recorded in the Jurassic Tuwaiq Mountain Formation of the Khashm Al-Qaddiyah area, Central Saudi Arabia. J. Earth Sci., 26, 224–235.

Zatoń, M., Wilson, M.A. and Zavar, E. (2011) Diverse sclerozoan assemblages encrusting large bivalve shells from the Callovian (Middle Jurassic) of southern Poland. Palaeogeography, Palaeoclimatology, Palaeoecology, 307, 232-244.

Zattin, M., Massari, F. and Dieni, I. (2008) Thermochronological evidence for Mesozoic-Tertiary tectonic evolution in the eastern Sardinia. Terra Nov., 20, 469–474.

Zeiss, A. (1968) Unteruchungen zur Paläontologie der Cephalopoden des Unter-Tithon des südlichen Frankenalb. Abhandlungen der Bayerischen Akademie der Wissenschaften mathematisch-naturwissenschaftliche Klasse, neue Folge 132, 1-191.

Zuo, F., Heimhofer, U., Huck, S., Adatte, T., Erbacher, J. and Bodin, S., 2019. Climatic fluctuations and seasonality during the Kimmeridgian (Late Jurassic): stable isotope and clay mineralogical data from the Lower Saxony Basin, Northern Germany. Palaeogeography, Palaeoclimatology, Palaeoecology, 517, 1–15.

Appendix

Detailed stratigraphic logs and analysed samples

1- Iscra

LOCATION
Urzulei Supramonte
40°06'17.43"N
9°27'27.01"E

THICKNESS
105 m

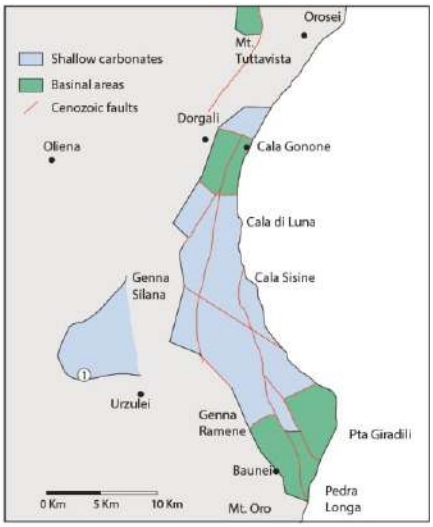

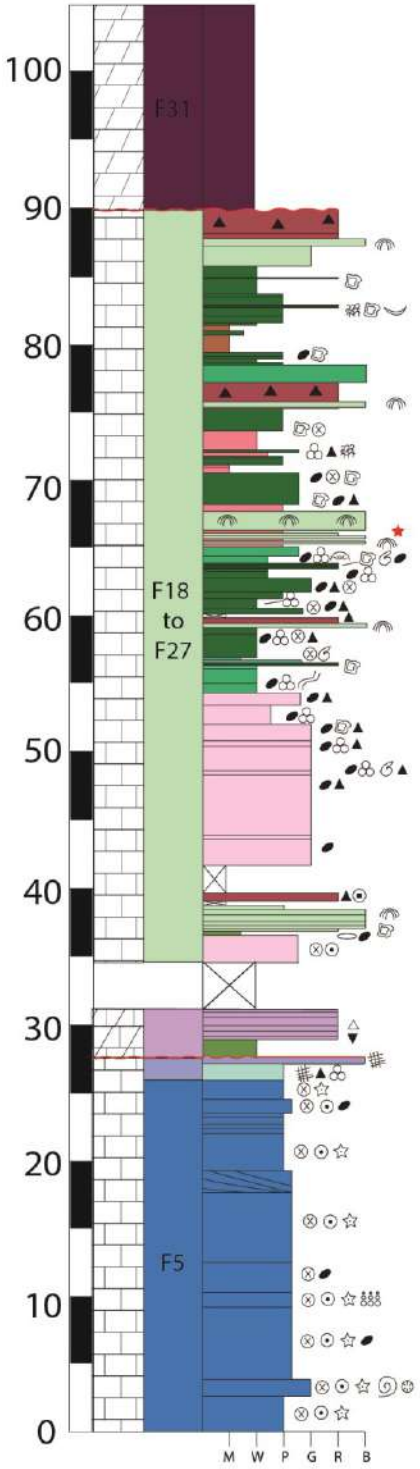

Sample	Stratigraphic height	Facies	$\delta^{13}C$	$\delta^{18}O$
TA2	100 m	F31	-	-
I537	88.7 m	F18	2.06	0.47
I524	87.4 m	F22	-1.73	-4.95
I501	85.1 m	F23	-0.19	-3.55
I480	82.0 m	F27	1.83	-2.51
I465	81.5 m	F19	-	-
I426	77.6 m	F23	-0.42	-3.39
I424	77.4 m	F18	2.16	0.69
I406	75.6 m	F22	-	-
I360	71.0 m	F21	-	-
I313	66.3 m	F19	-1.72	-1.70
I312	66.2 m	F22	-0.26	-3.65
I291	64.1 m	F23	-	-
I263	61.3 m	F26	-	-
I258	60.8 m	F26	-	-
I247	59.7 m	F22	0.47	-2.00
I244	59.4 m	F26	-	-
I198	54.8 m	F23	1.64	-1.75
I174	52.4 m	F20	2.30	-1.45
I140	49.0 m	F20	-	-
I137	48.7 m	F20	-	-
I71	42.1 m	F20	-	-
I45	39.5 m	F16	1.70	-0.44
I34	38.4 m	F23	2.06	-1.96
I05	35.5 m	F20	-	-
IS309A	30.9 m	F16	-0.99	-0.54
IS309	30.9 m	F16	-	-
IS291	29.1 m	F16	1.45	-2.25
IS287	28.7 m	F16	-0.99	-1.19
IS276	27.6 m	F25	-1.22	-1.68
IS273	27.3 m	F10	-0.87	-5.62
IS263	26.3 m	F9	-	-
IS244	24.4 m	F5	-	-
IS234	23.4 m	F5	-	-
IS186	18.6 m	F5	-	-
IS137	13.7 m	F5	-	-
IS101	10.1 m	F5	-	-
IS92	9.2 m	F5	-	-
IS45	4.5 m	F5	-	-
IS38	3.8 m	F5	-	-
IS04	0.4 m	F5	-	-

2- Codula Orbisi

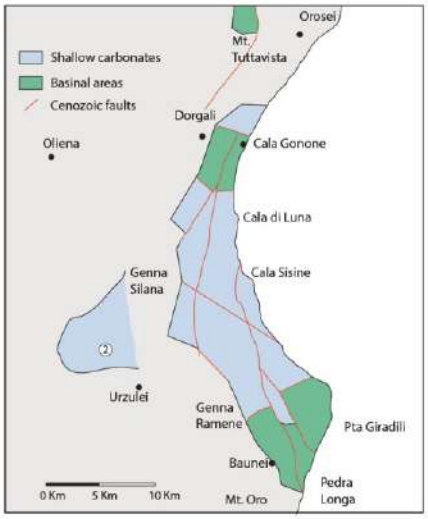

LOCATION
Urzulei Supramonte
40°07'51.63"N
9°29'33.53"E

THICKNESS
50 m

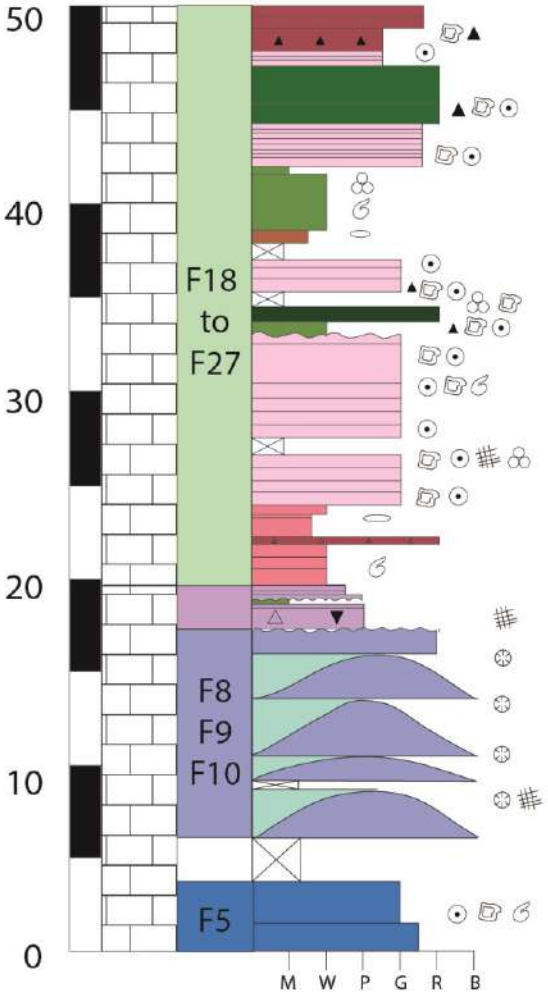

Sample	Stratigraphic height	Facies	$\delta^{13}C$	$\delta^{18}O$
CO504	50.4 m	F18	-	-
CO495	49.5 m	F18	1.62	-1.46
CO494	49.4 m	F18	-	-
CO484	48.4 m	F20	-	-
CO476	47.6 m	F26	1.58	-1.07
CO450	45.0 m	F26	-	-
CO435	43.5 m	F20	-	-
CO423	42.3 m	F20	-	-
CO417	41.7 m	F25	-	-
CO416	41.6 m	F25	-	-
CO385	38.5 m	F19	-	-
CO370	37.0 m	F20	-	-
CO353	35.3 m	F20	-	-
CO346	34.6 m	F27	-	-
CO337	33.7 m	F25	-	-
CO310	31.0 m	F20	-	-
CO302	30.2 m	F20	-	-
CO275	27.5 m	F20	-	-
CO264	26.4 m	F20	-	-
CO250	25.0 m	F20	-	-
CO240	24.0 m	F20	-	-
CO236	23.6 m	F21	-	-
CO227	22.7 m	F21	-	-
CO215	21.5 m	F21	-	-
CO218	21.8 m	F19	-1.41	0.11
CO198	19.8 m	F21	-	-
CO193	19.3 m	F21	-	-
CO188	18.8 m	F16	-	-
CO185	18.5 m	F25	0.01	-2.11
CO183	18.3 m	F25		
CO174	17.4 m	F17	-1.36	-3.87
CO162	16.2 m	F10	-	-
CO150	15.0 m	F10	-0.93	-3.12
CO145	14.5 m	F10	-	-
CO130	13.0 m	F10	-	-
CO118	11.8 m	F10	-	-
CO110	11.0 m	F10	-1.19	-3.93
CO98	9.8 m	F10	-	-
CO94	9.4 m	F10	-	-
CO83	8.3 m	F10	-0.97	-3.99
CO79	7.9 m	F10	-	-
CO76	7.6 m	F10	-	-
CO74	7.4 m	F10	-	-
CO29	2.9 m	F5	-0.98	-2.93
CO11	1.1 m	F5	-	-

3- Genna Silana

LOCATION
Urzulei Supramonte
40°09'30.26"N
9°30'24.08"E

THICKNESS
456 m

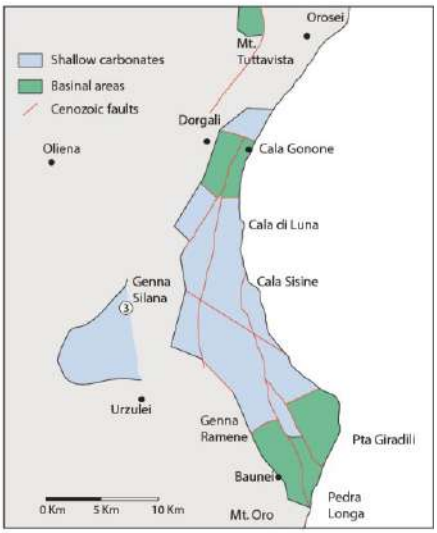

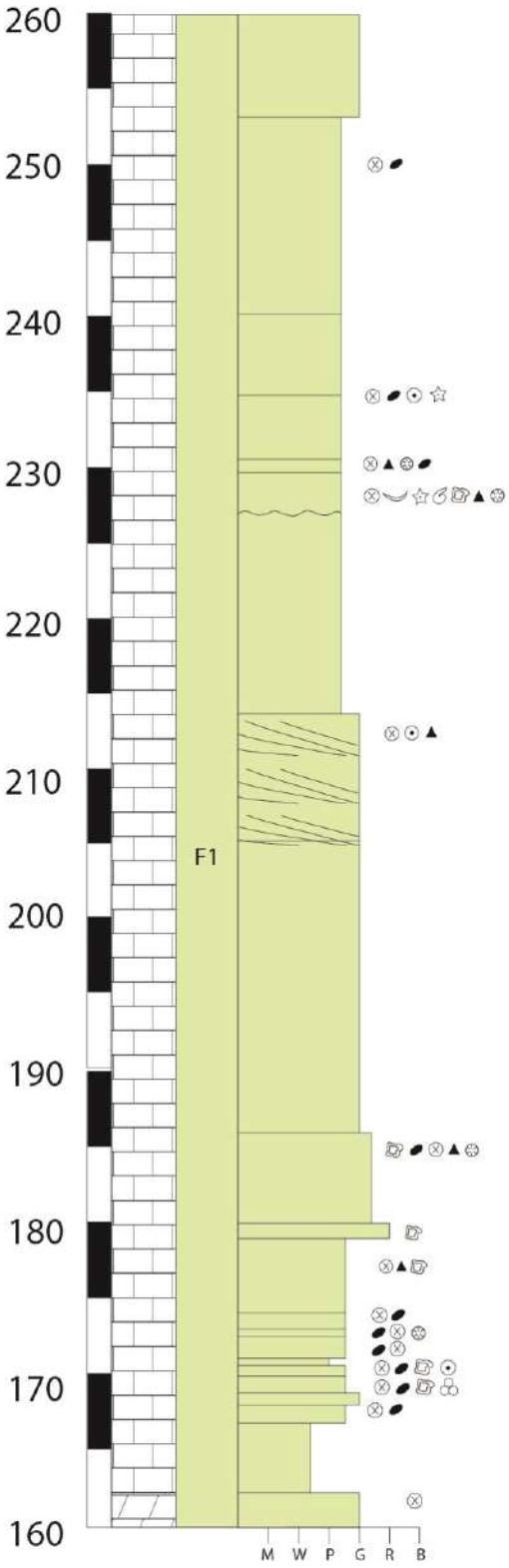

Sample	Stratigraphic height	Facies	$\delta^{13}C$	$\delta^{18}O$
GS931	253.1 m	F1	0.95	-3.07
GS740	234.0 m	F1	-	-
GS705	230.5 m	F1	-	-
GS696	229.6 m	F1	-	-
GS670B	227.0 m	F1	-	-
GS670A	227.0 m	F1	2.45	-1.32
GS538	213.8 m	F1	-	-
GS454	205.4 m	F1	-	-
GS257	185.7 m	F1	0.63	-3.00
GS201B	180.1 m	F1	-	-
GS201A	180.1 m	F1	-1.97	-4.40
GS130	173.0 m	F1	-2.06	-4.99
GS107C	170.7 m	F1	0.18	-2.93
GS107B	170.7 m	F1	-	-
GS107A	170.7 m	F1	-	-
GS100	170.0 m	F1	-	-
GS80	168.0 m	F1	-	-
GS55	165.5 m	F1	-7.81	-5.86
GS23A	162.3 m	F1	-8.51	-5.11
GS06	160.6 m	F1	2.45	0.28

3- Genna Silana

LOCATION
Urzulei Supramonte
40°09'30.26"N
9°30'24.08"E

THICKNESS
456 m

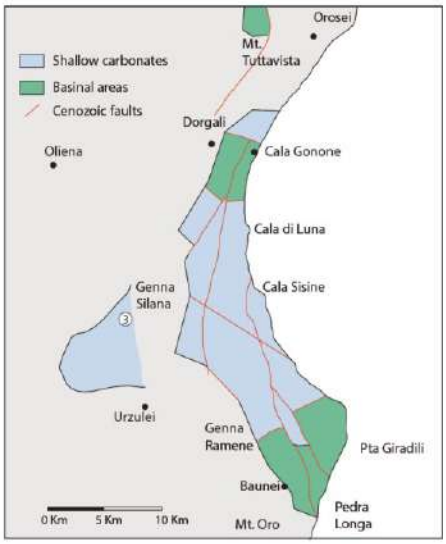

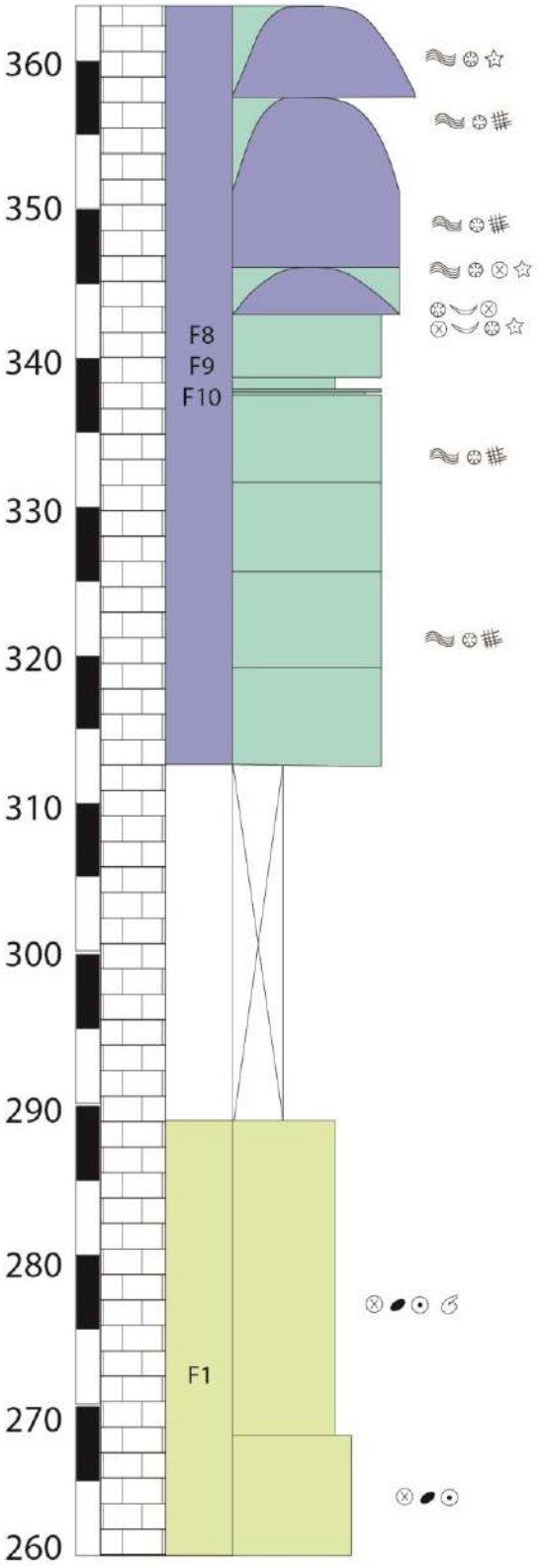

Sample	Stratigraphic height	Facies	$\delta^{13}C$	$\delta^{18}O$
GS1950	355.0 m	F10	-	-
GS1830	343.0 m	F10	-0.44	-5.23
GS1803	340.3 m	F9	-	-
GS1800	340.0 m	F9	-	-
GS1316	291.6 m	F1	-	-
GS1094	269.4 m	F1	-	-

3- Genna Silana

LOCATION
Urzulei Supramonte
40°09'30.26"N
9°30'24.08"E

THICKNESS
456 m

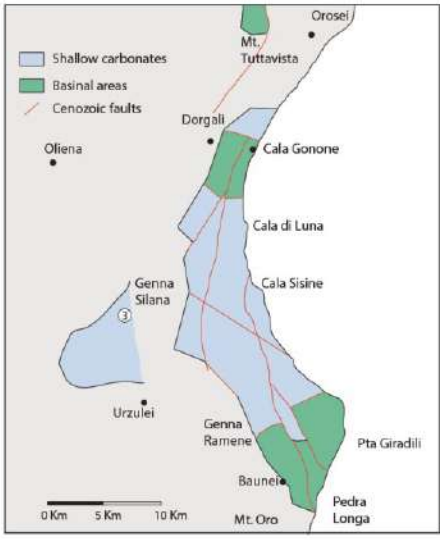

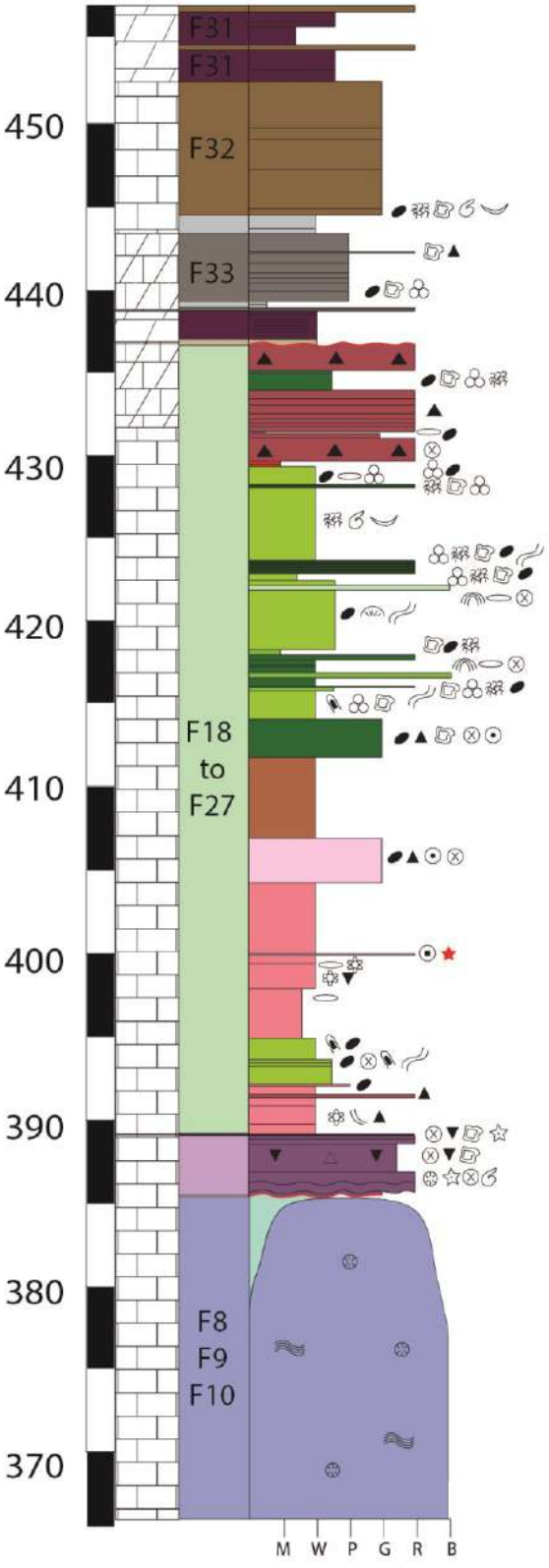

Sample	Stratigraphic height	Facies	$\delta^{13}C$	$\delta^{18}O$
GS2750	435.0 m	F18	1.42	-0.23
GS2739B	433.9 m	F18	-	-
GS2739A	433.9 m	F18	1.80	-0.10
GS2738B	433.8 m	F18	1.45	-1.40
GS2738	433.8 m	F18	-	-
GS2737	433.7 m	F18	2.04	-1.05
GS2736	433.6 m	F24	1.76	-1.80
GS2722	432.2 m	F24	-	-
GS2674	427.4 m	F27	2.49	-0.93
GS2670	427.0 m	F27	0.10	-0.83
GS2668	426.8 m	F24	-	-
GS2622	422.2 m	F26	2.39	-0.51
GS2612	421.2 m	F22	1.77	-2.22
GS2608	420.8 m	F26	-	-
GS2602	420.2 m	F26	-	-
GS2599	419.9 m	F24	-	-
GS2570	417.0 m	F26	-	-
GS2533	413.3 m	F19	2.35	-0.78
GS2489	408.9 m	F20	-	-
GS2444	404.4 m	F20	0.44	-0.18
GS2419	401.9 m	F21	-	-
GS2405	400.5 m	F21	-0.48	-0.80
GS2390	399.0 m	F24	1.38	-1.43
GS2377	397.7 m	F24	-	-
GS2362	396.2 m	F25	1.30	-1.60
GS2361	396.1 m	F21	1.25	-0.76
GS2354	395.4 m	F21	0.27	-1.11
GS2332	393.2 m	F21	-	-
GS2328	392.8 m	F17	-	-
GS2325	392.5 m	F17	-2.54	-2.82
GS2309	390.9 m	F17	-	-
GS2296A	389.6 m	F17	1.24	-2.49
GS2296B	389.6 m	F17	-	-
GS2294	389.4 m	F10	1.41	-1.51
GS2120	372.0 m	F10	0.72	-3.25
GS2090	369.0 m	F10	-	-

Sample	Stratigraphic height	Facies	$\delta^{13}C$	$\delta^{18}O$
GS3020	462.0 m	F32	2.78	0.39
GS2990	459.0 m	F32	-	-
GS2986	458.6 m	F32	2.96	0.07
GS2899	449.9 m	F32	1.61	-2.10
GS2874	447.4 m	F32	-	-
GS2866	446.6 m	F32	0.02	-2.74
GS2833	443.3 m	F33	-	-
GS2831	443.1 m	F33	2.22	-3.48
GS2820	442.0 m	F31	2.97	3.55
GS2810	441.0 m	F30	2.38	-1.30
GS2793	439.3 m	F18	-	-
GS2760	436.0 m	F18	0.21	-1.83
GS2755	435.5 m	F18	-	-
GS2754	435.4 m	F18	-	-

4- Ghispali

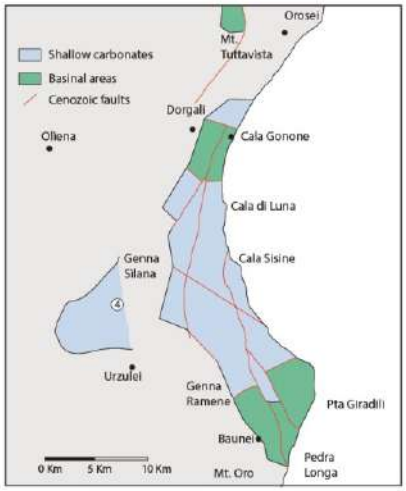

LOCATION
Urzulei Supramonte
40°06'45.77"N
9°30'24.19"E

THICKNESS
46 m

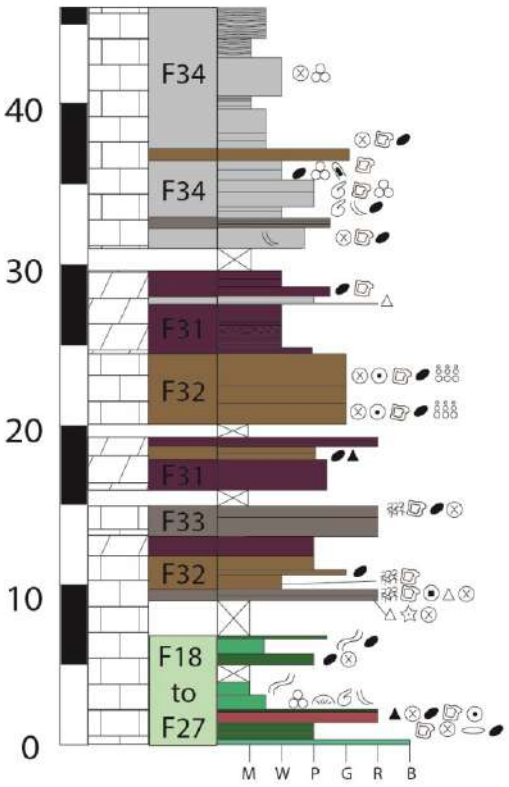

Sample	Stratigraphic height	Facies	$\delta^{13}C$	$\delta^{18}O$
G450	45.0 m	F34	-	-
G443	44.3 m	F34	-	-
G436	43.6 m	F34	-	-
G432	43.2 m	F34	-	-
G417	41.7 m	F34	-	-
G402	40.2 m	F34	-	-
G392	39.2 m	F34	-	-
G378	37.8 m	F32	-	-
G370	37.0 m	F34	-	-
G361	36.1 m	F34	-	-
G359	35.9 m	F34	-	-
G340	34.0 m	F34	-	-
G332	33.2 m	F33	-	-
G318	31.8 m	F34	-	-
G297	29.7 m	F31	-	-
G290	29.0 m	F31	-	-
G285	28.5 m	F31	-	-
G280	28.0 m	F34	-	-
G275	27.5 m	F31	-	-
G269	26.9 m	F31	-	-
G255	25.5 m	F31	-	-
G245	24.5 m	F31	-	-
G243	24.3 m	F32	-	-
G209	20.9 m	F32	-	-
G186B	18.6 m	F32	2.87	1.56
G186A	18.6 m	F32	2.03	-1.74
G183	18.3 m	F31	-	-
G179	17.9 m	F31	-	-
G170	17.0 m	F32	2.87	1.78
G161	16.1 m	F31	-	-
G147	14.7 m	F33	-	-
G133	13.3 m	F32	-	-
G124	12.4 m	F32	-	-
G107	10.7 m	F32	-	-
G101	10.1 m	F32	-	-
G93	9.3 m	F33	-	-
G91	9.1 m	F33	-	-
G71	7.1 m	F26	-	-
G67	6.7 m	F23	-	-
G55	5.5 m	F26	-	-
G30	3.0 m	F23	-	-
G21	2.1 m	F27	-	-
G19	1.9 m	F18	-	-
G10	1.0 m	F26	-	-
G02	0.2 m	F23	-	-

5-Cave

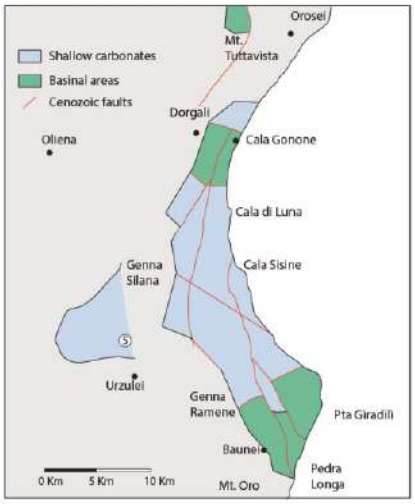

LOCATION
Urzulei Supramonte
40°06'11.43"N
9°30'34.79"E

THICKNESS
27 m

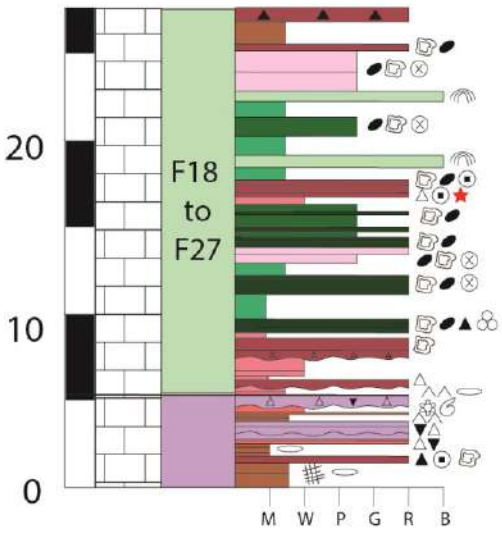

Sample	Stratigraphic height	Facies	$\delta^{13}C$	$\delta^{18}O$
UQ276	27.6 m	F18	-	-
UQ265	26.5 m	F19	-	-
UQ254	25.4 m	F18	-	-
UQ233	23.3 m	F20	-	-
UQ220	22.0 m	F23	-	-
UQ210	21.0 m	F26	-	-
UQ202	20.2 m	F25	-	-
UQ191	19.1 m	F22	-	-
UQ182	18.2 m	F25	-	-
UQ174	17.4 m	F26	-	-
UQ169	16.9 m	F26	-	-
UQ166	16.6 m	F25	-	-
UQ133	13.3 m	F25	-	-
UQ122	12.2 m	F27	-	-
UQ109	10.9 m	F25	-	-
UQ95	9.5 m	F26	-	-
UQ92	9.2 m	F27	-	-
UQ77	7.7 m	F18	-	-
UQ67	6.7 m	F21	-	-
UQ64	6.4 m	F21	-	-
UQ58	5.8 m	F18	-	-
UQ44	4.4 m	F16	-	-
UQ42	4.2 m	F21	-	-
UQ34	3.4 m	F16	-	-
UQ31	3.1 m	F16	-	-
UQ22	2.2 m	F19	-	-
UQ15	1.5 m	F18	-	-

6-Punta Mureddu

LOCATION
Punta Mureddu
40°09'54.66"N
9°34'49.46"E

THICKNESS
25 m

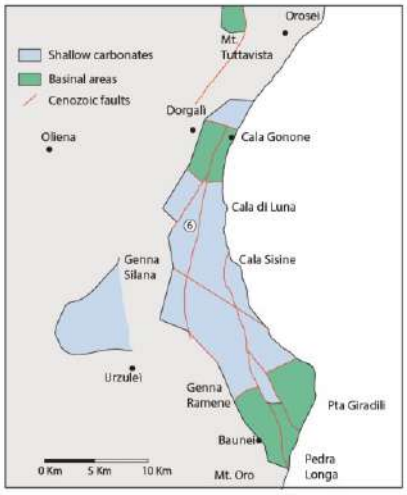

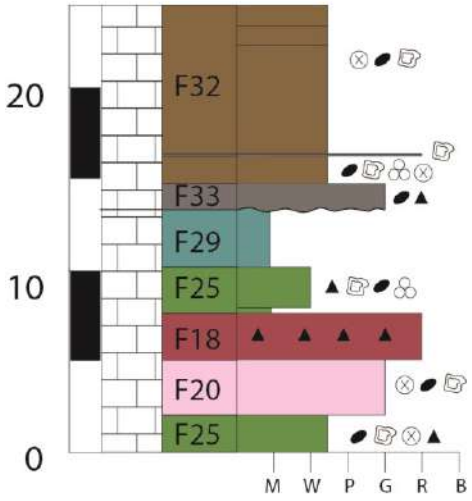

Sample	Stratigraphic height	Facies	$\delta^{13}C$	$\delta^{18}O$
BA2	21.0 m	F32	2.39	-0.69
BA3	16.0 m	F32	-	-
BA4	15.2 m	F32	-	-
BA5	14.3 m	F33	-	-
BA6	13.8 m	F33	-	-
BA7	12.1 m	F29	-	-
BA8	9.7 m	F25	-	-
BA1	8.5 m	F25	1.45	0.17
BA9	6.3 m	F18	1.75	0.06
BA10	4.1 m	F20	-	-
BA11	1.7 m	F25	2.31	-1.35

7-Genna Scalas

LOCATION
Baunei Supramonte
40°05'11.10"N
9°36'25.10"E

THICKNESS
82 m

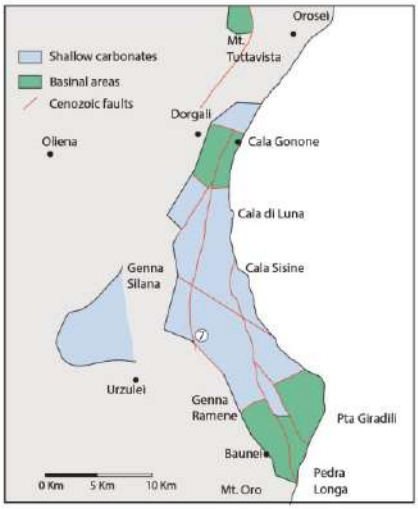

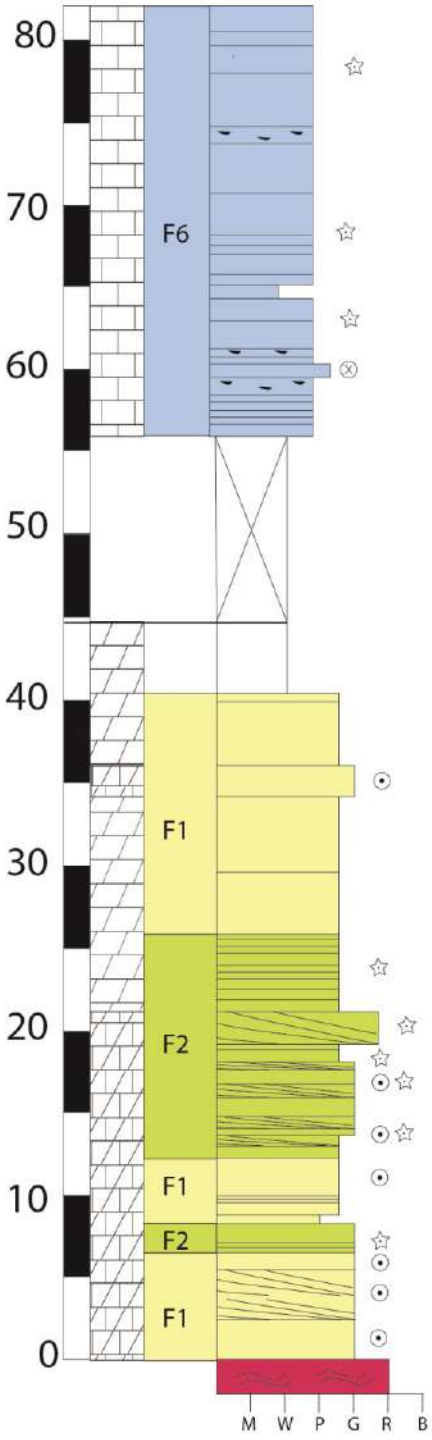

Sample	Stratigraphic height	Facies	$\delta^{13}C$	$\delta^{18}O$
KS241	78.1 m	F6	-	-
KS220	76.0 m	F6	-	-
KS210	75.0 m	F6	-	-
KS180	72.0 m	F6	-	-
KS167	70.7 m	F6	-	-
KS138	69.8 m	F6	-	-
KS115	67.5 m	F6	-	-
KS85	64.5 m	F6	-	-
KS70	63.0 m	F6	-	-
KS58	61.8 m	F6	-	-
KS45	60.5 m	F6	-	-
KS22	58.2 m	F6	-	-
KS15	57.5 m	F6	-	-
KS03	56.3 m	F6	-	-
SK426	42.6 m	DOL	-	-
SK390	39.0 m	DOL	-2.01	-5.17
SK380	38.0 m	F1	-	-
SK355	35.5 m	F1	-	-
SK285	28.5 m	F1	-	-
SK270	27.0 m	F1	-	-
SK245	24.5 m	F2	-	-
SK200	20.0 m	F1	2.54	0.53
SK182	18.2 m	F2	-	-
SK177	17.7 m	F2	-	-
SK133	13.3 m	F2	-	-
SK90	9.0 m	F1	-	-
SK82	8.2 m	F1	-	-
SK76	7.6 m	F2	1.43	0.02
SK55	5.5 m	F1	-	-
SK03	0.3 m	F1	0.40	-0.17

8-Genna Ramene

LOCATION
Baunei Supramonte
40°03'39.27"N
9°38'05.28"E

THICKNESS
77 m

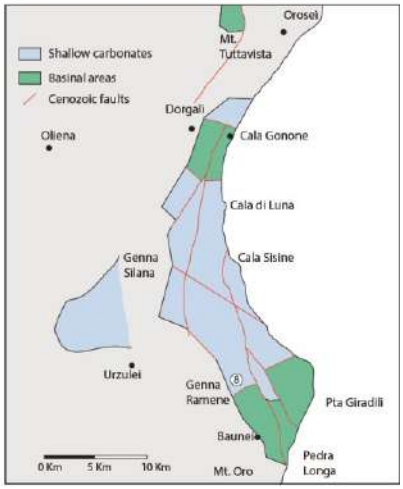

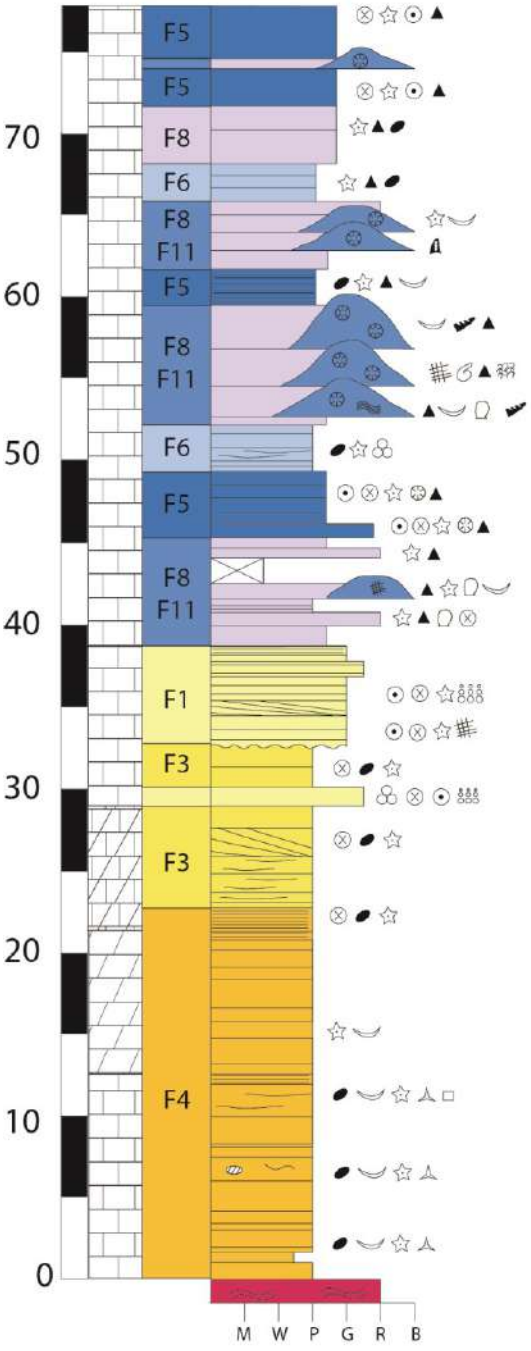

Sample	Stratigraphic height	Facies	$\delta^{13}C$	$\delta^{18}O$
R332	33.2 m	F3	-	-
R324	32.4 m	F3	-	-
R317	31.7 m	F3	-	-
R313	31.3 m	F3	-	-
R312	31.2 m	F1	0.77	-2.25
R295	29.5 m	F3	-	-
R281	28.1 m	F3	-	-
R267	26.7 m	F3	-	-
R257	25.7 m	F3	-	-
R253	25.3 m	F3	-	-
R244	24.4 m	F3	-	-
R230	23.0 m	F3	-	-
R225	22.5 m	F3	0.60	-2.64
R216	21.6 m	F4	1.40	-1.21
R209	20.9 m	F4	-	-
R205	20.5 m	F4	-3.69	-5.65
R194	19.4 m	F4	-	-
R184	18.4 m	F4	-	-
R165	16.5 m	F4	-	-
R155	15.5 m	DOL	3.03	1.16
R142	14.2 m	F4	2.40	-0.06
R133	13.3 m	F4	-	-
R122	12.2 m	F4	-	-
R121	12.1 m	F4	-	-
R112	11.2 m	F4	2.58	2.07
R108	10.8 m	F4	-	-
R104	10.4 m	F4	-	-
R96	9.6 m	F4	-	-
R86	8.6 m	F4	1.69	-0.68
R78	7.8 m	F4	-	-
R72	7.2 m	F4	-	-
R65	6.5 m	F4	-	-
R58	5.8 m	F4	-	-
R45	4.5 m	F4	-	-
R40	4.0 m	F4	-	-
R34	3.4 m	F4	-	-
R24	2.4 m	F4	-	-
R17	1.7 m	F4	-	-
R11	1.1 m	F4	0.91	-0.16
R00	0.0 m	F4	1.31	-0.26

Sample	Stratigraphic height	Facies	$\delta^{13}C$	$\delta^{18}O$
R740	74.0 m	F5	-0.11	-3.36
R716	71.6 m	F11	1.97	-2.04
R710	71.0 m	F8	-1.25	-3.75
R698	69.8 m	F8		
R685	68.5 m	F6	1.41	-2.03
R645	64.5 m	F8	1.63	-0.62
R640	64.0 m	F8	-	-
R621	62.1 m	F8	-	-
R615	61.5 m	F11	0.31	-3.09
R603	60.3 m	F5	0.41	-2.28
R589	58.9 m	F5	-	-
R577	57.7 m	F8	-	-
R572	57.2 m	F8	1.29	-2.80
R566	56.6 m	F8	1.12	-2.90
R548B	54.8 m	F11	-	-
R548A	54.8 m	F11	1.31	-2.23
R546	56.0 m	F8	1.58	-2.38
R540	54.0 m	F8	0.91	-3.55
R527	52.7 m	F11	0.26	-2.84
R523	52.3 m	F11	0.97	-2.48
R515B	51.5 m	F11	-	-
R515A	51.5 m	F11	0.85	-3.94
R508	50.8 m	F11	0.82	-3.37
R501	50.1 m	F6	2.25	-1.20
R490	49.0 m	F6	1.98	-2.62
R479	47.9 m	F6	2.21	-1.55
R473	47.3 m	F5	1.29	-3.61
R466	46.6 m	F5	0.53	-2.25
R460	46.0 m	F5	-	-
R451	45.1 m	F5	0.16	-3.51
R445	44.5 m	F5	0.52	-4.10
R437	43.7 m	F8	-0.47	-3.62
R428	42.8 m	F8	-0.78	-3.16
R406	40.6 m	F8	-0.71	-3.85
R398	39.8 m	F8	-0.62	-3.90
R393	39.3 m	F8		
R380	38.0 m	F8	0.30	-2.56
R373	37.3 m	F1	-	-
R367	36.7 m	F1	-0.70	-3.10
R364	36.4 m	F1	-	-
R355	35.5 m	F1	-	-
R350	35.0 m	F1	-	-
R341	34.1 m	F1	-	-

9-Baunei Supramonte

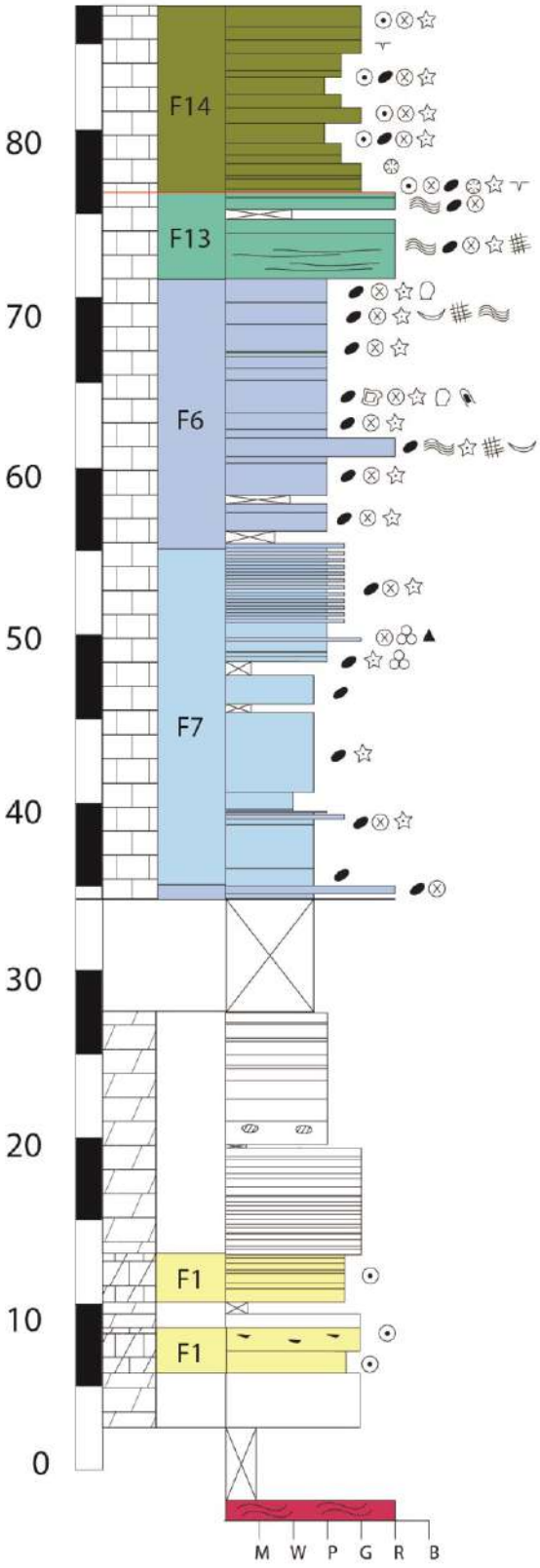

LOCATION
Baunei Supramonte
40°01'34.93"N
9°40'20.31"E

THICKNESS
86 m

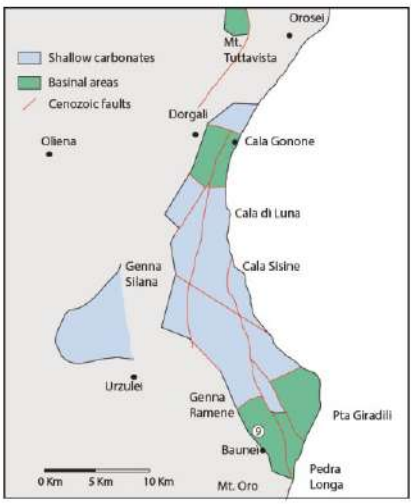

Sample	Stratigraphic height	Facies	$\delta^{13}C$	$\delta^{18}O$
SB69	61.9 m	F6	-	-
SB60	61.0 m	F5	-	-
SB55	60.5 m	F5	-	-
SB44	59.4 m	F5	-	-
SB37	58.7 m	F5	-	-
SB18	56.8 m	F5	-	-
SB09	55.9 m	F8	-	-
SB.M	54.1 m	F7	-	-
SB.L	51.5 m	F7	-	-
SB.I	49.8 m	F7	-	-
SB.H	49.0 m	F7	-	-
SB.G	48.1 m	F7	-	-
SB.F	44.3 m	F7	-	-
SB.C	38.8 m	F7	-	-
SB.B	34.5 m	F6	-	-
SB.A	34.0 m	F6	-	-
B22	25.8 m	DOL	-	-
B31	24.9 m	DOL	-	-
B45	23.5 m	DOL	-	-
B70	21.0 m	DOL	-	-
B80	20.0 m	DOL	-	-
B98	18.2 m	DOL	-	-
B113	16.7 m	DOL		
B120	16.0 m	DOL	-	-
B135	14.5 m	DOL	-	-
B144	13.6 m	DOL	-	-
B163	11.7 m	F1	-	-
B180	10.0 m	DOL	-	-
B198	8.2 m	F1	-	-
B205	7.5 m	F1	-	-
B218	6.2 m	DOL	-	-
B243	2.5 m	DOL	-	-

Sample	Stratigraphic height	Facies	$\delta^{13}C$	$\delta^{18}O$
SB305	85.5 m	F14	-	-
SB295	84.5 m	F14	-	-
SB289	83.9 m	F14	-	-
SB280	83.0 m	F14	-	-
SB261	81.1 m	F14	-	-
SB258	80.8 m	F14	-	-
SB250	80.0 m	F14	-	-
SB241	79.1 m	F14	-	-
SB225	77.5 m	F14	-	-
SB220	77.0 m	F14	-	-
SB217	76.2 m	F14	-	-
SB209	75.9 m	F14	-	-
SB203	75.3 m	F14	-	-
SB193	74.3 m	F13	-	-
SB181	73.1 m	F13	-	-
SB170	72.0 m	F13	-	-
SB156	70.6 m	F13	-	-
SB145	69.5 m	F6	-	-
SB132	68.2 m	F6	-	-
SB117	66.7 m	F6	-	-
SB106	65.6 m	F6	-	-
SB104	65.4 m	F6	-	-
SB96	64.6 m	F6	-	-
SB82	63.2 m	F6	-	-
SB72	62.2 m	F6	-	-

10-Franciscu 1

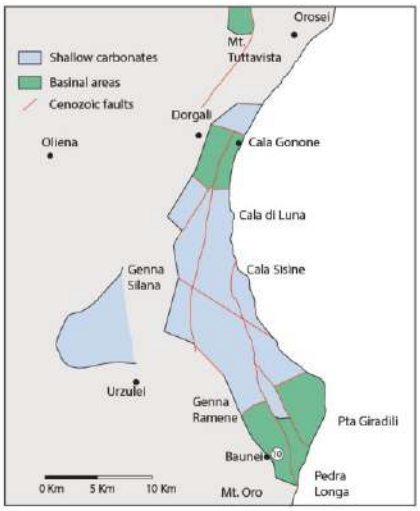

LOCATION
Baunei Supramonte
40°01'32.61"N
9°40'35.15"E

THICKNESS
13 m

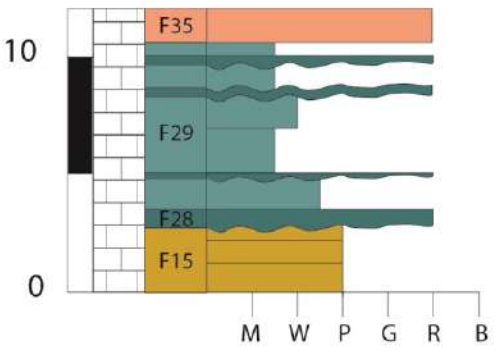

Sample	Stratigraphic height	Facies	$\delta^{13}C$	$\delta^{18}O$
1.120	12.0 m	F35	-	-
1.112	11.2 m	F29	-	-
1.105	10.5 m	F28	-	-
1.95	9.5 m	F29	-	-
1.91	9.1 m	F28	-	-
1.78	7.8 m	F29	-	-
1.70	7.0 m	F29	-	-
1.56	5.6 m	F29	-	-
1.51	5.1 m	F28	-	-
1.46	4.6 m	F29	-	-
1.37	3.7 m	F28	-	-
1.35	3.5 m	F28	-	-
1.33	3.3 m	F28	-	-
1.30	3.0 m	F28	-	-
1.23	2.3 m	F15	-	-
1.12	1.2 m	F15	-	-

10-Franciscu 2

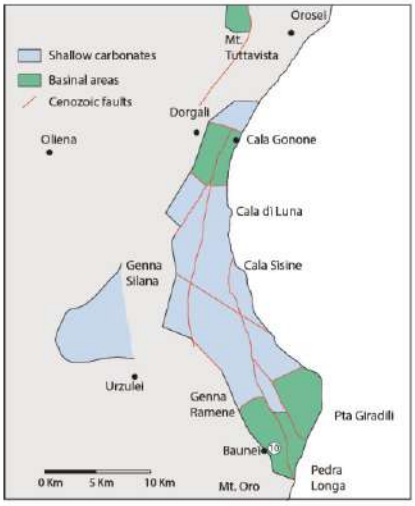

LOCATION
Baunei Supramonte
40°01'31.79"N
9°40'35.53"E

THICKNESS
18 m

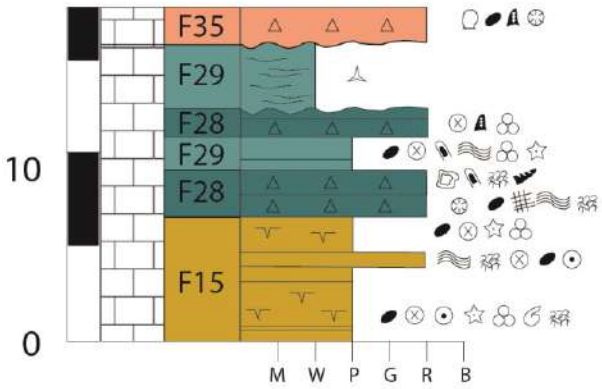

Sample	Stratigraphic height	Facies	$\delta^{13}C$	$\delta^{18}O$
F172	17.2 m	F35	0.25	-3.20
F165	16.5 m	F35	1.27	-1.96
F163	16.3m	F35	0.98	-0.34
F160	16.0 m	F29	0.92	-1.36
F156	15.6 m	F29	-	-
F147	14.7 m	F29	2.38	0.43
F140	14.0 m	F29	2.17	-0.57
F131	13.1 m	F29	2.10	0.03
F126	12.6 m	F29	1.99	0.03
F125	12.5 m	F28	2.06	-0.24
F120	12.0 m	F28	-0.93	-2.00
F111	11.1 m	F29	-0.66	-2.81
F98	9.8 m	F29	-0.40	-3.55
F91	9.1 m	F28	0.67	-2.41
F82	8.2 m	F28	-	-
F77	7.7 m	F28	0.60	-1.90
F62	6.2 m	F15	1.23	-1.09
F50	5.0 m	F15	0.74	-2.02
F43	4.3 m	F15	-0.89	-3.64
F38	3.8 m	F15	-1.49	-4.02
F30	3.0 m	F15	-0.78	-3.25
F15	1.5 m	F15	-0.53	-3.37
F08	0.8 m	F15	-0.58	-2.82
F05	0.5 m	F15	-0.68	-3.75

10-Franciscu 3

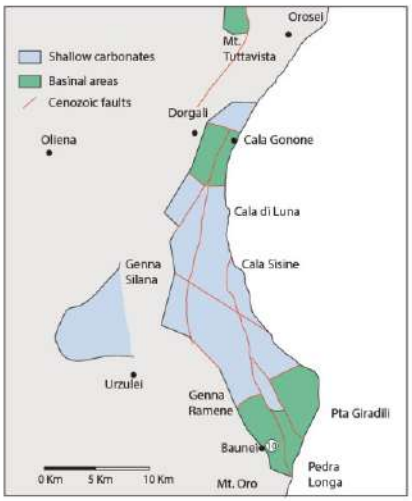

LOCATION
Baunei Supramonte
40°01'26.98"N
9°40'39.37"E

THICKNESS
10 m

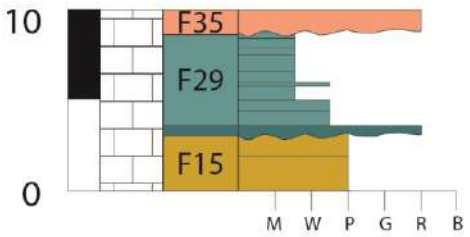

Sample	Stratigraphic height	Facies	$\delta^{13}C$	$\delta^{18}O$
2.99	9.9 m	F35	-	-
2.89	8.9 m	F35	-	-
2.86	8.6 m	F29	-	-
2.79	7.9 m	F29	-	-
2.70	7.0 m	F29	-	-
2.60	6.0 m	F29	-	-
2.58	5.8 m	F29	-	-
2.53	5.3 m	F29	-	-
2.49	4.9 m	F29	-	-
2.44	4.4 m	F29	-	-
2.33	3.3 m	F28	-	-
2.31	3.1 m	F15	-	-
2.23	2.3 m	F15	-	-
2.18	1.8 m	F15	-	-
2.03	0.3 m	F15	-	-

11-Punnaci 1

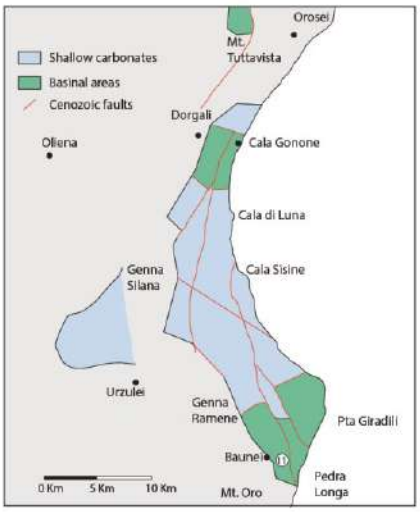

LOCATION
Baunei Supramonte
40°01'25.29"N
9°40'41.32"E

THICKNESS
16 m

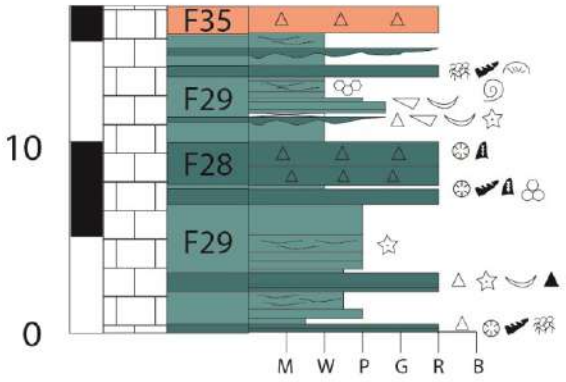

Sample	Stratigraphic height	Facies	$\delta^{13}C$	$\delta^{18}O$
3.160	16.0 m	F35	-	-
3.153	15.3 m	F29	-	-
3.147	14.7 m	F28	-	-
3.146	14.6 m	F28	-	-
3.143	14.3 m	F28	-	-
3.140	14.0 m	F29	-	-
3.134	13.4 m	F28	-	-
3.130	13.0 m	F28	-	-
3.126	12.6 m	F29	-	-
3.123	12.3 m	F29	-	-
3.121	12.1 m	F29	-	-
3.117	11.7 m	F29	-	-
3.113	11.3 m	F28	-	-
3.105	10.5 m	F29	-	-
3.99	9.9 m	F28	-	-
3.86	8.6 m	F28	-	-
3.76	7.6 m	F28	-	-
3.73	7.3 m	F28	-	-
3.61	6.1 m	F29	-	-
3.47	4.7 m	F29	-	-
3.42	4.2 m	F29	-	-
3.37	3.7 m	F29	-	-
3.33	3.3 m	F29	-	-
3.30	3.0 m	F28	-	-
3.23	2.3 m	F28	-	-
3.18	1.8 m	F29	-	-
3.07	0.7 m	F29	-	-
3.02	0.2 m	F28	-	-

12-Mt. Oro

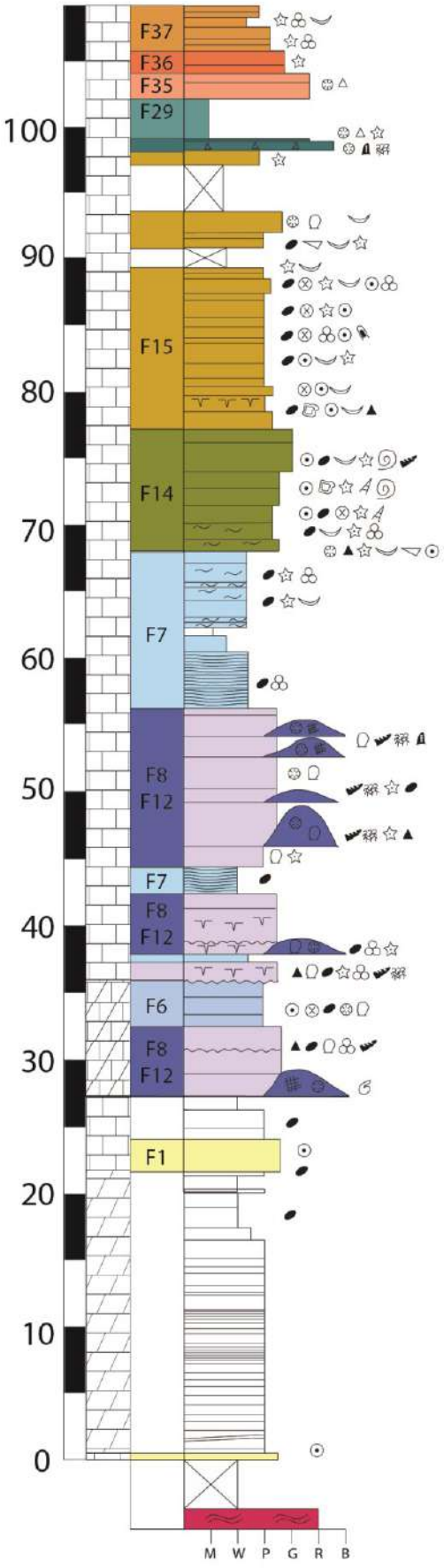

LOCATION
Baunei Supramonte
40°01'01.78"N
9°41'00.16"E

THICKNESS
108 m

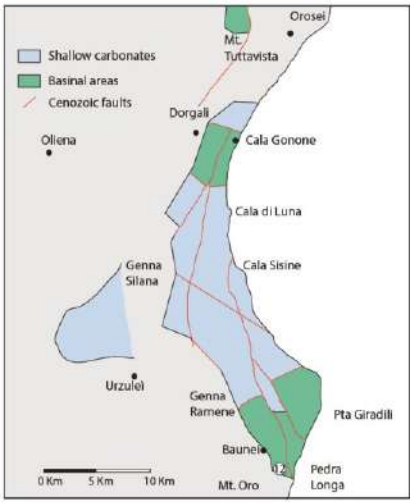

Sample	Stratigraphic height	Facies	$\delta^{13}C$	$\delta^{18}O$
O502	50.2 m	F12	-1.70	-3.80
O490	49.0 m	F12	-1.30	-3.31
O481	48.1 m	F8	-	-
O463	46.3 m	F8	-1.08	-3.29
O454	45.4 m	F8	-1.37	-3.49
O434	43.4 m	F8	-0.43	-2.09
O431	43.1 m	F8	2.54	-0.56
O421	42.1 m	F8	0.84	-1.95
O388	38.8 m	F8	0.27	-1.22
O381	38.1 m	F8	1.48	-1.14
O377	37.7 m	F7	1.58	-0.60
O363	36.3 m	F8	0.68	-1.62
O353	35.3 m	F8	0.72	-0.71
O340	34.0 m	F8	1.43	-1.08
O332	33.2 m	F8	1.37	-1.13
O312	31.2 m	F8	1.76	-0.99
O308	30.8 m	F8	-0.12	-2.79
O281	28.1 m	F12	0.54	-2.80
O256	25.6 m	F8	-	-
O247	24.7 m	F8	-3.25	-5.83
O238	23.8 m	F8	-3.44	-5.96
O229	22.9 m	F8	-5.80	-5.73
O201	20.1 m	DOL	-3.21	-6.27
O182	18.2 m	DOL	2.84	1.08
O173	17.3 m	DOL	0.09	-0.92
O164	16.4 m	DOL	1.97	0.96
O152	15.2 m	DOL	2.08	0.83
O144	14.4 m	DOL	2.06	0.45
O130	13.0 m	DOL	1.68	0.52
O125	12.5 m	DOL	-8.75	-3.97
O112	11.2 m	DOL	1.70	0.99
O102	10.2 m	DOL	1.62	0.76
O94	9.4 m	DOL	1.22	-0.70
O77	7.7 m	DOL	-2.96	-6.02
O72	7.2 m	DOL	1.05	0.38
O55	5.5 m	DOL	1.37	0.64
O48	4.8 m	DOL	1.34	-0.09
O41	4.1 m	DOL	-7.47	-4.05
O32	3.2 m	DOL	-	-
O29	2.9 m	DOL	1.44	0.02
O16	0.6 m	DOL	1.08	1.11
OO4	0.4 m	F1	-9.29	-4.53

Sample	Stratigraphic height	Facies	$\delta^{13}C$	$\delta^{18}O$
V1	106.3 m	F37	-0.13	-0.32
V2	106.0 m	F37	2.00	1.18
V3	105.5 m	F37	2.40	1.52
V4	105.0 m	F37	1.11	-0.59
V5	104.5 m	F36	1.49	-2.45
V6	104.0 m	F36	0.80	-2.35
V7	100.0 m	F29	-	-
V8	98.5 m	F29	1.65	-0.52
V9	98.1 m	F28	1.90	-0.19
MO.A	98.0 m	F28	-0.25	0.20
V10	97.5 m	F15	1.32	-0.20
V11	97.0 m	F15	1.67	0.22
O1145	92.5 m	F15	-	-
O1133	91.3 m	F15	-	-
O1125	90.5 m	F15	1.50	0.29
O1109	88.9 m	F15	-	-
O1101	88.1 m	F15	-	-
O1092	87.2 m	F15	0.88	-0.55
O1084	86.4 m	F15	1.23	-0.82
O1071	85.1 m	F15	-	-
O1056	83.6 m	F15	0.22	-1.76
O1046	82.6 m	F15	1.71	-0.44
O1037	81.7 m	F15	-	-
O1025	80.5 m	F15	-	-
O1020	80.0 m	F15	-	-
O1013	79.3 m	F15	2.18	0.24
O1001	78.1 m	F14	-	-
O988	76.8 m	F14	-	-
O973	75.3 m	F14	-	-
O958	73.8 m	F14	2.23	0.07
O951	73.1 m	F14	-	-
O933	71.3 m	F14	2.23	0.88
O924	70.4 m	F14	-	-
O918	69.8 m	F14	-	-
O906	68.6 m	F14	2.24	0.41
O892	67.2 m	F7	-	-
O888	66.8 m	F7	2.05	1.19
O879	65.9 m	F7	-	-
O870	65.0 m	F7	-	-
O860	64.0 m	F7	-	-
O849	62.9 m	F7	2.22	0.43
O592	59.2 m	F7	2.59	-0.10
O585	58.5 m	F7	2.38	-0.20
O575	57.5 m	F7	1.63	-0.40
O568	56.8 m	F7	1.76	-0.49
O560	56.0 m	F8	0.12	-2.75
O550	55.0 m	F12	-0.50	-4.19
O524	52.4 m	F12	-1.43	-2.72
O516	51.6 m	F12	-1.58	-3.58